Design and synthesis of new insertion electrode materials for Li-ion and Na-ion batteries identified via the Bond Valence Energy Landscape approach

eman ta zabal zazu

Universidad del País Vasco   Euskal Herriko Unibertsitatea

A Thesis Submitted in Fulfillment of the Requirements for the degree of Doctor in Philosophy in Physics

University of the Basque Country
CIC energiGUNE

Author
Agnieszka Wizner

Supervised by
Dr. Montse Casas Cabanas
Dr. Marine Reynaud

Tutor
Dr. Josu Mirena Igartua Aldamiz

August 2022

Dla Taty.

Acknowledgements

Sona, Roshan, Yarik and Marcus for all the beautiful moments we shared together. Thanks to my desk mate, Nick for our daily chats all over these five years, it has been a great pleasure to share the desk with you, even if you tried to bury it under your tones of papers. Big thanks to my soulmate, María Usoltseva, I do not think I would be finishing my PhD without your help. Thank you for always being there for me.

Big thanks to Xue and Marco for all these wonderful weekends in Toulouse, snowboarding, rowing, climbing and just sharing beautiful moments together!

Oczywiście nie może też zabraknąć podziękowań dla rodziny i przyjaciół z Polski, którzy mimo już ośmio letniej rozłąki są zawsze przy mnie i mnie wspierają. Dla Gosi Cz. która by poleciała za mną i na koniec świata (szczególnie jeśli by było dobre wino i kalmary) i której przyjaźń jest jedną z najpiękniejszych rzeczy, która mnie spotkała. Dla Gosi R. z którą dzielnie razem zmagałyśmy się z doktoratami i dzieliłyśmy jego trudy. Tobie już się udało, teraz moja kolej! Dla Piotra za ogromne wsparcie przez te wszystkie lata, za „cokolwiek” i „aczkolwiek”. Dzięki, Ty! Dla Zosi za znalezienie zawsze chwili, nawet w ostatnim momencie, by móc się zobaczyć przy każdym pobycie. I dla Kuby za wszystkie chwile w górach, skałach, nad morzem, jeziorami, rzekami i we wszystkich tych pięknych miejscach. Dziękuję, że jesteście.

Artur, dziękuję za motywujące słowa i biegówki dla odwrócenia uwagi od stresujących chwil. Mamo, dziękuję Ci za Twoje wsparcie na każdym kroku, wiarę we mnie i dodawanie sił codziennie.

Thank you. Dziękuję.

Abstract

Batteries are considered a key enabler for the decarbonization of our society. Li-ion batteries are now dominating the market for portable devices, hybrid and electric vehicles due to their light weight and outstanding energy density and power performance. However, the increasing demand for lithium and the unstable global context result in growing concerns about its availability and price, which is why Na-ion batteries have generated much interest in recent years. The abundance and low cost of sodium make it an appealing alternative to lithium. Additionally, apart from the high abundance, sodium is well distributed all over Earth, which considerably reduces the economic and geopolitical impact.

The cathode material is the key battery component, since it has the main influence on the eventual performance of the battery and its cost. The selected cathode material should provide fast insertion/extraction of the mobile cation and stable reversible capacity. Additionally, the ideal cathode material would possess a high specific capacity and deliver a high potential. This thesis targets to identify new cathode materials which can be used for rechargeable Li-ion and Na-ion batteries. To do so, the strategy employed in this work consists in using the Bond Valence Energy Landscape (BVEL) method to select structures from materials databases that present adequate migration pathways for Na and/or Li. In this work, two families of compounds were selected from the ICSD database and were experimentally validated: the CUBICON nitridophosphates $A^I_3M^{III}P_3O_9N$ and $A^I_2M^{II}_2P_3O_9N$, and the garnet fluorides, $Na_3Li_3M^{III}F_{12}$.

The synthesis protocols for synthesizing $A^I_3M^{III}P_3O_9N$ where A=Na/Li and M=V, $A^I_2M^{II}_2P_3O_9N$ where A = Na/Li, M= Fe, Co, Mn and $Na_3Li_3M^{III}F_{12}$ where M= V, Ti, Fe were established; and their exhaustive characterization and implementation in practical electrochemical cells to validate their performances as potential cathode materials was carried out. Our results show that the electrochemical performance of this family of materials varies with the chemical composition.

 The most remarkable results were obtained for the CUBICON $Na_3VP_3O_9N$, whose working potential was found to be very high, 4.0 V *vs.* Na^+/Na^0 and 4.1 V *vs.* Li^+/Li^0, being the highest operation voltage for the V^{IV}/V^{III} redox couple together with $Na_7V_3(P_2O_7)_4$. Additionally, we discovered a new family of alkali manganese

nitridophosphates $A_{1.1}Mn_{2.9}P_3O_8N_2$ (A = Na/Li) crystallizing in an orthorhombic structure which is, to the best of our knowledge, the first report of a direct synthesis of a lithium metal nitridophosphate.

On the other hand, the electrochemical response of the three garnet materials $Na_3Li_3M^{III}F_{12}$ (M= V, Ti, Fe) is probably hindered by the intrinsically poor electronic conductivity of fluoride compounds. However, the chemical oxidation of the titanium analogue lead to the formation of an orthorhombic phase of $Na_3Li(TiF_6)_2$ which reversibily accomodates one Li^+ at an average voltage of 3.1 V $vs.$ Li^+/Li^0, being the highest working voltage of the $Ti^{III/IV}$ redox couple.

Finally, pursuing the exploration of new fluoride compounds with the microwave-assisted solvothermal route, three vanadium fluorides were stabilized depending on the reaction conditions, with particular interest for the HTB-type $VF_3 \cdot 0.33H_2O$ phase which is reported for the first time. Although their operative voltage centered around 2 V $vs.$ Li^+/Li^0 prevent their real application as electrode materials, these compounds deliver a reversible capacity of >200 mAh.g^{-1} combining intercalation and conversion reactions.

Overall, the results presented in this thesis demonstrate that N- and F- based compounds still offer a huge chemical space that should be further explored to discover new attractive electrode materials.

Resumen

Las baterías se consideran un elemento clave para la descarbonización de nuestra sociedad. Las baterías de litio-ion dominan actualmente el mercado de los dispositivos portátiles y de los vehículos híbridos y eléctricos gracias a su ligereza y a su extraordinaria densidad y rendimiento energéticos. Sin embargo, la creciente demanda de litio y el inestable contexto mundial hacen que aumente la preocupación por su disponibilidad y precio, por lo que las baterías de sodio-ion han generado mucho interés en los últimos años. La abundancia y el bajo coste del sodio lo convierten en una atractiva alternativa al litio. Además, aparte de su gran abundancia, el sodio está bien distribuido por toda la Tierra, lo que reduce considerablemente el impacto económico y geopolítico.

El material del cátodo es el componente clave de la batería, ya que es el que más influye en el rendimiento final de la misma y en su coste. El material catódico seleccionado debe proporcionar una rápida inserción/extracción del catión móvil y una capacidad reversible estable. Además, el material de cátodo ideal debería poseer una alta capacidad específica y ofrecer un alto potencial. Se han desarrollado continuamente un gran número de químicas diferentes con numerosos análogos que pueden aplicarse con éxito tanto a las baterías de iones de litio como a las de iones de sodio. Sin embargo, el aumento constante de la demanda de mayor rendimiento y sostenibilidad exige el desarrollo de nuevos materiales mejorados.

El objetivo de esta tesis es identificar nuevos materiales catódicos que puedan ser utilizados en baterías recargables de Li-ion y Na-ion. El reto es encontrar nuevos compuestos que puedan mejorar tanto la capacidad específica como el voltaje. Por ello, esta tesis responde a las necesidades actuales de desarrollo de materiales avanzados para baterías.

En la búsqueda de nuevos materiales para electrodos pueden aplicarse dos enfoques diferentes. El primero es el diseño de nuevos materiales no reportados, y el segundo implica la revisión de estructuras ya conocidas con características compositivas y estructurales atractivas (o que requieran pequeñas modificaciones compositivas) necesarias para materiales de electrodos cuyo rendimiento electroquímico aún no ha sido evaluado. En nuestro trabajo, decidimos aplicar el segundo enfoque. El diseño de los nuevos materiales catódicos se basa en la modelización computacional y la metodología experimental. Para la parte computacional, la estrategia empleada en este trabajo consiste

en utilizar el método Bond Valence Energy Landscape (BVEL) para seleccionar estructuras de las bases de datos de materiales que presenten vías de migración adecuadas para el Na y/o el Li. Desarrollamos una metodología para examinar las bases de datos de materiales como Inorganic Crystal Structure Database (ICSD) o Crystallographic Open Database (COD) utilizando un enfoque de alto rendimiento basado en los cálculos del Bond Valence Energy Landscape (BVEL) para identificar los materiales que podrían ser buenos conductores iónicos de Li^+/Na^+ y que podrían ser aplicados como electrodos y electrolitos de estado sólido. Se analizaron 2736 entradas de compuestos de Na de la base de datos ICSD (versión 2013) utilizando estos cálculos BVEL. A través de esta lista de compuestos, se buscaron estructuras que presentaran una vía de migración 3D con energías de migración inferiores a 1.5 eV, que pudieran incluir un metal de transición 3d y con una masa molar relativamente baja para no penalizar la capacidad esperada.

Basado en esa estrategia, seleccionamos dos familias de compuestos, los nitrofosfatos CUBICON de fórmula general $Na_{3-n}M_{1+n}(PO_3)_3N$ y los fluoruros de granate de fórmula general $Na_3Li_3M^{III}F_{12}$, para los que se predijeron vías de migración 3D para el Na^+ con Em = 1.08 eV (M = Al, n=0), Em = 0.81 eV (M = Mg, n=1) y Em = 0.58 eV (M = V), respectivamente.

La primera familia, los nitrofosfatos CUBICON, tienen una capacidad teórica que varía desde ~65 $mAh.g^{-1}$ para la eliminación de un Na^+ del $Na_3M^{III}P_3O_9N$ hasta ~130 $mAh.g^{-1}$ para dos Na^+ eliminados del marco $Na_2M^{II}_2P_3O_9N$. En el caso del $Na_3M^{III}P_3O_9N$, la capacidad puede duplicarse utilizando dos pares redox del metal de transición.

Como primera elección para el trabajo experimental, se seleccionó el vanadio como metal de transición, ya que se espera que ofrezca un alto voltaje de trabajo y proporcione una gran capacidad gracias al uso de los pares redox $V^{III}/{IV}$ y V^{IV}/V, como en NASICON $Na_3V_2(PO_4)_3$. Luego, centrándonos en los metales 3d de bajo coste y abundantes en la tierra, se seleccionaron el hierro y el manganeso como metales de transición divalentes. Aunque es un elemento menos popular debido a su mayor coste y a la ética de la minería, la sustitución por cobalto suele tener un efecto beneficioso al elevar la tensión de trabajo y mejorar la ciclabilidad, por lo que también se incluyó este metal en la investigación.

Se establecieron los protocolos de síntesis para sintetizar $A^I_3M^{III}P_3O_9N$ donde A=Na/Li y M=V, $A^I_2M^{II}_2P_3O_9N$ donde A = Na/Li, M= Fe, Co, Mn y $Na_3Li_3M^{III}F_{12}$. donde M= V, Ti, Fe; y se llevó a cabo su exhaustiva caracterización e implementación en celdas

electroquímicas prácticas para validar sus prestaciones como potenciales materiales catódicos. Nuestros resultados muestran que el rendimiento electroquímico de esta familia de materiales varía con la composición química.

Los resultados más notables se obtuvieron para el CUBICON $Na_3VP_3O_9N$, cuyo potencial de trabajo resultó ser muy elevado, 4.0 V frente a Na^+/Na^0 y 4.1 V frente a Li^+/Li^0, siendo el mayor voltaje de operación para el par redox V^{IV}/V^{III} junto con $Na_7V_3(P_2O_7)_4$. Basándose en los cálculos DFT, se impide la extracción de más de un catión de sodio porque se predice que el potencial del par redox $V^{IV/V}$ está más allá de la ventana de estabilidad de voltaje de los electrolitos disponibles hasta ahora. Además, presentamos el éxito del intercambio iónico completo en $Li_3V(PO_3)_3N$ con la actividad electroquímica del par redox V^{IV}/V^{III} centrada alrededor de 3.9 V frente a Li^+/Li^0.

Centrándonos en los nitrofosfatos divalentes, presentamos que el $Na_2Fe_2(PO_3)_3N$ ofrece una capacidad estable de 60 mAh.g^{-1} frente al Li^+/Li^0 en configuración de iones híbridos con un voltaje medio de 3 V frente al Li^+/Li^0, lo que indica unas prestaciones mejoradas en comparación con las publicadas hasta ahora (capacidades de ~40 mAh.g^{-1} y alta polarización). La falta de resultados anteriores frente al Na metal sugería una extracción/inserción infructuosa de los iones Na^+ dentro de la estructura, sin embargo, aquí demostramos la movilidad estable, aunque limitada, de ~0.55 iones Na^+ a 2.9 V frente al Na^+/Na^0 mientras se cicla el $Na_2Fe_2(PO_3)_3N$ frente al Na metal. Otro aspecto destacado de esta parte fue la síntesis exitosa de $Na_2Co_2(PO_3)_3N$ por primera vez. Los estudios termogravimétricos de ambos miembros - $NaFe_2(PO_3)_3N$ y $Na_2Co_2(PO_3)_3N$ revelaron una notable estabilidad térmica.

Además, descubrimos una nueva familia de nitrurofosfatos de manganeso alcalinos $A_{1.1}Mn_{2.9}P_3O_8N_2$ (A = Na/Li) que cristalizan en una estructura ortorrómbica, lo cual es, hasta donde sabemos, el primer informe de una síntesis directa de un nitrurofosfato de metal de litio. Los cálculos DTF predijeron la actividad del par redox $Mn^{II/III}$ a un potencial compatible con los electrolitos orgánicos comunes (3.25 V frente a Na^+/Na^0 y 3.30 V frente a Li^+/Li^0), sin embargo, según las pruebas experimentales realizadas, no se logró la extracción de sodio y litio de estas estructuras. Los cálculos BVEL revelaron valores muy elevados de energías de percolación (>4 eV) indicando una difícil difusión de los cationes alcalinos dentro de la estructura, muy probablemente como resultado de la presencia de estrechos cuellos de botella en el curso de las vías de difusión de los cationes alcalinos.

Pasando a la segunda familia, fluoruros, comenzamos por los fluoruros de grenate de fórmula general $Na_3Li_3M^{III}F_{12}$. Dentro de la estructura de estos compuestos, tanto el Li como el Na ocupan sitios cristalográficos distintos (Na en 24c y Li en 24d), y se espera que ambos sean móviles dentro de la estructura. La energía de migración BVEL calculada considerando sólo los iones de Na como especies móviles resultó ser relativamente baja (Em = 0.70 eV), lo que sugiere una fácil eliminación de estos iones alcalinos de la estructura. Combinado con una capacidad teórica de ~130 mAh.g^{-1} considerando la inserción y/o extracción reversible de dos cationes alcalinos y un alto voltaje resultante de la electronegatividad F, estos materiales podrían ser atractivos materiales catódicos de Li-ion o Na-ion. Además de los compuestos reportados con Mn y V trivalentes, también decidimos explorar los compuestos basados en Fe, Ti y Co. Se espera que todos estos metales de transición trivalentes proporcionen un buen rendimiento electroquímico a través de las reacciones redox de los pares M^{III}/M^{II} y M^{III}/M^{IV}. Hasta donde sabemos, ninguno de estos compuestos ha sido probado previamente como material de electrodos. Se obtuvieron tres granates fluorados diferentes ($Na_3Li_3M^{III}F_{12}$ (M= V, Ti, Fe) mediante síntesis solvotérmica asistida por microondas (hierro y vanadio) y mecanosíntesis mediante molienda de bolas (los tres). Los intentos de sintetizar granates de manganeso y cobalto no tuvieron éxito. La respuesta electroquímica de los tres materiales de granate $Na_3Li_3M^{III}F_{12}$ (M= V, Ti, Fe) se ve probablemente obstaculizada por la conductividad electrónica intrínsecamente pobre de los compuestos de fluoruro. Sin embargo, la oxidación química del análogo de titanio conduce a la formación de una fase ortorrómbica de $Na_3Li(TiF_6)_2$ que acomoda reversiblemente un Li$^+$ a una tensión media de 3.1 V frente a Li$^+$/Li^0, siendo la tensión de trabajo más alta del par redox Ti^{III}/^{IV}.

Por último, siguiendo con la exploración de nuevos compuestos de fluoruro con la ruta solvotérmica asistida por microondas, se estabilizaron tres fluoruros de vanadio en función de las condiciones de reacción, con especial interés por la fase $VF_3 \bullet 0.33H_2O$ de tipo HTB que se reporta por primera vez. Aunque su tensión operativa centrada en torno a 2 V frente a Li$^+$/Li^0 impide su aplicación real como materiales de electrodos, estos compuestos ofrecen una capacidad reversible de >200 mAh.g^{-1} combinando las reacciones de intercalación y convergencia.

En general, podemos confirmar que los cálculos BVEL de alto rendimiento pueden ser aplicados con éxito como una herramienta en la búsqueda de nuevos materiales para

cátodos. Este método permite una rápida identificación de estructuras interesantes con atractivos rendimientos electroquímicos.

Además, los resultados presentados en esta tesis demuestran que los compuestos basados en el N y el F todavía ofrecen un enorme espacio químico que debería ser explorado más a fondo para descubrir nuevos materiales de electrodos atractivos.

Contents

Chapter 1 - General Introduction

Outline

1.1. State of the art

The ability to harness energy has entirely transformed the living conditions of humans. The steady growth of energy consumption over the past 200 years has been well aligned with the economic development and rising wealth. However, such an increasing prosperity resulted in a rapid growth of the population and happened at the expense of environmental deprivation. Economic and technological advancements are directly connected with the different energy resources available. As can be seen in Figure 1.1a, the Industrial Revolution in the 19th century resulted with the shift to coal as key energy source. It was mainly used for providing heat and powering steam engines.[1] The technological progress in the 20th century, with the introduction of combustion engines and oil-powered ships, brought new high energy sources like oil and natural gas. The rapid development also resulted in the increasing awareness of our complete dependence on fossil energy sources and their finite character. The limited abundance of the resources also caused political and economic conflicts. Moreover, a significant increase of the generated greenhouse gases was detected, having a direct damaging impact on the environment.
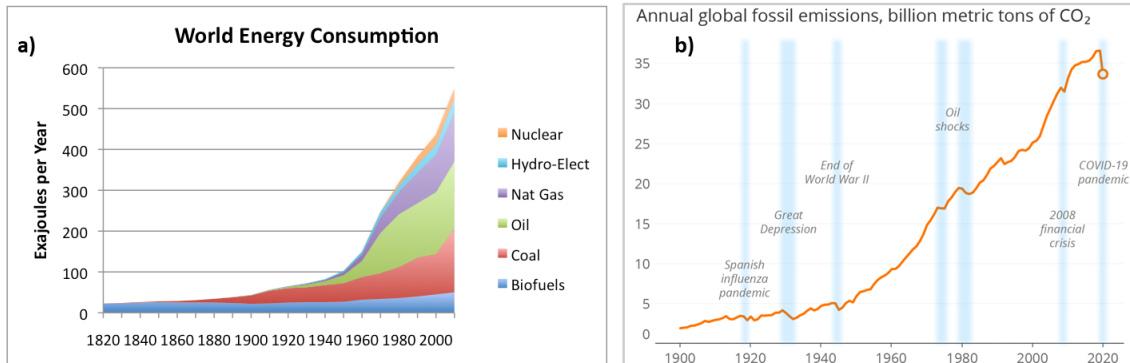
Figure 1.1: (a) World energy consumption by source over the past 200 years, based on Vaclav Smil estimates from Energy Transitions[2]: History, Requirements and Prospects together with BP Statistical Data for 1965 and subsequent; (b) Annual global fossil emissions.[3]

This trend can be well observed in Figure 1.1b presenting the annual global gas emissions from fossil fuels. Such an extreme increase of the emissions resulted with a rapid increase of the average global temperature of 1.1 °C over the last few decades.[3–5] To stop drastic climate changes, the world needs to apply drastic actions, the most important focused in a fast and large reduction of emissions. This requires a major shift towards clean and renewable energy sources such as wind, solar, biomass-derived and hydroelectric.[6,7] However, these are intermittent renewable sources, that therefore require efficient storage

systems. Additionally, transport is one of the main causes of greenhouse gas emissions and the transition towards low-emission vehicles has also led to an increased interest in alternative energy storage materials. The main challenge consists in connecting both clean and high-power qualities, creating eco-friendly, powerful and efficient energy materialss.[8,9] Among various innovative energy storage technologies, batteries have been considered as the key technology which could fulfill current demands at the global scale, as both high energy and power density can be achieved, which has led to a wide use in portable devices and electric cars.[10,11] The increasing demand for the constantly upgrading technology in terms of higher power and appearance, such as , smaller size, lighter weight, flexible design; challenges researchers to continuously investigate into new materials.

1.1.1. Li-ion and Na-ion batteries

The concept of batteries, presented in Figure 1.2 is believed to have existed for more than 2000 years with the discovery of "Baghdad battery" – collections of jars containing sheets of copper rolled up with an iron rod. When mixing them with an acidic liquid, such as wine or vinegar, copper and iron can react producing electricity. Although the original purpose is unclear, it is assumed that it might have been used to electroplate gold onto some objects. The first electrochemical cell was invented in the 18th century by Alessandro Volta. This cell, named Voltaic Pile, consisted of layers of copper and zinc divided by layers of cardboard or cloth soaked in brine or vinegar.[12] This breakthrough concept, with some modifications, is still commonly used today. The second milestone in the history of batteries was the invention of the rechargeable lead-acid battery in 1860 by the French physicist Gaston Planté. Within this cell, the anode was made of lead, the cathode of lead oxide, and a solution of sulfuric acid was used as an electrolyte. Apart from the low cost, the largest advantage of this battery was the significant improvement of the cell voltage (2V) compared to 1.1V of the primary cell.[13] Almost forty years later, in 1899, the first nickel-cadmium battery (NiCd) was invented. The energy density of the battery, compared to the lead-acid, was increased thanks to the combination of materials used. Seeking alternative chemistries to further elevate the working voltage, the development of the lithium-ion battery and its commercialization by Sony in 1991 was the next revolutionary step in the battery history. The development of lithium batteries was so innovative and important for the society that it has been awarded Nobel Prize in

2019. According to the Royal Swedish Academy of Sciences, "Lithium-ion (Li-ion) batteries have revolutionized our lives since they first entered the market in 1991. They have laid the foundation of a wireless, fossil fuel-free society, and are of the greatest benefit to humankind."
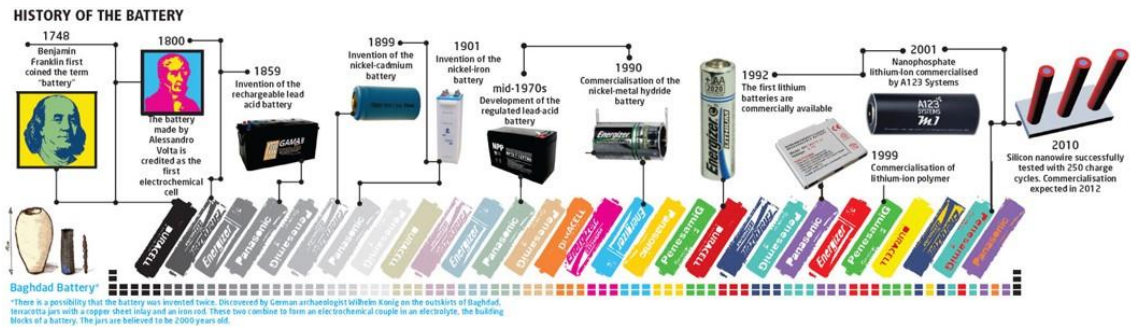
Figure 1.2: History of the battery with all the key breakthroughs over the time. From the first "Baghdad battery" invented more than 2000 years ago up to commercialization of the batteries in the 2000s. [14]

Figure 1.3 presents the comparison of the different battery technologies, which were described before, in terms of their volumetric (Wh.l^{-1}) and gravimetric (Wh.kg^{-1}) energy densities. Depending on the application, other additional criteria are considered, such as cost, cycle life, volume, etc. Among the presented technologies, Li-ion batteries surpass other systems in terms of their high energy density.
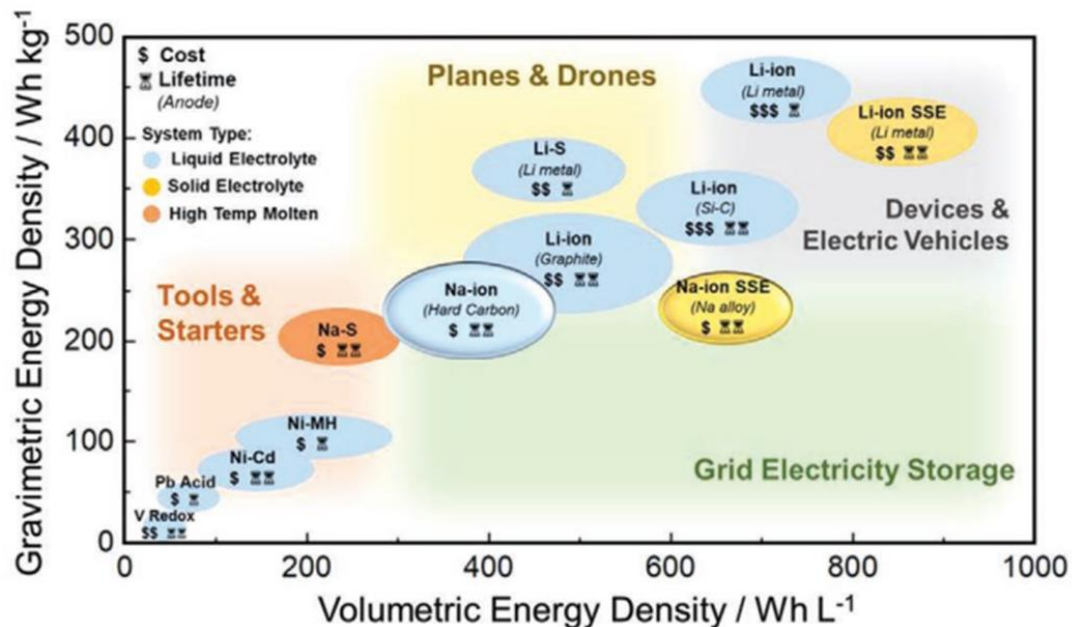
Figure 1.3: Variation of the volumetric (Wh.l^{-1}) and gravimetric (Wh.kg^{-1}) energy densities depending on the different battery technologies. [15]

14

A typical rechargeable Li-ion battery is constituted of two electrodes with different redox potentials – negative and positive - separated by an ionically conductive electrolyte, as shown in Figure 1.4. When connected to any electronic device, a spontaneous flow of electrons occurs from the negative electrode to the positive one through the external circuit. The alkali cations move in the same direction through the electrolyte, as shown in Figure 1.4a. The reverse process occurs while applying a potential difference between the two electrodes to charge the battery, as shown in Figure 1.4b.
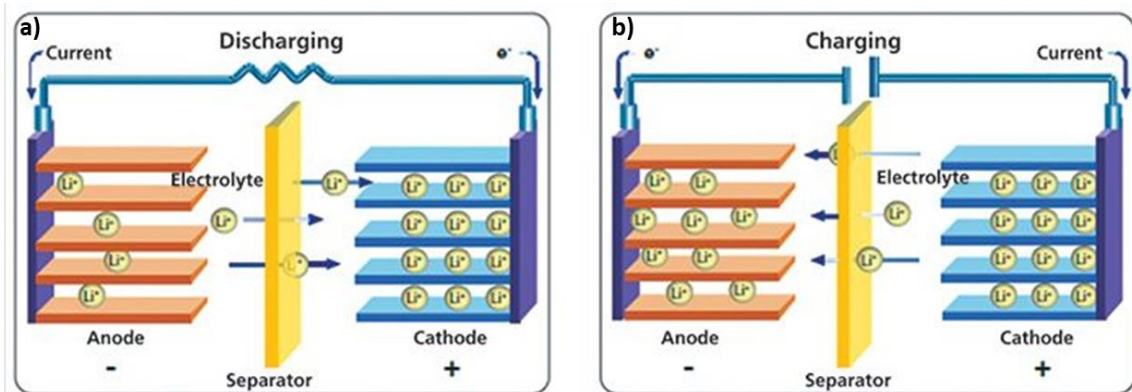
Figure 1.4: Working principle of Li-ion rechargeable battery during the charge and discharge process. Adapted from Wieboldt et. al.[16]

The first commercialized Li-ion battery was composed of a graphite anode and layered-oxide (Li_xMO_2, where M=Co, Ni or Mn) cathode.[17–19] Its working potential exceeded 3.6 V and the gravimetric energies were in the range of 120-150 $Wh.kg^{-1}$, exceeding five times the energy density of the lead-acid technology. This technology is still used in present portable electronic devices. Later, some research was conducted to replace the liquid electrolyte by a polymer layer with the eventual development of the lithium-ion polymer battery (LiPo). Moving to solid polymer batteries is a very active research topic today wing to safety concerns and to increase the energy density. Different cell formats exist, being cylindrical (Figure 1.5a) and pouch cells (Figure 1.5b) the most common.
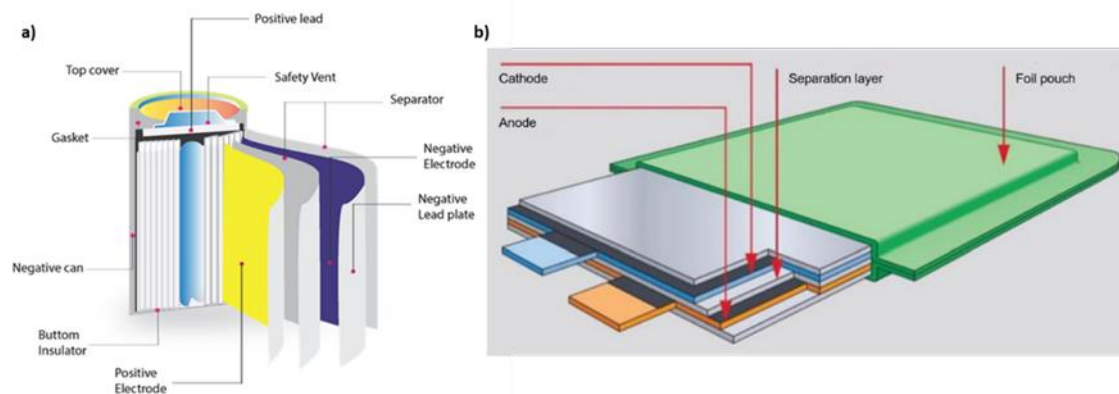
Figure 1.5: Schematic drawings of (a) a cylindrical Li-ion battery; (b) a Li-ion pouch battery.[20]

Li-ion batteries are dominating the market for portable devices, hybrid and electric vehicles due to their light weight and outstanding power and energy density.[21,8] However, with the rapidly increasing use of the electronic devices and vehicles, the increasing demand for lithium and the unstable global context results with growing concerns of its availability and price. Indeed, the major lithium sources are only in South America (mainly Chile) and Australia.[22] Additionally, the lithium market is currently dominated in 77% by China, resulting in an economical and geopolitical dependency of the lithium supply industries.[23] Therefore, the search for alternative battery technologies and chemistries is a natural and mandatory action.

- **Sodium-ion batteries**

The abundance and low cost of sodium make it an appealing alternative to lithium.[10,24,25] Figure 1.6a shows the significant difference in the abundance of Na as compared to Li and other elements. Apart from its high abundance, sodium is well distributed all over the Earth which considerably reduces the economic impact.

Research in sodium ion (Na-ion) batteries started in the 80s´alongside with the research in Li-ion batteries, however sidelined due to the obtained better performances of Li-ion technology.[26,27] As shown in Figure 1.6b, the growing concern about Li supplies recently renewed the interest in Na-ion batteries and is constantly increasing as demonstrated in the expanding number of academic publications and patents.
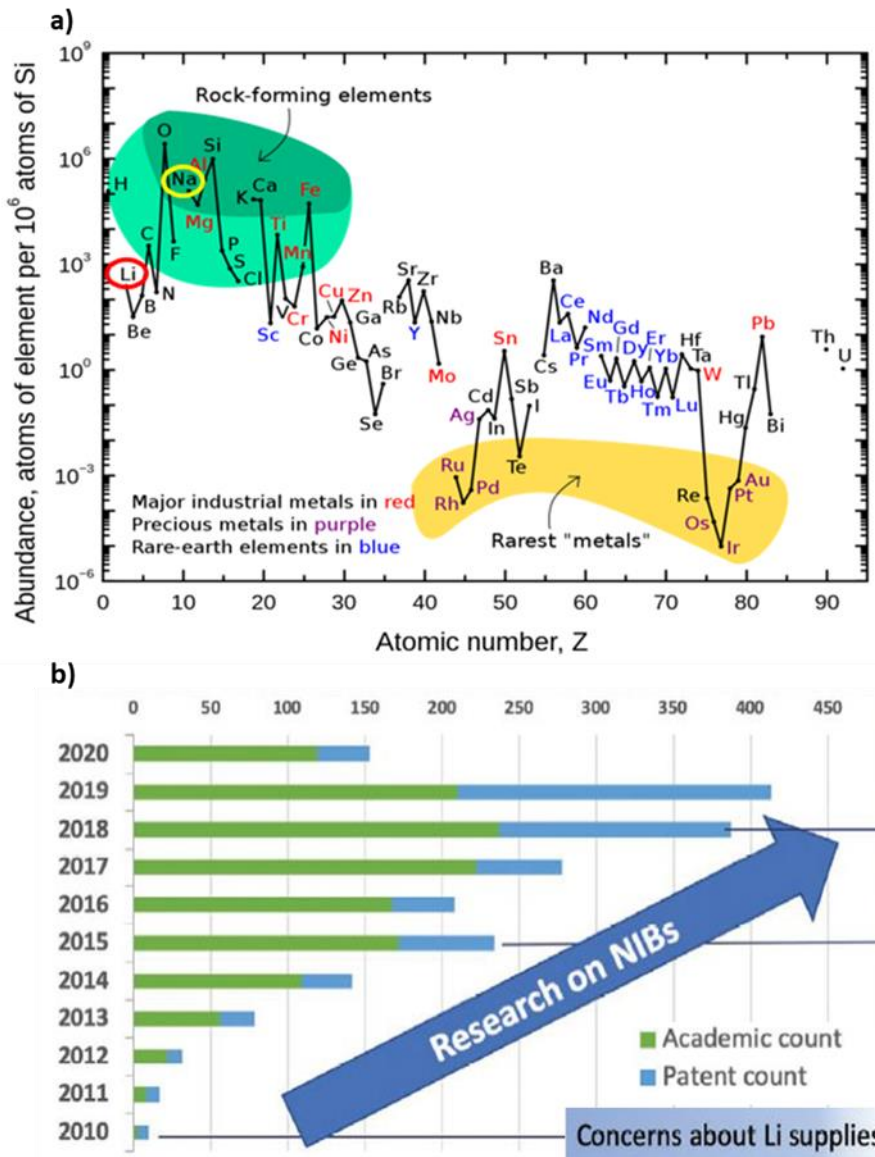
Figure 1.6: (a) Abundance of the chemical elements in Earth's upper continental crust as a function of atomic number with Na and Li marked in yellow and red, respectively[28]; (b) Number of academic publications and patents regarding sodium ion batteries until May 2020. Adapted from Goikolea et. al.[29]

As Na-ion and Li-ion batteries rely on the same working principles, the research in Na technology has strongly benefited from the great developments achieved in the Li field within last years. It has allowed to accelerate the research into new electrode materials to reach almost comparable energy density to the current Li-ion technology. Although Na^+ has a three times larger ionic radius and molar mass than Li^+, Na-ion batteries can be specially considered as an alternative for stationary energy storage systems. Furthermore, in Na-ion technology, aluminum can be implemented as a current collector at the anode side which reduces the cost compared to the more expensive copper current collector used for Li-ion batteries.

In theory Na-ion batteries are analogous to Li-ion batteries in terms of configuration and operation, both comprising of a cathode and anode, separated by an electrolyte thought which alkali cations migrate between electrodes. The differences appear while choosing appropriate electrode materials. In some cases, the sodiated analogue materials can be successfully implemented (like salts in electrolytes and some cathodes), but very often the operation mechanisms are very different resulting in different performance.

1.1.2.   Anodes for Li-ion and Na-ion batteries

Being the lightest metal with high specific capacity (3.86 Ah.g^{-1}) and extremely low electrode potential of –3.04 V *vs.* standard hydrogen electrode, lithium metal would be an ideal anode material for Li-ion batteries. However, electrochemical potential of the anode has to fall within the lowest unoccupied molecular orbital (LUMO) of used non-aqueous electrolytes, whereas the Li^+/Li^0 potential lies below this level. It leads to constant electrolyte reduction. Such unstable interface results in the formation of dendrites which might penetrate the electrolyte and cause internal short circuit. This might be very hazardous for the battery as can result with heat generation and even ignition.[30] As an alternative, carbonaceous materials were found to be most suitable candidates for anodes due to the possibility of intercalation of Li within the layers of the material. Among them, graphite was found to be the most attractive material as can reversibly accommodate 1 Li per 6 carbon atoms yielding a specific capacity of 372 mAh.g-^{1}.[31,32] Due to the low lithiation/delithiation potential of ~0.2 V *vs.* Li^+/Li^0, some electrolyte modifications had to be performed to be able to prevent graphite exfoliation. It was found that the addition of carbonates such as ethylene carbonate (EC) as electrolyte co-solvent prevents solvent co-intercalation and results with the formation of a sufficiently stable solid electrolyte interphase (SEI) on the graphite surface that supports stable reversible lithium intercalation.[33,34] This breakthrough invention induced the eventual commercialization of the lithium-ion battery in 1991. Since then, continuous research is conducted to improve the performance on graphite anodes (cycling stability, reversible capacity, first cycle coulombic efficiency) for example by developing suitable coatings or electrolyte additives.[35–38]

Moving to Na-ion batteries, here also metallic Na cannot be used as an anode due to the similar dendrite formation, and additionally low melting point of Na (97.7°C) which could lead to safety issues. Graphitic anodes, widely used for Li-ion batteries cannot be used

for Na-ion batteries, since the intercalation of Na^+ ions between graphite layers is thermodynamically less favorable than Na plating on the surface. [39,40] Various types of carbons have been widely investigated such as carbon nanofibers, carbon black, fibers, carbon microspheres, but the obtained energy densities were much worse while comparing with the ones of graphite for Li-ion batteries.[41–43] It was found that disordered carbons such as hard and soft carbons offer the most promising properties as anodes.[40,41] These carbons can deliver high specific capacities of ~400 mAh.g^{-1}, being close to the ones of graphite in Li-ion batteries, with the lowest oxidation voltages.[44] Although the performances still require further improvement, it was sufficient to apply this technology in the first Na-ion battery developed by Faradion in 2011.[45,46]

1.1.3. Cathodes for Li-ion and Na-ion batteries

The cathode material is the key component while designing the battery, since it has the main influence on the eventual performance of the battery. It has to provide fast insertion/extraction of the mobile cation and stable reversible capacity. Additionally, the ideal cathode material would possess high specific capacity and deliver a high potential. A great number of different chemistries have been continuously developed with many analogues which can be successfully applied for both Li-ion and Na-ion batteries. These materials can be classified into four main categories: layered oxides, polyanionic compounds, Prussian Blue derivatives and organic materials. Additionally, another group of conversion materials (such as transition metal fluorides, oxyfluorides or sulfides) also are also explored as potential cathode materials, however their working mechanism significantly differs from all aforementioned categories. All of these categories are gathered in Figure 1.7 together with their strong and weak points.
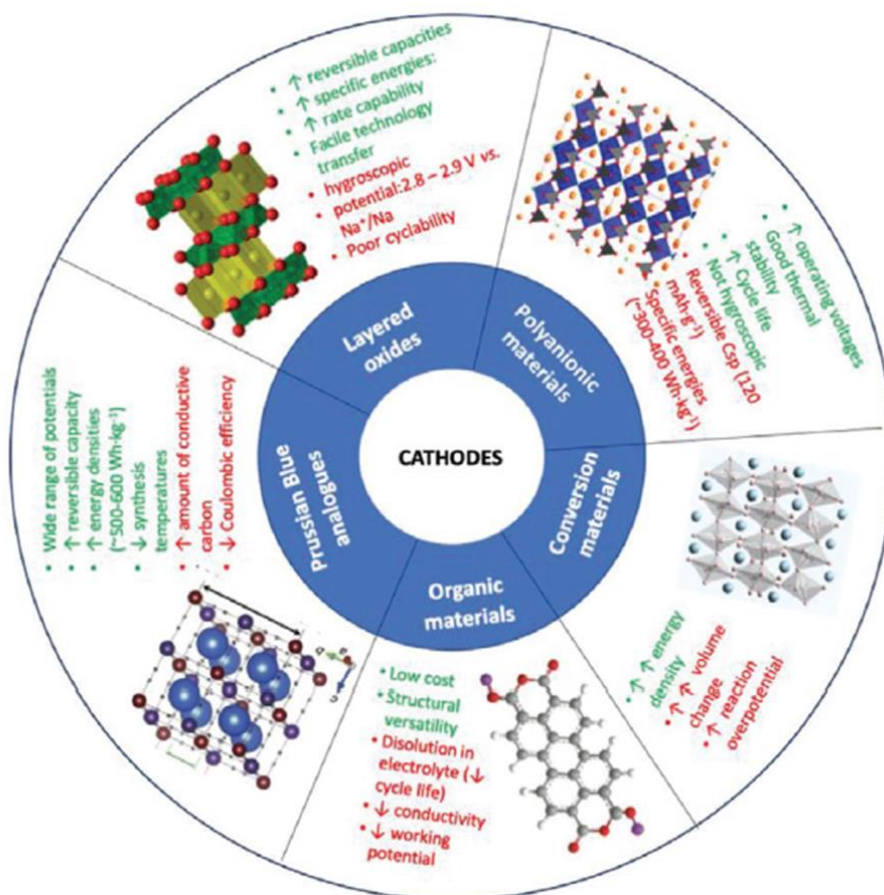
Figure 1.7: Different families explored as cathodes for Li-ion and Na-ion batteries with structures of the representatives and their strong and weak points (green and red, respectively). From Goikolea et. al.[29]

1.1.3.1. Sulfide based materials as the first intercalation system

The concept of intercalation of Li^+ ions into the host structure dates back to 1970 with the investigation of the binary and ternary sulfides such as TiS_2 and $FePS_3$.[26,47,48] The structure of TiS_2 is shown in Figure 1.8 and is composed of layers of TiS_6 octahedra separated by a large interlayer distance of 2.85 Å, as indicated in the figure. Such a large space facilitates Li^+ mobility through two-dimensional transport pathways.
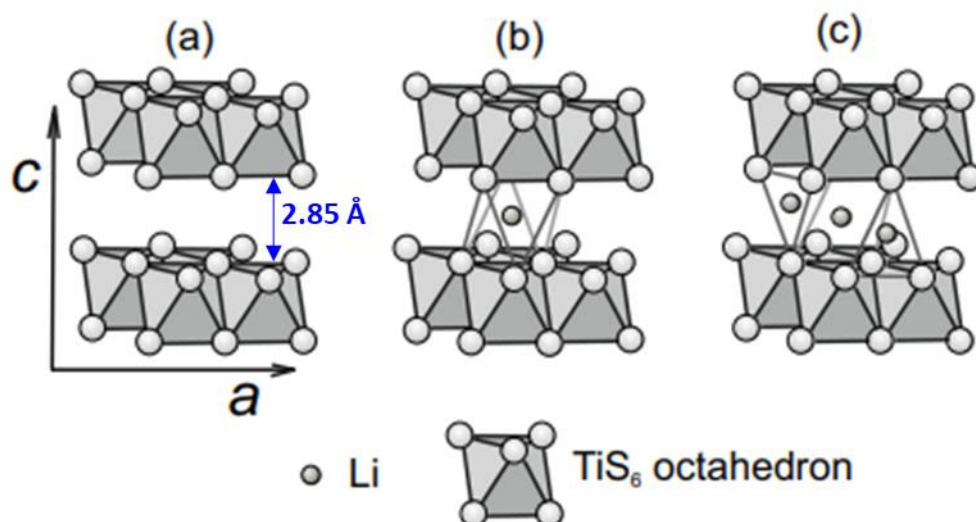
Figure 1.8: Structure of TiS₂ and the sequential lithium filling of octahedral (b) and tetrahedral (c) sites. Adapted from Suslov et. al.[49]

This reversible intercalation of Li^+ ions into TiS_2 cathode combined with the use of a LiAl anode was the first example of the rechargeable Li-ion battery, commercialized by Exxon in late1970s.[26] Although the performance of TiS_2 cathode was excellent (intercalation capacity of ~240 mAh.g^{-1}), the battery was a failure due the dendrite formation at the metallic anode upon cycling. Additionally, spontaneous release of toxic H_2S gas was observed upon contact with moisture causing TiS_2 difficult to handle.

1.1.3.2. Lithium transition metal oxides

In 1980 [50][51]Mizushima and Goodenough reported the high voltage $LiCoO_2$ (LCO) cathode at room temperature using organic electrolytes.[52] The structure of $LiCoO_2$ (shown in Figure 1.9a) is very similar to the structure of TiS_2, with alternating layers of CoO_6 octahedra and Li^+ ions in octahedral coordination.
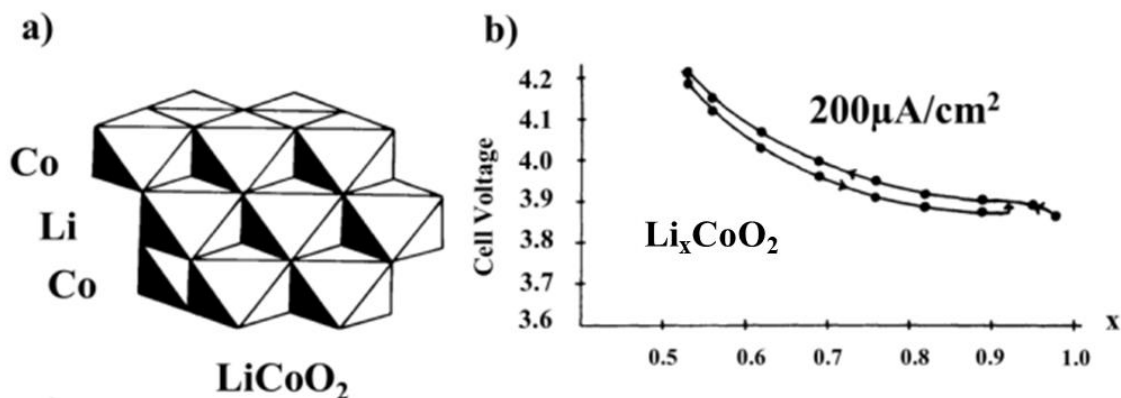
Figure 1.9: (a) The crystal structure of LiCoO₂; (b) the discharge/charge voltage versus composition profile of LiCoO₂ at current density of 200μA.cm⁻². Adapted from Mizushima et al.[52]

LiCoO₂ offers significantly higher Li⁺ insertion voltage of ~4.0 V *vs.* Li⁺/Li⁰ with a theoretical capacity of 274 mAh.g⁻¹. Complete delithiation of LiCoO₂ require very high voltage (5 V *vs.* Li⁺/Li⁰) which result with the decomposition of the organic electrolyte. Additionally, structural investigations revealed several detrimental phase transitions occurring above 4.2 V *vs.* Li⁺/Li⁰.[53] Therefore for the practical application, the voltage was limited to 4.2 V, leading to the reversible mobility of ~0.5 Li⁺ (Figure 1.9b). Pairing the LiCoO₂ cathode with LiC₆ graphite anode developed by Yoshino resulted with the first commercialization of the Li-ion battery in 1991, being one of the largest breakthroughs in the battery field. [54]

Since then, the family of lithium transition metal oxides with general formula LiMO₂ (M= Co, Ni, Mn) were extensively investigated as cathode materials.

LiNiO₂ was the second evaluated candidate due to its high operating voltage of 4.0 V *vs.* Li⁺/Li⁰, high theoretical capacity of 274 mAh.g⁻¹ and lower production cost while comparing with LiCoO₂.[55–58] The main obstacle in commercial use of LiNiO₂ is the cation mixing occurring due to the very similar ionic radii of Li⁺ and Ni^{II} leading to the non-stoichiometric composition of Li$_{1-x}$Ni$_{1+x}$O₂ (0<x<1).[55] This can lead to the appearance of Ni^{II} ions in the lithium sites strongly hindering the Li⁺ diffusion and eventually resulting with a significant decrease of the electrochemical performance. Additionally, during the charge-discharge processes, LiNiO₂ follows several phase transitions resulting with the decrease of the overall capacity.

LiMnO₂ has the highest theoretical capacity of 285 mAh.g⁻¹ among layered compounds. Two crystal structures of layered LiMnO₂ can be distinguished: monoclinic (layered), and the more thermodynamically stable orthorhombic phase.[59] The main problem with

LiMnO$_2$ in terms of application as cathode material is the strong Jahn-Teller effect of Mn^{III} which can easily undergo disproportion reaction of 2Mn^{III} → Mn^{IV} + Mn^{II} where Mn^{II} is highly soluble in the organic electrolyte.[60,61]

As a solution to improve the electrochemical performance of layered oxides, chemical substitution at the metal site resulted to be the most successful. Without changing the layered framework, partial substitution of the active metal ion by other electrochemically active or inactive metal ions can stabilize the structure throughout a wide compositional range but also increase the theoretical capacity. By following this approach, Tsutomu and Yoshinari introduced LiNi$_{1/3}$Co$_{1/3}$Mn$_{1/3}$O$_2$ (named as NMC111) with valences of Ni^{II}, Co^{III} and Mn^{IV} as a new cathode material.[62]
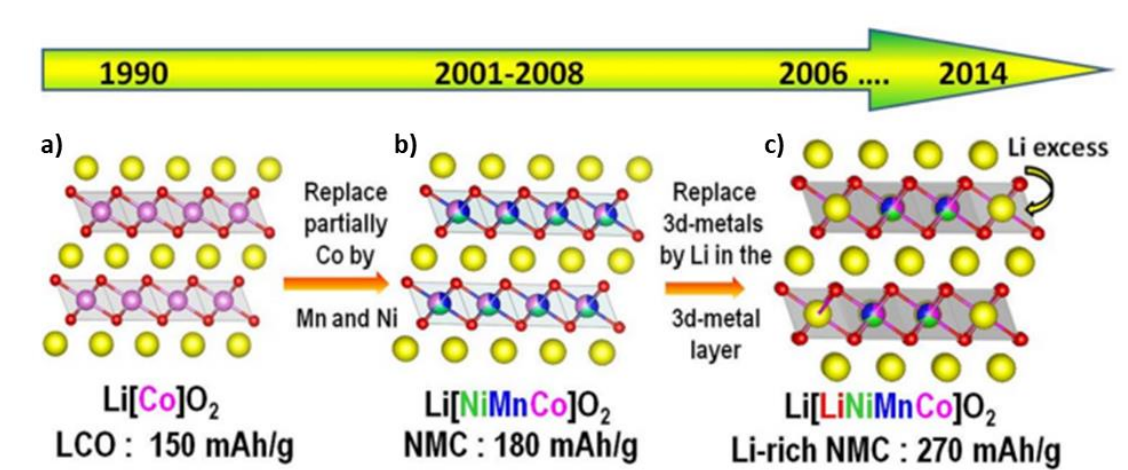
Figure 1.10: Chronological evolution of the layered oxide LiCoO2 chemistry (a) fueled by cationic substitution within the metal layers with (b) partial replacement of Co with Ni and Mn (NMC phase) within the metal layer (purple) and (c) more recently with Li (yellow) to form Li-rich NMC phases. From Rozier and Tarascon.[63]

This was a great improvement and advance in the layered oxide chemistry. Later on, the stability and electrochemical performance was improved by introducing an excess of Li forming so called Li-rich NMC phases.[64]. Figure 1.10 shows the evolution in time of the cationic substitution to form different NMC and Li-rich NMC phases together with their theoretical capacities.[63] Up to date NMC cathodes are widely used in multiple applications and Li-rich materials are still under development.

1.1.3.3. Sodium transition metal oxides

Since lithium layered oxides have experienced such a significant commercial success, it was a natural starting point in the search for promising sodium cathode materials to focus on analogous sodium layered oxides. These materials, with general formula of Na$_x$MO$_2$

(M = Co, Mn, Fe, Cr, V, Ni) are built by alternating layers of transition metal oxide TMO_6 octahedra and sodium polyhedra in the interlayer space. Depending on the stacking of oxygen layers and surrounding sodium environment there are different polytypes of sodium oxides: O3 (ABCABC), P2 (ABBA), P3 (ABBCCA) where O and P represent an octahedral or prismatic coordination environment of the Na^+ ions.[65] These typical structures of layered oxides are presented in Figure 1.11.
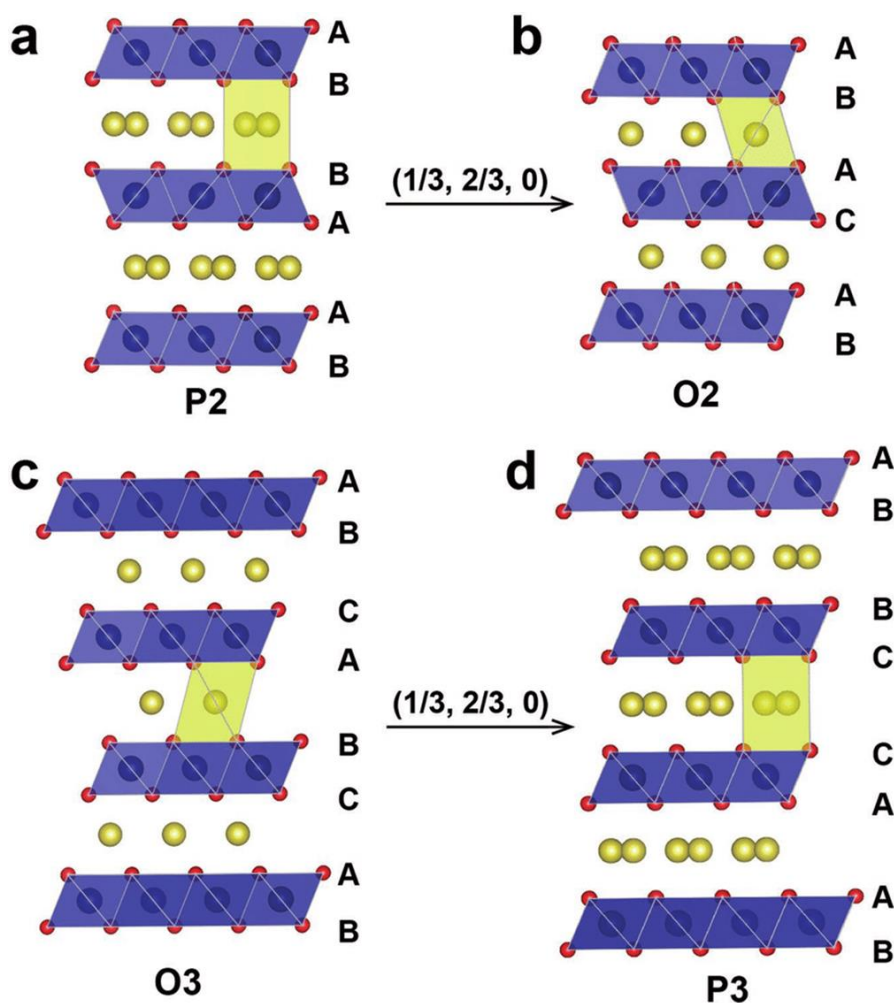

Figure 1.11: A schematic structures of (a) P2-type, (b) O2-type, (c) O3-type and (d) P3-type layered oxides. The blue and yellow balls represent the transition metal and Na ions, respectively. The arrows show the transformation of the P2 to O2 and O3 to P3-type, caused by the gliding (π/3 rotation) vectors, (2/3, 1/3, 0) and (1/3, 2/3, 0), respectively. From Wang et.al.[66]

The first evaluated system was Na_xCoO_2 in 1980s by Delmas et. al.[67] The most promising electrochemical performance was obtained for the composition of $Na_{0.8}CoO_2$, however only 50% of Na^+ was removed from the structure. Additionally, several structural transitions were observed upon cycling leading to poor cycling reversibility and large voltage hysteresis. Further work was focused on manganese and iron oxides due to their high redox potentials and capacity, as well as their low cost and low-toxicity.[68] Although

the first studies on $NaMnO_2$ resulted with obtaining a high capacity of 210 mAh.g^{-1} during the first charge, further cycling revealed severe problems with the structural transformations and capacity fading.[69] Additionally, Mn-based sodium layered oxides suffer large volume changes due to the strong Jahn Teller effect causing large structural distortions. Although there still is exhaustive research on sodium layered oxides, the results are fairly less successful than the lithium analogs, although several complex compositions have shown promise. In terms of long-term cycling these materials suffer multiple phase transitions resulting with voltage and capacity fading upon cycling. Another issue is the air and moisture sensitivity of these compounds, after exposure to air can undergo phase transitions to electrochemically less active structures.[70]

1.1.3.4. Spinel manganese oxide

Metal oxide-based spinel materials with general formula LiM_2O_4 (M=Co, Ni, Mn) provide a high energy density due to the high operating voltage of >4 V vs. Li^+/Li^0.

The $LiMn_2O_4$ spinel structure is shown in Figure 1.12 where the lithium ions are located in the center of the LiO_4 tetrahedra (indicated in light blue) and manganese ions in the center of MnO_6 octahedra (indicated in pink).
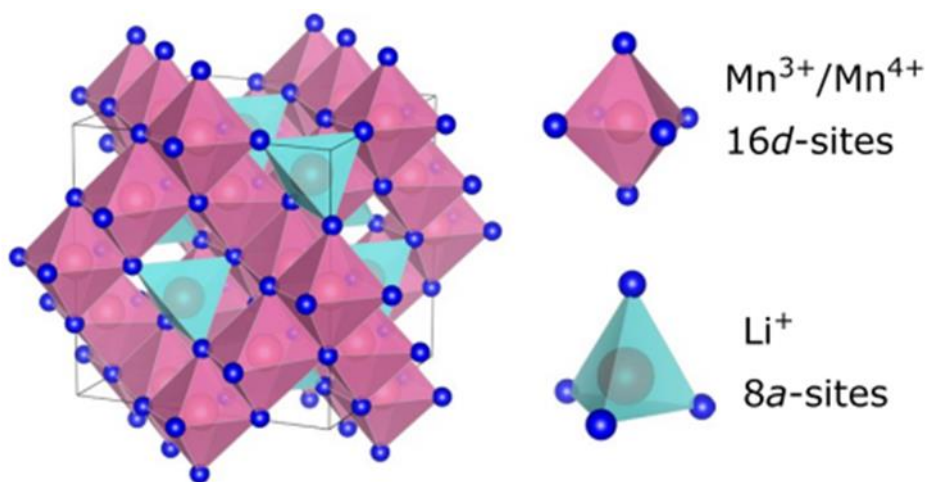
Figure 1.12: Crystal structure of LiM_2O_4 where the MnO_6 octahedra are indicated in pink and the LiO_4 tetrahedra are indicated in light blue. From Sun et. al.[71]

MnO_6 octahedra are connected to each other through their edges, while LiO_4 tetrahedra are interconnected with MnO_6 octahedra through their vertices forming a three-dimensional network for Li^+ ion diffusion.
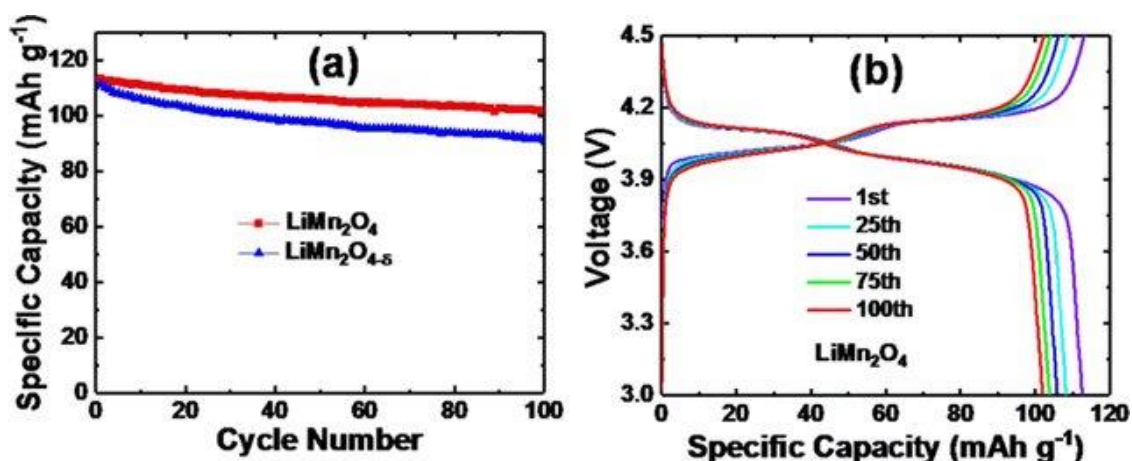
Figure 1.13: Electrochemical performances of LiMn₂O₄ and LiMn₂O₄₋δ. (a) Specific capacity vs. cycle number at 100 mA g⁻¹; (b) charge/discharge voltage vs. capacity curves. From Tan el. al.[72]

Electrochemical evaluation of $LiMn_2O_4$ revealed capacities of ~110 mAh.g⁻¹ at an average voltage of 4.1 V vs. Li^+/Li^0 as demonstrated in Figure 1.13.[72,73] Although the obtained capacities are lower than the ones from layered oxides, the good rate capability and high voltage placed $LiMn_2O_4$ as a widely used cathode material for high power application such as in electric vehicles.[74]

1.1.3.5. Prussian blue analogues

Prussian blue analogues with general formula $A_2M[Fe(CN)_6]$ where A=Li, Na, K and M= Fe, Co, Mn, Ni, Cu etc. are a large family of transition metal hexacyanoferrates which possess an open structure and abundant redox-active sites.[75–77] This open structure is characterized by a high structural stability and has large ionic channels which can easily accommodate alkali cations (see example in Figure 1.14). This feature is specially desired for Na-ion batteries as are adequate hosts for the larger Na^+ cation. Another advantage of these materials is their low cost.
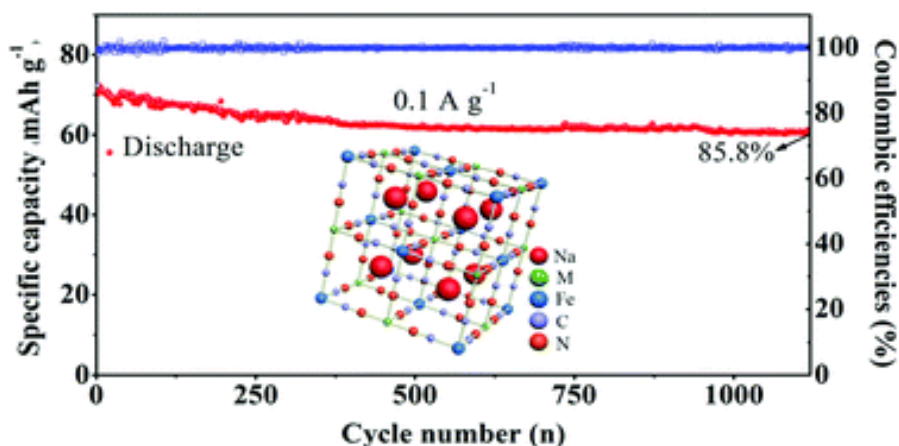
Figure 1.14: Structure and electrochemical characterization of the Na$_2$NiFe(CN)$_6$ cathode. Cycling performance at 0.1 A.g^{-1} between 2.0 and 4.1 V *vs.* Na$^+$/Na^0. From Huang ant al.[77]

Goodenough et. al. reported a manganese hexacyanoferrate (MnFe-PBA) possessing a discharge capacity of 120 mAh.g^{-1} at a voltage of 3.4 V *vs.* Na$^+$/Na^0, however due to the Jahn- Teller effect on the Mn^{III} a large decrease of the capacity was observed upon cycling [78] By changing manganese to nickel, significant improvement on the capacity retention was observed, as shown in Figure 1.14.[77] Varying the composition, these materials can reach high capacities of 160 mAh.g^{-1} at 3.0-3.5 V *vs.* Na$^+$/Na^0 .

1.1.3.6. Polyanionic compounds

Transition metal polyanionic compounds are typically composed by XO$_n$ species (X= non-metals such as P, S, B, C, N or semi-metals/metals like Si, Ge, As, Db, Se, Mo, W) connected with the MO$_6$ octahedra (M=transition metal) through the bridging oxygen atoms. The X–O bond has a high degree of covalency, due to the electronegativity difference between oxygen and non-metal or metals at high oxidation states forming high order bonds with oxygen. [79] Thanks to this, the XO$_n$ unit provides high thermal and mechanical stability of the polyanion framework while comparing with transition metal oxides. Additionally, the strong covalent X–O bond influences the ionic nature of the M-O bond increasing the distance between the antibonding orbitals, which can tune the working voltage of the compound.[80] This so-called inductive effect is explained in Figure 1.15.
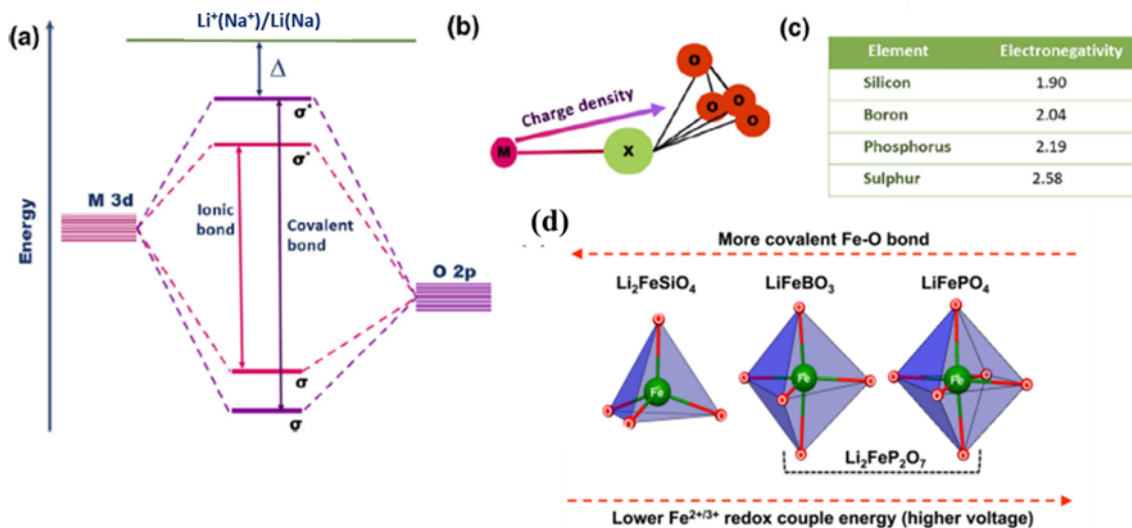
Figure 1.15: (a) Energy level diagram for the ionic and covalent bonds; **(b)** charge localization of the ionic bond around XO4 tetrahedra; **(c)** Electronegativity values of B, P, Si, and S elements, as on Pauling scale. Adapted from Sapra et. al.[81] **(d)** Dependence of the Fe^{III}/Fe^{II} voltage with the covalency of the Fe-O bond in the borate, silicate and phosphate compound. Adapted from Gutierrez et. al.[80]

The covalent interactions of the metal M ($3d$ orbitals) and oxygen O ($2sp$ orbitals) bonds result in the formation of anti-bonding (σ^*) and bonding (σ) orbitals, as shown in Figure 1.15a. The covalent M–O bond generates the repulsions between bonding and antibonding orbitals, raising the anti-bonding (σ^*) orbitals closer to the Fermi level in $Li^+(Na^+)/Li$ (Na) (as indicated by purple line). This results with the decrease of the energy difference (Δ) between these levels and consequently the operating voltage. The redox couple energy can be also tuned through the polyhedron connectivity and the type of the X atom, as demonstrated in Figure 1.15b and d. When the electronegativity of the X atom (Figure 1.15c) is higher than the one of M, the strength of the covalent M–O bond is reduced. The inductive effect pulls out the charge density from the M–X bond and enhances the energy difference (Δ) and consequently the operating voltage.[80] This dependence is well shown on the example of silicate, borate and phosphate compounds in Figure 1.15d. In phosphates, due to the highest electronegativity of phosphorous, the redox couple energy will be the highest, therefore this compound will deliver the highest working voltage.

i.   Phosphate-based cathode materials

Another great breakthrough in the Li-ion batteries was the reversible electrochemical Li^+ insertion into olivine $LiFePO_4$ by Padhi et. al.[82] The structure of $LiFePO_4$ is shown in Figure 1.16a. It is composed by FeO_6 octahedra (indicated in dark grey) linked to each other through corners in the b-c plane forming zigzag planes. The LiO_6 octahedra (in

green) are interconnected via edges forming chains along the *b* axis, which can be well seen in the right side of Figure 1.16a. Each FeO_6 octahedra shares edges with two LiO_6 octahedra. PO_4 tetrahedra, indicated in yellow, share one edge with the FeO_6 octahedra and two edges with LiO_6 octahedra. Li ions may diffuse along [001] plane as indicated in Figure 1.16a.
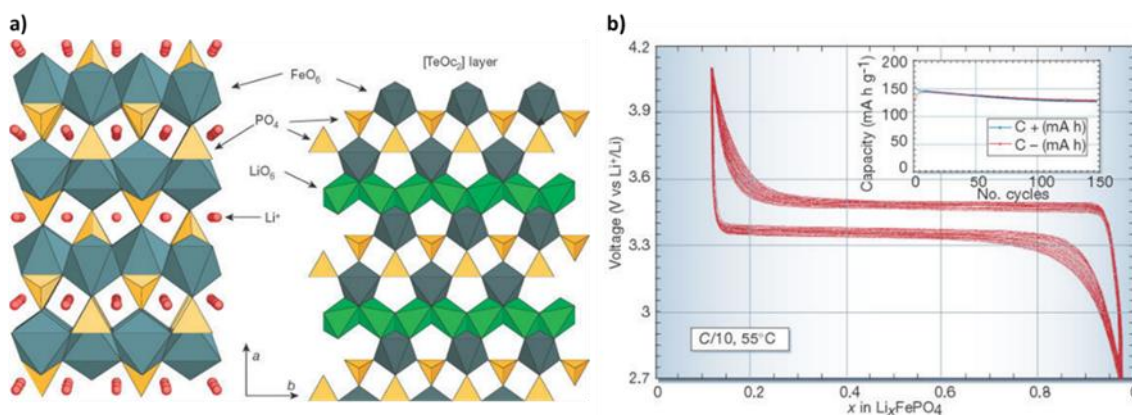
Figure 1.16: (a) The crystal structure of olivine LiFePO₄ in projection along [001] with the expanded view of the framework built on FeO₆ octahedra and PO₄ tetrahedra on the left and the restricted view of the Li, Fe and P distribution between two distorted hexagonal close packed (hcp) oxygen-dense layers; (b) Voltage vs. composition curve at 55 °C of an optimized LiFePO₄/C composite electrode (83% of active material) at a scan rate of C/10. The inset shows the capacity vs. the number of cycles. Adapted from Tarascon and Armand.[17]

One of the great benefits of this compound is the excellent stability of the delithiated $FePO_4$ phase. It has the same structure as $LiFePO_4$ with just a slight volume decrease (<7%) upon delithiation which translates into excellent electrochemical stability of the framework.[17] Additionally, $LiFePO_4$ possesses great thermal stability due to the strong covalent P–O bonds within the $(PO_4)^{3-}$ units.

While focusing on the application as a cathode material, the main advantage of $LiFePO_4$ is its low cost, non-toxicity and high theoretical capacity of 170 mAh.g^{-1}.[83–85] The Li^+ extraction/insertion occurs at ~3.45 V *vs.* Li^+/Li^0 upon a two-phase reaction, in agreement with a long plateau observed in Figure 1.16b.[83] $LiFePO_4$ also demonstrates a very stable capacity retention, as observed in the inset of Figure 1.16b. Material optimization such as carbon coating and decrease of the particle size was found to highly improve the electrochemical performance of $LiFePO_4$ translating into the successful commercialization of this compound.[84,86–88]

The great success of $LiFePO_4$ attracted the researchers' interest into the sodium analogue, olivine-$NaFePO_4$. With a high theoretical capacity of 154 mAh g^{-1} and operating potential

of 2.9 V vs. Na^+/Na^0 could be also a good candidate for Na-ion batteries. However, the main disadvantage of this material is that it cannot be obtained from a direct synthesis. Conventional reactions lead to the thermodynamically favored maricite phase which due to its one-dimensional structure has no Na^+ diffusion pathways.[89] Electrochemically active olivine $NaFePO_4$ can be obtained by extracting Li^+ ions from $LiFePO_4$ and inserting Na^+ ions into $FePO_4$, however practical performances are much lower due to its poor electronic conductivity and huge volume change between reduced and oxidized phase.[89,90]

ii. NASICON-type compounds

Sodium super ion conductor (NASICON) structures have the general formula of $Na_3MM`(XO_4)_3$ where M,M`=Fe, Ti, V, Cr, Nb, Ni etc. and X = P, S, Si, B. The first NASICON structure of $Na_{1+x}Zr_2P_{3-x}Si_xO12$ was proposed by Goodenough and Hong as a solid electrolyte with high conductivity and large three-dimensional diffusion channels. [91,92] Later on, the framework was exhaustively investigated with different metal ions for both solid electrolyte and cathode application.

Figure 1.17 shows the $Na_xM_2(PO_4)_3$ NASICON-type structure. It is built on a 3D framework of MO_6 octahedra (indicated in green) sharing all their corners with the PO_4 tetrahedra (indicated in blue). Interconnected MO_6 octahedra and PO_4 tetrahedra create large tunnels for fast ionic conduction, as can be observed in Figure 1.17a.
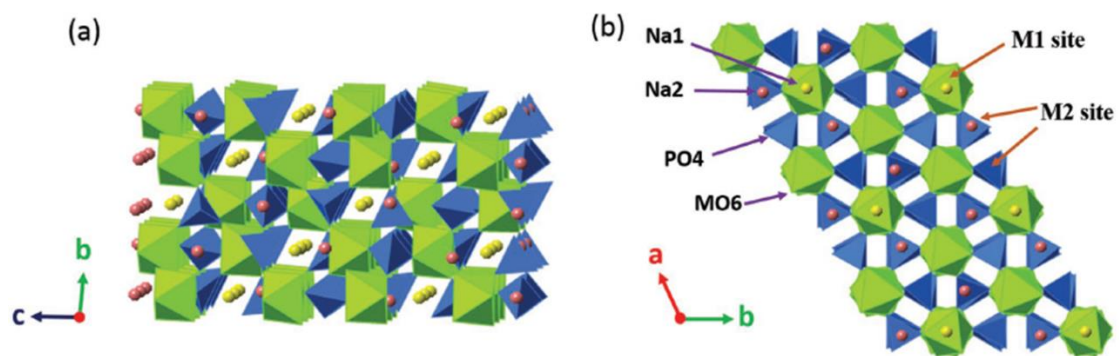

Figure 1.17: $Na_xM_2(PO_4)_3$ NASICON structure along (a) *a* and (b) *c* axis, respectively, where the MO_6 octahedra are indicated in green, PO_4 tetrahedra are indicated in blue and Na1 and Na2 atoms are shown as orange and yellow balls, respectively. From Fang et. al.[93]

One of the most interesting members of this family as cathode material is $Na_3V_2(PO_4)_3$ due to its three possible working redox couples: V^{III}/V^{II}, V^{IV}/V^{III}, and V^V/V^{IV}. $Na_3V_2(PO_4)_3$ is characterized by high operation potential of 3.4 V *vs.* Na^+/Na^0 for the redox couple V^{IV}/V^{III}.[94,95] Sodium ions occupy two different interstitial sites. Based on

the theoretical calculations, only Na ions at the Na(2) sites can be electrochemically extracted from the structure due to the weak bonding with the surrounding oxygen atoms, resulting with a theoretical capacity of 117 mAh g^{-1} (following the redox reaction of the V^{III}/V^{IV} couple).[96] Na$_3$V$_2$(PO$_4$)$_3$ can be also discharged to the low potential following the redox reaction of the V^{III}/V^{II} couple at ~1.6 V and additional Na$^+$ ion can be inserted at Na(2) site forming Na$_4$V$_2$(PO$_4$)$_3$.[94,97]

The first electrochemical tests of Na$_3$V$_2$(PO$_4$)$_3$ resulted with poor cycling reversibility and capacity fading caused by the intrinsic low conductivity of the phosphate framework.[98] The conductivity was highly improved while performing carbon coating to obtain Na$_3$V$_2$(PO$_4$)$_3$ /C material. As presented in Figure 1.18a, Na$_3$V$_2$(PO$_4$)$_3$ /C delivers a stable capacity of ~100 mAh g^{-1} at a current density of C/10.[99] The flat voltage plateau was observed at 3.4 V *vs.* Na$^+$/Na^0. Na$_3$V$_2$(PO$_4$)$_3$ /C also delivers stable capacity at high C rates, as demonstrated in Figure 1.18b.
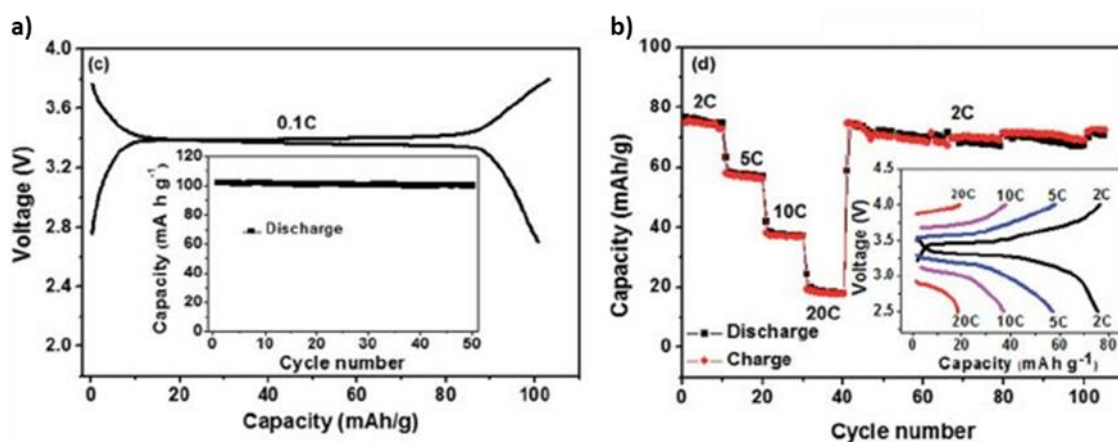
Figure 1.18: Electrochemical performances of Na$_3$V$_2$(PO$_4$)$_3$/C hierarchical nanofiber cathode materials for Na-ion batteries: (a) the first voltage–capacity curves at 0.1C rate measured in the voltage range of 2.7–3.8 V, and the inset shows the cycle stability of the Na$_3$V$_2$(PO$_4$)$_3$/C nanofiber cathode at 0.1C rate; (b) cycling performance of the Na$_3$V$_2$(PO$_4$)$_3$/C cathode at different current densities (increased from 0.2C to 20C), and the inset shows discharge–charge curves of the Na$_3$V$_2$(PO$_4$)$_3$/C nanofiber cathode at these different rates. Adapted from Liu et. al.[99]

iii. Fluorine-based transition metal compounds AM(XO$_4$)F (A=Li, Na; M= 3d transition metal; X = P, S)

One of the approaches to improve the electrochemical performance of the Li(Na)-ion battery is increasing of working potential of the cathode material. This can be obtained by using the inductive effect of the (PO$_4$)$^{3-}$ and (SO$_4$)$^{3-}$ groups and high electronegativity of the F$^-$ anion.

Various families of fluorosulfates and fluorophosphates have been investigated as positive electrode materials in both sodium and lithium-ion batteries. [100–104]

Two different types of structures have been found for LiFeSO$_4$F, tavorite and triphylite structures, as presented in Figure 1.19. Compared to the operating voltage of LiFePO$_4$ (~3.4 V *vs.* Li$^+$/Li^0),[84] the inductive effect of fluorine elevates the voltage of the Fe^{II}/Fe^{III} redox couple to 3.6 V *vs.* Li$^+$/Li^0 (tavorite)[105] and 3.9 V *vs.* Li$^+$/Li^0 (triphylite). [106,107] However, LiFeSO$_4$F exhibits only fair electrochemical performance due to the low intrinsic electrical conductivity and presence of defects in the host lattice.[108]
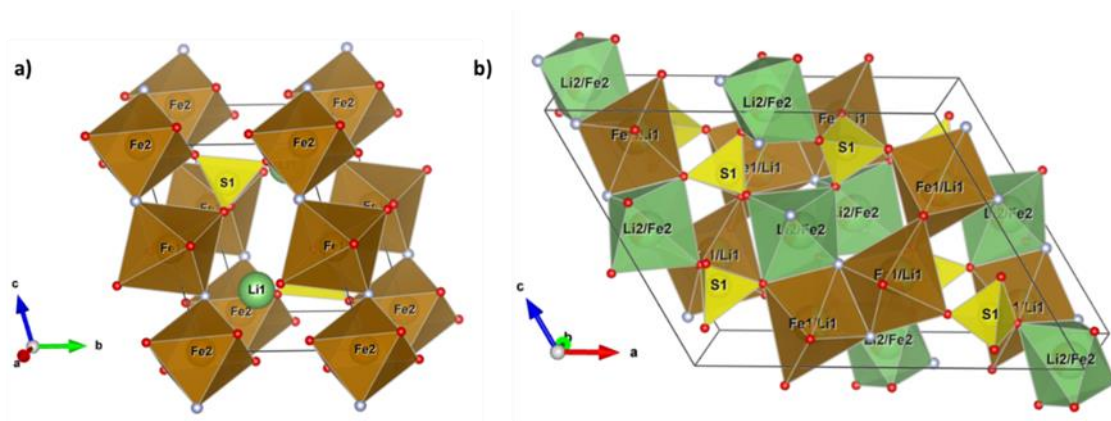
Figure 1.19: The crystal structures of (a) tavorite-type and (b) triphylite-type LiFeSO$_4$F. Iron octahedra are colored in brown, sulfur tetrahedra in yellow, whereas lithium in green. Oxygen atoms are colored in red, and fluorine in silver. In triphylite structure the octahedral positions are shared by Li$^+$/Fe^{II} ions, as indicated in the figure.

Moving to fluorophosphates, various families can be distinguished, such as: AMPO$_4$F, A$_2$MPO$_4$F, A$_3$M$_2$(PO$_4$)$_2$F$_3$, and A$_5$M(PO$_4$)$_2$F$_2$. Among them, Na$_3$M$_2$(PO$_4$)$_2$F$_3$ received most attention due to its outstanding electrochemical performances.
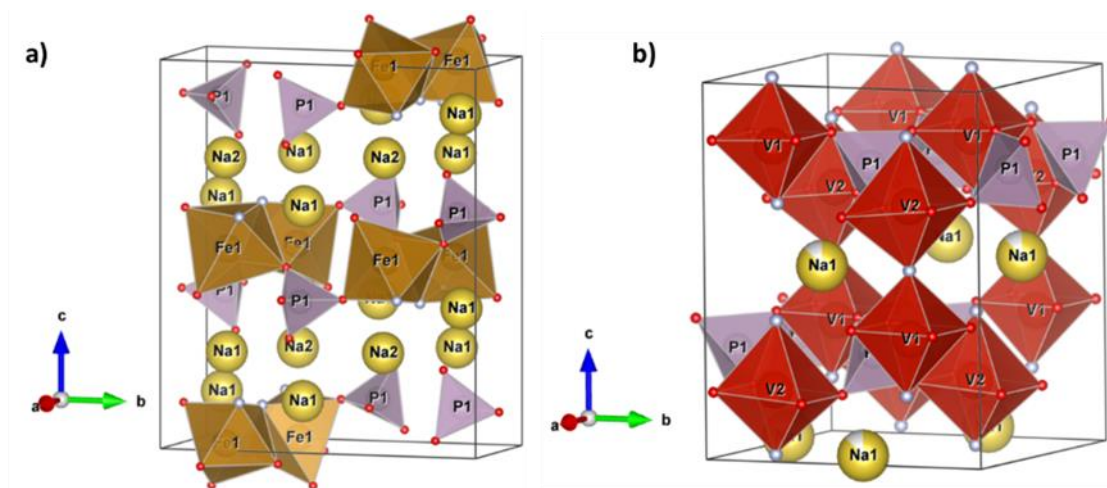
Figure 1.20: Crystal structure of (a) Na$_2$FePO$_4$F; (b) Nasicon-type Na$_3$V$_2$(PO$_4$)$_3$F$_3$. Fe and V octahedra are colored in brown and red, respectively. Na atoms are indicated as yellow balls, oxygen as red and finally fluorine as silver balls.

AMPO₄F

The large group of AMPO$_4$F fluorophosphates, where A is an alkali metal and M a transition metal is the first example of polyanionic fluorides applied for rechargeable batteries. Barker et. al.[109,110] reported for the first time the application of fluorophosphates as cathode materials on the example of NaVPO$_4$F and LiVPO$_4$F compounds. LiVPO$_4$F, adopting tavorite-type structure, was the first recognized cathode material delivering stable capacity for the $V^{IV/III}$ redox couple at ~4.2 V $vs.$ Li$^+$/Li^0, reaching approximately 115 mAh.g^{-1} at 0.5C.[110,111] Tailoring the composition resulted with obtaining novel fluorophosphate-based Li$_{1.1}$Na$_{0.4}$VPO$_{4.8}$F$_{0.7}$ reaching capacities of 156 mAh.g^{-1} at 4 V $vs.$ Li$^+$/Li^0 with prominent cycle stability (capacity retention of 98% after 100 cycles) and high energy and power capability.[112] Another member from this family, LiFePO$_4$F, also crystallizing in the tavorite framework, exhibits a theoretical capacity of 145 mAh.g^{-1} at 0.5C and redox voltage of 3.0 V $vs.$ Li$^+$/Li^0 with high capacity retention.[113]

A₂MPO₄F

Within the A$_2$MPO$_4$F family (A = Li, Na; M = Fe, Mn, Co, Ni), compounds crystallize in three structure types, depending on the connectivity of MO$_4$F$_2$ octahedra – triclinic (tavorite), monoclinic tunnel-like with $P2_1/n$ space group and two-dimensional orthorhombic with $Pbcn$ space group.[114–117] Layered Na$_2$FePO$_4$F (Figure 1.20a), with a space group of $Pbcn$ was presented as an attractive cathode material due to the high Na$^+$ mobility between the FePO$_4$F layers through two-dimensional pathways.[118] Discharge capacities of 100 mAh.g^{-1} at C/10 in the first cycle were first obtained by Recham et. al.[119] with a redox voltage of ~3.5 V $vs.$ Li$^+$/Li^0.[120]

A₃M₂(PO₄)₂F₃

A$_3$M$_2$(PO$_4$)$_2$F$_3$ (A = Li, Na; M = Al, V, Cr, Fe) compounds possess a three-dimensional framework with two distinct crystallographic sites for Li/Na cations and two channels for the cation migration. Na$_3$V$_2$(PO$_4$)$_2$F$_3$ crystallizing in the orthorhombic unit cell with the $Amam$ space group is the most widely explored vanadium based fluorophosphate due to its high theoretical capacity involving three electron transfer reaction (oxidation of V^{III} into V^{IV} and V^V). Successful extraction of two Na$^+$ ions was achieved experimentally following two plateaus at ~3.7 V and 4.2 V $vs.$ Na$^+$/Na^0 and delivering capacities of ~130 mAh.g^{-1}.[121]

Summarizing all discussed materials, it can be observed that there are almost no limitations in the design of the cathode material. Each presented family (layered oxides, polyanionic compounds) has their own advantages and disadvantages. However, the constantly increasing demand for higher performance and sustainability calls for the development of further improved materials.

1.2. Research motivation

This thesis is part of the ION-STORE project (founded by the Spanish Ministry of Economy, Industry and Competitiveness, MINECO, ref. ENE2016-81020-R) focused on the development of new battery materials. The project focusses on the positive electrode materials and solid electrolytes, whereas research conducted during this thesis will focus solely on the cathode materials. The aim is to find new compounds which could improve both specific capacity and working voltage. Seeking for alternatives to the lithium-ion battery technology, we focused on materials which could also be applied in sodium-ion batteries. This thesis therefore addresses the current needs for the development of advanced battery materials. The targeted design of the new cathode materials is based on joint computational modeling and experimental methodology, as explained below.

1.2.1. Research methodology

Two different approaches can be applied while looking for new electrode materials. The first is the design of new unreported materials, and the second involves revisiting already known structures with attractive compositional and structural features (or requiring minor compositional modifications) needed for electrode materials whose electrochemical performance has not been yet evaluated. In our work, we decided to apply the second approach. Performing this work experimentally, solely based on trial and error, would require an enormous number of hours in the laboratory, conducting syntheses and electrochemical testing, and eventually does not guarantee positive outcomes. Nowadays, computational methods can be employed to accelerate the discovery of materials.

DFT computations relying on quantum mechanics are widely used to identify structures and predict various ground state properties with high reliability and accuracy. [122–124] However, the high cost and limited access to the supercomputers on which these calculations are performed prevent their use to evaluate the properties of large numbers

of compounds in a fast and efficient manner. In the ION-STORE project, we developed a methodology to screen material databases such as the Inorganic Crystal Structure Database[125] or the Crystallographic Open Database[126] using an high-throughput approach based on Bond Valence Energy Landscape (BVEL) calculations [127] (explained in detail in the next section) to identify materials that could be good ionic Li^+/Na^+ conductors and could be potentially applied as electrodes and solid state electrolytes.[128] To do so, after a preliminary composition filtering to exclude expensive or irrelevant compounds, we evaluated the ionic migration pathways of Li^+ and Na^+ in the structures and their corresponding migration energy by means of BVEL (instead of using DFT or molecular dynamics calculations). After identifying interesting candidates, complementary DFT calculations[122] can eventually be performed to complete the materials assessement[127]. Finally, the selected candidates were validated experimentally by performing their syntheses, structural, physical and chemical characterizations and electrochemical tests. The scheme of this joined computational and experimental approach used to select the materials studied in this work is presented in Figure 1.21a. Figure 1.21b presents the results obtained from the screening of Na-based compounds in the ICSD database: the histogram shows the number of Na compounds as a function of their Na^+ migration energy (E_m) evaluated from BVEL calculations. Overall materials with $E_m < 1.5$ eV can be considered potential good ionic conductors. In the histogram, the blue and red arrows indicate the position of the families of garnet fluorides and CUBICON nitridophosphates along with their migration energies, that were selected for this thesis work.
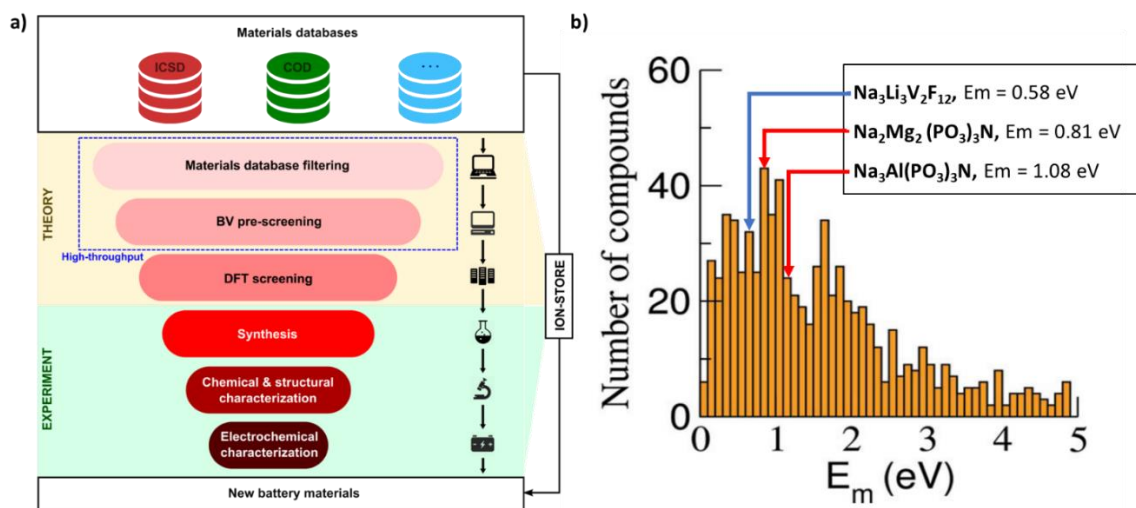
Figure 1.21: (a) Scheme of the joined theoretical and experimental approach applied to seek for new electrode materials for this thesis work; (b) Number of scanned Na-based compounds as a function of the migration energy E_m computed from BVEL calculations. The two families of compounds identified for this thesis work are indicated with the blue and red arrows.

After having identified the potential candidates for electrode materials, the selected compounds (or compositional variations) were evaluated experimentally. First, the effective synthesis methods were adapted or developed. Next, the structure of the compounds and their morphology were characterized by a combination of different techniques such as X-ray powder diffraction, scanning electron microscopy, nuclear paramagnetic resonance, elemental analysis, etc. Successfully synthesized and analyzed compounds were then subjected to electrochemical testing as electrode materials for sodium-ion or lithium-ion batteries. The initial tests were performed in coin cell or Swagelok in a half cell configuration. Eventually, the reaction mechanism was studied using *operando* XRD/Synchrotron XRD techniques.

1.2.2. Bond Valence Energy Landscape calculations

To evaluate the ability of a structure to release and uptake Li^+ or Na^+, one needs to identify the existing ion migration pathways and calculate their corresponding energy barriers. A very efficient and fast way is to use the Bond Valence method.[127] This method is based on Pauling's rules and valid mainly for ionic structures. Within this theory, each bond between ions i and j has a valence S_{ij}, which depends on the chemical nature of each element, the oxidation state of them and the observed bond length (R_{ij}). This bond valence can be characterized by an equation:

$$S_{ij} = \exp\left[\frac{R_0 - R_{ij}}{b}\right]$$

36

Where the softness parameter b and notional length of a bond of unit valence, R_o, are tabulated parameters characteristic for the *i-j* pair.[129]

The Bond Valence Sum (BVS) of a given ion *i*, is defined as the sum of the bond valences of its bonds with its N surrounding counter-ions *j*:

$$BVS(i) = \sum_{j}^{N} S_{ij}$$

Ideally, the BVS of each ion in a compound should be equal to the valence (oxidation state) of that ion. The BV approach is thus frequently used to validate newly determined crystal structures. However, this method has a limitation by considering only the first coordination shell and immobile ions. Therefore, it cannot be applied for alkali cations with high mobility such as K^+ or Na^+. Adams *et. al.*[130,131] introduced adjustments of the BV b and R_0 parameters called *soft*BV parameters in order to expand the use of the BV method for ionic conductors. This new set of parameters assumes not only the first coordination shell, but all counterions with interatomic distances up to 8 Å and equalize the b parameter to all anion types. Consequently, the BVS can be calculated for any arbitrary point in the unit cell. One can then sample the unit cell into hundreds of points and calculate in each point the bond valence sum mismatch ΔBVS for a given ion *i*, that is the difference of the calculated BVS(i) on that point and the expected valence (oxidation state) of that ion:

$$\Delta BVS(i) = |BVS(i) - V(i)|$$

This calculation of each point of the unit cell enables to map the possible positions of a given ion, such as Na or Li, in a structure.

The Bond Valence method can also be used to model and analyze the ion transport pathways in crystalline ion conductors. In 2011, Adams & Rao proposed to introduce in these calculations an effective local force field by introducing a Morse-type potential (steric repulsions) together with a screened Coulomb potential (electrostatic repulsions), in order to calculate a Bond-Valence Site Energy (BVSE, in eV) for an ion m given by the following formula[132,133]:

$$BVSE_m = D_0 \left[\sum_{j=1}^{Nx} \frac{\left(exp \left[\frac{R_0 - R_{mj}}{b} \right] - s_{min} \right)^2}{s_{min}^2} - N \right] + \sum_{i=1}^{Nm} E_{Coulomb,mi}$$

Where D_0 is bond dissociation energy, S_{min} the bond valence corresponding to $R=R_{min}$, and N_x and N_m are coordination numbers.

This approach enables to calculate the BVSE of a mobile ion in each point of the unit cell in a few seconds. This can allow to identify the potential conduction pathway which can be visualized using BV energy landscapes (BVEL).[127,129,130,134] The Bond_Str program within FullProf_Suite[135] is an effective tool create the BVEL maps, which later can be visualized in VESTA[136] program. By plotting isoenergy domains it is possible to directly visualize ion migration pathways. The threshold energy E_{th} for which these isoenergy domains percolate the unit cell in at least one dimension (i.e. form at least one infinite network that goes from cell to cell) can be taken, in general, as a rough estimate of the migration energy E_m of the mobile ion. Cathode materials can show various dimensionalities of the migration pathways (1D, 2D or 3D). For example, Figure 1.22 shows the BVEL of LiFePO$_4$, calculated using different energy cutoff values. It was found that LiFePO$_4$ requires the energy of $E_m = 0.91$ eV to create a 1D migration path for the Li$^+$ cations. To assess this value, it was compared with other calculations which provides energy barriers with high accuracy, such as nudged elastic band (NEB) and molecular dynamics based on the density functional theory as well as the experimental results.[124,137,138] The obtained results from the molecular dynamics and first-principle calculations are in the range from 0.215 eV[139] to 0.66 eV[140] whereas the experimental values of the activation energy also are reported in the wide range from 0.15 eV[141] to 0.63 eV.[142] The results obtained from the BVEL calculations suggest therefore an overestimation of the activation energy, which can be explained by the insufficient descriptors characterizing crystal structure and simplifications such as absence of the relaxation effects of the structure. However, despite this slight overestimation, the BVEL approach is highly convenient for thigh throughput calculations thanks to its simplicity, which allows fast evaluation of migration barriers and conductions pathways.
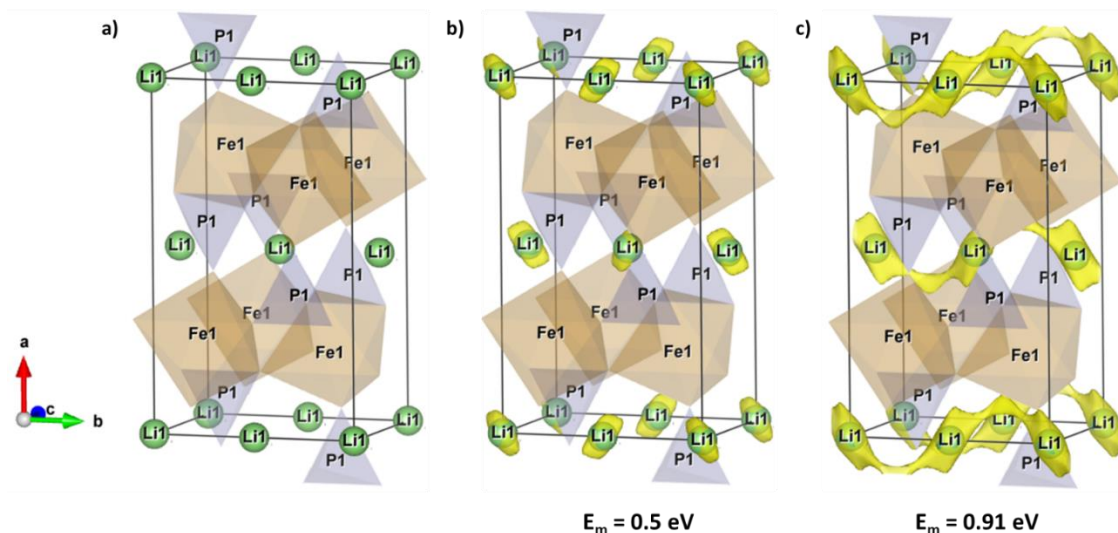
Figure 1.22: Bond Valence Energy Landscapes of Li^+ in $LiFePO_4$ calculated using different energy cutoff values, as indicated in the figure with the isosurface energy migration pathway connecting different Li^+ cations presented in (c). FeO_6 octahedra and PO_4 tetrahedra are indicated in brown and grey, respectively, while Li atoms in green.

2D migration pathways can be commonly found in layered oxide cathodes and the example is shown in Figure 1.23 using $LiCoO_2$ as a model. The 2D lithium diffusion pathway is shown in Figure 1.23b with a calculated migration energy of $E_m = 1.1$ eV. This value was compared with the ones obtained from the first principle calculations (0.83 eV[143]) and as in the case of LiFePO4 similar overestimation of ~0.3 eV was obtained for the BVEL calculations.
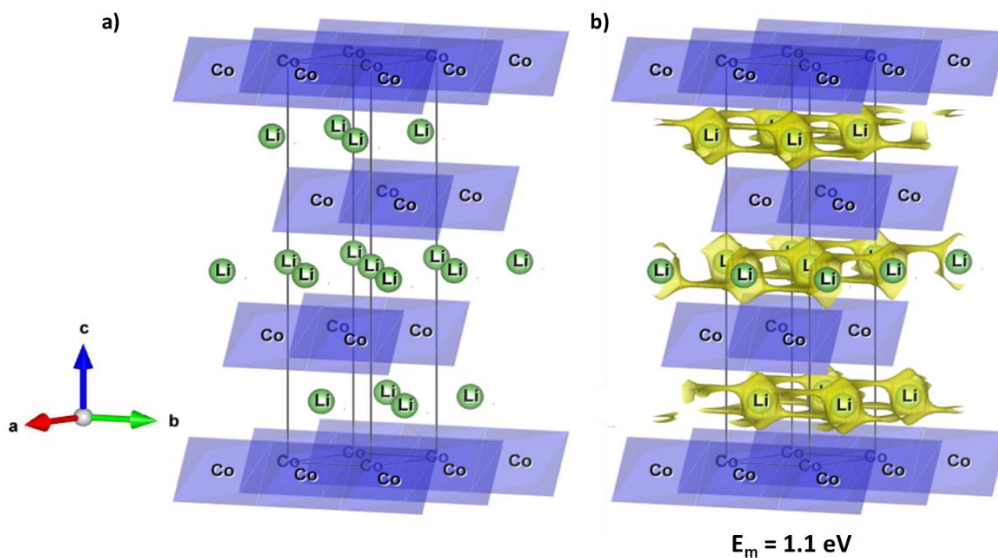
Figure 1.23: Bond Valence Energy Landscape of $LiCoO_2$ visualizing 2D migration pathway for the Li^+ mobility. CoO_6 octahedra are indicated in blue whereas lithium ions in green. The calculated isosurface migration pathway is shown in yellow.

The 3D migration pathway is also demonstrated on the example of $LiMn_2O_4$ (Figure 1.24). BVEL calculations indicate that the Li^+ ions exhibit a three-dimensional (3D) conduction pathway with calculated migration energy of $E_m = 0.85$ eV (Figure 1.24b). As in previous cases, this value was found to be higher than the reported one from the first principle calculations (0.52 eV).[144]

$E_m = 0.85eV$
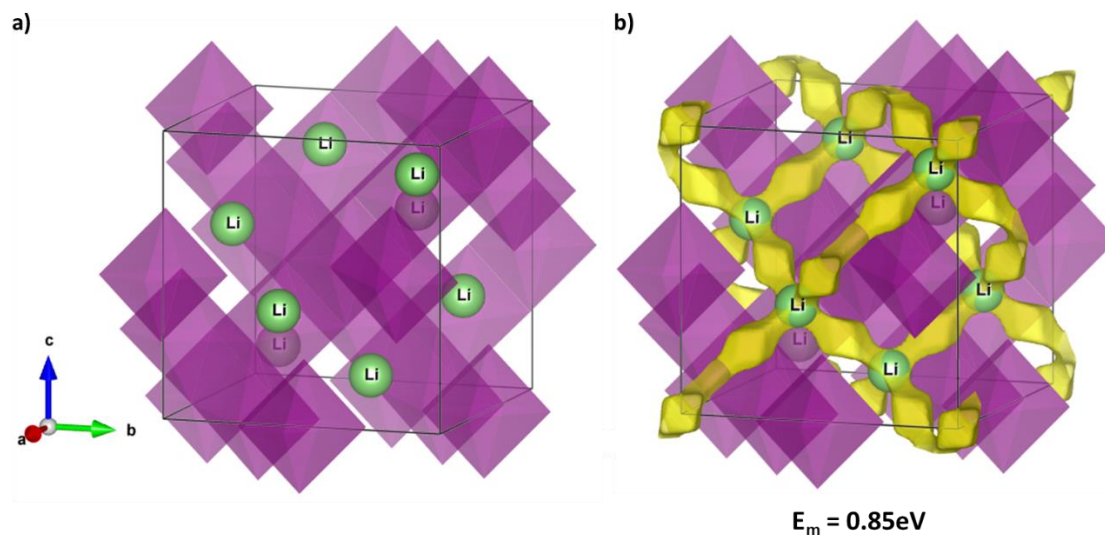
Figure 1.24: Bond Valence Energy Landscape of $LiMn_2O_4$ visualizing 3D migration pathway for the Li^+ mobility. MnO_6 octahedra are indicated in violet, whereas the Li atoms are shown as green balls.

Our group followed this approach and applied BVEL analyses to screen the databases to search for interesting candidates which could be further considered as potential electrode materials.[128] 2736 entries of Na compounds of the ICSD database (version 2013) were analyzed using these BVEL calculations (see Figure 1.21b). Through this list of compounds, we looked for structures presenting a 3D migration pathway with migration energies below 1.5 eV, that could include a 3d transition metal and with a relatively low molar mass in order not to penalize the expected capacity. For this thesis, we focused on two families of compounds, the CUBICON nitridophosphates of general formula $Na_{3-n}M_{1+n}(PO_3)_3N$ and the garnet fluorides of general formula $Na_3Li_3M_2F_{12}$, for which 3D migration pathways for Na^+ were predicted with $E_m = 1.08$ eV (M = Al, n=0), $E_m = 0.81$ eV (M = Mg, n=1) and $E_m = 0.58$ eV (M = V), respectively (Figure 1.21b). The CUBICON nitridophosphates have a theoretical capacity varying from ~65 mAh.g^{-1} for the removal of one Na^+ from $Na_3M^{III}(PO_3)_3N$ up to ~130 mAh.g^{-1} for two Na^+ removed from $Na_2M^{II}_2(PO_3)_3N$ framework. For $Na_3M^{III}(PO_3)_3N$, the capacity can be doubled while utilizing two redox couples of the transition metal. As a first choice, vanadium was selected as a transition metal since is expected to offer high working voltage and deliver

high capacity thanks to the use of both $V^{III/IV}$ and $V^{IV/V}$ redox couples, as in NASICON $Na_3V_2(PO_4)_3$.[98] Focusing on low cost and earth abundant 3d metals, iron and manganese were selected as divalent transition metals. Although being a less popular element owing to its higher cost and mining ethics, cobalt substitution usually has a beneficial effect by elevating the working voltage and improving the cyclability, therefore also this metal was included in the investigation.

The ion conduction paths of the Na^+ cations within the CUBICON $Na_{3-n}M_{1+n}(PO_3)_3N$ nitridophopshates were identified by the Bond Valence Energy Landscape (BVEL) calculations using the reported $Na_3V(PO_3)_3N$ structure (ICSD nr 188671),[145] shown in Figure 1.27.
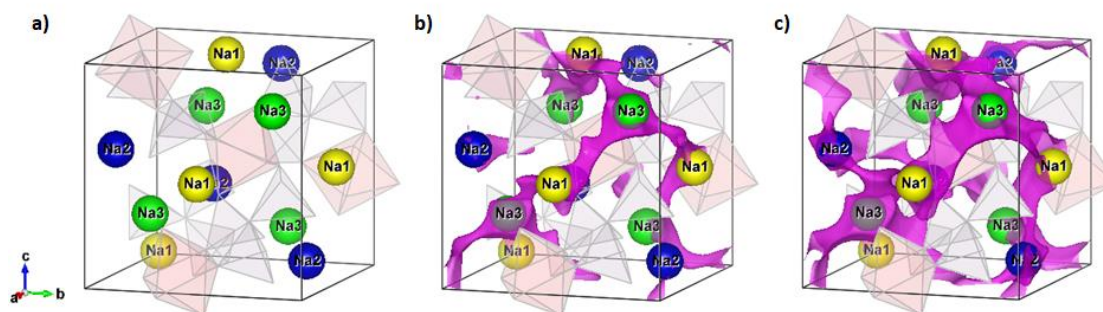
Figure 1.25: Bond Valence Energy Landscape maps of $Na_3V(PO_3)_3N$ showing the Na^+ 3D diffusion pathways for different energy cutoffs: (a) E = 0 eV, (b) E = 0.8 eV, (c) E = 1.85 eV. For better visualization, the energy values used to visualize the migration pathways are higher than the calculated percolation thresholds (0.7 eV and 1.8 eV, respectively).

The percolation of Na1 and Na3 sites through the structure is found with $E_m = 0.7$ eV, forming a 3D migration pathway (Figure 1.25b). This energy suggests a relatively high mobility of Na^+ ions located at these sites. However, the removal of the Na^+ ion at Na2 site requires an additional energy of 1.1 eV (Figure 1.25c), suggesting strong interactions of the Na^+ ions located at this site with the framework. These results suggest that Na1 and Na3 sites in $Na_3V(PO_3)_3N$ are expected to form a three-dimensional ion transport network, suggesting the possibility to extract two Na^+ ions from the structure and achieve full oxidation of V atoms to V^V reaching $NaV(PO_3)_3N$ composition. These results are in good agreement with the calculations reported for $Na_3Ti(PO_3)_3N$.[146]

On the other hand, the BVEL results of the $Na_3Li_3M^{III}_2F_{12}$ garnet family of compounds is shown in Figure 1.26b for M = Al (ICDSnr=9923). Within the garnet structure both Li and Na occupy distinct crystallographic sites (Na on 24c and Li on 24d) (Figure 1.26a), and both are expected to be mobile within the structure. The calculated BVEL migration energy considering only Na ions as mobile species was found to be relatively low

(E_{mig}=0.70 eV) (Figure 1.26b), which suggests facile removal of these alkali ions from the structure.
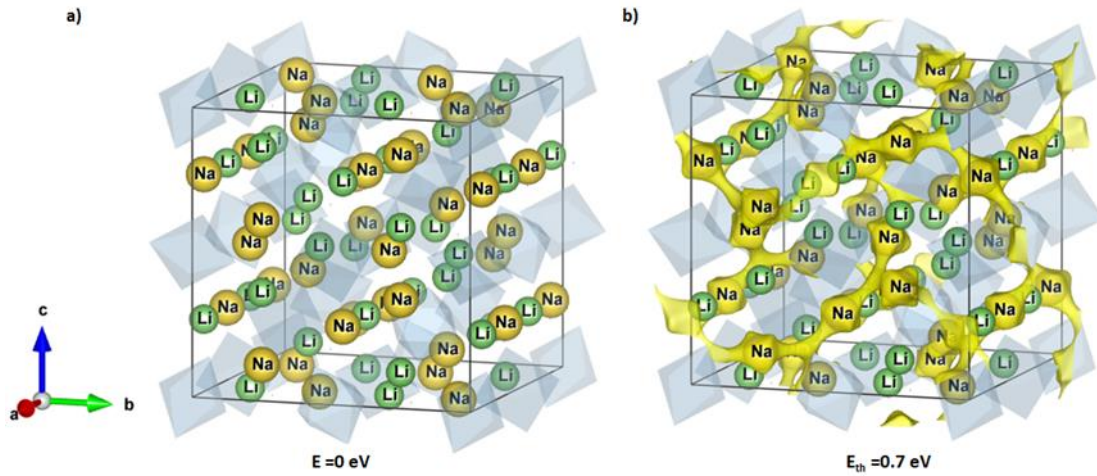
Figure 1.26: Bond Valence Energy Landscape maps of $Na_3Li_3Al_2F_{12}$ showing the Na^+ 3D diffusion pathways for (a) E = 0 eV and (b) E_m=0.7 eV. The AlO_6 octahedra are indicated in grey, and the Li and Na atoms are indicated in green and yellow.

Indeed, the Bond_Str program used to perform the BVEL calculations only enable to choose one mobile ionic species within the structure, while in the case of the garnet compounds $Na_3Li_3M^{III}_2F_{12}$, one could expect that both Na^+ and Li^+ cations can diffuse simultaneously. To check this possibility, we carried out additionnal BVEL calculations on this structure considering different possible scenarios:

a. Mobility of Na_{24c} cations with immobile Li_{24d} cations

b. Mobility of Li_{24d} cations with immobile Na_{24c} cations

c. Mobility of Na cations assuming only Na atoms in the structure (i.e. artificially replacing the Li^+ by Na^+ on the 24*d* sites for the BVEL calculations)

d. Mobility of Li cations assuming only Li atoms in the structure (i.e. artificially replacing the Na^+ by Li^+ on the 24*c* sites for the BVEL calculations)

Figure 1.27 shows the resulting BVEL isosurfaces calculated for the garnet $Na_3Li_3Ti_2F_{12}$ in each of the four possibilities described above. These can be considered as representative of the rest of the different garnets (Fe, V), as the obtained energy values for all of them are very similar. The migration energy values obtained from the calculations for each possibility are gathered in Table 1.1.
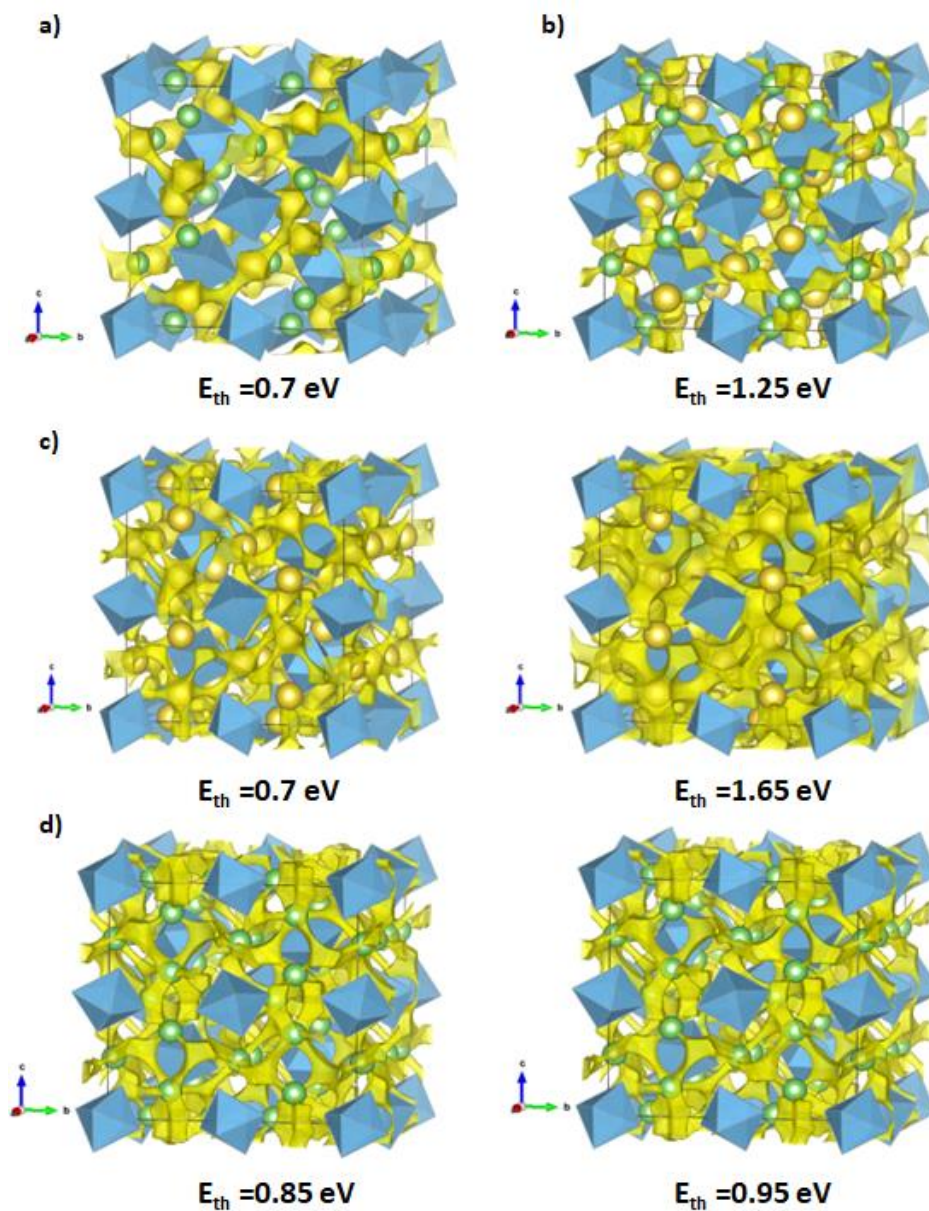
Figure 1.27: Bond Valence Energy Landscape maps of Na$_3$Li$_3$Ti$_2$F$_{12}$ showing the Na$^+$ /Li$^+$ diffusion pathways for different energy thresholds for four different possibilities: (a) mobility of Na$_{24c}$ cations with immobile Li$_{24d}$ cations with a resulting E$_{th}$ of 0.7 eV; (b) mobility of Li$_{24d}$ cations with immobile Na$_{24c}$ cations with a resulting E$_{th}$ of 1.25 eV; (c) mobility of Na cations assuming only Na atoms in the structure with a resulting E$_{th}$ of 0.75 eV and 1.65 eV corresponding to 24 c and 24 d sites respectively; (d) mobility of Li cations assuming only Li atoms in the structure with a resulting E$_{th}$ of 0.85 eV and 0.95 eV for 24 c and 24 d sites, respectively. Within garnet framework TiF$_6$ octahedra are represented in blue. Na$^+$ and Li$^+$ ions are indicated as yellow and green spheres, respectively.

Table 1.1: Calculated BVEL migration energies in $Na_3Li_3Ti_2F_{12}$ for different scenarios of ionic mobility

Mobile cation	Migration energy [eV]
a. Na_{24c} cations with immobile Li_{24d} cations	0.7
b. Li_{24d} cations with immobile Na_{24c} cations	1.2
c. Na cations assuming only Na atoms in the structure, occupying **24c** and **24d** sites	0.7 + additional 0.9 to remove from $24d$ site
d. Li cations assuming only Li atoms in the structure, occupying **24c** and **24d** sites	0.7 + additional 0.1 to remove from $24c$ site

Considering the first two options, in which only Li^+ or Na^+ cations are mobile (but not both), the most favorable scenario would be the mobility of the Na^+ ions from the $24c$ sites (example a), as the migration energy is relatively low (0.7eV) and is comparable to the calculated energy for $Na_3V(PO_3)_3N$ (Chapter 2); while the mobility of Li^+ ions from the $24d$ sites (example b) require additional 0.5 eV. This might be explained by the fact that in this latter case the immobile Na^+ cations on the $24c$ sites prevent the migration of the Li^+ ions on the $24d$ sites. Assuming only Na^+ ions within the structure occupying both $24c$ and $24d$ sites (example c), the removal of Na_{24d} cations would require additional 0.9 eV; i.e. the Na^+ cations would be rather trapped on this site. On the contrary, assuming only Li^+ ions within the structure occupying both $24c$ and $24d$ sites (example d), the removal of Li^+ ions from the $24c$ site would require only additional 0.1 eV, which could be interpreted as more facile access to second site of the cations after removing ones from the main site. However, the calculated difference between scenarios is quite low and might be within BVEL error. These results suggest that assuming that both Na_{24c}^+ and Li_{24d}^+ collaboratively migrates, then the Li^+ cations can be easily removed from the $24d$ sites. Therefore, one can expect that both Na and Li cations could be removed (and reinserted) upon oxidation (reduction) of these garnet compounds.

Combined with a theoretical capacity of ~130 mAh.g^{-1} considering the reversible insertion and/or extraction of two alkali cations and a high voltage resulting from F electronegativity, these materials could be appealing Li-ion or Na-ion cathode materials. Besides the reported compounds with trivalent Mn and V; Fe, Ti and Co were also targeted to be synthesized. All these trivalent transition metals are expected to provide good electrochemical performance through redox reactions of the M^{III}/M^{II} and M^{III}/M^{IV} couples.

Overall, both selected CUBICON and garnet materials are expected to outmatch the currently widely used cathode materials, as indicated in Figure 1.28.
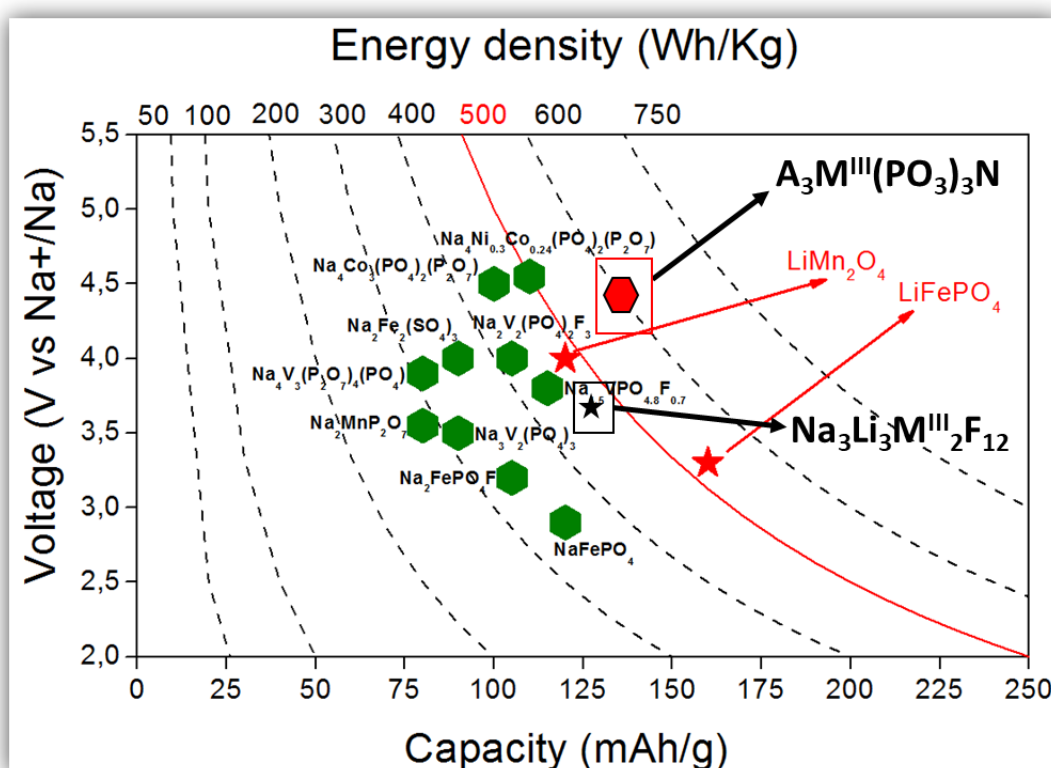
Figure 1.28: Schematic representation of the plot of potentials vs. capacity of the discussed cathode materials for Na-ion and Li-ion battery cathode materials together with the theoretical performance of the CUBICON nitridophosphate $A_3M^{III}(PO_3)_3N$, where in the graph $M=V^{III}$ and fluoride garnet families, $Na_3Li_3M^{III}_2F_{12}$ where in the graph $M=V^{III}$.

1.2.3.   Thesis outline

The thesis comprises seven chapters. In the first part of this Chapter 1, a brief review of the research and development of the lithium and sodium rechargeable battery with the focus on cathodes materials has been presented. In the second part of this chapter, the research context of this PhD has been presented, including research objectives and a

description of the research methodology. Chapters two to six are dedicated to the experimental part and are divided into two parts – Part A, which is focusing on the family of nitridophosphate compounds, and Part B, focusing on the selected fluoride families. Chapter seven is the concluding chapter with the summary of the entire work and future perspectives.

1.3. Conclusion

The intention of this chapter was to provide an insight into battery technology and its development through the years. The key breakthroughs in the battery history were presented with the main focus on the Li-ion and Na-ion technology. Since the aim of this thesis is the development of cathode materials, the research in this field was intended to be broadly discussed.

As Na-ion and Li-ion batteries rely on the same principles, the research in cathodes for the Na technology strongly benefits from the great developments achieved in the Li field within last years. It has allowed to accelerate the research into new electrode materials to reach comparable energy density to the current Li-ion technology. Cathode materials can be divided into different groups as layered oxides, polyanionic compounds, Prussian blue analogues and organic compounds, however the main research efforts have been put into the first two groups. Oxide materials provide high potentials and high energy density. $LiCoO_2$ was the first commercialized cathode material with an excellent electrochemical performance. Due to the economic and environmental issues, strong effort was put to replace toxic cobalt by more sustainable and environmentally friendly elements. The developed $LiMn_2O_4$ spinel material was another great success and currently is implemented at large scale such as electric vehicles. Thanks to their 3D framework, polyanionic compounds are characterized by a great structural stability upon long-term cycling. Additionally, fully delithiated/desodiated phases also usually remain stable, which translates into reaching high capacities and cycling stabilities with these materials. The open structures of these compounds favor the alkali ionic diffusion through various migration pathways. The use of the inductive effect of the $(XO_4)^{n-}$ groups together with the electronegative ions such as N^{3-}, F^-, S^{2-} allows to tune the working potential of the redox couple. Additionally, microstructural modifications such as decreasing the particle size to the nanoscale and carbon coating results in a significant increase of the

electrochemical performances of the evaluated materials, as was demonstrated in the LiFePO$_4$/C composite having a great commercial success.

Different strategies can be adapted to develop new electrode materials. One of them is to focus on already known materials (minerals, compounds reported in the material databases) and look for the key characteristics required for the good cathode material – open structure, pathways for the ionic mobility, the presence of the transition metal which could undergo redox reactions, etc. In our work we focused on this strategy and focused on the materials which are expected to provide high voltage and high capacity in Na-ion cells while having a low migration energy, which was evaluated by the BVEL method following a high throughput approach. Among thousands of screened compounds, we concentrated on two families of compounds – nitridophosphates and garnet fluorides – and the next chapters will present the experimental results on these materials.

PART A

Nitridophosphates

Part A

Outline

Introduction of Part A

Armand and Arroyo de Dompablo[147] predicted from theoretical calculations (DFT) that the substitution of oxygen by nitrogen in Li_2FeSiO_4 has a beneficial effect on both tuning of the voltage of redox couple and the overall specific capacity due to the redox activity of N^{III-} anion. As presented in Figure A.1a.; based on first principle calculations, the lithium intercalation voltage of the Fe^{II}/Fe^{III} and Fe^{III}/Fe^{IV} redox couples increases significantly with the amount of substituted oxygen by nitrogen in the structure. Figure A.1b shows fragment of the structure of $Li_2FeSiO_{3.5}N_{0.5}$. The calculated position of N atom is located in the vertex of SiO_4 and LiO_4 tetrahedra and there is no direct bond between N and Fe atoms.
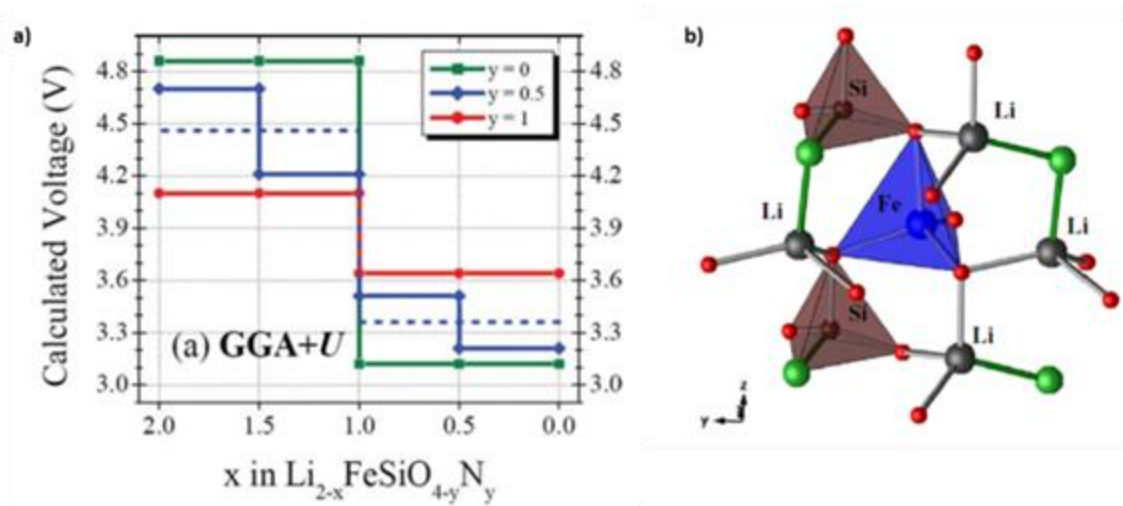
Figure A.1.: (a) Schematic voltage-Li composition curve for Li_2FeSiO_4 (green); $Li_2FeSiO_{3.5}N_{0.5}$ (blue) and Li_2FeSiO_3N (red) at low temperature obtained from the DFT + U method. The dashed line indicates the average voltage of $Li_2FeSiO_{3.5}N_{0.5}$, as the voltage processes at 3.5 and 4.2 V are associated with the redox activity of N ions.; (b) Fragment of the structure of $Li_2FeSiO_{3.5}N_{0.5}$ where the position of N atom in the vertex of SiO_4 and LiO_4 tetrahedra is denoted as green ball. [148]

It can be observed that the removal of the first Li^+ ion (oxidation of Fe^{II} into Fe^{III}) occurs at higher voltage in $Li_2FeSiO_{3.5}N_{0.5}$ (3.35 V *vs.* Li^+/Li^0) and Li_2FeSiO_3N (3.65 V *vs.* Li^+/Li^0), whereas the redox reaction of the Fe^{III}/Fe^{IV} redox couple corresponding to the removal of the second Li^+ occurs at much lower voltage for N-substituted compound (4.1 V *vs.* Li^+/Li^0) than in Li_2FeSiO_4 (4.86 V *vs.* Li^+/Li^0). This phenomenon can be explained by the strong inductive effect of nitrogen, which forms a more covalent Si-N bond as compared to a Si-O bond, on the Fe^{II} ion in the Fe-O-Si-N chain, raising the oxidation potential of Fe^{II}. Additionally, the nitrogen substitution has another large beneficial effect on the stabilization of the delithiated phase. While the Li_2MSiO_4 compounds are known

for their structural transformations occurring in the delithiated phase, according to the first principle calculations, N-substituted $Li_2FeSiO_{4-y}N_y$ possess higher thermodynamic stability.

Nitrogen substitution in polyanionic compounds can also have an effect on the changes in the local symmetry enabling greater structural diversity, and therefore enlarging the chemical and structural space.[149] Rousseau et. al.[150] performed *ab initio* simulations on the effect of the partial oxygen-to-nitrogen substitution on the energy density in sodium sulfate, $Na_2Fe_2(SO_4)_3$. After nitrogen substitution, the compound resulted with a composition of $Na_3Fe_2(SO_4)_2(SO_3N)$ with N atom located in the vertex of SO_3N tetrahedra. The introduction of nitrogen significantly increased the theoretical energy density from 480 Wh.kg^{-1} to 650 Wh.kg^{-1} as its redox activity also contributes in the further oxidation of the structure improving the overall specific capacity Contrary to Li_2FeSiO_4, introduction of nitrogen into $Na_2Fe_2(SO_4)_3$ structure has very mild effect on the voltage of the Fe^{II}/Fe^{III} redox couple which remains at its high level of 3.8 V., which might be related to lower inductive effect on the sulfate group than silicate. . All these attractive properties of the oxygen-to-nitrogen substitution represent a driving force to explore N substituted compounds as potential electrode materials.

The preparation of oxynitrides requires the use of NH_3 gas, or the use of alternative synthesis routes (solvothermal, hydrothermal) with nitride-based precursors as a source for N.[151,152] Marchand et. al.[153] investigated the introduction of nitrogen in the tetrahedral phosphorous environment, unveiling the new class of nitridophosphate materials. They observed that the introduction of nitrogen results with a significant modification of the physical and chemical characteristics of the compounds. For example, the investigated Na-M^{II}-P-O-N system (where M^{II} = Mn, Fe) possesses much higher thermal stability and chemical durability than corresponding phosphates and oxides. This system has been widely studied afterwards and it was observed that depending on the conditions of heat treatment under NH_3 flow and the composition, different families of compounds can be obtained.[154–157]

Among them, the interesting family of CUBICON nitridophosphates was reported with two distinct compositions of $M^I_3M^{III}P_3O_9N$ where M^I= Na, K; M^{III} = Al; Ga; Fe; Cr; Mn and $M^I_2M^{II}_2P_3O_9N$, where M^I = Na; M^{II} = Mg; Co.[157] The structure of $Na_3AlP_3O_9N$ was eventually solved for the first time by Conanec *et al*. in 1994, based on the studies of X-ray diffraction on a single crystal.[158] Almost twenty years later, Lee *et al*. reported the

crystal structure of $Na_2Mg_2P_3O_9N$ from the Rietveld refinement of the powder X-ray diffraction data and bond valence sum calculations.[159] Figure A.2. presents the crystal structure of both $M^I_3M^{III}P_3O_9N$ and $M^I_2M^{II}_2P_3O_9N$.
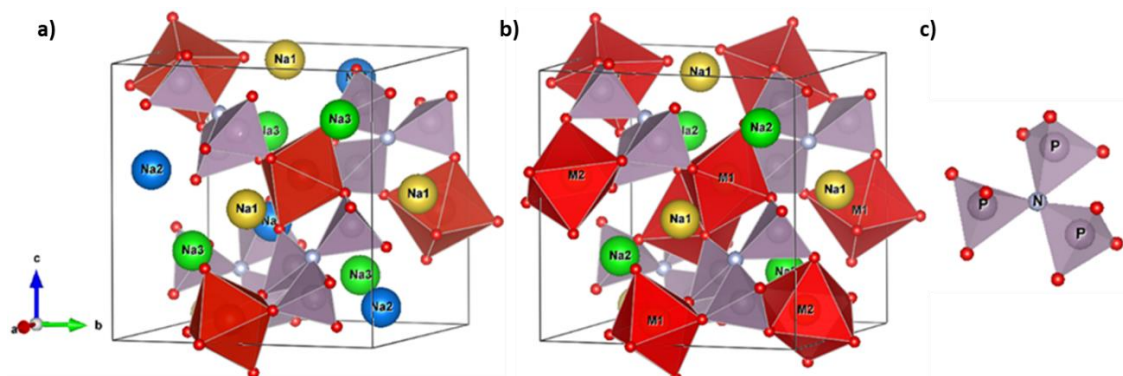
Figure A.2. Crystal structure of (a) $Na_3M^{III}(PO_3)_3N$ and (b) $Na_2M_2^{II}(PO_3)_3N$; (c) $(P_3O_9N)^{VI-}$ anion showing three phosphorous tetrahedra vertex-sharing the N atom.

These compounds crystallize in a cubic unit cell ($P\,2_13$ space group) and their structure can be described as isolated MO_6 octahedra interconnected through corners by $(PO_3)_3N$ units formed by three nitridophosphate PO_3N tetrahedra sharing a corner occupied by a nitrogen atom (Figure A.2.c). In the case of $Na_3M^{III}P_3O_9N$, sodium cations occupy three independent crystallographic sites (represented with yellow, green and blue spheres in Figure A.2.a); while in $Na_2M^{II}_2P_3O_9N$, the second divalent transition metal (M2) occupies the octahedral site corresponding to the position of Na2 atom in $Na_3M^{III}P_3O_9N$ (Figure A.2.b). The open structure of these compounds enables the migration of the alkali cation. Together with the strong inductive effect of the nitrogen in PO_3N group on the MO_6 octahedra, having great impact on the operating voltage, makes them attractive candidates for electrode materials.

The group of Khalifah explored several members of the $M^I_3M^{III}P_3O_9N$ and $M^I_2M^{II}_2P_3O_9N$ family (M = Fe[160], Ti[146]) as potential cathode and solid electrolytes.[146,160,161] First, they investigated the iron nitridophosphates $M_2Fe_2(PO_3)_3N$ (M = Li, Na).[160] While cycling in hybrid-ion configuration *vs.* Li^+/Li, average capacities of ~40 mAh.g^{-1} were obtained with large polarization (Figure A.3.a). They explained that such a poor performance was caused by the low Na^+ mobility within the $Na_2Fe_2(PO_3)_3N$ framework.

To improve the electrochemical performance, ion exchange of Na^+ by Li^+ was employed, claiming that the much smaller ion radius of Li^+ (0.74 Å) compared to Na^+ (0.92 Å) will significantly improve the kinetics of the alkali cation. Although only a small amount of

Li was introduced during the ion exchange (~0.3), the electrochemical performance of $Li_{2-x}Fe_2(PO_3)_3N$ significantly improved, reaching discharge capacities of ~120 mAh.g^{-1}, corresponding to 85% of theoretical capacity (Figure A.3.b).
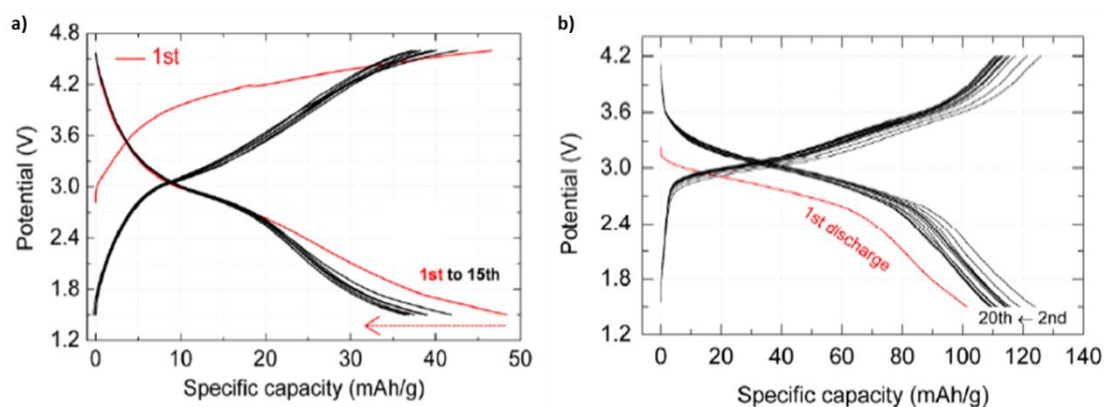
Figure A.3.: (a) Charge-discharge profile of Na$_2$Fe$_2$(PO$_3$)$_3$N cycled *vs*. Li at a C/20 rate; (b) Charge-discharge profile of Li$_{2-x}$Fe$_2$(PO$_3$)$_3$N cycled *vs*. Li at a C/10 rate.[160,161]

The second CUBICON system they investigated as cathode material was Na$_3$Ti(PO$_3$)$_3$N.[146] They performed coupled DFT and BVEL calculations on CUBICON Na$_3$TiP$_3$O$_9$N, where Na ions are occupying three independent crystallographic sites. These calculations reveal that the Na1 and Na3 sites exhibit lower migration energy, indicating possible mobility of two Na ions forming isotropic three-dimensional ion transport network. Two possible pathways between those sites have been identified (marked as L13 and S13 in Figure A.4.) and the DFT calculations indicate that the longer L13 pathway has lower energy. The high value of the diffusion energy for the Na$^+$ located in Na2 site suggests that this ion remains immobile within the Na$_3$TiP$_3$O$_9$N framework. [146]
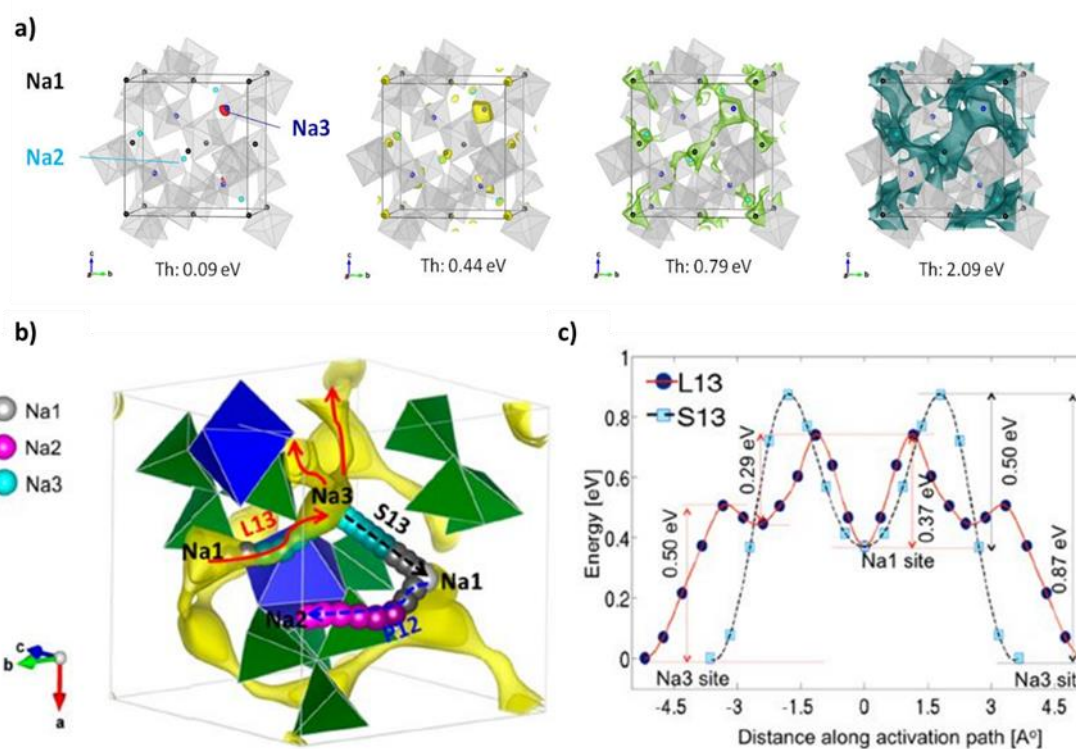
Figure A.4. : (a) Bond Valence Energy Landscape of Na₃Ti(PO₃)₃N calculated using different energy threshold values; (b) visualization of the potential diffusion pathways evaluated using DFT+U calculations superimposed on the BVS map; (c) DFT+U energies for points along Na1-Na3 pathways.[146]

The expected mobility of the Na$^+$ cation was inspected by cycling a cell composed of Na₃Ti(PO₃)₃N as active material *vs.* metallic Na (Figure A.5.). The performed test resulted with reversible Na$^+$ (de)intercalation with an average working potential of around 2.7 V *vs.* Na$^+$/Na originating from the redox activity of Ti^{III}/Ti^{IV} couple. The obtained capacities of ~60 mAh.g^{-1} at C/20, indicate the reversible mobility of less than one Na ion (theoretical capacity of 74 mAh.g^{-1}). Good reversibility and small volume changes allow the capacity to remain stable over the subsequent 50 cycles.
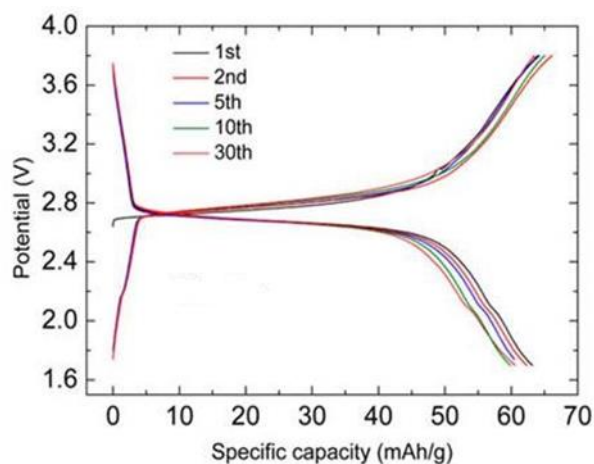
Figure A.5. : Electrochemical performance of Na$_3$Ti(PO$_3$)$_3$N - charge/discharge profile *vs*. Na metal at C/20 rate.[146]

From the shape of the voltage curve, the authors concluded that the mechanism is solid solution (no evidence of a plateau). DFT calculations from the same authors predict ordering of the Na vacancies on the Na$_1$ site in partially desodiated phases. However, as this ordering has only slightly positive formation energies relative to the desodiated Na$_2$TiP$_3$O$_9$N and fully sodiated Na$_3$TiP$_3$O$_9$N phases, it can be considered that the solid-solution mechanism can be accessible at room temperature, in agreement with the experimental results.

The experimental cycling results indicate the removal of one sodium ion which corresponds to the redox activity of the Ti$^{III/IV}$ redox couple (Figure A.4.), which suggests that the substitution of the Ti by other trivalent transition metal could result in reaching higher capacity through accessing two oxidation states.

Encouraged by these results, we directed our interest towards the evaluation of other transition metals which could be introduced into the framework of the Na$_3$MP$_3$O$_9$N and Na$_2$M$_2$P$_3$O$_9$N nitridophosphates. These results will be presented in the following three separate chapters.

In Chapter two, the trivalent Na$_3$V(PO$_3$)$_3$N and Li$_3$V(PO$_3$)$_3$N will be introduced as the first investigated members of the aforementioned nitridophosphate family. Two distinct synthesis methods (solid state under ammonia flow and solid-state using melamine as nitrogen source under argon flow) were used to synthesize Na$_3$V(PO$_3$)$_3$N. A Na-to-Li ion-exchange route to obtain Li$_3$V(PO$_3$)$_3$N will also be presented. Next, exhaustive structural and morphological analysis will be described. Both compounds were evaluated as a

cathode material in a half-cell configuration for both lithium-ion and sodium-ion batteries. Lastly, the cation insertion/extraction mechanism will be analyzed in detail by performing *operando* Synchrotron XRD measurements.

Chapter three will be dedicated to different solid solutions of CUBICON nitridophosphates focusing on low cost and earth abundant 3d metals such as iron and manganese. Additionally, cobalt also will be investigated due to the expected elevated working voltage. As in Chapter two, detailed analysis of the structure and electrochemical performance of all investigated materials will be presented.

Chapter four will introduce a novel family of sodium manganese nitridophosphates $A_{1.1}Mn_3P_3O_8N_2$ (A = Na/Li). Their crystal structure and proposed structural models will be introduced. Combination of complementary characterization techniques as well as theoretical calculations applied to solve the novel structure will be exhaustively discussed. Additionally, the potential application of these materials as cathodes for lithium-ion and sodium-ion batteries will be investigated by performing electrochemical measurements in half-cell configuration. The expected working voltage of both compounds will be calculated by DFT and the potential cation migration pathways will be evaluated by performing Bond Valence Energy Landscape (BVEL) calculations.

Finally, this part of the thesis will be summarized with the general conclusions and the perspectives for the future work.

Chapter 2 - Structural and electrochemical characterization of sodium and lithium vanadium nitridophosphates (Na$_3$V(PO$_3$)$_3$N and Li$_3$V(PO$_3$)$_3$N)

Outline

Chapter 2 - Structural and electrochemical characterization of sodium and lithium vanadium nitridophosphates ($Na_3V(PO_3)_3N$ and $Li_3V(PO_3)_3N$)

2.1. Introduction

Vanadium-based compounds were chosen as the first system to explore due to the possibility of going through two different oxidation states (V^{III}/V^{IV} and $V^{IV/V}$) associated with the extraction of two Na^+ ions at high voltage, as explained in the introduction.

The chapter, which focusses on both Na- and Li polymorphs of $A_3V(PO_3)_3N$, will be divided into two parts. In the first part, we will present two distinct synthesis routes leading to the preparation of $Na_3V(PO_3)_3N$. Next, the detailed structural and morphological analysis will be reported combined with DFT calculations, used to calculate the predicted working voltage of both V^{III}/V^{IV} and $V^{IV/V}$ redox couples together with the stability of the oxidized $Na_2V(PO_3)_3N$ and $NaV(PO_3)_3N$ phases. These predictions will be later evaluated by performing detailed electrochemical analysis using different electrolytes. Detailed analysis of the mechanism of Na^+/Li^+ insertion/extraction will be described based on the operando SXRD analysis.

The second part of the chapter will be devoted to $Li_3V(PO_3)_3N$, obtained by the Li/Na chemical ion exchange of $Na_3V(PO_3)_3N$. Structural analysis, electrochemical performance and NMR analysis uncovering Li mobility within the framework will be presented.

Prior to this work no publications reporting the electrochemical performance of $Na_3V(PO_3)_3N$ were found. However, during the course of this work, an US patent related to cubic ion conductors was uncovered, reporting an electrochemical performance of 35 $mAh.g^{-1}$ for $Na_3V(PO_3)_3N$ *vs.* Na^+/Na^0 cycled at C/20 rate and 73 $mAh.g^{-1}$ for ionically exchanged $Li_3V(PO_3)_3N$ cycled *vs.* Li^+/Li^0 at C/15 rate.[161]

2.2. Na₃V(PO₃)₃N

2.2.1.   Synthesis

Different nitridation techniques are described in the literature to obtain nitridophosphates. In all cases these are obtained through high temperature solid-state synthesis, either under ammonia flow (ammonolysis), either using melamine, or phosphorous nitride (PON) as nitrogen sources under argon. [161,162]

In this work we first prepared Na₃V(PO₃)₃N by the ammonolysis route, adapting the synthesis protocol reported by Kim and Kim.[145] Powders of NaPO₃ and V₂O₅ were taken in a molar ratio 1.1:1 and milled in a FRITSH Pulverisette 7 ball-miller under air for 20 min in a 45 ml zirconium oxide jar in a 1:20 powder-to-ball mass ratio (15 mm zirconium oxide balls were used). The as-prepared yellow mixture of precursors was placed into an alumina or graphite crucible and deposited in a tubular furnace for the heat treatment.

Na₃V(PO₃)₃N is expected to form according to the following reaction:

$$6NaPO_3 + V_2O_5 \xrightarrow{\quad T,\ NH_3 \quad} 2Na_3V(PO_3)_3N$$
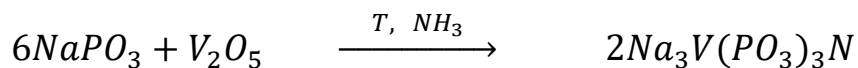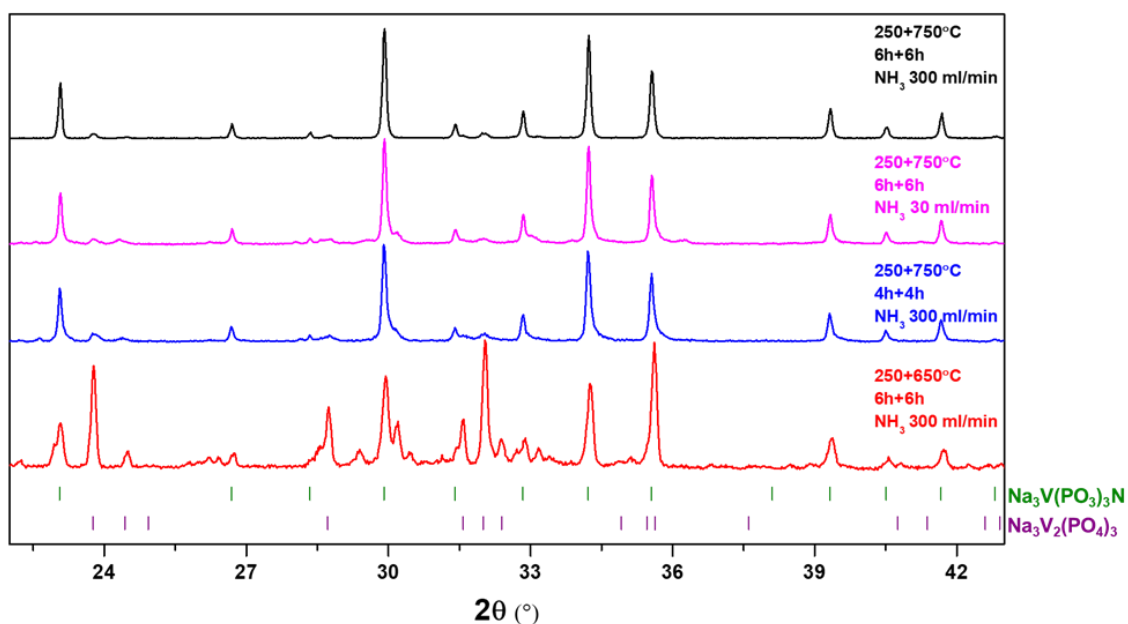
Figure 2.1: XRD patterns of the samples of $Na_3V(PO_3)_3N$ prepared under different conditions (temperature, time and NH_3 flow). Green and violet vertical bars indicate the position of the Bragg reflections of the $Na_3V(PO_3)_3N$ and NASICON-type $Na_3V_2(PO_4)_3$ phases, respectively.

$Na_3V(PO_3)_3N$ was indeed successfully obtained since the very first trials, but with a non-negligeable large amount of impurities (red curve in Figure). The synthesis conditions (temperature, time, flow of NH_3) were optimized during my master thesis to a two-step annealing process of 6 h each, first at 250 °C and the second one at 750 °C, both with a heating ramp of 10 °C/min, under constant ammonia flow of 300 ml/min.[163] Between these two steps, the powder was cooled down to room temperature, grinded manually in the mortar and placed back into the crucible for further heat treatment. After the second annealing step, the furnace was cooled down to room temperature and the recovered green powder from the crucible was grinded manually in the mortar.

Nonetheless, it was not possible to eliminate completely the impurities of NASICON-type $Na_3V_2(PO_4)_3$ phase (indicated by violet vertical bars in Figure); based on the Rietveld refinement (Figure 2.1a) ~5 % wt. was detected in all samples. To decrease the amount of impurities Liu[161] suggested the use of urea, which by decomposing into NH_3 and HNCO at around 350 °C reduces the oxygen concentration around the starting materials. Although the addition of urea during the synthesis of $Na_3Ti(PO_3)_3N$ successfully removed the NASICON-type impurities,[161] in our trials after adding urea to the precursors we observed increased amount of NASICON-type impurities (>7%).

Alternatively, the precursors ($NaPO_3$ and V_2O_5) were mixed with melamine in 1:5 molar ratio by ball milling, placed in the graphite crucible and heated for 10 h at 700 °C under

61

low Argon flow, following the synthesis protocol suggested by Zhang et al. [164] After the heat treatment the crucible was cooled down to room temperature, and the sintered product was manually grinded in the mortar. As a result, a green powder was obtained and the XRD confirmed the presence of only $Na_3V(PO_3)_3N$ phase, without NASICON-type impurity (seeFigure 2.2As this synthesis was realized at a later stage of the thesis, most of the characterization was performed on the sample obtained from the ammonolysis synthesis (with a small amount of NASICON-type impurities).

In each section the sample (ammonolysis, melamine or both) used for the analysis will be indicated.

2.2.2.   Chemical and structural characterization

2.2.2.1. X-ray and neutron powder diffraction

The purity of each sample was evaluated by powder XRD. X-ray diffraction patterns were refined with the help of the FullProf program[135] using the cubic structure of $Na_3V(PO_3)_3N$ proposed by Kim and Kim as starting values. [145]

Neutron powder diffraction (NPD) was also used to confirm the structure of $Na_3V(PO_3)_3N$ and the position of nitrogen atoms on the best sample produced by ammonolysis. NPD was performed on the ECHIDNA high-resolution diffractometer at ANSTO facilities (Australia). The NPD pattern was acquired using a wavelength of $\lambda = 1.622$ Å in the 2θ range $4 \leq 2\theta \leq 164°$ with a step size of 0.05°.

The XRD and NPD patterns of the sample of $Na_3V(PO_3)_3N$ produced by ammonolysis were analyzed with a combined Rietveld refinement, using a relative weight of 0.5:0.5 between both patterns. The lattice parameter, relative atomic positions, and isotropic displacement factor (B_{iso}) were refined, whereas the Na occupancies were fixed for the refinement. Figure 2.1 and the corresponding crystallographic data are shown in Table 2.1. Details regarding bond distances within the framework are gathered in Table 2.2.
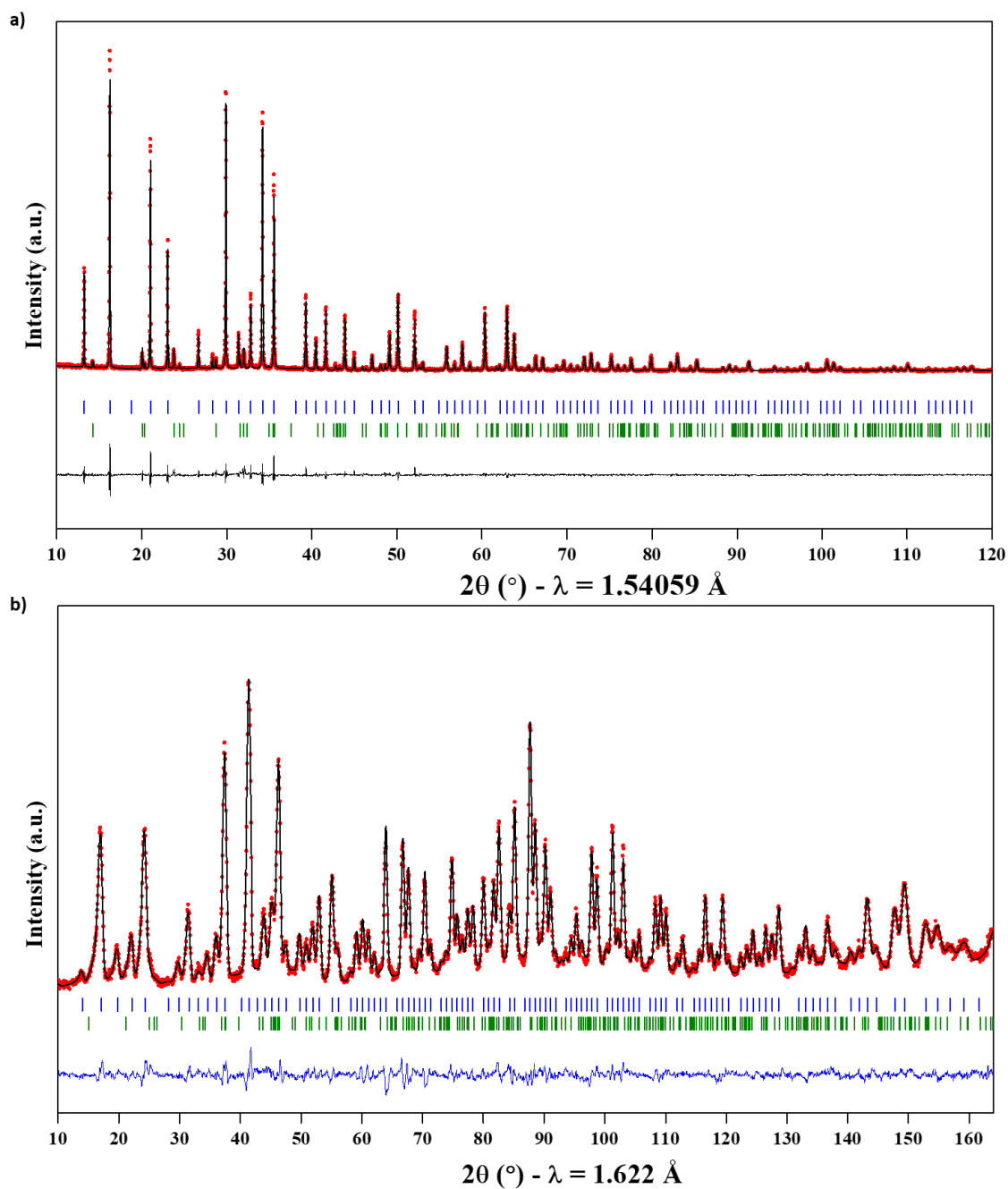
Figure 2.1: Rietveld-refined XRD (top) and NPD (bottom) patterns of Na$_3$V(PO$_3$)$_3$N obtained by ammonolysis synthesis. Red circles, black and blue lines represent the observed, calculated and difference patterns, respectively. The positions of the Bragg reflections of the *P*2$_1$3 space group are shown as blue vertical bars. Green bars denote a small (< 7 %) contribution of NASICON-type Na$_3$V$_2$(PO$_4$)$_3$.

63

Table 2.1: Crystallographic data and atomic coordinates of $Na_3V(PO_3)_3N$ obtained from ammonolysis determined from a combined refinement of XRD and NPD data.

S.G.: $P2_13$						
XRD: a =9.444(1) Å		$V = 842.32(2)$ Å^3		R_{Bragg} =4.9 %	$\chi^2 = 2.8$	
NPD: a =9.443(1) Å		$V = 842.06(3)$ Å^3		R_{Bragg} =4.4 %	$\chi^2 = 2.8$	
Atom	Wyckoff position	x/a	y/b	z/c	Occupancy	B_{iso}
P	12b	0.332(1)	0.082(1)	0.245(1)	1	0.56(2)
V	4a	0.579(2)	0.579(2)	0.579(2)	1	0.22(2)
Na1	4a	0.012(3)	0.012(3)	0.012(3)	1.0(2)	1.41(5)
Na2	4a	0.391(3)	0.391(3)	0.391(3)	0.97(2)	1.01(2)
Na3	4a	0.800(4)	0.800(4)	0.800(4)	0.96(3)	2.08(4)
O1	12b	0.271(2)	-0.0242(2)	0.349(2)	1	1.12(1)
O2	12b	0.372(2)	-0.001(2)	0.111(2)	1	1.07(1)
O3	12b	0.451(3)	0.167(3)	0.307(3)	1	1.03(1)
N	4a	0.196(1)	0.196(1)	0.196(1)	1	0.79(2)

Table 2.2: Bond distances within the $Na_3V(PO_3)_3N$ framework.

Bond type	bond distance [Å]
V-O(1)	1.982(5) Å x3
V-O(2)	1.993(6) Å x3
P-O(1)	1.540(6) Å
P-O(2)	1.533(6) Å
P-O(3)	1.545(6) Å
P-N	1.742(8) Å
Na(1)-O(1)	2.582(6) Å x3
Na(1)-N	2.951(8) Å
Na(1)-O(3)	2.643(6) Å x3
Na(2)-O(2)	2.306(7) Å x3
Na(2)-O(3)	2.472(7) Å x3
Na(3)-O(3)	2.326(7) Å x3
Na(3)-O(1)	2.956(7) Å x3

The combined XRD and NPD analysis allowed to confirm the structure of $Na_3V(PO_3)_3N$. Atomic positions and bond distances were found to be in very good agreement with the ones reported for this structure.[145] Two distinct V-O bond lengths indicate a slight distortion in the VO_6 octahedron. As in other $Na_3M(PO_3)_3N$-type materials, Na atoms occupy three crystallographically distinct sites. Na1 is coordinated to six O atoms and

one N atom forming an irregular NaO_6N polyhedron, while Na2 and Na3 are six-coordinated, forming distorted NaO_6 polyhedra.

Since the NPD technique offers in particular the possibility of distinguishing oxygen and nitrogen atoms thanks to their different scattering lengths (5.803 fm for O and 9.36 fm for N)[165], it was confirmed that the nitrogen atom is located in the vertex of the $(PO_3)_3N$ unit.

As explained earlier, the alternative synthesis route (with melamine) was used to verify whether the amount of the NASICON-type impurities can be reduced. The Rietveld refinement of the XRD pattern is shown in Figure 2.2 and the corresponding crystallographic data is reported in Table 2.3.
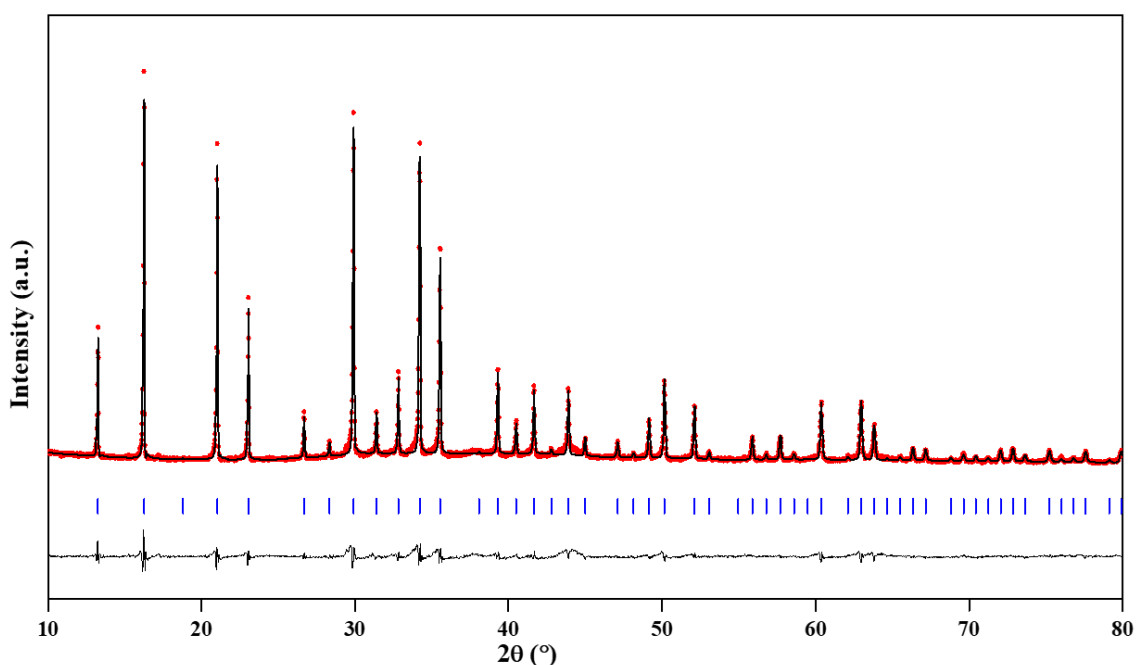
Figure 2.2: Rietveld refinement of the XRD pattern of Na$_3$V(PO$_3$)$_3$N obtained via melamine route. Red circles, black and black lines represent the observed, calculated and difference patterns, respectively. The positions of the Bragg reflections of the *P*2$_1$3 space group are shown as blue vertical bars.

Table 2.3: Crystallographic data and atomic coordinates of $Na_3V(PO_3)_3N$ obtained with the use of melamine.

S.G.: $P2_13$	$a = 9.444(6)$ Å	$V = 842.29(2)$ Å³	$R_{Bragg} = 8.6$ %		$\chi^2 = 4.6$	
Atom	**Wyckoff position**	x/a	y/b	z/c	Occupancy	B_{iso}
P	12b	0.334(3)	0.086(3)	0.245(3)	1	1.5(6)
V	4a	0.579(2)	0.579(2)	0.579(2)	1	1.4(5)
Na1	4a	0.015(5)	0.015(5)	0.015(5)	1.0(1)	1.6(3)
Na2	4a	0.390(4)	0.390(4)	0.390(4)	0.99(3)	1.6(3)
Na3	4a	0.803(4)	0.803(4)	0.803(4)	0.98(2)	1.6(3)
O1	12b	0.265(4)	-0.032(4)	0.347(4)	1	0.9(4)
O2	12b	0.372(2)	0.002(2)	0.111(2)	1	0.9(4)
O3	12b	0.454(3)	0.165(3)	0.305(3)	1	0.9(4)
N	4a	0.191(2)	0.191(2)	0.191(2)	1	0.8(6)

The absence of the NASICON-type phase in the XRD pattern confirms the improvement of the purity of the sample. Based on the refinement of the XRD pattern, the obtained phase can be well indexed with the $P\,2_13$ space group with the cell parameter a equal to 9.444(6) Å, analogous to the phase obtained via ammonolysis route. Additionally, no changes in the cell parameters and Na occupancies were observed confirming the same $Na_3V(PO_3)_3N$ structure. The small shoulder observed on the left side of all main peaks was originated by the slight movement of the powder within the holder while performing the measurement.

2.2.2.2. Electron microscopy and chemical composition analysis

The electron microscopy study was performed to analyze the morphology of the obtained powders. SEM images of $Na_3V(PO_3)_3N$ obtained with ammonolysis route are shown in Figure 2.3a and b. The particles exhibit a non-uniform shape with a wide particle size distribution, varying from 1 µm to 30 µm. The particles obtained through the melamine route also possess non-uniform shape although are larger (10-30 µm) and tend to agglomerate (Figure 2.3c and d).
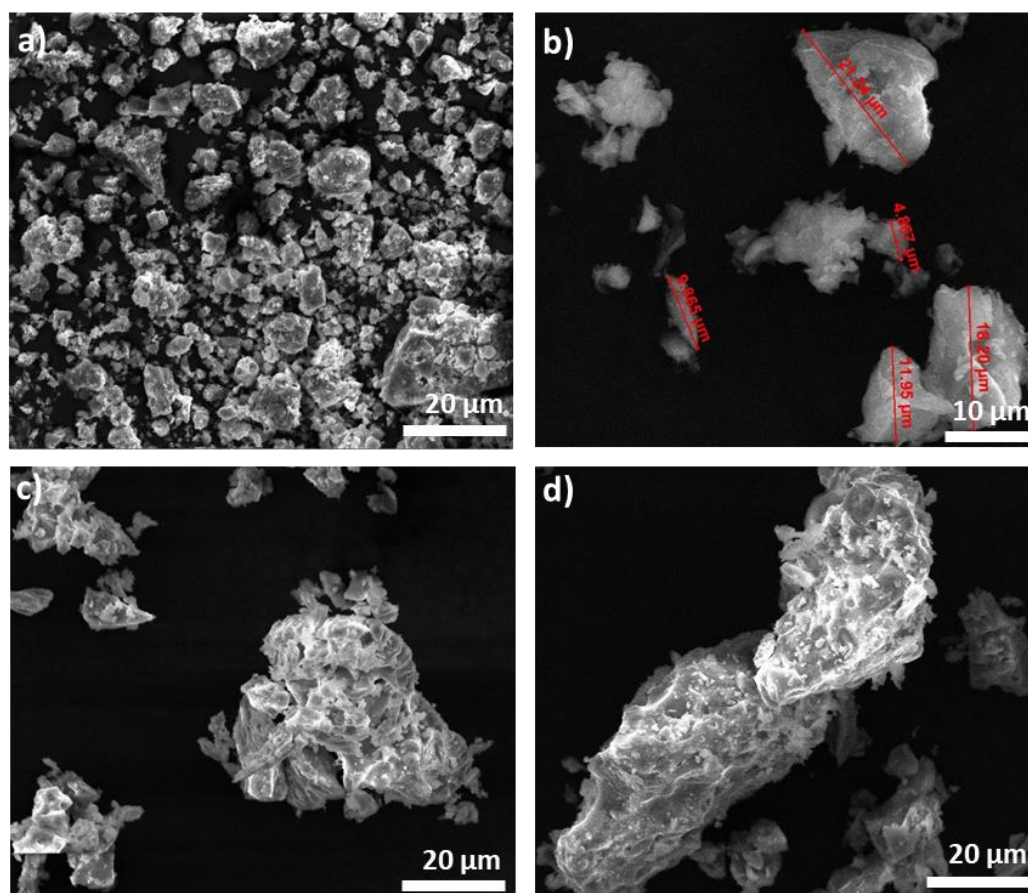
Figure 2.3: SEM images of Na₃V(PO₃)₃N synthesized with ammonolysis route (a&b); and with melamine (c&d).

The chemical composition, and precisely the ratio between Na, V and P atoms in the samples from both ammonolysis and melamine synthesis routes, was evaluated by EDX measurements and verified by inductively coupled plasma analysis (ICP). The results from both analyses are shown in Table 2.4 assuming a content of 3 P atoms in the nominal composition.

Table 2.4: Composition of Na₃V(PO₃)₃N obtained via both synthesis methods determined by EDX and ICP.

Element	Theoretical content	Experimental atomic content determined from EDX		Experimental atomic content determined from ICP	
		ammonolysis	melamine	ammonolysis	melamine
Na	3	3.1±0.16	3.1±0.16	2.9±0.03	2.8±0.04
P	3	3.0(fixed)	3.0 (fixed)	3.0 (fixed)	3.0(fixed)
V	1	0.9±0.05	0.9±0.05	0.9±0.05	0.9±0.03

Both EDX and ICP provide similar results. The lower amount of Na measured by ICP may come from the lower spectral intensity of this element, thus the results obtained from

EDX would be more reliable. The amount of nitrogen was evaluated using CHNOS Elemental Analysis and the results confirmed the expected content of one nitrogen atom per formula unit.

2.2.2.3. X-ray Absorption Spectroscopy analysis of $Na_3V(PO_3)_3N$

In the master thesis[163] the vanadium oxidation state was evaluated with the use of two different techniques: X-ray photoelectron spectroscopy (XPS) and electron paramagnetic resonance (EPR). Both of the techniques confirmed V^{III} oxidation state, however with a small amount of V^{IV} (not quantified). These results were complemented during the PhD with an X-ray Absorption Spectroscopy (XAS) study of $Na_3V(PO_3)_3N$.

XAS measurements were performed on a powder of $Na_3V(PO_3)_3N$, synthesized with the use of melamine, at the BOREAS beamline of the ALBA Synchrotron facility in Barcelona. Figure 2.4 shows the XAS spectra of V $L_{2,3}$ edge and O K-edge within $Na_3V(PO_3)_3N$. Since other experiments resulted with observation of the presence of both +3 and +4 oxidation states of vanadium, as a reference, XAS spectra for V^{III} and V^{IV} identical environments were computed using CTMXAS program.[166] This program calculates the L edge spectra based on the semi-empirical charge transfer multiplet (CTM) theory.[167] The calculations include the core and valence spin-orbit coupling, the core-valence two-electron integrals (multiplet effects), and finally the effects of strong correlations within the charge transfer model. To compute the spectra of V^{III} and V^{IV}, an O_h coordination symmetry was selected, and different crystal field parameters were evaluated, in particular the crystal field splitting, being the energy difference between the t_{2g} and e_g states. Eventually, by comparing the computed spectra with experimental ones, the most satisfying results were obtained with the crystal field splitting energy value (10dq) of 2.5 eV.
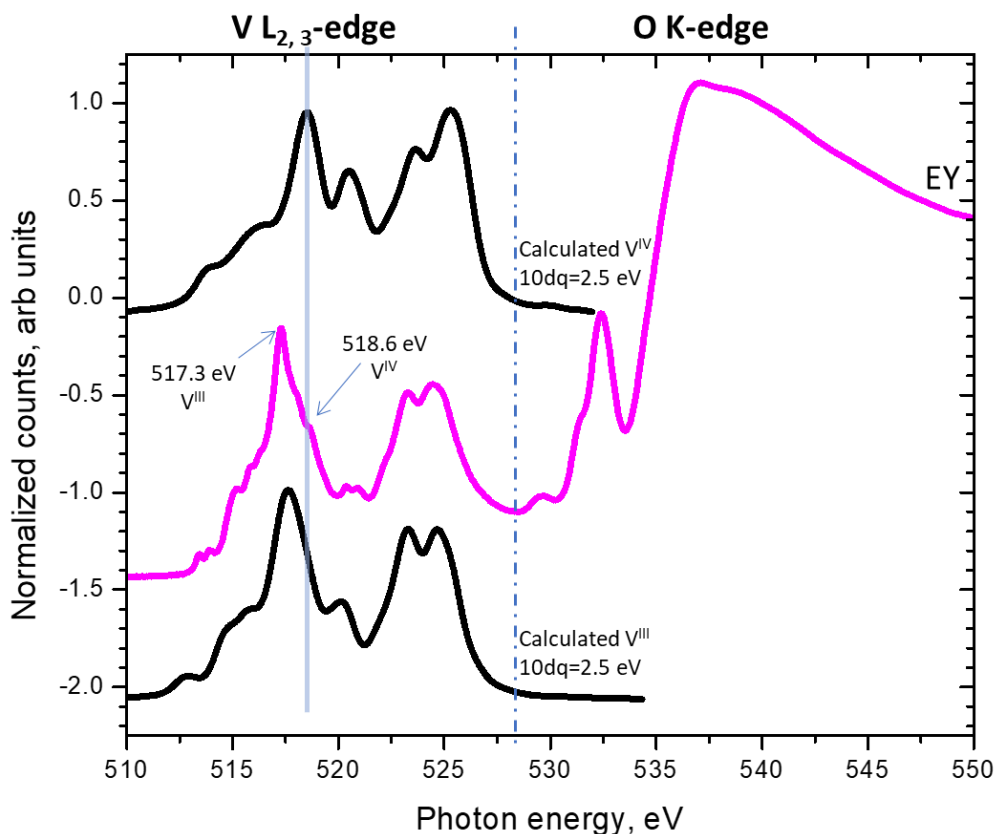
Figure 2.4: XAS V L$_{2,3}$-edge & O K-edge spectra of Na$_3$V(PO$_3$)$_3$N prepared from melamine route. Signals from electron detection mode (EY) corresponding to the surface are denoted in pink color. Black curves correspond to the calculated XAS V^{III} and V^{IV} L$_{2,3}$-edge spectra with Oh coordination symmetry and a crystal field splitting energy of 2.5 eV.

For the V L$_{2,3}$-edge region, the spectra exhibit two broad bands centered at 518 and 524 eV which can be attributed to the 2$p_{3/2}$ and 2$p_{1/2}$ levels, respectively. [168] The experimental spectrum of V L-edge was compared with the computed spectra and the good agreement between these two spectra confirms V^{III} oxidation state as the main component. However, a shoulder at 518.6 eV could suggest a small contribution of the V^{IV} oxidation state, being in good agreement with the observations from other techniques (XPS and EPR). These features are observed in the electron detection mode (EY), which corresponds to the surface.

The observed spectra for the O K-edge correspond to the transition from the O1s core level to unoccupied O2p level within the VO$_6$ octahedra. The features below 534 eV correspond to V3d – O2p hybridization, whereas the ones above correspond to V4sp-O2p hybridization.[167] The distribution of the two peaks at 529.5 and 532 eV and their intensity ratio is characteristic for the V^{III} oxidation state and is related to the t$_{2g}$-e$_g$ splitting.[168] The energy difference of 2.5 eV between these two peaks support well the calculated crystal field splitting energy.

The obtained results corroborate previous findings on the +3 oxidation state of vanadium. This technique additionally allowed to evaluate the observations of the +4 oxidation state and confirmed its presence on the surface, which might be related with the slight Na deficiency. Similar conclusions drawn Chen at. *al*[169] based on the analysis of the *in situ* X-ray absorption near-edge structure (XANES) spectra of $Na_3V(PO_3)_3N$.

2.2.2.4. Thermogravimetric analysis

Thermogravimetric analyses (TGA) of $Na_3V(PO_3)_3N$ (synthesized with melamine) were performed to evaluate $Na_3V(PO_3)_3N$ stability under Argon and under synthetic air were performed in the temperature range 30-1000 °C at 10 °C·min^{-1} heating rate. The aim of this measurement was to validate the stability of $Na_3V(PO_3)_3N$ in both inert and air atmospheres. The registered mass changes as a function of temperature in both measurements are shown in Figure 2.5.
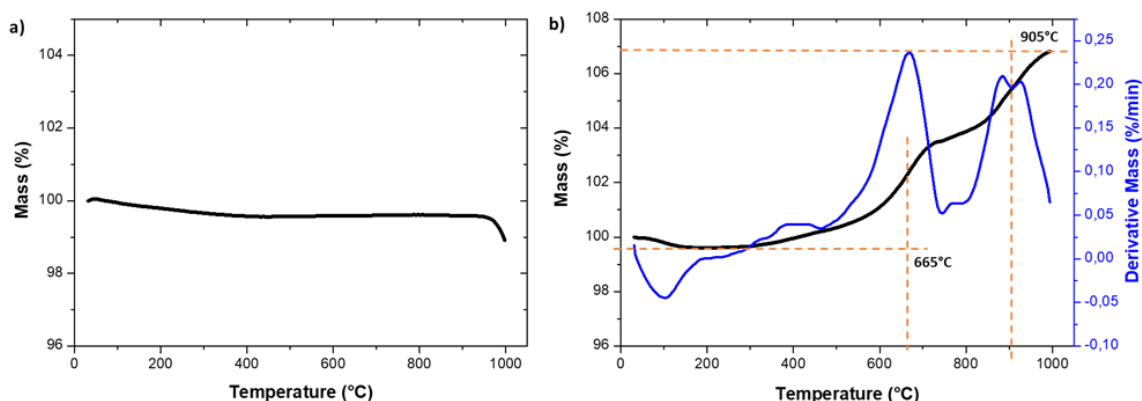
Figure 2.5: Mass(%) vs. temperature curves for $Na_3V(PO_3)_3N$ prepared from melamine under (a) Ar and (b) Air atmosphere measured from room temperature to 1000 ^{0}C at 10 °C·min^{-1} heating rate.

The results of the test performed under Ar atmosphere (Figure 2.5a) indicate a very high stability of $Na_3V(PO_3)_3N$ in inert atmosphere. Based on the TGA curve under air (Figure 2.5b), $Na_3V(PO_3)_3N$ tends to gain mass upon heating undergoing several transitions. Two main processes centered at 665 °C and 905 °C are observed (see the mass derivative curve, drawn in blue in Figure 2.5b), which are related to the oxidation of $Na_3V(PO_3)_3N$ with the nitrogen-oxygen substitution and eventual decomposition, a behavior typical of nitrido-based compounds [170].

To follow the observed phase transitions in detail, a high temperature XRD experiment under air flow was performed from RT to 900 °C at 10 °C·min^{-1} heating rate in a 2theta range of 10 - 60º. XRD patterns were recorded for 10 min every 100 °C up to 500 °C,

every 50 °C from 500 °C to 900 °C and ultimately a final pattern was recorded after cooling back to room temperature.
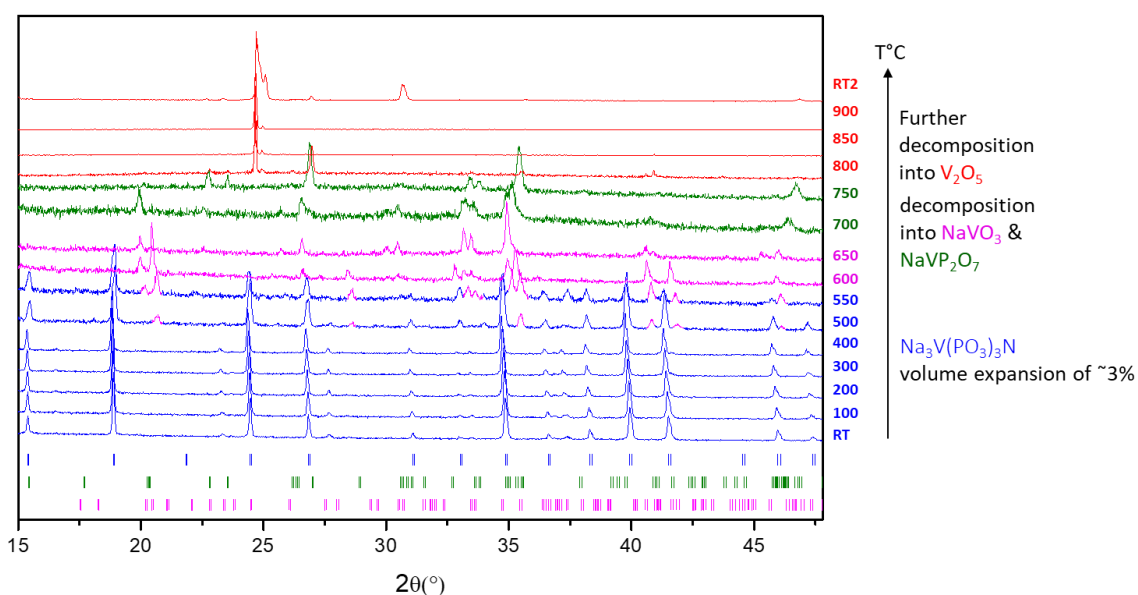
Figure 2.6: High temperature XRD measurement of $Na_3V(PO_3)_3N$ under air in the temperature range RT-900°C-RT Blue color of the curves corresponds to the region of the stability of $Na_3V(PO_3)_3N$, whose Bragg positions are marked as well with the blue bars; green bars indicate the phase of $NaVP_2O_7$, appearing at ~500°C. Red color corresponds to V_2O_5 phase forming >800°C.

The results of this measurement, presented in Figure 2.6, are in good agreement with the ones from the TGA analysis. Up to 450 °C the crystal structure of $Na_3V(PO_3)_3N$ is retained with small volume change of ~3%. Figure 2.7 shows the near-linear evolution of the cell parameter indicating gradual structure expansion with the increasing temperature.
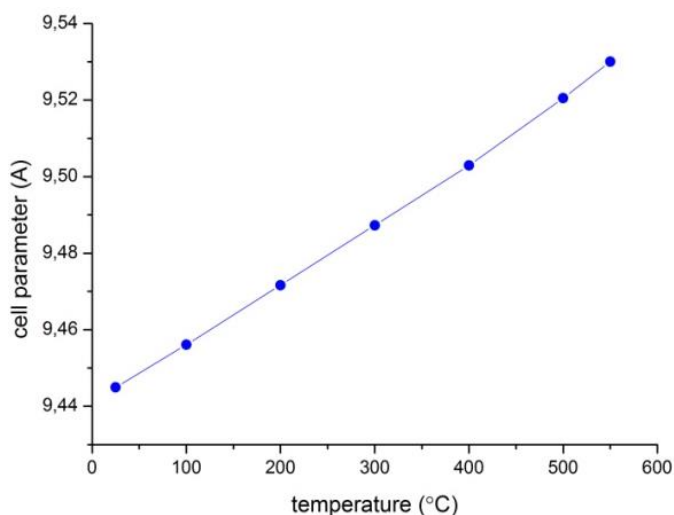
Figure 2.7: Evolution of the cell parameter of $Na_3V(PO_3)_3N$ with increasing temperature

At 500 °C peaks of new phases indexed as $NaVO_3$ and $NaVP_2O_7$ are appearing, indicating the beginning of the transformation of the nitridophosphate phase into pyrophosphates

71

and oxides, leading to complete decomposition at 600 °C. Above this temperature further structural changes can be observed with eventual decomposition into V_2O_5 oxide.

2.2.2.5. Solid-state Nuclear Magnetic Resonance analysis

High resolution ^{23}Na solid-state Nuclear Magnetic Resonance (NMR) experiments under fast Magic-Angle Spinning (MAS) were performed to study the local environment of sodium ions within the structure of $Na_3V(PO_3)_3N$. For the measurement the powder synthesized with melamine was used, where no impurities of NASICON-type phase were observed (expected at 79 ppm and -9 ppm)[171], indicating that all registered signals are expected to come from the $Na_3V(PO_3)_3N$ phase. Figure 2.8a shows the ^{23}Na spectrum where the observed signals are superimposed with their deconvolution.
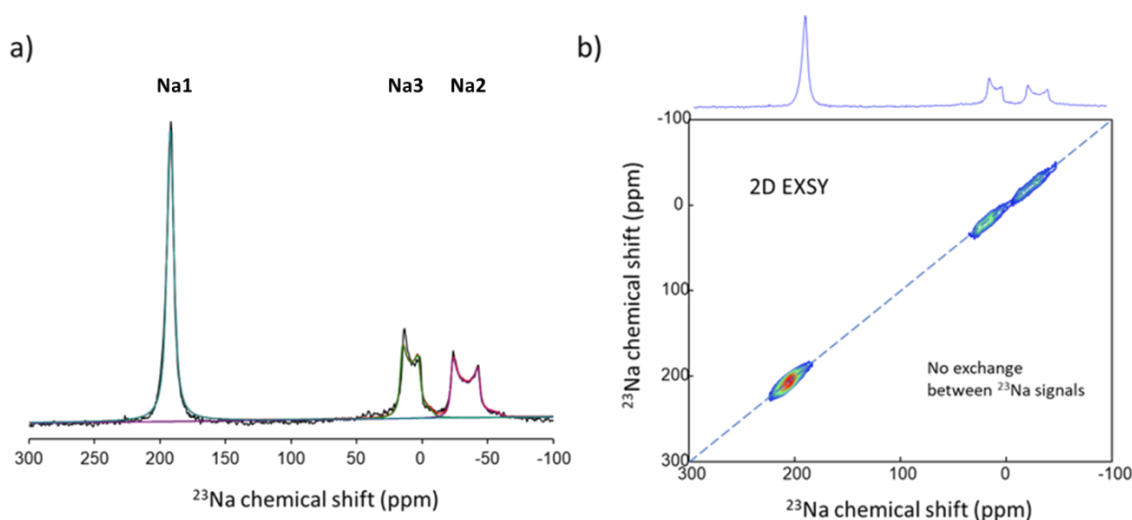
Figure 2.8: (a) ^{23}Na MAS solid state NMR spectrum of $Na_3V(PO_3)_3N$ prepared from melamine acquired at 50kHz; (b) ^{23}Na 2D EXSY spectra of $Na_3V(PO_3)_3N$ acquired at room temperature with mixing time 10ms.

As can be seen in Figure 2.8a, three main signals can be detected in the spectrum, in agreement with the crystal structure, where Na ions occupy three different crystallographic sites. The absence of additional signals in the spectrum indicates that there are no Na-containing impurities in the sample in agreement with the XRD data. In order to fit the spectrum, two different components were used: a single Lorentzian shape for the signal at 192 ppm and two quadrupolar shapes for the signals at 20 and -16.3 ppm. The quantification of the different Na signals should take into account the intensity of the full rotational band pattern. Due to the paramagnetic broadening of the signals this is not normally feasible. The details of the performed fitting can be found in Table 2.5.

Table 2.5: ^{23}Na MAS solid state NMR fitting parameters where QCC is the quadrupole coupling constant, h is the asymmetry of the quadrupole coupling tensor and LW is the lie width of the Lorentzian line.

Signal	Assigned Na site	Shift (ppm)	QCC (kHz)	h	LW (ppm)
1	Na1	192.3	-	-	6.4
2	Na3	20.0	560	0.03	-
3	Na2	-16.3	692	0.07	-

$Na_3V(PO_3)_3N$ contains paramagnetic vanadium V^{III} ions, whose two unpaired electrons are responsible for the shifts and shape of the signals. These shifts are determined by the unpaired electron densities that are transferred from the orbitals containing the electrons into the *s* orbitals of the Na nuclei detected in the NMR experiment. Therefore, paramagnetic interactions depend strongly on the structural arrangement of the different Na atoms in the material. A detailed analysis of the Na-V distances was performed in order to assign the signals to the corresponding Na atoms. Table 2.6 gathers the distances between each Na site and the three nearest V atoms and Figure 2.9 presents the environments of the three Na sites, as determined from the XRD data.

Table 2.6: Na-V distances in $Na_3V(PO_3)_3N$ used for the chemical shift assignment.

atoms	distance	atoms	distance	atoms	distance
Na(1)-V	3.986(4) Å	Na(2)-V	3.100(5) Å	Na(3)-V	3.606(5) Å
Na(1)-V	3.986(4) Å	Na(2)-V	5.345(5) Å	Na(3)-V	4.609(5) Å
Na(1)-V	3.986(4) Å	Na(2)-V	5.793(5) Å	Na(3)-V	4.609(5) Å
Σ	**11.958(4) Å**		**14.238(5) Å**		**12.824(5) Å**
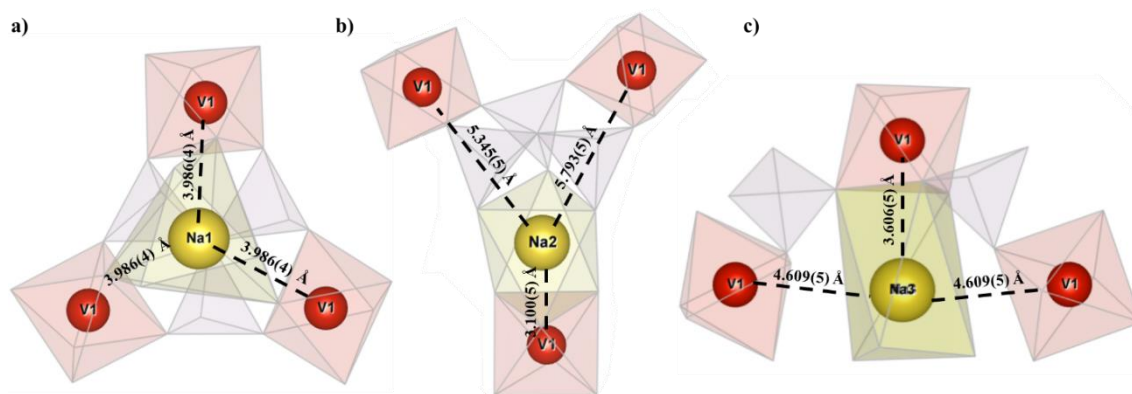
Figure 2.9: Representation of the three Na environments in Na₃V(PO₃)₃N highlighting the nearest Na – V contacts for (a) Na1; (b) Na2; and (c) Na3. The V atoms are labeled and indicated in red. The VO₆ octahedra are shown in red, Na polyhedra in light yellow and PO₃N tetrahedra in light grey.

Since paramagnetic shifts are an additive property, all the existing nearby vanadium positions should be considered for the analysis of ssNMR spectra (and not only the minimum distance). Therefore, due to the nearest vicinity of three vanadium atoms, the Lorentzian shape signal was assigned to the Na1 site. The large shift observed for Na1 is explained by the Fermi contact interactions of this nuclei with the unpaired electrons of the adjacent vanadium centers. The other two signals were assigned to the Na3 and Na2 sites based on the sum of the Na-V distances (Table 2.6 and Figure 2.9) and were clearly determined by a quadrupolar splitting with characteristic peak-doublet shapes. The observation of well-defined quadrupolar signals for positions 3 and 2 demonstrate that these sodium sites are well ordered and homogenous. A significant proportion of vacancies or defects in the structure would result in broader complex patterns for these signals. Additionally, the calculation of the volume of the Na polyhedra, gave the following results: Na(1)O₆N - 24.0653 Å³; Na(2)O₆ - 17.1485 Å³ and Na(3)O₆ - 19.0979 Å³. The largest volume is observed for the Na1 position, and this is in agreement with the absence of quadrupolar splitting. Local motions of the Na⁺ ions within the polyhedra eliminate the quadrupolar interactions and since the Na1 polyhedra has the largest volume, these interactions are not detected. This observation corroborates the aforementioned assignation of the signals.

In order to assess the possibility of Na⁺ exchange processes, 2D ²³Na – ²³Na Exchange Spectroscopy (EXSY) experiments were performed. 2D EXSY experiments are a well stablished NMR technique to probe the mobility between different crystallographic sites of alkali cations and can provide the first insight of the local dynamics within the structure. In the literature numerous publications can be found demonstrating the

successful application of this technique to follow the Li exchange processes within the Li sites.[172–174] Na-Na chemical exchange has been also studied although in a small number of materials, e.g. in Na_2FePO_4F where no cross peaks could be detected indicating too slow Na ion exchange to be possibly registered.[175]

The resulting 2D EXSY spectrum obtained for $Na_3V(PO_3)_3N$ at a mixing time of 10 ms is shown in Figure 2.8b. All three ^{23}Na NMR signals (Na2, Na3 and Na1) are only observed at the diagonal of this homonuclear correlation. The absence of off-diagonal signals in this spectrum correlating different sodium positions demonstrates that there is no measurable exchange of Na^+ ions between different crystallographic sites at room temperature in the timescale of 10 ms used in the experiment. Plausibly Na mobility is too slow to be captured by this experiment and requires previous chemical or electrochemical partial desodiation to follow the exchange between Na sites, which anticipates sluggish intercalation kinetics.

2.2.3. DFT calculations

First-principles calculations were carried out to predict the redox potential corresponding to the extraction of two sodium ions from the $Na_3V(PO_3)_3N$ framework. These calculations were performed by the modeling and computational simulation group at CIC energiGUNE.

The energy cutoff was set to 500 eV, and a $4 \times 4 \times 4$ k-point grid was used. DFT+U scheme of Dudarev et al. [176] was applied to describe the localized nature of V $3d$ states. Within this Hubbard model the magnetic character is assumed to be paramagnetic with the magnetic planes being parallel to the (111) plane.[177] This assumption will be evaluated afterwards. The U value chosen for V was 3.70 eV.[178] Ground state energies were computed by performing a global energy minimization, where atomic positions were allowed to relax with a residual force threshold of 0.02 eV / Å.

As evaluated from the bond-valence calculations, Na2 site is expected to be the least mobile. Therefore, the calculations were done considering only two different arrangements for the Na^+ cations in the oxidized phase $Na_2V^{IV}(PO_3)_3N$: with vacancies at Na1 and at Na3 sites.

The cell voltage of the reactions was calculated by approximating the following equations:

$$V \approx - \frac{E(Na_3 V^{III}(PO_3)_3 N) - E(Na_2 V^{IV}(PO_3)_3 N) - E(Na)}{F}$$

$$V \approx - \frac{E(Na_2 V^{IV}(PO_3)_3 N) - E(Na V^{V}(PO_3)_3 N) - E(Na)}{F}$$

Where F is the Faraday constant, E values represent the computed DFT energy value of $Na_3V(PO_3)_3N$, $Na_2V(PO_3)_3N$, and bulk Na metal ground states, respectively. The ground state energies were computed for $Na_3V(PO_3)_3N$, $Na_2V(PO_3)_3N$ and $NaV(PO_3)_3N$; and intercalation voltages were computed from $NaV(PO_3)_3N$ to $Na_2V(PO_3)_3N$ and $Na_2V(PO_3)_3N$ to $Na_3V(PO_3)_3N$. Results from the calculations are shown in Figure 2.10.
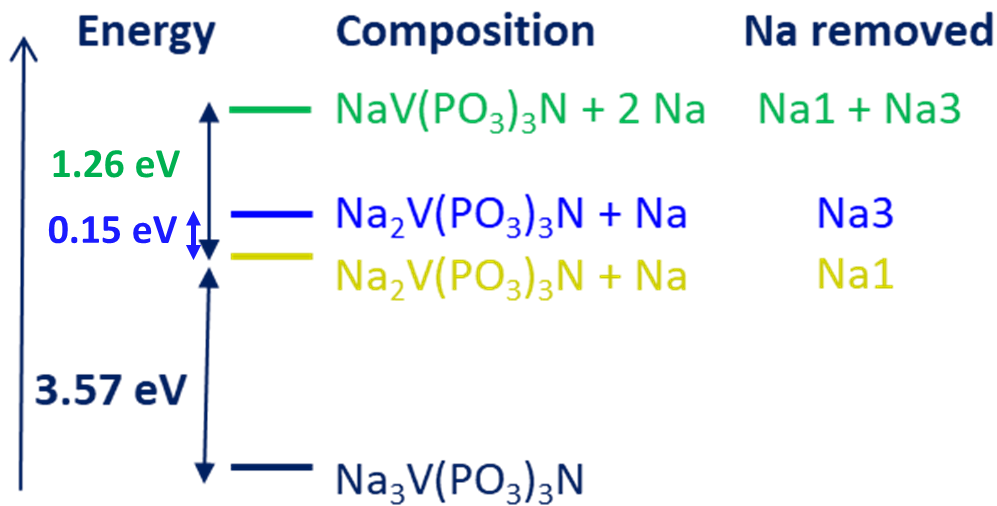
Figure 2.10: Ground states for the different compositions considering the removal Na ion from Na1 and/or Na3 site. Yellow and blue levels represent $Na_2V(PO_3)_3N$ states with Na1 and Na3 vacancies respectively, green with both Na1 and Na3 vacancies.

A calculated average intercalation voltage of 3.57 V *vs.* Na^+/Na^0 (removal of the Na^+ from the Na1 site) was obtained between $Na_3V(PO_3)_3N$ and $Na_2V(PO_3)_3N$. The removal of Na^+ from the Na3 site was 0.15 eV higher that of Na1, therefore it is expected that the latter is first removed. This value agrees very well with the expected voltage for the V^{III}/V^{IV} redox couple in $Na_3V(PO_3)_3N$ – between 3.4 V *vs.* Na^+/Na^0 as in NASICON $Na_3V_2(PO_4)_3$ [98] and 4.0 V *vs.* Na^+/Na^0 as in $Na_3V_2(PO_4)_2F_3$,[112] due to the lower inductive effect of nitrogen comparing with the effect of fluorine. The extraction/insertion of a second Na^+ from the Na3 site, between $Na_2V(PO_3)_3N$ and $NaV(PO_3)_3N$, is calculated to be associated

with an average voltage increase of 1.26 V, i.e. up to 4.83 V *vs.* Na^+/Na^0. This value is very close to the electrolyte stability limit, however, is still expected to be reachable experimentally.

Similar voltage calculations using DFT theory were performed by Debbichi and Lebegue [179] on the $Na_3Ti(PO_3)_3N$ system. For their calculations also only two arrangements of the Na^+ cations were considered, with the vacancies at Na1 and Na3 site. The calculated voltage of 2.69 V agrees perfectly with the reported experimental value of 2.7 V.[146]

As mentioned before, DFT calculations were used to explore the magnetic ordering and inspect its effect on the geometry of the structure. Two different hypotheses were evaluated with both ferromagnetic and antiferromagnetic ordering. Eventually it was confirmed that for $Na_3V(PO_3)_3N$, the antiferromagnetic state is the most stable. The antiferromagnetic state was also reported as the most stable state for $Na_3Ti(PO_3)_3N$.[146,179]

2.2.4.   Magnetic properties

Magnetic measurements were performed in a Quantum Design PPMS in order to evaluate the magnetic behavior of $Na_3V(PO_3)_3N$ and compare the results with the ones obtained from theoretical calculations. Magnetic susceptibility was recorded as a function of the temperature between 2 and 300 K in both zero-field-cooled (ZFC) and field-cooled (FC) conditions with an applied magnetic field of 10 kOe.
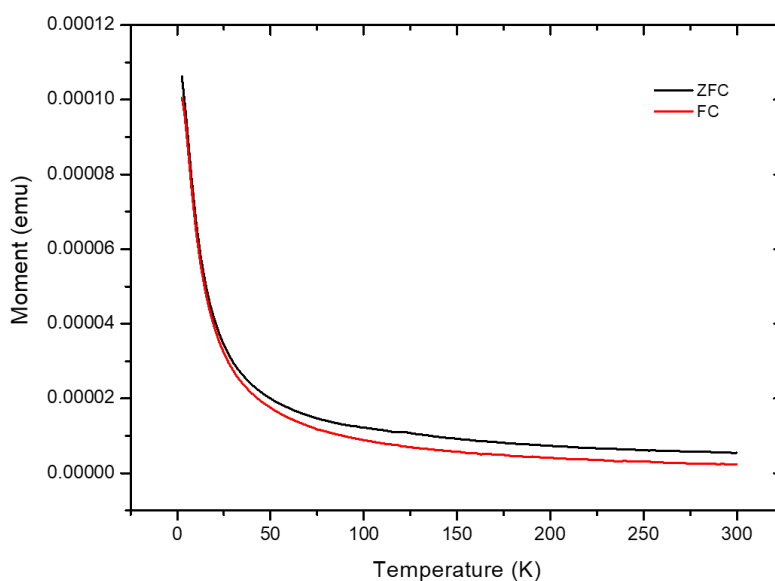
Figure 2.11: ZFC and FC $Na_3V(PO_3)_3N$ magnetic susceptibility curves.

The data presented in Figure 2.11 shows that there is no long-range magnetic ordering down to 2 K and suggest that $Na_3V(PO_3)_3N$ is either paramagnetic or has weak/frustrated antiferromagnetic coupling. These findings support well the results from the DFT calculations.

2.2.5.   Electrochemical characterization

In order to confirm the theoretical calculations suggesting redox reaction of both V^{III}/V^{IV} and V^{IV}/V^V redox couples occurring within the stability window of commonly used electrolytes, the electrochemical properties of $Na_3V(PO_3)_3N$ as a cathode material for Na-ion and Li-ion batteries were explored. In addition to validating reversible mobility of Na ions in half cells versus Na, some experiments were performed in a hybrid-ion cell configuration with Li metal and Li-based electrolyte, to test the possible insertion of Li+ ions into the electrochemically desodiated phase $Na_{3-x}V(PO_3)_3N$. Since the insertion voltage for polyanionic electrode materials against sodium anode is usually ~0.3 V lower than the one against lithium, the predicted voltage of V^{IV}/V^V redox couple *vs.* Li^+/Li^0 is expected to lie ~5.1 V *vs.* Li^+/Li^0, which could exceed the stability window of carbonate-based electrolytes (in this case 1M $LiPF_6$ in EC:DMC). Therefore, additional tests using ionic liquid electrolyte were performed.

- **Carbonate-based electrolytes**

Electrode materials were prepared by ball milling (SPEX) the active material ($Na_3V(PO_3)_3N$ synthesized using ammonolysis route) with carbon C_{65} and PVDF in a mass ratio of 80:10:10 for 20 min under air. N-Methylpyrrolidone (NMP) was added to the mixed powders and the obtained viscous slurry was coated on aluminum foil. These as-prepared electrodes were used to assemble cells against lithium and sodium metal anodes using 1M $LiPF_6$ or $NaPF_6$ in EC:DMC as electrolyte respectively.

The half-cells were cycled in galvanostatic mode at C/40 rate (which corresponds to the exchange of one electron in 40 hours) in various voltage windows within the 2.5-5.0 V range. The best results in terms of capacity, low polarization and capacity retention were obtained within the 3.8 – 4.8 V *vs.* Li^+/Li^0 and 3.5 – 4.5 V *vs.* Na^+/Na^0 voltage windows. Cyclic voltammograms (CV) were also performed in the voltage window 3.0 – 4.8 V *vs.*

Li$^+$/Li^0 and 3.0 – 4.5 V *vs.* Na$^+$/Na^0 voltage at a scanning rate of 0.05 mV/s to follow the reduction-oxidation processes.

Figure 2.12a shows the selected galvanostatic charge-discharge curves of Na$_3$V(PO$_3$)$_3$N *vs.* Na$^+$/Naº together with the corresponding cyclability curve.
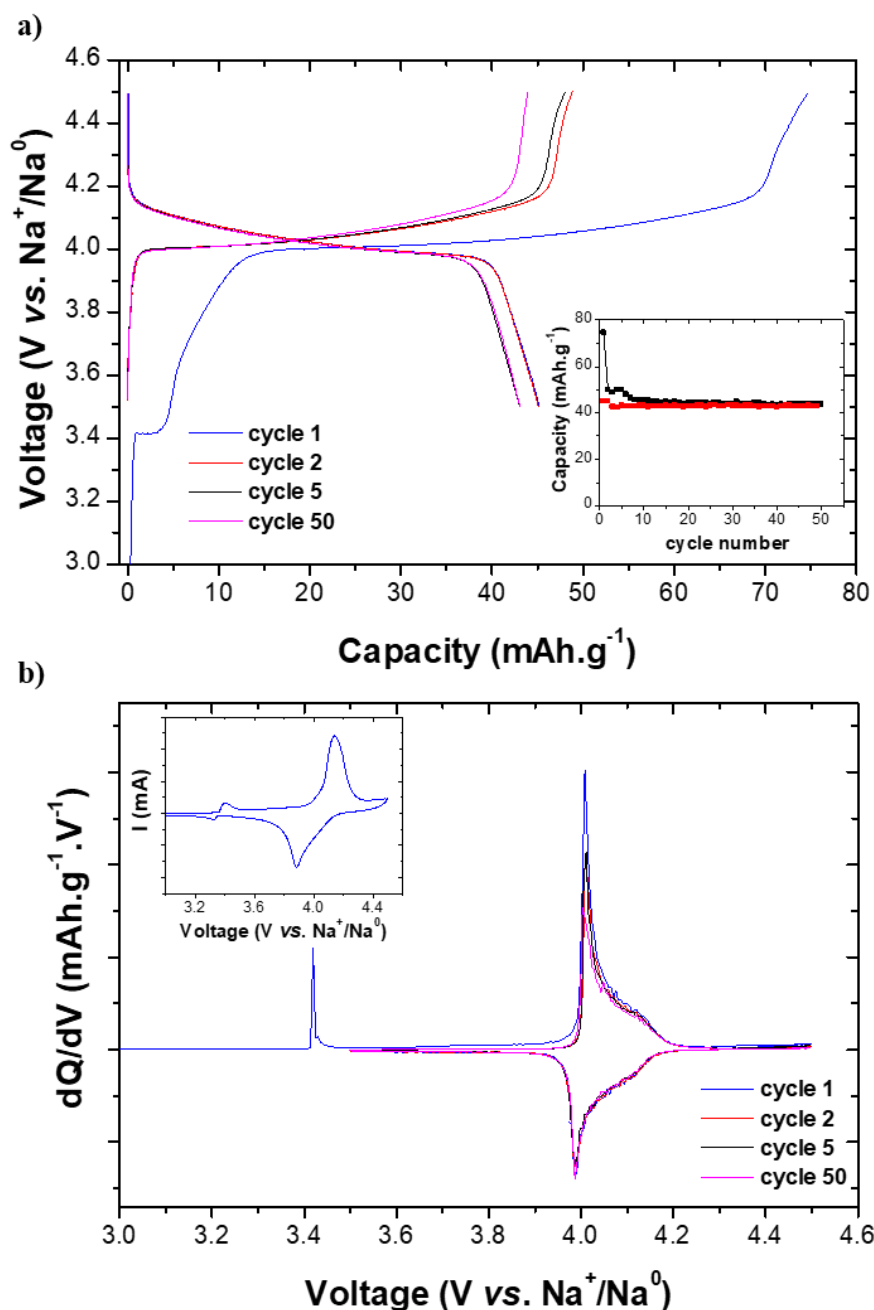
Figure 2.12: (a) Voltage-capacity curve for Na$_3$V(PO$_3$)$_3$N for cycles 1,2,5 and 50 measured between 3.5 and 4.5 V at a C/40 rate *vs.* Na metal anode and corresponding capacity vs cycle number shown in the inset of (a); (b) dQ/dV curves corresponding to the data of (a) and first cycle CV curve of Na$_3$V(PO$_3$)$_3$N measured between 3 V and 4.5 V with a scan rate of 0.05 mV/s in inset of (b).

The theoretical capacity of 74 mAh.g^{-1} corresponding to the removal of one sodium ion was achieved at the first charge. Such reaction is centered around 4.0 V *vs.* Na$^+$/Na^0,

associated to the remarkably high voltage activity of the V^{III}/V^{IV} redox couple. In the discharge, around 0.6 Na^+ ion were reinserted resulting in a stable capacity of around 50 $mAh.g^{-1}$ in the following cycles. The origin of such first cycle irreversibility is not clear. First hypothesis could be supported by the finding from the XAS analysis indicating partial preoxidation of vanadium in the pristine material, which was also suggested by Chen et al.[169] Additionally, other phenomena such as internal atom rearrangements hampering the mobility of Na^+ ions or the irreversible evolution of N_2 could also be involved. Both of these hypotheses will be later evaluated by gas chromatography analysis (section 2.2.7.1.) and *operando* XRD measurement (section 2.2.5.2.). As shown in the capacity retention plot (inset in Figure 2.12a), subsequent cycling proceeds with a remarkable stable capacity over 50 cycles.

Derivative dQ/dV curves (Figure 2.12b) reveal a shoulder at higher voltage values, both at charge and discharge and also visible in the cyclic voltammogram (inset in Figure 2.12), which suggests two separate processes for the alkali extraction/insertion separated by a small voltage step in agreement with the DFT calculations, which suggest different voltage for the removal of Na1 and Na3. The small plateau observed in the first charge at 3.4 V *vs.* Na^+/Na^0 is attributed to the oxidation of the NASICON-type $Na_3V_2(PO_4)_3$ phase.[98] Extremely small voltage hysteresis of 0.035 V between charge and discharge can be observed. The mechanism of Na mobility will be closely evaluated in the following section.

The performance of $Na_3V(PO_3)_3N$ *vs.* Na was also tested at higher cycling rates. Figure 2.13a shows the charge and discharge capacities at different C-rates: C/40, C/20 and C/10; whereas in Figure 2.13b the galvanostatic charge-discharge curves of the first, second and fifth cycles are plotted for C/40, C/20 and C/10.
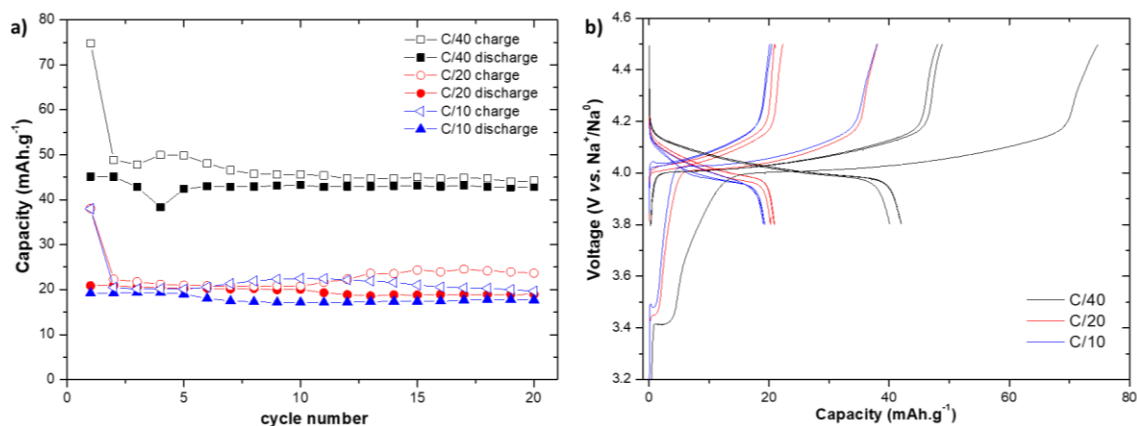
Figure 2.13: (a) Charge & discharge capacity as a function of number of cycles at three different C-rates: C/40, C/20 and C/10 of Na₃V(PO₃)₃N cycled *vs*. Na in the voltage window 3.5 – 4.5 V; (b) selection of the voltage-capacity curves for Na₃V(PO₃)₃N for cycles 1,2 and 5 between 3.5 and 4.5 V cycled at (black) C/40; (red) C/20 and (blue) C/10 rate *vs*. Na metal anode.

The obtained capacity has significantly decreased at such C-rates, reaching around 20 mAh.g^{-1}. In each cell we observe a similar irreversible capacity after the first charge, but subsequent cycling shows relatively stable capacity. It can also be observed that the polarization increases with the cycling rate which could be related with the overall decrease of the capacity while comparing with the C/40 rate. These results suggest that the electrode optimization such as carbon-coating or nano-sizing is required to improve the electronic and ionic conductivity. Despite different attempts were done in this regard (e.g. ball-milling), no improvement in the electrochemical performance was observed.[163]

Next, the performance of Na₃V(PO₃)₃N was evaluated in a hybrid-ion configuration, using metallic Li as an anode in a LiPF₆ electrolyte. Figure 2.14a shows the galvanostatic charge-discharge curves together with the corresponding cyclability plot, whereas Figure 2.14b shows the CV curve at a scan rate of 0.05 mV s^{-1} and the derivative plots of the galvanostatic curve.
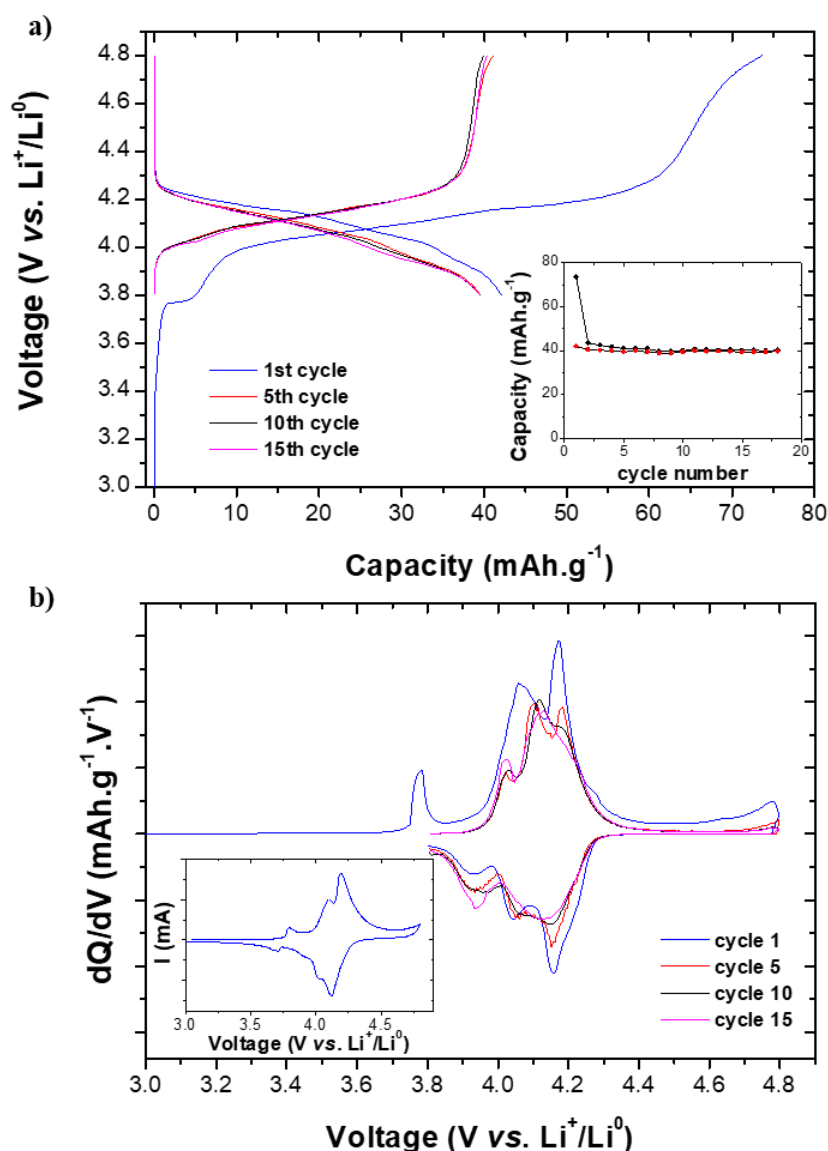
Figure 2.14: (a) Voltage-capacity trace; (b) dQ/dV curves, measured between 3.8 and 4.8 V at a C/40 rate *vs.* Li metal anode. Cyclability of Na₃V(PO₃)₃N obtained from ammonolysis is shown in the inset of (a); CV curve of the first cycle of Na₃V(PO₃)₃N between 2.8 V and 4.8 V with a scan rate of 0.05 mV/s in inset of (b).

Similarly to the previous results, the obtained capacity of 75 mAh.g^{-1} during the first charge corresponds to the removal of one sodium ion. Again, a significant irreversible capacity can be observed in the following charge process, which will be investigated in sections 2.2.5.2. and section 2.2.7.1. Subsequent cycling proceeds with a remarkably stable capacity with very small voltage hysteresis of 0.065 V. The performance is very similar to the one obtained while cycling Na₃V(PO₃)₃N *vs.* Na. Following the derivative curves, the electrochemical activity of Na₃V(PO₃)₃N is centered around 4.1 V *vs.* Li$^+$/Li^0, which is very similar to the value obtained while cycling *vs.* Na (~4.0 V *vs.* Na$^+$/Na^0). To the best of our knowledge, such an unusual phenomenon had never been previously noticed in other cathode materials, as due to the difference in the voltage between Na$^+$/Na^0

(-2.71 V) and Li^+/Li^0 (-3.04 V *vs.* SHE), redox potentials measured *vs.* Li are expected to be ~0.3 V higher than *vs.* Na. The small difference of ~0.1 V in the insertion/extraction voltage between both alkali metal reference electrodes (Na *vs.* Li) observed for $Na_3V(PO_3)_3N$ suggests that the interactions between the framework of $Na_3V(PO_3)_3N$ and the mobile Na^+ cations might be greater due to *ad hoc* matching in site size, than with the inserted Li^+ cations. On the contrary, the typical difference of ~0.3 V between Na and Li system could be observed in the case of the NASICON-type impurity – small plateau at 3.7 V *vs.* Li^+/Li^0. The shape of the peaks in the derivative and CV curves differs from the ones observed while cycling *vs.* Na and suggest multiple processes occurring during cation extraction/reinsertion, possibly related to Li^+ and Na^+ exchange. This hypothesis will be further evaluated while investigating the mechanism of the insertion/deisertion reaction.

The performance of $Na_3V(PO_3)_3N$ *vs.* Li was also tested at higher cycling rates. Figure 2.15 shows the charge and discharge capacities at C/40, C/20 and C/10. In each cell the irreversible capacity was observed after the first charge, however subsequent cycling shows stable capacity at C/40 and C/20 rates. At C/10 progressive fading of the capacity upon cycling was observed. However, in this case the capacity decreased only slightly when increasing the rate from C/40 to C/20, which suggests improved ionic transport, resulting with an average of 35 mAh.g^{-1} at C/20. While increasing the cycling rate to C/10, the gradual decrease of the capacity was observed reaching only ~20 mAh.g^{-1} after 15 cycles.
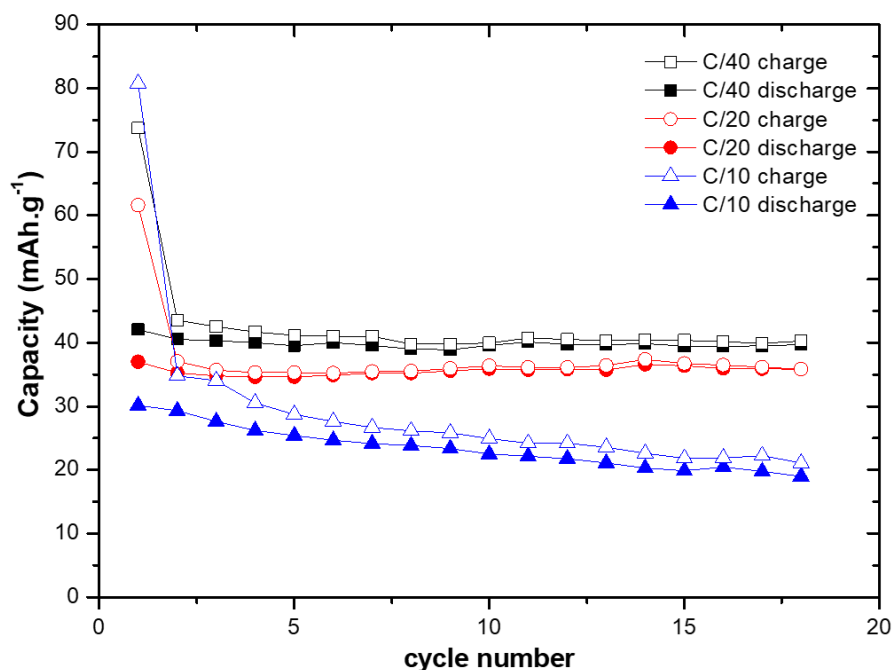
Figure 2.15: (a) charge; (b) discharge capacity as a function of number of cycles at three different C-rates: C/40, C/20 and C/10 of Na₃V(PO₃)₃N prepared from ammonolysis route cycled *vs.* Li in the voltage window 3.8 – 4.8. V.

Based on the DTF calculations, the calculated average intercalation voltage between $Na_3V(PO_3)_3N$ and $Na_2V(PO_3)_3N$ is expected at 3.57 V *vs.* Na^+/Na^0. Compared with the experimental results, this predicted voltage is about 0.4 V lower than the experimental one (4.0 V *vs.* Na^+/Na^0). The extraction/insertion of a second Na^+, between $Na_2V(PO_3)_3N$ and $NaV(PO_3)_3N$, is calculated to be associated with an average voltage increase of 1.26 V, therefore the experimental voltage would be expected at ~5.2 V *vs.* Na^+/Na^0. Searching for the removal of second sodium, the voltage window was opened to 5.0 V while the rate was maintained at C/40, but no additional activity was observed (not shown).

The $Na_3V(PO_3)_3N$ synthesized with the use of melamine was also evaluated as a cathode material to compare its electrochemical performance with the results obtained from the ammonolysis synthesis. The same testing conditions were employed while cycling *vs.* both Na and Li. The obtained galvanostatic charge-discharge curves are presented in Figure 2.16.
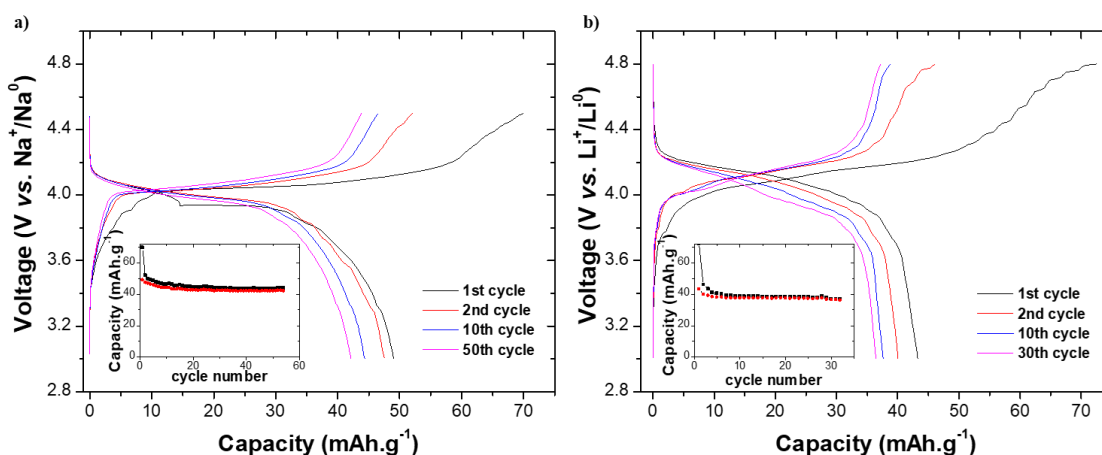
Figure 2.16: Voltage-capacity trace of Na₃V(PO₃)₃N obtained from melamine route measured (a) between 3.0 and 4.5 V at a C/40 rate vs. Na metal anode; (b) between 3.0 and 4.8 V at a C/40 rate vs. Li metal anode. In the insets cyclability of Na₃V(PO₃)₃N vs. both Na and Li anodes.

The capacity of the charge process indicates the removal of one Na^+ ion from the structure, which is almost identical as the performance of the material obtained via ammonolysis route. During the discharge, for both samples, the capacity is lower, again indicating irreversible capacity in the first cycle, however here slightly smaller for the Na cell than Li. In both cases, subsequent cycling proceeds with relatively stable capacity, as can be visible in the cyclability plots in the inset of Figure 2.16. Also, as in the previous experiments, the polarization is very small (0.048 *vs.* Na^+/Na^0 and 0.08 V *vs.* Li^+/Li^0) and the working voltage of the V^{III}/V^{IV} redox couple was remarkably high (~4 V) in both cells with just small difference of 0.1 V between Na and Li.

A capacity retention test was performed to study the electrochemical performance of Na₃V(PO₃)₃N obtained from the melamine route at higher cycling rates. The cell was cycled in the voltage window 3.0 – 5.0 V vs. Li metal as anode in the following conditions: 5 cycles at C/40, 5 cycles at C/20, 5 cycles at C/10, 5 cycles at C/5 and 10 cycles back at C/40 rate. Results of these measurements are presented in Figure 2.17.
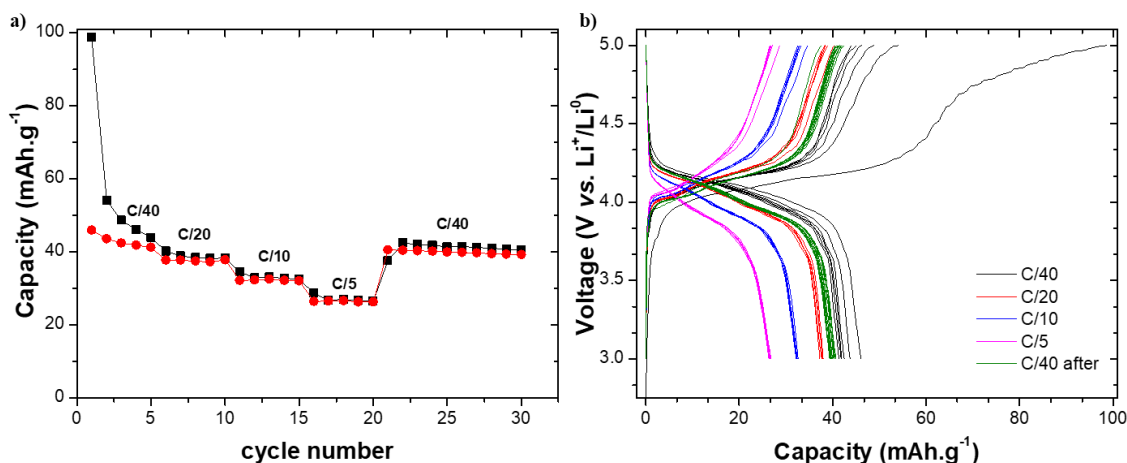
Figure 2.17: (a) Rate capability test of Na₃V(PO₃)₃N obtained from melamine route performed vs. Li metal at four different C-rates: C/40, C/20, C/10 and C/5 in a voltage window 3.0 – 5.0 V. (b) voltage-capacity curves of Na₃V(PO₃)₃N cycled at (black) C/40; (red) C/20; (blue) C/10; (violet) C/5 and (green) C/40 rate in a 3. 0 – 5.0 V voltage window.

The performed test shows an improved retention of the capacity with increasing rate for the melamine sample, compared with the sample synthesized from the ammonolysis route. For example, at C/20 rate the obtained capacity of ~40 mAh.g-1 is almost twice the one at the same C-rate obtained for the sample synthesized from the ammonolysis route (Figure 2.15). However, as can be seen in Figure 2.17b, with increasing cycling rate the polarization highly increases.

Based on these results it can be concluded that the attempts to use more than one Na⁺ ion were unsuccessful due to the instability of the organic liquid electrolytes at high voltage. In next tries, we decided to evaluate possibility of elevating the working voltage by using ion liquid electrolytes, which are expected exhibit a wider electrochemical stability window, in collaboration with Deakin University (Melbourne, Australia).

- **Ionic liquid electrolytes**

Room temperature ionic liquids are a very attractive alternative to conventional liquid electrolytes due to their exceptionally high thermal and electrochemical stability. For example, ionic liquid electrolytes based on imidazolium, pyridinium and tetra-alkyl-ammonium cations, coupled with bis(trifluromethanesulfonyl)imide anions, are particularly tailored for lithium battery systems operating >5 V *vs.* Li⁺/Li⁰. [180–183]

The first test was performed against Na metal anode and using C₃mpyrFSI with 3.2M NaFSI as electrolyte. Figure 2.18a shows the voltage-capacity curve obtained at C/10 rate in a voltage window 3.5 – 5.2 V *vs.* Na⁺/Na⁰. The upper voltage cut-off was increased to

search for the second redox process of V^{IV}/V^V couple. A capacity of 71 mAh.g^{-1} was achieved even at C/10. At higher voltage a pseudo plateau at ~4.8 V *vs.* Na$^+$/Na^0 is observed, followed by long plateau at ~5.0 V *vs.* Na$^+$/Na^0, assigned to the electrolyte degradation reaction, since the resulting capacity exceeds the theoretical capacity corresponding to the removal of two Na$^+$ (144 mAh.g^{-1}). A drastic decrease of the capacity in the following discharge and next cycle is observed, confirming electrolyte degradation.
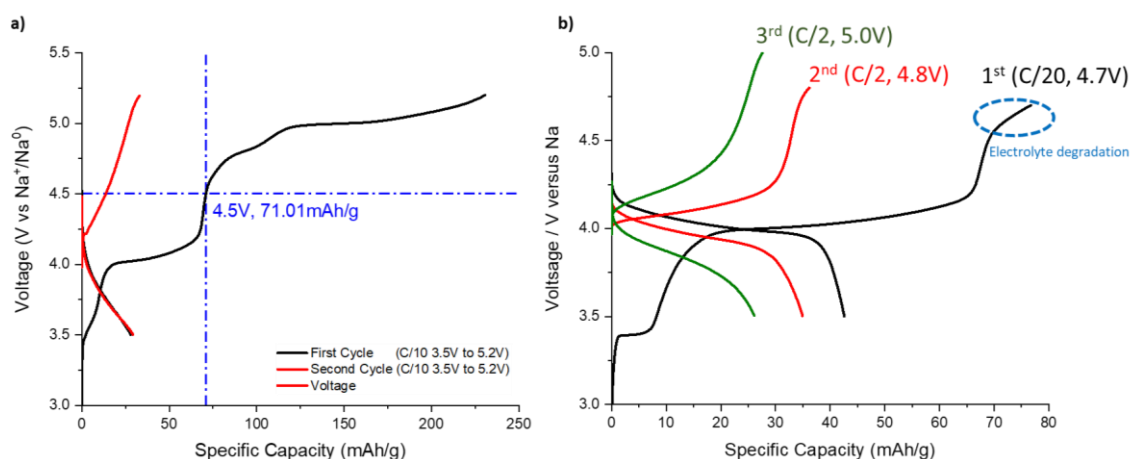
Figure 2.18: Galvanostatic charge-discharge curves of Na$_3$V(PO$_3$)$_3$N prepared from the ammonolysis route cycled *vs.* Na metal anode at (a) C/10 rate in voltage window 3.5 – 5.2 V; (b) various C/rates and voltage windows, as indicated in the figure, using ionic liquid electrolytes.

Next, Na$_3$V(PO$_3$)$_3$N was cycled against Li metal, using C$_3$mpyrFSI with 3.2M LiFSI as electrolyte (Figure 2.18b). At C/10, electrolyte degradation was observed above 4.5 V *vs.* Na$^+$/Na^0. Next tests were performed at C/2 rate with two cut-off voltages of 4.8 V and 5.0 V. Such a high C-rate resulted in a high capacity drop, and yet no activity of V^{IV}/V^V couple was registered below 5.0 V. Although the aimed redox activity of the second vanadium couple was not achieved, the performed tests demonstrated that one Na$^+$ ion can be successfully removed at much higher cycling rates, than with the use of carbonate-based liquid electrolytes. Further experiments would be needed to understand the impact of the electrolyte nature in the rate capability.

2.2.6.   Chemical oxidation

To get first insight into the structural changes occurring upon desodiation of Na$_3$V(PO$_3$)$_3$N, chemical oxidation was carried out. Oxidized Na$_{3-x}$V(PO$_3$)$_3$N was prepared by mixing Na$_3$V(PO$_3$)$_3$N powder with the solution of NO$_2$BF$_4$ in acetonitrile in the molar ratio of 1:1.1 under argon or 24h at room temperature. This reactant is widely used for oxidation reactions thanks to its very high redox potential, 5.1 V *vs.* Li$^+$/Li^0.[184]

Oxidation is expected to occur following the reaction:

$$Na_3V(PO_3)_3N + NO_2BF_4 \rightarrow Na_2V(PO_3)_3N + NaBF_4 + NO_2 \uparrow$$
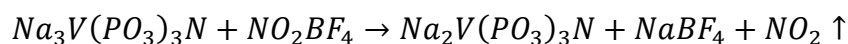
The obtained solution was filtered, washed three times with ethanol to remove the impurities of formed NaBF$_4$ and dried in the vacuum oven at 80 °C overnight. The XRD patterns of both pristine Na$_3$V(PO$_3$)$_3$N and oxidized Na$_{3-x}$V(PO$_3$)$_3$N are compared in the inset of the Figure 2.19.
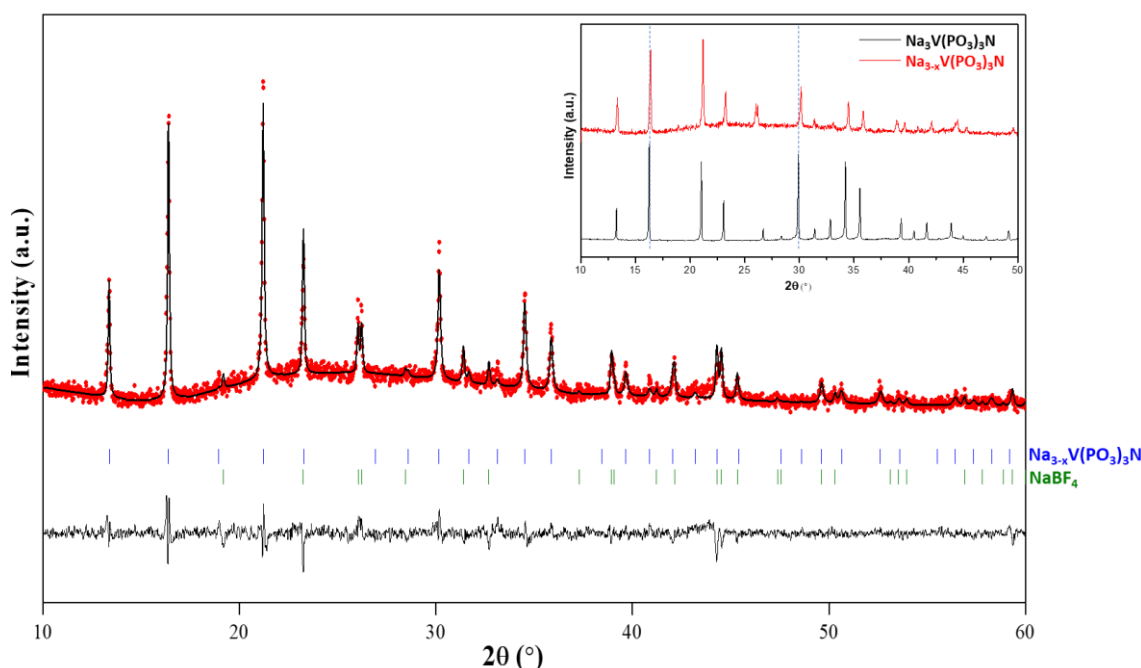
Figure 2.19: Rietveld refinement of the XRD pattern of chemically oxidized Na$_{3-x}$V(PO$_3$)$_3$N. Red circles, black and horizontal black lines represent the observed, calculated and difference patterns, respectively. The positions of the Bragg reflections of the $P2_13$ space group are shown as blue vertical bars. Green bars denote a 12% contribution of NaBF$_4$ impurity. In the inset comparison of the XRD patterns of Na$_3$V(PO$_3$)$_3$N (black line) and Na$_{3-x}$V(PO$_3$)$_3$N (red line) with the shift of the pattern indicated by the blue dashed line.

A small shift of all peaks to the higher 2θ values can be observed in the oxidized sample, as indicated by the blue dashed lines, suggesting a decrease of the cell parameters. Additionally, a change of the intensities in several peaks can be also observed after chemical oxidation. Rietveld refinement of the obtained XRD pattern of Na$_{3-x}$V(PO$_3$)$_3$N was performed to analyze the structure after performing the oxidation (Figure 2.19). Table 2.7 gathers the crystallographic data determined from the refinement.

Table 2.7: Crystallographic data and atomic coordinates of $Na_{3-x}V(PO_3)_3N$ determined from the refinement of XRD data.

S.G.: $P2_13$						
a =9.358(4) Å		V = 819.48(5) Å^3		R_{Bragg} =8.4 %	χ^2 = 1.43	
Atom	Wyckoff position	x/a	y/b	z/c	Occupancy	B_{iso}
P	12b	0.349(2)	0.077(2)	0.262(2)	1	0.72(6)
V	4a	0.497(3)	0.497(3)	0.497(3)	1	0.65(5)
Na2	4a	0.351(5)	0.351(5)	0.351(5)	0.96(2)	0.92(8)
Na3	4a	0.886(7)	0.886(7)	0.886(7)	0.57(2)	1.28(7)
O1	12b	0.158(4)	-0.018(4)	0.306(4)	1	0.92(6)
O2	12b	0.407(2)	0.042(2)	0.042(2)	1	0.98(6)
O3	12b	0.487(4)	0.245(4)	0.245(4)	1	1.13(6)
N	4a	0.194(2)	0.194(2)	0.194(2)	1	0.65(8)

The obtained XRD pattern was successfully refined with the $P2_13$ space group indicating no changes in the framework. Based on the refinement (Table 2.7), the unit cell parameter has decreased to 9.358(4) Å (compared to the cell parameter of 9.444(1) Å of pristine $Na_3V(PO_3)_3N$), which explains shift of all the peaks ito higher 2θ value. The refined occupancies of Na indicate that all Na from the Na1 was removed upon the oxidation. Additionally, vacancies on the Na3 site were observed suggesting a total removal of ~1.5 Na from the structure.

To verify these findings, ICP measurement was performed to analyze the atomic ratio in $Na_{3-x}V(PO_3)_3N$. Table 2.8 gathers the obtained results.

Table 2.8: Composition of $Na_{3-x}V(PO_3)_3N$ determined by ICP.

Element	Theoretical content	Experimental atomic ratio determined from ICP
Na	2	1.6±0.04
P	3	3(fixed)
V	1	1.0±0.02

Based on the performed measurement, the amount of Na in $Na_{3-x}V(PO_3)_3N$ was found to be 1.6, being in very good agreement with the findings from the refinement of the XRD pattern (taking into account ~12% of the $NaBF_4$ impurities identified in the refinement).

^{23}Na solid state NMR experiment was performed on the chemically oxidized $Na_{3-x}V(PO_3)_3N$ to study the local distribution of Na atoms and to compare these results with the spectra of pristine $Na_3V(PO_3)_3N$. Results are presented in Figure 2.20.
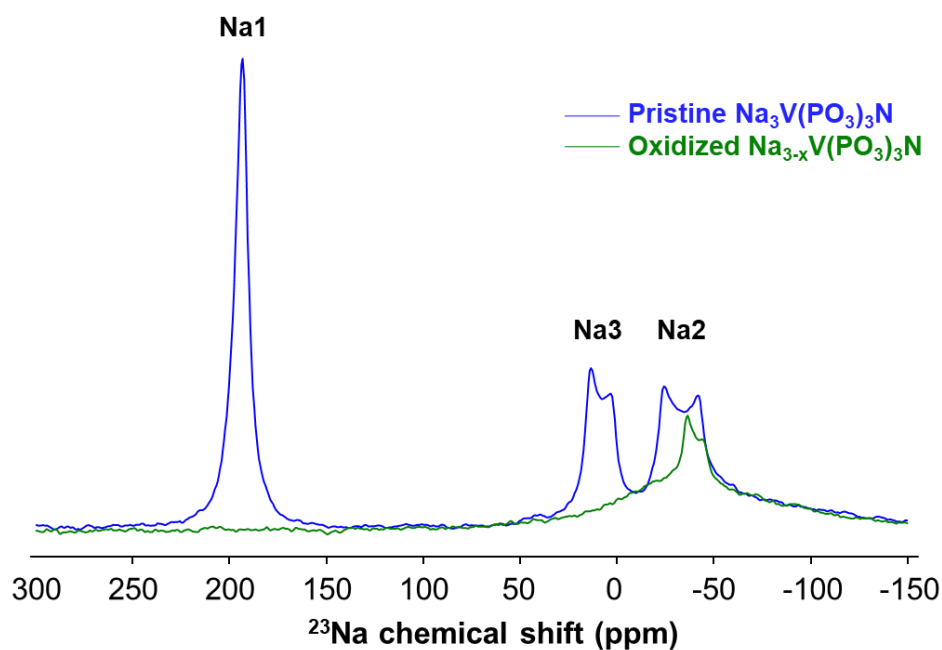
Figure 2.20: Comparison of the ^{23}Na NMR of the pristine Na$_3$V(PO$_3$)$_3$N (blue line) and chemically oxidized Na$_{3-x}$V(PO$_3$)$_3$N (green line) with the Na sites assigned as in the figure.

The Na sites in the pristine Na$_3$V(PO$_3$)$_3$N were assigned according to the discussion in chapter 2.2.2.5. While following the obtained spectra for the oxidized Na$_{3-x}$V(PO$_3$)$_3$N (green line) it can be observed that the only clear signal can be registered at ~ -45 ppm, which in pristine Na$_3$V(PO$_3$)$_3$N was assigned to Na2 site. Additionally, the shoulder at a left side of this signal can be related to the remaining Na at the Na3 site. Clearly no signal was observed at ~200 ppm, which indicate absence of Na at Na1 site. These results couple very well the findings from the Rietveld refinement of the XRD pattern and BVEL calculations on the removal of more than one Na from both Na1 and Na3 sites and confirms that the Na at the Na2 site remains most strongly coordinated to the structure.
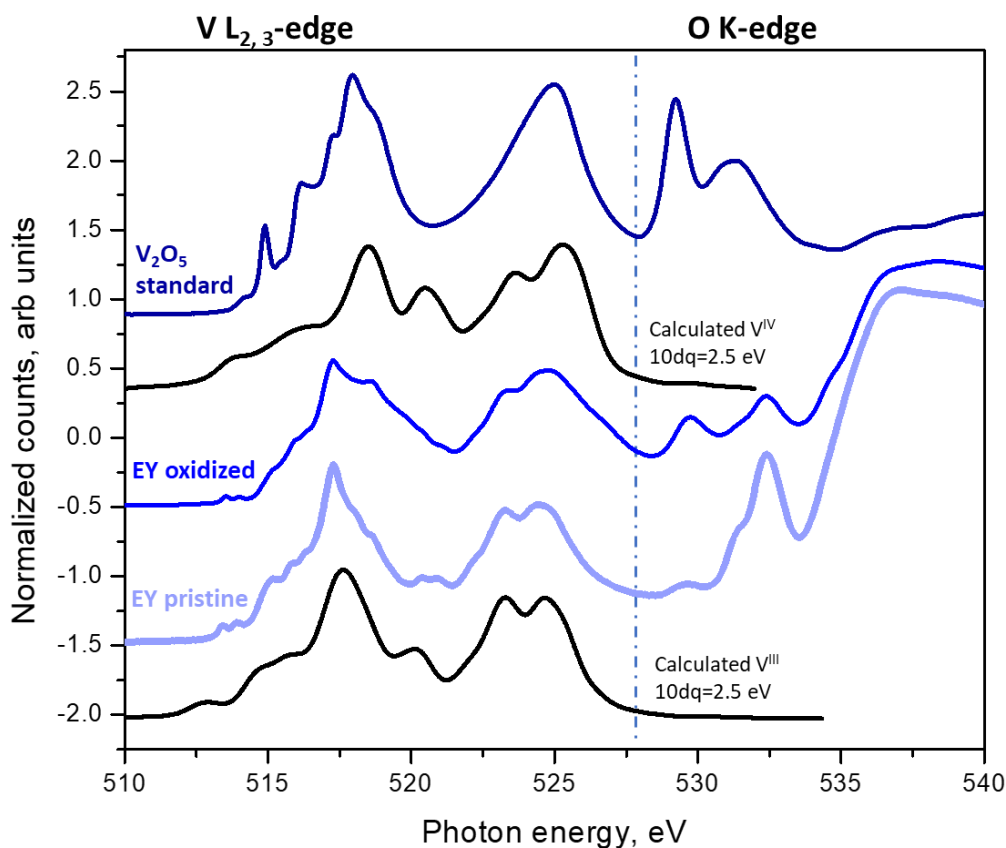
Figure 2.21: XAS V L$_{2,3}$-edge & O K-edge spectra in Na$_3$V(PO$_3$)$_3$N. Signals from electron detection mode (EY) of the pristine Na$_3$V(PO$_3$)$_3$N are denoted in light blue color, whereas for the chemically oxidized Na$_{3-x}$V(PO$_3$)$_3$N in blue color. Black curves correspond to the calculated XAS V^{III} and V^{IV} L$_{2,3}$-edge spectra with Oh coordination symmetry and a crystal field splitting energy of 2.5 eV. Dark blue color corresponds to the signal from the electron yield mode (EY) of V$_2$O$_5$ used as a standard for the V^V oxidation state.

Likewise relevant changes were observed by means of X-ray absorption spectroscopy (Figure 2.21). In the V L$_{2,3}$-edge region, a large broadening of two main bands centered at 518 and 525 eV can be observed. The shoulder at 518.6 eV in the pristine sample attributed to the small contribution of the V^{IV} oxidation state is much better defined in the oxidized sample, as indicated by the light green vertical line. Double peaks between 520-521 eV being the signature peaks of the V^{III} state are no longer visible in the spectra of the oxidized sample. Finally, significant changes in the intensity ratio of the peaks below 534 eV in the O K-edge indicate the change in the electron occupancy of the t$_{2g}$-e$_g$ orbitals. All these features indicate complete oxidation of vanadium in Na$_{3-x}$V(PO$_3$)$_3$N into V^{IV}. Although the removal of 1.5 Na (as determined earlier) implies the further oxidation of vanadium, no signs of V^V were observed compared to the reference V^V spectrum (dark blue color in Figure 2.21), which could suggest an eventual oxidation state of ~ +4.5.

This experiment demonstrated that NO_2BF_4 is very strong oxidizing agent and can be successfully used to oxidize $Na_3V(PO_3)_3N$. The refined composition of $Na_{1.5}V(PO_3)_3N$ in the oxidized sample indicates the removal of 1.5Na. By electrochemical oxidation of $Na_3V(PO_3)_3N$ it is only possible to remove one Na indicating that higher voltage is required to reach second Na atom, being in perfect agreement with DFT voltage calculations. Additionally, it has been confirmed that the sodium in the Na2 sites is the least mobile, corroborating the BVEL results.

2.2.7. Evaluation of the Na insertion/extraction mechanism

2.2.7.1. Ex situ XRD

Swagelok-type cells comprising $Na_3V(PO_3)_3N$ as a positive electrode and Li (Na) metal as negative electrode were first charged up to selected voltage values (indicated in Figure 2.22). Next, the swageloks were opened in the glovebox and the positive electrodes were washed three times in DMC to remove the traces of the electrolyte. Once dried, the electrodes were loaded into a sensitive XRD holder to collect the XRD patterns. For the cells cycled *vs.* Na anode two patterns were collected: at 4.0 V *vs.* Na^+/Na^0 and at full charge – at 4.5 V *vs.* Na^+/Na^0. In turn, three patterns were collected for the cell cycled *vs.* Li: at 4.0 V *vs.* Li^+/Li^0, full charge – at 4.8 V *vs.* Li^+/Li^0 and full discharge at 3.8 V *vs.* Li^+/Li^0. *Ex situ* XRD patterns of cycled electrodes are shown in Figure 2.22 b and d together with that of the corresponding pristine electrode.
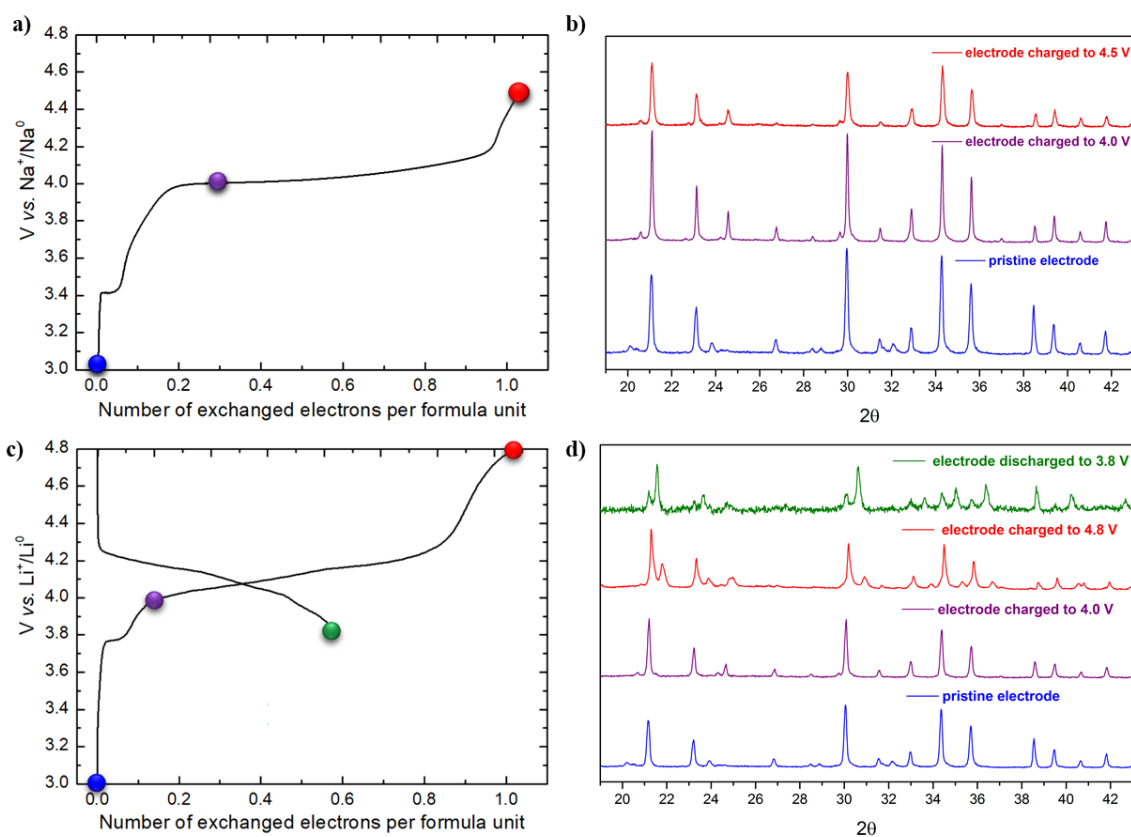
Figure 2.22: Electrochemical curves of Na$_3$V(PO$_3$)$_3$N of the full charge vs (a) Na and full charge and discharge vs (c) Li. Colored spheres indicate the voltages up to which each cell was cycled and opened to collect the XRD pattern. (b&d) corresponding ex situ XRD patterns measured from the recovered electrodes.

Almost no change in shape or peak position can be observed in the cells cycled *vs.* Na (Figure 2.22b). The refined cell parameter of the fully charged cell is just slightly smaller than the one of the pristine material (Table 2.9) indicating almost no change in the volume of the cell occurs upon removal of one Na.

Table 2.9: Cell parameter *a* value of Na$_3$V(PO$_3$)$_3$N cycled *vs.* Na and Li at different charge states.

	Na$_3$V(PO$_3$)$_3$N *vs.* Na	Na$_3$V(PO$_3$)$_3$N *vs.* Li
	a [Å]	a [Å]
Pristine	9.4393(4)	9.4393(4)
Charged up to 4.0 V	9.4353(2)	9.4366(3)
Charged up to 4.5 V (4.8 V)	9.4253(1)	9.4234(4) + 9.2092(8)
Discharged up to 3.8 V	-	9.4415(2) + 9.2158(3)

A quite different behavior can be observed in the cells charged *vs.* Li (Figure 2.22d) as a secondary cubic phase appears at higher angles when charging the cell above 4.0 V *vs.* Li$^+$/Li^0. The cell parameters of this second phase are significantly smaller than the pristine

phase (Table 2.9), which may indicate a spontaneous Na^+/Li^+ ion exchange of the partially discharged electrode.

This hypothesis was evaluated by soaking electrodes corresponding to different states of charge in LP30 electrolyte (*i.e.* the electrolyte used in the cells cycled *vs.* Li). Figure 2.23 shows the XRD patterns of the pristine $Na_3V(PO_3)_3N$ electrode; electrode soaked in LP30 electrolyte for 12h; electrode charged to 4.1 V; electrode charged to 4.1 V and soaked in LP30 electrolyte for 12h.
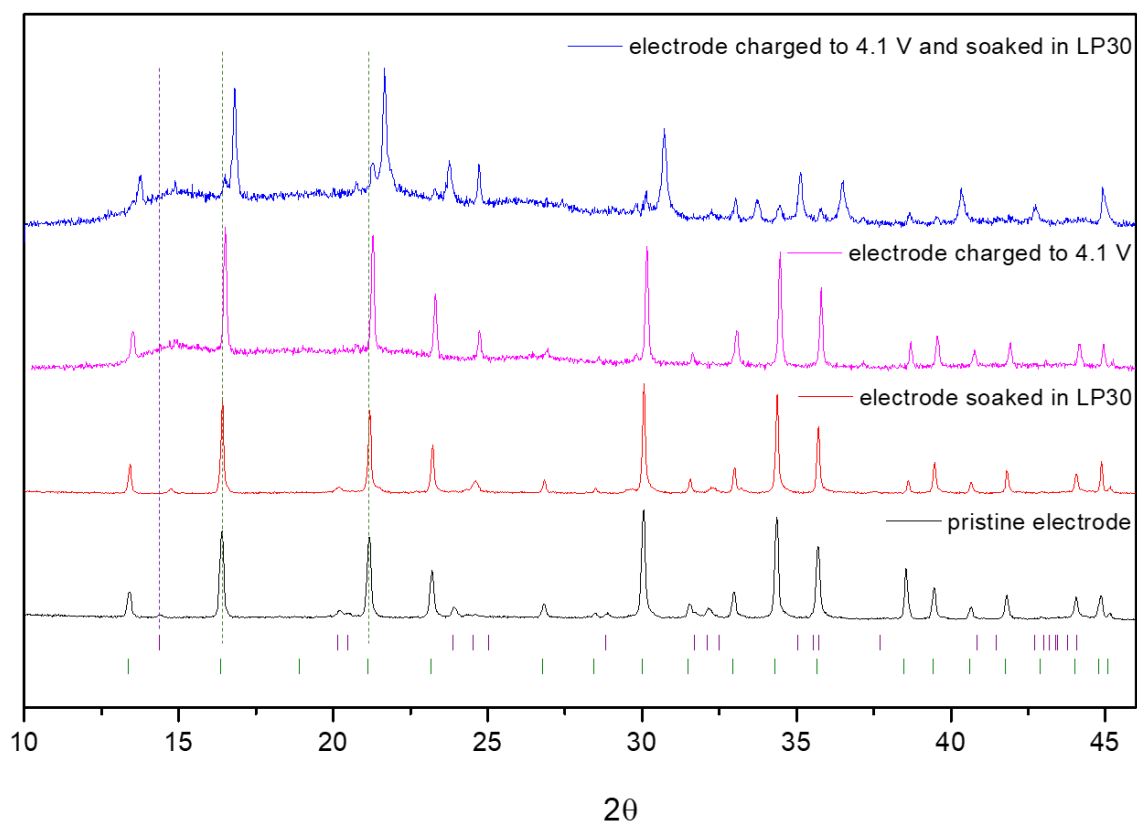
Figure 2.23: XRD patterns of (black) pristine $Na_3V(PO_3)_3N$ electrode; (red) $Na_3V(PO_3)_3N$ electrode soaked in LP30 electrolyte for 12h; (pink) $Na_3V(PO_3)_3N$ electrode charged to 4.1 V; (blue) $Na_3V(PO_3)_3N$ electrode charged to 4.1 V and soaked in LP30 electrolyte for 12h. Green bars refer to the positions of the Bragg reflections of the $Na_3V(PO_3)_3N$ phase. Violet bars denote a small (< 7 %) contribution of NASICON-type $Na_3V_2(PO_4)_3$.

No changes in the XRD pattern are observed after soaking the pristine $Na_3V(PO_3)_3N$ phase (Figure 2.23, red curve), contrary to the NASICON secondary phase for which spontaneous Na^+/Li^+ ion exchange was observed (indicated by vertical violet dashed line). Different results were obtained when the electrode was charged up to 4.1 V and next soaked in LP30 as only very small peaks of the $Na_3V(PO_3)_3N$ phase remain after soaking (Figure 2.23, blue curve). The new cubic phase appears at higher angles, analogous to the results obtained from the *ex situ* experiment. This confirms that,

concomitant to the electrochemical process of Na extraction from the structure, the exchange of Na^+ ions with the Li^+ ions occurs from the electrolyte in the charged material.

2.2.7.2. Operando XRD

Operando XRD measurements were performed to follow observed changes in the structure of $Na_3V(PO_3)_3N$ under cycling conditions. Since the resolution of the collected XRD patterns in operando XRD experiments at the laboratory diffractometer was not sufficient to establish the reaction mechanism, *operando* synchrotron XRD measurements were performed at the BL04-MPSD beamline of ALBA Synchrotron in Barcelona. The home-made *in situ* cell was used for the measurements (details in Annex - experimental section). A laminate of $Na_3V(PO_3)_3N$ with a ratio of 80% active material : 10% C_{65} carbon : 10% PVDF solution in NMP and a mass loading of ~3 mg.cm^{-2} was used as positive electrode.

The cells were cycled at a C/20 rate *vs.* Na and Li metal. The cell cycled *vs.* Na was charged up to 4.5 V and then discharged down to 3.0 V, whereas the cell *vs.* Li was charged to 4.5 V and the discharge unfortunately had to be stopped at 3.9 V, due to a connection failure. In both cases, the XRD patterns were collected in the 2θ range 0° – 44° for 5 min, every 30 min. The results of these two experiments are described below.

- **$Na_3V(PO_3)_3N$ *vs.* Na**

One complete cycle (one charge and one discharge) was registered. The measurement lasted for around 43 hours. The collected SXRD patterns as well as the corresponding electrochemical curve are shown in Figure 2.24.

Unexpectedly, the cell cycled *vs.* Na resulted in a high capacity in the charge process (beyond the theoretical capacity corresponding to one exchanged Na^+), possibly due to a side process involving oxidation of the electrolyte, resulting also with a lower capacity in the discharge.
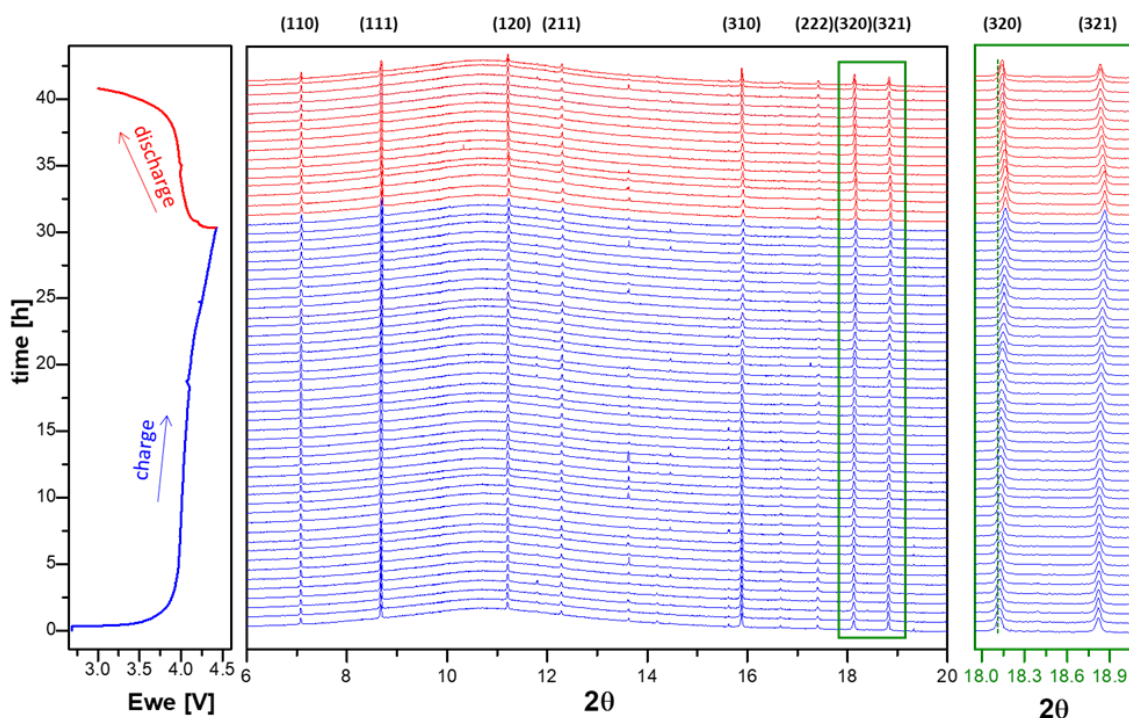
Figure 2.24: Results obtained for the *in situ* cell comprising Na₃V(PO₃)₃N as an active material cycled *vs*. Na metal at C/20 rate. On the left, electrochemical curve indicating charge process in blue and discharge in red; on the right, collected SXRD patterns with the zoom of the selected peaks of the Na₃V(PO₃)₃N phase, as indicated by the orange and green regions.

Based on the collected SXRD patters, only very subtle changes can be detected within the structure of $Na_3V(PO_3)_3N$ upon cycling. A slight shift of the peaks towards higher 2θ value can be observed in the charge with a reversible shift to the lower 2θ value in the discharge, as visible in the zoom of the (320) and (321) peaks. This observation corroborates our preliminary conclusions on the zero-strain nature of this material (at least for the V^{II}/V^{IV} process).[185]

In order to have an insight into the structural changes occurring upon cycling, Rietveld refinements were performed. Each collected SXRD pattern was successfully refined with the $P2_13$ space group. The details on the changes of the lattice parameter, volume and the Na occupancies in each site, obtained from the refinements, are gathered in Table 2.10 , whereas Figure 2.25 shows the variation of the cell parameter (Figure 2.25a) and Na occupancy (Figure 2.25b) upon time.

Table 2.10: Refined lattice parameters, cell volume and Na occupancies of acquired from the refinement of the corresponding XRD patterns at OCV, fully charged and fully discharged state of $Na_3V(PO_3)_3N$ cycled *vs*. Na metal.

Charge state	Na occupancy	a (Å)	V (Å^3)
OCV	Na1 0.989(4) Na2 1.0(2) Na3 1.0(5)	9.446(2)	842.84(3)
End of charge – 4.5 V	Na1 0.204(5) Na2 1.0(3) Na3 0.853(3)	9.425(5)	837.23(3)
End of discharge – 3.8 V	Na1 0.611(5) Na2 1.0(2) Na3 1.0(2)	9.440(4)	841.23(2)
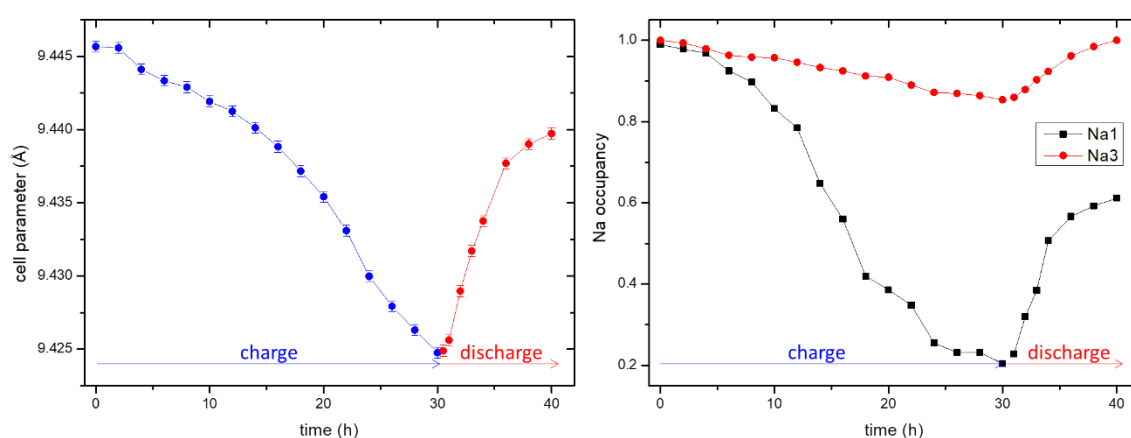
Figure 2.25: (a) variation of the $Na_3V(PO_3)_3N$ cell parameter in time upon charge and discharge during the *operando* process; (b) variation of the Na occupancy (both Na1 and Na3 site) in time upon charge and discharge during the *operando* process.

Refinement of the Na occupancies revealed that during charge, Na^+ ions are being partially extracted from the Na1 and Na3 sites, as predicted from the BVEL and DFT calculations. This finding confirms that the two peaks or shoulders observed in the derivative dQ/dV curves in Figure 2.12 and Figure 2.14 indeed correspond to the removal of Na^+ ions from Na1 and Na3 site at slightly different voltages. In total, around one Na^+ was extracted from the structure, in agreement with previous electrochemical tests. During the discharge, a total of 0.55 Na^+ ions were reinserted, fully filling Na3 site, while around 0.4 Na^+ ions from the Na1 site were not able to be re-inserted into the structure. Zhang et. al.[164] obtained comparable performance and likewise observed high irreversible capacity for the first charge. Based on the analysis of the *in situ* XRD, they observed that upon cycling Na^+ ions are extracted from the Na1 and Na3 sites, however, upon discharge part of the Na^+ ions are not re-inserted into Na1 (Na3 according to their notation) site suggesting high diffusion barrier for this site.

The obtained amount of the extracted/inserted Na^+ ions from the refinements corresponds perfectly with the capacities obtained during the charge/discharge processes. No indication of structural rearrangements that could be at the origin of the irreversible capacity typically observed in the first cycle for this material were found. The progressive variation of the lattice parameters together with the absence of additional phases suggest a solid-solution mechanism of sodiation-desodiation process. This hypothesis could be supported by the work of Chen et al.[169] where combined analysis of GITT, *in situ* synchrotron XRD and *in situ* XAS measurements likewise suggested solid-solution reaction mechanism recognized based on the one electron transfer process.

- **$Na_3V(PO_3)_3N$ *vs.* Li**

The second cell was cycled *vs.* Li metal in hybrid configuration. The collected SXRD patterns are gathered in Figure 2.26, together with the corresponding electrochemical curve indicating the charge and discharge process in blue and red, respectively.
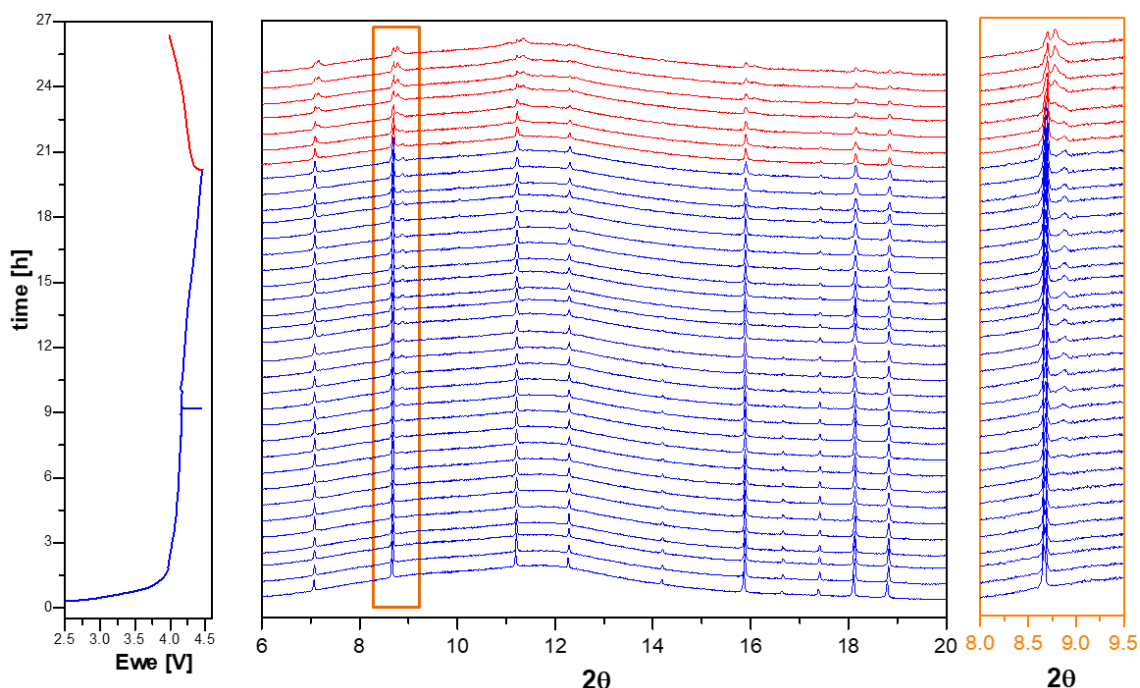
Figure 2.26: Results obtained for the *in situ* cell comprising $Na_3V(PO_3)_3N$ as an active material cycled *vs.* Li metal at C/20 rate. On the left, electrochemical curve, indicating charge process in blue and discharge in red, on the right collected SXRD patterns, with the zoom of the selected peak, as indicated by the orange region.

The evolution of the cell parameters and the % fraction of these two phases derived from the Rietveld refinements of the SXRD patterns is presented in Figure 2.27. The details on the changes of the lattice parameter and volume obtained from the refinements, are gathered in Table 2.11. In agreement with the *ex situ* XRD data, a secondary cubic phase

appears at higher angles, visible in the enlarged image in Figure 2.27. The cell parameter of this second phase ($a = 9.213(2)$ Å at 4.5 V) is significantly smaller than the one of the pristine phase ($a = 9.4397(3)$ Å) and almost equal to observed earlier in the *ex situ* measurement. Therefore, the occupancy of the different phases was refined considering both Li and Na atoms in both phases. Since Li occupancy cannot be refined using the SXRD data, the amount of Na was refined and it was assumed that Li occupies the vacancies. A similar lattice parameter reduction associated to a Li^+/Na^+ ion exchange in isotypic compounds $Na_2Fe_2(PO_3)_3N$ and $Na_2Mg_2(PO_3)_3N$ were previously reported. [160,186]
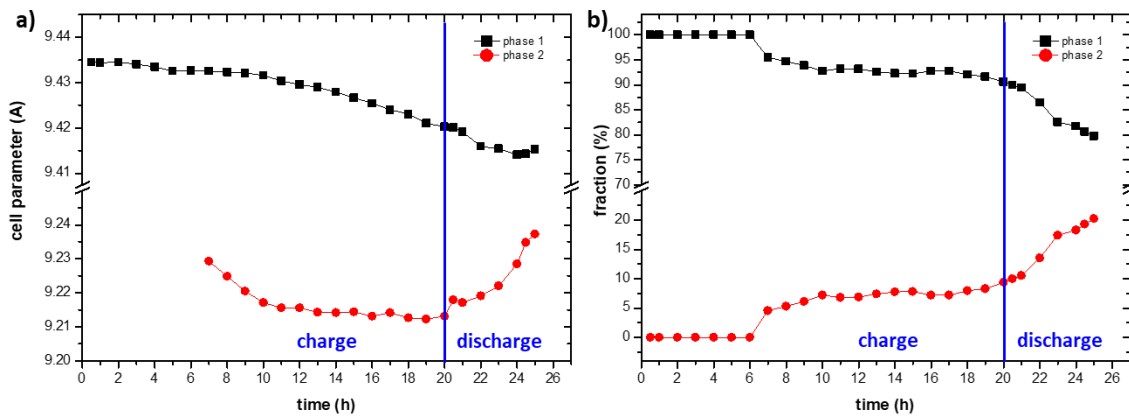
Figure 2.27: Variation of the (a) cell parameter; (b) fraction (%) *vs.* time of the two refined phases of $Na_3V(PO_3)_3N$ and $Na_{3-x}Li_xV(PO_3)_3N$ during the in situ cycling *vs.* Li.

Table 2.11: Refined Na occupancy, lattice parameters and cell volume acquired from the refinement of the corresponding XRD patterns at OCV, charged and discharged state of $Na_3V(PO_3)_3N$ cycled *vs.* Li metal.

Charge state	Na occupancy	a (Å)	V (Å³)
OCV	Na1 0.985(4) Na2 1.0(2) Na3 1.0(5)	9.447(3)	843.32(4)
End of charge – 4.5 V	Na1 0.169(6) Na2 1.0(3) Na3 0.476(3)	9.420(5)	835.98(5)
End of discharge – 3.9 V	Na1 0.151(4) Li1 0.739(4) Na2 1.0(2) Na3 0.696(5) Li3 0.155(5)	9.415(3)	834.74(6)

Table 2.12: Refined Na/Li occupancy, lattice parameters and cell volume acquired from the refinement of the corresponding XRD patterns at OCV, charged and discharged state of the second phase, $Na_{3-x}Li_xV(PO_3)_3N$, cycled *vs*. Li metal.

Charge state	Na occupancy	a (Å)	V (Å³)
End of charge – 4.5 V	Li1 0.002(3) Na2 1.0(3) Li3 0.431(4)	9.213(2)	782.03(4)
End of discharge – 3.9 V	Li1 0.611(5) Na2 1.0(2) Li3 0.849(3)	9.247(3)	806.77(4)

Based on the Na occupancies from Table 2.11 and Table 2.12 and taking into account phase fractions, at the end of the charge 1.355 Na^+ was utilized. Since only one Na^+ ion was extracted from the structure, it suggests that remaining 0.355 Na^+ took part in the spontaneous ion exchange with the Li^+ ions from the electrolyte. Through refining the second, $Na_{3-x}Li_xV(PO_3)_3N$ phase, it was observed that all Na located in the Na2 site remains intact, while sodium ions both Na1 and Na3 are entirely exchanged with lithium ions. At the end of the charge, almost all Li^+ ions from the Li1 and around half from the Li3 site were extracted (Table 2.11 and Table 2.12). Interesting phenomenon can be observed while following the discharge process. Instead of increasing of the cell parameters for the $Na_3V(PO_3)_3N$, as detected while charging *vs*. Na anode, it slightly decreased. This can be explained by observed insertion of the Li^+ ions in the Na1 and Na3 sites, as shown in Table 2.11 since Li^+ ion has much smaller ion radii than Na^+ (0.74 Å *vs*. 1.02 Å).[187] Within the second, $Na_{3-x}Li_xV(PO_3)_3N$ phase also partial insertion of the Li^+ ions was detected, as shown in Table 2.12.

It is expected that $Na_3V(PO_3)_3N$ will follow exactly the same desodiation mechanism independently on the used counter electrode. In Figure 2.26 it can be observed that no changes in the shape or the position could be noticed when cycling against the Li anode and therefore only small changes in lattice parameters were found. These corroborate the assumed solid-solution mechanism of the desodiation reaction.

2.2.8. Evaluation of factors affecting electrochemical performance

Based on the performed *ex situ* and *operando* XRD measurements, no changes in the $Na_3V(PO_3)_3N$ framework were observed that could explain the irreversible capacity

unavoidably observed in the first cycle. This might suggest that these changes were too subtle to be registered by XRD or undetectable.

Different scenarios of the nitrogen effect can be taken into account, which could be compared to the reported anionic redox effects of oxygen:

- irreversible redox reaction of nitrogen with the release of N_2 (similarly to irreversible reaction when oxygen leaves the structure as O_2)[188]

- reversible redox reaction of nitrogen, which could be compared to the reversible formation of peroxo-like $(O_2)^{n-}$ species occurring for oxygen.[189–192]

First hypotheses is the irreversible oxidation of the N^{3-} from the $Na_3V(PO_3)_3N$ structure upon electrochemical cycling process. This reaction would be associated with the release of the N_2, and can be found in the literature on the example of$LiFeSiO_3N$.[193] As explained by Armand and Arroyo y de Dompablo[193], such a phenomena was related to the redox activity of the N^{3-} ions, expected to occur in a voltage range $3.5 – 4.2$ V, and can be observed as additional plateau in the electrochemical curve. While cycling $Na_3V(PO_3)_3N$ in the electrochemical curves we did not observe additional plateau, however the redox activity of the N^{3-} ions could be overlapped with the plateau corresponding to the redox reaction of the V^{III}/V^{IV} couple. This hypothesis is supported with the observed irreversible capacity which would be ascribed to the partial oxidation of N^{3-} into N_2.

Second hypothesis, the reversible reaction of nitrogen, would be related with the formation of oxynitride species, which could also correspond to the additional capacity registered in the electrochemical curve. However, since this reaction is supposed to be reversible, the additional capacity would be expected to reappear in the next cycles, whereas it was observed only in the first one.

To test these different hypotheses, we decided to perform distinct tests attempting to analyze the eventual influence of nitrogen. In the first one, the assumed release of the N_2 gas is expected to be registered by *ex situ* gas chromatography mass spectrometry (GC-MS) analysis. Next, since the oxidation of nitrogen could translate in the subtle changes in the structure and particularly the P-O and P-N bonds (not observed by XRD), a set of *ex situ* Raman measurements will be performed at different charge-discharge stages.

2.2.8.1. Gas analysis

GC-MS analysis was performed at the Laboratoire de Réactivité et Chimie des Solides (LRCS) in Amiens using a self-made set-up that allows measuring evolved gasses from chemical or electrochemical reactions. Details on this experiment can be found in the experimental section.

As the expected amount of released gases is relatively low (with a 18 mm electrode of $Na_3V(PO_3)_3N$ of mass loading of ~5 mg.cm^{-2} this would correspond ~0.035 ml), we decided to analyze the gases released upon chemical oxidation using a solution of NO_2BF_4 in a suitable solvent (acetonitrile or sulfolane). The redox potential of NO_2^+/NO_2 is ca. 5.1 V vs. Li^+/Li and is effective for oxidizing $Na_3V(PO_3)_3N$. NO_2 is expected to be detected together with N_2, according to the mechanism presented in section 2.2.5. The results obtained from the MS analysis of the gases released from the chemically oxidized $Na_3V(PO_3)_3N$ using NO_2BF_4 in sulfolane are gathered in Figure 2.28. By vertical blue line is indicated the moment of the opening the valve and beginning of the registering the gases from the experiment.

Figure 2.28 shows the changes in intensity registered for the selected gases: Ar (reference), N_2, NO and NO_2. The high increase in NO_2 confirms the oxidation reaction. A very small change in the curve for N_2 suggests that a small amount of this gas was also registered, however as the shape of the curve remains flat it rather would be assigned to the slight leak of the air. The most interesting was the registered high amount of NO which might suggest some parallel reactions arising from the reaction of N^{3-} to NO in $Na_3V(PO_3)_3N$.
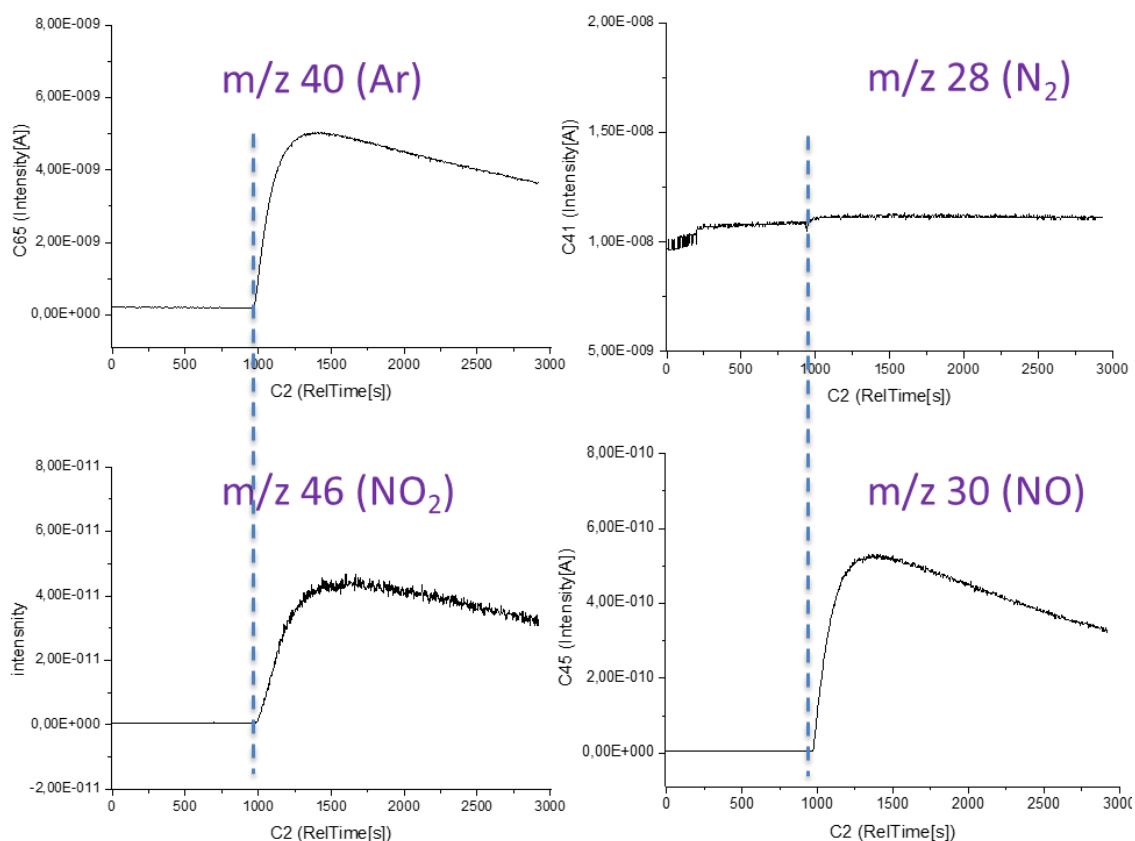
Figure 2.28: Trace of the intensity in time of the selected m/z ratio corresponding to the specific gases obtained from the MS analysis of the chemically oxidized Na₃V(PO₃)₃N using NO₂BF₄ in sulfolane. By vertical blue line is indicated the moment of the opening the valve and beginning of the registering the gases from the experiment.

The next set of experiments were performed by electrochemical oxidation of Na₃V(PO₃)₃N. The tests were performed in two types of cells: a modified Swagelok cell, and an EL-cell (details in annex). The advantage of the EL-cell is the larger surface area of the electrode, so as to maximize the amount of gases, however Swagelok cells provide much tighter closure and better contact between electrodes. Both Swagelok and EL-cell were assembled in the argon filled glovebox using a self-standing electrode of Na₃V(PO₃)₃N as cathode and metallic lithium as an anode. The cells were charged once at C/20 rate with the cut-off voltage set up at 4.5-4.8 V *vs.* Li⁺/Li⁰ with 5 h hold. The obtained voltage-capacity curves are shown in Figure 2.29. The Swagelok cell was stopped at 4.5 V due to the set limit of time of the reaction, however the obtained capacity corresponds to the removal of one Na indicating complete charge. The capacity of the EL-cell also corresponds to the removal of one Na, however the shape of the curve at high voltage (>4.6 V) rather corresponds to the oxidation of the LP30 electrolyte. The MS analysis of the formed gases was performed for both cells, however since in the EL-cell was observed oxidation of the electrolyte which has impact on the formed gases, only the

results from the Swagelok cell will be presented. Figure 2.30 shows the intensity changes in the gas flow observed for the detected gases of the Swagelok cell.
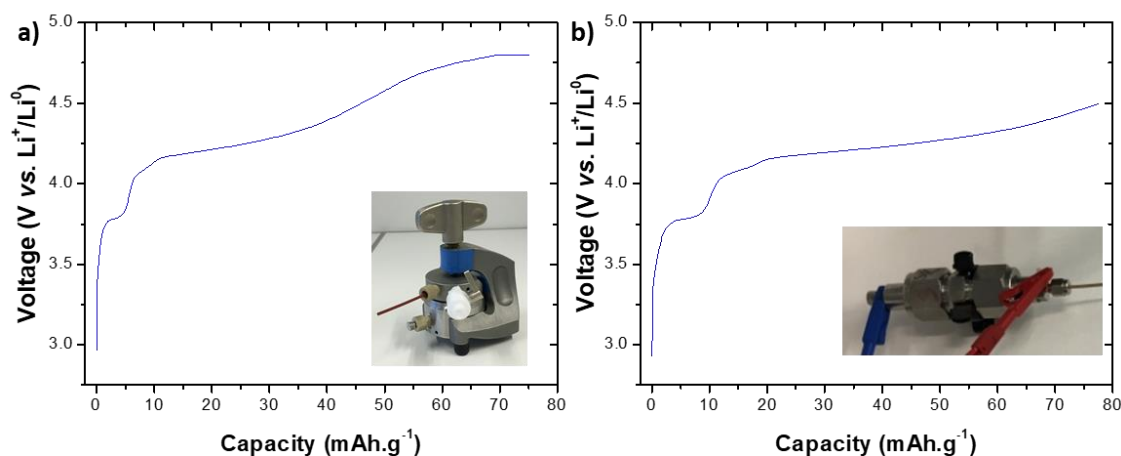
Figure 2.29: Voltage-capacity curve of the Na₃V(PO₃)₃N charged once *vs.* Li+/Li at C/20 rate in (a) EL-cell; (b) Swagelok cell.
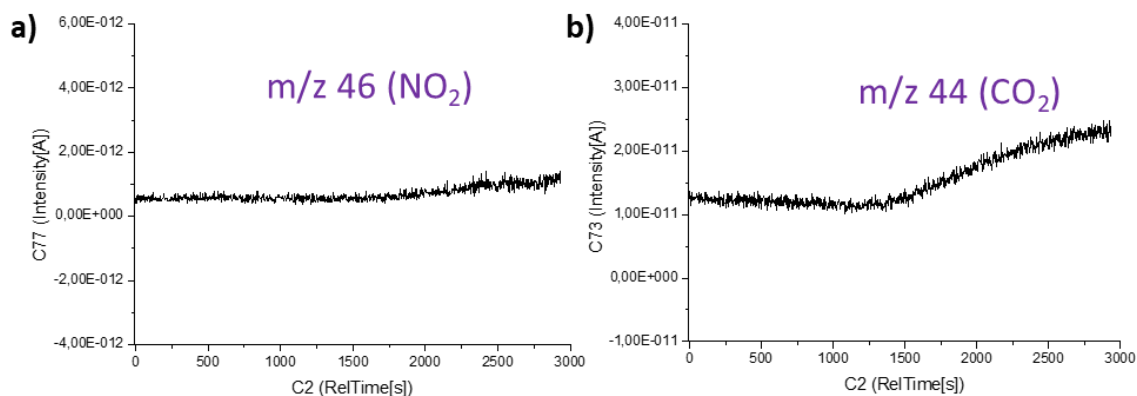
Figure 2.30: Results from the MS analysis of the gases released from Swagelok cell.

In the Swagelok cell a very small amount of NO_2 and a relative high amount of CO_2 were detected. CO_2 is expected to be released upon the electrolyte oxidation, whereas NO_2 in this case is supposed to come from the oxidation of Na₃V(PO₃)₃N. In the EL-cell only a small amount of CO and CO_2 were detected, confirming the electrolyte oxidation, as observed in the electrochemical curve. No N_2 or NO gas was registered in none of the cells. These results do not couple the findings from the analysis of the gases from the chemical oxidation, which might be related to the insufficient amount of the nitrogen-type gases formed from the electrochemical oxidation or to a low cut-off voltage. The use of higher mass loading and a wider voltage window would be suggested for the future.

Summarizing performed experiments, both MS and GC MS can be used to analyze the gases after chemical and electrochemical oxidation. An optimization of the electrode size

and the time of the experiment (longer hold) is required to obtain a higher amount of gases.

Evolution of several N-containing gases was detected, mainly NO, which suggests oxidation of nitrogen. This phenomenon could be responsible for the irreversible capacity, however this finding require coupling with other techniques to understand the changes occurring in the $Na_3V(PO_3)_3N$ structure upon oxidation.

2.2.8.2. Raman spectroscopy

To further evaluate eventual changes in $Na_3V(PO_3)_3N$ during electrochemical operation a series of different *ex situ* Raman measurements were performed – pristine electrode, at the end of the first charge, at the end of the first discharge and at the end of the second charge. For these *ex situ* experiments, self-standing electrodes of $Na_3V(PO_3)_3N$, charged to the desired state were removed from the cell, washed in DEC solvent, dried, placed between two glass plates and sealed with molten wax in the glovebox as demonstrated in Figure 2.32. The obtained spectra were gathered in Figure 2.32.
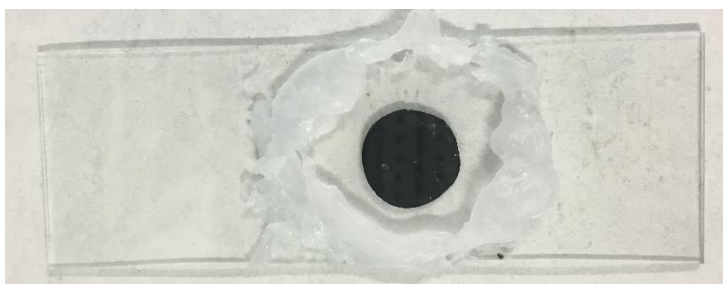
Figure 2.31: $Na_3V(PO_3)_3N$ electrode sealed between two glass plates for ex situ Raman measurement.
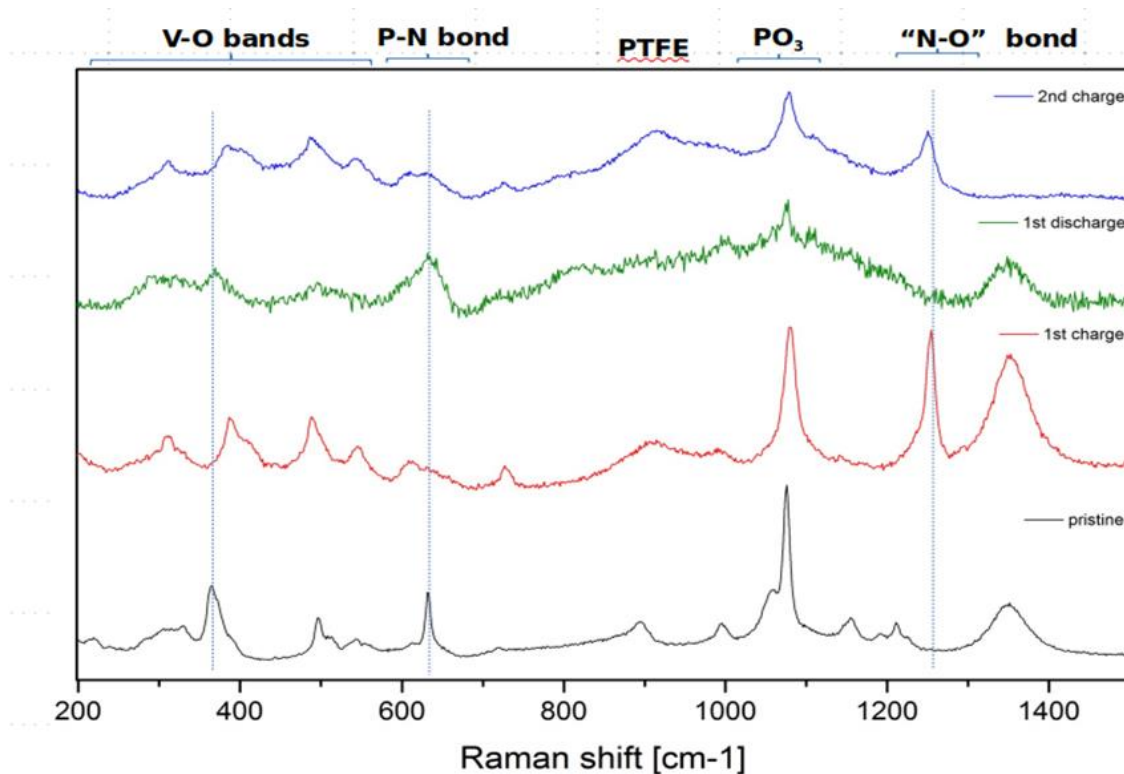
Figure 2.32: Ex situ Raman spectra of Na₃V(PO₃)₃N collected at distinct charge states, as indicated in the figure. Identified ranges of distinct bonds are also marked in the figure. The band at 1350 cm⁻¹ corresponds to carbon used to prepare the self-standing electrode, and its absence in the 2ⁿᵈ discharge curve might be related with the focus on the large particle od the active material.

The analysis of the spectra and the assignation of the bands were performed based on the literature and available Raman data for similar compounds such as phosphorous oxynitride glasses. [194–199]

Multiple changes in the spectra were observed upon charging and discharging. The reversible shift of the V-O bands confirms the oxidation-reduction of vanadium. The bands at 620 cm⁻¹ and 1280 cm⁻¹ were assigned to the nitrogen-phosphorous and nitrogen-oxygen bonds, respectively.[194,195] These observations would suggest reversible changes in the bonding nature upon cycling such as large elongation or shortening of the bonds in the (PO₃)₃N unit. However, based on the detailed analysis of the refinements of the SXRD patterns from the *operando* measurement (section 2.2.6.2.), no changes in the P-N bond were observed (1.71(5)Å for the pristine material and 1.69(5) Å at the end of the charge)

Summarizing both performed experiments, the activity of nitrogen from Na₃V(PO₃)₃N upon cycling cannot be excluded. Although no direct release of N₂ gas was observed, the registered small amount of NO in the mass spectrometry together with the registration of the new N-O bond by Raman analysis suggest the oxidation of nitrogen into oxide. Yet

these findings are not sufficient to claim it as an anionic redox activity of nitrogen and a source of the irreversible capacity and would require further investigation.

2.3. Li$_3$V(PO$_3$)$_3$N

A natural step after the evaluation of Na$_3$V(PO$_3$)$_3$N was the replacement of Na by Li, as has previously been done for the Fe counterpart. Li$^+$ has a much smaller ion radius (0.74 Å)[187] than Na$^+$ (0.92Å),[187] thus replacing Na atoms with Li atoms is expected to enhance the mobility of the ions within the structure. Indeed it has been demonstrated by Liu et. al.[160] that Li$_2$Fe$_2$(PO$_3$)$_3$N possesses much higher Li$^+$ ionic conductivity compared to the Na$^+$ conductivity in the Na counterpart. In the previous part we demonstrated that Li$^+$ ions can be reversibly intercalated in the Na$_3$V(PO$_3$)$_3$N structure at ~4.0 V *vs.* Li$^+$/Li^0. The lower molecular weight of Li$_3$V(PO$_3$)$_3$N together with anticipated higher ionic mobility of Li$^+$ ions is expected to translate into improved electrochemical performance of this compound. The theoretical capacity corresponding to the reversible (de)intercalation of one Li$^+$ ion is equal to 83 mAh.g^{-1} and can be doubled if the second redox couple of vanadium (V^{IV}/V^V) is reached.

2.3.1. Synthesis and structural characterization

Several attempts of performing direct synthesis of Li$_3$V(PO$_3$)$_3$N either by ammonolysis, or with the use of melamine were unsuccessful, and therefore the chemical ion-exchange indirect method was attempted. The group of Khalifah[160] already attempted this strategy in Na$_2$Fe$_2$(PO$_3$)$_3$N, however, although they successfully removed both of sodium ions from Na$_2$Fe$_2$(PO$_3$)$_3$N, only a small amount of Li was inserted into the structure resulting with the final composition of Li$_{0.3}$Fe$_2$(PO$_3$)$_3$N.[160] Difficulties with the insertion of more lithium were explained by the oxidation of iron upon the ion-exchange reaction.

We decided to adapt the reaction conditions with taking precautions to maximally limit the exposure of the sample to air. Ion exchange was performed by first grinding Na$_3$V(PO$_3$)$_3$N with LiBr in a molar ratio of 1:8 in the Ar filled glovebox. Next, the mixture of powders was compressed into a pellet, placed into a graphite crucible and then rapidly transferred into a tubular furnace for the heating process which was carried out at 330 °C for 20 h under constant flow of Ar gas. After cooling down to the room temperature the crucible was transferred back to the glovebox, the recovered pellet was manually grinded

in a mortar and the powder was washed 3 times with methanol and next twice with acetone (in order to remove all traces of formed NaBr, $Li_{1-x}Na_xBr$ as well as unreacted LiBr), filtered and dried. The color of the powder changed from green to brown, as visible in the images:

Figure 2.33: (left) powder of pristine $Na_3V(PO_3)_3N$ before pressing into pellets; (right) powder of ionically exchanged $Li_3V(PO_3)N$ obtained after grinding the pellets.

2.3.2. X-ray and synchrotron powder diffraction study

The inset in Figure 2.34 where the comparison of the XRD patterns of $Na_3V(PO_3)_3N$ and $Li_3V(PO_3)_3N$ can be found shows a clear shift of all the peaks to higher 2θ values after the ion-exchange reaction with small intensity changes between peaks, which indicates that the CUBICON structure is retained. Next, a synchrotron XRD measurement (Figure 2.34) was performed to get detailed insight into the structure of $Li_3V(PO_3)_3N$.
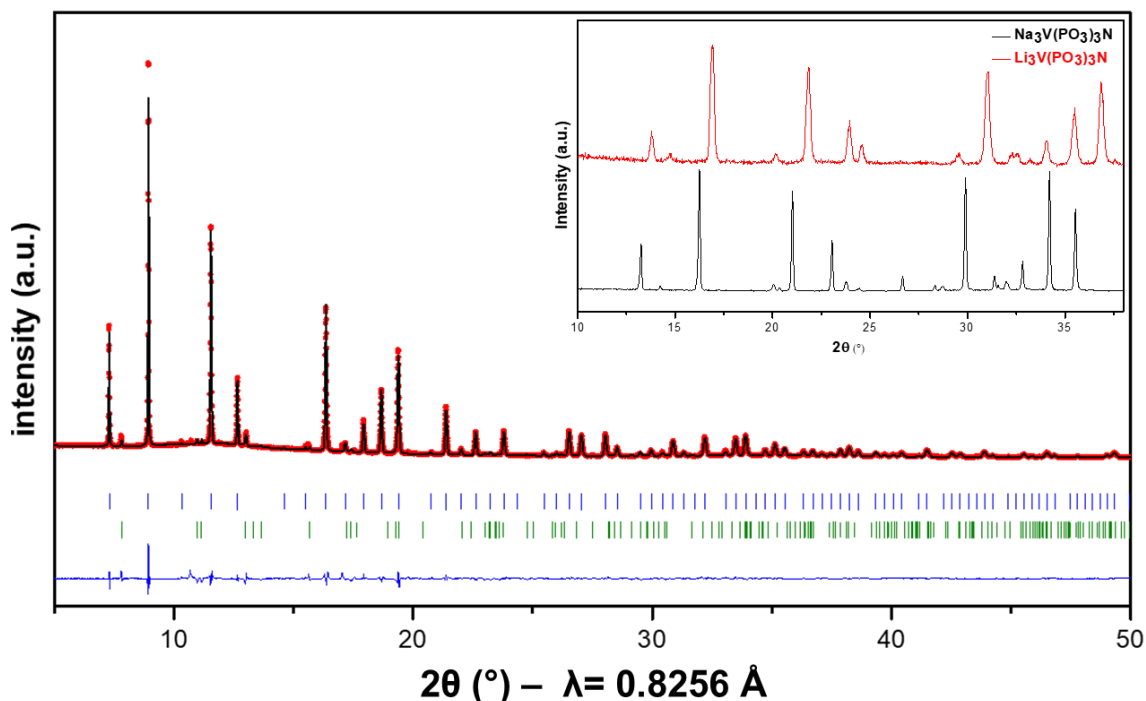
Figure 2.34: Rietveld refinement of the synchrotron XRD pattern of Li₃V(PO₃)₃N. Red circles, black and blue lines represent the observed, calculated and difference patterns, respectively. The positions of the Bragg reflections of the $P2_13$ space group are shown as blue vertical bars. Green bars denote a small (< 3 %) contribution of NASICON-type $Li_xNa_{3-x}V_2(PO_4)_3$ phase. In the inset the XRD patterns of pristine Na₃V(PO₃)₃N (black) and ionically exchanged Li₃V(PO₃)₃N (red) are shown with a clear shift of the peaks.

Rietveld refinement of the SXRD pattern (Figure 2.34) confirmed the cubic lattice with $P2_13$ space group and the successful removal of Na^+ ions. Table 2.13 gathers the refined crystallographic parameters of the formed $Li_3V(PO_3)_3N$ phase. Since the $Na_3V(PO_3)_3N$ used for the ion-exchange reaction had ~5% of NASICON-type impurity, this phase was also taken into account while performing the refinement. As can be observed in the inset of Figure 2.34, the peaks corresponding to the NASICON-type phase also shifted into higher 2θ values suggesting the Na^+/Li^+ ion exchange also in this phase. For the Rietveld refinement, in the beginning the $Na_3V_2(PO_3)_4$ phase was used. It was observed that the amount of Na decreased significantly, however some amount of Na was still presente. Since the Li occupancy is not possible to be refined in the SXRD data, it was assumed that the observed vacancies in the Na sites are occupied with Li, resulting with the final estimated composition of $Li_2Na(PO_4)_3$. The refined amount of this phase was found to be ~5%.

Table 2.13: Crystallographic details and atomic coordinates of Li₃V(PO₃)₃N obtained from the refinement of the SXRD data.

S.G.: $P2_13$	a =9.178(1) Å	V = 772.29(2) Å³	R_{Bragg} =5.6 %		χ^2 = 4.8
Atom	Wyckoff position	x/a	y/b	z/c	B_{iso}
P	12b	0.341(1)	0.088(1)	0.260(1)	0.9(2)
V	4a	0.073(1)	-0.073(1)	0.427(1)	0.8(3)
Li1	4a	0.038(3)	0.038(3)	0.038(3)	1.3(5)
Li2	4a	0.379(7)	0.379(7)	0.379(7)	1.2(5)
Li3	4a	0.662(6)	0.162(6)	0.338(6)	1.2(6)
O1	12b	0.273(2)	-0.016(2)	0.374(2)	0.6(6)
O2	12b	0.392(2)	-0.002(2)	0.128(2)	0.5(6)
O3	12b	0.445(3)	0.184(3)	0.325(3)	0.9(6)
N	4a	0.200(3)	0.200(3)	0.200(3)	0.3(8)

Rietveld refinement was performed using the initial structure model of Na₃V(PO₃)₃N with the replacement of the Na^+ ions by Li^+ ions and a cell parameter of 9.20 Å, which was extrapolated from the refined cell parameter obtained for the $Li_xNa_{3-x}V(PO_3)_3N$ phase in the discharged state during the *operando* cycling of Na₃V(PO₃)₃N *vs.* Li (9.29 Å). As

mentioned before, the Li occupancy could not be refined, therefore eventual remains of Na were verified in all three sites. Since no residues of Na were found, therefore it was assumed that the final composition was $Li_3V(PO_3)_3N$. This assumption will be later verified by performing EDX analysis and verifying the amount of sodium in the structure. Nevertheless, the neutron powder diffraction would be additionally suggested to refine the Li occupancy and validate the eventual vacancies.

Table 2.14 shows the comparison of $Li_3V(PO_3)_3N$ and $Na_3V(PO_3)_3N$ cell parameters and volume. The exchange results in a ~10% decrease of the cell volume. Figure 2.35 shows the comparison of the structures, while Table 2.15 gathers the interatomic distances between the atoms in both compounds.

Table 2.14: Comparison of the cell parameter and volume of the cell of $Li_3V(PO_3)_3N$ and $Na_3V(PO_3)_3N$.

$Li_3V(PO_3)_3N$	$Na_3V(PO_3)_3N$
S.G.: $P2_13$	S.G.: $P2_13$
$a = 9.166(3)$ Å	$a = 9.445(2)$ Å
$V = 770.135(2)$ Å^3	$V = 842.58(3)$ Å^3
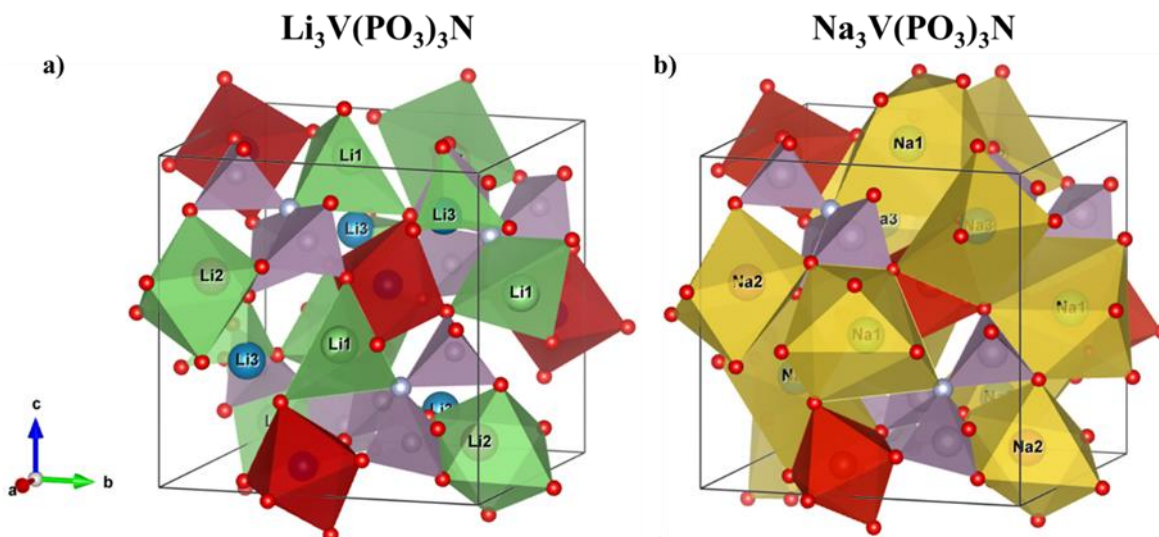
Figure 2.35: (a) crystal structure of $Li_3V(PO_3)_3N$ with three different types of Li polyhedra indicated in green; (b) crystal structure of $Na_3V(PO_3)_3N$ with three different types of Na polyhedra indicated in yellow; in both VO_6 octahedra indicated in red and chain of $(PO_3)_3N$ polyhedra indicated in grey, nitrogen atoms are represented as silver ball in the shared vertex of PO_3N tetrahedra.

Table 2.15: Comparison of interatomic distances in the structures of Na₃V(PO₃)₃N and Li₃V(PO₃)₃N.

	$Na_3V(PO_3)_3N$	$Li_3V(PO_3)_3N$
V-O(1)	1.982(5) Å x3	1.975(5) Å x3
V-O(2)	1.993(6) Å x3	1.984(5) Å x3
P-O(1)	1.540(6) Å	1.543(6) Å
P-O(2)	1.533(6) Å	1.531(5) Å
P-O(3)	1.545(6) Å	1.429(6) Å
P-N	1.742(8) Å	1.742(7) Å
Li/Na(1)-O(1)	2.582(6) Å x3	2.283(6) Å x3
Li/Na(1)-N	2.951(8) Å	2.277(8) Å
Li/Na(1)-O(3)	2.643(6) Å x3	3.022(7) Åx3[*]
Li/Na(2)-O(2)	2.306(7) Å x3	2.382(16) Å x3
Li/Na(2)-O(3)	2.472(7) Å x3	1.948(16) Å x3
Li/Na(3)-O(3)	2.326(7) Å x3	2.005(13) Å x3
Li/Na(3)-O(1)	2.956(7) Å x3	3.145(11) Åx3[*]

[*]observed atomic distance, too long to be considered as a bond

As visible in the Figure 2.35, the main difference between two structures is the environment of the alkali cation. Whereas in $Na_3V(PO_3)_3N$ all sodium ions are in distorted octahedral configuration, in $Li_3V(PO_3)_3N$ three different types of Li polyhedra are formed – a highly distorted $Li(1)O_3N$ terahedron, a distorted $Li(2)O_6$ octahedron and $Li(3)O_3$ trigonal pyramid with Li in the vertex. The observed Li(1)-O(3) and Li(3)-O(1) distances are too long to be considered as a bond, based on the ionic radius of these element determined by Shannon.[200] While analyzing the position and the V-O and P-O and P-N bonds, no major change in the vanadium octahedra and chains of $(PO_3)_3N$ polyhedra can be observed indicating very stable framework of $A_3V(PO_3)_3N$ (A=Li,Na).

2.3.3.   BVEL analysis

The mobility of Li^+ cations within the $Li_3V(PO_3)_3N$ structure was evaluated by Bond Valence Energy Landscape (BVEL) calculations, which were performed using the refined $Li_3V(PO_3)_3N$ structure. The resulting bond valence maps are shown in Figure 2.36.
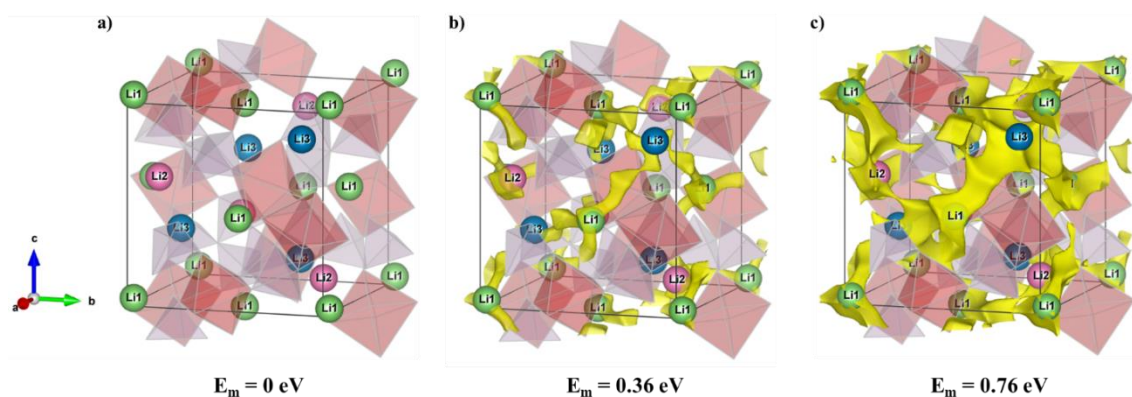
Figure 2.36: Bond Valence Energy Landscape maps of Li₃V(PO₃)₃N showing the Li⁺ diffusion pathways for different energy thresholds: (a) E_m = 0 eV, (b) E_m = 0.36 eV, (c) E_m = 0.76 eV.

The minimum required percolation threshold for the Li1 and Li3 sites was found to be 0.36 eV. This value is half of the calculated energy required to connect Na1 and Na3 sites in $Na_3V(PO_3)_3N$ (0.75 eV) implying a much higher mobility of the Li⁺ ions. Additionally, the energy required to connect the remaining Li2 site to the migration pathway was also found to be relatively low (0.4 eV). In comparison, Na2 requires additional energy of 1.1 eV to participate in the percolation pathway within $Na_3V(PO_3)_3N$. These results thus predict a lower energy three-dimensional migration pathway for Li⁺ ions.

2.3.4. Electron microscopy and chemical composition

Electron microscopy measurements coupled with EDX analysis were performed to analyze the morphology of $Li_3V(PO_3)_3N$ and confirm Na removal. Figure 2.37 shows the SEM image of $Li_3V(PO_3)_3N$ and Table 2.16 the determined composition of the measured atoms.

Table 2.16: Composition of Li₃V(PO₃)₃N determined by EDX.

Element	Theoretical atomic ratio	Experimental atomic ratio determined from EDX
Na	0	0.0
V	1	1.0(fixed)
P	3	3.0±0.15
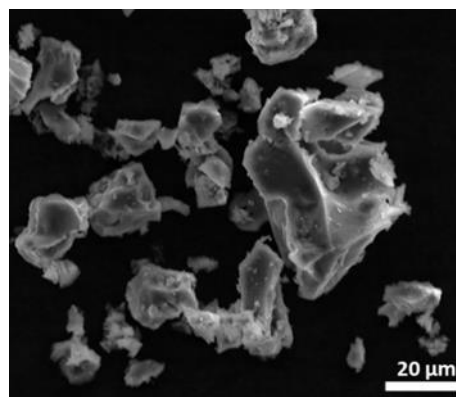
Figure 2.37: SEM image of Li₃V(PO₃)₃N.

EDX data confirm the absence of the Na signals in the spectra. The measured ratio between phosphorous and vanadium also was found to be as expected (3:1). The SEM image of the powder presented in the Figure 2.37 shows that the particles of $Li_3V(PO_3)_3N$ have similar non-uniform shape and size as the ones of $Na_3V(PO_3)_3N$, in agreement with the fact that, since this compound was obtained by ion-exchange synthesis, no changes in the morphology are expected. The amount of nitrogen was evaluated using CHNOS Elemental Analysis and the results confirmed the expected content of one nitrogen atom per formula unit.

2.3.5. Solid State Nuclear Magnetic Resonance analysis

^7Li MAS NMR measurements were performed to study the local environment and dynamics of lithium ions in $Li_3V(PO_3)_3N$. Additionally, ^{23}Na MAS NMR measurements were performed to determine the possible presence of remaining sodium. Figure 2.38a shows the ^7Li MAS solid-state NMR spectrum of the $Li_3V(PO_3)_3N$ sample, whereas Figure 2.38b shows the ^{23}Na MAS solid-state NMR spectrum of $Li_3V(PO_3)_3N$, overlapped with the ^{23}Na MAS NMR spectra of the pure $Na_3V(PO_3)_3N$ phase (discussed in the section 2.2.2.5.) as reference.
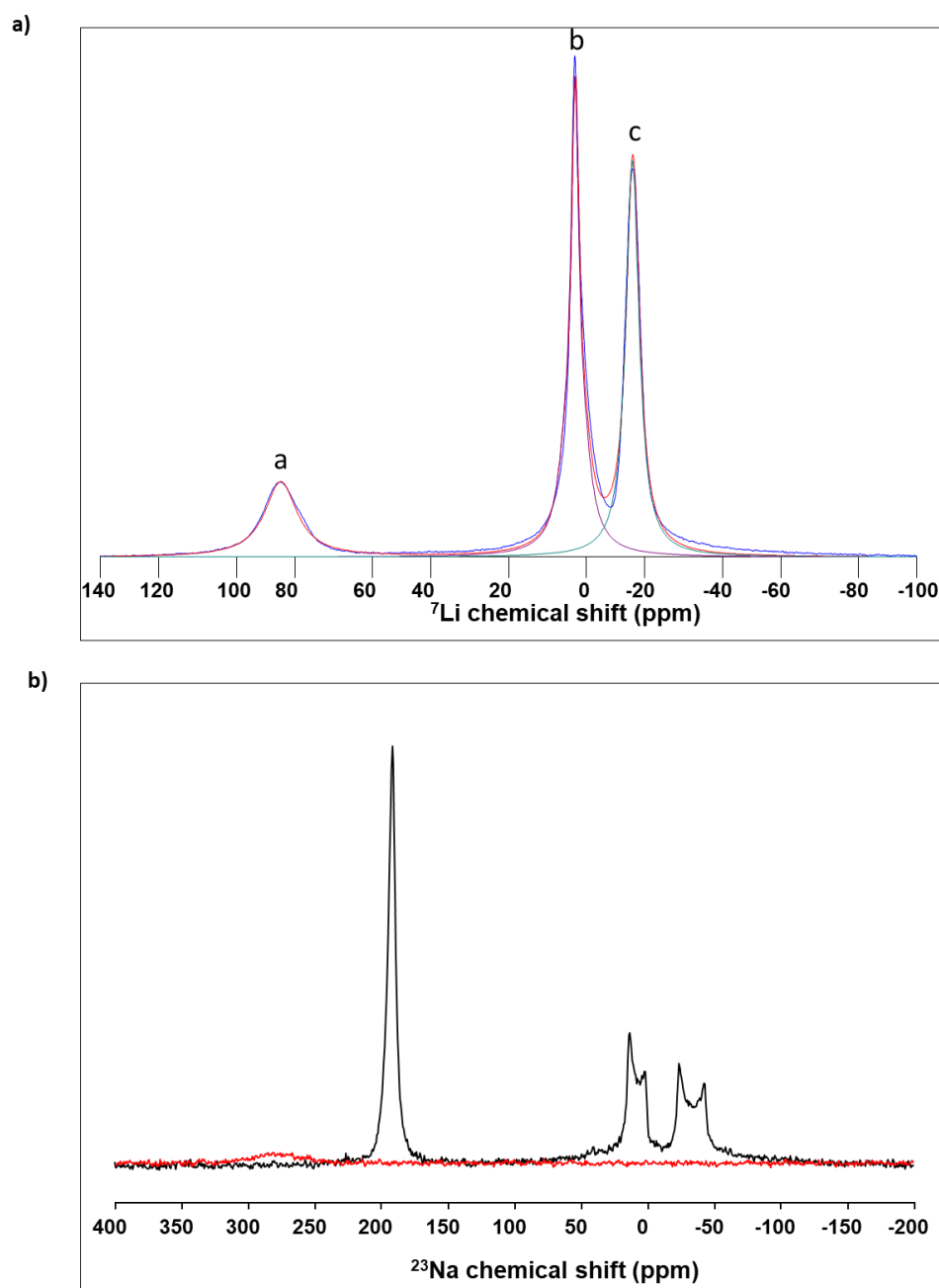
Figure 2.38: (a) ^{7}Li MAS solid-state NMR spectrum of the Li$_3$V(PO$_3$)$_3$N sample acquired at 50 kHz MAS rotation using 1.3 mm rotor with assigned resonances to corresponding Li sites in Li$_3$V(PO$_3$)$_3$N; (b) ^{23}Na MAS solid-state NMR spectra of the (red) Li$_3$V(PO$_3$)$_3$N; (black) Na$_3$V(PO$_3$)$_3$N.

As can be seen in Figure 2.38a, three distinct resonances can be detected at ~87 ppm, ~1 ppm and -17 ppm (indicated as: a, b & c) which were fitted considering the values listed in the Table 2.17.

Table 2.17: ^{7}Li MAS solid-state NMR fitting parameters.

Signal	Shift (ppm)	LW (ppm)
a	87.6	11.1
b	-16.8	4.9
c	0.2	4.4

The shift of the first of the signals is clearly out of the expected range for lithium containing diamagnetic materials (± 10 ppm). This shift is therefore explained by the paramagnetic interaction of the ^{7}Li nucleus with the unpaired electrons of vanadium. To assign the signal to the corresponding Li site, a detailed analysis of the Li-V distances was performed, as shown in Figure 2.39 and Table 2.18.
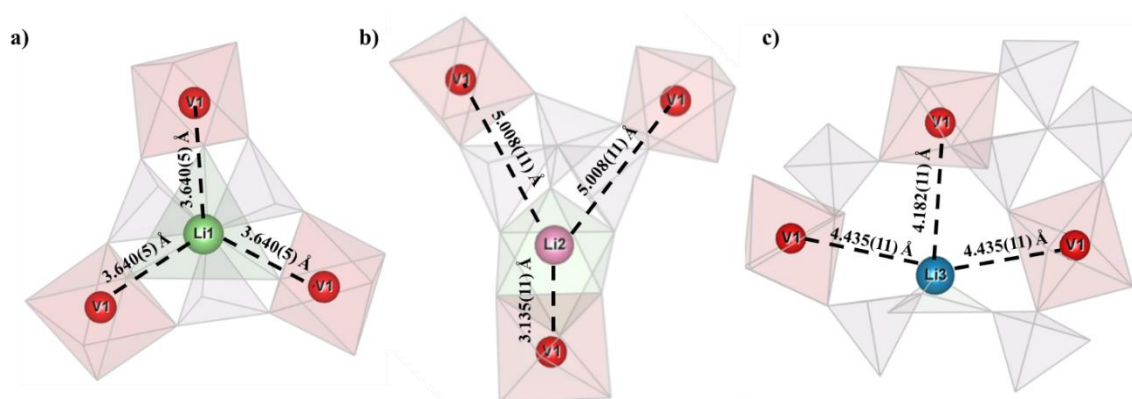
Figure 2.39: Representation of the three Li environments in Li₃V(PO₃)₃N highlighting the nearest Li – V contacts for (a) Li1, green; (b) Li2, pink and (c) Li3, blue. The V atoms are labeled and indicated in red. The VO₆ octahedra are shown in red, Li polyhedra in light green and PO₃N tetrahedra in light grey.

Table 2.18: Li-V distances in Li₃V(PO₃)₃N used for the chemical shift assignment.

atom	distance	atom	distance	atom	distance
Li(1)-V	3.640(5) Å	Li(2)-V	3.135(11) Å	Li(3)-V	4.182(11) Å
Li(1)-V	3.640(5) Å	Li(2)-V	5.008(11) Å	Li(3)-V	4.435(11) Å
Li(1)-V	3.640(5) Å	Li(2)-V	5.008(11) Å	Li(3)-V	4.435(11) Å
Σ	**10.992(5) Å**		**13.151(11) Å**		**13.052(11) Å**

Paramagnetic shifts are an additive property. Therefore, even if Li2 (Figure 2.39b) has the shortest Li-V distance, the sum of the distances to the three nearest vanadium atoms resulted the largest, 13.151(11) Å. The Li(1)O₄ tetrahedron (Figure 2.39a) is equidistant to three nearest vanadium atoms, resulting with the lowest sum of 10.920(5) Å. Finally, the sum of the Li-V distances for the Li3 site is equal to 13.052(11) Å. Based on these

results, the three signals at 87 ppm, 0 ppm and -17 ppm are assigned to the Li1, Li3 and Li2 sites, respectively.

In the Figure 2.38b, the ^{23}Na MAS solid-state NMR spectra of $Li_3V(PO_3)_3N$ and $Na_3V(PO_3)_3N$ are shown superimposed. As can be observed, the sodium signal in $Li_3V(PO_3)_3N$ is extremely low indicating only trace amounts of sodium in the lithiated sample. SXRD measurement revealed the presence of a small (<5%) amount of the partially lithiated NASICON phase of presumed $Li_2Na(PO_4)_3$ composition, however without a reference spectrum it is not possible to corroborate these results with NMR technique. Yet it was confirmed that the amount of sodium is extremely small and is not expected to have any impact on the physicochemical properties of $Li_3V(PO_3)_3N$.

An investigation of exchange processes between Li^+ ions at different sites was performed using 2D exchange spectroscopy (2D EXSY) in the same conditions as it has been done for $Na_3V(PO_3)_3N$ (Figure 2.8).
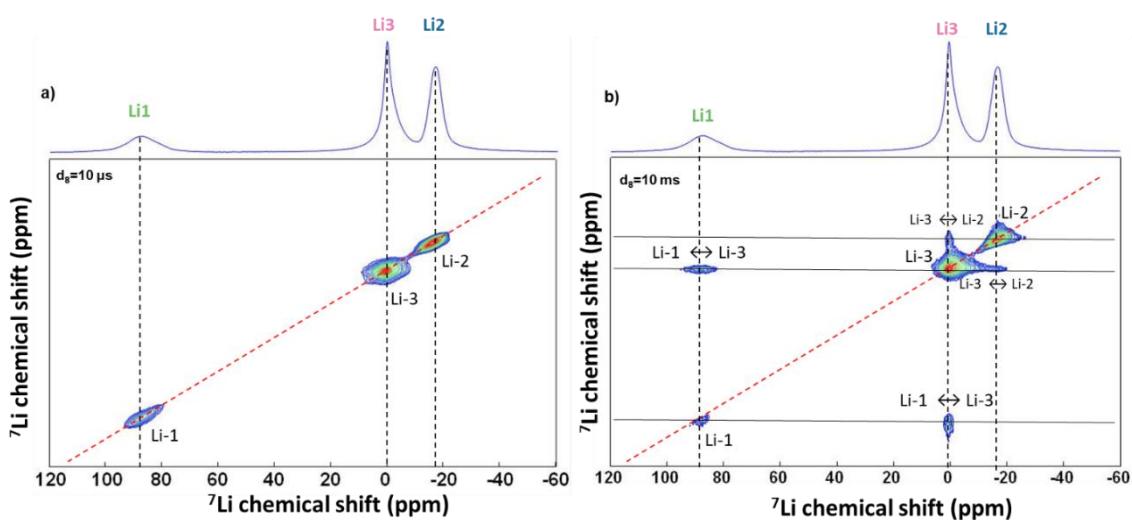
Figure 2.40: ^{7}Li 2D EXSY spectra of $Li_3V(PO_3)_3N$ acquired at 50 kHz with mixing times: (a) t_{mix}=10 µs; (b) t_{mix}=10 ms.

Figure 2.40 shows the 2D EXSY spectra of $Li_3V(PO_3)_3N$ at two different mixing times, 10 µs and 10 ms. Evolution of the cross-peak intensity as a function of a mixing time allows the assessment of the rate of the exchange process. At low mixing times (10 µs in Figure 2.40a) only the diagonal signals autocorrelating the three main Li resonances are present. By increasing the time to 10 ms (Figure 2.40b) clear off-diagonal signals can be visible correlating resonances of lithium positions Li1 and Li3. Additionally, a low

intensity cross peaks between Li3 and Li2 positions can be observed. No exchange signals are detected directly correlating positions Li1 and Li2.

The rate of the exchange process for both sets of cross peaks was investigated by following the evolution of the normalized volume of the cross-peak surface as a function of mixing time (Figure 2.41).
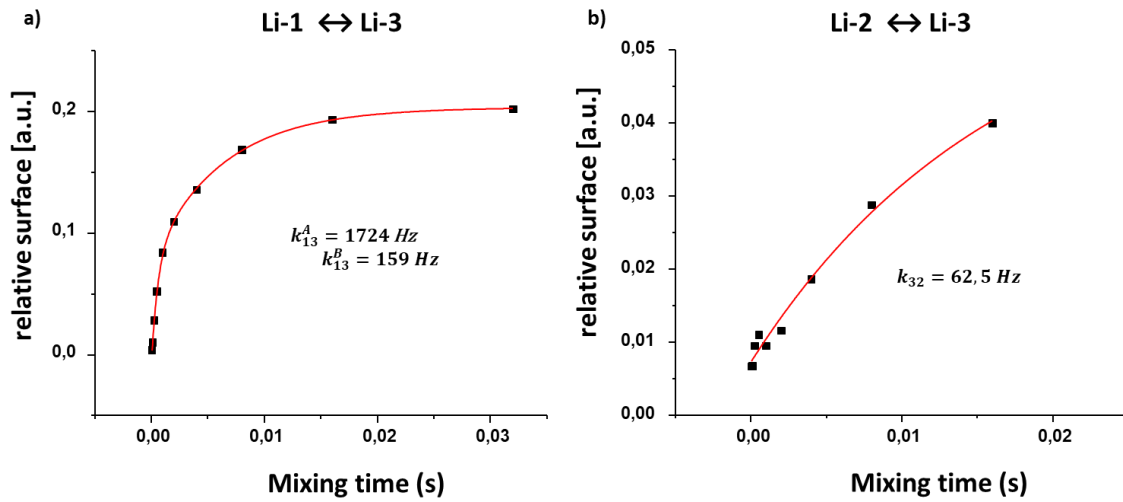
Figure 2.41: (a) Relative volume of the Li1-Li3 cross peaks surface as a function of mixing time with the second-order exponential fit (red line); (b) Relative volume of the Li3-Li2 cross peaks surface as a function of mixing time with the first-order exponential fit (red line). k_{xy} is the exchange rate between two sites.

The results correlating signals Li1 and Li3 (Figure 2.41a) could not be fitted considering a single exponential function and are perfectly reproduced by a double exponential. From this fitting, the Li1-Li3 exchange rates (k_{13}) are equal to 1724 and 159 s^{-1} (Figure 2.41a.). These values indicate a fast and facile mobility of the Li ions between Li1 and Li3 sites. Additionally, small cross peaks between Li2 and Li3 (Figure 2.41b) indicate the possible exchange between these two sites. The hopping rate of this exchanges is smaller and equal to 62.5 s^{-1}. Summarizing, the lithium mobility within Li$_3$V(PO$_3$)$_3$N is expected to follow this equation:

$$Li1 \overset{k_{13}}{\leftrightarrow} Li3 \overset{k_{32}}{\leftrightarrow} Li2 \quad k_{13} > k_{32}$$
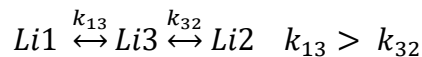
where k is the exchange rate between sites. The two different values of k_{13} are expected to origin from the impact of the Li3 ↔ Li2 exchange which decelerates the exchange between Li1 and Li3. These results are found to be in very good agreement with the conclusions from BVEL calculations which also shows fast Li$^+$ mobility between Li1 and Li3 sites. Additionally, the energy required to connect the remaining Li2 site to the

migration pathway was also found to be relatively low (0.4 eV). These results confirm the lower energy three-dimensional migration pathway for Li^+ ions and remain in good agreement with the conclusions from the BVEL analysis.

2.3.6.   Electrochemical characterization

The electrochemical performance of $Li_3V(PO_3)_3N$ was evaluated in Swagelok-type cells against Li metal and using a commercial LP30 electrolyte. The half cells were cycled at a C/20 C-rate in two different voltage windows: 3.0 – 4.5 V and 3.0 – 5.0 V *vs.* Li^+/Li^0. The higher upper voltage (5.0 V) was chosen to verify if the second redox process of V^{IV}/V^V couple could be detected. The corresponding charge-discharge curves are shown in Figure 2.42.
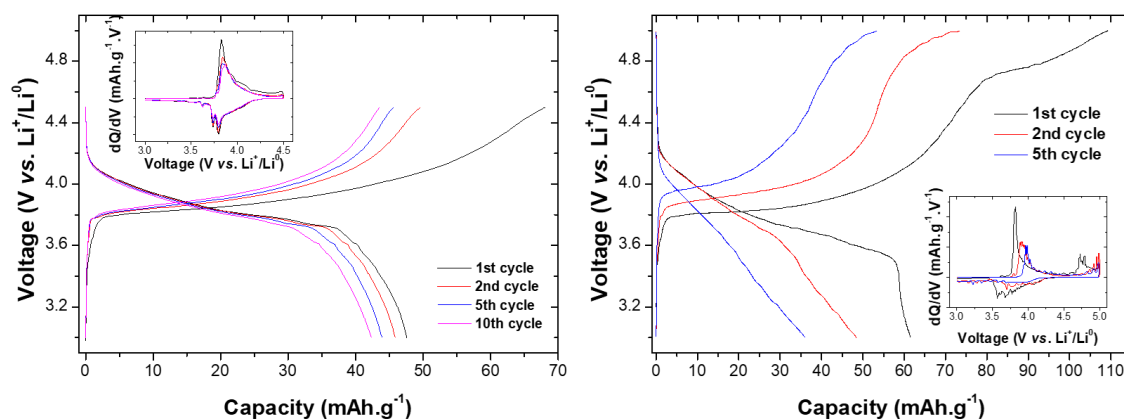
Figure 2.42: Galvanostatic charge-discharge profile of Li₃V(PO₃)₃N against a Li anode at C/20 rate in (a) 3.0-4.5V and (b) 3.0-5.0 V *vs.* Li⁺/Li⁰ voltage windows together with the corresponding derivative dQ/dV curves in insets.

The electrochemical activity of $Li_3V(PO_3)_3N$ is centered around ~3.9 V *vs.* Li^+/Li^0. Following the first charge curve in the Figure 2.42, the obtained capacity of ~70 mAh.g^{-1} corresponds to the removal of ~0.8 Li^+. Based on the first ten cycles it is visible that the cyclability is worse comparing to $Na_3V(PO_3)_3N$, after each cycle small drop of the capacity can be observed. Additionally, as in the electrochemical curves of $Na_3V(PO_3)_3N$, the irreversible capacity in the first cycle was observed. Such a phenomena could be related with structural reorganization occurring upon mobility of Li^+ ions and would require *operando* SXRD measurement to follow these eventual changes.

Opening the voltage window to 5.0 V *vs.* Li^+/Li^0 resulted in worsening of the performance. Although the capacity of the first charge corresponds to the removal of ~1.3 Li^+ and an additional plateau at ~4.8 V *vs.* Li^+/Li^0 can be observed, it is absent in the

subsequent discharge. While such a behavior normally would be explained by the oxidation of the electrolyte, large polarization and significant decrease of the capacity in subsequent cycles would rather suggest internal structural changes occurred after removal of additional lithium ion. To verify if eventually these changes can be related with the redox activity of the second V^{IV}/V^V couple, *ex situ* XAS measurement is required. Additionally, *ex situ* SXRD would be crucial to verify the eventual structural changes.

2.4. Conclusions

In this chapter we presented the synthesis, detailed structural analysis and electrochemical performance of CUBICON $Na_3V(PO_3)_3N$ and $Li_3V(PO_3)_3N$. $Na_3V(PO_3)_3N$ can be successfully synthesized using two methods, either using an ammonia flow at high temperature (ammonolysis), or with the use of melamine, mixed together with the precursors and annealed under Argon. Thermogravimetric studies revealed remarkable high thermal stability in inert atmosphere (>900°C). $Na_3V(PO_3)_3N$ offers a stable capacity with very low voltage hysteresis, although only one sodium out of the expected two could be removed. The working potential was found to be very high, 4.0 V *vs.* Na^+/Na^0 and 4.1 V *vs.* Li^+/Li^0, with a remarkable small difference in the insertion voltage between both alkali metal reference electrodes. To the best of our knowledge this is the Na-ion cathode material with the highest operation voltage for the V^{IV}/V^{III} redox couple together with $Na_7V_3(P_2O_7)_4$.[201] Based on the DFT calculations, the extraction of more than one sodium cation seems to be prevented because the potential of the redox couple V^V/V^{VI} is predicted to be beyond the voltage stability window of the electrolytes available up to now. Additionally, although not achieved from direct synthesis, pure $Li_3V(PO_3)_3N$ was prepared through ion exchange. Its electrochemical activity of the V^{IV}/V^{III} redox couple centered around 3.9 V *vs.* Li^+/Li^0. 2D ^7Li-^7Li EXSY NMR experiments revealed clear off-diagonal signals in $Li_3V(PO_3)_3N$ connecting Li positions at sites 1-3 and 2-3 which can be translated into fast diffusion pathway for Li^+ ions within the framework. These results remain in good agreement with the BVEL calculations, where the obtained activation energy of 0.36 eV value is half of the calculated energy required to connect Na1 and Na3 sites in $Na_3V(PO_3)_3N$ (0.75 eV) implying a much higher mobility of the Li^+ ions in $Li_3V(PO_3)_3N$. However, preliminary electrochemical tests resulted in a similar performance compared to $Na_3V(PO_3)_3N$ (although with enhanced capacity fading) that would require further understanding and material optimization.

Although electrochemical tests revealed the reversible mobility of ~1 alkali cation per formula unit, the obtained very high working voltage of the V^{III}/V^{IV} redox couple places $Na_3V(PO_3)_3N$ $Li_3V(PO_3)_3N$ as attractive potential cathode materials. Since the second redox couple was not possible to be reached due to the calculated voltage exceeded voltage stability window of the currently available electrolytes, in our next work we intended to increase the capacity by changing the composition and test the divalent nitridophosphates.

Chapter 3 - Na$_2$M$_2$(PO$_3$)$_3$N (M = Mn, Fe, Co) nitridophosphates as potential cathode materials for Sodium- and Lithium-Ion batteries

Outline

Chapter 3 - Na$_2$M$_2$(PO$_3$)$_3$N (M = Mn, Fe, Co) nitridophosphates as potential cathode materials for Sodium- and Lithium-Ion batteries

3.1. Introduction

In this chapter, the divalent Na$_2$M$_2$(PO$_3$)$_3$N (M = Fe, Mn, Co) nitridophosphate family will be explored. Although the incorporation of a second transition metal within the CUBICON framework increases the molecular weight with respect to trivalent Na$_3$M(PO$_3$)$_3$, the redox reaction of both transition metals still is expected to translate into theoretical specific capacities of ~140 mAh.g^{-1}. Focusing on low cost and earth abundant 3d metals, iron and manganese were first selected. Although being less popular dopant owing to its higher cost and mining ethics, Co substitution usually has a beneficial effect by elevating the working voltage and improving the cyclability, therefore also this metal was included in the investigation.[116,202,203]

First, Na$_2$Fe$_2$(PO$_3$)$_3$N will be revisited. Liu et. al.[160] reported the synthesis of Na$_2$Fe$_2$(PO$_3$)$_3$N using the ammonolysis route and its electrochemical performance in hybrid-ion configuration (using Li metal as anode and a Li electrolyte). These tests resulted with capacities of ~40 mAh.g^{-1} and large polarization although a capacity of 100-120 mAh.g^{-1} was obtained after an ion exchange process that resulted in Li$_{0.3}$Fe$_2$(PO$_3$)$_3$N. The performance of Na$_2$Fe$_2$(PO$_3$)$_3$N *vs.* Na was not reported. In our work, first we will focus on the evaluation of the electrochemical performance of Na$_2$Fe$_2$(PO$_3$)$_3$N *vs.* Na. Additionally, Na$_2$Fe$_2$(PO$_3$)$_3$N will be tested in a hybrid-ion configuration against Li anode to compare its performance *vs.* Na anode and the one reported by Liu.[160] Detailed insight into the Na insertion/extraction mechanism will be also discussed from an *operando* Synchrotron XRD experiment.

The next part will be focused on the Co-based and Mn-based nitridophosphates. First, we will prepare the iron-mixed compositions with the aim to investigate the influence of the foreign metal (Co^{II} and Mn^{II}) on the capacity and working voltage. Eventually, we will aim to prepare the two end members, Na$_2$Co$_2$(PO$_3$)$_3$N and Na$_2$Mn$_2$(PO$_3$)$_3$N, which so far

have never been reported. The synthesis of $Na_2Co_2(PO_3)_3N$ together with the detailed structure characterization and electrochemical properties will be presented.

Last, the preparation of the CUBICON manganese nitridophosphate will be described. As in the literature no structural description can be found apart from the cell parameter value[162], different synthesis conditions will be explored.

3.2. Iron nitridophosphate

First, we focused on the synthesis of $Na_2Fe_2(PO_3)_3N$, where different precursors and nitridation methods were evaluated. Two distinct synthesis routes were applied to synthesize the targeted compound – ammonolysis and solid-state synthesis under Ar using melamine ($C_3H_6N_6$) as the nitrogen source, as was already described for the synthesis of $Na_3V(PO_3)_3N$ in Chapter 2.

3.2.1.   Synthesis and structural characterization

To prepare the samples for ammonolysis, powders of $NaPO_3$, Fe_2O_3 or FeC_2O_4 and $NH_4H_2PO_4$ were mixed in a stoichiometric ratio and the obtained mixtures were loaded into graphite crucibles and heated for 12 h at 630°C under constant flow of NH_3 (details on the synthesis can be found in the Annex – experimental part). Two different Fe precursors (Fe_2O_3 or FeC_2O_4) were evaluated due to their different decomposition temperatures – 1500 °C (under Ar) for Fe_2O_3 *vs.* 550 °C (under Ar) for FeC_2O_4). Although there are no reported temperatures of the decomposition of both products under ammonia, it was assumed that FeC_2O_4 is less stable.

Alternatively, for the second synthesis route, the same precursors were mixed with a 5x molar excess of melamine by ball milling (SPEX 8000M) for 30 min. The obtained mixture was first heated at 300°C for 2 h and next at 600°C for 8 h under a slow flow of Ar (<2 ml/min).

Figure 3.1 shows the XRD patterns of the $Na_2Fe_2(PO_3)_3N$ synthesized using the aforementioned methods. The blue curve corresponds to the ammonolysis route using Fe_2O_3 ; the red curve to the ammonolysis route using FeC_2O_4 ; and the black curve to the melamine route using FeC_2O_4.
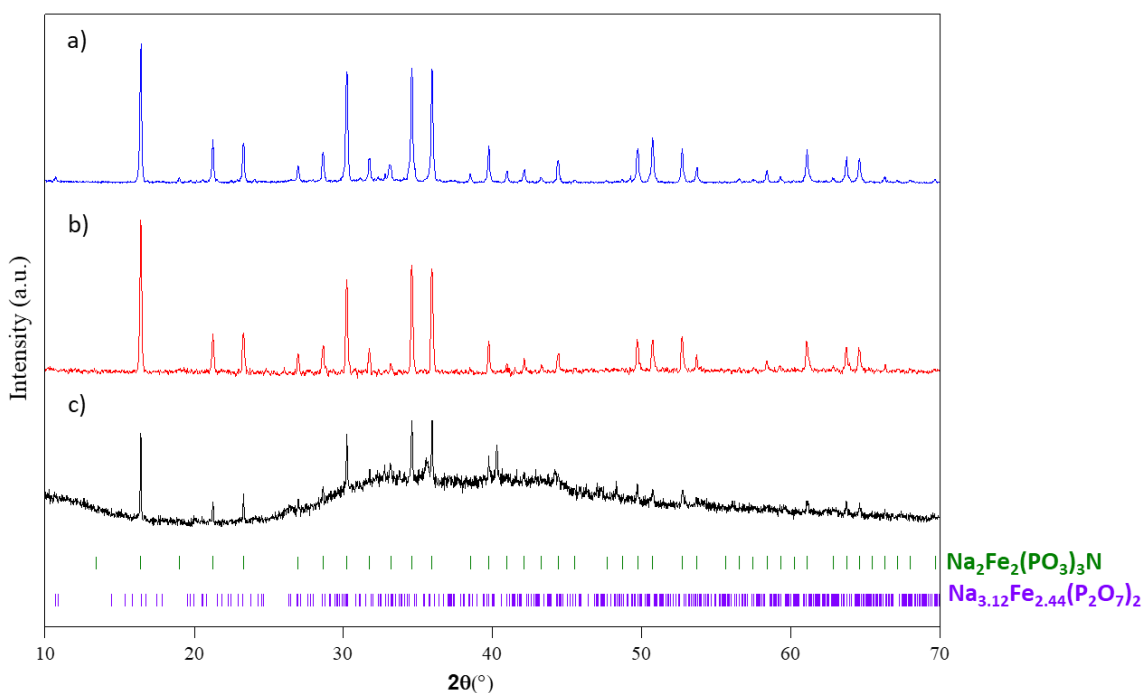
Figure 3.1: XRD patterns of Na$_2$Fe$_2$(PO$_3$)$_3$N prepared by (a, blue curve) ammonolysis route using Fe$_2$O$_3$ as Fe precursor; (b, red curve) ammonolysis route using FeC$_2$O$_4$ as Fe precursor; (c, black curve) melamine route using FeC$_2$O$_4$ as Fe precursor. Bragg reflections of the Na$_2$Fe$_2$(PO$_3$)$_3$N phase and the Na$_{3.12}$Fe$_{2.44}$(P$_2$O$_7$)$_2$ phase are shown as green and violet vertical bars, respectively.

The original synthesis procedure[162] suggests the use of Fe$_2$O$_3$ as Fe precursor. However, based on the obtained XRD pattern (Figure 3.1a, blue curve), the powder contained impurities indexed as Na$_{3.12}$Fe$_{2.44}$(P$_2$O$_7$)$_2$ phase.

In the next try, the less stable iron oxalate FeC$_2$O$_4$ precursor was used and indeed the resulting powder had higher purity (Figure 3.1b, red curve). Different temperatures of the synthesis were screened, and it was found that pure Na$_2$Fe$_2$(PO$_3$)$_3$N can be stabilized in a very narrow temperature range (630-635°C). Higher temperatures lead to the formation of a high amount of Fe$_2$P and FeP impurities.

The sample prepared from melamine and FeC$_2$O$_4$ precursors also resulted with Na$_2$Fe$_2$(PO$_3$)$_3$N as the main phase. However, the samples contained a high amount of amorphous-type phase and unindexed impurities (Figure 3.1c, black curve), which were not possible to eliminate by changing the reaction conditions.

Figure 3.2 and Table 3.1 show the results of the Rietveld refinement of the XRD pattern of Na$_2$Fe$_2$(PO$_3$)$_3$N synthesized from Fe$_2$O$_3$ as Fe precursor. Figure 3.3 and Table 3.2, correspond to the results of Na$_2$Fe$_2$(PO$_3$)$_3$N obtained by ammonolysis from FeC$_2$O$_4$.
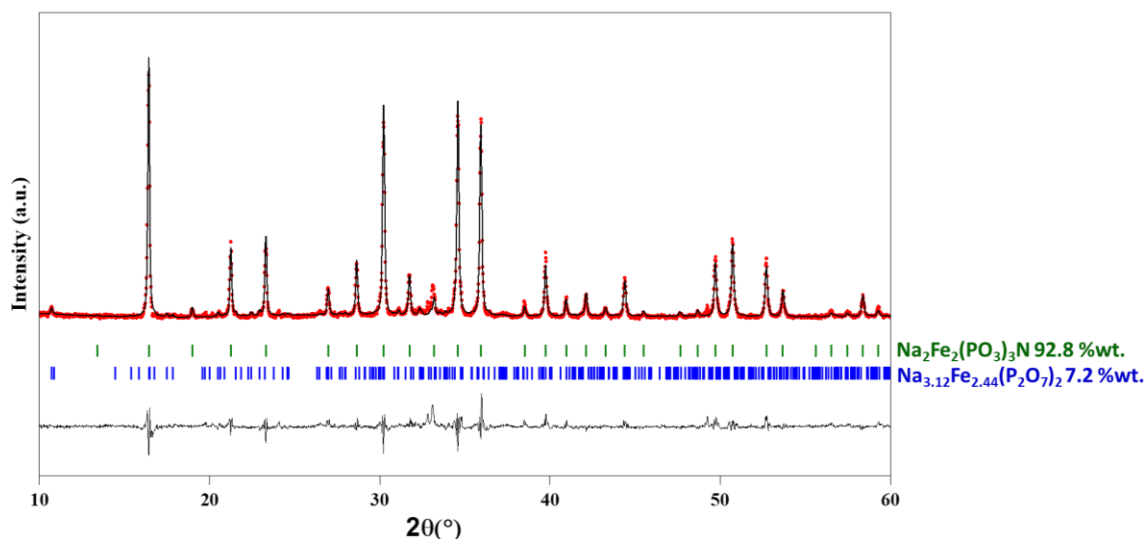
Figure 3.2: Rietveld refinement of the XRD pattern of $Na_2Fe_2(PO_3)_3N$ synthesized by ammonolysis route from Fe_2O_3 as Fe precursor. Black line and red circles represent the calculated and observed patterns, respectively. Bragg reflections of the $P2_13$ space group are shown as green vertical bars. Blue bars denote a small (~7 %) contribution of $Na_{3.12}Fe_{2.44}(P_2O_7)_2$ phase.

Table 3.1: Structural parameters of $Na_2Fe_2(PO_3)_3N$ prepared by ammonolysis route from Fe_2O_3 as Fe precursor determined from the Rietveld refinement of the XRD pattern.

S.G.: $P2_13$	$a = 9.344(2)$Å	$V = 815.71(1)$Å^3		$R_{Bragg} = 8.73\%$	$\chi^2 = 2.38$	
Atom	**Wyckoff position**	*x/a*	*y/b*	*z/c*	**Occupancy**	B_{iso}
P1	12*b*	0.343(2)	0.093(2)	0.261(2)	1.0	1.5(6)
Fe1	4*a*	0.577(2)	0.577(2)	0.577(2)	1.0	1.6(8)
Fe2	4*a*	0.393(4)	0.393(4)	0.393(4)	1.0	0.5(7)
Na1	4*a*	0.032(2)	0.032(2)	0.032(2)	1.0(5)	1.4(6)
Na2	4*a*	0.792(4)	0.792(4)	0.792(4)	1.0(4)	1.0(6)
O1	12*b*	0.203(4)	0.021(3)	0.882(3)	1.0	1.6(7)
O2	12*b*	0.400(4)	0.017(5)	0.139(5)	1.0	1.4(8)
O3	12*b*	0.482(3)	0.203(3)	0.312(2)	1.0	1.7(7)
N1	4*a*	0.181(2)	0.181(2)	0.181(2)	1.0	1.6(8)
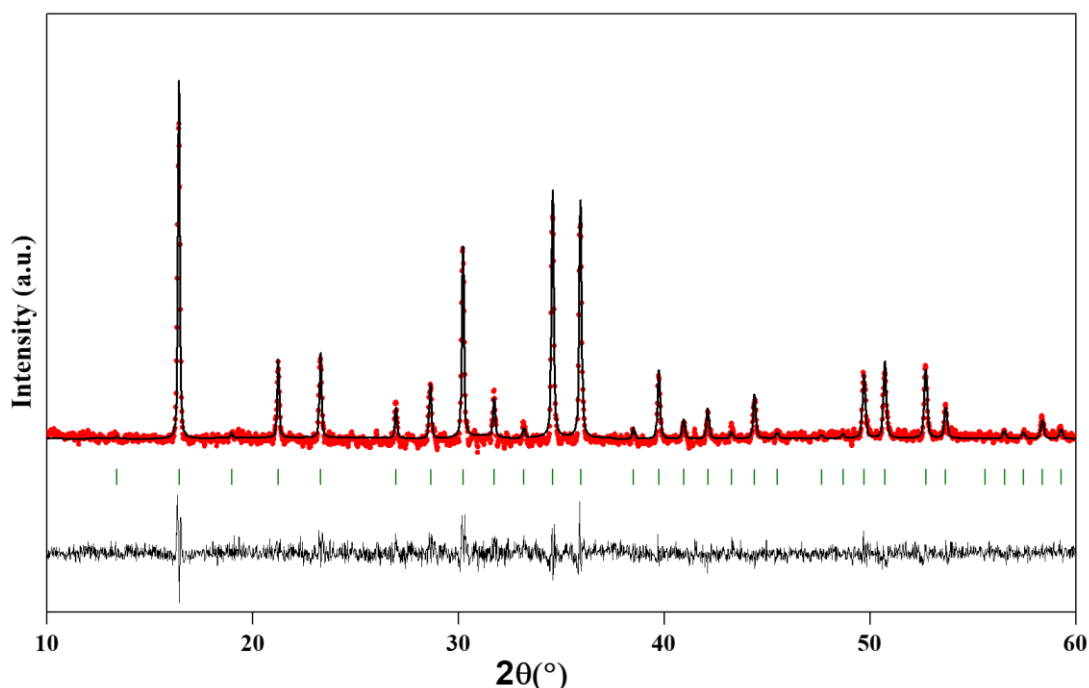
Figure 3.3: Rietveld refinement of the XRD pattern of $Na_2Fe_2(PO_3)_3N$ prepared by ammonolysis route using FeC_2O_4 as Fe precursor. Black line and red circles represent the calculated and observed patterns, respectively. The blue line is the difference curve between the calculated and observed patterns. The Bragg reflections of the CUBICON's $P2_13$ unit cell are shown as green vertical bars.

Table 3.2: Structural parameters of $Na_2Fe_2(PO_3)_3N$ prepared by ammonolysis route from FeC_2O_4 as Fe precursor determined from the Rietveld refinement of the XRD pattern.

S.G.: $P2_13$	$a = 9.342(3)$Å		$V = 796.04(3)$Å^3		$R_{Bragg} = 7.51\%$	$\chi^2 = 5.13$
Atom	**Wyckoff position**	**x/a**	**y/b**	**z/c**	**Occupancy**	**B_{iso}**
P1	12b	0.343(4)	0.093(5)	0.262(5)	1.0	1.2(8)
Fe1	4a	0.577(2)	0.577(2)	0.577(2)	1.0	1.1(7)
Fe2	4a	0.399(3)	0.399(3)	0.399(3)	1.0	1.1(6)
Na1	4a	0.043(3)	0.043(3)	0.043(3)	0.98(7)	1.6(9)
Na2	4a	0.789(4)	0.789(4)	0.789(4)	1.0(6)	1.6(9)
O1	12b	0.226(9)	0.016(7)	0.868(7)	1.0	1.7(8)
O2	12b	0.401(9)	0.005(9)	0.133(6)	1.0	1.6(9)
O3	12b	0.460(8)	0.193(8)	0.322(7)	1.0	0.7(9)
N1	4a	0.205(9)	0.205(9)	0.205(9)	1.0	1.2(4)

The Rietveld refinement of the XRD patterns (Figure 3.2 and Figure 3.3) confirms the cubic structure with $P2_13$ space group, isostructural with other reported nitridophospates.[145,146,160,164,185,204] The refined cell parameters of 9.344(2) Å (from Fe_2O_3) and 9.342(2) Å (from FeC_2O_4) are in good agreement with the one reported by Liu et al. (9.3459(1) Å)[160] From the comparison of the structural parameters of both materials (Table 3.1 and Table 3.2), it can be observed that the used Fe precursor has no

influence on the structure. The refined sodium occupancy showed that in both samples both sodium sites are fully occupied. The refinements confirm that the sample obtained from FeC_2O_4 is single phased, whereas the one obtained from Fe_2O_3 contains a small impurity of $Na_{3.12}Fe_{2.44}(P_2O_7)_2$ phase (~7 wt.%). This may suggest that the lower decomposition temperature of FeC_2O_4 *vs.* Fe_2O_3 helps in completing the reaction.

Finally, the poor quality of the pattern of $Na_2Fe_2(PO_3)_3N$ synthesized with melamine as nitrogen source did not allow to perform a Rietveld refinement, instead Le Bail profile matching was performed (Figure 3.4). The refined cell parameter of 9.343(4) Å indicates that the correct $Na_2Fe_2(PO_3)_3N$ phase was obtained, however contrary to $Na_3V(PO_3)_3N$, this method does not result in obtaining a pure phase for $Na_2Fe_2(PO_3)_3N$. Therefore, due to the higher purity, the samples prepared by the ammonolysis technique were used for further characterizations.
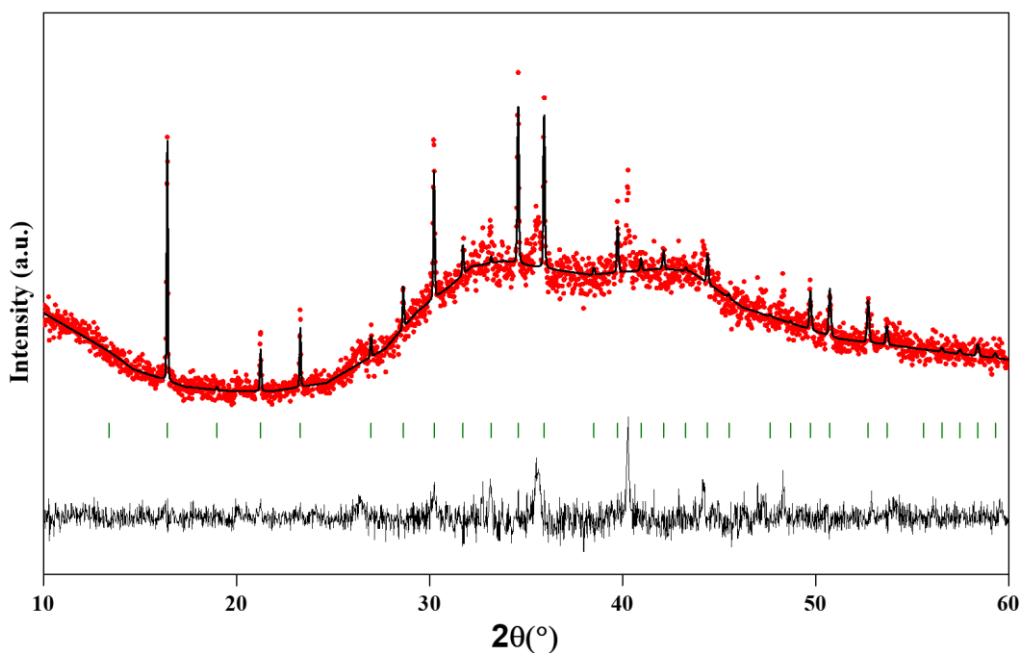
Figure 3.4: Profile matching of the XRD pattern of $Na_2Fe_2(PO_3)_3N$ synthesized with melamine as a nitrogen source. Black line and red circles represent the calculated and observed patterns, respectively. The black horizontal line is the difference curve between the calculated and observed patterns. Bragg reflections of the CUBICON's $P2_13$ unit cell with a = 9.343(7) Å are shown as green vertical bars.

3.2.2. Chemical and morphological analysis

- SEM, EDX & ICP

The SEM images of the powders of $Na_2Fe_2(PO_3)_3N$ prepared by the ammonolysis synthesis from the two different precursors (Fe_2O_3 and FeC_2O_4) are shown in Figure 3.5 a&b.
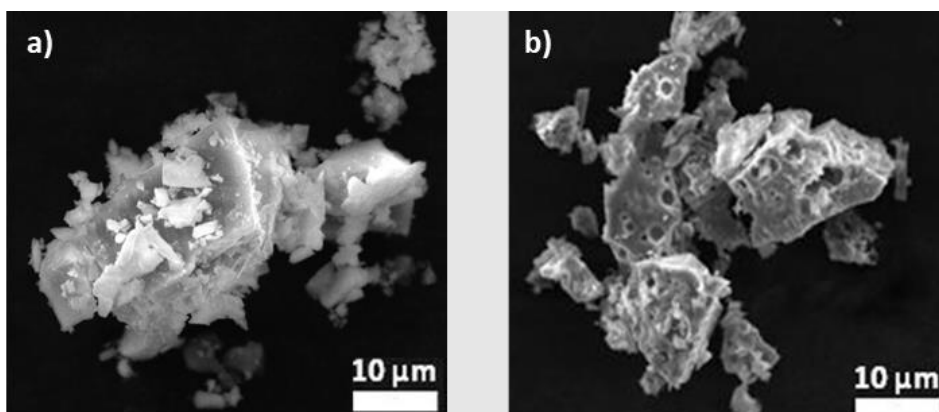
Figure 3.5: SEM images of (a) $Na_2Fe_2(PO_3)_3N$ synthesized from Fe_2O_3 as Fe precursor; (b) $Na_2Fe_2(PO_3)_3N$ synthesized from FeC_2O_4 as Fe precursor.

Some differences can be distinguished regarding the size and shape of the particles. More diversity in the particle size can be observed for the ones synthesized from Fe_2O_3 (Figure 3.5a), with (~1-5 μm) size particles forming ~20 μm agglomerates. The analyzed particles have non-uniform shape. The particles of $Na_2Fe_2(PO_3)_3N$ synthesized from FeC_2O_4 (Figure 3.5b) have in average a larger size varying from 2 to 20 μm, also have non-uniform shape. Small holes can be observed in the walls of the particles, which are absent in the particles synthesized from Fe_2O_3 and are assumed to result from the C_2O_4 decomposition. Since the same synthesis protocol was used to obtain both powders, the difference in the particles is expected to origin from the different nature of the Fe precursors.

The atomic ratio between elements in $Na_2Fe_2(PO_3)_3N$ was evaluated by EDX and ICP-AES analysis. Results from these two techniques are gathered in Table 3.3. The experimental ratios are in good agreement with the theoretical ones. The slightly lower amount of sodium determined by EDX could be related with the evaporation of this element under the incident beam, since the ICP technique confirmed the expected ratio.

Table 3.3: Composition of Na₂Fe₂(PO₃)₃N synthesized from FeC₂O₄ as Fe precursor, determined by EDX and ICP.

Element	Theoretical content	Experimental atomic ratio determined from EDX	Experimental atomic ratio determined from ICP
Na	2	1.7±0.08	2.0±0.02
P	3	3 (fixed)	3(fixed)
Fe	2	2.0±0.05	1.9±0.02

3.2.3.   Thermogravimetric analysis

The thermal stability of $Na_2Fe_2(PO_3)_3N$ synthesized from FeC_2O_4 was evaluated by performing a thermal gravimetric analysis (TGA) under both inert (Ar) and synthetic air atmospheres in the temperature range of RT-1000°C. The TGA curves are shown in Figure 3.6.
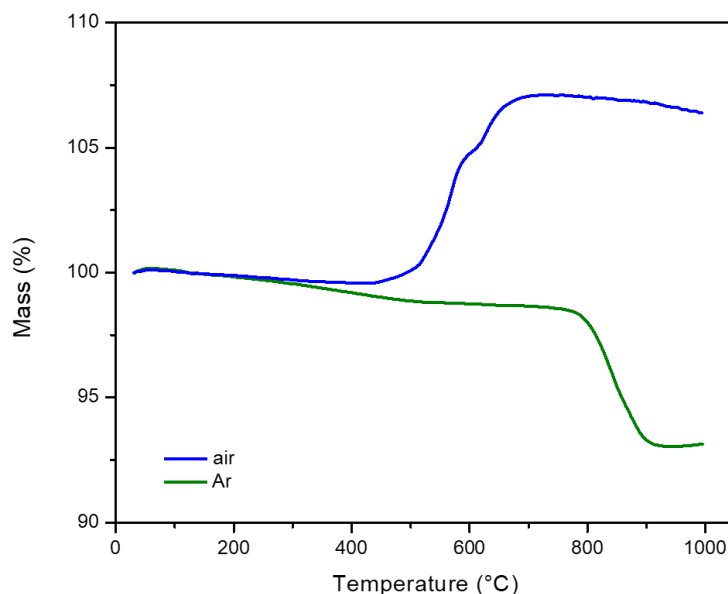
Figure 3.6: TG curves of Na₂Fe₂(PO₃)₃N synthesized from FeC₂O₄ under Ar (green) and air (blue) flows within the temperature range of 30–1000°C at 10°C.min⁻¹ heating rate.

$Na_2Fe_2(PO_3)_3N$ exhibits exceptional thermal stability in inert atmosphere with the decomposition starting above 800°C. The obtained powder melted and sticked to the crucible, therefore it was not possible to perform XRD analysis of it, however by analogy to the decomposition products of $Na3V(PO_3)_3N$ (Chapter 2.2.2.4), it is expected that $Na_2Fe_2(PO_3)_3N$ decomposed into Fe_2O_3. Under air, $Na_2Fe_2(PO_3)_3N$ is stable up to ~500°C. Above this temperature, an increase of the net weight was observed resulting either from the framework decomposition upon replacement of N^{III-} by O^{II-} and/ or oxidation of Fe^{II} to Fe^{III}.

Exceptional thermal stability up to 500°C in air indicates superior thermal properties of this material with respect to $Na_3V(PO_3)_3N$, which is more convenient for battery application.

3.2.4.   Electrochemical characterization

As mentioned in the introduction, Liu et. al.[160] synthesized $Na_2Fe_2(PO_3)_3N$ using same ammonolysis route. No electrochemical performance of $Na_2Fe_2(PO_3)_3N$ *vs.* Na was reported, while cycling $Na_2Fe_2(PO_3)_3N$ in hybrid-ion configuration *vs.* Li metal anode resulted in obtaining capacities of ~40 mAh.g^{-1} and large polarization. Such poor performance was claimed to result from the limited Na^+ ion mobility in $Na_2Fe_2(PO_3)_3N$. For this reason, Liu *et al.*[160] carried out a chemical Na^+/Li^+ ion exchange using LiBr in a molar ratio of 1:8 (Na to Li) prior to electrochemical evaluation *vs.* Li. However, although they successfully removed both of the sodium ions from $Na_2Fe_2(PO_3)_3N$, only a small amount of Li was inserted into the structure resulting with the final composition of $Li_{0.3}Fe_2(PO_3)_3N$.[160] Difficulties with the insertion more lithium were explained by the oxidation of iron upon the ion-exchange reaction.

Since the obtained $Li_{0.3}Fe_2(PO_3)_3N$ iron was at oxidized +III state, the electrochemical tests were initiated in discharge to intercalate Li^+ into the structure. ~1.4 Li^+ was inserted in the structure, corresponding to a capacity of ~100 mAh.g^{-1}. A relatively stable capacity of 120 mAh.g^{-1} was obtained in subsequent cycles, corresponding to the reversible mobility of 1.7 Li^+. The cyclic voltammetry analysis revealed two separate redox potentials at 3.55 V / 3.5 V *vs.* Li^+/Li and 3.1 V/ 2.95 V *vs.* Li^+/Li from $Fe^{II/III}$ redox couple.

In our work, we decided to revisit the electrochemical properties of the $Na_2Fe_2(PO_3)_3N$ *vs.* both Na and Li anode. The material synthesized from FeC_2O_4 was used due to the higher purity. $Na_2Fe_2(PO_3)_3N$ cathodes were prepared by mixing the active material with 30% carbon (Acetylene Black) and 10% poly(vinylidene) fluoride (PVDF, Alfa Aesar) in N-methyl-2-pyrrolidone (NMP, Aldrich) and pasting the obtained slurry onto an Al foil using a doctor blade. The as-prepared laminate was then dried overnight in the vacuum oven at 120°C and punched into small disks with a mass loading of active material around 2-3x10^{-3} g/cm^2. The tests were performed in half-cell configuration with metallic sodium or lithium as a negative electrode and $LiPF_6/NaPF_6$ in EC:DMC (1:1 vol)

as electrolyte in 2032-type coin cells. The prepared cells were studied by cycling in galvanostatic mode at a rate of one electron exchange in 40 hours (C/40 rate) for 50 cycles; between 1.5 and 4.5 V vs Na$^+$/Na and 1.5 and 5.0 V vs Li$^+$/Li using a MACCOR battery tester. All electrochemical measurements were performed at room temperature. The obtained galvanostatic charge-discharge curves are presented in Figure 3.7.
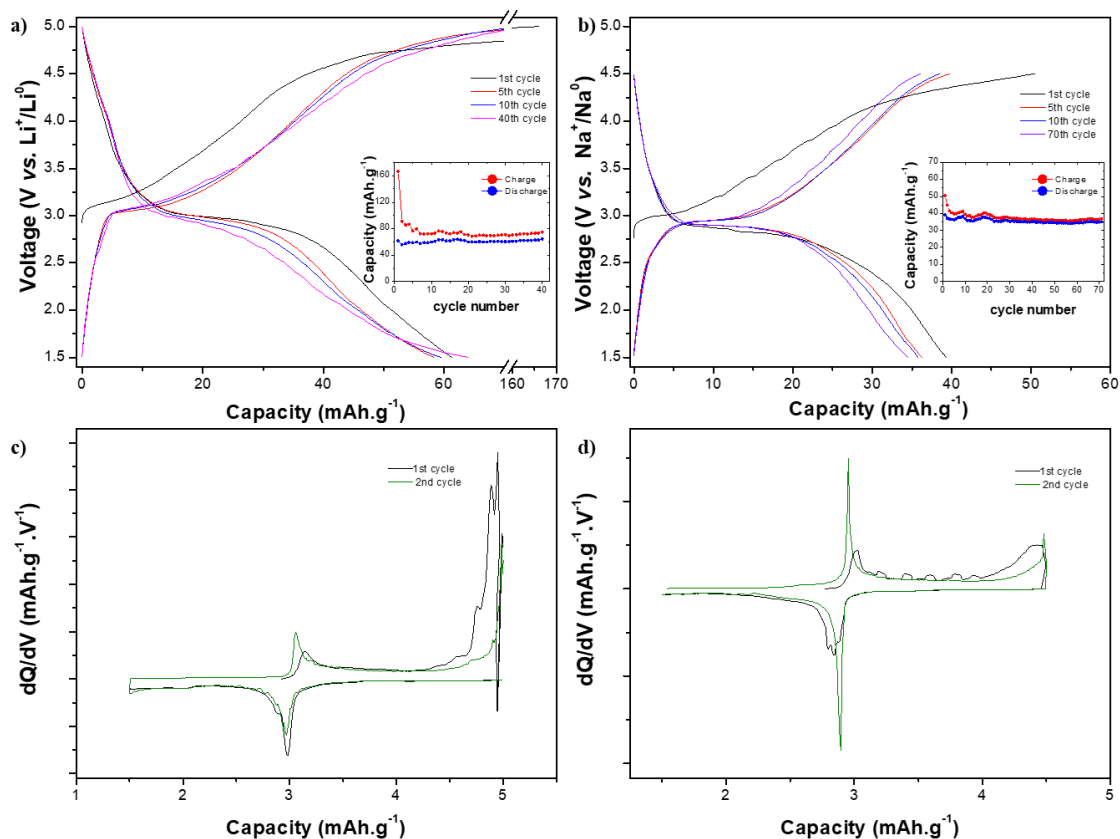
Figure 3.7: (a&b) Voltage-capacity profile of Na$_2$Fe$_2$(PO$_3$)$_3$N against (a) Li$^+$/Li^0 and (b) Na$^+$/Na^0 metal at C/40 rate. The inset shows the evolution of the charge and discharge capacity during the first 40 (Li) and 70(Na) cycles; (c&d) corresponding derivative dQ/dV for the first two cycles against (c) Li$^+$/Li^0 and (d) Na$^+$/Na^0 metal.

Analyzing the charge-discharge curves of Na$_2$Fe$_2$(PO$_3$)$_3$N cycled against Na and Li metal several differences can be observed. The capacities achieved for Na$_2$Fe$_2$(PO$_3$)$_3$N (~60 mAh.g^{-1}, Figure 3.7a and c) corresponds to the mobility of around one alkali cation per f.u. The large additional capacity of ~100 mAh.g^{-1} at >4.6 V *vs.* Li$^+$/Li^0 is ascribed to the oxidation of the Li electrolyte. On the other hand, when cycled against Na metal (Figure 3.7b and d), the obtained capacities are almost reduced to half (~35 mAh.g^{-1}) and corresponding to the mobility of around 0.55 Na$^+$ per f.u. In both cells the capacity remains relatively stable over 40 to 70 cycles (inset in Figure 3.7a and b).

From the derivative dQ/dV curves it can be observed that the electrochemical activity of the Fe^{II}/Fe^{III} redox couple is centered at 3.0 V *vs.* Li^+/Li^0 and 2.9 V *vs.* Na^+/Na^0 and only one process is observed.

As mentioned in the introduction, the literature only reports the electrochemical performance of $Na_2Fe_2(PO_3)_3N$ *vs.* Li metal with the capacities of ~40 mAh.g^{-1} and high polarization.[160] Lack of the results *vs.* Na metal suggests unsuccessful extraction/insertion of Na^+ ions within the framework. Here we demonstrated the stable, although limited mobility of ~0.55 Na^+ ions at 2.9 V *vs.* Na^+/Na^0 while cycling $Na_2Fe_2(PO_3)_3N$ *vs.* Na metal. While cycling the cell in the hybrid-ion configuration (*vs.* Li metal and using Li electrolytes) a higher capacity, than previously reported was obtained. Compared to other iron-based polyanionic compounds such as $NaFePO_4$ [205] or Na_2FePO_4F [206], the electrochemical performance of $Na_2Fe_2(PO_3)_3N$ is however less competitive. However, it seems that the limitation origins with the use of only one Fe^{II}/Fe^{III} redox couple. The possible activation of the second one would double the capacity and place $Na_2Fe_2(PO_3)_3N$ as a competitive electrode material.

3.2.4.1. Evaluation of the Na insertion/extraction mechanism

An *operando* synchrotron XRD experiment was performed to further analyze the mechanism of $Na_2Fe_2(PO_3)_3N$ oxidation and reduction during the first cycle. The experiment was performed at ALBA synchrotron, MSPD beamline. Details on the experiment can be found in the Annex - experimental part. The material was cycled in a special electrochemical cell with a Be window acting as current collector and Na metal as counter electrode at C/40 rate. One complete cycle (1 charge and 1 discharge) was registered. Figure 3.8 shows the obtained electrochemical charge-discharge profile together with its derivative curve. The collected SXRD patterns as well as the corresponding electrochemical curve are shown in Figure 3.9.
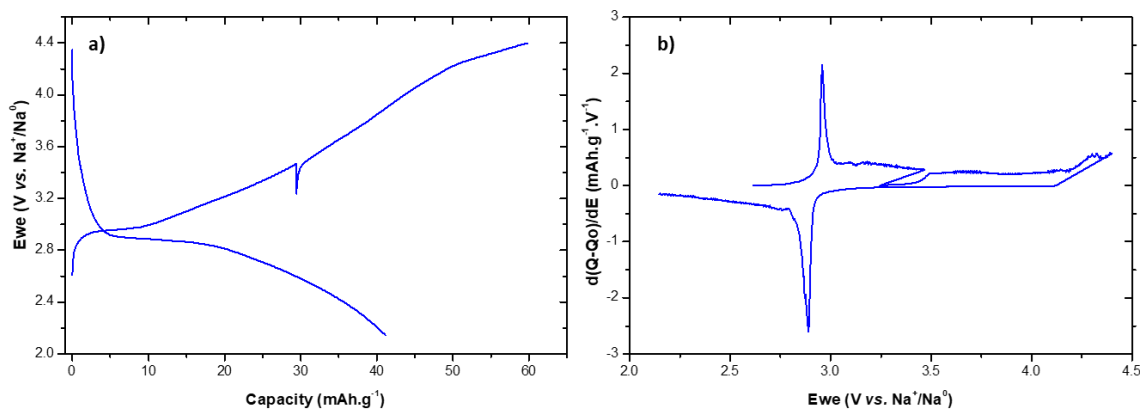
Figure 3.8: (a) Galvanostatic charge-discharge curve of $Na_2Fe_2(PO_3)_3N$ cycled *vs.* Na at C/40 rate with (b) corresponding derivative dQ/dV curve.

The capacity of ~60 mAh.g^{-1} obtained during the first charge corresponds to the removal of one Na$^+$, whereas during discharge ~0.65 Na$^+$ were reinserted into the $Na_2Fe_2(PO_3)_3N$ structure. Based on the derivative curve (Figure 3.8b), the redox process of the Fe^{II}/Fe^{III} couple is centered at 2.95 V *vs.* Na$^+$/Na^{0,} in agreement with previous electrochemical tests performed in Swagelok cell.
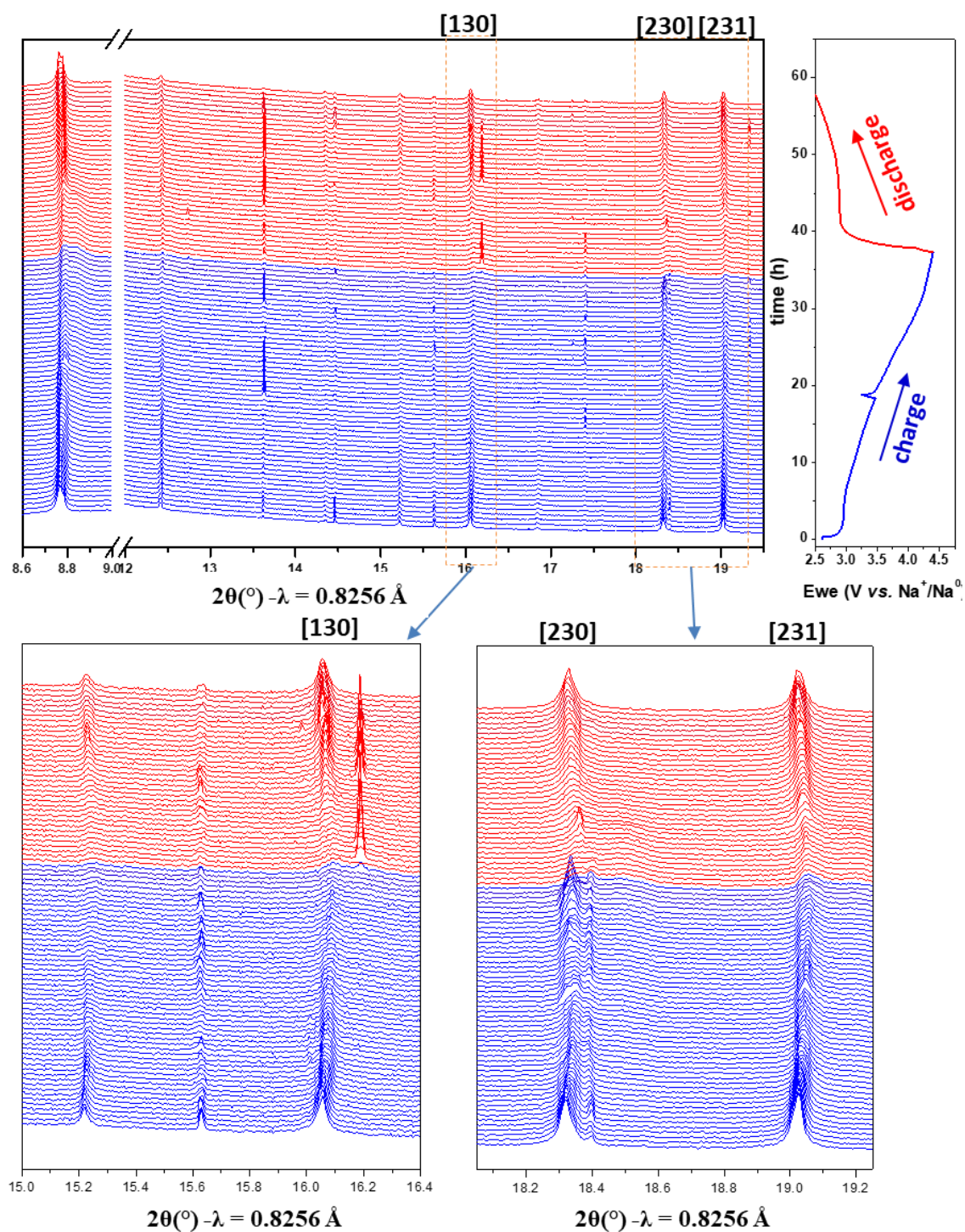
Figure 3.9: Results obtained for the first measured *in situ* cell comprising Na₂Fe₂(PO₃)₃N as an active material cycled vs. Na metal at C/40 rate. On the top left, collected SXRD patterns, on the top right, corresponding electrochemical curve, indicating charge process in blue and discharge in red. Below, evolution of the [130], [230] and [231] peaks showing reversible shift and the clear appearance of a secondary phase in the higher 2theta range.

While analyzing the SXRD patterns (Figure 3.9) and mainly focusing on the highlighted reflections, the shift of the peaks can be observed with the clear appearance of a second phase in the higher 2theta angles whose intensity increases with the increasing voltage.

134

This feature suggests a biphasic mechanism, with the coexistence of a Na-rich and a Na-poor phase in this region. During the discharge, the biphasic region can be observed through the whole process.

Table 3.4: Refined Na occupancy and lattice parameter of Na$_{2-x}$Fe$_2$(PO$_3$)$_3$N at different charge states acquired from the refinement of the corresponding XRD patterns.

Charge state	formula	Na1 occ	Na2 occ	a (Å)	wt.%
Pristine	Na$_2$Fe$_2$(PO$_3$)$_3$N	0.98(7)	1.0(6)	9.342(3)	100%
End of charge	Na$_{1.1}$Fe$_2$(PO$_3$)$_3$N	0.73(4) (ph1) + 0.42(3) (ph2)	0.87(4) (ph1) + 0.35(3) (ph2)	9.324(3) ph1 9.271(5) ph2	Ph1 31%, ph2 69%
End of discharge	Na$_{1.65}$Fe$_2$(PO$_3$)$_3$N	0.76(4)	0.88(5)	9.339(4)	100%

Rietveld refinements of the selected SXRD patterns (recorded every two hours) were performed. Table 3.4 shows the refined Na occupancies and lattice parameters before cycling, at end of charge and end of the discharge. Figure 3.10 shows the evolution of the cell parameter of both, Na-rich and a Na-poor phases upon cycling together with the changing weight fraction of these phases. The refined cell parameters corroborate the biphasic mechanism. Indeed, in the biphasic region two sets of peaks were well indexed with the $P2_13$ space group, corresponding to the two Na$_{2-x}$Fe$_2$(PO$_3$)$_3$N phases. The cell parameter of the new phase was smaller in agreement with the smaller Na content, and evolves throughout the charge and discharge process as its Na content also varies. Considering the fraction of the phases and Na$^+$ occupancies at the end of the charge, it can be deduced that ~1 Na$^+$ was removed which is in perfect agreement with the obtained capacity during the first charge. At the end of the discharge, the presence of only one phase was detected with the cell parameter almost equal to the pristine material, however several vacancies were observed at the Na sites. The eventual refined composition was found to be Na$_{1.65}$Fe$_2$(PO$_3$)$_3$N. From the electrochemical curve (Figure 3.8) it can be observed that not all capacity was recovered, ~0.65Na$^+$ was reinserted, which is in good agreement with the findings from the refinement of the SXRD pattern. Such an
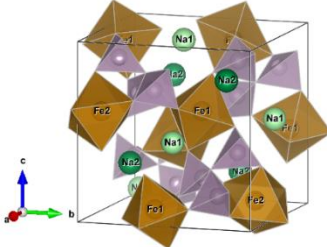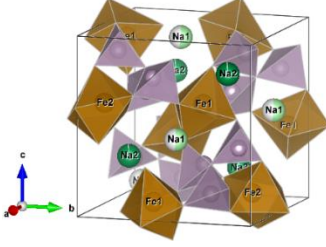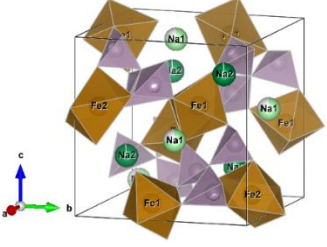
irreversible capacity has been already observed in $Na_3V(PO_3)_3N$ and discussed in Chapter 2.

A detailed structural analysis of the $Na_2Fe_2(PO_3)_3N$ phase sequence is presented in Table 3.5. The performed analysis reveals the decrease of the FeO_6 octahedra volume, together with the changes of the Fe-O distances, being in good agreement with the change of the ionic radius from Fe^{III} (0.645 Å), to Fe^{II} (0.78 Å).[200] These results confirm the oxidation of iron upon charging from Fe^{II} to Fe^{III}. Additionally, it can be observed that at the discharged state the oxidation state of iron instead of Fe^{II} is closer to $Fe^{2.4}$ (as obtained from the bond valence data) which could explain the observed vacancies in Na. This hypothesis would require further detailed *ex situ* XAS analysis.
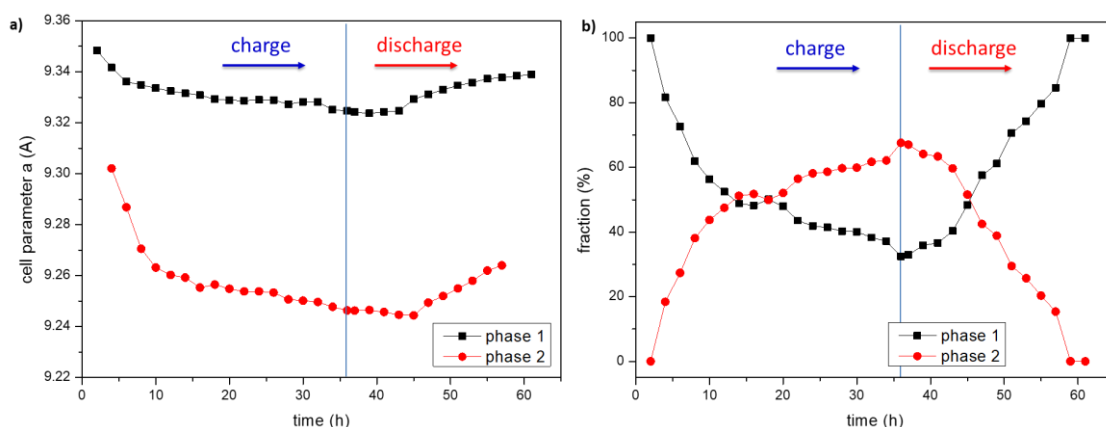
Figure 3.10: (a) Variation of the cell parameters in the two phases of $Na_2Fe_2(PO_3)_3N$ upon time during charge and discharge; (b) variation of the fraction (in %) of both phases upon time during charge and discharge.

Table 3.5: Crystallographic characterization (lattice parameters, polyhedral details, and selected bond lengths) of $Na_2Fe_2(PO_3)_3N$ at three stages of the *operando* measurement – beginning, end of charge and end of discharge.

Pristine $Na_2Fe_2(PO_3)_3N$	End of charge $NaFe_2(PO_3)_3N$	End of discharge $Na_{1.65}Fe_2(PO_3)_3N$
Lattice parameters: $a = 9.342(2)$ Å	**Lattice parameters:** <u>31 wt.% Ph1:</u> $a = 9.324(3)$ <u>69% wt.% Ph2</u> $a =+$ $9.271(5)$	**Lattice parameters:** $a = 9.339(4)$ Å
Fe polyhedra details: • $Fe(1)O_6$ Average bond length $=2.119$ Å Polyhedral volume $= 12.3643$ Å^3 Distortion index (bond length) $= 0.03039$ • $Fe(2)O_6$ Average bond length $= 2.1748$ Å Polyhedral volume $= 13.4433$ Å^3 Distortion index (bond length) $= 0.00721$	**Fe polyhedra details of ph2:** • $Fe(1)O_6$ Average bond length $= 2.0918$ Å Polyhedral volume $= 11.1980$ Å^3 Distortion index (bond length) $= 0.04160$ • $Fe(2)O_6$ Average bond length $= 2.1081$ Å Polyhedral volume $= 11.5995$ Å^3 Distortion index (bond length) $= 0.04352$	**Fe polyhedra details:** • $Fe(1)O_6$ Average bond length $= 2.0406$ Å Polyhedral volume $= 10.9146$ Å^3 Distortion index (bond length) $= 0.00382$ • $Fe(2)O_6$ Average bond length $= 2.1009$ Å Polyhedral volume $= 11.5775$ Å^3 Distortion index (bond length) $= 0.00506$
Selected bond distances: 3x Fe1 – O1 2.06(15) Å 3x Fe1 – O2 2.18(15) Å 3x Fe2 – O2 2.19(15) Å 3x Fe2 – O3 2.16(15) Å P – O1 1.60(15) Å P – O2 1.71(15) Å P – O3 1.42(16) Å P – N 1.63(16) Å 3x Na1 – O1 2.23(15) Å 3x Na1 – O3 2.96(15) Å Na1 – N 2.67(15) Å 3x Na3 – O1 3.10(15) Å 3x Na3 – O2 3.03(16) Å 3x Na3 – O3 2.33(15) Å	**Selected bond distances of ph2:** 3x Fe1 – O1 2.01(16) Å 3x Fe1 – O2 2.18(16) Å 3x Fe2 – O2 2.20(13) Å 3x Fe2 – O3 2.02(13) Å P – O1 1.93(7) Å P – O2 1.67(6) Å P – O3 1.44(5) Å P – N 1.65(6) Å 3x Na1 – O1 2.15(13) Å 3x Na1 – O3 3.12(13) Å Na1 – N 2.43(13) Å 3x Na3 – O1 3.11(7) Å 3x Na3 – O2 2.88(7) Å 3x Na3 – O3 2.23(7) Å	**Selected bond distances:** 3x Fe1 – O1 2.05(7) Å 3x Fe1 – O2 2.03(5) Å 3x Fe2 – O2 2.09(7) Å 3x Fe2 – O3 2.11(6) Å P – O1 1.33(7) Å P – O2 1.80(6) Å P – O3 1.28(7) Å P – N 1.71(7) Å 3x Na1 – O1 3.44(8) Å 3x Na1 – O3 3.21(8) Å Na1 – N 2.46(7) Å 3x Na3 – O1 3.20(7) Å 3x Na3 – O2 3.02(7) Å 3x Na3 – O3 2.51(6) Å

3.2.4.2. Chemical oxidation

Since the electrochemical measurements resulted with the oxidation of only one Fe^{II}/f.u., the chemical oxidation was performed to verify if both Fe^{II} ions can be oxidized using this route. As for the chemical oxidation of $Na_3V(PO_3)_3N$ (Chapter 2 section 2.2.5.), NO_2BF_4 solution in acetonitrile was used as oxidizing agent. Two different molar ratios were investigated, targeting the removal of one and two Na^+ ions. Figure 3.11 shows the XRD patterns of the pristine and oxidized phases.
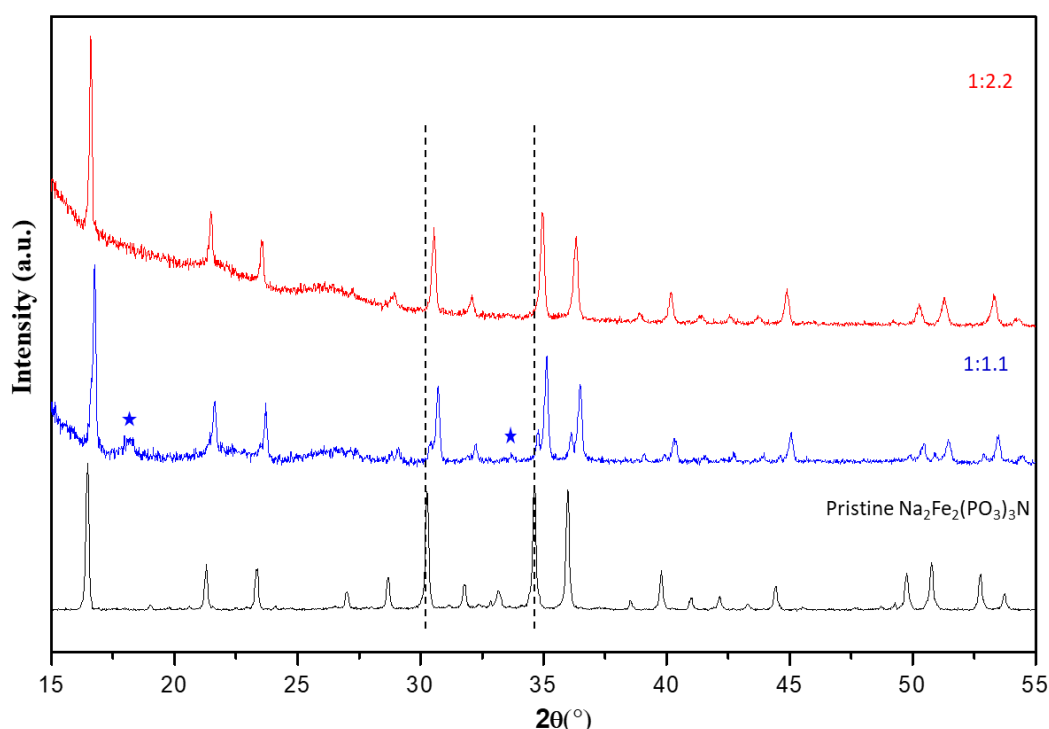
Figure 3.11: XRD patterns of pristine $Na_2Fe_2(PO_3)_3N$ and after oxidation reaction with NO_2BF_4 in ACN. The active material to oxidizing reagent (AM:OR) ratio is given in the figure. Additional peaks in the blue pattern (indicated with asterisks) correspond to the small amount of the $NaBF_4$ impurity.

Two distinct phases can be distinguished while using an equivalent molar ratio of the oxidizing agent to remove 1 Na^+ ion, suggesting that part of the pristine $Na_2Fe_2(PO_3)_3N$ did not undergo the oxidation. In the second sample, with a higher amount of NO_2BF_4, the oxidation resulted in a single phase. Figure 3.12 shows the Rietveld refinement of the obtained pattern, and Table 3.6 the crystallographic data obtained from the refinement.
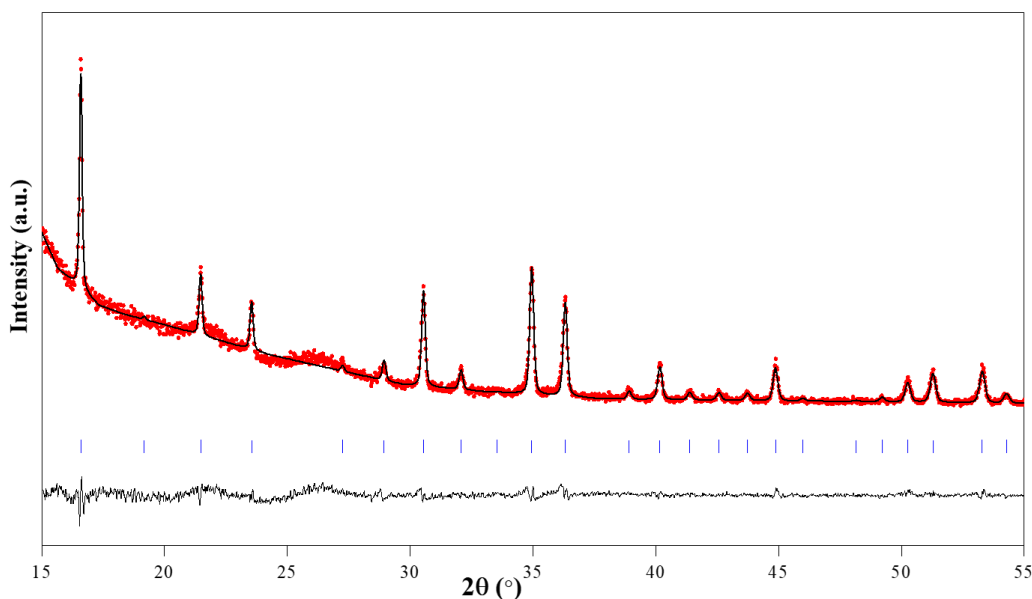
Figure 3.12: Rietveld refinement of the XRD pattern of chemically oxidized Na₂₋ₓFe₂(PO₃)₃N. Red circles, black and horizontal black lines represent the observed, calculated and difference patterns, respectively. The positions of the Bragg reflections of the _P2₁3_ space group are shown as blue vertical bars.

Table 3.6: Crystallographic data and atomic coordinates of Na₂₋ₓFe(PO₃)₃N determined from the refinement of XRD data.

S.G.: _P2₁3_						
_a_ =9.249(5) Å		**V = 791.2(5) Å³**		**R_Bragg = 6.9 %**	**χ² = 1.47**	
Atom	Wyckoff position	_x/a_	_y/b_	_z/c_	Occupancy	_B_iso
P	12_b_	0.341(2)	0.096(2)	0.263(2)	1	0.52(6)
Fe1	4_a_	0.576(4)	0.576(4)	0.576(4)	1	1.21(4)
Fe2	4_a_	0.388(4)	0.388(4)	0.388(4)	1	1.29(4)
Na2	4_a_	0.789(5)	0.789(5)	0.789(5)	0.98(5)	0.29(6)
O1	12_b_	0.208(4)	0.017(4)	0.429(4)	1	0.42(5)
O2	12_b_	0.397(2)	0.001(3)	0.142(3)	1	0.48(5)
O3	12_b_	0.481(2)	0.169(2)	0.314(2)	1	0.43(5)
N	4_a_	0.199(3)	0.199(3)	0.199(3)	1	0.55(6)

Based on the Rietveld refinement of the XRD pattern of this sample (Table 3.6), the obtained material can be well indexed with the same cubic structure with _P2₁3_ space group and lattice parameter of 9.249(5) Å. Based on the refinement, one Na is being fully removed from the Na1 site and this removal is associated with the shrinking of the unit cell volume (as demonstrated in Table 3.7). While comparing these results with the ones from the _operando_ measurement, it can be observed, that the decrease of the cell parameter was indeed observed in the second (Na-poor) phase. In the experiment here,

all Na1 site was depleted therefore it explains the smaller value of the refined cell parameter.

Table 3.7: Lattice parameter of Na$_{2-x}$Fe$_2$(PO$_3$)$_3$N at different charge states acquired from the refinement of the corresponding XRD patterns and from the chemically oxidized states.

Charge state	a (Å)	Wt.%
Pristine Na$_2$Fe$_2$(PO$_3$)$_3$N	9.342(3)	100%
Chemical oxidation 1	9.334(3)+ 9.244(4)	Ph1 12%
		Ph2 88%
Chemical oxidation 2	9.249(5)Å	100%

These results indicate that the complete removal of one sodium from the Na$_2$Fe$_2$(PO$_3$)$_3$N framework is possible with the use of a strong oxidizing agent such as NO$_2$BF$_4$. However, the removal of the second Na$^+$ ion upon chemical oxidation was not achieved, suggesting very high stability of the oxidized NaFe$_2$(PO$_3$)$_3$N phase requiring very high additional energy to transform into less favorable desodiated Fe$_2$(PO$_3$)$_3$N state.

In order to increase the voltage of the redox activity centered around 2.9 V vs. Na$^+$/Na in Na$_2$Fe$_2$(PO$_3$)$_3$N, we decided to explore the substitution of Fe by other bivalent transition metals known to operate at higher voltages (Mn^{II}, Co^{II}). This hypothesis can be supported theoretical calculations and experimental tests.[207–209] Ong et. al. [207] calculated the Na and Li voltages for the different families such as layered AMO$_2$, olivine and maricite AMPO$_4$, and the NASICON A$_3$V$_2$(PO$_4$)$_3$ structures. The results of these calculations are gathered in Figure 3.13. It can be observed that in each family the polymorph with Mn and Co transition metal has a higher voltage than the corresponding Fe member.
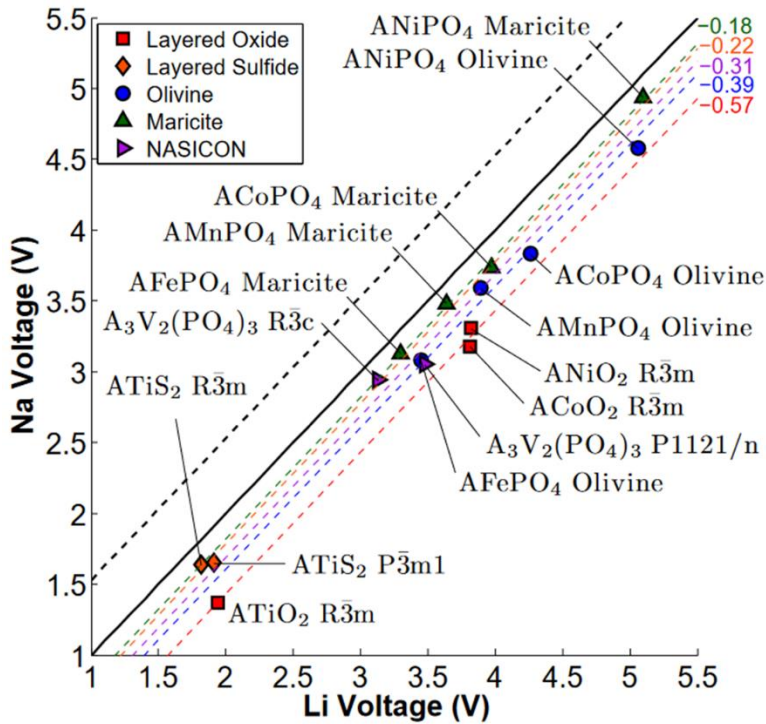
Figure 3.13: Calculated Na voltage *vs.* calculated Li voltage for different structures. The black dashed line indicates the +0.53 V difference between the cohesive energies of Na and Li, while the other colored dashed lines indicate the fitted average voltage difference ΔV_Na-Li. From Ong et.al.[207]

Pagot et. al.[208] evaluated substitution of Fe^{II} ions in $LiFePO_4$ by CO^{II}, Ni^{II} and Mn^{II}. They observed that while controlling the molar ratio of the TM ions, the working potential can be increased from 3.5 V up to 4.8 V and the capacities also can be improved reaching 160 mAh.g^{-1}. The material with the highest cobalt content showed the best performances in terms of the highest working voltage (>4.5 V); good capacities of ~125 mAh.g^{-1} and good rate capabilities.

Encouraged by these results we decided to screen different solid solutions of Fe/Co and Fe/Mn mixed $Na_2M_xM´_{2-x}(PO_3)_3N$ compositions. To have a first insight into the working voltage of the end members ($Na_2Co_2(PO_3)_3N$ and $Na_2Mn_2(PO_3)_3N$), the modeling and computational simulation group at CIC energiGUNE performed series of spin-polarized DFT calculations as implemented in the Vienna ab initio simulation package (VASP). [210–212] In order to properly account for the localized nature of Fe, Co and Mn 3d states, DFT+U scheme of Dudarev et al.[176] was applied with U values of 5.30, 3.32 and 3.90 eV for Fe, Co and Mn, respectively. These U parameters are similar to those from the Materials Project.[213]

The average equilibrium voltage, $V_{j \to i}$, of $Na_y M_2(PO_3)_3 N$ (M = Co, Fe and Mn) for sodium compositions between y_i and y_j (with $y_i < y_j$) was given by the negative change in the Gibbs free energy per charge carrier. [214] For zero-temperature calculations, it can be approximated by simply considering the change in total DFT energies as follow:[215]

$$
V_{j \to i} \approx -\frac{E\left(Na_{y_j} M_2(PO_3)_3 N\right) - E\left(Na_{y_i} M_2(PO_3)_3 N\right) - (y_j - y_i) E(Na)}{(y_j - y_i) e}, \qquad (1)
$$

where e is the electron charge, $E\left(Na_{y_j} M_2(PO_3)_3 N\right)$ and $E\left(Na_{y_i} M_2(PO_3)_3 N\right)$ are the total energies of the corresponding nitridophosphate ground state structures at compositions y_i and y_j, and $E(Na)$ is the total energy (per atom) of bulk bcc sodium. For computing average equilibrium voltages using equation (1), the structures with the lowest-energy magnetic arrangement in each case were considered. Table 3.8 summarizes the results.

Table 3.8: DFT computed zero-temperature average equilibrium voltages for $Na_{2 \to 1} M_2(PO_3)_3 N$ and $Na_{1 \to 0} M_2(PO_3)_3 N$ (M = Co, Fe and Mn).

	$V_{j \to i}$ (in V)
$Na_2Co_2(PO_3)_3N \rightarrow Na_1Co_2(PO_3)_3N$	3.75
$Na_1Co_2(PO_3)_3N \rightarrow Na_0Co_2(PO_3)_3N$	4.53
$Na_2Fe_2(PO_3)_3N \rightarrow Na_1Fe_2(PO_3)_3N$	2.79
$Na_1Fe_2(PO_3)_3N \rightarrow Na_0Fe_2(PO_3)_3N$	3.38
$Na_2Mn_2(PO_3)_3N \rightarrow Na_1Mn_2(PO_3)_3N$	3.44
$Na_1Mn_2(PO_3)_3N \rightarrow Na_0Mn_2(PO_3)_3N$	4.15

It can be observed that the calculated voltage for the removal of one electron for $Na_2Fe_2(PO_3)_3N$ (2.79 V) is in good agreement with the experimental results (2.9 V), and, as expected, the voltage calculated for Co and Mn is higher. Although the calculated voltage for the removal of the second electron in $Na_2Fe_2(PO_3)_3N$ (3.38 V) is accessible from the theoretical point of view, it was not possible to be reached experimentally. In our next work we will evaluate if the substitution of Fe^{II} by Co^{II} and Mn^{II} will unlock the possibility of the two electron exchange.

3.3. Mixed cobalt-iron nitridophosphates

3.3.1.   Synthesis and structural characterization

Syntheses were realized using the ammonolysis synthesis route using $NaPO_3$, FeC_2O_4, CoO and $NH_4H_2PO_4$ precursors. Different temperatures were screened, ranging from 600 to 700 °C with eventually 650 °C identified to be suitable for the synthesis. Higher temperature resulted in a high amount of Co_2P and CoP impurities.

The evolution of the lattice parameters with the amount of Fe and the corresponding XRD patterns are summarized in Table 3.9 and shown in Figure 3.14, respectively.
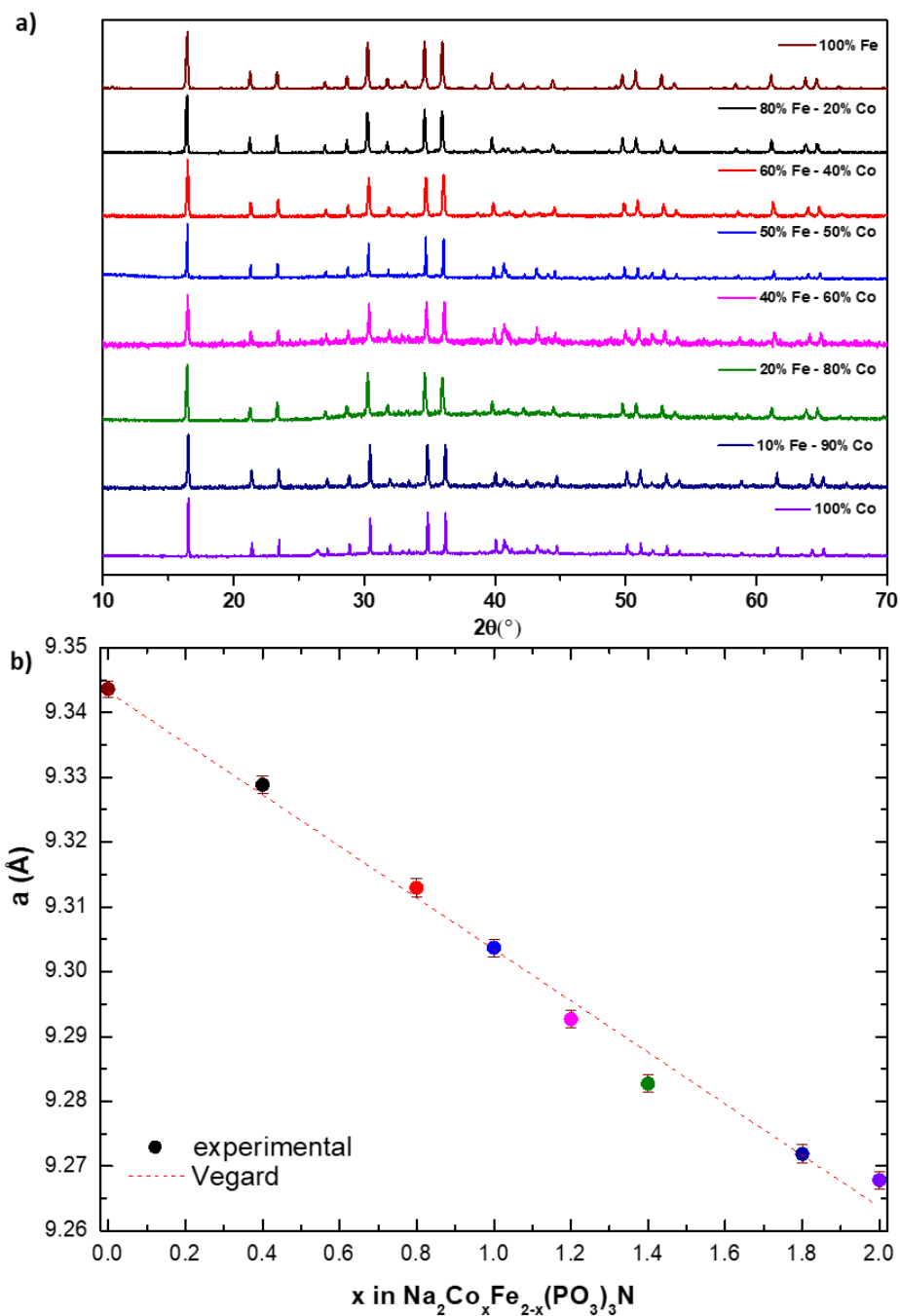
Figure 3.14: (a) Evolution of the XRD pattern with a changing content x of Co in Na₂CoₓFe₂₋ₓ(PO₃)₃N $(0 \leq x \leq 2)$ (b) Variation of a cell parameter a with changing content x of Co in Na₂CoₓFe₂₋ₓ(PO₃)₃N $(0 \leq x \leq 2)$.

Table 3.9: Evolution of the lattice parameters with the changing composition in $Na_2Co_xFe_{2-x}(PO_3)_3N$ ($0 \leq x \leq 2$).

x	composition	Lattice parameter [Å]
0	$Na_2Fe_2(PO_3)_3N$	9.344(2)
0.4	$Na_2Co_{0.4}Fe_{1.6}(PO_3)_3N$	9.329(2)
0.8	$Na_2Co_{0.8}Fe_{1.2}(PO_3)_3N$	9.313(3)
1	$Na_2CoFe(PO_3)_3N$	9.304(2)
1.2	$Na_2Co_{1.2}Fe_{0.8}(PO_3)_3N$	9.293(4)
1.6	$Na_2Co_{1.6}Fe_{0.4}(PO_3)_3N$	9.279(2)
1.8	$Na_2Co_{1.8}Fe_{0.2}(PO_3)_3N$	9.272(2)
2	$Na_2Co_2(PO_3)_3N$*	9.2678(2)*

Stabilization of the $Na_2Co_xFe_{2-x}(PO_3)_3N$ phase was successful up to x=0.9 and all XRD patterns could be well indexed with the $P2_13$ space group. The attempts of the synthesis of pure $Na_2Co_2(PO_3)_3N$ phase in the same conditions resulted with obtaining an amorphous phase. (*) The XRD pattern and cell parameter provided in Figure 3.14 and Table 3.9 were found after changing the synthesis method (described below in the section 3.6.). The incorporation of the smaller Co^{II} into the framework resulted with slight changes in the polyhedra volumes compared to $Na_2Fe_2(PO_3)_3N$, however without almost any impact on the atomic positions. The quasi-linear decrease of the lattice parameter with decreasing amount of Fe indicates that the $Na_2Co_{2x}Fe_{2-2x}(PO_3)_3N$ solid solutions follows Vegard`s law. Figure 3.15 shows the Rietveld refinement of the $Na_2FeCo(PO_3)_3N$ phase. A small amount of impurity (~1.5%) was identified as $NaFe_3(PO_4)_3$.
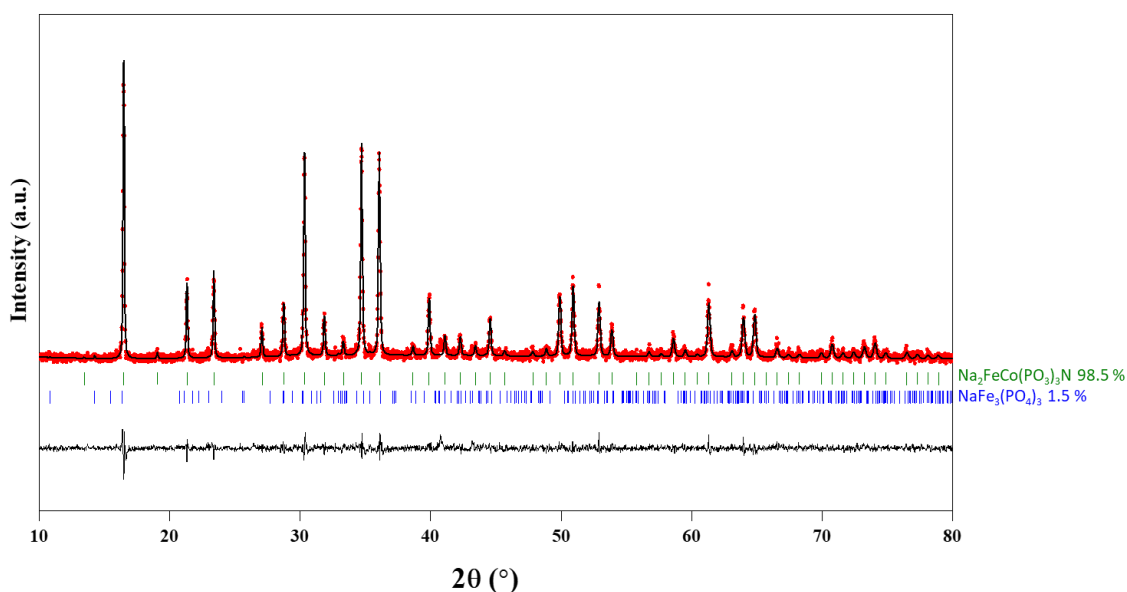
Figure 3.15: Rietveld refinement of the XRD pattern of $Na_2FeCo(PO_3)_3N$. Black line and red circles represent the calculated and observed patterns, respectively. The horizontal black line is the difference curve between the calculated and observed patterns. The Bragg reflections of the CUBICON's $P2_13$ unit cell with a = 9.304 Å are shown as green vertical bars. Blue vertical bars are indicating the Bragg reflections of the 1.5% impurities of $NaFe_3(PO_4)_3$.

145

Table 3.10: Crystallographic data and atomic coordinates of Na₂FeCo(PO₃)₃N determined from the refinement of XRD data.

S.G.: $P2_13$

a =9.304(2) Å		V = 805.3(2) Å³		R_{Bragg} = 6.8 %	χ^2 = 1.58	
Atom	Wyckoff position	x/a	y/b	z/c	Occupancy	B_{iso}
P	12b	0.342(2)	0.089(2)	0.258(2)	1	0.68(5)
Fe1	4a	0.578(3)	0.578(3)	0.578(3)	0.5	0.35(7)
Co1	4a	0.578(3)	0.578(3)	0.578(3)	0.5	0.35(7)
Fe2	4a	0.399(3)	0.399(3)	0.399(3)	0.5	0.34(6)
Co2	4a	0.399(3)	0.399(3)	0.399(3)	0.5	0.34(6)
Na1	4a	0.038(5)	0.038(5)	0.038(5)	1.0(2)	0.69(4)
Na2	4a	0.792(5)	0.792(5)	0.792(5)	1.0(2)	0.72(4)
O1	12b	0.217(3)	0.006(3)	0.875(3)	1	0.65(5)
O2	12b	0.391(3)	0.001(3)	0.144(3)	1	0.51(5)
O3	12b	0.450(2)	0.178(2)	0.317(3)	1	0.48(5)
N	4a	0.204(2)	0.204(2)	0.204(2)	1	0.55(6)

3.3.2.   Electrochemical characterization

Various Na₂Co₂ₓFe₂₋₂ₓ(PO₃)₃N compositions were investigated in order to evaluate the influence of cobalt substitution on electrochemical performance: 0.8 Fe – 0.2 Co; 0.5 Fe – 0.5 Co; 0.2 Fe – 0.8 Co.

As in previous tests, half-cell configuration was selected with metallic sodium or lithium as a negative electrode and LiPF₆/NaPF₆ in EC:DMC (1:1 vol) as electrolyte in 2032-type coin cells. The cathodes were prepared in analogous manner as for Na₂Fe₂(PO₃)₃N (section 3.1.2).
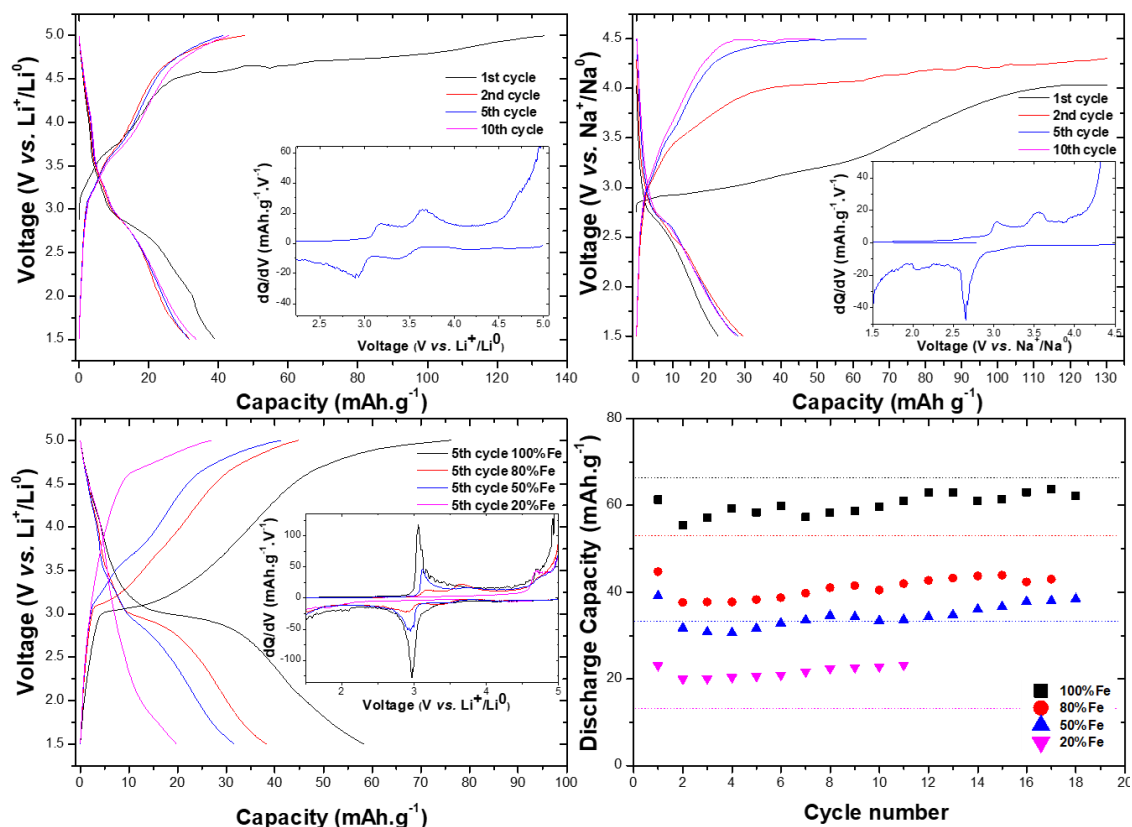
Figure 3.16: (a) galvanostatic charge-discharge curves of Na₂CoFe(PO₃)₃N cycled vs. Li at C/40 rate. In the inset derivative dQ/dV curves of Na₂CoFe(PO₃)₃N of the fifth cycle; (b) galvanostatic charge-discharge curves of Na₂CoFe(PO₃)₃N cycled vs. Na at C/40 rate. In the inset derivative dQ/dV curves of Na₂CoFe(PO₃)₃N of the fifth cycle; (c) galvanostatic charge-discharge curves of the fifth cycle of Na₂CoₓFe₂₋ₓ(PO₃)₃N cycled vs. Li where x=0, 0.2, 0.5, 0.8; together with corresponding derivative curves in the inset; (d) dependence of the amount of Fe in Na₂CoₓFe₂₋ₓ(PO₃)₃N on the discharge capacity with the expected capacity from Feᴵᴵᴵ/Feᴵᴵ as only active redox couple indicated by dashed line.

Figure 3.16 a) and b) gather the electrochemical performance of Na₂CoFe(PO₃)₃N cycled *vs.* Li and Na – the galvanostatic charge-discharge profiles together with the derivative curves of the fifth cycle. While cycling *vs.* Li (Figure 3.16 a) large irreversible capacity can be obtained in the first charge, whereas while cycling *vs.* Na, in the first and second cycle. The capacity of the subsequent discharge decreases significantly, reaching even lower values than while cycling Na₂Fe₂(PO₃)₃N. Similarly to pure Na₂Fe₂(PO₃)₃N, the capacity obtained while cycling against Na anode is lower than while cycling against Li anode, suggesting greater difficulties in the Na⁺ mobility within the framework. In the derivative dQ/dV curves (insets in Figure 3.16 a &b), there are two sets of redox peaks (3.7 V *vs.* Li⁺/Li⁰ and 3.5 V *vs.* Na⁺/Na⁰ in the charge and 3.4 V *vs.* Li⁺/Li⁰ and 2.7 V *vs.* Na⁺/Na⁰ in the discharge), which could correspond to the Coᴵᴵ/ᴵᴵᴵ redox couple, and falls very well with calculated voltage of this couple (Table 3.8), however almost no additional capacity is registered which could result from the activity of Coᴵᴵ. Further tests were performed with different stoichiometries (Na₂Co₀.₄Fe₁.₆(PO₃)₃N (0.2 Co),

147

$Na_2CoFe(PO_3)_3N$ (0.5 Co) and $Na_2Co_{1.6}Fe_{0.4}(PO_3)_3N$ (0.8 Co), as presented in Figure 3.16c &d. These results were overlapped with the results from pristine $Na_2Fe_2(PO_3)_3N$ for better comparison. Following the galvanostatic charge-discharge curves (Figure 3.16c), with increasing amount of cobalt in the structure is observed decrease of the capacity and high increase of the polarization. Following the derivative dQ/dV curves, no additional signal which could correspond to the Co^{II}/Co^{III} redox couple could be observed, and the average potential is equal to the one of $Na_2Fe_2(PO_3)_3N$, which means that the registered electrochemical activity corresponds only to the iron redox couple. Figure 3.16d shows the influence of the Co content x in $Na_2Co_{2x}Fe_{2-2x}(PO_3)_3N$ on the discharge capacity. The expected capacity from Fe^{II}/Fe^{III} as only active redox couple is indicated by dashed line. It can be observed that in the two cells with high amount of Fe and small of Co, the obtained capacity is lower than expected from only Fe^{II}/Fe^{III}. However, in the cells with 0.5 of Fe and 0.5 of Co and 0.2 Fe and 0.8 Co the registered capacity exceeds the ones only from Fe^{II}/Fe^{III} suggesting activity of Co^{II}/CoI^{II} redox couple. This eventual activity will be further explored while analyzing pure $Na_2Co_2(PO_3)_3N$ in the next section.

3.4. Cobalt nitridophosphate

As mentioned before, the first tries of the synthesis of $Na_2Co_2(PO_3)_3N$ were realized in same conditions as $Na_2Co_xFe_{2-x}(PO_3)_3N$ – solid-state ammonolysis at 650 °C. Unfortunately, an amorphous phase was obtained. Increasing the annealing temperature resulted with obtaining amorphous phase and mix of $Na_4P_2O_7$, Co_2P and CoP impurities. This finding indicates that even very small as 5% amount of Fe is essential for the stabilization of the Co phase in the reducing atmosphere. Similar observations were found for the Mn-based CUBICON structure, which also requires small addition of the foreign cation. Therefore, we explored alternative routes to produce the pure Co CUBICON compound.

3.4.1. Synthesis and structural characterization

Eventually, $Na_2Co_2(PO_3)_3N$ was synthesized adding melamine to the mixture of precursors, as used in the alternative synthesis of $Na_3V(PO_3)_3N$ (Chapter 2.2.) The use of this method resulted with successful synthesis of $Na_2Co_2(PO_3)_3N$ after adjusting the synthesis conditions. Precursors were mixed together and heated in the inert atmosphere

of Ar gas at 600 °C. Figure 3.17 presents the Rietveld refinement of the SXRD pattern, obtained from the SXRD measurement of the borosilicate capillary filled with the powder of $Na_2Co_2(PO_3)_3N$ (details in Annex) and the refined structural parameters are gathered in Table 3.11. Contribution of Co_2P as well as graphite impurities (coming from the crucible used during the synthesis), ~15% in total, are indicated in the SXRD pattern as orange and violet bars, respectively. The performed refinement confirmed that the synthesized $Na_2Co_2(PO_3)_3N$ is isostructural to previously obtained $Na_2Fe_2(PO_3)_3N$ and other CUBICON nitridophosphates. The refined cell parameter of 9.2678(2) Å remains in good agreement with the one reported by Conanec et. al. (9.26(1) Å)2[4]. Except the cell parameter, no details on the crystallographic structure could be found in the literature. Therefore, the successful synthesis of the crystalline $Na_2Co_2(PO_3)_3N$ phase in this work is worth highlighting.
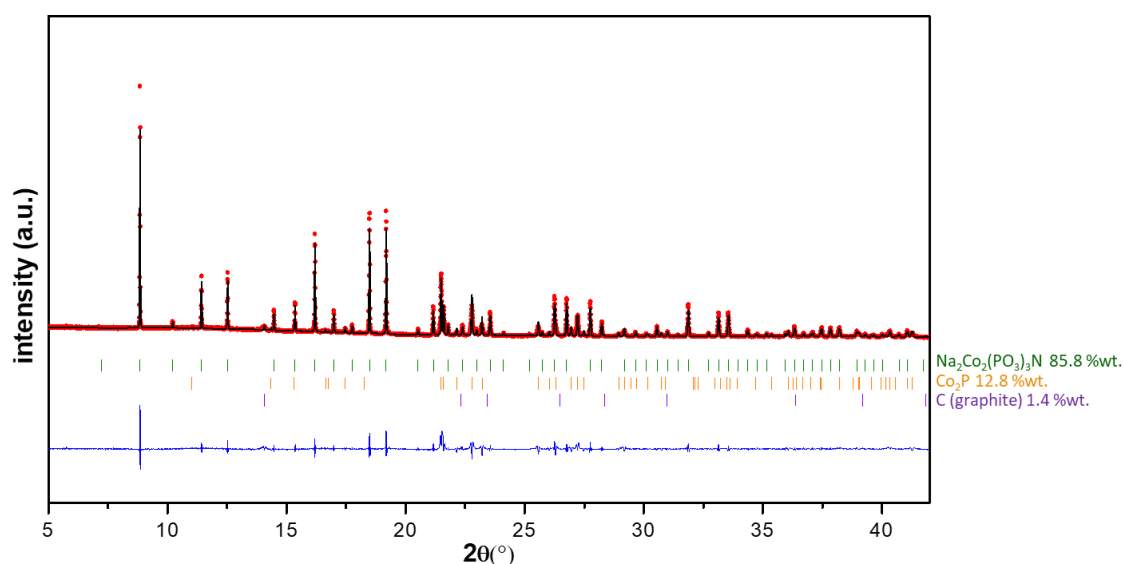
Figure 3.17: Rietveld refinement of the SXRD pattern of $Na_2Co_2(PO_3)_3N$. Black line and red circles represent the calculated and observed patterns, respectively. Bragg reflections of the $P2_13$ space group are shown as green vertical bars. Orange and violet bars denote a small contribution of Co_2P and graphite, respectively.

Table 3.11: Structural parameters of $Na_2Co_2(PO_3)_3N$ determined from the Rietveld refinement of the SXRD pattern.

S.G.: $P2_13$	$a = 9.2678(2)$Å	$V = 796.04(3)$Å^3		$R_{Bragg} = 7.51$ %	$\chi^2 = 5.13$
Atom	**Wyckoff position**	x/a	y/b	z/c	B_{iso}
P1	12b	0.343(4)	0.093(5)	0.262(5)	1.2(8)
Co1	4a	0.577(2)	0.577(2)	0.577(2)	1.1(7)
Co2	4a	0.399(3)	0.399(3)	0.399(3)	1.1(6)
Na1	4a	0.043(3)	0.043(3)	0.043(3)	1.6(9)
Na2	4a	0.789(4)	0.789(4)	0.789(4)	1.6(9)
O1	12b	0.226(9)	0.016(7)	0.868(7)	1.7(8)
O2	12b	0.401(9)	0.005(9)	0.133(6)	1.6(9)
O3	12b	0.460(8)	0.193(8)	0.322(7)	0.7(9)
N1	4a	0.205(9)	0.205(9)	0.205(9)	1.2(4)

3.4.2.   Chemical and morphological analysis

An SEM image of the powder of $Na_2Co_2(PO_3)_3N$ is shown in Figure 3.18 Non-uniform shape of the particles can be observed, very similar to other investigated nitridophophosphates. The size of the particles varies from few to 20 μm.
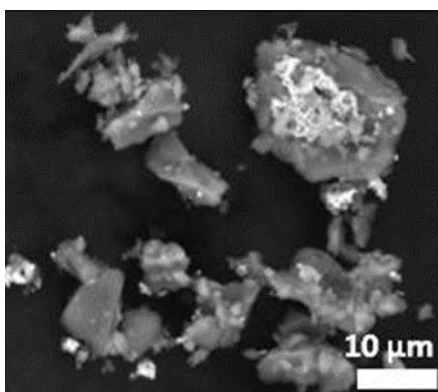
Figure 3.18: SEM image of $Na_2Co_2(PO_3)_3N$.

The atomic ratio was evaluated by EDX and ICP-AES analysis. Results from these two techniques are gathered in

Table 3.12. The obtained ratios from both techniques are in good agreement with the theoretical one.

Table 3.12 : Composition of Na₂Co₂ (PO₃)₃N determined by EDX and ICP.

Element	Theoretical content	Experimental atomic ratio determined from EDX	Experimental atomic ratio determined from ICP
Na	2	1.7±0.08	2.0±0.02
P	3	3 (fixed)	3(fixed)
Co	2	1.8±0.09	1.9±0.02

3.4.3.   Thermogravimetric analysis

The thermal stability of $Na_2Co_2(PO_3)_3N$ was evaluated by performing thermal gravimetric analysis (TGA) under both inert (Ar) and air atmosphere in the temperature range of RT-1000 °C. The TGA curves are shown in Figure 3.63.19.
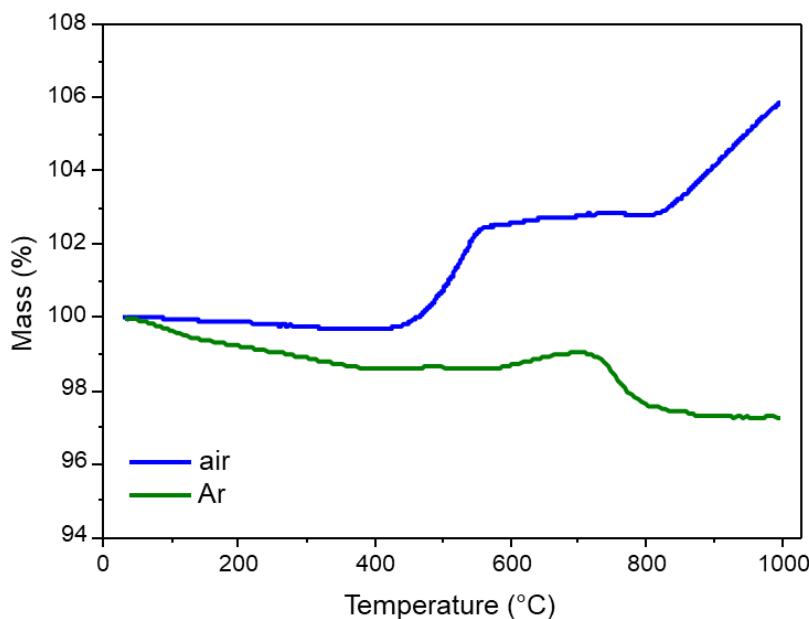
Figure 3.19: TGA curves of Na₂Co₂(PO₃)₃N under Ar (green) and air (blue) flows within the temperature range of 30–1000 °C at 10 °C.min⁻¹ heating rate.

Similar to the iron polymorph, $Na_2Co_2(PO_3)_3N$ exhibits high thermal stability in inert atmosphere up to >600 °C. Under air, $Na_2Co_2(PO_3)_3N$ decomposes above 500 °C with the onset of ~450 °C related to the mass gain upon structural oxidation accompanied with the release of nitrogen. No thermal decomposition up to 500 °C indicates good thermal stability of this material.

3.4.4.   Electrochemical characterization

Na$_2$Co$_2$(PO$_3$)$_3$N was studied in half-cell configuration following the same cathode preparation method and conditions as for Na$_2$Fe$_2$(PO$_3$)$_3$N (section 3.1.2). Attempts of cycling Na$_2$Co$_2$(PO$_3$)$_3$N *vs.* Na failed, already in the first cycle electrolyte oxidation was observed above 4.2 V vs. Na$^+$/Na and no further activity was registered (not shown). Figure 3.20 shows the galvanostatic charge-discharge profiles obtained versus Li, together with the derivative curves of the first, fifth and tenth cycles.
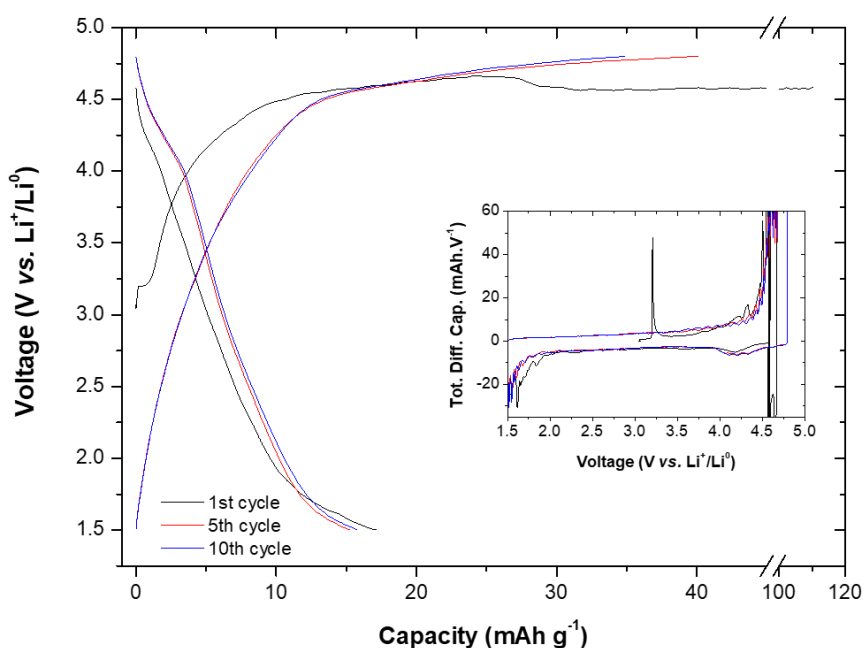
Figure 3.20: Galvanostatic charge-discharge curves of Na$_2$Co$_2$(PO$_3$)$_3$N cycled *vs.* Li at C/40 rate of the first, fifth and tenth cycles. In the inset derivative dQ/dV curves of the corresponding cycles.

While following the galvanostatic charge/discharge curve, no clear redox activity of the Co^{II}/Co^{III} couple could be detected. As in the previous cells with mixed Fe/Co ratios, large irreversible capacity could be observed in all cycles. Additionally, the shape of the curve in the high voltage region (~4.5V *vs.* Li$^+$/Li^0) suggests electrolyte oxidation. Based on the findings from the electrochemical analysis of Na$_2$Co$_{1.6}$Fe$_{0.4}$(PO$_3$)$_3$N (Figure 3.16), and DFT calculations, signal from the cobalt redox couple is expected to appear around 3.7 V *vs.* Li$^+$/Li^0 in the charge and 3.4 V *vs.* Li$^+$/Li^0 in the discharge, however in the derivative curve in the inset in Figure 3.20 no activity in this region can be observed. In the first charge, a small plateau at ~3.2 V *vs.* Li$^+$/Li^0 can be observed, however no reversible process in discharge was found. Although in the derivative curve small process at ~4.5 V *vs.* Li$^+$/Li^0 in charge and 4.2V *vs.* Li$^+$/Li^0 in the discharge can be observed, the obtained

capacity of the cell reveals almost no electrochemical activity of the Co^{II}/Co^{III} redox couple.

3.5. Mixed manganese-iron nitridophosphates

3.5.1. Synthesis and structural characterization

Pursuing the synthesis of mixed manganese/iron CUBICON nitridophosphate, we observed that at maximum one manganese per formula unit can be inserted in the framework, leading to the composition of $Na_2MnFe(PO_3)_3N$. We assumed that the insertion of higher amount of manganese is limited due to the higher ionic radius of Mn^{II} (0.83 Å *vs*. 0.78 Å of Fe^{II})[194].
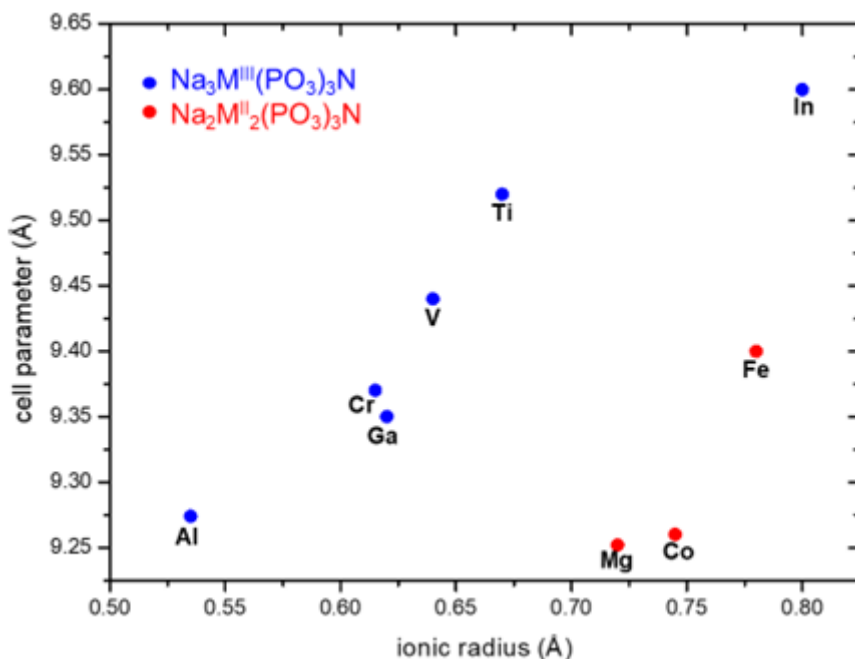
Figure 3.21: Evolution of the cell parameter of the $Na_3M^{III}(PO_3)_3N$ and $Na_2M^{II}_2(PO_3)_3N$ compositions depending on the ionic radius of the trivalent M^{III} (blue) or divalent M^{II} (red) cation. The values of the cell parameters of the CUBICON compounds for M= V, Al, Mg, Co & Fe were determined in this work, the values for the other metals are those reported by Conanec et. al.[169]

To verify this statement, we plotted the evolution of the cell parameter as a function of an ionic radius in both $Na_3M^{III}(PO_3)_3N$ and $Na_2M^{II}_2(PO_3)_3N$ compositions (Figure 3.21). It can be observed that for both compositions the cell parameter of the CUBICON structure increases with the ionic radius of the metal M. The largest reported unit cell parameter of 9.6 Å was found for $Na_3In(PO_3)_3N$ with ionic radius of 0.8 Å of In^{III}. Taking this into account, the presence of two divalent cations of manganese with even larger

radius of 0.83 Å indeed could be exceeding the framework stability. Synthesis and structural characterization.

In addition to an expected increase of the working voltage, Mn substitution composition could offer the possibility of using two Mn redox couples (MnIII/II and MnIV/III). All samples were synthesized by ammonolysis route using the same conditions as for $Na_2Fe_2(PO_3)_3N$, using MnO and FeC_2O_4 as TM precursors. Figure 3.21a shows the XRD patterns of the different $Na_2Mn_xFe_{2-x}(PO_3)_3N$ samples prepared, with x= 0, 0.2, 0.4, 0.5, 0.6, 0.8, 1, whereas Table 3.13 gathers the corresponding refined lattice parameters..
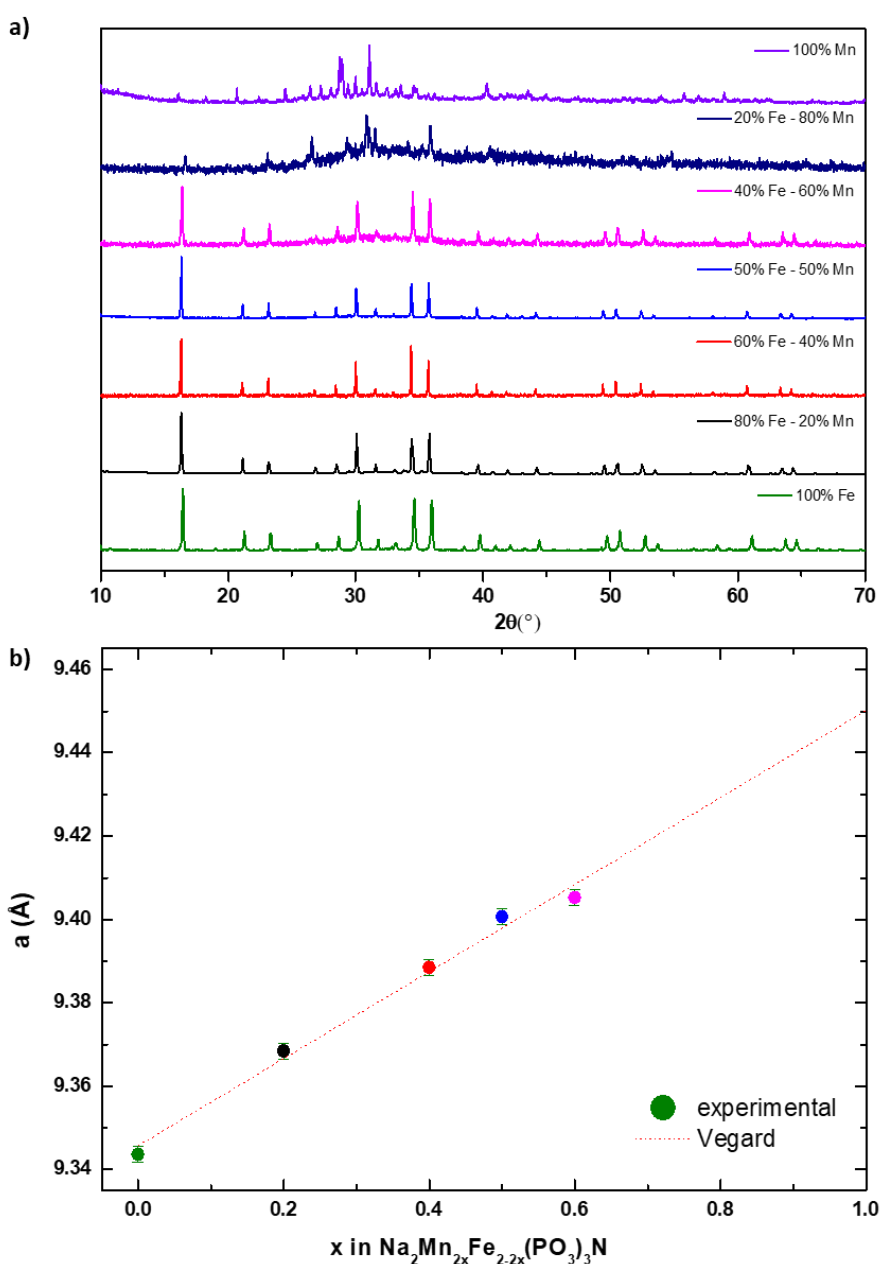
Figure 3.21: (a) Evolution of the XRD patterns with a changing content x of Mn in $Na_2Mn_{2x}Fe_{2-2x}(PO_3)_3N$; (b) Variation of the cell parameter *a* in a changing content x of Mn in $Na_2Mn_{2x}Fe_{2-2x}(PO_3)_3N$.

Table 3.13: Evolution of the refined lattice parameters of $Na_2Mn_{2x}Fe_{2-2x}(PO_3)_3N$ (x=0, 0.2, 0.4, 0.5 and 0.6).

x	composition	Lattice parameter [Å]
0	$Na_2Fe_2(PO_3)_3N$	9.344(2)
0.2	$Na_2Mn_{0.4}Fe_{1.6}(PO_3)_3N$	9.368(3)
0.4	$Na_2Mn_{0.8}Fe_{1.2}(PO_3)_3N$	9.388(2)
0.5	$Na_2MnFe(PO_3)_3N$	9.401(2)
0.6	$Na_2Mn_{1.2}Fe_{0.8}(PO_3)_3N$	9.405(3)

The increase of the cell parameters visible in the XRD patterns in Figure 3.21 as well as in Table 3.13 confirms the gradual substitution of Fe^{II} by Mn^{II}. According to these results, the substitution of Fe^{II} by Mn^{II} in $Na_2Mn_{2x}Fe_{2-2x}(PO_3)_3N$ was successful up to x=0.5. Above that value the sample became multiphasic (including Mn oxides, Mn phosphates and pyrophosphates) and the cell parameter did not increase with respect to $Na_2MnFe(PO_3)_3N$ (x=0.5). In addition, for x>0.5 the appearance of an amorphous phase can be observed, suggesting that the 1:1 Mn:Fe ratio is the maximum that can be accepted by the crystalline CUBICON phase. We presume that the larger ionic radius of Mn^{II} (0.83Å *vs.* 0.78 Å of Fe^{II})[200] prevents the stabilization of the pure CUBICON manganese nitridophosphate phase. A similar behavior was observed by Recham et al. for Na_2MnPO_4F,[119] for which the bigger radius of Mn results in creating repulsive interactions within the structure, leading to a structural transformation involving the change from a two-dimensional layered structure (Na_2FePO_4F) to a three-dimensional one for Na_2MnPO_4F.

$Na_2MnFe(PO_3)_3N$ was subjected to further analyses. Rietveld refinement of the XRD pattern of this phase is shown in Figure 3.22 and the crystallographic details obtained from the refinement are gathered in Table 3.6.
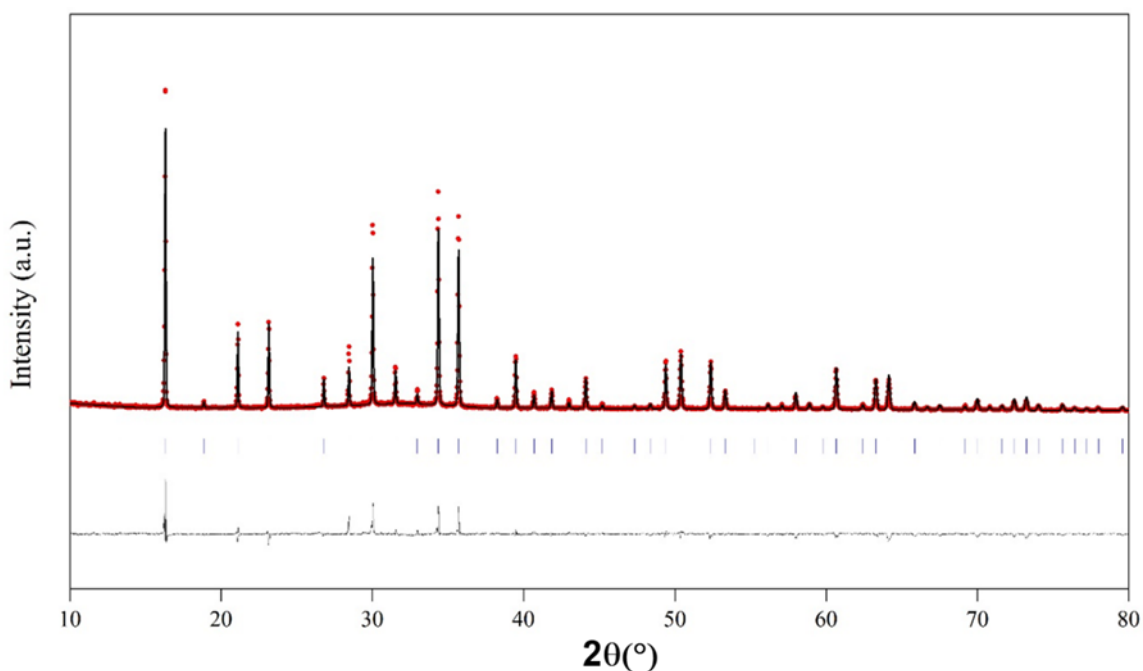
Figure 3.22: Rietveld refinement of the XRD pattern of $Na_2FeMn(PO_3)_3N$. Black line and red circles represent the calculated and observed patterns, respectively. The horizontal black line is the difference curve between the calculated and observed patterns. The Bragg reflections of the CUBICON's $P2_13$ unit cell are shown as blue vertical bars.

Table 3.14: Crystallographic data and atomic coordinates of $Na_2FeMn(PO_3)_3N$ determined from the refinement of XRD data.

S.G.: $P2_13$						
a =9.401(3) Å		V = 830.7(3) Å^3		R_{Bragg} = 8.2 %	χ^2 = 1.90	
Atom	Wyckoff position	x/a	y/b	z/c	Occupancy	B_{iso}
P	12b	0.341(3)	0.091(3)	0.258(3)	1	0.98(7)
Fe1	4a	0.581(4)	0.581(4)	0.581(4)	0.5	0.75(6)
Mn1	4a	0.581(4)	0.581(4)	0.581(4)	0.5	0.75(6)
Fe2	4a	0.398(3)	0.398(3)	0.398(3)	0.5	1.11(5)
Mn2	4a	0.398(3)	0.398(3)	0.398(3)	0.5	1.11(5)
Na1	4a	0.037(5)	0.037(5)	0.037(5)	0.98(5)	0.89(6)
Na2	4a	0.795(5)	0.795(5)	0.795(5)	1.0(5)	0.79(6)
O1	12b	0.213(4)	0.007(4)	0.876(3)	1	0.62(4)
O2	12b	0.389(2)	0.009(3)	0.134(3)	1	0.49(4)
O3	12b	0.454(2)	0.180(2)	0.314(2)	1	0.48(4)
N	4a	0.201(3)	0.201(3)	0.201(3)	1	0.45(5)

Since Fe and Mn are not possible to be distinguished by XRD, for the refinement it was assumed that Mn is occupying both Fe1 and Fe2 sites. Based on the refinement and particularly analyzing the refined atomic positions and comparing them with the ones of $Na_2Fe_2(PO_3)_3N$ (Table 3.2), it can be observed that the framework remained practically

unchanged. The ~5% increase of the volume (830.7(3) Å^3 for $Na_2FeMn(PO_3)_3N$ *vs.* 796.04(3) Å^3 for $Na_2Fe_2(PO_3)_3N$) remains in good agreement with the larger size of the ionic radius of Mn^{II} (0.83Å) than one of Fe^{II} (0.78 Å)[200]

3.5.2.　Electrochemical characterization

The stabilized $Na_2FeMn(PO_3)_3N$ was evaluated as a potential cathode material in half-cell configuration with metallic sodium and lithium as a negative electrode and $LiPF_6$or $NaPF_6$ in EC:DMC (1:1 vol) as electrolyte in 2032-type coin cells.

As for $Na_2Fe_2(PO_3)_3N$, cathodes were prepared by mixing the active material with 30% carbon (Acetylene Black) and 10% poly(vinylidene) fluoride (PVDF, Alfa Aesar) in N-methyl-2-pyrrolidone (NMP, Aldrich) and pasting the obtained slurry onto an Al foil using a doctor blade. The as-prepared laminate was then dried overnight in the vacuum oven at 120°C and punched into small disks with the mass loading of active material around 2-3x10^{-3} g/cm^2. The prepared cells were studied by cycling in galvanostatic mode at a rate of one electron exchange in 40 hours (C/40 rate) for 50 cycles; between 1.5 and 4.5 V vs Na$^+$/Na and 1.5 and 5.0 V vs Li$^+$/Li using a MACCOR battery tester. All electrochemical measurements were performed at room temperature.

Figure 3.23 shows the galvanostatic charge-discharge profiles of $Na_2FeMn(PO_3)_3N$ cycled *vs.* Li and Na anodes together with the derivative curves of the first and fifth cycles.
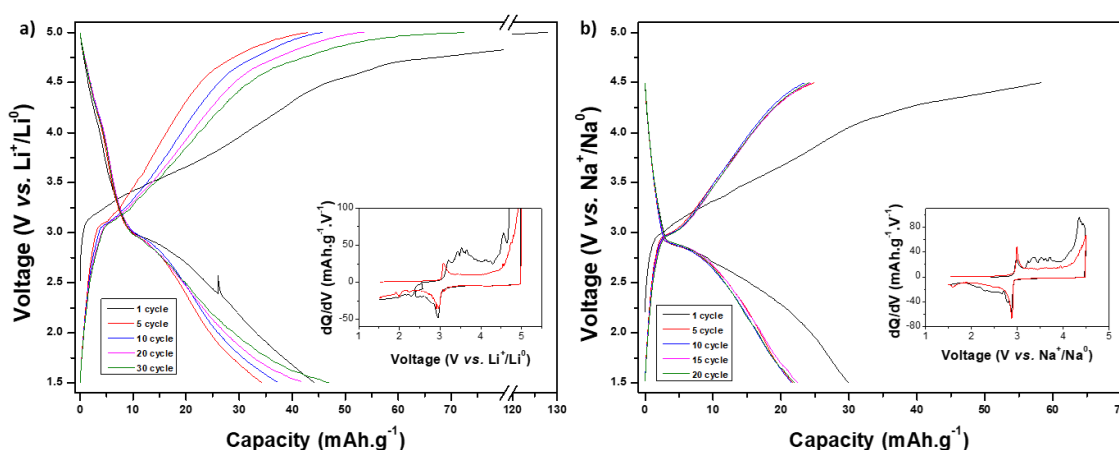
Figure 3.23: (a&b) Voltage-capacity profile of Na$_2$FeMn(PO$_3$)$_3$N against (a) Li$^+$/Li^0 and (b) Na$^+$/Na^0 metal at C/40 rate; in the insets corresponding derivative dQ/dV curves of the first and fifth cycles.

Based on the obtained capacity values from the galvanostatic curves, substitution of Fe by Mn did not result in any improvement in the electrochemical performance of this

material. On the contrary, the obtained capacity was lower than that of the pure iron nitridophosphate (~40 mAh.g^{-1} *vs.* theoretical 65.5 mAh.g^{-1} for the removal of one Na$^+$).

Following the derivative dQ/dV curves, no additional signal which could correspond to the Mn^{II}/Mn^{III} redox couple could be observed, and the average potential is almost identical to the one of Na$_2$Fe$_2$(PO$_3$)$_3$N, which means that the registered electrochemical activity corresponds only to the iron redox couple. Similarly to pure Na$_2$Fe$_2$(PO$_3$)$_3$N, the capacity obtained while cycling against Na anode is lower than while cycling against Li anode, suggesting greater difficulties in the Na$^+$ mobility within the framework. The working voltage of the Fe^{II}/Fe^{III} redox couple is centered at 3.05 V *vs.* Li$^+$/Li^0 and 2.95 V *vs.* Na$^+$/Na^0, slightly higher than pure Na$_2$Fe$_2$(PO$_3$)$_3$N due to the high polarization.

This behavior has already been observed in the literature for other polyanionic compounds such as Na$_2$Fe$_{1-x}$Mn$_x$PO$_4$F, for which the electrochemical performance of the Mn-based phase was worse than for the Fe-based phase.[119] The origin could be found in the poorer electronic conductivity arising from the higher ionicity of the Mn-O bond as well as the distortions caused by the strong Jahn-Teller effect on Mn^{III}.

3.6. Manganese-based nitridophosphates

Our efforts to prepare Na$_2$Fe$_{1-x}$Mn$_x$PO$_4$F (x>1) initially failed. The group of Khalifah, who has recently published several CUBICON nitridophosphate compositions for battery applications, also failed to synthesize Na$_2$Mn$_2$(PO$_3$)$_3$N and identified Na$_3$Mn(PO$_3$)$_3$N as an amorphous phase;[168] but sodium-based CUBICON nitridophosphates were mentioned by Conanec et. al.[24] However, only the cell parameter was given (a = 9.33(1) Å for Na$_2$Mn$_2$(PO$_3$)$_3$N and a = 9.35(1) Å for Na$_3$Mn(PO$_3$)$_3$N).[162] In this section our attempts to prepare Na$_3$Mn(PO$_3$)$_3$N will be described.

3.6.1.   Synthesis and structural characterization

The solid-state ammonolysis route was again selected using powders of NaPO$_3$ and Mn$_2$O$_3$ in a stoichiometric ratio as precursors under reducing atmosphere of NH$_3$. Na$_3$Mn(PO$_3$)$_3$N and Na$_2$Mn$_2$(PO$_3$)$_3$N are expected to form according to the following reactions:

$$3NaPO_3 + MnO_2 \xrightarrow{\quad T,\ NH_3 \quad} Na_3Mn(PO_3)_3N \qquad\qquad \text{(a)}$$

$$2NaPO_3 + Mn_2O_3 + NH_4H_2PO_4 \xrightarrow{T, \ NH_3} Na_2Mn_2(PO_3)_3N \qquad (b)$$
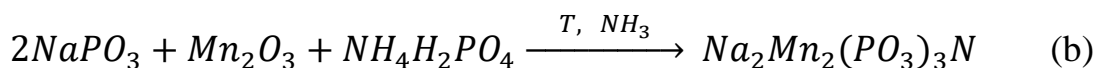
as a first target. Two types of crucibles – alumina and graphite, were used for the annealing step. Figure 3.24 shows the obtained XRD patterns of both synthesized powders.
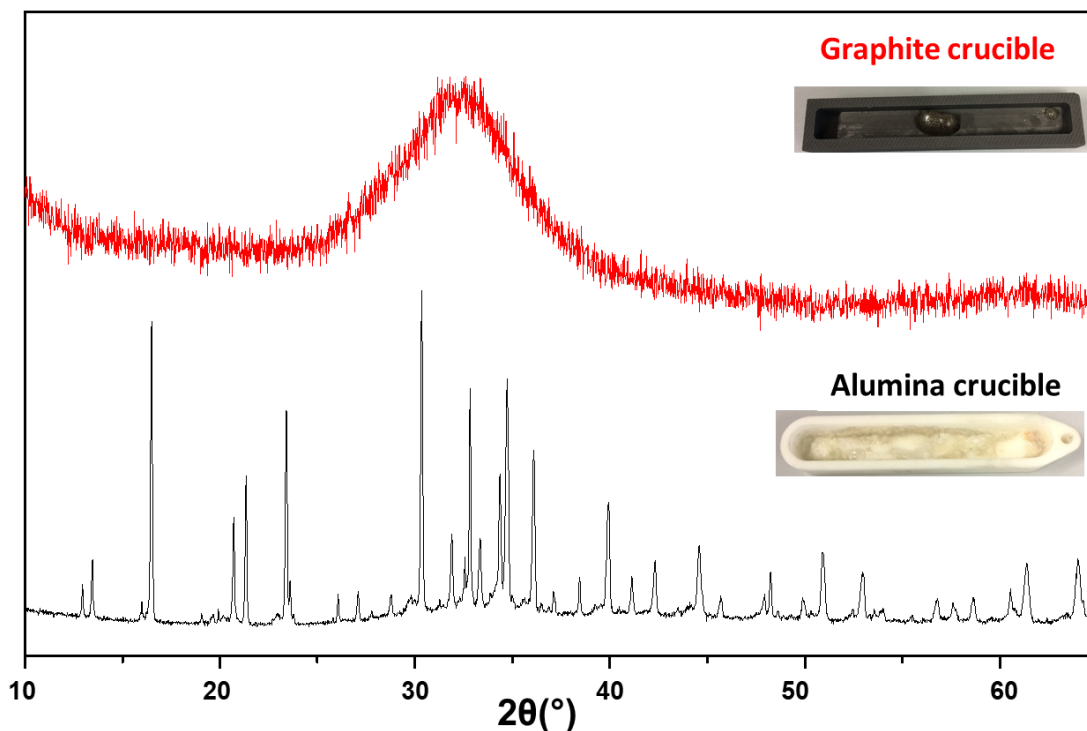
Figure 3.24: XRD patterns of the samples obtained targeting the Na₃Mn(PO₃)₃N phase by ammonolysis using alumina and graphite crucibles, as indicated in the figure.

The white powder of the targeted $Na_3Mn(PO_3)_3N$ composition (black curve in Figure 3.24) obtained using the alumina crucible was found to exhibit the CUBICON structure, however highly contaminated with different Mn and Al oxides. The presence of aluminum oxides was explained using the alumina crucible for the synthesis. On the other hand, an amorphous phase was obtained from the synthesis performed using the graphite crucible (red curve Figure 3.24).

Since the only difference between both syntheses was the crucible material, we suspected that the stabilization of the crystalline CUBICON Mn phase might not be possible unless a foreign cation such as Al^{III} is introduced in the structure. To validate this hypothesis, $Na_3Mn_xAl_{1-x}(PO_3)_3N$ was prepared with different Mn:Al ratios in carbon crucibles to investigate the necessary amount of Al to stabilize the CUBICON structure. Since the synthesis of $Na_3Al(PO_3)_3N$ can be found in the literature,[24] the same conditions

159

(ammonolysis at (800 °C with Al_2O_3 as Al precursor) were applied and pure phase was obtained.

Figure 3.25 gathers the collected XRD patterns from the obtained powders of the $Na_3Mn_xAl_{1-x}(PO_3)_3N$ series ($0 \leq x \leq 2$). As seen in the XRD patterns from the high background between 25° and 40°, the contribution of the amorphous part is larger with increasing amount of manganese. In addition, no changes in the position of the peaks of the CUBICON phase were observed indicating no change in the cell parameters. The results also indicate that already 10% of Al is enough to stabilize the CUBICON phase, however with a high contribution of the amorphous phase. On the contrary, a pure $Na_3Al(PO_3)_3N$ phase is obtained with the cell parameter of 9.294(2) Å, slightly higher than the reported one (9.274(1) Å).[24]
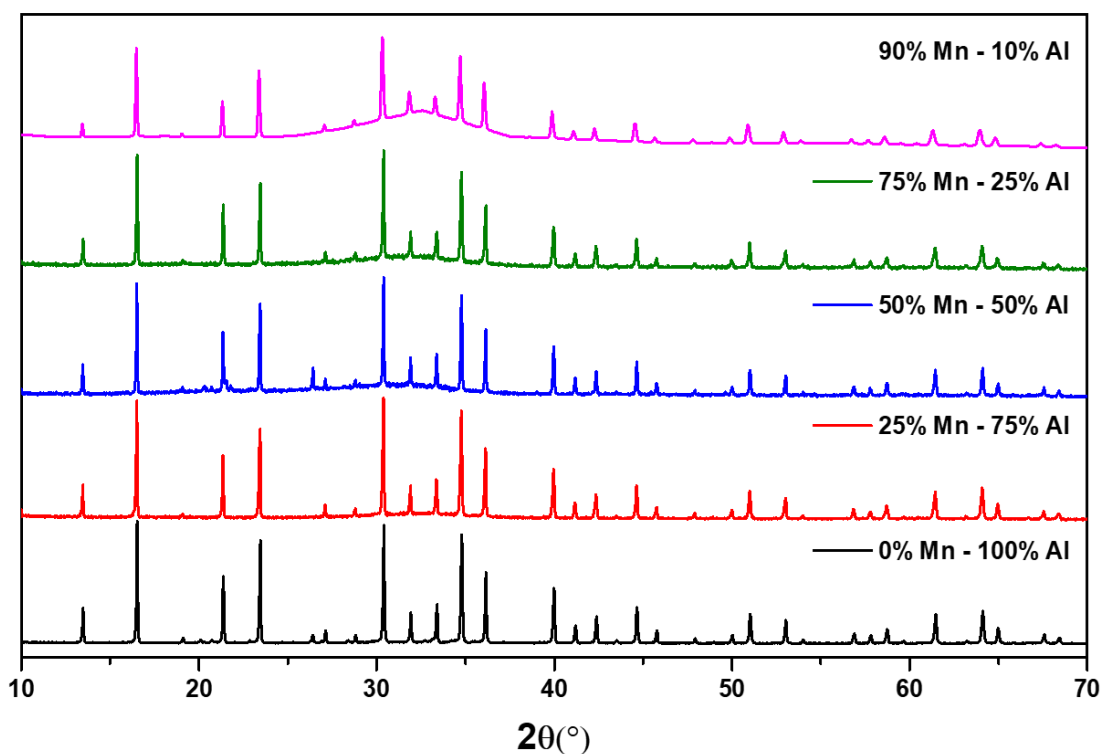
Figure 3.25: XRD pattern of series of the targeted $Na_3Mn_xAl_{1-x}(PO_3)_3N$ syntheses. The targeted Mn:Al ratios are indicated in the curves.

Eventual changes in the lattice resulting from the difference of the ionic radius of Mn^{III} vs. Al^{III} (0.645 Å vs. 0.535 Å)[52] were evaluated by performing the Rietveld refinement of the obtained XRD patterns (see Table 3.15 for a summary of cell parameter evolution with increasing Al content). Only a slight increase in the cell parameter occurs from $Na_3Al(PO_3)_3N$ to $Na_3Mn_{0.9}Al_{0.1}(PO_3)_3N$, which might indicate that very litthe Mn is incorporated in the structure.

160

Table 3.15: Evolution of the lattice parameters of the crystalline phase with the changing composition in targeted Na$_3$Mn$_x$Al$_{1-x}$(PO$_3$)$_3$N

Targeted composition	Lattice parameter [Å]
Na$_3$Mn$_{0.9}$Al$_{0.1}$(PO$_3$)$_3$N	9.313(4)
Na$_3$Mn$_{0.8}$Al$_{0.2}$(PO$_3$)$_3$N	9.312(2)
Na$_3$Mn$_{0.75}$Al$_{0.25}$(PO$_3$)$_3$N	9.301(1)
Na$_3$Mn$_{0.5}$Al$_{0.5}$(PO$_3$)$_3$N	9.308(3)
Na$_3$Mn$_{0.25}$Al$_{0.75}$(PO$_3$)$_3$N	9.293(3)
Na$_3$Al(PO$_3$)$_3$N	9.294(2)

The structure of targeted composition of Na$_3$Mn$_{0.75}$Al$_{0.25}$(PO$_3$)$_3$N was evaluated by neutron powder diffraction performed on the ECHIDNA high-resolution diffractometer at ANSTO facilities (Australia) (details can be found in the Annex). The NPD pattern (Figure 3.26) was acquired using a wavelength of $\lambda = 1.622$ Å in the 2θ range $4 \leq 2\theta \leq 164°$ with a step size of 0.05°.
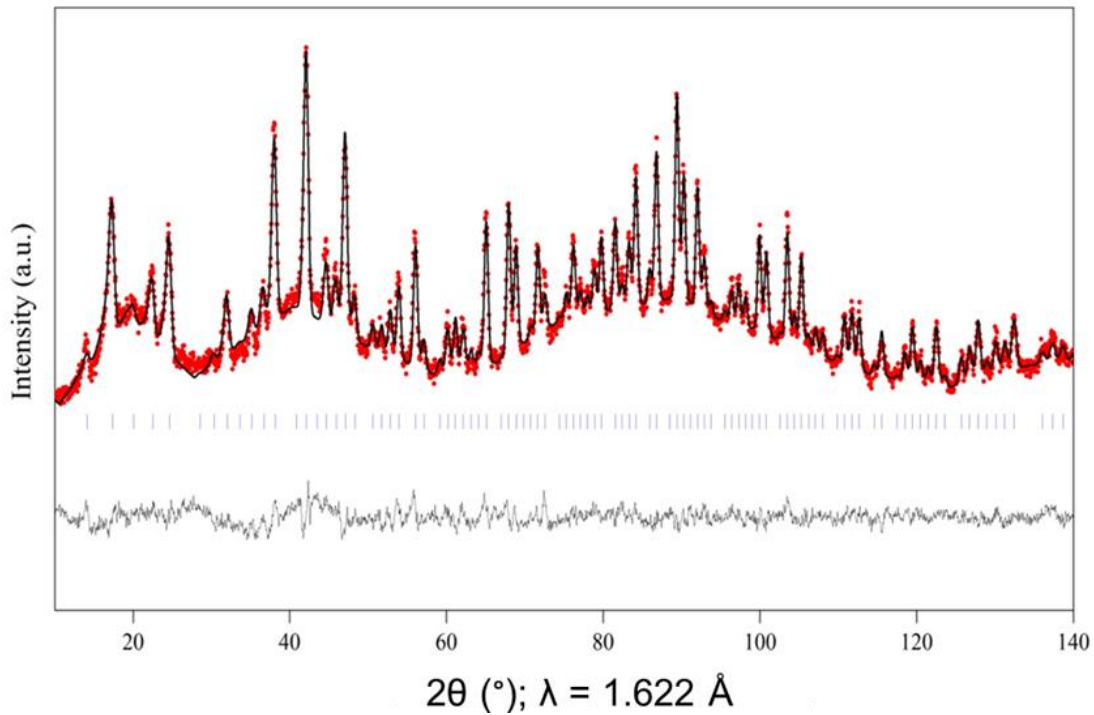
Figure 3.26: Rietveld refinement of the NPD pattern of Na$_{2.61}$Mn$_{0.37}$Al$_{0.6}$(PO$_3$)$_3$N. Red circles, black vertical and black horizontal lines represent the observed, calculated and difference patterns, respectively. The positions of the Bragg reflections of the *P*2$_1$3 space group are shown as blue vertical bars.

Table 3.16: Structural parameters of $Na_{2.61}Mn_{0.37}Al_{0.6}(PO_3)_3N$ determined from the Rietveld refinement of the NPD pattern.

S.G.: $P2_13$	$a = 9.289(5)$Å		$V = 803.3(3)$Å^3		$R_{Bragg} = 9.62\%$	$\chi^2 = 2.07$
Atom	**Wyckoff position**	**x/a**	**y/b**	**z/c**	**Occupancy**	**B_{iso}**
P1	12*b*	0.325(4)	0.080(4)	0.2410(3)	1	0.6(4)
Mn	4*a*	0.653(5)	0.653(5)	0.653(5)	0.123(3)	0.9(7)
Al	4*a*	0.653(5)	0.653(5)	0.653(5)	0.201(2)	0.9(7)
Na1	4*a*	0.017(6)	0.017(6)	0.017(6)	0.328(5)	0.1(6)
Na2	4*a*	0.402(2)	0.402(2)	0.402(2)	0.215(5)	1.5(8)
Na3	4*a*	0.807(2)	0.807(2)	0.807(2)	0.327(3)	1.1(7)
O1	12*b*	0.262(3)	-0.030(2)	0.349(4)	1	1.3(9)
O2	12*b*	0.369(3)	0.002(5)	0.100(3)	1	1.1(8)
O3	12*b*	0.449(3)	0.159(4)	0.310(5)	1	1.4(9)
N1	4*a*	0.193(1)	0.193(1)	0193(1)	0.33333	0.1(7)

The Rietveld refinement of the obtained NPD pattern (Figure 3.26 and Table 3.16) indicates that the phase can be well indexed with the $P2_13$ space group with lattice parameter of 9.289(5) Å, being slightly lower than the one obtained from the refinement of the XRD pattern (9.301(1) Å). The refined occupancies suggest the presence of Mn within the structure, however much less than the targeted value. In addition. refinement of the occupancies of Na atoms indicates vacancies in the Na2 site. Attempts of introducing partial substitution of Na by Mn or Al on this site were unsuccessful. Based on the performed refinement, the obtained powder has a composition of $Na_{2.61}Mn_{0.37}Al_{0.6}(PO_3)_3N$. As the scattering length of oxygen and nitrogen atoms can be easily distinguished by neutron diffraction, it was confirmed that the nitrogen atom is located in the vertex of the $(PO_3)_3N$ unit. Based on these results and following the changes in the XRD patterns in Figure 3.25 with the increasing amount of the manganese, it is presumed that the major part of the manganese is present in the amorphous phase, which is responsible for the high background observed in the NPD pattern.

3.6.2. Morphological and chemical analysis

3.6.2.1. SEM and TEM analysis

Electron microscopy study was performed to analyze the morphology of obtained powders. SEM images of two selected compositions – the amorphous sample with $Na_3Mn(PO_3)_3N$ targeted composition from the graphite crucible and

$Na_{2.61}Mn_{0.37}Al_{0.6}(PO_3)_3N$ (sample with targeted ratio Mn:Al 75:25); are shown in Figure 3.27.
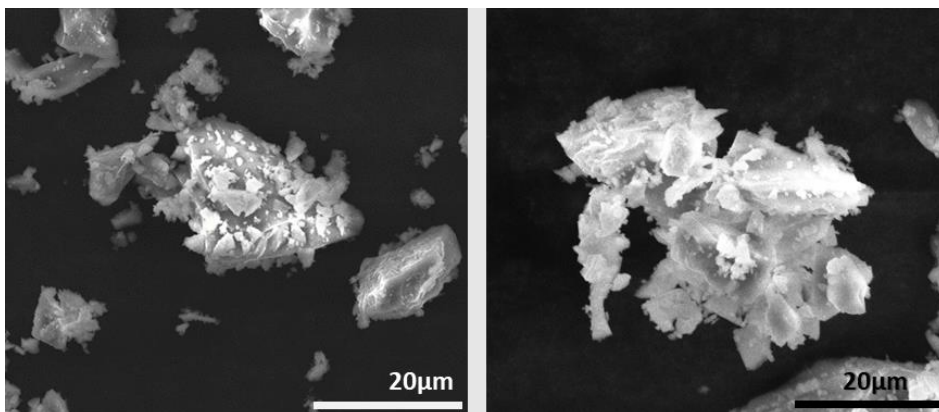
Figure 3.27: SEM images of (a) amorphous of targeted composition of $Na_3Mn(PO_3)_3N$ and (b) $Na_{2.61}Mn_{0.37}Al_{0.6}(PO_3)_3N$.

No significant changes between these samples can be observed. In both cases, the small particles have a tendency to pile into large agglomerates. Both samples exhibit particles of a non-uniform shape and a wide particle size distribution, varying from 5 µm to 40 µm.

TEM analysis was performed to explore the chemical differences between the crystalline and the amorphous phase. Figure 3.28 shows an example of crystalline and amorphous particles, identified according to their electron diffraction patterns. The electron diffraction patterns of the crystalline particles confirmed the $P2_13$ space group.
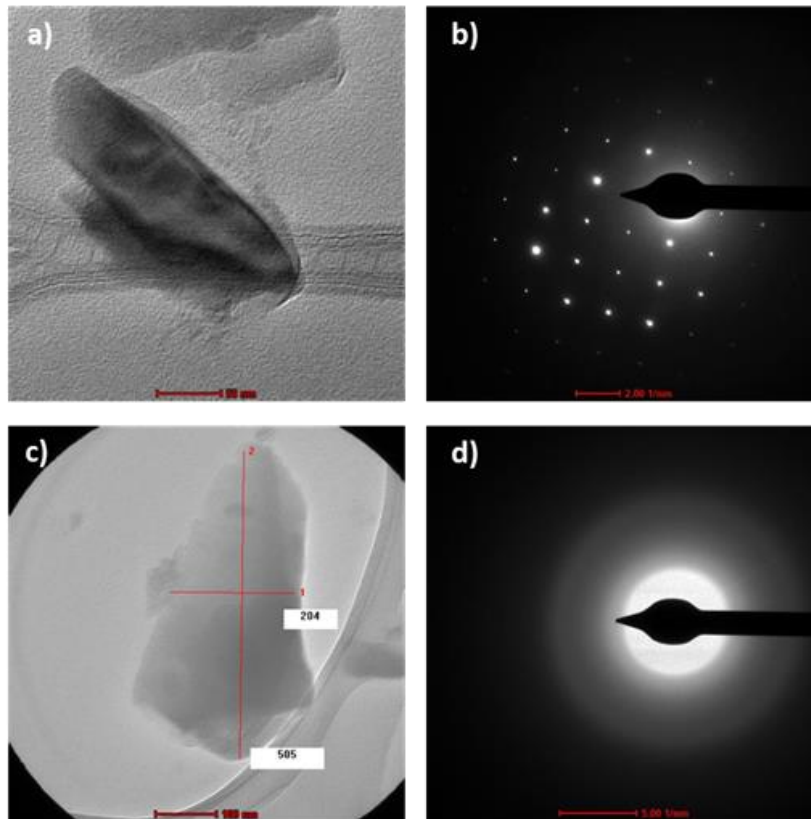
Figure 3.28: a&c – TEM images of particles of $Na_{2.61}Mn_{0.37}Al_{0.6}(PO_3)_3N$ together with b&d – acquired electron diffraction patterns revealing their crystalline and amorphous character, respectively.

Next, energy-dispersive X-ray spectroscopy (EDX) technique was employed to analyze the element distributions in the two different types of the particles. Table 3.17 shows the average experimental atomic ratio determined from the measurements performed on ten different particles, both amorphous and crystalline.

Table 3.17: Composition of $Na_{2.61}Mn_{0.37}Al_{0.6}(PO_3)_3N$ determined by EDX.

Element	Theoretical atomic ratio	Experimental atomic ratio determined from EDX – crystalline particles	Experimental atomic ratio determined from EDX – amorphous particles
N	1	1.01±0.05	1.72±0.09
Na	3	2.21±0.1	1.96±0.1
P	3	3.00 (fixed)	3.00 (fixed)
Mn	1	0.24±0.06	0.72±0.09
Al	x	0.88±0.04	0.44±0.02

The results indicate that the crystalline particles possess less manganese, and almost double amount of aluminum than the amorphous ones. The obtained amount of sodium was found to be lower than expected and obtained from the refinements of the NPD pattern and is expected to result from the observed evolution of the particle under the beam (disappearance of the diffraction pattern).

3.6.2.2. X-ray Absorption Spectroscopy

XAS analysis was performed to validate the oxidation state of manganese in obtained $Na_{2.61}Mn_{0.37}Al_{0.6}(PO_3)_3N$. Figure 3.30 shows the XAS Mn $L_{2,3}$-edge spectra together with the simulated spectra of Mn^{III} and Mn^{II}.
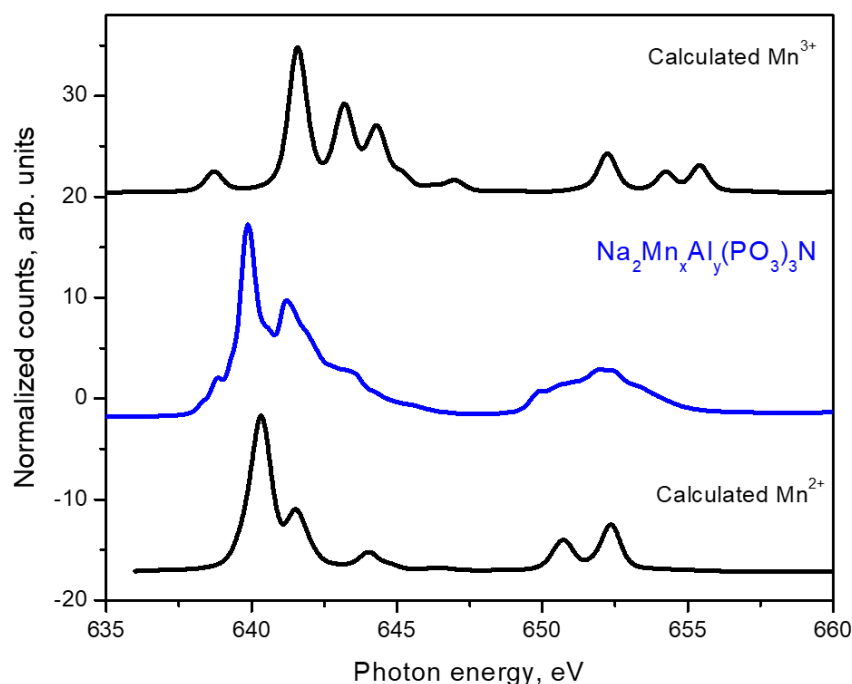
Figure 3.30: XAS Mn $L_{2,3}$-edge spectra in $Na_{2.61}Mn_{0.37}Al_{0.6}(PO_3)_3N$. Signals from electron detection mode (EY) corresponding to the surface are denoted in blue color. Black curves correspond to the calculated XAS Mn $L_{2,3}$-edge spectra with Oh coordination symmetry for Mn^{II} and Mn^{III}.

XAS data was collected using the total electron yield mode, corresponding to the chemical state of the surface layer of the material (probing depth of around 2-5 nm). [167] As a reference, the spectra for both Mn^{II} and Mn^{III} were computed with Oh coordination symmetry with the program CTM4XAS. [166,216] The features in the experimental Mn $L_{2,3}$-edge match very well the computed spectra for Mn^{II}

Based on these results, it can be concluded that the stabilization of Mn^{III} is difficult in reducing atmosphere, and the reduction of MnO_2 or Mn_2O_3 directly into Mn^{II} is favored. However, it has not been possible to obtain pure $Na_2Mn_2(PO_3)_3N$. In fact, Mn was only found in crystalline CUBICON when stabilized with other metal such as Al or Fe, as shown before. Considering the high amount of aluminum in the composition, which is electrochemically inactive, very poor electrochemical performance of the synthesized compounds is expected and the initial tests confirmed this assumption (not shown).

3.7. Conclusions

In this chapter, different CUBICON nitridophosphate compositions were investigated focusing on low cost and earth abundant 3d metals such as iron and manganese. Additionally, cobalt also was investigated in search from a more elevated working voltage.

 $Na_2Fe_2(PO_3)_3N$ offers a stable capacity of 60 mAh.g^{-1} corresponding to the reversible mobility of one alkali ion per f.u. *vs.* Li in hybrid-ion configuration with average voltage of 3 V *vs.* Li$^+$/Li^0, indicating improved performances from the ones reported so far (capacities of ~40 mAh.g^{-1} and high polarization)..[18] The lack of the reported results *vs.* Na metal suggested unsuccessful extraction/insertion of Na$^+$ ions within the framework, however here we demonstrated the stable, although limited mobility of ~0.55 Na$^+$ ions at 2.9 V *vs.* Na$^+$/Na^0 while cycling $Na_2Fe_2(PO_3)_3N$ *vs.* Na metal Analysis of the operando synchrotron XRD measurement suggests biphasic mechanism of Na insertion/extraction with the presence of both Na-rich and Na-poor phases. Attempts of chemically oxidize $Na_2Fe_2(PO_3)_3N$ with a strong oxidizing agent such as NO_2BF_4 resulted with the complete removal of one sodium from the cubic framework. The removal of the second Na$^+$ ion upon chemical oxidation was not achieved, suggesting a very high stability of the oxidized $NaFe_2(PO_3)_3N$ phase requiring very high additional energy to transform into less favorable desodiated $Fe_2(PO_3)_3N$ state.

In the next step, various solid solutions of $Na_2Mn_{2x}Fe_{2-2x}(PO_3)_3N$ and $Na_2Co_{2x}Fe_{2-2x}(PO_3)_3N$ were prepared, in perspective to improve the electrochemical performance by partial substitution of Fe by Mn and Co. The solid solution of $Na_2Co_{2x}Fe_{2-2x}(PO_3)_3N$ was explored by ammonolysis, stabilizing crystalline phases up to 95% of Co and 5% Fe. $Na_2Co_2(PO_3)_3N$ was succesfully synthesized for the first time by changing the synthesis method and using melamine as a source of nitrogen. The initial electrochemical tests did not reveal any electrochemical activity of the $Co^{II/III}$ redox couple.

On the other hand, due to the size difference, it was possible to exchange one Fe for one Mn and stabilize the $Na_2MnFe(PO_3)_3N$ structure. Unfortunately, electrochemical analysis resulted with no activity of the Mn^{II}/Mn^{III} redox couple. Attempts to prepare $Na_3Mn(PO_3)_3N$ were unsuccessful andonly with the presence of a foreign atom such as Al^{III} or Fe^{II} it is possible to introduce small amount of Mn into the CUBICON structure of $Na_3MFe(PO_3)_3N$.

Chapter 4 - A new family of manganese nitridophosphates, $AMn_3P_3O_8N_2$ (A = Li, Na)

Outline

Chapter 4 - A new family of manganese nitridophosphates, $AMn_3P_3O_8N_2$ (A = Li, Na)

4.1. Introduction

As concluded from the previous chapter, the synthesis of CUBICON manganese nitridophosphate could not be achieved, but the stabilization of this cubic structure requires the presence of an additional metal (such as Fe or Al, as demonstrated) and the maximum amount of Mn introduced in the structure was 0.5. Additionally, the highly reductive character of the ammonia flow used to stabilize the CUBICON structure favors the reduction of the manganese oxide precursors directly into Mn^{II}. For this reason, pursuing our effort towards the stabilization of a pure manganese nitridophosphate, we decided to explore the solubility limit of Mn into $Na_2Mn_{2x}Mg_{2-2x}(PO_3)_3N$. The pure magnesium CUBICON compound $Na_2Mg_2(PO_3)_3N$[17] was indeed reported to be stabilized after a longer annealing at higher temperature (850 °C) as compared to the other CUBICON compounds studied in the previous chapters (700-800 °C). By gradually increasing the amount of manganese in $Na_2Mn_{2x}Mg_{2-2x}(PO_3)_3N$ we observed that, instead of the appearance of amorphous phase as previously observed for the other mixed compositions (MnAl and MnFe), a new phase was obtained.

In this chapter we will describe a new family of manganese nitridophosphates with the general formula of $AMn_3P_3O_8N_2$ (A = Li, Na). As it is an entirely new structure, the detailed structural analysis based on combined synchrotron and neutron diffraction study will be presented. The DFT calculations, performed to validate the proposed structure, will be also shown. Next, the exhaustive physical-chemical analysis will be described to fully characterize this new family. In the first part the sodium polymorph, $NaMn_3P_3O_8N_2$, will be described. The second part will be dedicated to the lithium-based polymorph, being the first lithium-based nitrogen-based polyanionic compound synthesized directly, and not via ion-exchange route like other known compounds.[18,50,66]

4.2. NaMn$_3$P$_3$O$_8$N$_2$

4.2.1. Synthesis, structural analysis and chemical composition study

As described in the introduction, we first explored the incorporation of Mn into Na$_2$Mn$_{2x}$Mg$_{2-2x}$(PO$_3$)$_3$N, following the synthesis protocol reported for Na$_2$Mg$_2$(PO$_3$)$_3$N.[159] To do so, NaPO$_3$, MnO and NH$_4$H$_2$PO$_4$ precursors were first ball milled in stoichiometric amounts for 20 min under air in order to obtain a homogeneous mixture. Next, the powder was placed into a graphite crucible and heated up to 800 °C for 12 hours under a constant flow of anhydrous ammonia (30 mL.min^{-1}). The recovered light grey powders were grinded manually in the mortar and subjected to the XRD analysis.

Figure 4.1 shows the XRD patterns obtained for the samples with various Mg:Mn ratios (100:0, 50:50, 25:75, 0:100). The synthesis of the pure-magnesium CUBICON compound Na$_2$Mg$_2$(PO$_3$)$_3$N was successfully reproduced (black pattern). The LeBail refinement of this XRD pattern leads to a refined CUBICON cell parameter of a = 9.243(4) Å, in agreement with the literature (9.252(1) Å)[24].
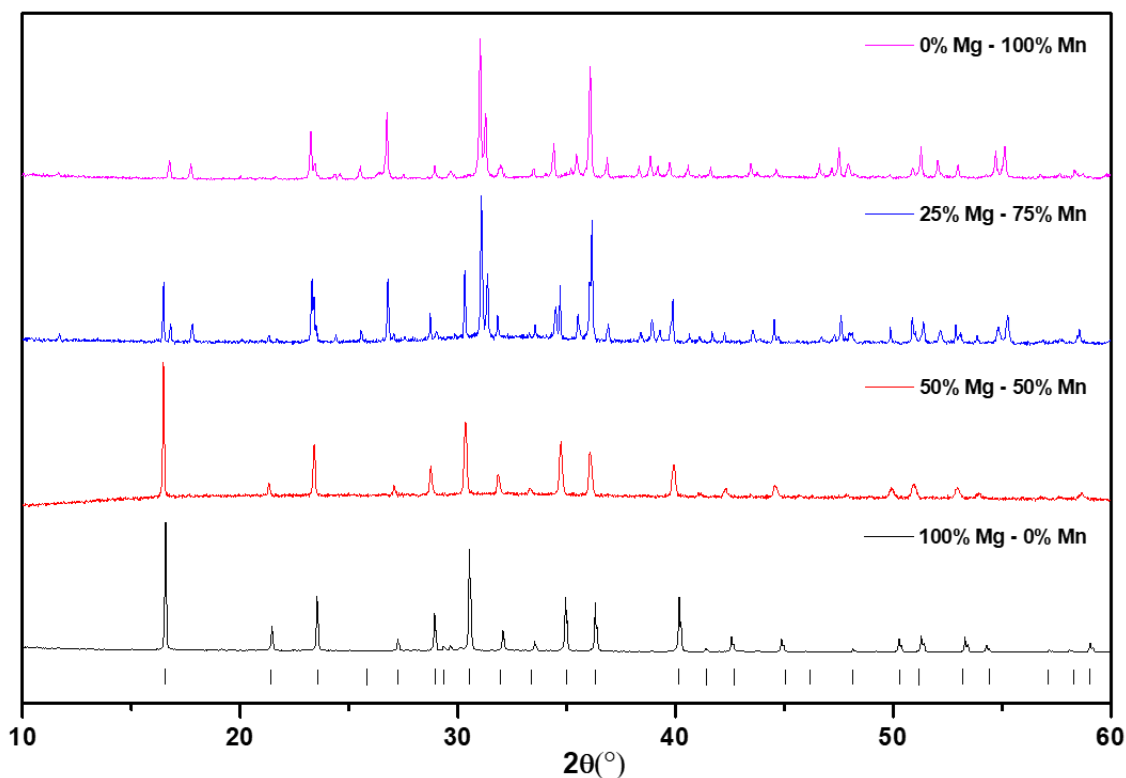
Figure 4.1: XRD patterns of the series of the Na$_2$Mn$_{2x}$Mg$_{2-x}$(PO$_3$)$_3$N samples. The targeted Mg:Mn ratios are indicated next to the curves. Vertical black lines indicate the position of the Bragg reflections of the Na$_2$Mg$_2$(PO$_3$)$_3$N phase.

The XRD pattern of the $Na_2MgMn(PO_3)_3N$ sample, corresponding to a Mg:Mn ratio of 50:50 (red curve in Figure 4.2), can also be well indexed as the CUBICON phase. The larger lattice parameter of 9.308(2) Å (Table 4.1) confirms partial substitution of Mg^{II} by larger Mn^{II} (0.72 Å and 0.83 Å, respectively)[52]. However, conversely to the trials of substitution of aluminum or iron by manganese in the CUBICON structure for which an amorphous phase appeared, new diffraction peaks were observed in addition to the CUBICON phase at higher a Mg:Mn ratio of 25:75 (blue curve in Figure 4.1). The refinement of the CUBICON phase in the sample enabled to determine a lattice parameter of 9.319(3) Å. Assuming that the system verifies a Vegard's law, this indicates that the maximum Mn content accommodated by the CUBICON would be 58% (Figure 4.2.).
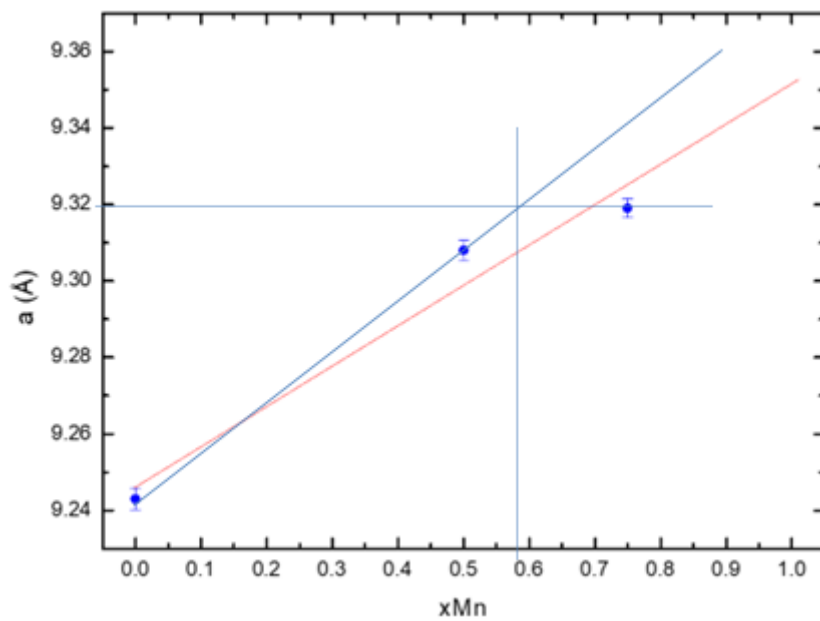
Figure 4.2: Variation of the cell parameter a as a function of the Mn content x in Na2Mn2xMg2-2x(PO3)3N. The red line shows the expected evolution in the hypothesis that Vegard's law applies to the system.

Table 4.1: Evolution of the lattice parameter of the CUBICON structure as a function of the Mn content x in $Na_2Mn_{2x}Mg_{2-x}(PO_3)_3N$.

composition	Lattice parameter [Å]
$Na_2Mg_2(PO_3)_3N$	9.243(4)
$Na_2MnMg(PO_3)_3N$	9.308(2)
$Na_2Mn_{1.5}Mg_{0.5}(PO_3)_3N$	9.319(3)

The XRD pattern of the sample with 100% of manganese does not exhibit the CUBICON peaks anymore, and instead all reflections correspond to the secondary phase obtained for a 75:25 ratio. This pattern (pink curve in Figure 4.1) could not be identified with the indexation programs (DIFFRAC.EVA[217], HighScore[218]) as of any known structure, and

therefore it was concluded that a new material had been isolated. In order to solve the structure, we first indexed the diffraction peaks using the DICVOL[219,220] program implemented in the FullProf Suite program.[221,222] The obtained orthorhombic cell with lattice parameters a = 4.8835(1) Å, b = 10.6008(2) Å, c = 15.1888(2) Å and a unit cell volume of V = 786.307(12) Å^3 accommodates four formula units per unit cell. Next, the three-dimensional elementary cell was constructed exploring different possible space groups using direct methods with the EXPO2014 software[223–225].
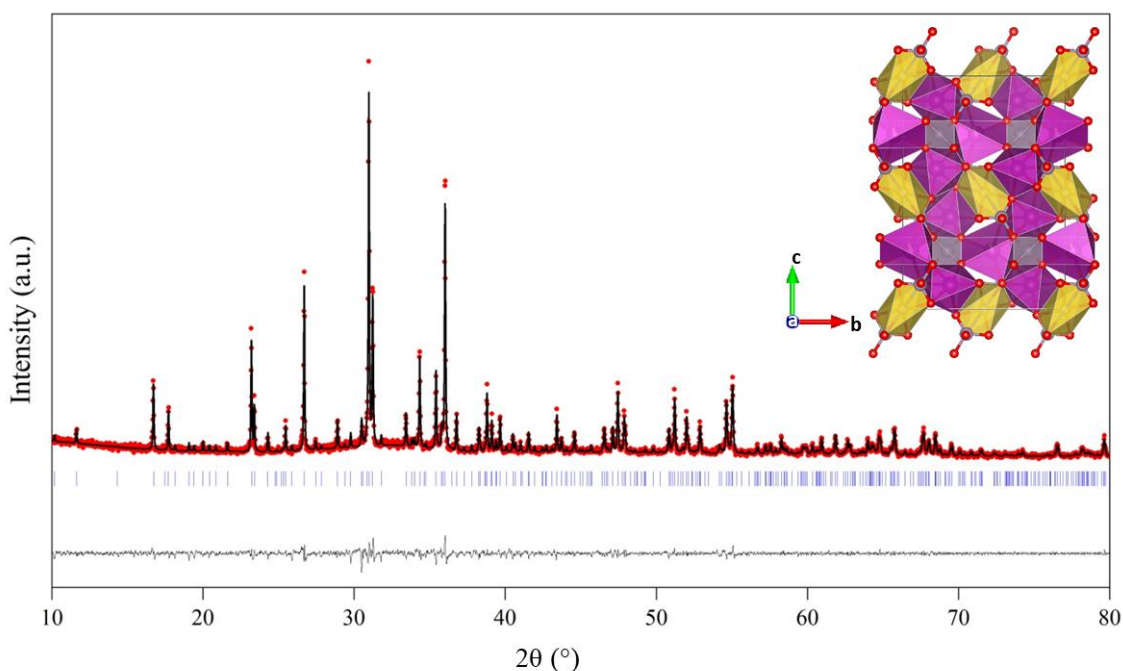
Figure 4.3: Rietveld refinement of the XRD pattern of the new Mn phase using a preliminary composition of NaMn$_3$P$_3$O$_{10}$. Red circles, black lines and grey lines represent the observed, calculated and difference patterns, respectively. Vertical blue bars indicate the positions of the Bragg reflections of the *Pbcn* space group. In the inset proposed model of the NaMn$_3$P$_3$O$_{10}$ structure along the *a* axis.

The best structural model was obtained with the space group *Pbcn,* which was confirmed by performing a Rietveld refinement of the XRD data using a preliminary composition of NaMn$_3$P$_3$O$_{10}$ (Figure 4.3). In a first approximation, we began from the NaMn$_3$P$_3$O$_{10}$ structural model where all anions were considered as oxygen atoms since oxygen and nitrogen exhibit similar X-ray scattering power. However, a high value of isotropic thermal agitation factor (B$_{iso}$) of 2.83 Å^3 was obtained for one (O3) of the five distinct crystallographic sites corresponding to the vertices of the phosphorous tetrahedra, suggesting that this position was occupied by a nitrogen atom rather than an oxygen one.

To have a more precise insight into the chemical composition, EDX and inductively coupled plasma (ICP) measurements were performed and to determine the ratio between

Na, Mn and P atoms. The amount of nitrogen was verified by elemental analysis. The results from these three analyses are shown in Table 4.2 assuming a content of 3 P atoms in the nominal composition.

Table 4.2: Composition of analyzed sample determined by EDX, ICP and elemental analysis.

Element	Assumed theoretical atomic ratio	Experimental atomic ratio determined from EDX	Experimental atomic ratio determined from ICP	Experimental amount determined from Elemental analysis
Na	1	1.0±0.05	1.1±0.1	-
P	3	3.00 (fixed)	3.00 (fixed)	-
Mn	3	3.0±0.08	2.6±0.1	-
N	?	-	-	2

Results from both EDX and ICP measurements were found to be in good agreement with the proposed stoichiometry of $NaMn_3P_3O_{10}$. The lower amount of Mn measured by ICP may come from lower spectral intensity of this element, thus the results obtained from EDX would be more reliable. The amount of nitrogen was evaluated using CHNOS Elemental Analysis and the results revealed content of two nitrogen atom per formula unit. Taking these results into account, the determined stoichiometry is $NaMn_3P_3O_8N_2$.

To confirm these results, the Modeling and Computational group in CIC energiGUNE performed DFT calculations of the ground-state energy for different nitrogen distributions by substituting oxygen for nitrogen at each of the five crystallographic sites occupied by O in the initially proposed structural model of $NaMn_3P_3O_{10}$ (Figure 4.5a). The DFT calculations were carried out using the Vienna Ab initio Simulation Package (VASP).[210,211] To describe the localization of the 3d electrons in Mn, the recently developed strongly constrained and appropriately normed (SCAN)[226] meta-generalized gradient approximation (meta-GGA) functional was used. This functional has been shown to systematically improve without empirical corrections the description of various types of bonding[227] and accurately predict the stability of different polymorphs in compound containing Mn-O bonds.[228,229] Subsequently, the SCAN functional was used to reach the ground-state minimum energy. The self-consistent cycle was stopped using an energy threshold of 10-4 eV.

As shown in Table 4.3, the lowest ground-state minimum energy was found for the position O3, confirming the experimental data. Interestingly, the structure with the lowest

energy per formula unit has the smallest volume: $NaMn_3P_3O_8N_2$ with nitrogen on the O3 distribution leads to the most compact structure (Figure 4.4). While comparing with the experimental volume determined from the Rietveld refinement, an underestimation of ~3% from the theoretical calculations was noticed. This reduced volume is expected from SCAN functional which tends to slightly underestimate the cell volume of manganese-containing systems whereas other GGA+U approaches tend to systematically overestimate it.[227–229] Nevertheless, the SCAN functional provides the best prediction in physical properties, including energy and crystal structure, as it provides a more accurate description of the chemical bonds within the crystal as well as the electron density overlap. More importantly, these theoretical results corroborate the XRD results regarding the preferential occupation site of the nitrogen atoms among the different anionic sites forming the phosphorous-centered tetrahedra.

Table 4.3: Calculated lattice parameters, volume, and the energy per formula unit of the different structures with the different N distributions for $NaMn_3P_3O_8N_2$. Energy difference per formula unit with respect to the lowest energy system, ΔE energy.

	a (Å)	b (Å)	c (Å)	Volume (Å^3)	Energy (eV)	ΔE (eV/f.u.)
N in O1 site	4.79	11.13	14.56	775.86	-762.35	+3.68
N in O2 site	4.93	10.56	14.94	778.05	-764.11	+3.24
N in O3 site	4.82	10.47	15.11	762.77	-777.07	+0.0
N in O4 site	4.72	10.65	15.38	772.78	-764.00	+3.27
N in O5 site	4.87	10.61	15.38	794.02	-763.64	+3.36
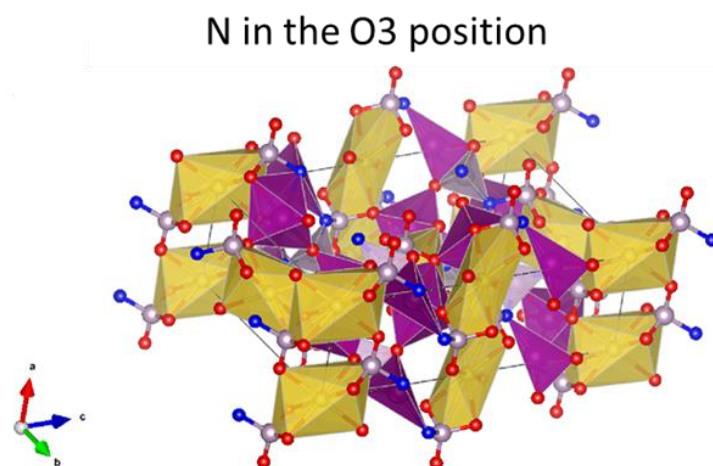
Figure 4.4: Crystal structure of $NaMn_3P_3O_8N_2$ where manganese atoms are in the center of the polyhedrons (dark purple), the sodium, phosphorus and oxygen atoms are shown in yellow, grey and red, respectively. The position of nitrogen atoms was determined from the DFT calculations and shown in blue.

Finally, the structural model built using the information from the preliminary XRD refinement, chemical analyses and DFT, was further validated by neutron powder diffraction was used because the neutron scattering contrast of N and O allows obtaining more precise results: b_N = 9.36 fm vs. b_O = 5.803 fm.[24] Based on the Rietveld refinement of the NPD pattern (Figure 4.5), nitrogen fully occupies the O3 site (named as N3) which confirms previous findings. In addition, some cation (Na/Mn) mixing was found on the metal sites. The structural parameters and atomic positions obtained from the refinement of the NPD pattern are given in Table 4.4. On the other hand, Synchrotron XRD was used to fully validate the structural model. The resulting refinement of the SXRD pattern is presented in Figure 4.7 and Table 4.5. Based on these results, the final refined Na:Mn ratio is 1.1:2.9 and the refined composition $Na_{1.1}Mn_{2.9}P_3O_8N_2$. Although in the SXRD pattern several peaks were identified as the MnO precursor, the share of this phase is extremely low (<1%). The proposed crystal structure of $Na_{1.1}Mn_{2.9}P_3O_8N_2$ is shown in Figure 4.8.
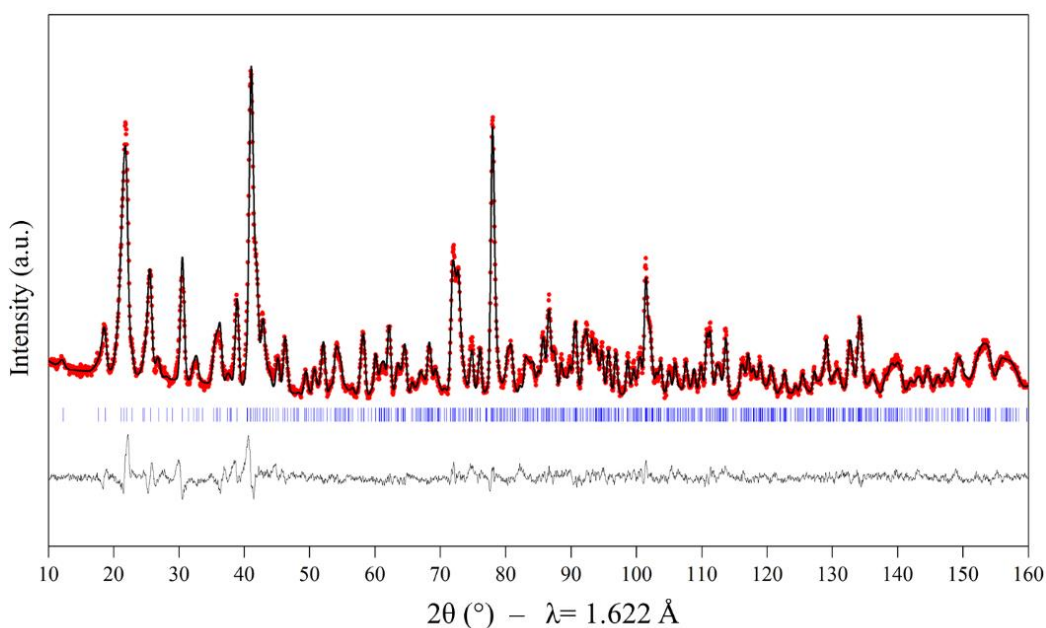
Figure 4.5: Rietveld refinement of the NPD pattern of $Na_{1.1}Mn_{2.9}P_3O_8N_2$ (final composition adapted to the refined one, as explained in the text). Red circles, black lines and grey lines represent the observed, calculated and difference patterns, respectively. Vertical blue bars indicate the positions of the Bragg reflections of the *Pbcn* space group.

Table 4.4: Structural parameters of $Na_{1.1}Mn_{2.9}P_3O_8N_2$ determined from the Rietveld refinement of the NPD pattern.

S.G.: *Pbcn*				$\chi^2 = 2.45$	RBragg = 6.28%	
$a = 4.8787(2)$ Å $b = 10.5815(4)$ Å $c = 15.1862(6)$ Å V = 783.97(5) Å^3						
Atom	Wyckoff site	*x/a*	*y/b*	*z/c*	Occupancy	B_{iso} (Å^2)
Na1	4*c*	0	0	0	1.0	1.4(5)
Mn1	8*d*	0.011(4)	0.2927(13)	0.3965(11)	1.0	0.5(3)
Mn2 /Na2	4*c*	0	0.049(3)	¼	0.908(19) 0.093(19)	0.5(8)
P1	8*d*	0.437(3)	0.1080(10)	0.1058(9)	1.0	0.70(16)
P2	4*c*	0	0.7741(16)	¼	1.0	1.0(3)
O1	8*d*	0.173(3)	0.4709(9)	0.1113(9)	1.0	1.17(17)
O2	8*d*	0.2463(19)	0.1123(9)	0.3887(8)	1.0	1.06(17)
N3	8*d*	0.2974(15)	0.1832(6)	0.1905(5)	1.0	0.93(10)
O4	8*d*	0.314(3)	0.1725(9)	0.0250(7)	1.0	0.74(15)
O5	8*d*	0.317(2)	0.3591(9)	0.3068(7)	1.0	0.77(18)
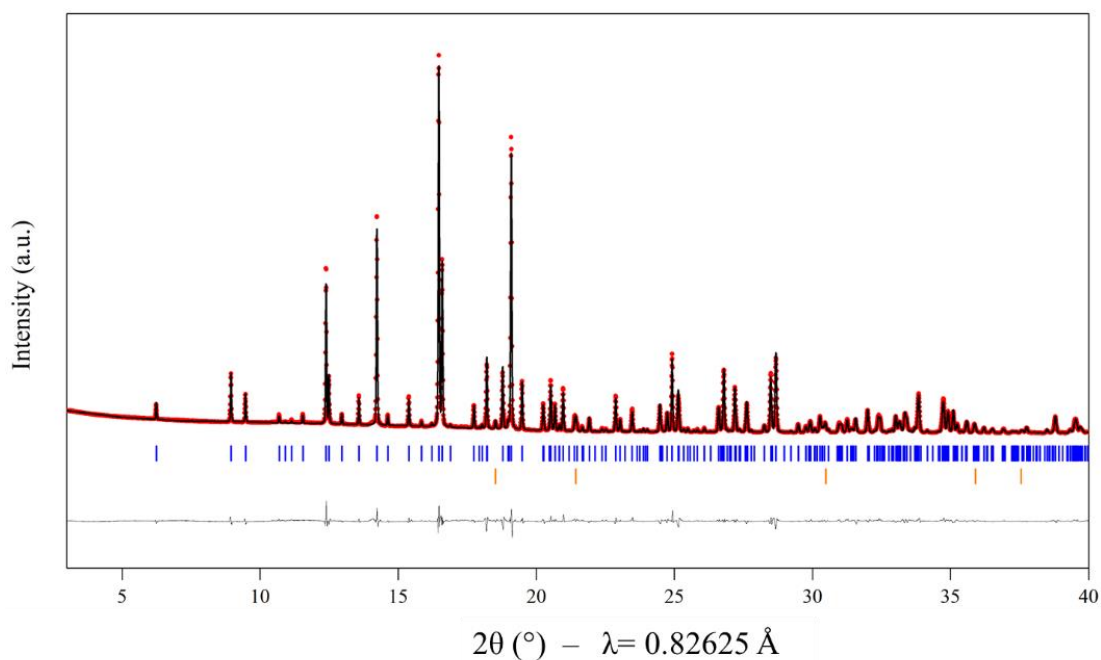
Figure 4.6: Rietveld refinement of the SXRD pattern of $Na_{1.1}Mn_{2.9}P_3O_8N_2$. Red circles, black lines and grey lines represent the observed, calculated and difference patterns, respectively. Vertical blue bars indicate the positions of the Bragg reflections of the *Pbcn* space group. Vertical orange bars indicate the position of the Bragg reflection of the <1% unreacted precursor of MnO.

Table 4.5: Structural parameters of $Na_{1.1}Mn_{2.9}P_3O_8N_2$ determined from the Rietveld refinement of the SXRD pattern.

S.G.: *Pbcn*				$\chi^2 = 59.7$		RBragg = 5.19%
a = 4.884(1) Å b = 10.601(2) Å c = 15.189(2) Å V = 786.307(19) Å^3						
Atom	Wyckoff site	x/a	y/b	z/c	Occupancy	B_{iso} (Å^2)
Na1	4c	0	0	0	1.0	1.4(3)
Mn1	8d	0.0127(8)	0.2935(3)	0.3968(3)	1.0	0.88(8)
Mn2 /Na2	4c	0	0.0422(6)	¼	0.874(10) 0.126(10)	1.33(16)
P1	8d	0.4396(13)	0.1057(6)	0.1066(5)	1.0	0.78(14)
P2	4c	0	0.7731(8)	¼	1.0	0.94(19)
O1	8d	0.172 (3)	0.4717(13)	0.1124(11)	1.0	0.8(4)
O2	8d	0.242(3)	0.1126(13)	0.3906(11)	1.0	1.0(4)
N3	8d	0.298(4)	0.1807(19)	0.1892(13)	1.0	0.8(5)
O4	8d	0.321(3)	0.1728(15)	0.0242(10)	1.0	0.8(4)
O5	8d	0.317(3)	0.3627(15)	0.3059(10)	1.0	0.6(4)
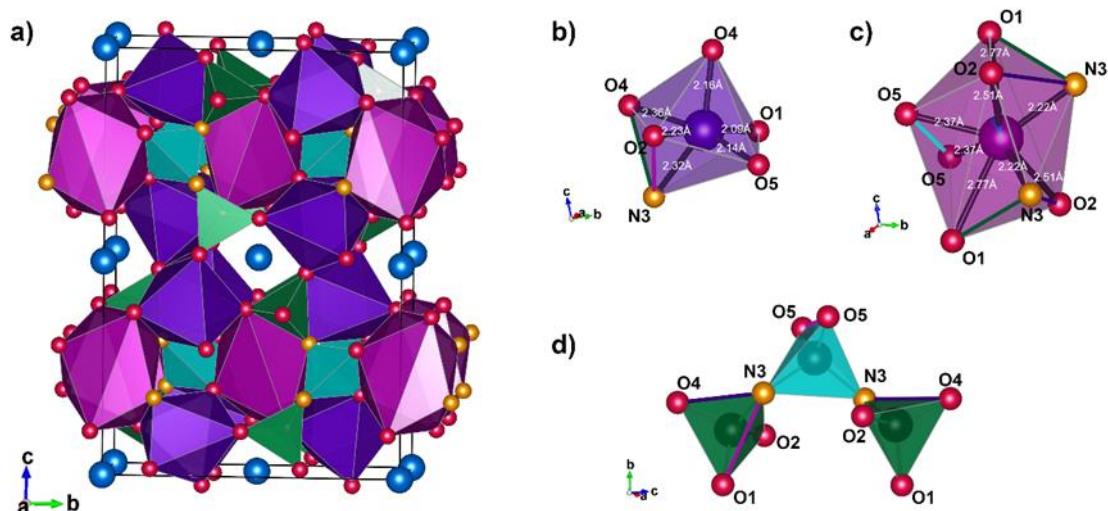
Figure 4.7: (a) Crystal structure of $Na_{1.1}Mn_{2.9}P_3O_8N_2$. Na, O and N atoms are shown as blue, red and orange balls, respectively. The $(Mn1)O_5N_1$ octahedra and $(Mn2/Na2)O_6N_2$ polyhedra are displayed in purple and pink, respectively. The $(P1)O_3N$ and $(P2)O_2N_2$ octhedra are shown in green and cyan, respectively. (b) and (c) views of the coordination environment of Mn1 and Mn2/Na2 sites, respectively with indicated bond lengths. The edges shared with other polyhedra are highlighted with their corresponding colors. (d) Polyanionic chain of $(P_3O_8N_2)^{-VII}$ made of three phosphorous tetrahedra sharing their N corners. The edges shared with other polyhedra are highlighted with their corresponding colors.

Manganese atoms occupy two distinct crystallographic sites, labelled Mn1 and Mn2: Mn1 is located in a distorted MnO_5N octahedron, while Mn2 is surrounded by six oxygen atoms and two nitrogen atoms (Figure 4.7b and c, respectively). These two kinds of manganese-centered polyhedra are connected both through O corners and through all their O-N edges, forming a 3D framework. Phosphorous atoms occupy two distinct crystallographic sites: P1 is coordinated to three oxygens and one nitrogen, while P2 is

coordinated to two oxygens and two nitrogens. These two kinds of tetrahedra share their N corners and thus form short twisted chains of $P_3O_8N_2$, as shown in (Figure 4.7d). Such short chains of three tetrahedra differ from the $(PO_3)_3N$ units of three PO_3N tetrahedra observed in the CUBICON-type compounds $Na_3M(PO_3)_3N$ and $Na_2M_2(PO_3)_3N$ described in Chapter 2 and 3.[158,162,145,160,146,185,230] The complex arrangement of manganese and phosphorous polyhedra results in narrow channels along the *a*-axis, in which Na3 occupies an octahedral site coordinated to six oxygen atoms.

Table 4.6 gathers the interatomic distances within the crystal structure of $Na_{1.1}Mn_{2.9}P_3O_8N_2$ obtained from the refinements of both SXRD and NPD patterns (of the same sample). The major difference can be observed in the Mn-O distances between the manganese polyhedra. The volume of the partially substituted $[(Mn2/Na2)O_6N_2]$ polyhedra is almost twice larger than the $[(Mn1)O_5N_1]$ distorted octahedra (25.51 Å^3 *vs.* 13.71 Å^3, respectively). Within the $[PO_3N]$ tetrahedra, the P-N bond is ~10% longer than the two other P-O bonds (which was also observed in CUBICON-type compounds $Na_3M(PO_3)_3N$ and $Na_2M_2(PO_3)_3N$ as shown for example in Table 2.15 for $Na_3V(PO_3)_3N$ and Table 3.5 for $Na_2Fe_2(PO_3)_3N$).

Table 4.6: Selected interatomic distances within the crystal structure of $Na_{1.1}Mn_{2.9}P_3O_8N_2$ deduced from the Rietveld refinement of the Synchrotron XRD and NPD patterns.

Bond	Bond distance (SXRD)	Bond distance (NPD)
Mn1-O1	2.097(4)	2.092(7)
Mn1-O2	2.221(4)	2.230(7)
Mn1-N3	2.333(5)	2.315(7)
Mn1-O4	2.395(4)	2.358(7)
Mn1-O4	2.128(4)	2.161(7)
Mn1-O5	2.156(4)	2.139(8)
Mn2/Na2-O1 ×2	2.739(3)	2.772(5)
Mn2/Na2-O2 ×2	2.551(3)	2.515(5)
Mn2/Na2-N3 ×2	2.264(4)	2.219(7)
Mn2/Na2-O5 ×2	2.268(3)	2.365(9)
Na3-O1 ×2	2.362(3)	2.345(4)
Na3-O2 ×2	2.362(3)	2.390(4)
Na3-O4 ×2	2.440(3)	2.414(4)
P1-O1	1.523(3)	1.549(6)
P1-O2	1.559(3)	1.548(6)
P1-N3	1.638(5)	1.658(5)
P1-O4	1.551(4)	1.526(6)
P2-N3 ×2	1.667(5)	1.649(5)
P5-O5 ×2	1.557(4)	1.532(6)

Although the solved structure of $Na_{1.1}Mn_{2.9}P_3O_8N_2$ cannot be found in the literature, it exhibits structural similarities to the one reported for $Na_2Ca_3Si_3O_{10}$ [231,232] and shown in Figure 4.8. Similar lattice parameters can be found ($C2/c$ monoclinic cell with $a = 16.249$ Å, $b = 5.147$ Å, $c = 11.347$ Å, $\beta = 92.97°$, $V = 947.78$ Å^3; ICSD record #36399) and stoichiometry (Ca:Si:O atomic ratio: 3:3:10). In addition, $Na_2Ca_3Si_3O_{10}$ also contains short chains of three SiO_4 tetrahedra linked through their oxygen corners, very similar to the chain of two PO_3N and one PO_2N_2 tetrahedra formed in $Na_{1.1}Mn_{2.9}P_3O_8N_2$. Calcium is eightfold coordinated by oxygen in two kinds of distorted CaO_6 also sharing O-O edges with each other and with one of the two kinds of SiO_4 tetrahedra. Ca-O distances of 2.308 (3); 2.435 (4); 2.367 (3) Å (2x each) in $Ca(1)O_6$ octahedra and 2.325 (4); 2.6592 (4); 2.302 (3); 2.411 (3); 2.317 (4); 2.417 (3) in $Ca(2)O_6$ octahedra are very similar to the Mn-O distances in two manganese polyhedra of $Na_{1.1}Mn_{2.9}P_3O_8N_2$. The arrangement of CaO_6 octahedra in $Na_2Ca_3Si_3O_{10}$ yet differs as forms 2D connected frameworks which are bridged by the Si_3O_{10} chains instead of a 3D network formed in $Na_{1.1}Mn_{2.9}P_3O_8N_2$ by the manganese polyhedra. Eventually, $Na_2Ca_3Si_3O_{10}$ structure comprises two Na per formula unit, contrary to $Na_{1.1}Mn_{2.9}P_3O_8N_2$ with 1.1 Na per formula unit.
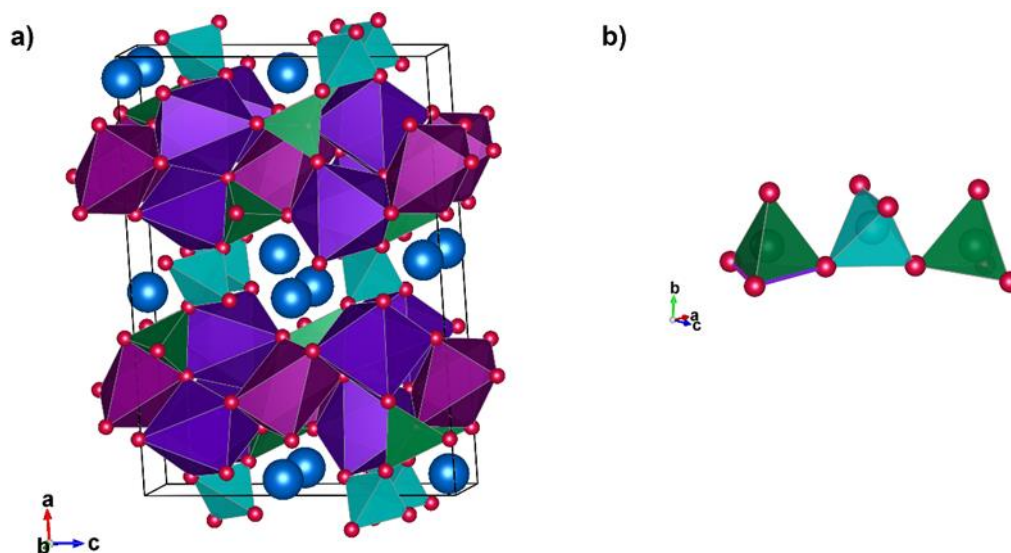
Figure 4.8: (a) Representation of the crystal structure of $Na_2Ca_3Si_3O_{10}$. [231,232] Na and O atoms are shown as blue and red balls, respectively. The two crystallographically-distinct CaO_6 octahedra are displayed in purple and pink, respectively. The two types of SiO_4 tetrahedra are shown in green and cyan, respectively. (b) Polyanionic chain of $[Si_3O_{10}]^{-VIII}$ made of two SiO_4 tetrahedra sharing O corners. The edges shared with CaO_6 octahedra are highlighted with their corresponding colors.

4.2.2. Electron diffraction and high-resolution Transmission Electron Microscopy study

- **Transmission Electron Microscopy (TEM)**

To further confirm the indexation of the *Pbcn* space group and the crystal structure of $Na_{1.1}Mn_{2.8}P_3O_8N_2$, Transmission Electron Microscopy (TEM) was used with the collaboration of Francisco Bonilla from CIC energiGUNE. Selected area electron diffraction (SAED) patterns of crystals oriented along distinct zone axes were collected and compared with the simulated patterns of the *Pbcn* space group. As can be seen in Figure 4.9, the SAED patterns acquired along different zone axes, corresponding to five individual particles (P1-P5), can be fully indexed with the *Pbcn* orthorhombic cell. Likewise, the SAED patterns were collected along the three main axes [100], [010] and [001] were effectively indexed with the *Pbcn* cell, as shown in Figure 4.10 (a-c).
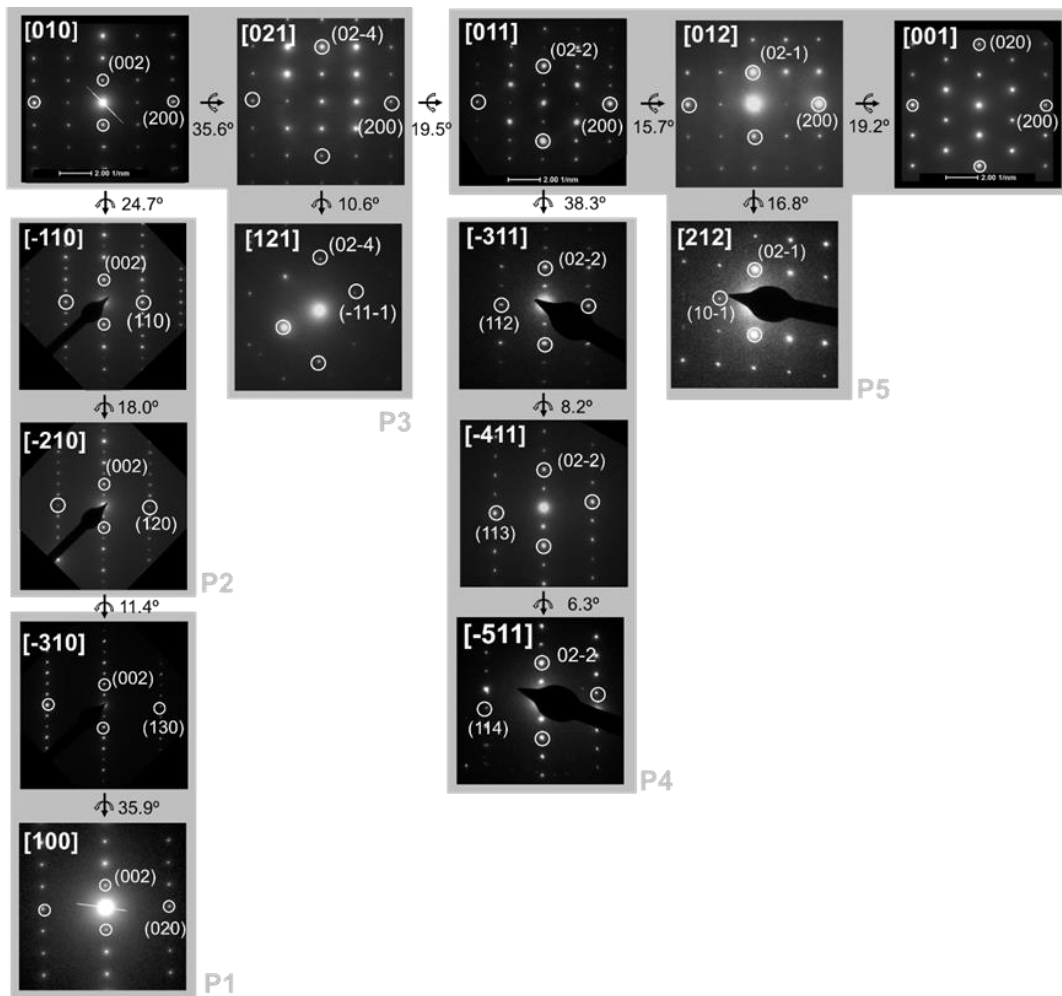
Figure 4.9: SAED patterns for different particles (P1-P5) of $Na_{1.1}Mn_{2.9}P_3O_8N_2$ obtained along high-order zone axes. All patterns can be fully indexed with the Pbcn orthorhombic cell determined from powder diffraction. Angles between images correspond to the horizontal (horizontal arrow) or vertical (vertical arrow) rotations of crystals needed to go from one zone axis to another.
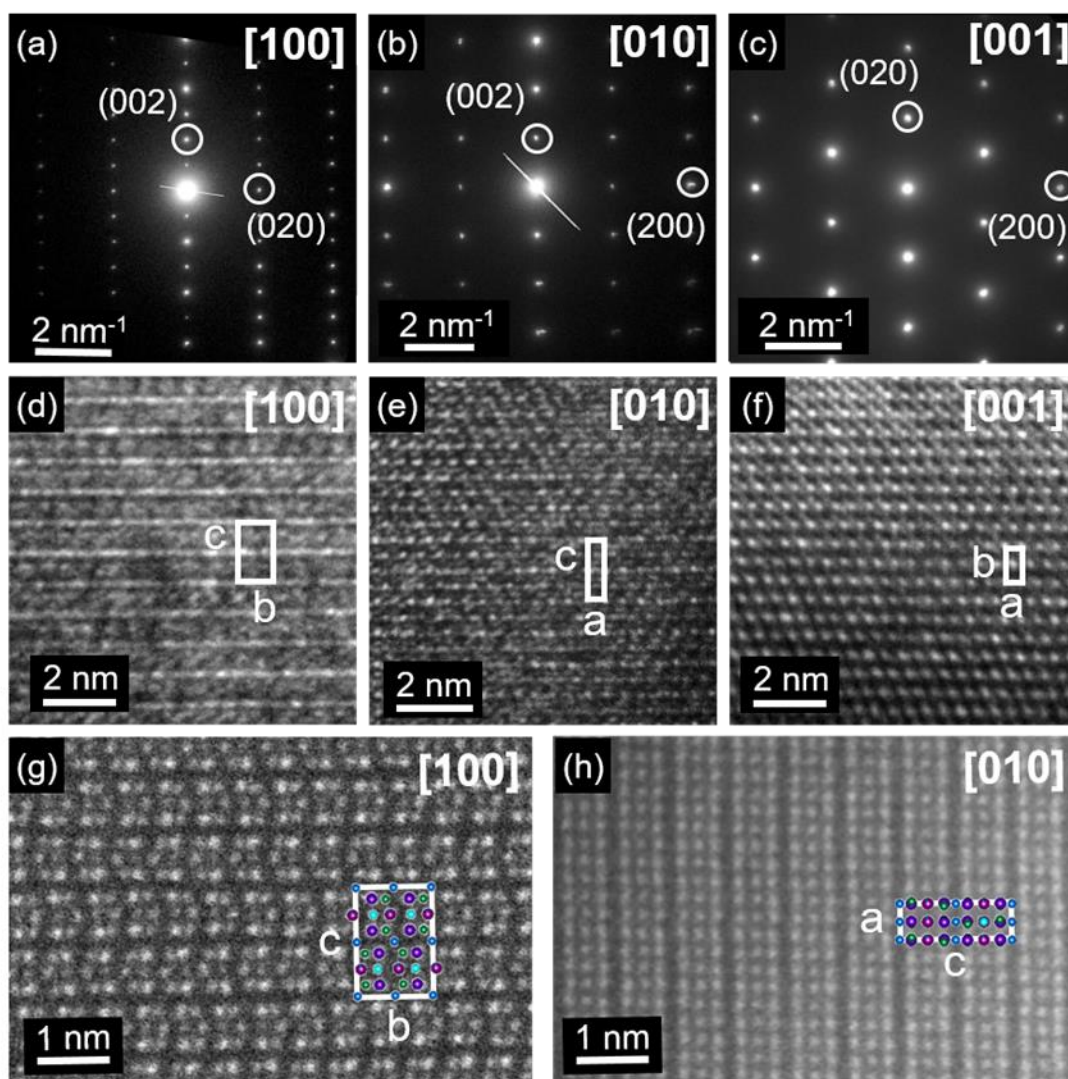
Figure 4.10: Representative SAED patterns of crystals of $Na_{1.1}Mn_{2.8}P_3O_8N_2$ oriented along the main axes (a) [100], (b) [010] and (c) [001]. High-resolution TEM images of crystals of $Na_{1.1}Mn_{2.8}P_3O_8N_2$ oriented along the main axes (d) [100], (e) [010] and (f) [001]. High-resolution STEM images (g) of a particle of $Na_{1.1}Mn_{2.8}P_3O_8N_2$ oriented along [100] and (h) of a particle oriented along [010]. (d-h) The unit cell is indicated with white squares and (g-h) the position of atoms of Na, Mn and P are indicated with colored circles.

Additionally, high-resolution high-angle annular dark field (HAADF) STEM images were collected to give an insight on the chemical distribution on the atomic scale. High-resolution TEM images of crystals of $Na_{1.1}Mn_{2.8}P_3O_8N_2$ oriented along the main axes [100], [010] and [001] are shown in Figure 4.10 (d), (e), (f), respectively. Figure 4.10 (g) and (h) shows the high-resolution STEM images of crystals oriented along [100] and [010] axes. The projections of the structural model of $Na_{1.1}Mn_{2.8}P_3O_8N_2$ along the [100] (*a*) and [010] (*b*) axes match well with the bright columns of Mn and P atoms observed in the HAADF-STEM images, corroborating the crystal structure established from powder diffraction.

- **Scanning Electron Microscopy (SEM)**

Electron microscopy study was performed to analyze the morphology of $Na_{1.1}Mn_{2.8}P_3O_8N_2$ crystals. SEM images shown in Figure 4.11 indicate a non-uniform shape of the particles and a wide particle size distribution, varying from 1 µm to 30 µm. Additionally, small particles tend to agglomerate.
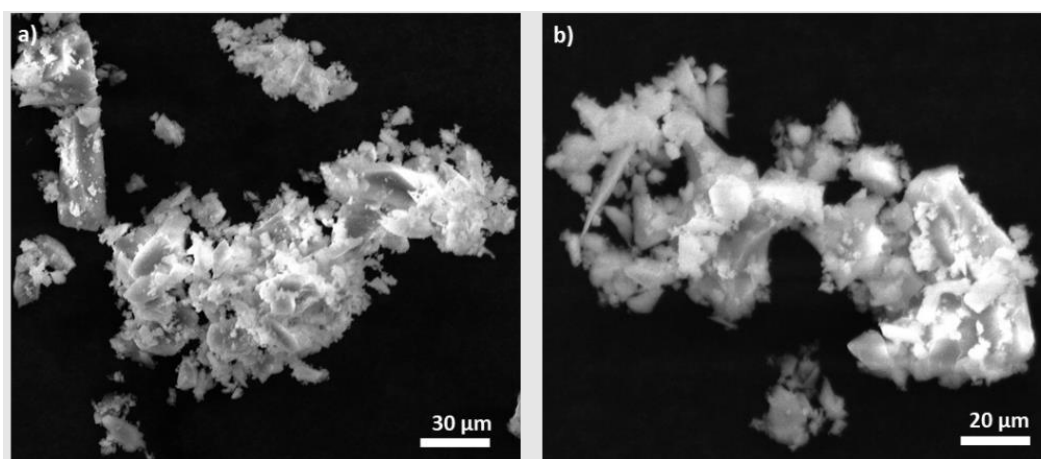
Figure 4.11: SEM images of Na$_{1.1}$Mn$_{2.8}$P$_3$O$_8$N$_2$.

4.2.3.   Air and thermal stability analysis

To explore the stability properties of this new phase $Na_{1.1}Mn_{2.8}P_3O_8N_2$, three different tests were performed. First, the air stability of the structure was examined by exposing a powder sample in air and collecting the XRD patterns after 1h, 24h, 48h and 7 days. The obtained XRD patterns are gathered in Figure 4.12.
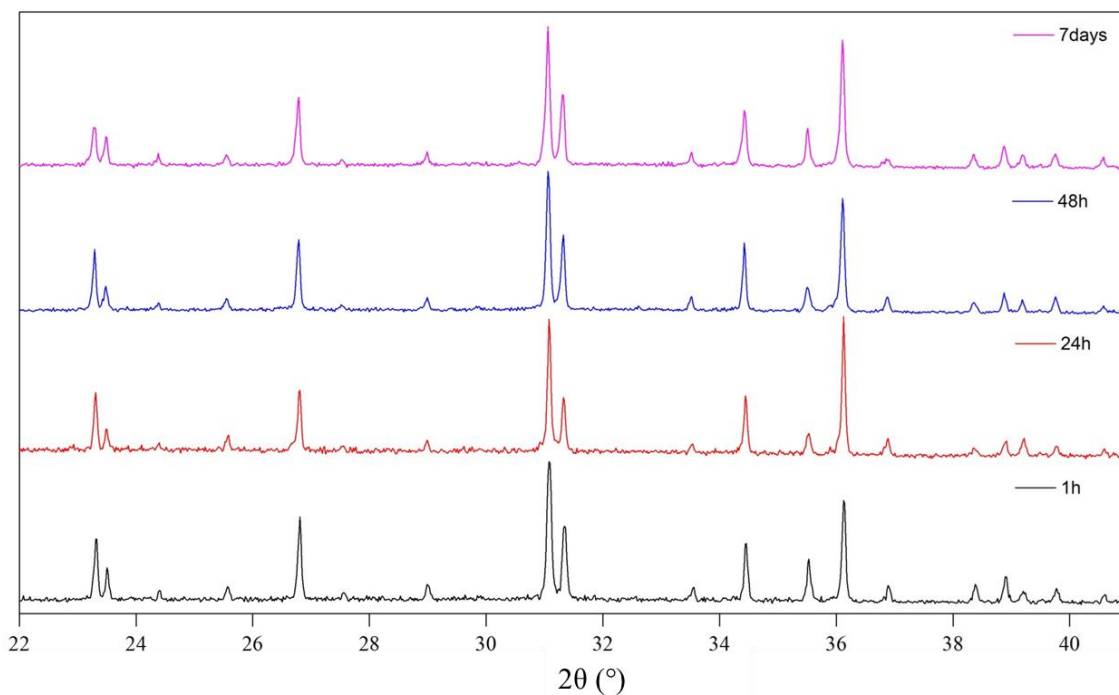
Figure 4.12: Comparison of the XRD patterns of Na$_{1.1}$Mn$_{2.8}$P$_3$O$_8$N$_2$ after air exposure at 1h, 24h, 48h and 7 days, as indicated in the figure.

Based on obtained results, it can be observed that structure of Na$_{1.1}$Mn$_{2.8}$P$_3$O$_8$N$_2$ remains unchanged for 48 h. After 7 days small differences in the intensity ratios can be detected, which could suggest slight alteration of the compound. Although no additional analysis was done, elemental analysis should be done to verify the oxygen-nitrogen ratio in the structure.

Next, the thermogravimetric analysis of Na$_{1.1}$Mn$_{2.8}$P$_3$O$_8$N$_2$ was performed under synthetic air, in the temperature range 30-1000 °C at 10 °C.min^{-1} heating rate to evaluate the thermal stability of the structure. The registered mass changes as a function of temperature together with the corresponding DTA curve are shown in Figure 4.13.
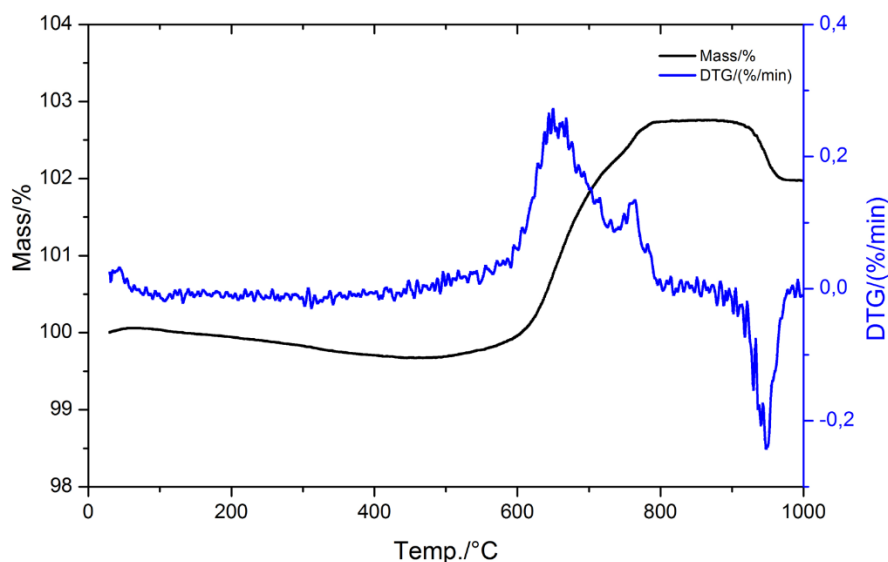
Figure 4.13: Thermogravimetric analyses (relative mass loss curves) obtained for Na$_{1.1}$Mn$_{2.9}$P$_3$O$_8$N$_2$ under synthetic air measured from room temperature to 1000 ^{0}C at 10 $^{\circ}$C.min^{-1} heating rate.

Based on the TGA curve, Na$_{1.1}$Mn$_{2.8}$P$_3$O$_8$N$_2$ remains stable until 600 ºC, which could be a great advantage for this compound if it could be used as a cathode material. The mass gain observed above this temperature is attributed to the release of nitrogen and simultaneous uptake of oxygen which is the typical signature of nitrogen-containing compounds.[233]

Finally, high temperature XRD measurements were performed to analyze the observed structural changes occurring at elevated temperatures. The experience was performed from RT to 900 °C at 10 °C.min^{-1} heating rate in a 2theta range of 10 - 60º. XRD patterns were recorded every 50 °C up to 900 °C and are shown in Figure 4.14.
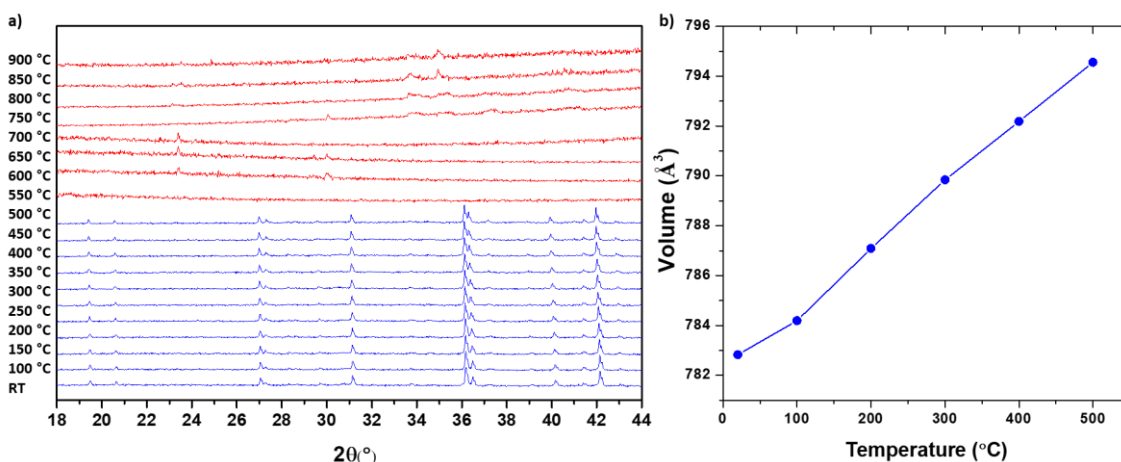
Figure 4.14: (a) Evolution of the XRD patterns of $Na_{1.1}Mn_{2.8}P_3O_8N_2$ upon heating under air in the temperature range RT-900 °C. Blue colour of the curves corresponds to the region of the stability of $Na_{1.1}Mn_{2.8}P_3O_8N_2$, while the red colour the region of the decomposition of the phase. (b) Variation of the $Na_{1.1}Mn_{2.8}P_3O_8N_2$ cell volume upon temperature in the stability range of RT – 500 °C.

The collected XRD patterns indicate the decomposition of the $Na_{1.1}Mn_{2.8}P_3O_8N_2$ structure at 500 °C into an amorphous phase. The difference of the decomposition temperatures between TGA and HT XRD measurement arise from the longer exposure of the powder to the high temperature during the later measurement, required to collect the XRD pattern. Figure 4.14b shows the dependence of the increasing temperature on the volume of the cell in the crystalline range (RT – 500 °C). Exceptional stability of the structure observed by lack of changes in the XRD patterns was confirmed by solely ~1.5% volume change. Several peaks appearing >750 °C were indexed with the $Mn_2P_2O_7$ phase, known as a common decomposition product of the phosphates at high temperatures.[234,235]

4.2.4.   Magnetic measurements

Magnetic measurements were performed to analyse the magnetic character of $Na_{1.1}Mn_{2.8}P_3O_8N_2$. The zero-field cooled (ZFC) AC susceptibility measurements were performed while cooling from 300 K to 2.5 K under an AC magnetic field of 10 Oe amplitude at a frequency of 10 kHz. The AC field cooled (FC) susceptibility measurements were performed similarly to ZFC, cooling down to 2.5 K under an additional applied DC magnetic field of 1 T. Figure 4.15 shows the FC and ZFC susceptibility measurements of $Na_{1.1}Mn_{2.9}P_3O_8N_2$. The increase of the susceptibility with the decrease of the temperature can be observed in the beginning of the experiment, until reaching ~30 K. Below this temperature, the susceptibility initially slightly decreases until reaching a minimum near 15 K, below which it increases. The maximum observed

185

at 33 K can be identified as the Néel temperature T_N, which marks the transition from paramagnetic to antiferromagnetic ordering. The difference between FC and ZFC susceptibility measurements is not expected in the paramagnetic state, which suggests that ferromagnetic impurities are present, possibly Mn oxide, which indeed was observed in the Synchrotron XRD pattern.
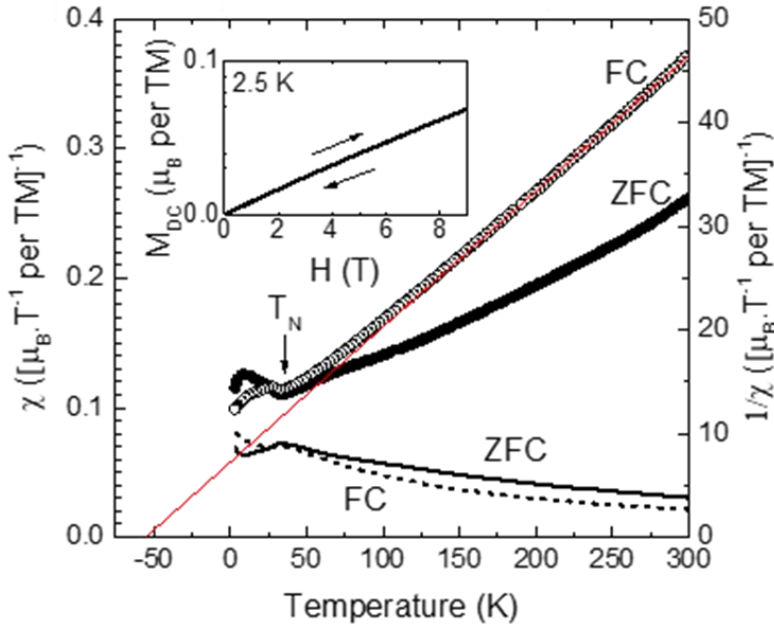
Figure 4.15: Susceptibility (left axis) and inverse susceptibility (right axis) of Na$_{1.1}$Mn$_{2.9}$P$_3$O$_8$N$_2$ in ZFC and FC (1T DC) modes. The fit with the Curie-Weiss law is shown by the red line. Inset: DC magnetization versus magnetic field at 2.5 K. The Néel temperature of 33 K is indicated by an arrow.

The FC inverse susceptibility curves was used to calculate the effective moment μ_{eff}, as shown in the Figure 4.15. By performing the linear fitting of the curve, the μ_{eff} was extracted from the slope in the high temperature limit, according to the equations:

$$y = b * x + a$$

$$\frac{1}{\chi} = \frac{1}{C} * T - \frac{\theta}{C}$$

$$C = \frac{N_A \cdot \mu_{eff}^2}{3k_B}$$

where θ is the Weiss constant, C the Curie constant, N_A Avogadro's number, k_B Boltzmann's constant and μ_{eff} is the effective moment in units of μ_B per Mn, μ_B being Bohr's magneton. The value μ_{eff} deduced from the fit of the FC inverse susceptibilities of 5.85 μ_B per Mn is very close to the theoretical value expected for pure Mn^{II} (5.92 μ_B per Mn), confirming the expected oxidation state. The Weiss constant is negative, close

to -60 K, which is a further indication that the main interaction in the paramagnetic state is antiferromagnetic.

4.2.5. Solid State Nuclear Magnetic Resonance analysis

^{23}Na solid-state MAS NMR was carried out to study the local environment of sodium within the structure of $Na_{1.1}Mn_{2.9}P_3O_8N_2$. Three main signals are detected in the spectrum, which were labelled using the letters *a*, *b* and *c* in Figure 4.16.
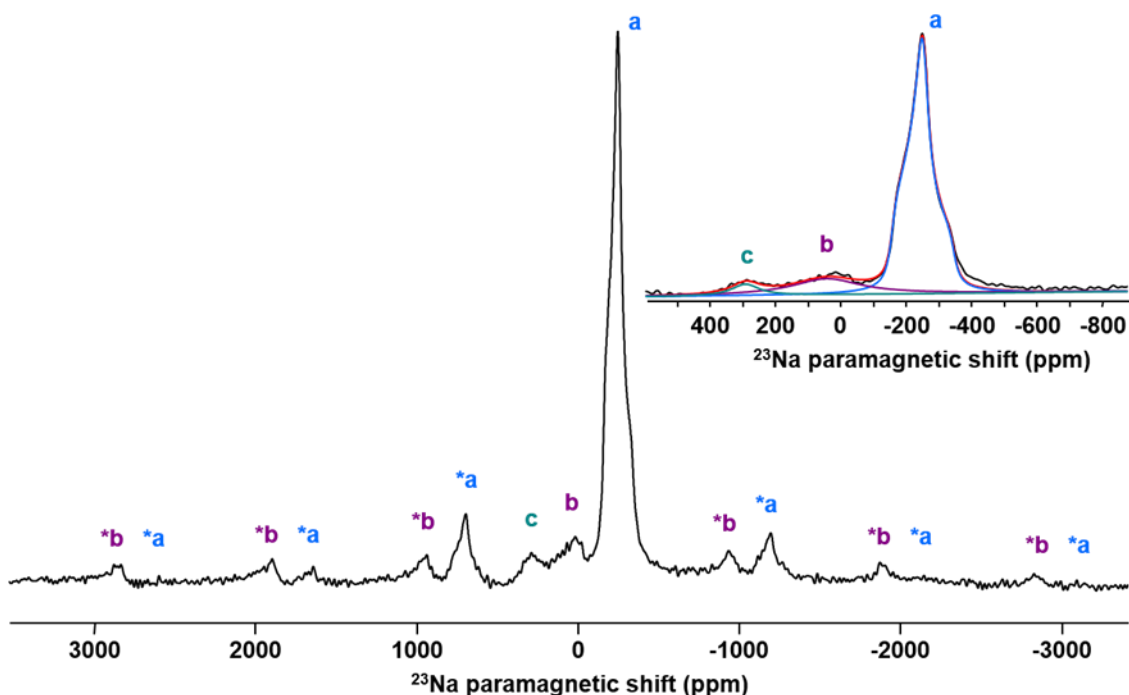
Figure 4.16: ^{23}Na solid-state MAS NMR spectrum of $Na_{1.1}Mn_{2.9}P_3O_8N_2$. The isotropic resonances of the three signals are labelled by the letters *a* (in blue), *b* (in purple) and *c* (in cyan) and their respective spinning sidebands are indicated with asterisks. Inset: result of the fit of the central part of spectrum using three components. The experimental spectrum is plotted in black, while the red line is the fit, which is deconvoluted into the *a* (in blue), *b* (in purple) and *c* (in cyan) components.

Table 4.7: Fitted NMR parameters of the ^{23}Na spectra in $Na_{1.1}Mn_{2.9}P_3O_8N_2$.

Component	δ [ppm]	η	C$_Q$ [kHz]	Quantification [%]
a	-155	0.96	2729	80
b	40			15
c	285			5

The most intense resonance at around -155 ppm (signal labelled *a* in blue in Figure 4.16) is assigned to the main sodium component in $Na_{1.1}Mn_{2.9}P_3O_8N_2$, "Na1" in the octahedral environment. The quadrupolar shape of this signal was fitted considering the values given in Table 4.7. The asymmetry of the quadrupolar shape indicates the presence of structural

deviations from a perfect octahedral disposition around Na1 sites, which indeed was observed while analyzing the bond distances within the octahedra (Table 4.6). The shift of this resonance is strongly determined by the paramagnetic nature of the compound. The second signal at ~40 ppm (signal labelled *b* in purple in Figure 4.16) is ascribed to the sodium at the manganese sites in the structure (Mn2, MnO_6N_2). This assignment is based on the large intrinsic broad character of this signal characterized by a very extensive set of MAS rotational sidebands in the spectrum. This large broadening is related to the dipolar broadening generated by strong paramagnetic interactions of Na in the Mn sites. The intensity ratio between the signals ascribed to Na1 (*a*) and Na2 at the Mn2 site (*b*) should take into consideration the individual intensities of the central peak and all the MAS rotational sidebands, although the correct excitation of the MAS sidebands far away from the carrier frequency could be underestimated due to pulse imperfections. In any case, the relative intensities between these two signals are expected to be in the range calculated by other techniques (90:10). Finally, the minor resonance at ~290 ppm, for which no spinning side bands are observed, is assigned to a paramagnetic impurity containing Na^+.

4.2.6. Electrochemical activity evaluation and voltage calculations

The electrochemical properties of the $Na_{1.1}Mn_{2.9}P_3O_8N_2$ were tested in half-cell configuration versus both metallic sodium and lithium as a negative electrodes and $LiPF_6/NaPF_6$ in EC:DMC (1:1 vol) as electrolytes in 2032-type coin cells. The theoretical capacity corresponding to the removal of one Na^+ is equal to 61.3 mAh.g^{-1}.

Two types of electrodes were prepared, with different kind and amount of carbon (10% of C_{65} and 15% of Ketjen Black respectively). The change of carbon from C_{65} to Ketjen Black was done due to the higher surface area of the latter which was expected to translate into higher conductivity and more homogeneous mixing. The electrode was prepared by mixing the active material ($Na_{1.1}Mn_{2.9}P_3O_8N_2$) with carbon and 10% poly(vinylidene) fluoride (PVDF, Alfa Aesar) in N-methyl-2-pyrrolidone (NMP, Aldrich) and casting the obtained slurry onto an Al foil using a doctor blade. The as-prepared laminate was then dried overnight in the vacuum oven at 120 °C and punched into small disks with the mass loading of active material around 3x10^{-3} g.cm^{-2}.

The prepared cells were studied in galvanostatic mode at a rate of one electron exchange in 40 hours (C/40 rate), between 1.0 and 4.5 V vs Na^+/Na and 1.0 and 5.0 V vs Li^+/Li using a MACCOR battery tester. All electrochemical measurements were performed at room temperature.

Galvanostatic charge-discharge curves are presented in Figure 4.17. Figure 4.17 a&b correspond to the cells with 10% of C_{65}; whereas Figure 4.17 c&d to 15% of Ketjen Black.
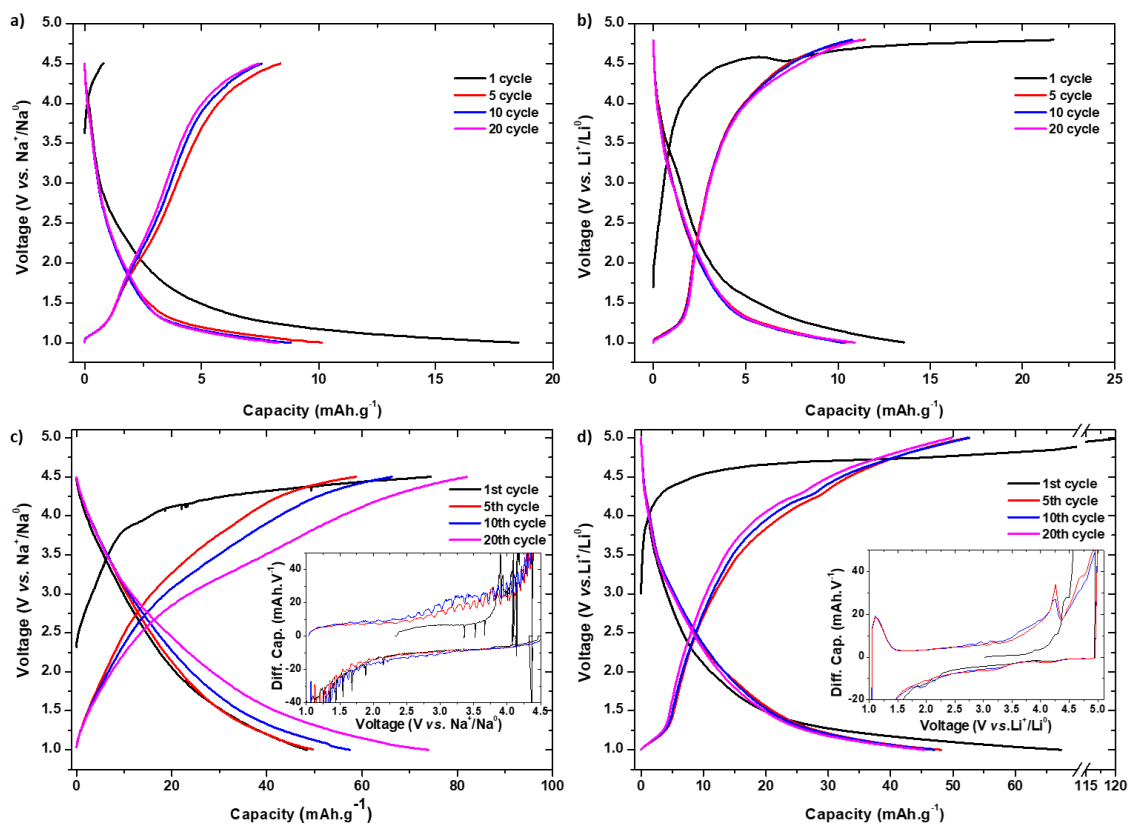
Figure 4.17: (a&b) Galvanostatic charge discharge curves of $Na_{1.1}Mn_{2.9}P_3O_8N_2$ against (a) Na^+/Na^0 and (b) Li^+/Li^0 metal at C/40 rate with the electrode prepared with 10% of C_{65}; (c&d) Galvanostatic charge discharge curves of $Na_{1.1}Mn_{2.9}P_3O_8N_2$ against (c) Na^+/Na^0 and (d) Li^+/Li^0 at C/40 rate with the electrode prepared with 15% of ketjen black. Inset of (c &d) – derivative dQ/dV curves of the 1st, 5th and 10th cycle.

It can be observed that although the change of carbon to Ketjen Black slightly improved the capacity, the overall electrochemical performance of $Na_{1.1}Mn_{2.9}P_3O_8N_2$ is poor as exhibits a very significant polarization and a very large irreversible capacity in the first cycle. A small signal in the charge in the derivative curves can be observed at 4.2 V *vs.* Li^+/Li^0 (inset of Figure 4.17d), however it does not appear in the discharge. This indicates a probable oxidation reaction of the electrolyte coupled to the non-faradaic behavior of Ketjen Black rather instead of the redox reaction of the manganese couple.

These results may be explained either from the inactivity of the Mn^{II}/Mn^{III} redox couple within the tested voltage window; or by kinetic limitations associated with poor ionic and/or electronic mobility. To verify these hypotheses, DFT calculations were performed to determine the expected redox potential associated with the oxidation of Mn^{II} to Mn^{III} concomitant with the extraction of one alkali cation per formula unit. The voltage was calculated at ab-initio level, using the following equation (with $x = 1$):

$$V(x) \approx - \frac{E_{Na_1Mn_3P_3O_8N_2} - E_{Mn_3P_3O_8N_2} - E_{Na_{(s)}}}{e}$$

A computed average voltage of 3.25 V *vs.* Na^+/Na^0 was obtained which clearly falls within the voltage stability window of common organic electrolytes, and then discards the first hypothesis.

To verify the second hypothesis of the kinetic limitations, further calculations were performed. The Bond Valence Energy Landscape (BVEL)[236,237,127] were calculated for to assess the possibility of Na^+ diffusion within this compound. Figure 4.18 shows the calculated BVEL maps in which the isosurfaces colored in yellow define the regions of the alkali cation mobility for a given bond-valence energy of 1.5 eV above the lowest site energy of the alkali site. The threshold energy E_{th} for which these isosurfaces start to percolate the unit cell in at least one dimension can be taken, in general, as a rough estimate of the activation energy for cation migration E_m. Here, very high values of percolation energy of $E_{th} = 4.6$ eV were calculated, which clearly indicates a difficile diffusion of the alkali cations within the structure, probably hampered by the presence of narrow bottlenecks in the inflexible covalent polyanionic framework along the *a* direction (rectangular bottle neck of 3.1 Å × 2.5 Å).
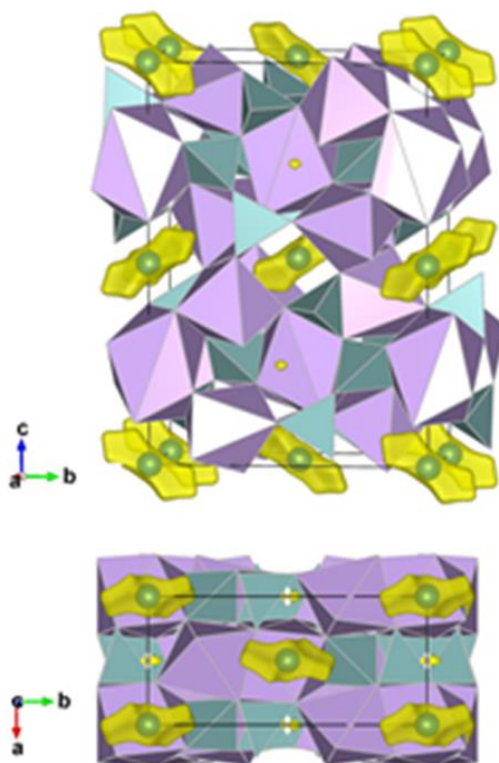
Figure 4.18: BVEL isosurfaces (yellow regions) calculated for Na$_{1.1}$Mn$_{2.9}$P$_3$O$_8$N$_2$ for a given bond-valence energy of 1.5 eV above the lowest site energy of the alkali site (Na$^+$ shown as green balls). Manganese and phosphorous polyhedra are shown in lilac and teal colors, respectively.

In view of these results, the lithium counterpart, Li$_{1.1}$Mn$_{2.9}$P$_3$O$_8$N$_2$ was prepared and investigated to determine whether the smaller Li$^+$ cation can influence on the different organization of the polyhedra within the framework, require smaller diffusion channels and improve its electrochemical performance.

4.3. LiMn$_3$P$_3$O$_8$N$_2$

4.3.1. Synthesis and structural analysis

Although all reported lithium metal nitridophosphates were so far obtained by the Na$^+$/Li$^+$ ion-exchange route,[160,186,238] we decided to try the direct synthesis method by changing the precursors used for the sodium counterpart (NaPO$_3$) for the lithium one (Li$_3$PO$_4$). Eventually the LiMn$_3$P$_3$O$_8$N$_2$ was expected to be synthesized according to the reaction:

$$Li_3PO_4 + MnO + 2\,NH_4H_2PO_4 \rightarrow Li_3MnP_3O_8N_2$$
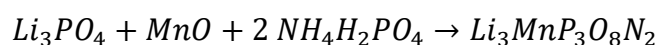
An analogous synthesis route was employed as for the synthesis of Na$_{1.1}$Mn$_{2.9}$P$_3$O$_8$N$_2$. The precursors were first ball milled for 20 min, next placed in the graphite crucible and

subjected to annealing under constant ammonia flow (30 ml.min^{-1}). After annealing, the sample was cooled down to room temperature and manually grinded in a mortar and eventually a light-grey powder was obtained. By performing various tries, it was observed that increasing the temperature up to 850 °C was required to eliminate the co-synthesized impurities of $LiMnPO_4$ and unreacted precursors of Li_3PO_4 and MnO observed in previous tries.
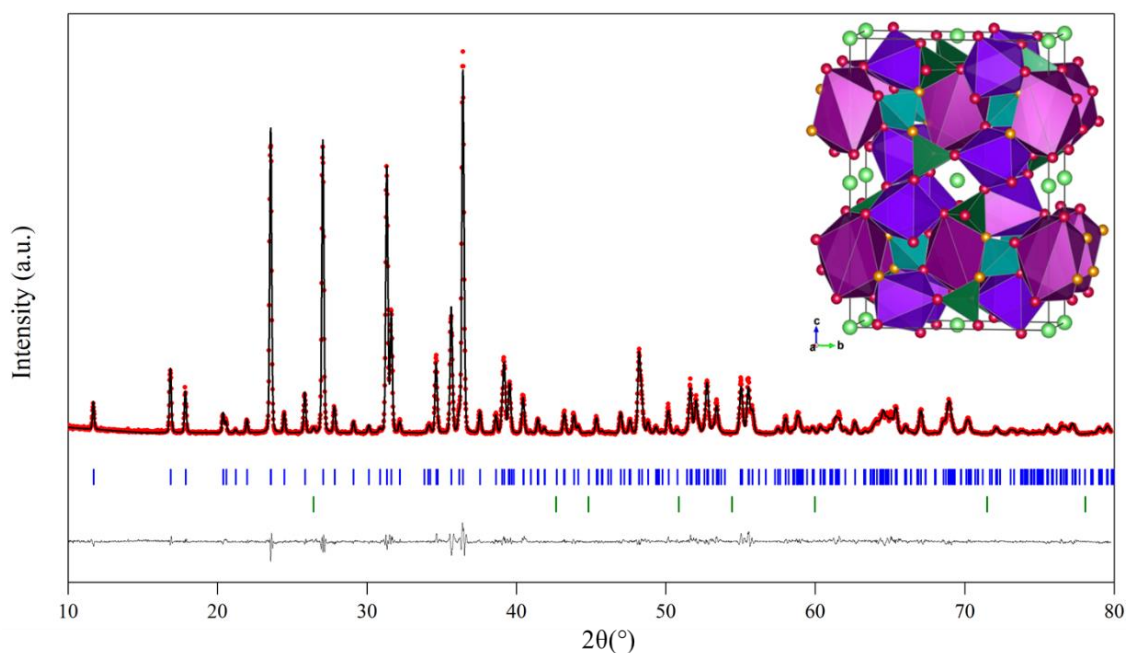
Figure 4.19: Results of the Rietveld refinement of the XRD pattern of a sample of Li$_{1.1}$Mn$_{2.9}$P$_3$O$_8$N$_2$ (eventual composition adapted to the results from the refinement). Red circles, black lines and grey lines represent the observed, calculated and difference patterns, respectively. Vertical blue bars indicate the positions of the Bragg reflections of the *Pbcn* space group. Vertical green bars indicate the position of the 0.6% graphite impurity from the crucible; Inset: Crystal structure of Li$_{1.1}$Mn$_{2.9}$P$_3$O$_8$N$_2$. Li, O and N atoms are shown as light green, red and orange balls, respectively. The (Mn1/Li1)O$_5$N$_1$ octahedra and (Mn2/Li2)O$_6$N$_2$ polyhedra are displayed in purple and pink, respectively. The (P1)O$_3$N and (P2)O$_2$N$_2$ octahedra are shown in dark green and cyan, respectively.

The XRD pattern of the Li$_{1.1}$Mn$_{2.9}$P$_3$O$_8$N$_2$ sample could be perfectly indexed using an orthorhombic unit cell having the *Pbcn* space group similar to that of Na$_{1.1}$Mn$_{2.9}$P$_3$O$_8$N$_2$, with slightly reduced lattice parameters: $a = 4.7835(2)$ Å, $b = 10.5063(4)$ Å, $c = 15.0972(6)$ Å and unit cell volume V = 758.75(5) Å^3, in agreement with the smaller size of Li$^+$ cation as compared to Na$^+$. We therefore performed a Rietveld refinement of the data for a Li$_{1.1}$Mn$_{2.9}$P$_3$O$_8$N$_2$ sample starting from the structural model determined for Na$_{1.1}$Mn$_{2.9}$P$_3$O$_8$N$_2$, while removing Na from the framework. Fourier difference maps performed with the GFourier program (Figure 4.20) enabled to locate the Li atoms around the 4*a* Wyckoff position (0,0,0), and revealed a clear ellipsoidal shape for both electronic and nuclear density maps.
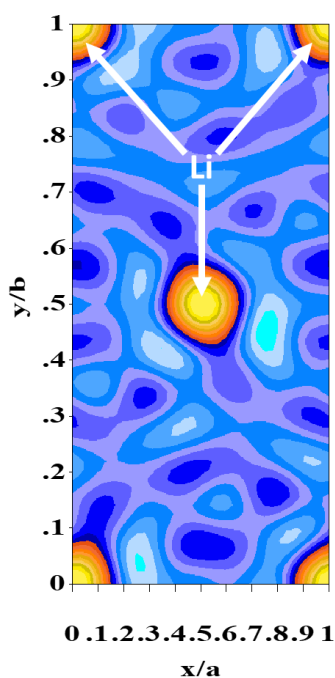
Figure 4.20: Difference Fourier map around the Li position for $Li_{1.1}Mn_{2.9}P_3O_8N_2$ calculated from the XRD data using a structural model without Li atoms.

As in $Na_{1.1}Mn_{2.9}P_3O_8N_2$, a small amount of Li was found yin the octahedral site of Mn2, therefore the eventual composition was found to be $Li_{1.1}Mn_{2.9}P_3O_8N_2$. The results of the refinement of the atomic positions together with the structural information obtained from the data set are gathered in Table 4.8. The crystal structure obtained from the refinement of the XRD pattern, being almost identical to the structure of the sodium counterpart, is shown in the inset of Figure 4.19.

Table 4.8: Structural parameters of $Li_{1.1}Mn_{2.9}P_3O_8N_2$ determined from the Rietveld refinement of the XRD pattern.

S.G.: *Pbcn*			$\chi^2 = 2.07$		RBragg = 3.75%	
$a = 4.7835(2)$ Å	$b = 10.5063(4)$ Å		$c = 15.0972(6)$ Å	$V = 758.75(5)$ Å^3		
Atom	Wyckoff site	x/a	y/b	z/c	Occupancy	B_{iso} (Å^2)
Li1	4c	0	0	0	1.0	1.2(7)
Mn1	8d	0.0185(4)	0.2835(16)	0.4008(12)	1.0	0.93(6)
Mn2 /Li2	4c	0	0.0266(2)	¼	0.984(3) 0.0016(3)	1.2(7)
P1	8d	0.423(6)	0.093(3)	0.103(2)	1.0	0.72(9)
P2	4c	0	0	0	1.0	0.7(1)
O1	8d	0.200(11)	0.457(6)	0.103(4)	1.0	0.03(8)
O2	8d	0.254(11)	0.096(5)	0.399(4)	1.0	0.03(8)
N3	8d	0.301(19)	0.168(7)	0.190(5)	1.0	0.03(8)
O4	8d	0.286(14)	0.162(5)	0.021(4)	1.0	0.03(8)
O5	8d	0.310(14)	0.345(6)	0.307(4)	1.0	0.03(8)

4.3.2. Chemical composition and electron microscopy

The chemical composition, and precisely the ratio between Li, Mn and P atoms in $Li_{1.1}Mn_{2.9}P_3O_8N_2$ was evaluated by EDX measurements and verified by inductively coupled plasma analysis (ICP). The results from both analyses are shown in Table 4.9 assuming a content of three P atoms in the nominal composition. The obtained results match well the expected theoretical ratios.

Table 4.9: Composition of $Li_{1.1}Mn_{2.9}P_3O_8N_2$ determined by EDX and ICP.

Element	Theoretical atomic ratio	Experimental atomic ratio determined from EDX	Experimental atomic ratio determined from ICP
Li	1.1	-	0.9±0.1
P	3	3.00 (fixed)	3.00 (fixed)
Mn	2.9	2.9±0.1	2.9±0.06
N	2	-	-

The amount of nitrogen was evaluated using CHNOS Elemental Analysis and the resulted amount of 1.8 N per formula unit is slightly smaller than the theoretical one.

An electron microscopy study was performed to analyze the morphology of $Li_{1.1}Mn_{2.8}P_3O_8N_2$ crystals. SEM images shown in Figure 4.21 indicate very similar appearance to the crystals of $Na_{1.1}Mn_{2.8}P_3O_8N_2$ with a non-uniform shape of the particles and a wide particle size distribution, varying from few to 20 µm. Additionally, small particles tend to agglomerate into ~30 µm clusters.
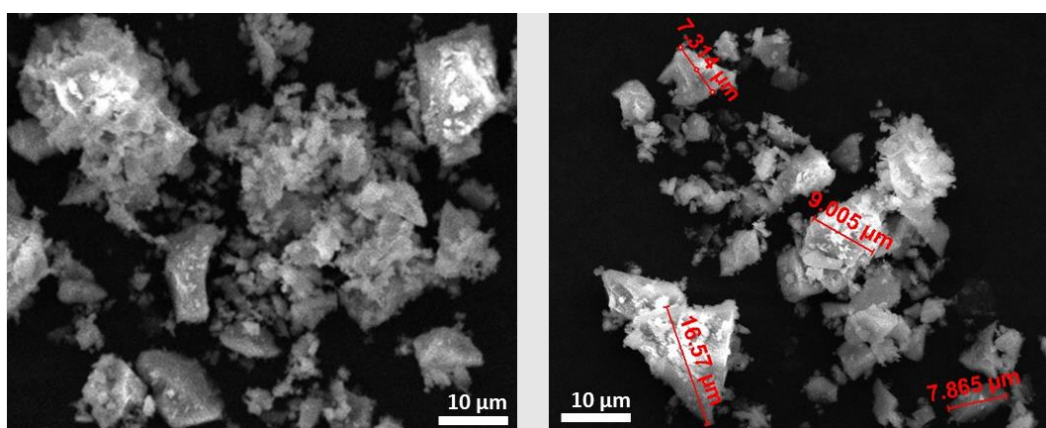
Figure 4.21: SEM images of $Li_{1.1}Mn_{2.8}P_3O_8N_2$.

4.3.3. Thermogravimetric analysis and high temperature XRD measurement

Thermogravimetric analysis of $Li_{1.1}Mn_{2.8}P_3O_8N_2$ were performed under synthetic air, in the temperature range 30-1000 °C at 10 °C.min^{-1} heating rate. The registered mass changes as a function of temperature together with the corresponding DTA curve are shown in Figure 4.22.
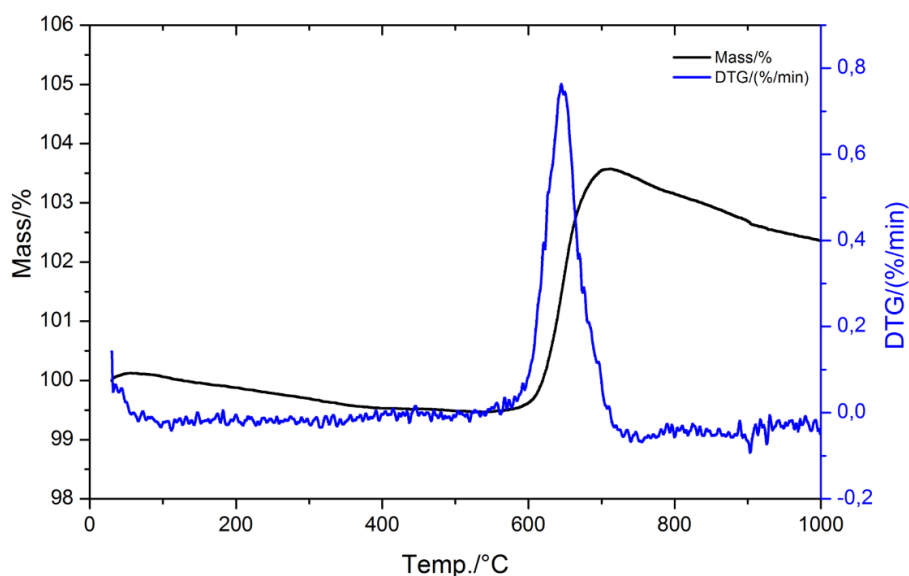
Figure 4.22: Thermogravimetric analysis (relative mass gain curve) obtained for $Li_{1.1}Mn_{2.9}P_3O_8N_2$ under synthetic air measured from room temperature to 1000 ^{0}C at 10 °C.min^{-1} heating rate.

Very similar results were obtained as for the sodium counterpart. The sample of $Li_{1.1}Mn_{2.9}P_3O_8N_2$ remains very stable up to approximately 600 ℃. Above this temperature a rapid mass gain can be observed, which, as in the case of $Na_{1.1}Mn_{2.8}P_3O_8N_2$ and other nitrogen-containing compounds, is the typical behavior related to the release of nitrogen and simultaneous uptake of oxygen.[233]

To observe the phase transition in detail, an *in-situ* high temperature XRD experiment under air flow was performed from RT to 900 °C at 10 °C.min^{-1} heating rate in a 2theta range of 10 - 60º. XRD patterns were recorded every 50 °C from RT to 900 °C. Figure 4.22 shows the collected XRD patterns, with different observed regions signaled by different colors.
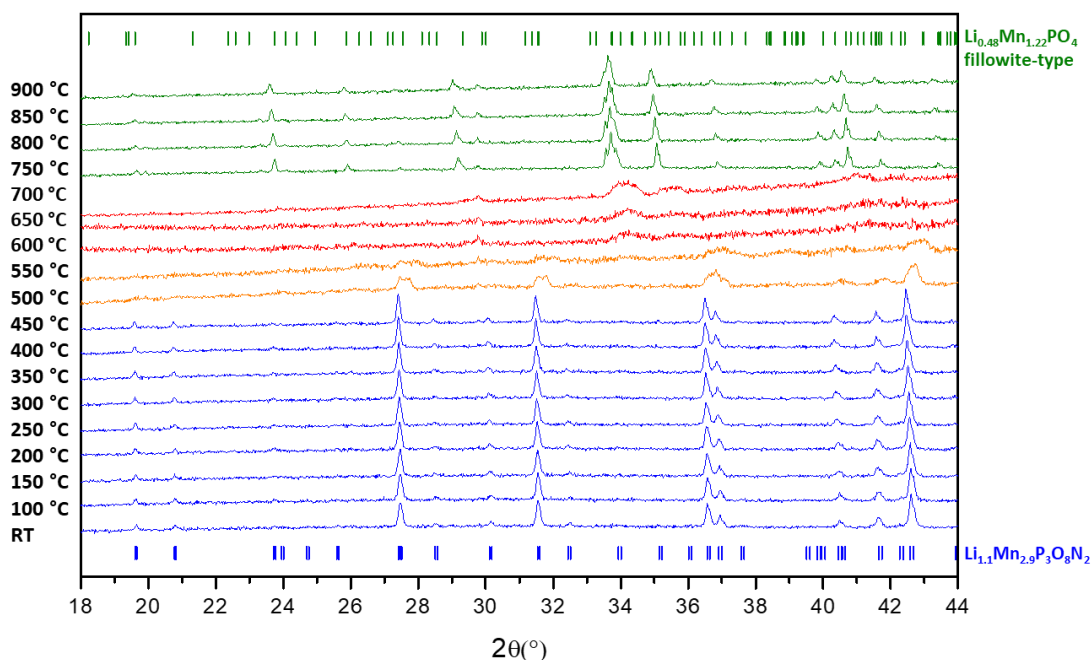
Figure 4.23: Evolution of the XRD patterns of $Li_{1.1}Mn_{2.9}P_3O_8N_2$ upon heating under air in the temperature range RT-900 °C. Blue color of the curves corresponds to the region of the stability of $Li_{1.1}Mn_{2.9}P_3O_8N_2$, while orange and red the region of the decomposition of the phase.

The first region, corresponding to the stability of the $Li_{1.1}Mn_{2.8}P_3O_8N_2$ structure, is indicated in blue. The framework remains stable up to 450 °C. Next, between 500 and 550 °C, the substantial broadening of the peaks indicates changes in the structure with eventual amorphization, as indicated by the red color of the curves. Contrary to $Na_{1.1}Mn_{2.8}P_3O_8N_2$, at 750 °C a recrystallization to a different phase was observed and indexed as fillowite-type "$Li_{0.48}Mn_{1.22}PO_4$". Although no crystallographic data were found on this latter compound, the indexation was made on the known sodium counterpart, $Na_{0.48}Mn_{1.22}PO_4$,[239] by changing the alkali cation and refining the unit cell parameters.

4.3.4. Magnetic measurements

The magnetic character of $Li_{1.1}Mn_{2.9}P_3O_8N_2$ was analyzed by performing magnetic measurements, in the same conditions as the measurement of $Na_{1.1}Mn_{2.8}P_3O_8N_2$. The zero-field cooled (ZFC) AC susceptibility measurements have been performed while cooling from 300 K to 2.5 K under an AC magnetic field of 10 Oe amplitude at a frequency of 10 kHz. The AC field cooled (FC) susceptibility measurements have been performed similarly to ZFC, cooling down to 2.5 K under an additional applied DC magnetic field of 1 T. Figure 4.24 shows the FC and ZFC susceptibility measurements of $Li_{1.1}Mn_{2.9}P_3O_8N_2$. The increase of the susceptibility with the decrease of the temperature

196

can be observed in the beginning of the experiment, until reaching ~40 K, slightly higher than observed for $Na_{1.1}Mn_{2.9}P_3O_8N_2$. Below this temperature, the susceptibility initially decreases until reaching a minimum near 15 K, below which it increases. The maximum observed at 38 K can be identified as Néel temperature T_N, which marks the transition from paramagnetic to antiferromagnetic ordering. The difference of just 5 K between $Li_{1.1}Mn_{2.9}P_3O_8N_2$ and $Na_{1.1}Mn_{2.9}P_3O_8N_2$ indicates the remarkably similar behaviour of these two materials. However, contrary to $Na_{1.1}Mn_{2.9}P_3O_8N_2$, no noticeable difference is observed between FC and ZFC susceptibility measurements, which is consistent with an antiferromagnetic ordering and indicates a high purity of the sample.
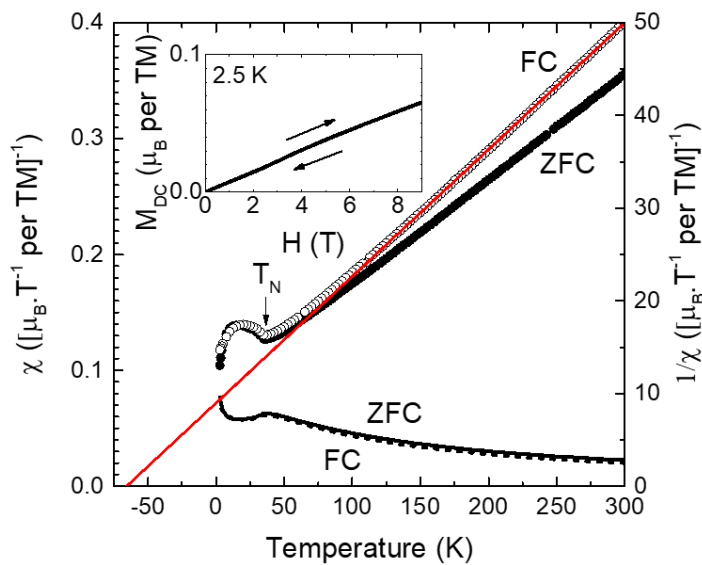
Figure 4.24: Susceptibility (left axis) and inverse susceptibility (right axis) of $Li_{1.1}Mn_{2.9}P_3O_8N_2$ in ZFC and FC (1T DC) modes. The fit with the Curie-Weiss law is shown by the red line. Inset: DC magnetization versus magnetic field at 2.5 K. The Néel temperature of 33 K is indicated by an arrow.

The FC inverse susceptibility curve was used to calculate the effective moment μ_{eff}, as shown in Figure 4.15. By performing the linear fitting of the curve, the μ_{eff} was extracted from the slope in the high temperature limit, in the same manner as for $Na_{1.1}Mn_{2.9}P_3O_8N_2$ (section 4.2.5). The value μ_{eff} deduced from the fit of the FC inverse susceptibilities of 5.71 μ_B per Mn (slightly lower than the one obtained for $Na_{1.1}Mn_{2.9}P_3O_8N_2$) is very close to the theoretical value expected for pure Mn^{II} (5.92 μ_B per Mn), confirming the expected oxidation state. The Weiss constant is negative, close to -62 K, which is a further indication that the main interaction in the paramagnetic state is antiferromagnetic.

4.3.5. Solid State Nuclear Magnetic Resonance analysis

The ^{7}Li solid-state NMR spectrum of $Li_{1.1}Mn_{2.9}P_3O_8N_2$ is shown in Figure 4.25. The most intense resonance at around 45 ppm (signal labelled *a* in blue in Figure 4.25) is attributed to the Li3 in octahedral environment, while the tiny peak at around 0 ppm is assigned to the lithium cations on the Mn2 site, being in perfect agreement with the results from the XRD. Based on the fitting, the relative intensities between these two gaussian signals are observed to be 96 : 4, as indicated in Table 4.10. These results corroborate the finding from the XRD and magnetic measurement concerning the absence of the impurities in $Li_{1.1}Mn_{2.9}P_3O_8N_2$.
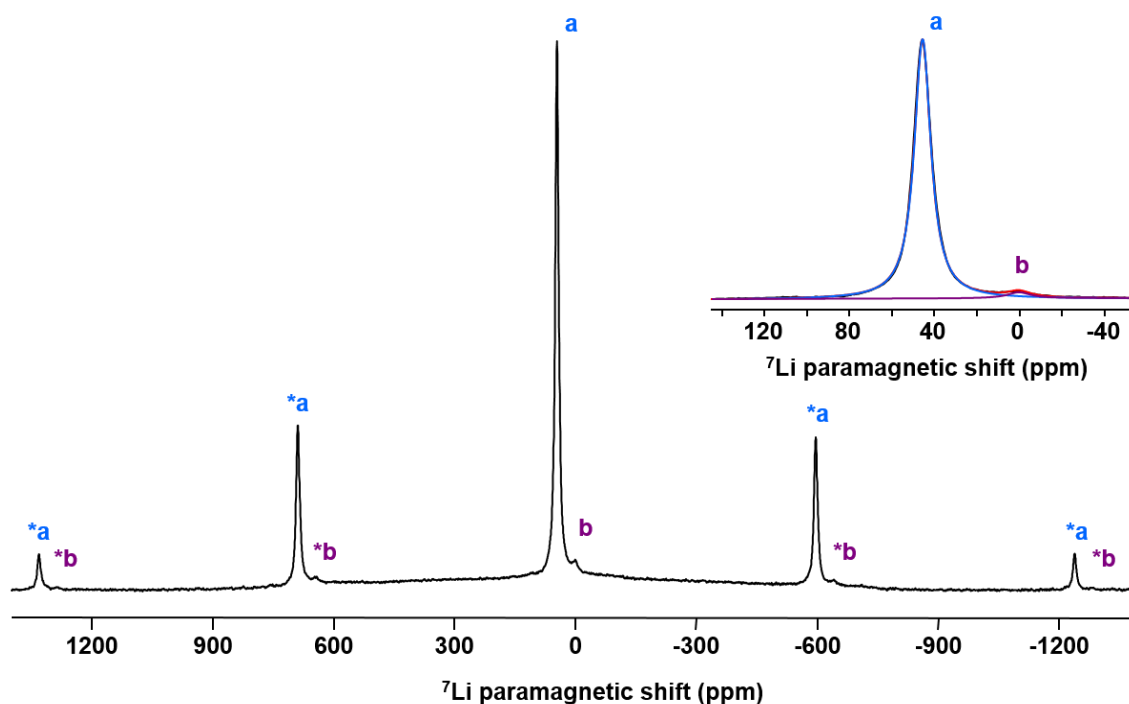
Figure 4.25: ^{7}Li solid-state MAS NMR spectrum of $Li_{1.1}Mn_{2.9}P_3O_8N_2$. **The isotropic resonances of the two signals are labeled by the letters *a* (in blue) and *b* (in purple), and their respective spinning sidebands are indicated by asterisks. In inset: result of the fit of the central part of the spectrum using two components. The experimental spectrum is plotted in black, while the red line is the fit, which is deconvoluted into the *a* (in blue) and *b* (in purple) components.**

Table 4.10: Fitted NMR parameters of the ^{6}Li spectra in $Li_{1.1}Mn_{2.9}P_3O_8N_2$.

Component	δ [ppm]	Quantification [%]
a	46	96
b	0	4

4.3.6. Electrochemical activity evaluation and voltage calculations

As it was explained in section 4.2.7.; $Na_{1.1}Mn_{2.9}P_3O_8N_2$ remains electrochemically inactive due to the narrow bottleneck limiting Na cation diffusion pathway. Although the framework only slightly changed for $Li_{1.1}Mn_{2.9}P_3O_8N_2$, still we decided to verify the performance of this compound with a smaller alkali cation as a potential cathode material.

First, DFT voltage predictions were performed by the Modeling and Computational group to identify the expected working voltage of the Mn^{II}/Mn^{III} redox couple in $Li_{1.1}Mn_{2.9}P_3O_8N_2$. Similar voltage calculations were performed as for $Na_{1.1}Mn_{2.9}P_3O_8N_2$, using the energies calculated within DFT.[215,240]

$$V = -\frac{E(Li_nH) - E(Li_{n-x}H) - xE(Li)}{xe}$$

where H is the host structure, and e is the electronic charge.

These calculations predict an average voltage of 3.3 V *vs.* Li^+/Li^0. Therefore, the computed voltage difference between Na and Li system is only 0.05 V. While this might seem surprising at first sight, it is in alignment with the experimental results of $Na_3V(PO_3)_3N$ (Chapter 2).

The electrochemical properties of the $Li_{.1}Mn_{2.9}P_3O_8N_2$ were tested in half-cell configuration with metallic sodium or lithium as a negative electrode and $LiPF_6/NaPF_6$ in EC:DMC (1:1 vol) as electrolyte in 2032-type coin cells.

Two types of electrodes were prepared, with different kind and amount of carbon (same formulation and conditions as for $Na_{1.1}Mn_{2.9}P_3O_8N_2$). Galvanostatic charge-discharge curves together with their derivative curves are presented in Figure 4.17 where a&b correspond to the cells with 10% of C_{65}; whereas c&d with 15% of Ketjen Black.
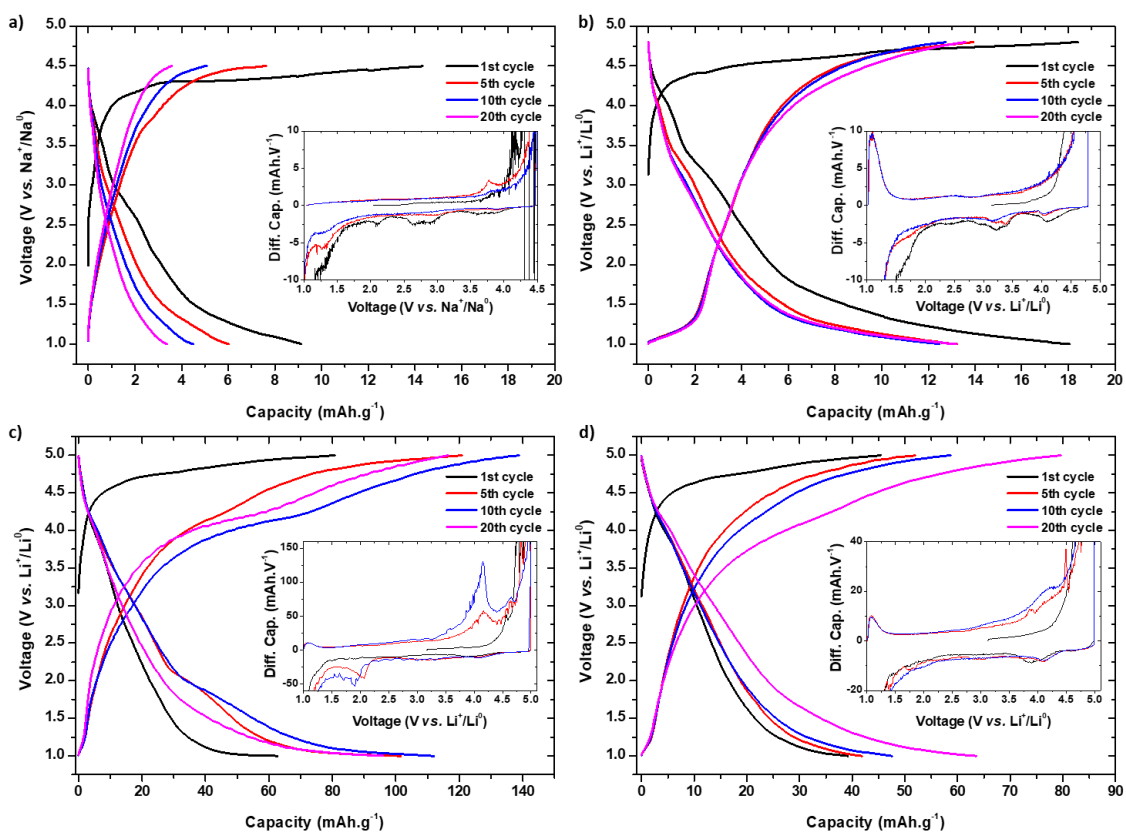
Figure 4.26: (a&b) Galvanostatic charge discharge curves of Li₁.₁Mn₂.₉P₃O₈N₂ against (a) Na⁺/Na⁰ and (b) Li⁺/Li⁰ metal at C/40 rate with the electrode prepared with 10% of C₆₅; (c&d) Galvanostatic charge discharge curves of Li₁.₁Mn₂.₉P₃O₈N₂ against Li⁺/Li⁰ at (a) C/40 rate; (b) C/20 rate; with the electrode prepared with 15% of ketjen black. Inset of (a, b,c & d) – derivative dQ/dV curves of the 1ˢᵗ, 5ᵗʰ and 10ᵗʰ cycle.

The very low capacities obtained for the cells prepared with C_{65} carbon suggest no electrochemical performance like for $Na_{1.1}Mn_{2.9}P_3O_8N_2$, however a small anodic peak can be observed at ~3.3 V *vs.* Li^+/Li^0 in the derivative curves of the cell cycled *vs.* Li anode (inset in Figure 4.26b), being in perfect agreement with the voltage obtained from DFT calculations. The use of Ketjen Black significantly improved the capacity, as can be observed in Figure 4.26c, although previously presented signal in the derivative curves was absent and a large signal in the charge and very slight in the discharge curves at ~4.0 V *vs.* Li^+/Li^0 (inset in Figure 4.26c) was observed instead. This could be attributed to the redox reaction of the Mn^{II}/Mn^{III} redox couple (although higher than one predicted by the DFT calculations). Additionally, the shape of the curves at high voltages (>4.5 V) suggests the occurrence of side reaction such as oxidation of the electrolyte. Attempting to reduce the influence of this side reactions, the cell was further cycled faster, at a C/20 rate. As shown in Figure 4.26d, this resulted with a large drop of the capacity, however indeed significantly decreased the side reactions. The observed signals at ~4 V in the dq/dV curves which were tentatively assigned to the redox reaction of the Mn^{II}/Mn^{III}

200

couple are less visible in charge, however became more intense in discharge at ~4.0 V *vs.* Li^+/Li^0. The observed gradual increase of the capacity could be explained by the slight modifications in the structure and/or the oxidation of the nitrogen and would require further analysis such as *ex situ* XRD and *ex situ* Raman or XAS measurements. However, as overall electrochemical performance of $Li_{1.1}Mn_{2.9}P_3O_8N_2$ was very poor, no further electrochemical investigations were conducted. Additionally, the BVEL calculations performed for $Li_{1.1}Mn_{2.9}P_3O_8N_2$ revealed also very high values of percolation energy $E_{th} = 4.2$ eV, which clearly indicates a difficile diffusion of the alkali cations within the structure and no improvement in the lithium compound with respect to the sodium one.

4.4. Conclusions

In this chapter, we have unveiled a novel family of sodium manganese nitridophosphates $A_{1.1}Mn_3P_3O_8N_2$ (A = Na/Li). Their unknown orthorhombic crystal structure was solved and confirmed by a combination of complementary characterization techniques as well as theoretical calculations. The preparation of the lithium counterpart, to the best of our knowledge, is the first direct synthesis of lithium nitrogen-based polyanionic compound.

DTF calculations predicted activity of the $Mn^{II/III}$ redox couple at a potential compatible with common organic electrolytes (3.25 V *vs.* Na^+/Na^0 and 3.30 V *vs.* Li^+/Li^0), however based on the performed experimental tests, sodium and lithium extraction from these structures was not significantly achieved. The BVEL calculations revealed indeed very high values of percolation energies (>4 eV) indicating a difficile diffusion of the alkali cations within the structure, most probably resulting from the presence of narrow bottlenecks on the course of the alkali cations diffusion pathways.

Although the goal of synthesizing an attractive cathode material was not fulfilled, we have demonstrated that the research into nitrogen-containing polyanionic compound should be pursued as novel materials are yet to be discovered.

General conclusions for Part A

The Part A of this thesis has introduced the interesting family of nitridophospates with the general formulae of $A_3M(PO_3)_3N$ and $A_2M_2(PO_3)_3N$, where A = Na, Li and M = V, Fe, Co, Mn.

In Chapter two we presented the synthesis, detailed structural analysis and electrochemical performance of $Na_3V(PO_3)_3N$. This compound can be successfully synthesized using two methods, either using the flow of ammonia at high temperature (ammonolysis), either with the use of melamine, mixed together with the precursors and annealed under Argon. Thermogravimetric studies revealed remarkable high thermal stability. Electrochemical studies of $Na_3V(PO_3)_3N$ were performed as a potential cathode material for Na-ion and Li-ion batteries and it was shown for the first time that $Na_3V(PO_3)_3N$ offers a stable capacity with very low voltage hysteresis, although only Na1 is found to be extracted and reinserted. The working potential was found to be very high, 4.0 V *vs.* Na^+/Na^0 and 4.1 V *vs.* Li^+/Li^0, with a remarkable small difference in the insertion voltage between both alkali metal reference electrodes. To the best of our knowledge this is the Na-ion cathode material with the highest operation voltage for the V^{IV}/V^{III} redox couple together with $Na_7V_3(P_2O_7)_4$. [201] Based on the DFT calculations, the extraction of more than one sodium cation is prevented because the potential of the redox couple V^V/V^{VI} is predicted to be beyond the voltage stability window of the electrolytes available up to now. Additionally, we presented the successful complete ion exchange into $Li_3V(PO_3)_3N$ with the electrochemical activity of the V^{IV}/V^{III} redox couple centred around 3.9 V *vs.* Li^+/Li^0.

Next, Chapter three was dedicated to different solid solutions of CUBICON nitridophosphates focusing on low cost and earth abundant 3d metals as iron and manganese. Additionally, cobalt also was investigated due to the expected elevated working voltage. $Na_2Fe_2(PO_3)_3N$ offers a stable capacity of 60 mAh.g^{-1} *vs.* Li in hybrid-ion configuration with average voltage of 3 V *vs.* Li^+/Li^0, indicating improved performances compared to the ones reported so far (capacities of ~40 mAh.g^{-1} and high polarization). [18] The lack of previous results *vs.* Na metal suggested unsuccessful extraction/insertion of Na^+ ions within the framework, however here we demonstrated the stable, although limited, mobility of ~0.55 Na^+ ions at 2.9 V *vs.* Na^+/Na^0 while cycling $Na_2Fe_2(PO_3)_3N$ *vs.* Na metal. Analysis of the operando synchrotron XRD measurement

suggests a biphasic mechanism of Na insertion/extraction with the presence of both Na-rich and Na-poor phases. The chemical oxidation of $Na_2Fe_2(PO_3)_3N$ with a strong oxidizing agent such as NO_2BF_4 resulted with the complete removal of one sodium from the cubic framework. The removal of the second Na^+ ion was not achieved, suggesting very high stability of the oxidized $NaFe_2(PO_3)_3N$ phase requiring very high additional energy to transform into less favorable desodiated $Fe_2(PO_3)_3N$ state.

The $Na_2Co_{2x}Fe_{2-2x}(PO_3)_3N$ solid solution was also prepared, with the successful synthesis of $Na_2Co_2(PO_3)_3N$ for the first time. The first electrochemical tests resulted with poor electrochemical performance and only a slight redox activity of the $Co^{II/III}$ couple around 3.7 V $vs.$ Li^+/Li^0 and 3.5 V $vs.$ Na^+/Na^0 in the charge and 3.4 V $vs.$ Li^+/Li^0 and 2.7 V $vs.$ Na^+/Na^0 in the discharge for $Na_2Co_{1.6}Fe_{0.4}(PO_3)_3N$, however $Na_2Co_2(PO_3)_3N$ was found to be totally inactive. Thermogravimetric studies of both end members - $NaFe_2(PO_3)_3N$ and $Na_2Co_2(PO_3)_3N$ revealed remarkable high thermal stability.

Finally, the stabilization of Mn-based CUBICON structure was not possible, and it was shown that Mn-based CUBICON phases require the presence of a foreign atom such as Al^{III} or Fe^{II} to stabilize the cubic structure. However, in Chapter four we introduced a new sodium manganese nitrodophosphate $A_{1.1}Mn_3P_3O_8N_2$ (A = Na/Li). These materials were found to crystallize in an orthorhombic structure, that was resolved and confirmed by a combination of complementary characterization techniques as well as theoretical calculations. The preparation of the lithium counterpart, to the best of our knowledge, is the first direct synthesis of lithium nitrogen-based polyanionic compound. DTF calculations predicted activity of the $Mn^{II/III}$ redox couple at a potential compatible with common organic electrolytes (3.25 V $vs.$ Na^+/Na^0 and 3.30 V $vs.$ Li^+/Li^0), however based on the performed experimental tests, sodium and lithium extraction from these structures was not achieved. BVEL calculations revealed very high values of percolation energies (>4 eV) indicating a difficile diffusion of the alkali cations within the structure, most probably resulting from the presence of narrow bottlenecks on the course of the alkali cations diffusion pathways.

These results demonstrate that the BVEL method allows identifying interesting insertion materials to be used as positive electrodes in Li and Na batteries and can even result in the discovery of new compounds. Despite the electrochemical performance of these systems was not competitive with other state of the art materials, research into nitrogen-

containing polyanionic compound should be maintained as novel attractive materials are yet to be discovered.

Garnet-type and Vanadium VF$_3$-type fluorides

Part B

Outline

Introduction of Part B

Despite the difficulty in handling the fluorides and fluorinating reagents like highly reacting and dangerous fluorine gas, fluorine-type compounds are used in a broad range of applications – electronics, catalysis, medicine, agriculture and nuclear energy.[102,241] Having the highest electronegativity and a small polarizability, fluorine is able to form strong and stable bonds with other elements. In particular, metal-fluorine bonds have a very high ionicity, resulting in high reduction reaction potentials. This phenomenon is well illustrated while analyzing the operating voltages in different compounds having same redox couple.[100,242] As shown in Figure B.1. on the example of Fe^{II}/Fe^{III} and V^{III}/V^{IV} redox couples, compounds with fluorine directly bonded to the transition metal (redox center) operate at higher voltages than the related oxides and phosphates.
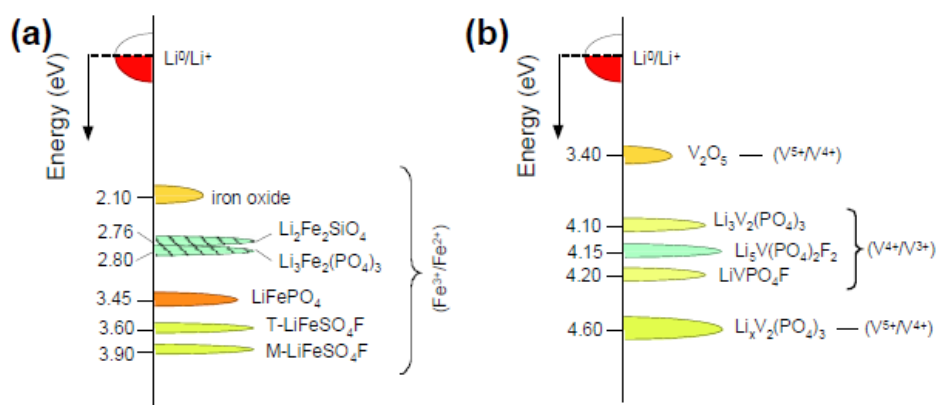
Figure B.1.: Energy of the (a) iron and (b) vanadium redox couples within the phosphate frameworks relative to the Fermi level of metallic lithium.[100]

The effect of the fluorine substitution on the operating voltage has been investigated by Arroyo y de Dompablo et al. by performing first principles calculations.[242] They demonstrated that more ionic M-F bond results with the stabilization of the energy of the antibonding $3d$ orbitals of the transition metal, increasing the lithium insertion voltage. In the field of electrode materials, 3D polyanionic compounds have been widely explored due to their tunable redox potential and structural stability.[101,79,243] The inductive effect of the polyanionic $(XO_4)^{n-}$ group was found to be responsible for the elevating of the redox potential of the polyanionic framework due to the strong X-O covalent bond.[244,245] Fluorine substitution further enhances the inductive effect of the adjacent transition metal ions consequently increasing the working voltage.

Various families of fluorosulfates and fluorophosphates have been investigated as positive electrode materials in both sodium and lithium-ion batteries.[100–104]

Apart from polyanionic F-based compounds introduced in Chapter 1, metal fluorides have been found to exhibit great potential as cathode materials for both lithium and sodium ion batteries. Remarkably the lower molecular weight of metal fluorides results in increased capacities and specific energies. Three main families of fluoride compounds studied as cathode materials are described below.

- ***Perovskite*-type AMF$_3$**

The first example of ternary metal fluorides is the family of *perovskite*-type AMF$_3$ (A = Li, Na; M = Fe, Mn, Co and Ni) with the orthorhombic structure and *Pnma* space group (Figure B.). This structure can easily accommodate alkali cations within its open framework. Theoretical capacity of 197 mAh.g^{-1} was achieved at a rate of 0.076 mA.cm^{-2} at an average voltage of 2.7 V *vs.* Na$^+$/Na^0 for NaFeF$_3$ being the highest capacity obtained for the iron-based cathode materials for sodium-ion batteries.[246,247] Although the working voltages are lower than the corresponding sulphates or phosphates, much lower molecular weight of the fluorides results in higher capacities delivered by these materials.

- ***Cryolite*-type A$_3$MF$_6$**

Fluorides with general formula A$_3$MF$_6$ crystallize in the *cryolite*-type structure with MF$_6$ octahedra located in the edge of the crystal lattice (Figure B.2c).[248] Two polymorphs (α & β) of *cryolite* A$_3$MF$_6$ were found. Within this family, Li$_3$FeF$_6$ and Li$_3$VF$_6$ have been extensively studied by the group of García-Alvarado.[249–251]

Orthorhombic α-Li$_3$FeF$_6$ with space group *Pna*2$_1$, delivers full theoretical capacity of 140 mAh.g^{-1} at a current density of 0.1 mA.cm^{-2} at ~3.1 V *vs.* Li$^+$/Li^0 for the Fe$^{III/II}$ redox couple. Monoclinic β-Li$_3$VF$_6$ with space group *C*2/*c* also delivers theoretical capacity of 144 mAh.g^{-1} corresponding to the complete reduction of V^{III} to V^{II} at an average voltage of 2 V *vs.* Li$^+$/Li^0. [250]

- ***weberite*-type Na$_2$MM`F$_7$**

Another group of appealing metal fluorides recently proposed as cathode materials for sodium-ion batteries are *weberite*-type compounds with Na$_2$MM`F$_7$ structure.[252] Based on theoretical calculations, these materials can offer high voltage and high energy density

and possess low-energy two-dimensional pathways for Na^+ diffusion. Figure B.2b shows the crystal structure of mineral Na_2MgAlF_7, being the parent of the *weberite* compounds. By replacing Mg^{II} and Al^{III} with other divalent and trivalent cations, such as Fe^{II} and V^{III}, high theoretical capacities may be obtained at ~3.6 V *vs.* Na^+/Na^0. Based on the calculations, a theoretical capacity of 187 mAh.g^{-1} can be obtained by the oxidation of both cations and extraction of two Na^+ ions.[252]
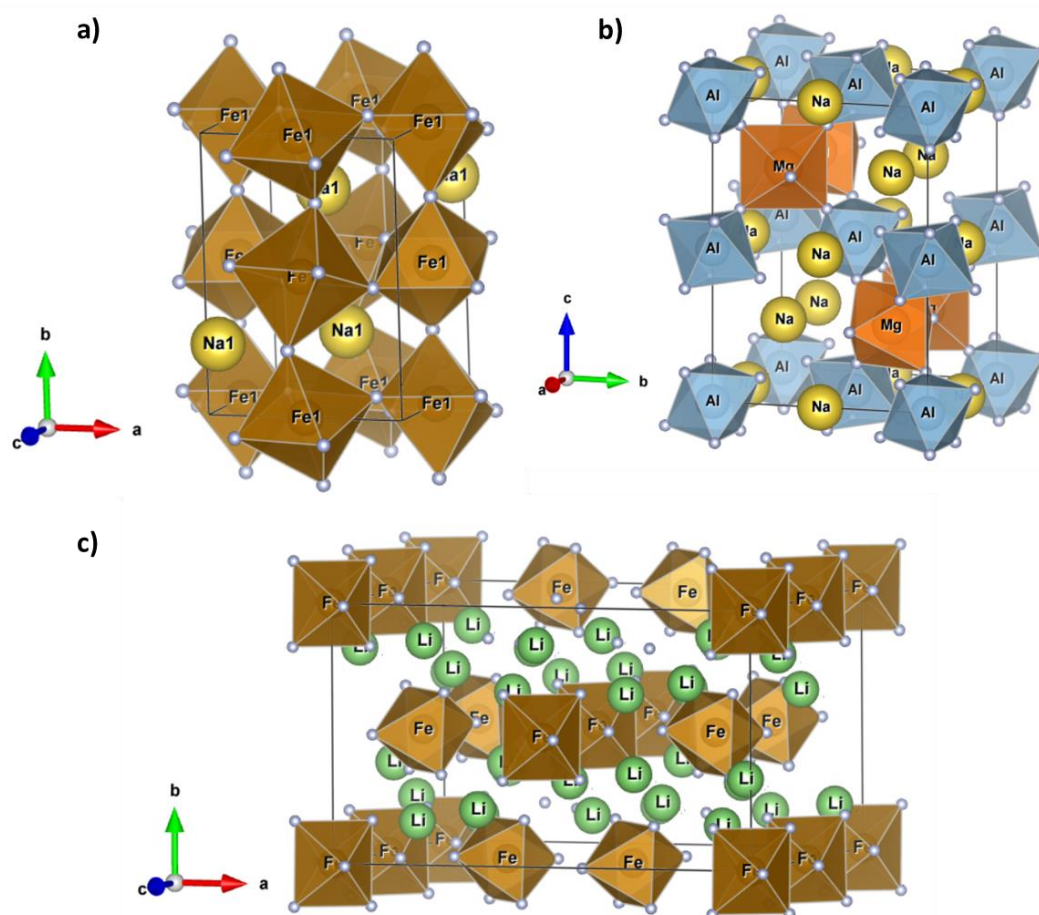
Figure B.2: crystal structures of (a) *perovskite*-type $NaFeF_3$; (b) *weberite* Na_2MgAlF_7; (c) *cryolite*-type α-Li_3FeF_6. Fe, Al and Mn octahedra are colored in brown, blue and orange, respectively. Na atoms are indicated as yellow balls, lithium as green balls, and finally fluorine as silver balls.

In this work we have focused our attention in two families of fluoride materials – first, garnet fluorides, that to our knowledge were not previously explored as potential cathode materials, and VF_3-type compounds due to the very high theoretical capacities which could offer very attractive electrochemical performances. The novel synthesis method applying the use of the microwave will be employed and the detailed structural analysis will be provided. Next, the as-synthesized materials will be used in half-cell configuration and electrochemically tested to investigate their properties as potential cathode materials.

Chapter 5 - Garnet-type fluorides as cathode materials for Na-ion and Li-ion batteries

Outline

Chapter 5 - Garnet-type fluorides as cathode materials for Na-ion and Li-ion batteries

5.1. Introduction

Originally, garnet compounds correspond to natural orthosilicates with general formula $A_3B_2Si_3O_{12}$, where A refers to a eight-coordinated divalent cation such as Ca^{II}, Mg^{II}, Fe^{II}, Mn^{II} and B to a six-coordinated trivalent cation such as Al^{III}, Fe^{III}, Cr^{III}. These materials crystallize in a face-centered cubic structure with *Ia-3d* space goup.[253] Their structure flexibility allows for various chemical substitutions resulting in a wide group of compounds, such as replacement of silicon by other elements, e.g. $A_3B_5O_{12}$, where A = Ca, Mg, Y, Ln, La and B = Al, Fe, Mn, Ni, V, Ga, Ge.[254–257]

Garnet-type oxides are well known Li-ion conductors making them one of the most promising electrolytes for all-solid-state Li-ion batteries.[258–263] The cubic structure of these compounds is able to accommodate additional Li^+ ions thanks to the rearrangement of the Li^+ ions in the interstitial spaces, which allows increasing the number of charge carriers, and therefore the ionic conductivity. Within this family, $Li_7La_3Zr_2O_{12}$ (LLZO) exhibits one of the highest Li-ion conductivities at room temperature for a solid material ($\sim 10^{-3}$ S.cm^{-1}) and very high stability against metallic Li.[262]

As for electrode application, the electrochemical insertion of Li^+ ions into the garnet framework was investigated by the group of Goodenough on $Li_3Nd_3W_2O_{12}$.[259] Four Li^+ ions were inserted with the reversible redox reaction of W^{VI}/W^V at $0.8 – 0.85$ V *vs.* Li^+/Li^0 and W^V/W^{IV} at 0.4-0.5 V *vs.* Li^+/Li^0 with a discharge capacity of 310 mAh.g^{-1} at 0.05 C rate. Despite this example involves high cost and low abundant elements, it proves that garnet compounds can be successfully applied as intercalation electrode materials.

The garnet fluorides of interest in this chapter with the general formula $Na_3Li_3M_2F_{12}$, (M= Ti, Fe, V, Co, Cr) were first synthesized and characterized in the '60s.[264,265] These materials attract the attention due to the presence of fluorine which is expected to result in higher operating voltages as compared to oxides when used as cathode material, but also to the presence of both Na^+ and Li^+ cations within the structure. It is the only known garnet family with mixed alkali cations.

The only natural mineral of the fluoride garnets family is the *cryolithionite* $Na_3Li_3Al_2F_{12}$. Its crystal structure, solved by Menzer[266] in 1927, can be indexed in the *Ia-3d* space group ($a = 12.122$ Å). The crystal structure is shown in Figure and the detailed crystallographic data is shown in Table 5.1.[255,267] Within this three-dimensional framework, each AlF_6 octahedron (red) is joined to six others through vertex-sharing LiF_4 tetrahedra (green). Na cations (represented as yellow spheres) occupy eight-fold interstitial positions forming dodecahedra/distorted cubes. Interestingly, it is the only garnet structure where the tetrahedral cation-anion distance is longer than the octahedral cation-anion one. Later, in late '60s, several fluorine-based compounds crystallizing in the garnet $Na_3Li_3M_2F_{12}$ structure have been described, with M= trivalent metal ion (Al, Fe, Co, Ti, Ga, In, Mn, V, Sc, Rh).[264,265,268–270]
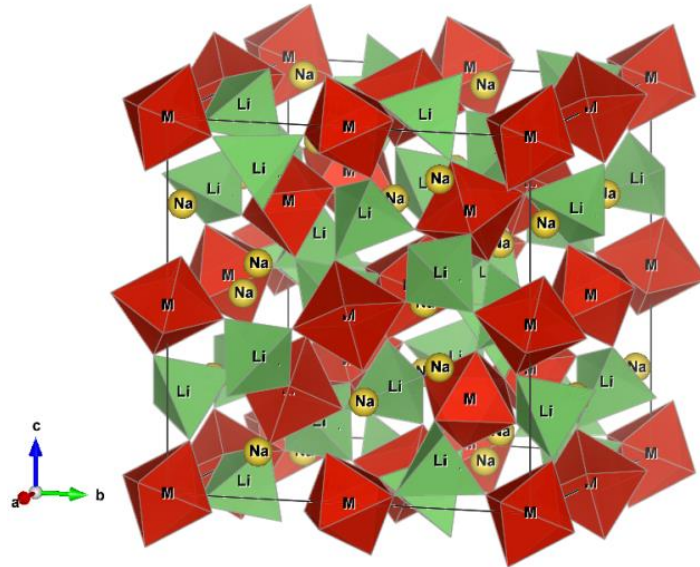
Figure 5.1: Unit cell representation of $Na_3Li_3M_2F_{12}$ where MF_6 octahedra are indicated in red, LiF_4 tetrahedra in green and Na atoms are shown in yellow.

Table 5.1: Crystallographic data and atomic coordinates of $Na_3Li_3M_2F_{12}$.

Cubic, S.G.: *Ia-3d*

Atom	Wyckoff position	x/a	y/b	z/c
M	16*a*	0	0	0
Na	24*c*	¼	⅛	0
Li	24*d*	¼	⅜	0
F	96*f*	*x*	*y*	*z*

The $Na_3Li_3M^{III}_2F_{12}$ family of compounds was identified by our group to be attractive candidates for electrode materials from high-throughput BVEL calculations (described in Chapter 1).[271] Its calculated low ion migration energy for Na^+ (<0.70 eV) is expected to

result with fast mobility of alkali metals within the structure. Combined with a theoretical capacity of ~130 mAh.g^{-1} considering the reversible insertion and/or extraction of two alkali cations and a high voltage resulting from F electronegativity, these materials could be appealing Li-ion or Na-ion cathode materials. Besides the reported compounds with trivalent Mn and V, we also decided to explore the Fe, Ti and Co-based compounds. All these trivalent transition metals are expected to provide good electrochemical performance through redox reactions of the M^{III}/M^{II} and M^{III}/M^{IV} couples. To our knowledge, none of these compounds have been previously tested as electrode materials.

All the literature records regarding the synthesis of this family of materials date back to the '60s – late '70s of the past century.[255,264,265,267,270,272,273] Four different types of syntheses were proposed:

a) Solid state synthesis at 800 °C (for M=V, Cr and Fe) and 650 °C (for M = Mn, Sc, Rh) in platinum and gold sealed tubes, respectively, according to reaction:

$$3LiF + 3NaF + 2MF_3 \rightarrow Na_3Li_3M_2F_{12} \ (M = \ V, Cr, Fe, Sc, In, Rh)$$
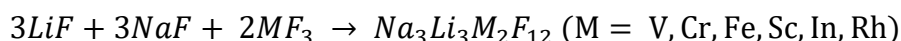
b) Fluorination in a nickel crucible for M=Co with the use of F$_2$ gas at 480°C during 2h, according to reaction:

$$3LiF + 3NaF + 2CoO + 6F_2 \rightarrow Na_3Li_3Co_2F_{12} + O_2$$
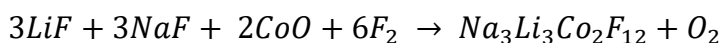
c) Two-step reaction for M=Ti: first heating the mixture of 3 NaF, 3 LiF and 2 TiO$_2$ at 300°C for 2h under constant flow of F$_2$, followed by mixing obtained powders with Si and heating the mixture in monel (nickel alloy) tube at 800°C under nitrogen flow to reduce Ti^{IV} to Ti^{III} according to reaction:

$$2 \, (3NaF, 3LiF, 2TiF_4) + \ Si \ \rightarrow \ 2 \, Na_3Li_3Ti_2F_{12} + \ SiF_4 \uparrow$$
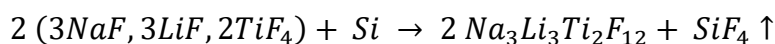
d) Coprecipitation in aqueous solution for M=Al, Fe, Cr.[270] First, selected precursors for the synthesis were dissolved in water (1) and (3) or HCl aqueous solution (2); next they were mixed with 45% HF aqueous solution and methanol in a 1:10 molar ratio; stirred at room temperature to give a precipitate, filtered, washed with methanol and dried. The expected reactions are:

(1) $NaOH + 3LiOHxH_2O + 2NaAlO_2 + \ 12HF \ \rightarrow \ Na_3Li_3Al_2F_{12}$

(2) $NaOH + 3LiOHxH_2O + 2NaFeO_2 + \ 12HF \ \rightarrow \ Na_3Li_3Fe_2F_{12}$

(3) $NaOH + 3LiOHxH_2O + 2CrCl_3 \cdot x6H_2O + \ 12HF \ \rightarrow \ Na_3Li_3Cr_2F_{12}$
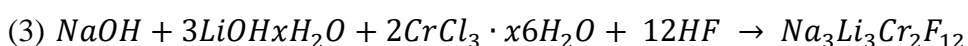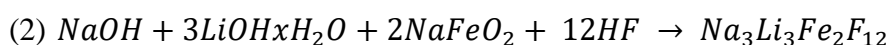
Materials' characteristics (color, cell parameter) and synthesis routes are summarized in Table 5.2.

Attempts to synthesize Mn^{III}, Co^{III} and Ni^{III} garnets using coprecipitation in aqueous solution method were reported to be unsuccessful and no precipitation occurred. This was explained by the change of the valency of the cations into the divalent state in presence of HF.

Table 5.2: Characteristic parameters (color and *a* cell parameter) of fluoride $Na_3Li_3M^{III}_2F_{12}$ garnets together with their synthesis routes developed by different groups [264,265,270,272,273]

metal	Color	*a* (Å)	synthesis route
Ti	violet	12.498 ±0.003[264]	1° Solid-state under F_2, 300°C
			2° solid state in monel tube under nitrogen, 800°C
V	light green	12.409±0.006 [264] 12.434±0.006 [273]	Solid-state in platinum sealed tubes, 800°C
Cr	Green	12.328±0.002 [264] 12.340±0.006 [273] 12.334±0.004 [270]	Solid-state in platinum sealed tubes, 800°C Aqueous solution
Fe	white	12.393±0.002 [264] 12.404±0.005 [273] 12.407±0.002 [270]	Solid-state in platinum sealed tubes, 800°C Aqueous solution
Al	white	12.119±0.004 [270]	Aqueous solution
Co	light brown	12.326±0.002	Solid-state under F_2, 480°C
Sc	white	12.607±0.003	Solid-state in gold sealed tube, 500°C
In	white	12.693±0.003	Solid-state in gold sealed tube, 500°C
Rh	black	12.415±0.003	Solid-state under F_2, 500°C
Ni	tan	12.165±0.030	Solid-state under F_2, 500°C

We decided to employ two synthesis methods – mechanochemical using ball milling and a novel microwave-assisted solvothermal synthesis method. This latter route requires the use of the hydrofluoric acid. Contrary to other acids, HF has a highly corrosive nature, it can penetrate the skin extremely easily and decalcify bones leading to destruction of the deep tissue layers. While handling the HF acid, personal protective clothing including goggles, laboratory coat and neoprene gloves were always employed. Special laboratory safety training was also carried out to prevent potential risks.

5.2. Synthesis of garnet fluoride Na$_3$Li$_3$M$_2$F$_{12}$ (M = Fe, Mn, V, Co, Ti)

As mentioned previously, garnet fluorides were traditionally obtained via solid state synthesis in sealed tubes. This method allows to obtain pure compositions but requires long thermal treatments. Coprecipitation in aqueous HF solution was proven to be a successful alternative synthesis route decreasing the time of the reaction as well as allowing the control of the kinetics of the reaction.[270]

For the synthesis of the selected garnet compounds (Fe, Mn, Co, Ti and V), two synthesis routes were evaluated – microwave-assisted solvothermal reaction (MW) and mechanosynthesis using ball milling (BM). The use of microwave for the solvothermal synthesis of inorganic compounds has been widely used as it significantly reduces time and cost. [274–276] The main disadvantage of this method applied to the synthesis of fluorides is the requirement of the use of hazardous HF. On the other hand, mechanosynthesis allows to obtain fluoride compounds by mixing the powders of precursors without HF, though it requires longer reaction time. The synthesis methods used in this work depending on the targeted composition are gathered in Table 5.3.

Table 5.3: Selected synthesis routes for each garnet composition.

Garnet	Synthesis route
$Na_3Li_3Fe_2F_{12}$	Microwave and/or ball milling
$Na_3Li_3V_2F_{12}$	Microwave and/or ball milling
$Na_3Li_3Mn_2F_{12}$	ball milling
$Na_3Li_3Ti_2F_{12}$	ball milling
$Na_3Li_3Co_2F_{12}$	ball milling

For the preparation of $Na_3Li_3V_2F_{12}$ and $Na_3Li_3Fe_2F_{12}$, the microwave-assisted solvothermal synthesis route was selected. It was the first attempt of adapting this innovative method for the synthesis of garnet fluorides. Stoichiometric amounts of NaF, LiF and MCl_3 (M=V,Fe) were mixed together with 9.8 ml of methanol and 0.181 ml of an aqueous solution of 40% HF in a 50 ml Teflon autoclave for 15min under air. Next, the reactor was tightly closed and placed in the CEM MARS5 microwave in order to be exposed to microwave irradiation for 30 min at 160 °C (details on the microwave-assisted sythesis can be found in annex). The garnet was expected to be formed according to the following reaction:

$$3LiF + 3NaF + 2MCl_3 + 6HF \rightarrow Na_3Li_3M_2F_{12} + 6HCl$$
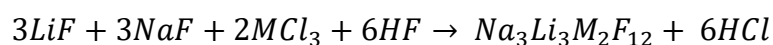
The recovered green powder was washed once with methanol and twice with ethanol (to remove formed HCl), filtered and dried overnight at 60 °C.

Due to the known problems of reduction of Mn^{III} and Co^{III} in presence of HF, garnets with these transition metals were prepared by mechanosynthesis using dry ball milling. $Na_3Li_3Ti_2F_{12}$ was also prepared by this method for practical reasons (availability of reactants). $Na_3Li_3V_2F_{12}$ and $Na_3Li_3Fe_2F_{12}$ were also prepared using the mechanosynthesis method in order to compare the powders obtained by this synthesis method with the solvothermal one.

The mixture of fluoride precursors (sodium, lithium and trivalent metal fluorides) was placed in the 45 ml zirconium oxide jar in a 1:20wt powder-to-ball ratio (15 mm zirconium oxide balls) and closed tightly in a nitrogen filled glovebox to prevent the formation of impurities upon oxidation reaction. Next, the mixture was milled in a FRITSH Pulverisette 7 ball-miller for 18 h (36 cycles of 30 min with 600 rpm speed + 2 min of pause after each cycle). The ball milling conditions were selected according to the

previously published synthesis protocol of $(NH_4)M^{2+}Fe^{3+}F_6$ (M = Mn, Co, Ni, Cu) fluorides.[277] The garnet fluorides were expected to form according to the following reaction:

$$3LiF + 3NaF + 2MF_3 \rightarrow Na_3Li_3M_2F_{12}$$

After finishing the milling steps, the jars were opened, the powder was recovered and subjected to further analysis.

5.3. Structural and chemical characterizations

The XRD characterization of the synthesized samples were performed after each synthesis in order to validate the composition and the purity of the obtained powders.

- $Na_3Li_3V_2F_{12}$

The first trials of the microwave-assisted solvothermal synthesis of $Na_3Li_3V_2F_{12}$ already resulted with a compound which could be indexed with the garnet structure and *Ia-3d* space group, however accompanied with some impurities and a high amount of LiF/NaF precursor residues. The blue color of the solution obtained after synthesis (Figure 5.2) might indicate partial oxidation of vanadium III into V^{IV} resulting in an insufficient amount of vanadium precursor to react with LiF and NaF. However, this hypothesis was evaluated by performing a synthesis with excess of VCl_3 precursor, and similar results were obtained (with even darker blue solution and unreacted LiF and NaF impurities) suggesting that the excess of VCl_3 does not improve the reactivity of the precursors. Therefore, for the next tries stoichiometric ratio of precursors was used.

Figure 5.2: Image of the solution after microwave-assisted synthesis of Na₃Li₃V₂F₁₂.

Different microwave conditions (time and temperatures) were evaluated, and the resulting XRD patterns are presented in Figure 5.3. Conditions of 190 °C and 30 min were selected

as the optimal ones based on the purity of obtained powders. The NaF residue was successfully removed by washing the powder twice with water. LiF has much smaller solubility in water therefore a small amount of this impurity was still detected. Figure 5.4a shows the Rietveld refinement of the XRD pattern of the washed sample. No change in the garnet structure is observed after washing the powder, indicating its high stability in water.
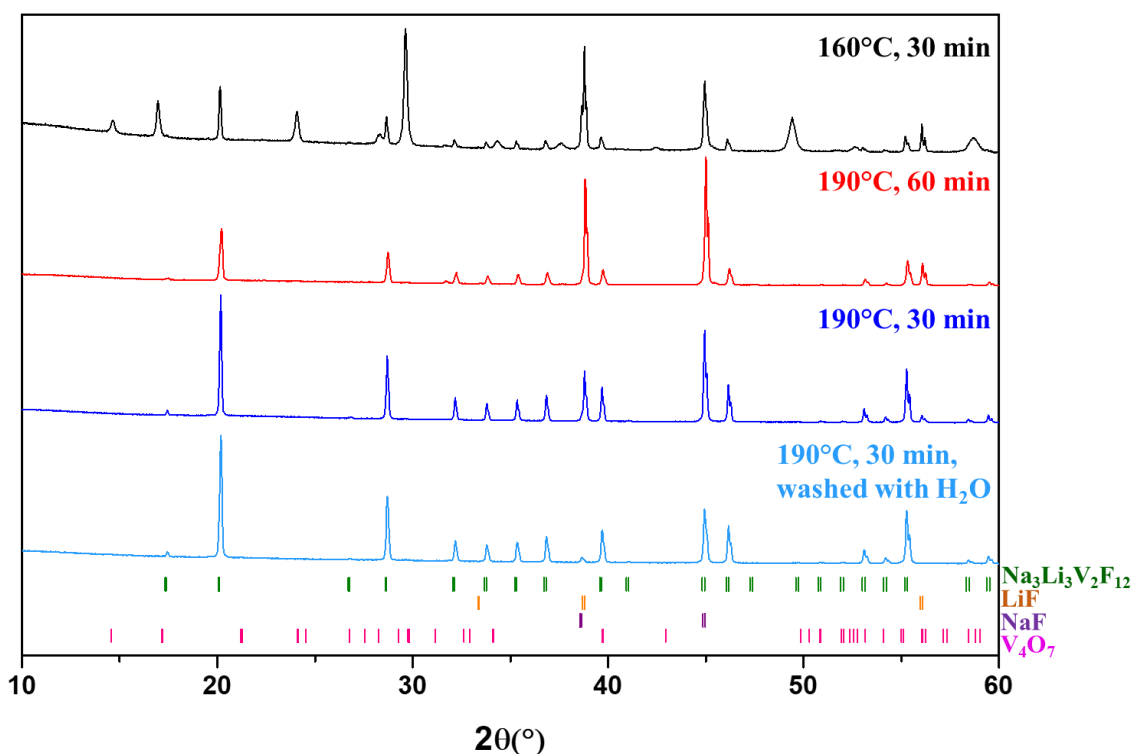
Figure 5.3: XRD patterns of $Na_3Li_3V_2F_{12}$ obtained at different synthesis conditions. The position of the Bragg peaks corresponding to $Na_3Li_3V_2F_{12}$, LiF, NaF and V_4O_7 phases are represented as green, orange, violet, and pink, respectively.

As shown in Figure 5.4b, a purer sample of $Na_3Li_3V_2F_{12}$ was obtained by ball-milling, no clear peaks of LiF/ NaF were observed, however the broadening of the peaks of the main phase could result with hiding the peaks of the impurities in the background. The larger broadening of the diffraction peaks however suggest a smaller size of the crystallites for the sample obtained by ball-milling as compared to the one obtained from microwave-assisted solvothermal synthesis.
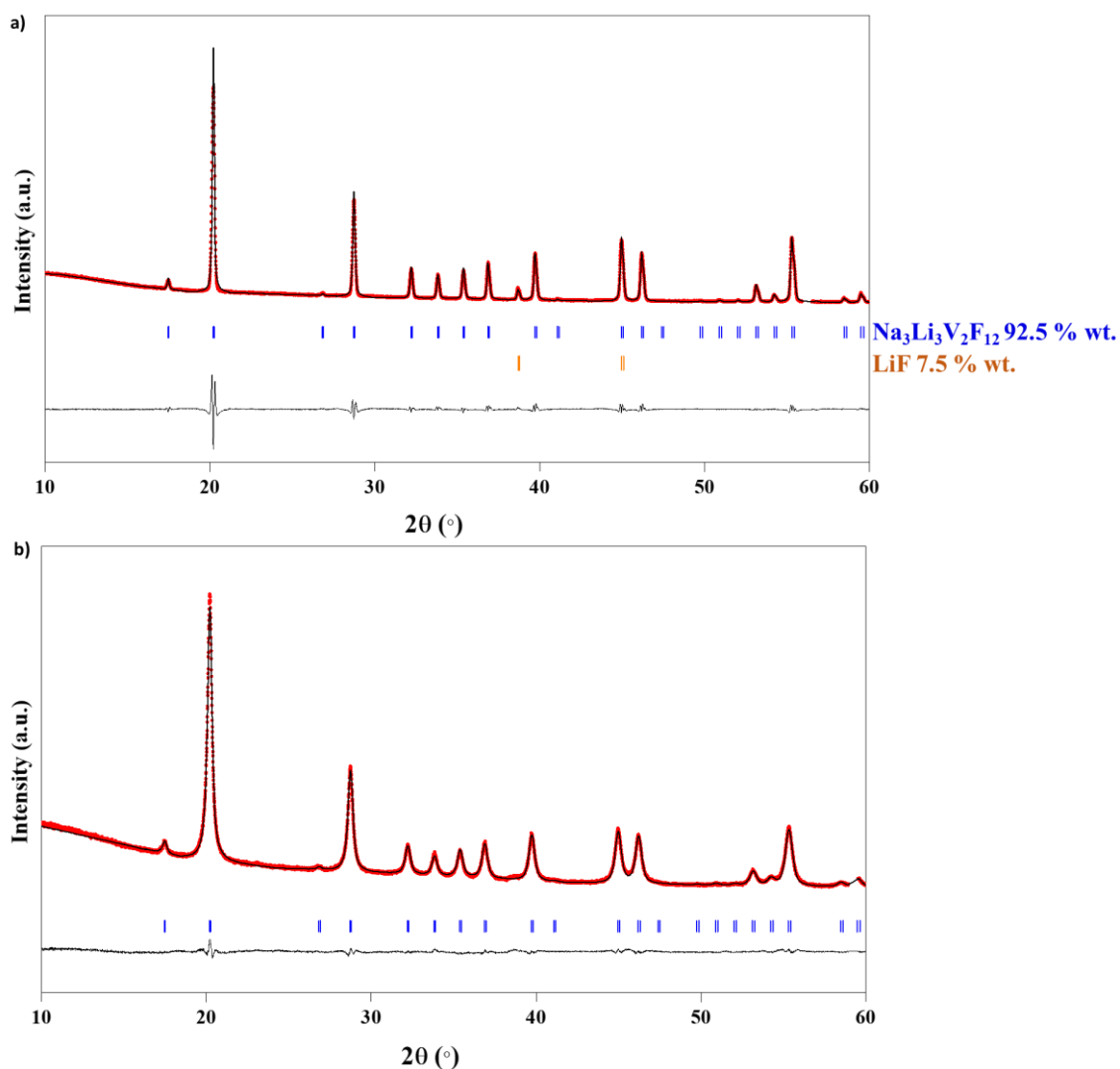
Figure 5.4: Rietveld refinements of the XRD patterns of Na$_3$Li$_3$V$_2$F$_{12}$, obtained via (a) microwave-assisted solvothermal and (b) ball milling syntheses. Red circles, black and grey lines represent the observed, calculated and difference patterns, respectively. The positions of the Bragg reflections of the *Ia*-3*d* space group are shown as blue vertical bars. Orange bars in (a) indicate a small (~7.5%) contribution of LiF impurity.

The crystallographic data and the structural details of Na$_3$Li$_3$V$_2$F$_{12}$ obtained from the refinements of the XRD patterns of the samples synthesized by microwave-assisted solvothermal and ball milling routes are shown in Table 5.4 and Table 5.5, respectively.

Table 5.4: Crystallographic data and atomic coordinates of $Na_3Li_3V_2F_{12}$ obtained from microwave-assisted solvothermal synthesis.

S.G.: *Ia-3d*	a =12.424(1) Å	V = 1917.87(4) Å^3	R_{Bragg} =3.33%	χ^2 = 2.57		
Atom	Wyckoff position	x/a	y/b	z/c	B_{iso}	Occ
V	16*a*	0	0	0	1.65(2)	1
Na	24*c*	¼	⅛	0	2.59(9)	1
Li	24*d*	¼	⅜	0	0.71(2)	1
F	96*f*	-0.030(1)	0.046(1)	0.146(1)	2.08(2)	1

Table 5.5: Crystallographic data and atomic coordinates of $Na_3Li_3V_2F_{12}$ obtained from ball milling synthesis.

S.G.: *Ia-3d*	a =12.422(4) Å	V = 1916.85(2) Å^3	R_{Bragg} =3.91%	χ^2 = 2.13		
Atom	Wyckoff position	x/a	y/b	z/c	B_{iso}	Occ
V	16*a*	0	0	0	1.33(4)	1
Na	24*c*	¼	⅛	0	2.43(6)	1
Li	24*d*	¼	⅜	0	1.92(5)	1
F	96*f*	-0.029(1)	0.045(1)	0.144(1)	1.47(3)	1

As can be seen in the tables, the refined cell parameters of $Na_3Li_3V_2F_{12}$ are equivalent for both methods: a_{BM} = 12.422(4) Å, whereas a_{MW} = 12.424(1) Å, indicating that both methods result with the successful synthesis of $Na_3Li_3V_2F_{12}$. The refined amount of remaining LiF impurity from the microwave synthesis is 7.5 wt. %. A significant difference in the crystallinity of the particles can be observed, as those obtained from ball milling route are much less crystalline, resulting with broad peaks in the XRD patterns. In this sample peak broadening was modelled isotropically and fully attributed to the finite size of the crystallites, with an average size of 21.1 nm as obtained using the Scherrer formula from the refined profile parameters (after subtraction of instrumental parameters), whereas the crystallites from the microwave route have an average size of 78.5 nm.

- **$Na_3Li_3Fe_2F_{12}$**

The iron fluoride garnet, $Na_3Li_3Fe_2F_{12}$, was also successfully synthesized using both methods. The Rietveld refinements of the XRD patterns of $Na_3Li_3Fe_2F_{12}$ synthesized using microwave-assisted solvothermal and ball-milling syntheses are presented in Figure

5.5 a) and b), respectively. The refined crystallographic data are presented in Table 5.6 and Table 5.7. The microwave-assisted solvothermal synthesis conducted under the same conditions as selected for $Na_3Li_3V_2F_{12}$ – 190 °C, 30 min, resulted in a white powder, indexed as$Na_3Li_3Fe_2F_{12}$.A small peak at 39° might originate from a trace of LiF, however the intensity is so low that was not taken into account for the refinement. The average size of the crystallites was 89.4 nm, as calculated using the Scherrer formula. The lack of LiF/NaF impurities in the XRD pattern suggests complete reaction of precursors without side oxidation reactions. On the other hand, a light-pink powder was obtained from the ball milling synthesis and was also indexed as $Na_3Li_3Fe_2F_{12}$ phase with <2% amount of Fe_2O_3 impurities, with an average size of the crystallites of 22.9 nm.
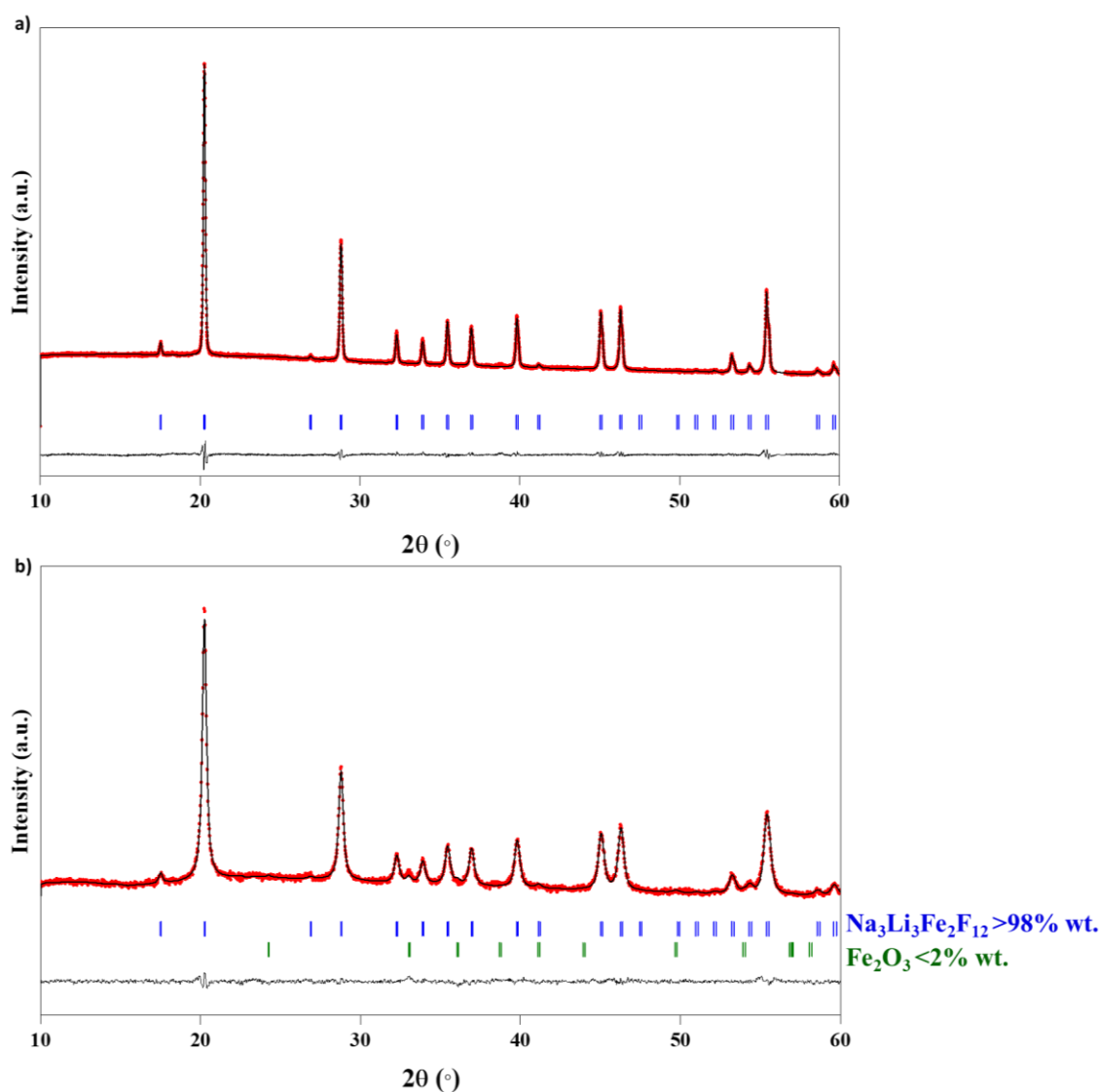
Figure 5.5: Rietveld refinements of the XRD patterns of Na₃Li₃Fe₂F₁₂, obtained via (a) microwave-assisted solvothermal and (b) ball milling syntheses. Red circles, black and grey lines represent the observed, calculated and difference patterns, respectively. The positions of the Bragg reflections of the *Ia-3d* space group are shown as blue vertical bars. Green bars in (b) indicate a small (<2%) contribution of Fe₂O₃ impurities.

Table 5.6: Crystallographic data and atomic coordinates of Na₃Li₃Fe₂F₁₂ obtained from microwave-assisted solvothermal synthesis.

S.G.: *Ia-3d*	*a* =12.400(1) Å	*V* = 1906.73(3) Å³	R_{Bragg} =4.78%		χ^2 = 2.06	
Atom	Wyckoff position	*x/a*	*y/b*	*z/c*	B_{iso}	*Occ*
Fe	16a	0	0	0	1.08(6)	1
Na	24c	¼	⅛	0	1.76(5)	1
Li	24d	¼	⅜	0	1.49(6)	1
F	96f	-0.030(1)	0.047(1)	0.147(1)	1.12(4)	1

Table 5.7 : Crystallographic data and atomic coordinates of Na₃Li₃Fe₂F₁₂ obtained from ball milling synthesis.

S.G.: *Ia-3d*	*a* =12.404(5) Å	*V* = 1908.25(1) Å³		R$_{Bragg}$ =2.22%	χ² = 1.55	
Atom	Wyckoff position	*x/a*	*y/b*	*z/c*	*B$_{iso}$*	*Occ*
Fe	16a	0	0	0	0.17(2)	1
Na	24c	¼	⅛	0	1.79(3)	1
Li	24d	¼	⅜	0	1.37(2)	1
F	96f	-0.030(3)	0.046(3)	0.146(3)	0.21(2)	1

The obtained data indicate that both synthesis routes results with synthesizing same Na₃Li₃Fe₂F₁₂ garnet phase – no difference in cell parameter or atomic positions can be observed. The microwave synthesis route resulted in the pure phase, whereas in the ball-milling route apart from the garnet phase, very small (<2%) amount of Fe_2O_3 oxide impurity.

- **Na₃Li₃Ti₂F₁₂**

The titanium fluoride garnet, Na₃Li₃Ti₂F₁₂, was synthesized using the ball milling method. The Rietveld refinement of the XRD pattern of the powder, as well as the crystal structure details are presented in Figure 5.6 and Table 5.8.
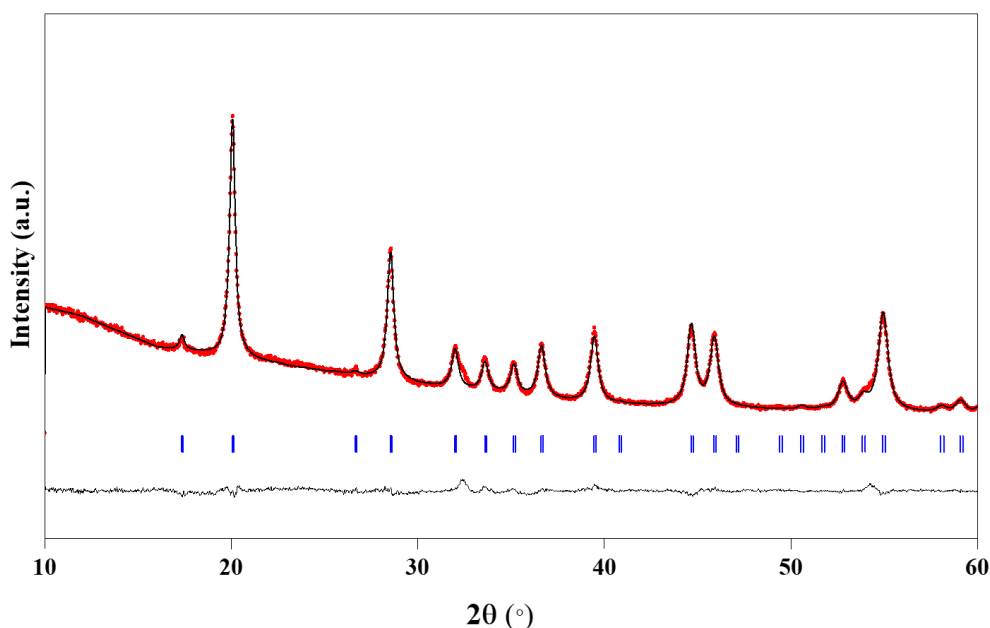
Figure 5.6: Rietveld refinement of the XRD pattern of Na₃Li₃Ti₂F₁₂, obtained via ball milling synthesis. Red circles, black and grey lines represent the observed, calculated and difference patterns, respectively. The positions of the Bragg reflections of the *Ia-3d* space group are shown as blue vertical bars.

Table 5.8: Crystallographic data and atomic coordinates of Na₃Li₃Ti₂F₁₂ obtained from ball milling synthesis.

S.G.: *Ia-3d*	*a* =12.504(2) Å		*V* = 1954.93(1) Å³		R_{Bragg} =3.87 %	χ^2 = 3.15
Atom	Wyckoff position	*x/a*	*y/b*	*z/c*	B_{iso}	*Occ*
Ti	16a	0	0	0	0.38(3)	1
Na	24c	¼	⅛	0	0.13(2)	1
Li	24d	¼	⅜	0	1.91(2)	1
F	96f	-0.030(5)	0.046(5)	0.149(5)	0.82(4)	1

The XRD pattern of the dark violet powder was refined as a pure Na₃Li₃Ti₂F₁₂ phase, with an average size of the crystallites of 17.7 nm, as obtained using the Scherrer formula. No impurity of titanium oxide or remainings of LiF/NaF precursors was detected.

With the ball milling synthesis Na₃Li₃V₂F₁₂, Na₃Li₃Fe₂F₁₂ and Na₃Li₃Ti₂F₁₂ were stabilized with high purity, whereas attempts of obtaining Na₃Li₃Co₂F₁₂ and Na₃Li₃Mn₂F₁₂ were unsuccessful, possibly due to the reduction of the precursors and the formation of the amorphous phase as was explained by Naka.[104,272,277]

In Table 5.9 all the characteristic information of the garnets obtained via both synthesis routes is gathered (color, cell parameter, average crystallite size and an image of the obtained powder). The refined cell parameters are in good agreement with the literature.[264]

Table 5.9: Characteristic information of synthesized garnets (color, cell parameter, average crystallite size and an image of the obtained powder).

Structure	Synthesis route	color	a (Å)	*Average crystallite size*	
$Na_3Li_3V_2F_{12}$	Both (MW-microwave or BM-ball milling)	Dark green	12.424(1) Å (BM) 12.422(4) Å (MW)	2-3 µm (MW); ~300 nm (BM)	
$Na_3Li_3Fe_2F_{12}$	Both (MW-microwave or BM-ball milling)	White (MW) Light pink (BM)	12.400(1) Å (MW) 12.404(5) Å (BM)	3-5 µm (MW); ~200 nm (BM)	
$Na_3Li_3Ti_2F_{12}$	Ball milling	violet	12.504(2) Å	~500 nm	

5.4. Morphological and chemical analysis

5.4.1.   Scanning Electron microscopy (SEM)

SEM images of all synthesized garnets are gathered in Figure 5.7. Images (a) and (b) correspond to $Na_3Li_3V_2F_{12}$ and $Na_3Li_3Fe_2F_{12}$ synthesized by the microwave-assisted solvothermsl route. Significant differences between the shape of the particles can be observed – those of $Na_3Li_3V_2F_{12}$ resemble hollow round shells of an average size of 2-3 µm whereas particles of $Na_3Li_3Fe_2F_{12}$ have much sharper edges with platelet shapes and an average size of 3-5 µm. The size was estimated based on around 10 measurements of each sample.
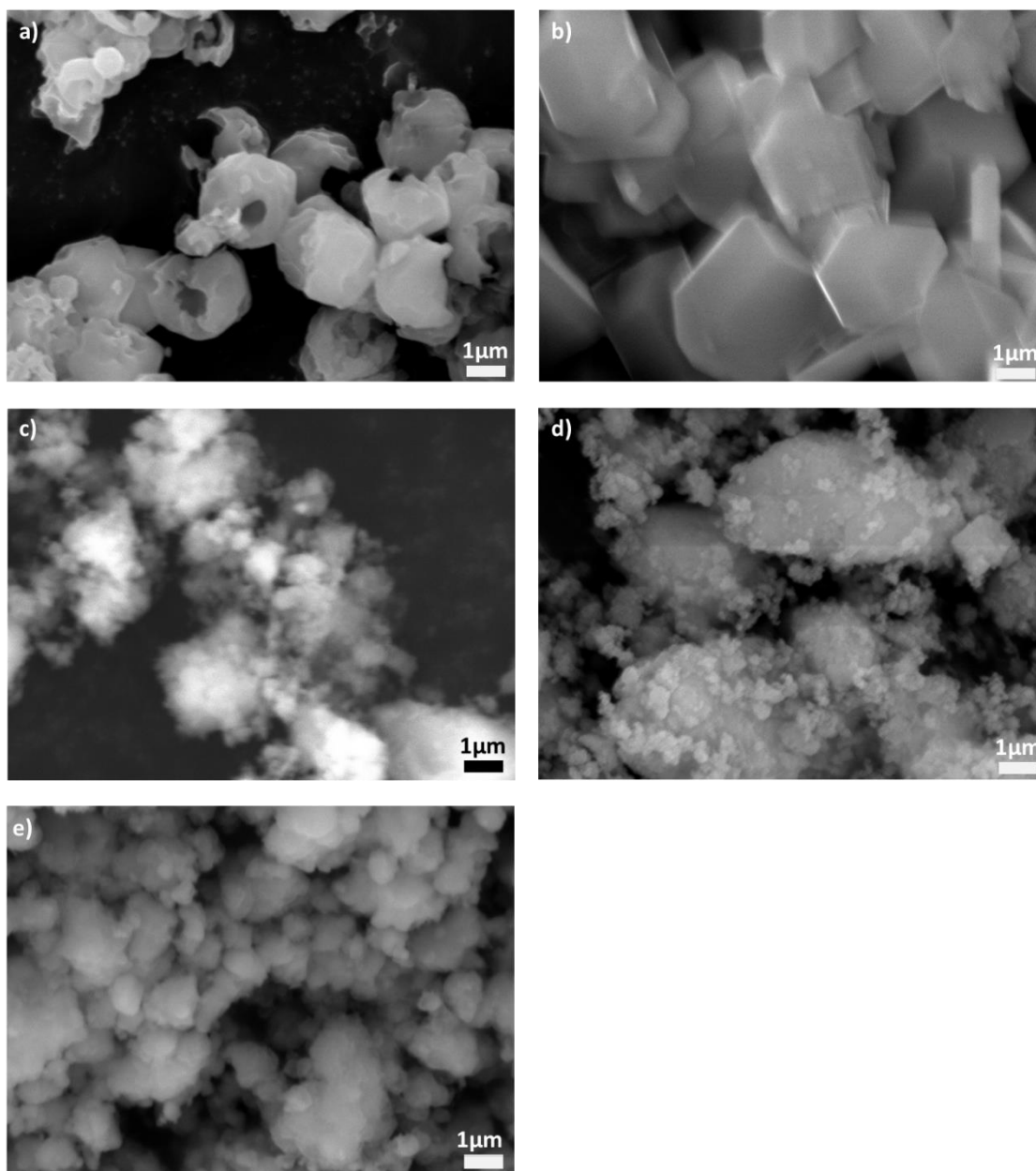
Figure 5.7: SEM images of (a) Na₃Li₃V₂F₁₂ obtained via microwave-assisted solvothermal synthesis; (b) Na₃Li₃Fe₂F₁₂ obtained via microwave -assisted solvothermal synthesis; (c) Na₃Li₃V₂F₁₂ obtained via ball-milling synthesis; (d) Na₃Li₃Fe₂F₁₂ obtained via ball-milling synthesis; (e) Na₃Li₃Ti₂F₁₂ obtained via ball-milling synthesis.

Images (c) and (d) correspond to $Na_3Li_3V_2F_{12}$ and $Na_3Li_3Fe_2F_{12}$ synthesized by the ball-milling route. In both samples,s the shape of the nanometric particles is non-uniform, with average size around 5 µm. These particles tend to form large agglomerates of several microns. The last image – (e), shows $Na_3Li_3Ti_2F_{12}$ particles obtained from the ball milling synthesis. As in the former images, nanometric primary particles (<500 nm) are obtained, which agglomerate in more uniform secondary particles of several microns. From the XRD refinements, using the Scherrer formula, the average size of the crystallites of all

three garnets synthesized by ball-milling route was estimated to be approximately 20 nm. These results are in good agreement with the findings from the SEM measurements, as it can be visible that the agglomerates are formed by a large amount of very small particles, whose precise size cannot be measured with SEM resolution.

5.4.2. Chemical composition

Chemical analysis was performed on $Na_3Li_3V_2F_{12}$ and $Na_3Li_3Fe_2F_{12}$ synthesized by both microwave-assisted solvothermal and ball-milling routes, and $Na_3Li_3Ti_2F_{12}$ obtained from the ball milling synthesis. The results of the elemental ratio evaluated by EDX and ICP are gathered in Table 5.10 and Table 5.11 .

Table 5.10: Composition of $Na_3Li_3M_2F_{12}$ M=(Fe,V,Ti) determined by EDX.

Element	Theoretical atomic ratio	Experimental atomic ratio determined from EDX				
		BM $Na_3Li_3Fe_2F_{12}$	MW $Na_3Li_3Fe_2F_{12}$	BM $Na_3Li_3Ti_2F_{12}$	BM $Na_3Li_3V_2F_{12}$	MW $Na_3Li_3V_2F_{12}$
Na	3	2.8±0.14	2.8±0.14	2.9±0.15	3.0±0.15	3.1±0.16
Li	3	-	-	-	-	-
Fe/V/Ti	2	2.0 (fixed)	2.0 (fixed)	2.0 (fixed)	2.0 (fixed)	2.0 (fixed)
F	12	10.8±0.54	10.0±0.5	11.0±0.55	10.2±0.51	9.9±0.5

Table 5.11: Composition of $Na_3Li_3M_2F_{12}$ M=(Fe,V,Ti) determined by ICP.

Element	Theoretical atomic ratio	Experimental atomic ratio determined from ICP				
		BM $Na_3Li_3Fe_2F_{12}$	MW $Na_3Li_3Fe_2F_{12}$	BM $Na_3Li_3Ti_2F_{12}$	BM $Na_3Li_3V_2F_{12}$	MW $Na_3Li_3V_2F_{12}$
Na	3	3.08±0.02	3.16±0.04	3.13±0.03	3.11±0.02	3.14±0.03
Li	3	3.13±0.03	3.15±0.04	3.16±0.03	3.05±0.03	3.02±0.03
Fe/V/Ti	2	2.0 (fixed)	2.0 (fixed)	2.0 (fixed)	2.0 (fixed)	2.0 (fixed)
F	12	-	-	-	-	-

Due to too low energy of the emitted X-rays, lithium was not detected by EDX. The experimental ratio of the elements was calculated based on the average atomic % of ten measurements. Final ratios were calculated by fixing the transition metal to its stoichiometric value. The obtained results are close to the theoretical ratios, considering the low accuracy of the EDX quantification (±5% relative error).[278] Fluorine ions tend to migrate due to repulsions from the negatively charged electron beam, therefore the obtained value can be lower than the real one,[279] as is our case. However, these results demonstrate that the samples contain a large amount of fluorine, which is, within error, close to the stoichiometric value. Additionally, the results obtained for the samples

synthesized in two different synthesis routes are almost identical, once more confirming that both synthesis techniques result with obtaining the proper garnet phase.

On the other hand, with the use of ICP technique, sodium, lithium and transition metals were detected and quantified. The detection of fluorine was impossible due to the high ionization potential of this element.[280] As in the previous case, the final ratios were calculated using the transition metal content as reference. The quantified amounts of sodium and lithium are in good agreement with the theoretical values (although slightly overestimated in some cases, which could be related to the presence of small amount of the NaF/LiF residues).

5.4.3.   Thermogravimetric analysis

Thermogravimetric analysis of the $Na_3Li_3Fe_2F_{12}$ garnet obtained from the microwave synthesis (see Figure 5.8) was carried out by heating the powder from room temperature to 900 °C with a heating ramp of 5°C/min under constant flow of synthetic air (20 % of oxygen +80 % of nitrogen). $Na_3Li_3Fe_2F_{12}$ is expected to decompose following this reaction:

$$Na_3Li_3Fe_2F_{12} + O_2 \rightarrow Fe_2O_3 + 3NaF + 3LiF + 6HF \uparrow$$
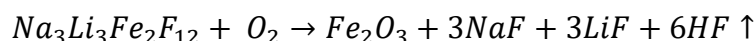
According to the TGA result, the decomposition of the $Na_3Li_3Fe_2F_{12}$ garnet structure starts at ~450 °C and is completed at ~840 °C with a mass loss of 16.03 wt%. This experimental mass loss is in good agreement with the calculated theoretical mass loss (15.36 wt%) and literature[270], indicating that no side reactions occurred during the thermal process.

The recovered dark red powder was identified as a mixture of Fe_2O_3, LiF and NaF, as indicated by the Rietveld refinement of the XRD pattern shown in Figure 5.9.
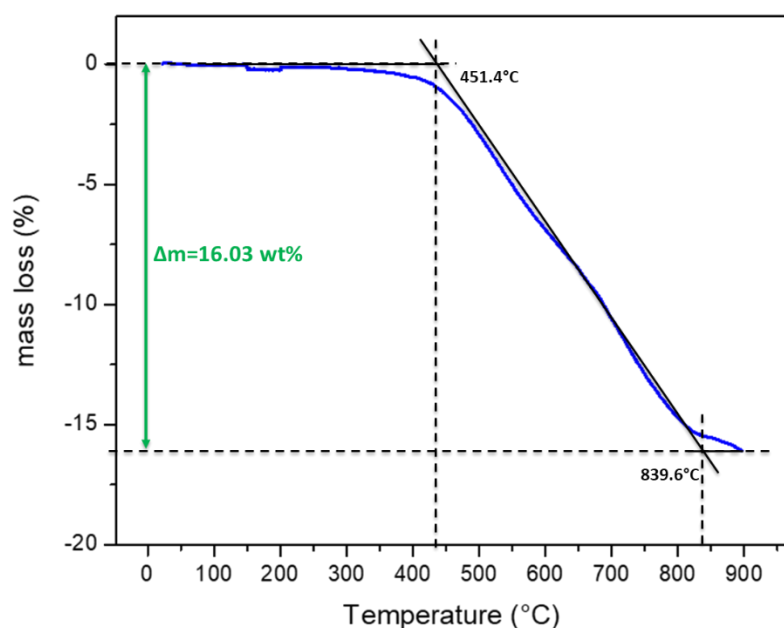
Figure 5.8: Thermogravimetric measurement of $Na_3Li_3Fe_2F_{12}$ under air.
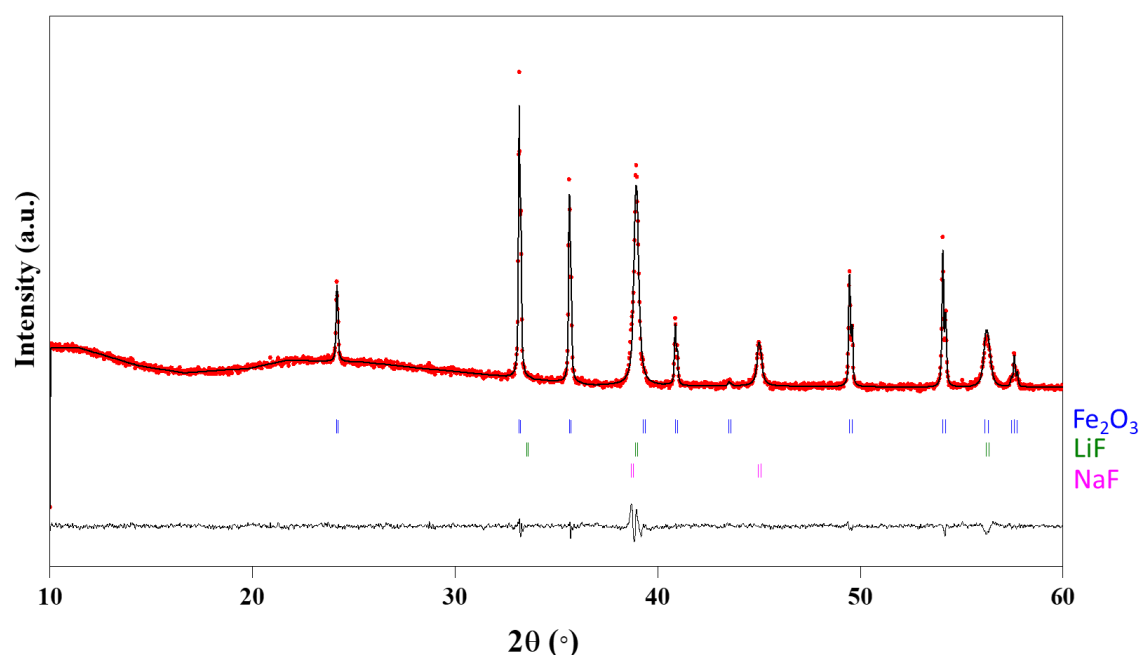
Figure 5.9: Rietveld refinement of the XRD pattern of the powder obtained after thermogravimetric analysis. Red circles, black and grey lines represent the observed, calculated and difference patterns, respectively. The positions of the Bragg reflections of the different phases are shown as vertical bars.

Due to the corrosive nature of the samples (release of dangerous HF upon heating), the analysis was only performed on $Na_3Li_3Fe_2F_{12}$. For $Na_3Li_3V_2F_{12}$ and $Na_3Li_3Ti_2F_{12}$ similar results are expected with the formation of the corresponding oxides (V_2O_5 for $Na_3Li_3V_2F_{12}$, and Ti_2O_3 for $Na_3Li_3Ti_2F_{12}$,) together with NaF and LiF.

5.4.4. X-ray Absorption Spectroscopy

Soft X-ray absorption spectroscopy (XAS) analysis was conducted on pristine powders of the three $Na_3Li_3M_2F_{12}$ garnets (M = Fe, V, Ti) at the BOREAS beamline of the ALBA Synchrotron facility in Barcelona (details can be found in Annex – Experimental section, part A.2.3). The aim of this measurement was to validate the oxidation state of the transition metal and evaluate the environment of fluorine and sodium. For the measurement, $Na_3Li_3V_2F_{12}$ and $Na_3Li_3Fe_2F_{12}$ obtained from the microwave-assisted solvothermal synthesis and $Na_3Li_3Ti_2F_{12}$ synthesized by ball milling were used. The computed spectra were generated with the program CTM4XAS. [166,216]

Transition metal (V, Ti and Fe) $L_{2,3}$-edges as well as F and Na K-edges were analyzed. XAS data was collected using both total electron and fluorescence yield detectors. Signals from electron detection mode (EY) correspond to the chemical state of the surface layer of the material (probing depth of around 2-5 nm). Fluorescence yields (FY) correspond to the probing depths of approximately 100 - 500 nm into the particle, thus having a notable contribution from the bulk crystal structure, especially considering the particle size of the materials. [167]

5.4.4.1. 3d Transition Metal $L_{2,3}$-edges

Within the garnet structure, the transition metals are expected to be at the trivalent oxidation state in an octahedral MF_6 environment. The three studied garnet phases $Na_3Li_3M_2F_{12}$ (M = Fe, V, Ti) represent different $3d$ systems: V^{III} is a $3d^2$ system with two $3d$ occupied electrons, Fe^{III} is a $3d^5$ system with five $3d$ occupied electrons (half-filled) and Ti^{III} is a $3d^1$ system with one $3d$ occupied electron. These characteristics have a significant impact on the type of ground state and symmetry effects of each metal, as shown below.

- **$Na_3Li_3V_2F_{12}$**

Figure 5.10 shows the XAS spectra of V $L_{2,3}$- and O K-edges, the latter was also measured in this case due to the close adsorption energy value, which falls within the default measurement region of vanadium L-edge region. The theoretical spectra for V^{III} and V^{IV} were computed using the CTM4XAS software for the ideal structure (no charge

compensation taken into account for V^{IV}), with O_h coordination symmetry and a crystal field splitting energy of 2.5 eV, also shown in Figure 5.10 as reference.
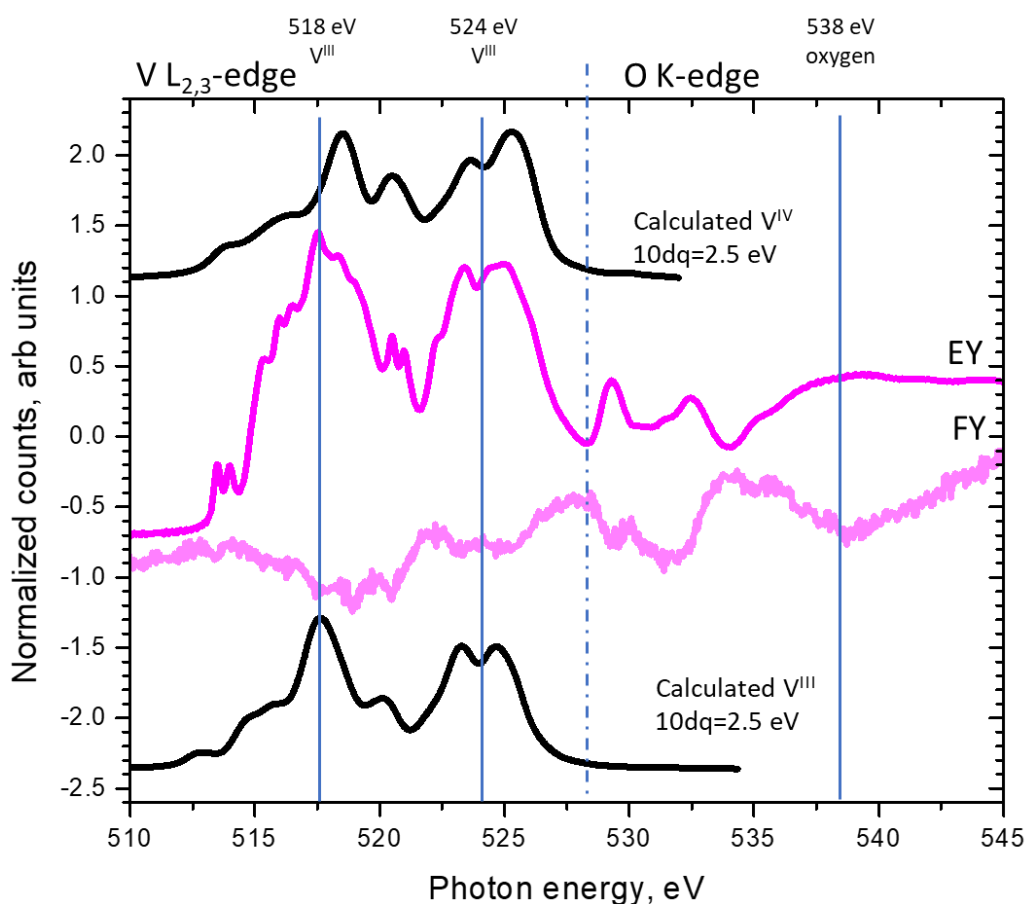
Figure 5.10: XAS V L₂,₃-edge & O K-edge spectra in Na₃Li₃V₂F₁₂. Signals from electron detection mode (EY) corresponding to the surface are represented in pink color; whereas signals from fluorescence mode (FY) corresponding to the interior, are represented in light pink color. Black curves correspond to the calculated XAS V^III and V^IV L₂,₃-edge spectra with Oh coordination symmetry and a crystal field splitting energy of 2.5 eV.

For the V L-edge region, the experimental spectrum exhibits two broad bands centered at 518 and 524 eV which can be attributed to the $2p_{3/2}$ and $2p_{1/2}$ levels, respectively. [168] The position of these bands is in good agreement with the computed V^{III} spectrum. V^{IV} oxidation state is a priori not observed. In the signal from the fluorescence mode (FY, indicated in Figure 5.10 as light pink curve) the signal to noise ratio is much smaller, which is expected to result from the self-absorption.

As in the garnet structure all V atoms are expected to be bonded with F forming VF_6 octahedra, no features in the O K-edge were expected to be present. Surprisingly, a small band at 538 eV was observed indicating the presence of V-O bond within the structure. The observed spectra for the O K-edge correspond to the transition from the O1s core

level to unoccupied Op level. The features below 534 eV correspond to V3d–O2p hybridization, whereas the ones above correspond to V4sp–O2p hybridization. The ratio between the two peaks at 529.5 and 532 eV corresponds to a 3:2 intensity ratio, which is characteristic for the V^{III} oxidation state and is related to the t_{2g}-e_g splitting.[168] The energy difference of 2.5 eV between these two peaks supports well the calculated crystal field splitting energy.

The presence of the V-O bond in the garnet structure can be related to the synthesis method used to obtain this compound. Microwave-assisted synthesis was realized in the methanol solution with the use of 40% HF, which involves presence of water. It has been shown for $FeF_3 \cdot 3H_2O$, $Fe_2F_5(H_2O)_2$ and $Fe_3F_8(H_2O)_2$ that the microwave-assisted solvothermal synthesis favors the partial substitution of fluorine atoms with OH groups within the hexagonal tungsten bronze structure due to the hydrolysis.[281,282] These results might suggest similar process occurring during the formation of the garnet. This hypothesis can be verified, and the amount of OH can be quantified, by performing thermogravimetric analysis, as was demonstrated for $FeF_3 \cdot 3H_2O$. The loss of OH group is expected to occur above 130°C. Another solution could be a XAS analysis of the garnet sample obtained by the mechanosynthesis, where no oxygen should be observed.

- **$Na_3Li_3Fe_2F_{12}$**

Figure 5.11 shows the XAS spectra of F K-edge and Fe L$_{2,3}$-edge in $Na_3Li_3Fe_2F_{12}$ next to the spectra of F K-edge and Fe L$_{2,3}$-edge in FeF_2 and FeF_3 from the literature.[283]
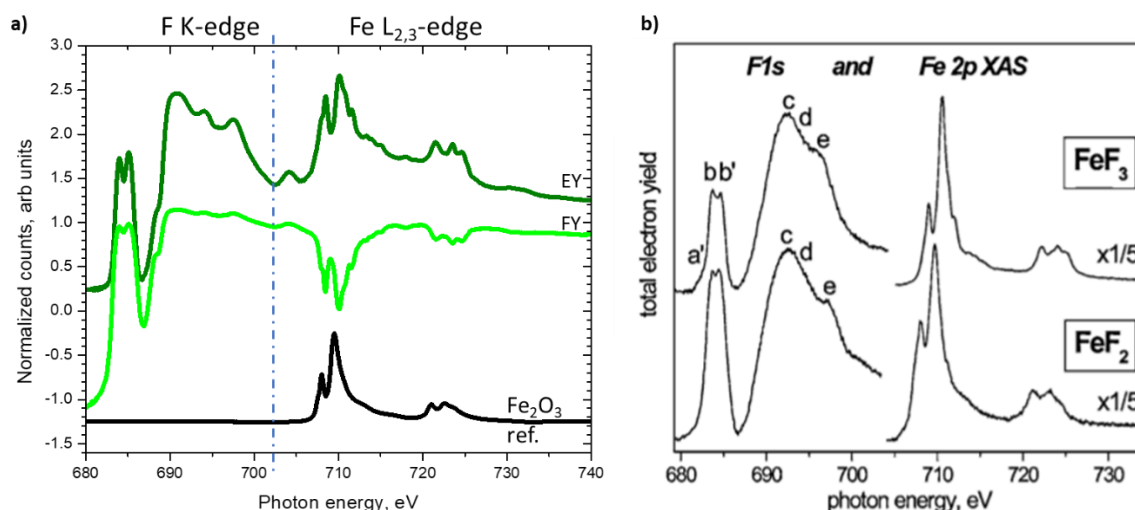
Figure 5.11: (a) XAS F K-edge & Fe L$_{2,3}$-edge spectra in Na$_3$Li$_3$Fe$_2$F$_{12}$. Signals from electron detection mode (EY) corresponding to the surface are represented in dark green color; whereas signals from fluorescence mode (FY) corresponding to the bulk, are represented in light green color. (b) XAS F K-edge & Fe L$_{2,3}$-edge spectra in FeF$_2$ and FeF$_3$ from reference. [283]

The Na$_3$Li$_3$Fe$_2$F$_{12}$ Fe L$_{2,3}$-edge spectrum exhibits two main separate features, centered at 710 and 722 eV, which can be attributed to the Fe L$_3$- and Fe L$_2$-edges, respectively. The first group of peaks attributed to the L$_3$-edge correspond to the 2p-3d transition into the low-energy t$_{2g}$ and high-energy e$_g$ states.[167] The relative intensity ratio of the peaks at 708.5 and 711 eV (with the dominating peak at 711 eV) matches well the position of the double peaks in FeF$_3$. However, the final determination of the oxidation state of Fe needs to be supported with the analysis of F K-edge, which will be presented in the 5.4.4.2. section, because the spectra of FeF$_2$ and FeF$_3$ presented in Figure 5.11b exhibit a very similar shape, which results from the very similar octahedral coordination of Fe in these compounds.

The "negative" intensity in the Fe L$_{2,3}$-edge fluorescence yield spectrum arises from a high self-absorption, however the shape and energy are the same as in the electron yield; indicating that the surface and bulk states are the same.

- **Na$_3$Li$_3$Ti$_2$F$_{12}$**

The XAS spectra of Ti L$_{2,3}$-edge is shown in Figure 5.12. Spectra for both Ti^{III} and Ti^{IV} were computed with octahedral coordination symmetry and a crystal field splitting energy of 1.4 eV for Ti^{III} and 2.6 eV for Ti^{IV} as reference.
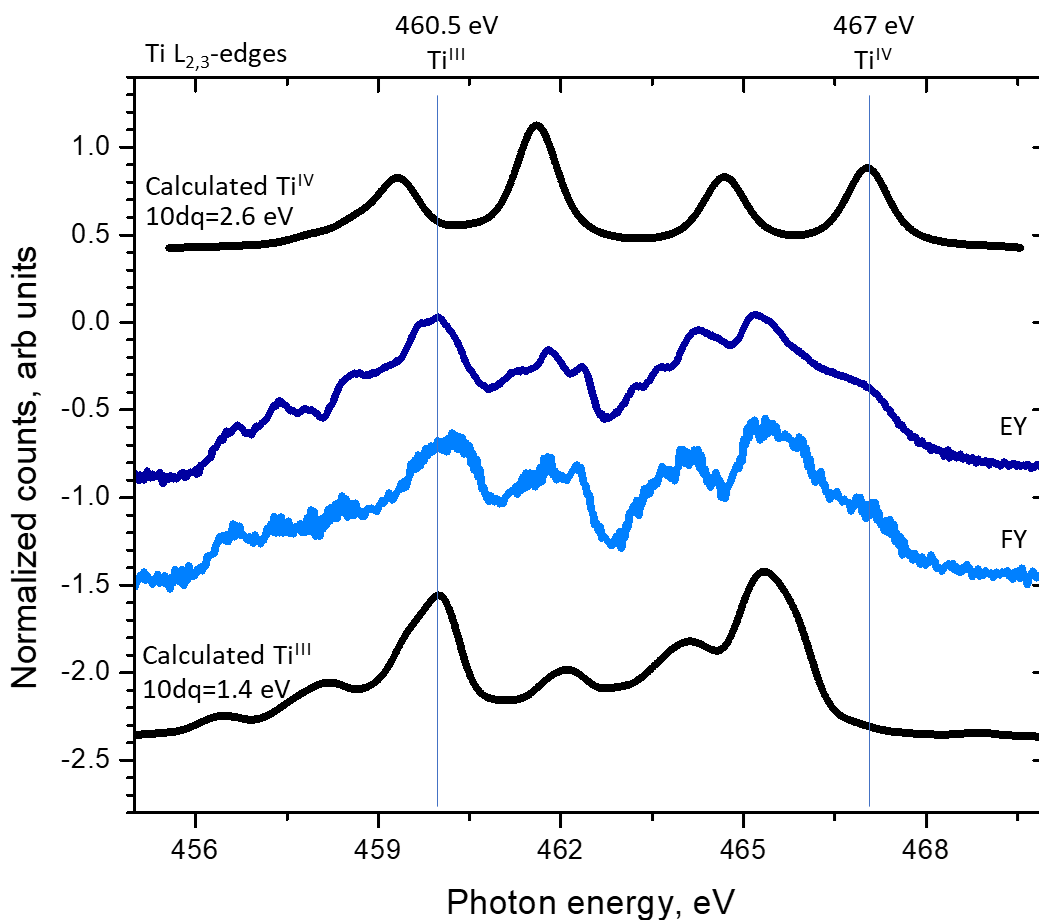
Figure 5.12: XAS Ti L$_{2,3}$-edge spectra in Na$_3$Li$_3$Ti$_2$F$_{12}$. Signals from electron detection mode (EY) corresponding to the surface are represented in dark blue color; whereas signals from fluorescence mode (FY) corresponding to the bulk, are represented in light blue color. Black curves correspond to the calculated XAS Ti L$_{2,3}$-edge spectra with Oh coordination symmetry and a crystal field splitting energy of 1.4 eV for Ti^{III} and 2.6 eV for Ti^{IV}.

The features in the experimental Ti L$_{2,3}$-edge spectrum match well the computed spectra for Ti^{III}. However, there is an additional absorption feature at 467 eV which is attributed to Ti^{IV}. Therefore, it is concluded that the pristine material has mainly Ti^{III} and a low amount of Ti^{IV}, both in the surface and the bulk, since the spectra from electron and fluorescence yields are similar.

The presence of Ti^{IV} within the garnet structure could be related either to Na/Li deficiency, or the partial substitution of F by O. As the refinement of the XRD pattern does not reveal any vacancies in Na or Li, the analysis of the O K-edge and the use of the neutron diffraction would be recommended in further investigation to have detailed insight into the garnet structure.

5.4.4.2. F K-edges

In all the garnet fluorides $3d$ transition metals are octahedrally coordinated to fluorine atoms. The covalent bonding between the $3d$ TM atom and the surrounding F atom takes place due to the mixing of the valence M$3d$, $4s$ and F$2p$ states. The analysis of F K-edge X-ray absorption spectroscopy in garnets was conducted to probe the metal-ligand covalency (hybridization) in MF$_6$$^{-III}$ based on the presence of pre-edge features. The results from this analysis are expected to support the conclusions from the evaluation of the L-edges of transition metals.

Two distinct regions can be distinguished in the spectra, indicated by the dashed line in Figure 5.13a. First, the features in the pre-edge region (<688 eV) corresponding to F $2p$ orbitals hybridizing with M($3d$) states. In the second region (>688 eV) the features correspond to F $2p$ orbitals hybridizing with empty M ($4sp$) states. A comparison between the different garnets obtained, together with spectra from the literature, is shown in Figure 5.13.

According to their electronic structure, the $3d$ states of Ti^{III} and V^{III} are partially occupied (with one and two electrons respectively); whereas the d orbital in Fe^{III} has 5 electrons. The influence of the decreasing number of free $3d$ states in fluorine spectra was exhaustively studied by Vinogradov *et.al.*[284] Figure 5.13b reveals the changes in the F1s absorption spectra of binary fluorides upon changing the valence configuration of the 3d atoms. The experimental spectra of Ti^{III} ($3d^1$), V^{III} ($3d^2$) and Fe^{III} ($3d^5$) match well the corresponding reported spectra according to their configuration, confirming the proper identification of MF$_6$ octahedra. [167,284–287] While the analysis of the Fe L$_{2,3}$-edge resulted with unclear determination of the oxidation state of Fe, the analysis of the F K-edge helped to confirm the expected Fe^{III} state.

Figure 5.13: (a) XAS F K-edge spectra of (blue) $Na_3Li_3Ti_2F_{12}$; (green) $Na_3Li_3Fe_2F_{12}$; (pink) $Na_3Li_3V_2F_{12}$ garnet. Signals from electron detection mode (EY) corresponding to the surface are represented in dark color; whereas signals from fluorescence mode (FY) corresponding to the interior, are represented in light color. Features in the 700-730 eV range in green (Fe garnet) spectra are ascribed to the Fe $L_{2,3}$-edge. The dashed line divides the F K-edge spectra into the pre-edge (left side) and the main edge region (right side); (b) Near-edge F1s absorption in: (1)K_2TiF_6 ($3d^0$), (2) VF_3 ($3d^2$), (3) CrF_3 ($3d^3$), (4) CrF_3 ($3d^4$), (5) FeF_3 ($3d^5$) from Vinogradov _et.al._ [284]

Analysis of the F K-edge electron yield (EY) and fluorescence yield (FY) allows to follow the surface and bulk states of fluorine within the garnet structure. As visible in Figure 5.13a, in $Na_3Li_3Ti_2F_{12}$ garnet both electron and fluorescence yield are very similar in shape and energy position; indicating that the surface and bulk states of F are the same, which is consistent with Ti $L_{2,3}$-edge analysis.

In the case of $Na_3Li_3Fe_2F_{12}$, the high self-absorption of Fe $L_{2,3}$-edge results in a distorted shape of the fluorescence yield spectrum within the main region, however the pre-edge region is very similar to the electron yield therefore indicating equal F environments in the bulk and at the surface.

For $Na_3Li_3V_2F_{12}$, the relative intensity of the pre-edge peaks changes between electron and fluorescence yields. The pre-edge peak at 685 eV represents covalent mixing between V($3d$ - t_{2g}) and F($2p$) states, while the pre-edge peak at 687 eV represents covalent mixing between V($3d$ -e_g) and F($2p$) states which indicates differences in the hybridization between bulk and the surface. This could suggest slightly different composition in the bulk and in the surface of the garnet, which could be related to the observed presence of the V-O bond in the analysis of the V $L_{2,3}$-edge.

5.4.4.3. Na K-edges

The Na K-edge spectra (Figure 5.14) correspond to electronic transitions from filled Na $1s$ orbitals to empty $2p$ states. For each garnet sample the spectrum exhibits two broad bands centered at 1075 and 1080 eV and low frequency oscillations at higher energies. These features are typical for Na in a disordered environment such as a glass.[288] These results are in good agreement with the sodium environment of distorted NaF_8 dodecahedra within the garnet structure.[273]

Figure 5.14: XAS Na K-edge spectra of (blue) $Na_3Li_3Ti_2F_{12}$; (green) $Na_3Li_3Fe_2F_{12}$; (pink) $Na_3Li_3V_2F_{12}$ garnet. Signals from electron detection mode (EY) corresponding to the surface are represented in dark color; whereas signals from fluorescence mode (FY) corresponding to the interior, are represented in light color.

The Na K-edge spectra of all samples are similar in electron and fluorescence detection modes, indicating that the chemical states of Na are the same on the surface and in the bulk.

Summarizing, XAS analysis of the garnet samples allowed to validate the expected oxidation state of the transition metals and eventually corroborate the proper composition. By performing the analysis of the fluorine and sodium K -edges, the expected environment of both atoms was also confirmed.

5.5. Preliminary evaluation of the electrochemical properties of $Na_3Li_3M_2F_{12}$ (M = V, Fe, Ti) as Na-ion and Li-ion positive electrode materials

All attempts to prepare classical NMP-based slurries for further coating on Al foils were unsuccessful (either by hand mixing of the garnet material and carbon or using ball milling) due to the separation of the mixed powders from NMP, therefore electrodes were prepared following two alternative methods:

1) Powder of active material was manually grinded in a mortar with carbon (Ketjen Black) in a mass ratio of 80:20 for 30 min. Next, the obtained mix was dried in a vacuum oven for 12h at 120°C and was directly used in powder form.

2) Self-standing electrodes were prepared by mixing powder of active material with carbon Ketjen Black and an aqueous solution of PTFE in a mass ratio 70:20:10. Few drops of ethanol were used to facilitate mixing and preparation of the film, from which disks of diameter 12 mm were punched. The prepared disks were next dried in a vacuum oven for 12 h at 120 °C. Mass loading of prepared electrodes was ~2.5 mg.cm^{-2}.

The as-prepared electrode materials were used to assemble the cells against lithium and sodium metal anodes using $LiPF_6$ or $NaPF_6$ in EC:DMC electrolytes. The half-cells were cycled in galvanostatic mode at C/40 and C/20 rate which corresponds to the exchange of one electron in 40 and 20 hours respectively. Different voltage windows were explored and 1.5 – 4.5 V (for the cells tested *vs.* Na anode) and 1.5 – 4.7 V (for the cells tested *vs.* Li anode) were finally chosen. Both cation insertion or extraction are possible to occur for the $Na_3Li_3V_2F_{12}$ and $Na_3Li_3Ti_2F_{12}$ garnets, therefore cells were either launched in charge or discharge. Cells comprising $Na_3Li_3Fe_2F_{12}$ as active material were launched in discharge due to the more probable reduction reaction to Fe^{II} than oxidation to Fe^{IV}.

Due to the high amount of carbon used to prepare the electrode materials, blank cells with only Ketjen Black powder *vs.* Na and Li anodes were assembled. Figure 5.15 shows the galvanostatic charge-discharge curves of Ketjen Black cycled *vs.* Na (a) and Li (b) anode at C/40 rate in the same voltage windows as subsequently cycled garnet materials. Derivative dQ/dV curves were additionally plotted in order to verify the existence/absence of faradaic processes occurring during cycling.

Figure 5.15: (a&b) Galvanostatic charge-discharge curves; (c&d) derivative dQ/dV curves of blank cells with Ketjen Black as an active material vs (a&c) Na; (b&d) Li; cycled at C/40 rate.

As expected, relatively high capacities are obtained in both tests as a result of the capacitive activity of Ketjen Black carbon. Indeed, this type of carbon exhibits a high surface area ($1400 \, m^2.g^{-1}$) which favors non-faradaic charge storage, as confirmed by the shape of the galvanostatic curves obtained. In the derivative curves, some features can be observed in both cells. In the cell cycled *vs.* Na (Figure 5.15a&c) a drop of ~0.5 V can be observed during the OCV measurement prior applying the current, followed by noisy shape of the discharge current, which could correspond to the internal problems of the contact between electrodes. A similar feature appears in the beginning of the subsequent charge (peaks ~2 V), however later the shape of the curve implies appropriate cycling. In both cells irreversible peaks at the end of charge (~4.05 V *vs.* Na^+/Na^0 and 4.30 V *vs.* Li^+/Li^0) suggest slight electrolyte oxidation which is favored with low C-rate used (C/40). In summary, Ketjen Black does contribute to the overall capacity of the prepared electrodes. From the capacity values obtained, it can be considered that since only 20% of carbon is used in the prepared electrode, a capacity of ~20 $mAh.g^{-1}$ can be considered as the Ketjen Black contribution.

- **Na$_3$Li$_3$V$_2$F$_{12}$**

Na$_3$Li$_3$V$_2$F$_{12}$ synthesized by the ball milling route was used for the electrochemical tests. Its smaller particle size is expected to improve the contact with carbon and to exhibit less kinetic limitations, which is expected to translate into better electrochemical performance.

Figure 5.16 shows the galvanostatic charge-discharge profiles of Na$_3$Li$_3$V$_2$F$_{12}$ cycled *vs.* Na and Li anode (a&c) together with its derivative dQ/dV curves (b&d).

Figure 5.16: Galvanostatic charge-discharge profile of Na$_3$Li$_3$V$_2$F$_{12}$ as a powder; cycled *vs.* Na (a) and *vs.* Li (c) in a voltage window 2.0-4.5 V together with the derivative dQ/dV curves (b&d).

While cycling the powder electrode *vs.* both Na and Li metal the upper cut-off voltage of 4.5 V was not reached and electrolyte oxidation was observed. In subsequent discharge *vs.* Na, no redox process was observed suggesting no insertion or extraction of any alkali cation. While cycling the electrode material *vs.* Li metal, the obtained discharge capacities were higher than the ones obtained for the Na cells, and additionally several peaks at ~2 V *vs.* Li$^+$/Li^0 in the derivative curve could suggest small activity of the V^{III} in this voltage range and will require further analysis.

Self-standing electrodes were expected to provide better homogeneity between garnet and carbon, however the electrochemical performance of garnet in this form was worse (not shown), and the exceptionally low value of the obtained capacity indicates no electrochemical performance.

- **$Na_3Li_3Fe_2F_{12}$**

For $Na_3Li_3Fe_2F_{12}$ garnet also the sample obtained from the ball milling synthesis was chosen.

Each cell was launched in discharge, followed by the subsequent charge-discharge in the voltage window: $1.5 – 4.5$ V *vs.* Na^+/Na^0 and $1.5 – 4.7$V *vs.* Li^+/Li^0. In this case, similar capacities and performance were obtained while using powder (Figure 5.17a and b) and self-standing electrodes (Figure 5.17c and d).

Figure 5.17: Galvanostatic charge-discharge profile of $Na_3Li_3Fe_2F_{12}$ as (a&b) powder; (c&d) self-standing electrode cycled *vs.* Na anode (a&c) in a voltage window 1.5-4.5 V; *vs.* Li anode (b&d) in a voltage window 1.5-4.7 V at C/40 rate.

Figure 5.18: Derivative dQ/dV (Q: specific capacity, V: cell voltage) curve for $Na_3Li_3Fe_2F_{12}$ *vs.* Na anode (a); Li anode (b) at C/20 rate (self-standing electrode).

While the discharge capacity was quite low (~10 mAh.g^{-1} *vs.* Na and ~ 20 mAh.g^{-1} *vs.* Li, see Figure 5.17) a reversible capacity of of ~30-40 mAh.g^{-1} *vs.* Na and 50-60 mAh.g^{-1} *vs.* Li was obtained. Derivative dQ/dV curves (Figure 5.18) were plotted for a closer analysis of the charge-discharge curves. While cycling the cell *vs.* Li, a peak at 2.6 V *vs.* Li$^+$/Li^0 can be observed in the first discharge. It could correspond to the redox reaction of Fe^{III}/Fe^{II}, however no corresponding oxidation process could be observed in the subsequent charge. The problem with the reversibility of this process might result from the internal changes in the structure upon chemical reduction. To confirm this hypothesis, *ex situ* XRD would be required to follow the structural changes upon cycling.

The observed activity at ~4 V in charge in both cells (*vs.* Li and *vs.* Na anode) is not reversible, therefore it is assumed to correspond to fluorine induced side reactions, [289] rather than the redox activity of the Fe^{III}/Fe^{IV} couple.

- **$Na_3Li_3Ti_2F_{12}$**

The electrochemical characterization of titanium $Na_3Li_3Ti_2F_{12}$ garnet was performed using the powder method. Figure 5.19 a&b shows the galvanostatic charge-discharge curves of $Na_3Li_3Ti_2F_{12}$ cycled at C/40 rate, whereas Figure 5.19 c&d corresponding derivative curves.

Figure 5.19: Galvanostatic charge-discharge profile of Na₃Li₃Ti₂F₁₂ as a powder; cycled *vs.* Na anode (a&c) in a voltage window 1.5-4.4 V; Li anode (b&d) in a voltage window 1.5-4.7 V at C/40 rate, together with the corresponding derivative dQ/dV curves (c&d).

As shown in Figure 5.19, the obtained capacities are very similar to the ones obtained for Na₃Li₃Fe₂F₁₂, suggesting a certain activity of the garnet apart from the carbon. However, the derivative curve for the cell cycled *vs.* Na (Figure 5.19c) does not reveal clear peaks that could be related to the redox reaction of Ti^{III}/Ti^{IV}. On the contrary, the small peaks centered at 2.95 V *vs.* Li^+/Li^0 in the charge and 2.6 V *vs.* Li^+/Li^0 observed during discharge in the cell cycled *vs.* Li (Figure 5.19d) correspond to the region of activity of the Ti^{III}/Ti^{IV} redox couple and could suggest redox activity of the garnet. The observed activity ~4 V *vs.* Na^+/Na^0 and ~3.8 V *vs.* Li^+/Li^0 is assumed to correspond to fluorine induced side reactions.

The performed electrochemical tests unfortunately resulted with relatively poor performances of the garnet fluorides. The obtained capacities are higher than the capacity calculated to correspond to the carbon contribution, indicating some activity of the materials, however only in the Na₃Li₃Ti₂F₁₂ garnet cycled *vs.* Li anode reversible redox processes that can be assigned to the transition metal couple were observed in the dQ/dV curves. The insulating nature of the fluorides is expected to be the main reason of the

problems with the electrochemistry. Electrode processing such as extended ball-milling with carbon or the use of carbon nanotubes may be needed to enhance the electrochemical performance.

5.6. Chemical oxidation & reduction

As the results from the electrochemical were not completely conclusive, chemical oxidation/reduction reactions were performed on all garnets to confirm that no Na^+/Li^+ cations can be extracted from the structure.

- **$Na_3Li_3V_2F_{12}$ – chemical oxidation**

Due to the high stability of garnet phase in water, the first test was performed using an aqueous solution of potassium persulfate, $K_2S_2O_8$. Persulfate is a known oxidizing agent and is widely used for the delithiation/desodiation reactions due to appropriate redox potential (~5 V *vs.* Li^+/Li; ~4.7 V *vs.* Na^+/Na, 2.6 V *vs.* SHE) and facile use.

In a first step, $K_2S_2O_8$ was dissolved in water to prepare 0.5M solution, next the powder of $Na_3Li_3V_2F_{12}$ was added and the suspension was stirred for 24 h at room temperature under air. As can be seen on the photographs in Figure 5.20; the mixture changed the color from dark green to light green upon 24 h stirring. The obtained green powder was filtered, washed three times with water and dried overnight at 60 °C.

Figure 5.20: Mixture of $Na_3Li_3V_2F_{12}$ in aqueous solution of $K_2S_2O_8$ in the beginning of the reaction (left); and after 24h of stirring (right).

From the BVEL calculations it is difficult to predict which alkali cation will be removed, therefore the expected reaction is as follows:

$$A_3V_2F_{12} + 0.5\,K_2S_2O_8 \;\rightarrow\; A_5V_2F_{12} + 0.5\,A_2SO_4 + \; 0.5\,K_2SO_4$$

The XRD patterns of pristine $Na_3Li_3V_2F_{12}$ and $(Na,Li)_{6-x}V_2F_{12}$ phases are shown in Figure 5.21. In the XRD patterns of $(Na,Li)_{6-x}V_2F_{12}$ the position and the relative intensities of the peaks did not change, which suggests unsuccessful oxidation. The LiF observed in the pristine material was partially removed with water. In the XRD pattern of $(Na,Li)_{6-x}V_2F_{12}$ additional peaks were indexed as the K_2NaVOF_5 phase, which could indicate a partial decomposition reaction of the garnet when reacted with $K_2S_2O_8$. Based on the Rietveld refinement, the sample obtained after oxidation contains 88% of garnet $Na_3Li_3V_2F_{12}$, phase, 10% of K_2NaVOF_5 and 2% of LiF (Figure 5.22).

The refined cell parameters of $(Na,Li)_{6-x}V_2F_{12}$ are the same as those of the pristine phase, which together with the lack of changes in the XRD pattern would indicate no oxidation occurring in the garnet structure.

Figure 5.21: XRD pattern of Na₃Li₃V₂F₁₂ and (Na,Li)₆₋ₓV₂F₁₂ (chemically oxidized with K₂S₂O₈). Position of Bragg peaks corresponding to Na₃Li₃V₂F₁₂, LiF and K₂VOF₅ phases are represented as green, orange and violet, respectively.

Figure 5.22: Rietveld refinement of (Na,Li)₆₋ₓV₂F₁₂ . Position of Bragg peaks corresponding to Na₃Li₃V₂F₁₂, K₂VOF₅, and LiF phases are represented as green, violet and orange, respectively.

A second chemical oxidation attempt was performed for $Na_3Li_3V_2F_{12}$ by mixing the powder of the garnet with another oxidizing agent, NO_2BF_4 (similar redox potential of ~5 V *vs.* Li^+/Li; ~4.7 V *vs.* Na^+/Na), in an acetonitrile solution in a 1:2.5 molar ratio. The as-prepared suspension was stirred for 24h at 70 °C in the glovebox under Ar. The resulting suspension was filtered, washed three times with acetonitrile and dried overnight

246

at room temperature. Figure 5.23 presents the XRD patterns of both pristine $Na_3Li_3V_2F_{12}$, and $(Na,Li)_{6-x}V_2F_{12}$.

Figure 5.23: XRD pattern of $Na_3Li_3V_2F_{12}$, and $(Na,Li)_{6-x}V_2F_{12}$ chemically oxidized with NO_2BF_4 in ACN.

The XRD pattern of the obtained sample does not differ from the XRD pattern of pristine $Na_3Li_3V_2F_{12}$ indicating that oxidation with NO_2BF_4 was also not successful.

To confirm the conclusions from the XRD analysis and exclude the possibility that garnet could be a zero-strain material, X-ray absorption spectra of V $L_{2,3}$-edge $(Na,Li)_{6-x}V_2F_{12}$ Figure 5.24 shows the acquired $L_{2,3}$-edge & O K-edge spectra of $(Na,Li)_{6-x}V_2F_{12}$ together with spectra of pristine $Na_3Li_3V_2F_{12}$ and the calculated V^{III} and V^{IV} $L_{2,3}$ edge spectra with Oh coordination symmetry and a crystal field splitting energy of 2.5 eV as reference.

Figure 5.24: XAS V L$_{2,3}$-edge & O K-edge spectra in Na$_3$Li$_3$V$_2$F$_{12}$ and (Na,Li)$_{6-x}$V$_2$F$_{12}$. Signals from electron detection mode (EY) corresponding pristine Na$_3$Li$_3$V$_2$F$_{12}$are represented in black color; whereas signals from EY mode corresponding to (Na,Li)$_{6-x}$V$_2$F$_{12}$ are represented in red color. Blue curves correspond to the calculated XAS V^{III} and V^{IV} L$_{2,3}$-edge spectra with Oh coordination symmetry and a crystal field splitting energy of 2.5 eV.

The spectrum exhibits two main broad bands centered at 518 and 524 eV, which are attributed to V^{III} state as in the pristine phase. A slight difference between two experimental spectra can be noticed in the O K-edge, in the energy range of 528 – 534 eV (indicated in Figure 5.24). The change in this region corresponds to the increase of the V3d – O2p hybridization.[168] The variation of the intensities of the two peaks at 529 and 532 eV from 3:2 to 2:3 may indicate partial oxidation of V^{III} into V^{IV} however the absence of the characteristic bands of V^{IV} state in the V L$_{2,3}$-edge indicate that the amount of the V^{IV} states at the surface is very low.

A final attempt with a large excess of NO$_2$BF$_4$ (1:6) resulted with complete decomposition into NaBF$_4$ and LiF, and aqueous solution containing vanadium ions.

All these results imply that both electrochemical and chemical oxidation of V^{III} into V^{IV} is very difficult and suggests a very high stability of the Na$_3$Li$_3$V$_2$F$_{12}$ phase. DFT

calculations on the stability of both $Na_3Li_3V_2F_{12}$ and oxidized $(Na,Li)_{6-x}V_2F_{12}$ phases as well as the predicted voltage of the $V^{III/IV}$ redox couple would be recommended to support this conclusion.

- **$Na_3Li_3V_2F_{12}$ – chemical reduction**

As chemical oxidation resulted unsuccessful, the following trials were focused on chemical reduction of $Na_3Li_3V_2F_{12}$ with the eventual possibility to accommodate additional alkali cation, as was presented in the case of garnet $Li_3Nd_3W_2O_{12}$.

For this reaction, LiI was selected as reducing agent and lithium source, which has an operating redox potential of 2.6 V *vs.* Li^+/Li. [290–292] Li insertion is expected to occur following this reaction:

$$Na_3Li_3V_2F_{12} + \frac{3}{2}\, LiI\ \rightarrow Na_3Li_4V_2F_{12} + \frac{1}{2}\, LiI_3$$
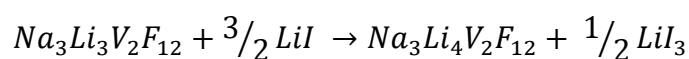
The chemical lithiation was performed in an Ar-filled glovebox due to the highly hydroscopic nature of LiI. $Na_3Li_3V_2F_{12}$ was suspended in a 0.5 M solution of LiI in acetonitrile. Three different V:Li molar ratios were investigated: 1:1.5; 1:3 and 1:6. The mixtures were stirred for 24 h at 70 °C. Next, the precipitates were washed three times with acetonitrile to remove the remaining LiI. The obtained powders were dried overnight at room temperature.
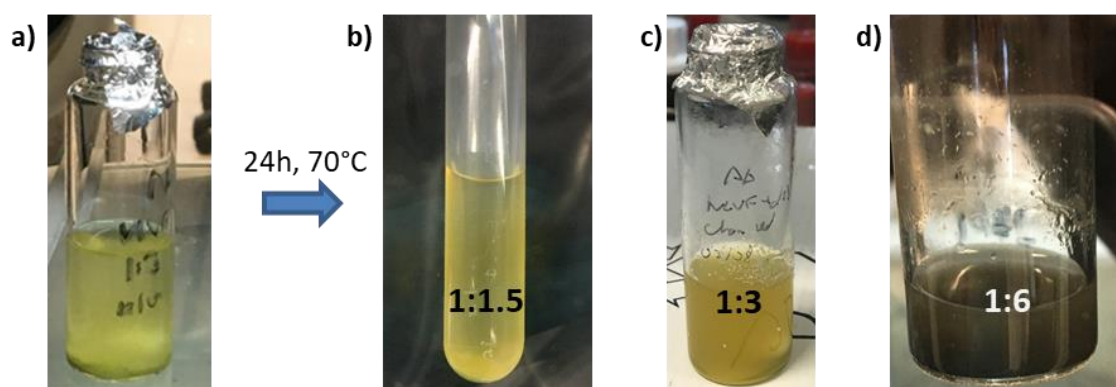
Figure 5.25: (a) $Na_3Li_3V_2F_{12}$ in acetonitrile solution of LiI prior to the reaction; (b,c&d) solution after 24h of stirring at 70 °C with the used V:Li molar ratio indicated in the photo.

Figure 5.25 shows the suspension of $Na_3Li_3V_2F_{12}$ in acetonitrile solution of LiI before and after the reactions. Only for the 1:6 V:Li molar ratio the color of the obtained solution changed from light yellow to dark brown.

XRD patterns of each obtained powder of the $Na_3Li_{3+x}V_2F_{12}$ phase are gathered in Figure 5.26. Although the signals corresponding to the garnet phase can be observed, a large amount of impurities was detected already when using the smallest amount of the reducing agent.
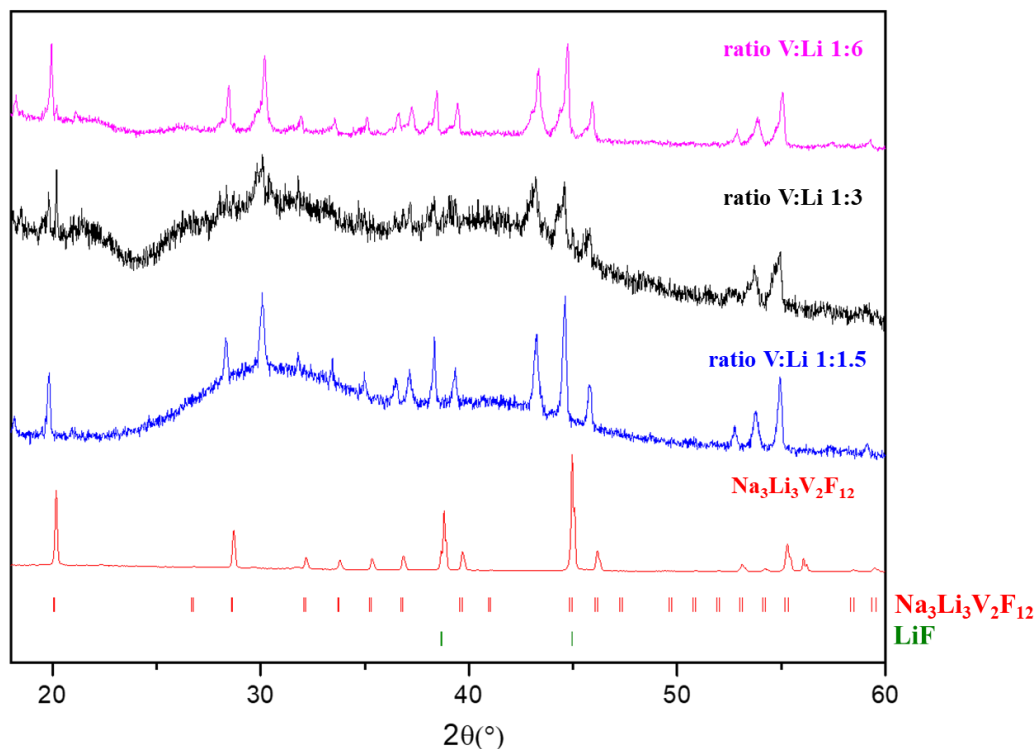
Figure 5.26: XRD pattern of $Na_3Li_3V_2F_{12}$ and $Na_3Li_{3+x}V_2F_{12}$ (chemically reduced by acetonitrile solution of LiI with the V:Li ratio indicated in the figure). Position of Bragg peaks corresponding to $Na_3Li_3V_2F_{12}$ and LiF phases are represented as red and green respectively.

Since the amount of recovered material was rather low, the patterns are noisy and in the black XRD pattern (ratio V:Li 1:3) exhibit a shoulder on the left side of each peak that derives from a shift of the powder in the XRD holder while performing the measurement.

Based on the performed experiments, it can be concluded that in the oxidizing medium $Na_3Li_3V_2F_{12}$ remains very stable, whereas in the reducing one already with the small amount of LiI occurs the decomposition.

- **$Na_3Li_3Fe_2F_{12}$ – chemical reduction**

$Na_3Li_3Fe_2F_{12}$ garnet was also attempted to be chemically reduced by a LiI acetonitrile solution with a Fe:Li molar ratio of 1:6.
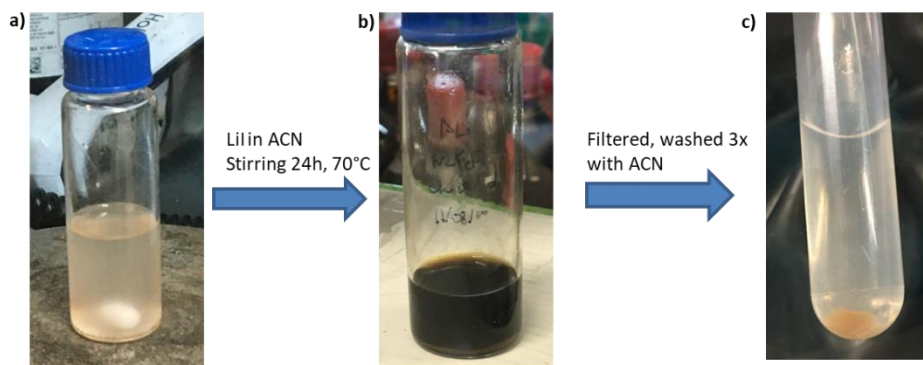
Figure 5.27: (a) Na₃Li₃Fe₂F₁₂ in acetonitrile (ACN) solution of LiI prior to the reaction; (b) solution after stirring 24 at 70 °C; (c) powder in acetonitrile after washing three times.

Figure 5.27 shows the changes in the color of the solution upon reduction reaction. After stirring for 24 h the light pink solution changed color into black, however the washed powder was eventually slightly darker than the powder of pristine $Na_3Li_3Fe_2F_{12}$.

The XRD pattern of $Na_3Li_3Fe_2F_{12}$ and $Na_3Li_{3+x}Fe_2F_{12}$ are shown in Figure 5.28. A small change in the ratio of the intensities of the peaks can be observed, especially in the doublet at 45 and 46°. The lack of changes in the position of the signals corresponding to the garnet phase suggest unsuccessful reduction reaction. The XRD pattern of the reduced phase could be refined with garnet structure with same unit cell parameters as the pristine phase.
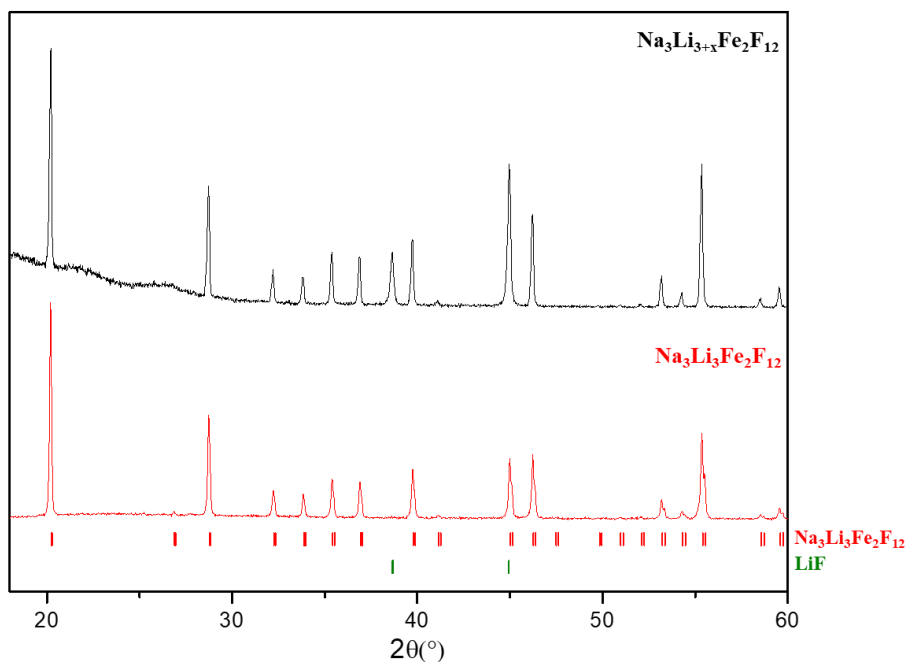
Figure 5.28: XRD patterns of Na₃Li₃Fe₂F₁₂ and Na₃Li₃₊ₓFe₂F₁₂. Vertical green and red bars indicate the position of the Bragg indexes of the Na₃Li₃Fe₂F₁₂ and LiF phases, respectively.

While comparing with the results obtained for both garnets, $Na_3Li_3Fe_2F_{12}$ exhibits much higher stability in the reducing atmosphere than $Na_3Li_3V_2F_{12}$. However, no lithium insertion could be demonstrated.

- **$Na_3Li_3Ti_2F_{12}$ – chemical oxidation**

Contrary to Fe and V systems, the chemical oxidation of $Na_3Li_3Ti_2F_{12}$ using NO_2BF_4 in acetonitrile solution resulted in the transformation of the garnet into a new phase that could not be indexed as a cubic garnet (see Figure 5.29).
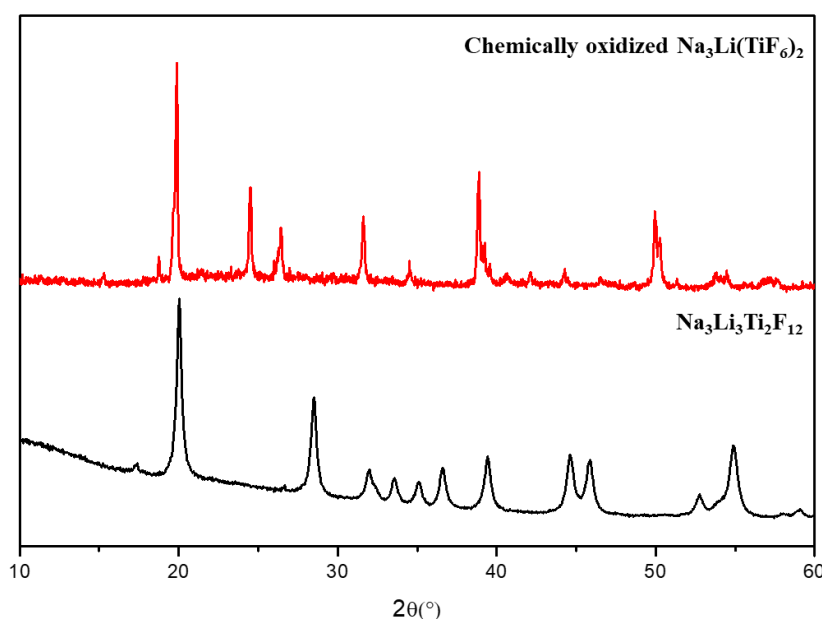
Figure 5.29: XRD patterns of pristine garnet $Na_3Li_3Ti_2F_{12}$ and chemically oxidized phase, identified as being $Na_3Li(TiF_6)_2$.

The peaks of the new obtained phase were indexed as the $Na_3Li(TiF_6)_2$ compound (which can also be written as $Na_3LiTi_2F_{12}$, by analogy to the garnet material) indicating chemical oxidation of Ti^{III} to Ti^{IV} and extraction of two Li^+ cations.[293] The oxidation of Ti^{III} to Ti^{IV} is thus here related to a structural transformation from cubic to tetragonal symmetry. The structure of $Na_3Li(TiF_6)_2$ was determined by Popov et. al.[293] while investigating mixed-cation hexafluoro complexes of Group IV elements. No further studies or potential application of this phase have been reported to date. As explained in the beginning of this subsection, from the BVEL calculations (Chapter 1) it was not clear which alkali cation can be removed from the structure. Based on the results obtained for $Na_3LiTi_2F_{12}$, it can be observed that only Li cations are removed.

In the next part, this $Na_3LiTi_2F_{12}$ phase will therefore be characterized and discussed to a further extent.

5.7. $Na_3Li(TiF_6)_2$ as an alternative electrode material

5.7.1. Structural and morphological characterization

The violet powder obtained from the chemical oxidation of the garnet $Na_3Li_3Ti_2F_{12}$ was then subjected to detailed analysis. First, the profile matching of the obtained XRD pattern (Figure 5.30) was performed to validate the correct indexation of the synthesized phase with the reported $Na_3LiTi_2F_{12}$ phase. [293]
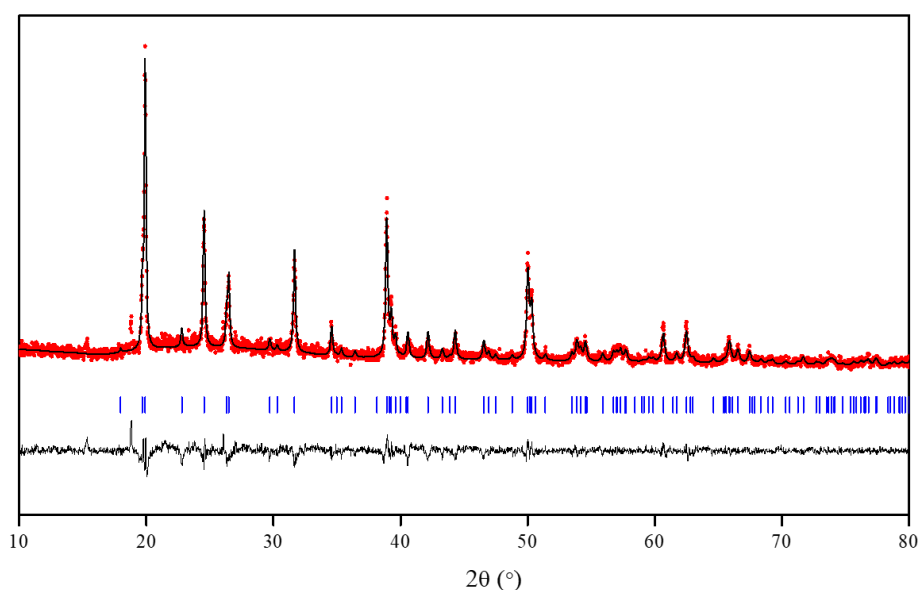
Figure 5.30: Le Bail profile matching of the XRD pattern of oxidized $Na_3Li(TiF_6)_2$ phase.

The reported crystal structure of $Na_3Li(TiF_6)_2$, shown in Figure 5.31, consists of alternating layers of edge-shared TiF_6 octahedra (represented in blue) and $Na(1)F_6$ polyhedra (represented in yellow) forming $NaTiF_{10}$ dimers. These layers are linked by the vertex shared LiF_4 tetrahedra and $Na(2)F_8$ polyhedra forming a three-dimensional framework. Atomic coordinates of all atoms are given in Table 5.12.
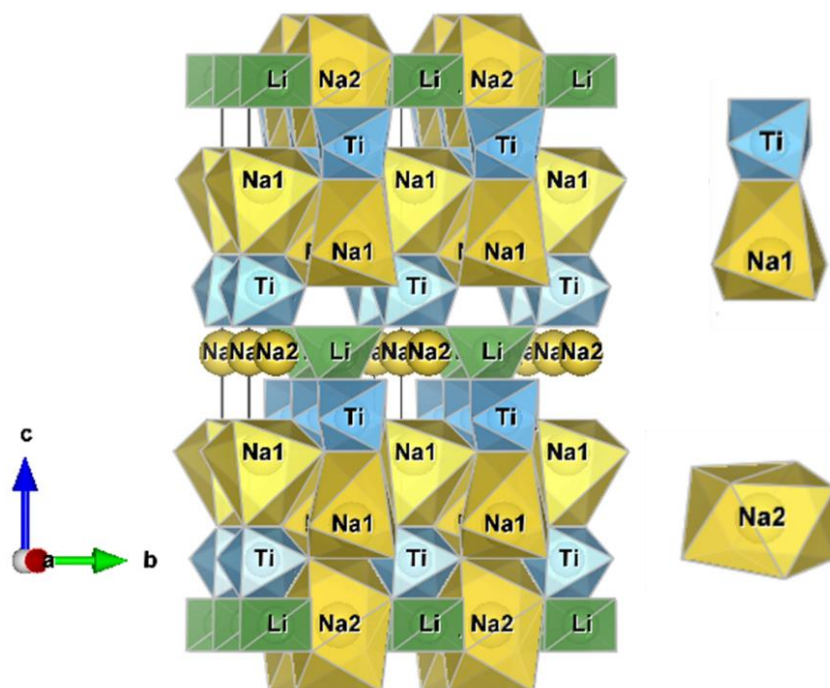
Figure 5.31: Crystal structure of Na₃Li(TiF₆)₂. TiF₆ octahedra are represented in blue, Na(1)F₆ and Na(2)F₈ polyhedra in blue and LiF₄ tetrahedra in green. Na(2)F₈ polyhedra in the middle of the figure were removed for the visibility of formed layers of the Ti and Na(1) octahedra. On the right are highlighted dimer of the edge-shared NaTiF₁₀ and distorted Na(2)F₈ dodecahedron.

Table 5.12: Crystallographic data and atomic coordinates of Na₃Li(TiF₆)₂. The values of the cell parameters are obtained from the LeBail profile matching, whereas the atomic positions are from the reported structure of Na₃Li(TiF₆)₂ [293]

S.G.: *P*-42₁*c*	a =5.126(1) Å c =18.026(6) Å	V = 473.60(2) Å³		R_{Bragg} =30.6%	χ^2 = 3.00	
Atom	Wyckoff position	*x/a*	*y/b*	*z/c*	B_{iso}	*Occ*
Ti	4*d*	0	0	0	1.0	1
Na1	4*d*	0	½	0.185(5)	1.0	1
Na2	2*b*	0	0	½	1.0	1
Li	2*a*	½	½	½	1.0	1
F1	8*e*	0.298(2)	0.147(4)	0.198(3)	1.0	1
F2	8*e*	0.233(4)	0.657(5)	0.456(5)	1.0	1
F3	8*e*	0.290(4)	0.456(3)	0.116(3)	1.0	1

In order to get further insight in the oxidation reaction and evaluate its possible topotactical character, the structure of Na₃Li(TiF₆)₂ was compared with the structure of Na₃Li₃Ti₂F₁₂ garnet.

Table 5.13 gathers the interatomic distances within both structures. In the garnet framework, Ti is octahedrally coordinated in TiF₆ octahedra of equal Ti-F distances of 1.986(3) Å. In Na₃Li(TiF₆)₂ the octahedra are slightly distorted, characterized by Ti-F distances varying from 1.833(4) Å to 1.892(4) Å. The shorter Ti-F bond distances of

Na$_3$Li(TiF$_6$) octahedra arise from the smaller ionic radius size of Ti^{IV} (0.605 Å) compared to Ti^{III} (0.67 Å).[200] Within Na$_3$Li(TiF$_6$)$_2$ two independent Na$^+$ ions are forming distorted Na(1)F$_6$ octahedra and distorted Na(2)F$_8$ dodecahedra (Figure 5.31). The average Na(2)-F distances in the dodecahedra (2.439 Å) are very similar to the ones in the garnet structure where all Na ions are forming distorted NaF$_8$ dodecahedra with average Na-F distances of 2.489 Å. LiF$_4$ tetrahedra of Na$_3$Li(TiF$_6$)$_2$ are slightly larger than those of the garnet structure, with Li-F distances changing from 1.989 Å to 1.827 Å.

Seeking a relationship between these two structures, first, their frameworks with only TiF$_6$ octahedra were visualized with a help of the VESTA program.[136] Figure 5.32a and b present the garnet and Na$_3$Li(TiF$_6$)$_2$ structures, respectively with indicated Ti-Ti distances between TiF$_6$ octahedra. As most of the distances were elongated or contracted, the framework of the garnet was rotated until finding the proper orientation, where the distances in the two structures would be similar. It was found that all TiF$_6$ have to rotate around their center to transform on structure into the other. Dark blue color indicates the rearrangement at which Ti octahedra would be at similar position in both structures. It can be observed that the Ti-Ti distances are more comparable. Next, to selected framework of Ti octahedra, surrounding Na and Li polyhedral were added and their relationships were investigated. In the garnet structure (Figure 5.32c), each TiF$_6$ octahedra shares all vertices with six LiF$_4$ tetrahedra and edge-sharing six NaF$_8$ polyhedra (two layers of three polyhedra) forming a three-dimensional network. The TiF$_6$ octahedral environment changes after the structure transformation into Na$_3$Li(TiF$_6$)$_2$. Removal of two lithium atoms from the structure results with the presence of only two LiF$_4$ tetrahedra connected to TiF$_6$ octahedra through vertex sharing fluorine. Rearrangement of the sodium polyhedra also changes significantly. They are either edge-sharing (indicated in yellow in Figure 5.32d), or vertex-sharing (indicated in orange in Figure 5.32d) TiF$_6$ octahedra. These results suggest that the chemical oxidation is related to the structural rearrangements occurring after removal of two Li atoms and final adaptation of the tetragonal unit cell.

Table 5.13: Comparison of interatomic distances in the structures of garnet $Li_3Na_3Ti_2F_{12}$ and $Na_3Li(TiF_6)_2$.

	$Na_3Li(TiF_6)_2$[293]	$Li_3Na_3Ti_2F_{12}$
Ti-F(1)	1.833(4) Å x2	1.986(3) Å x6
Ti-F(2)	1.892(4) Å x2	
Ti-F(3)	1.854(3) Å x2	
Na(1)-F(1)	2.376(3) Å x2	2.597(3) Å x4
Na(1)-F(1)	2.415(5) Å x2	2.382(3) Å x4
Na(1)-F(3)	2.252(4) Å x2	
Na(2)-F(2)	2.293(3) Å x4	
Na(2)-F(3)	2.585(3) Å x4	
Li-F(2)	1.898(3) Å x4	1.827(3) Å x4
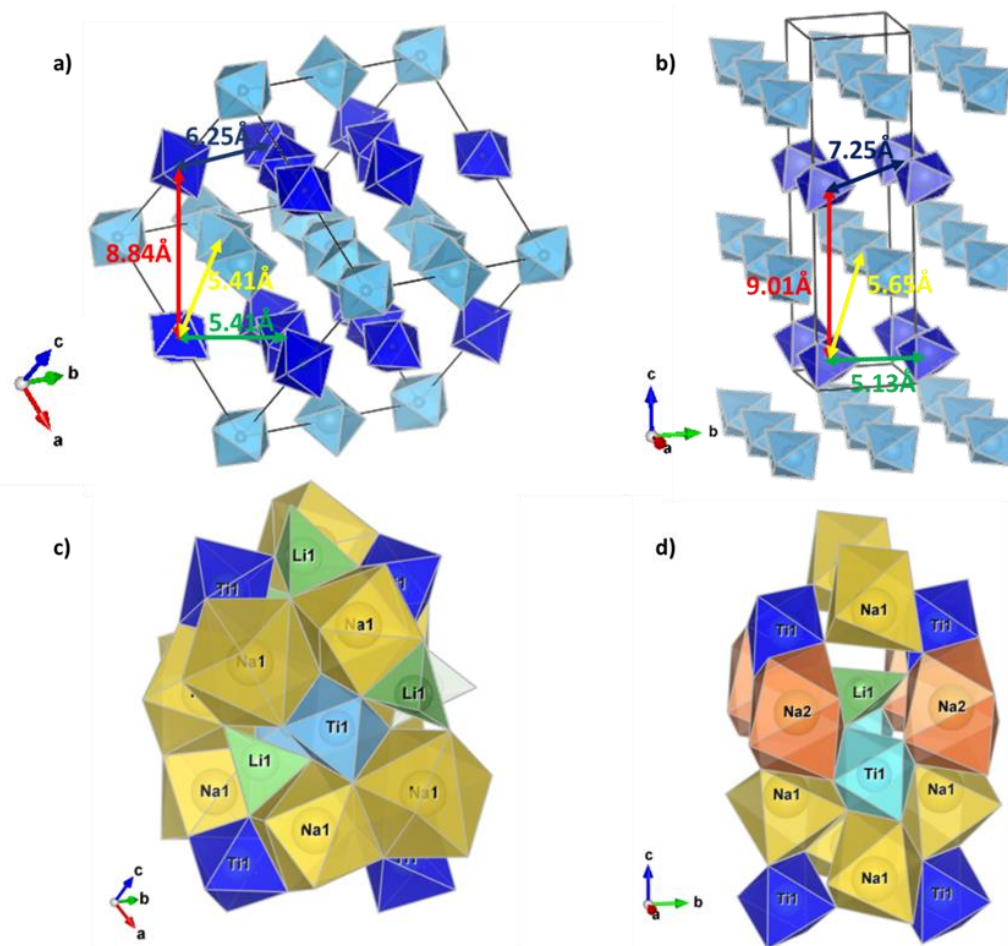
Figure 5.32: Visualization of the crystal structure of (a&c) $Na_3Li_3Ti_2F_{12}$ and (b&d) $Na_3Li(TiF_6)_2$ at different orientations, where the distances in two structures are more or less similar, as indicated in the figure. By blue color are represented TiF_6 octahedra. Dark blue color indicates the rearrangement at which Ti octahedra would be at similar position in both structures. By yellow are indicated Na octahedra which are edge-sharing Ti octahedra; whereas by orange, the octahedra which are vertex-sharing Ti octahedra.

256

The morphology of $Na_3Li(TiF_6)_2$ was evaluated by SEM. Figure 5.33 shows the images of both $Na_3Li_3Ti_2F_{12}$ (a) and $Na_3Li(TiF_6)_2$ (b) samples. Garnet $Na_3LiTi_2F_{12}$ was synthesized with the ball-milling route, thus the nano-sized particles are grouping in agglomerates of non-uniform shape. Particles of $Na_3Li(TiF_6)_2$ have very similar nanoscopic size with a tendency to agglomerate. Based on the XRD, the peaks of the $Na_3Li(TiF_6)_2$ are much sharper than the ones of $Na_3Li_3Ti_2F_{12}$, which might suggest recrystallization of the $Na_3Li(TiF_6)_2$ particles upon the reaction, however no visible morphological change can be observed. Based on the refinement of the XRD patterns of both structures, the average crystallite size obtained using the Scherrer formula, is estimated to be approximately 24 nm for the garnet $Na_3LiTi_2F_{12}$, whereas particles of $Na_3Li(TiF_6)_2$ are around ~38 nm, confirming a possible growth during the reaction.
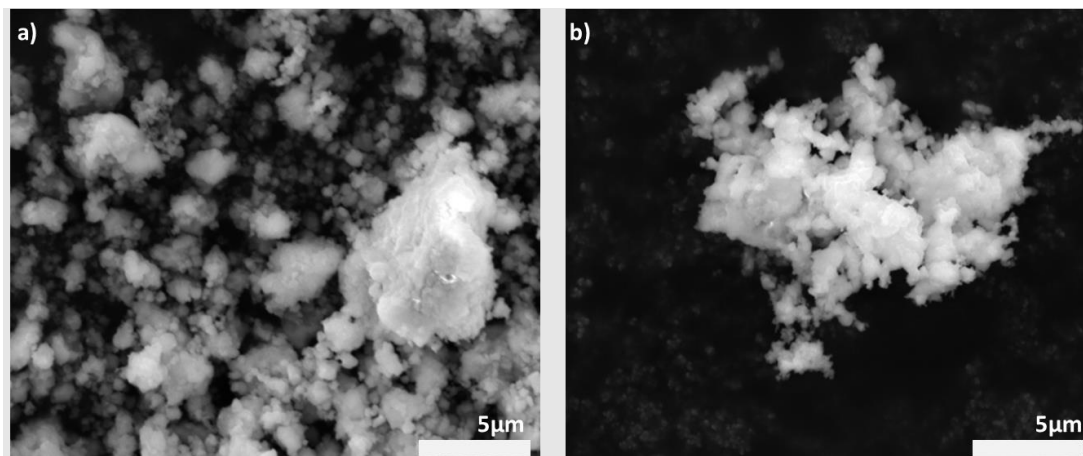
Figure 5.33: SEM images of (a) pristine $Na_3Li_3Ti_2F_{12}$ garnet, (b) $Na_3Li(TiF_6)_2$.

The results of the elemental ratio evaluated by EDX and ICP are gathered in Table 5.14. The experimental ratio of the elements in the EDX analysis was calculated based on the average atomic % of ten measurements. Final ratios were calculated by fixing the transition metal to its stoichiometric value. The obtained results are slightly lower than the theoretical ratios, however, as was explained in section 5.2.4.1, the measured amount of fluorine can be lower due to its migration upon beam radiation.

Table 5.14: Composition of Na$_3$Li(TiF$_6$)$_2$ determined by EDX and ICP

Element	Theoretical content	Experimental atomic ratio determined from EDX	Experimental atomic ratio determined from ICP
Na	3	2.7±0.14	3.1±0.03
Li	1	-	1.2±0.02
Ti	2	2.0 (fixed)	2.0 (fixed)
F	12	9.1±0.46	-

With the use of ICP technique, sodium, lithium and titanium were detected and quantified. The detection of fluorine was impossible due to the high ionization potential of this element.[280] The final ratio was calculated using the transition metal content as reference. The quantified amount of sodium and lithium is in good agreement with the theoretical values confirming the expected composition of the Na$_3$Li(TiF$_6$)$_2$ phase.

5.7.2.   X-ray absorption spectroscopy study

X-ray absorption spectroscopy analysis was conducted on Na$_3$Li(TiF$_6$)$_2$, at the Ti L$_{2,3}$- and F K-edges to confirm the observed chemical oxidation of Ti^{III} to Ti^{IV}. XAS data was collected using both total electron and fluorescence yield detectors. Signals from electron detection mode (EY) correspond to the chemical state of the surface layer of the material, whereas fluorescence yields (FY) correspond to approximately 100 - 500 nm into the particle. Results were compared with the ones obtained for the Na$_3$Li$_3$Ti$_2$F$_{12}$ garnet to follow the changes occurring in both the bulk and on the surface upon chemical oxidation. As a reference, spectra for both Ti^{III} and Ti^{IV} were computed with octahedral coordination symmetry and a crystal field splitting energy of 1.4 eV for Ti^{III} and 2.6 eV for Ti^{IV}. The computed spectra were generated with the program CTM4XAS. [166,216]
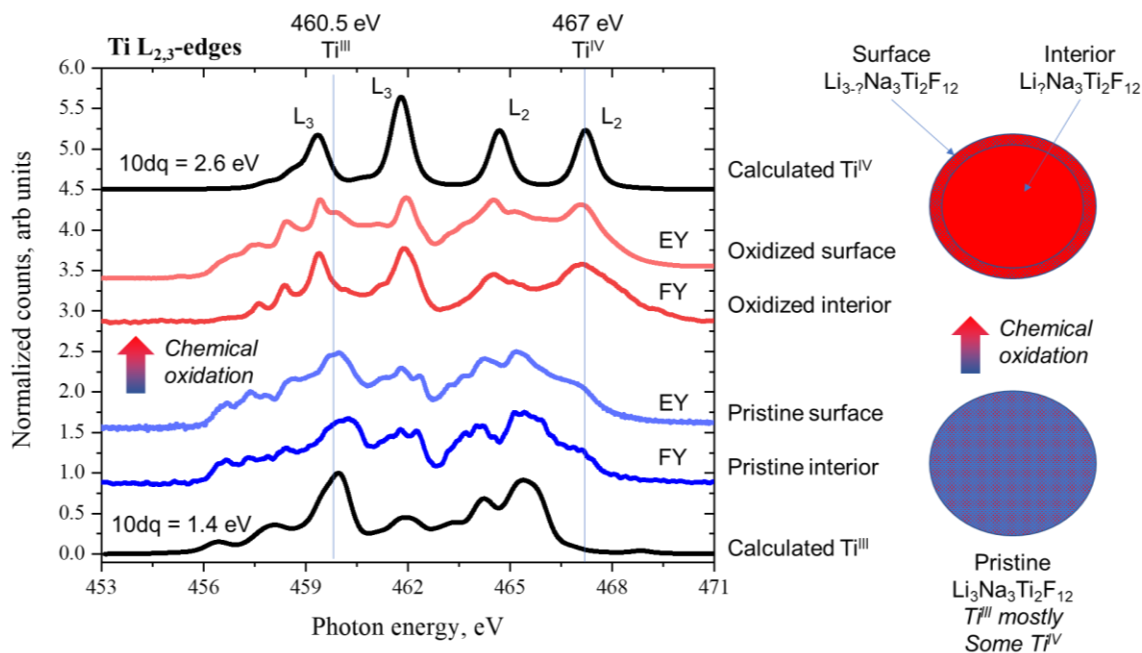
Figure 5.34: Integrated X-ray absorption spectra of Ti L$_{2,3}$-edge in pristine Li$_3$Na$_3$Ti$_2$F$_{12}$ garnet (indicated in blue) and Na$_3$Li(TiF$_6$)$_2$ (indicated in red). Black curves correspond to the calculated XAS Ti^{III} and Ti^{IV} L$_{2,3}$-edge spectra with Oh coordination symmetry and a crystal field splitting energies of 1.4 and 2.6 eV, respectively. On the right, proposed composition of the pristine and oxidized material with the assumed arrangement of the Ti species.

As explained in 5.4.4.1. section, the pristine material likely has both Ti^{III} and Ti^{IV} in the surface and the bulk since the spectra from electron and fluorescence yields are similar. Upon chemical oxidation the shape and energy positions of the peaks changed both in the surface and in the bulk. In the fluorescence yield, the position of the four most intense peaks matches the calculated spectrum of Ti^{IV} which means that the interior of Na$_3$Li(TiF$_6$)$_2$ is composed of Ti^{IV} states. Same peaks are also observed in the surface indicating a majority composition of Ti^{IV} states, however additional peak at 460.5 eV indicates copresence of a low amount of Ti^{III}.

Analysis of the fluorine K-edge X-ray absorption spectroscopy of Na$_3$Li(TiF$_6$)$_2$ was conducted to probe the metal-ligand covalency in TiF$_6^{-II}$ anion based on the presence of pre-edge features (Figure 5.34a).[287]
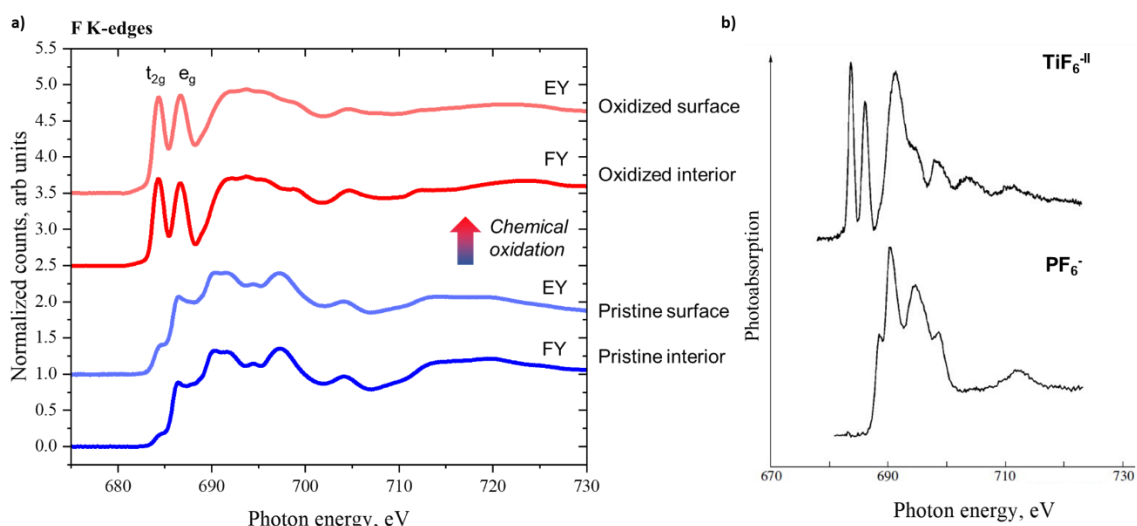
Figure 5.35: (a) XAS spectra of F K edge in pristine Li₃Na₃Ti₂F₁₂ garnet and Na₃Li(TiF₆)₂ (oxidized garnet) collected at ALBA synchrotron; (b) XAS spectra of F K edge in K₂TiF₆ and KPF₆ crystals, from Vinogradov *et.al.* [284]

Two distinct regions can be distinguished in the spectra. First are the features in the pre-edge region (<688 eV) corresponding to F $2p$ orbitals hybridizing with empty Ti($3d$) states. In the main region (>688 eV) the features correspond to F $2p$ orbitals hybridizing with empty Ti ($4sp$) states. The spectra obtained for Na₃Li(TiF₆)₂ were compared with the spectra of pristine Na₃Li₃Ti₂F₁₂ garnet and K₂TiF₆ and KPF₆ from the work of Vinogradov *et.al.* [284] (Figure 5.35b).

In pristine Na₃Li₃Ti₂F₁₂ garnet F K-edge electron yield (EY) and fluorescence yield (FY) are very similar in shape and energy position; indicating that the surface and bulk states of F are the same, which is consistent with Ti L₂,₃-edge analysis. The F K-edge spectra in Na₃Li(TiF₆)₂ are in good agreement with the F K-edge in TiF₆$^{-II}$ octahedral environment.[284] The pre-edge peak at 684 eV represents covalent mixing between Ti($3d$ - t₂g) and F($2p$) states, while the pre-edge peak at 687 eV represents covalent mixing between Ti($3d$ - eg) and F($2p$) states. The relative intensity of these pre-edge peaks changes between electron and fluorescence yields. In the fluorescence yield (FY), the t₂g peak is slightly more intense than the eg peak, which is similar to pre-edge features in O K-edge spectra of TiO₂.[294] These observations are consistent with Ti L₂,₃-edge analysis indicating that the bulk is composed of Ti^{IV} states and the surface has some remaining Ti^{III}. Although the amount of the Ti^{III} could not be quantified, it is expected to be very low and have no impact on the electrochemical performance of Na₃Li(TiF₆)₂.

5.7.3. Electrochemical evaluation as Na-ion and Li-ion positive electrode material

Since the chemical oxidation of $Na_3Li_3Ti_2F_{12}$ garnet resulted in a structural transformation, the electrochemical activity of the oxidized material was evaluated in powder form using the material obtained after ball milling $Na_3Li(TiF_6)_2$ with carbon (Ketjen Black) in a molar ratio 85:15. The prepared half-cell was cycled *vs.* Li metal at C/20 rate. Figure 5.36 shows the galvanostatic charge-discharge profile of $Na_3Li(TiF_6)_2$ together with the corresponding derivative curve.
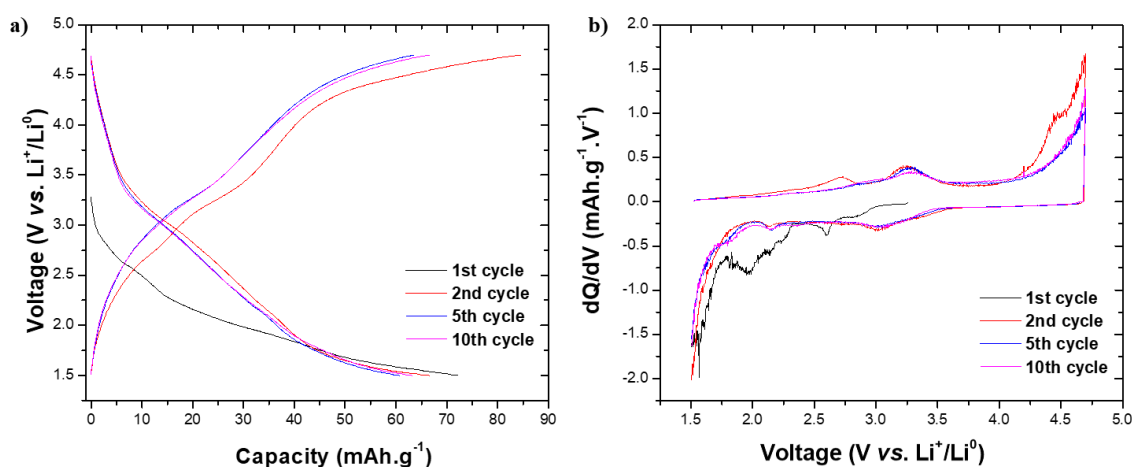
Figure 5.36: (a) Galvanostatic charge-discharge profile; (b) corresponding dQ/dV curve of $Na_3Li(TiF_6)_2$ cycled *vs.* Li in a voltage window 1.5-4.7 V

The obtained capacity of ~70 $mAh.g^{-1}$ during the first discharge corresponds to the insertion of one Li^+ associated with the reduction of Ti^{IV} to Ti^{III}. Subsequent charge-discharge processes result with a stable capacity of around 60 $mAh.g^{-1}$. The additional capacity obtained during the first charge, corresponding to the peak at 4.5 V *vs.* Li^+/Li in the dQ/dV curve, is expected to be associated with the electrolyte oxidation. Analysis of the dQ/dV curves reveals that the reversible Li^+ insertion/extraction occurs at an average voltage of 3.1 V *vs.* Li^+/Li corresponding to the reaction of $Ti^{III/IV}$ redox couple. Interestingly, it is around 0.3 V higher than observed in $Na_3Li_3Ti_2F_{12}$ garnet. Additionally, it is worth highlighting that it is the highest working voltage of this redox couple among polyanionic compounds. So far, the highest redox potential attributed to $Ti^{III/IV}$ redox couple was observed in sodium titanium nitridophosphate, $Na_3Ti(PO_3)_3N$[146] (2.95 V *vs.* Li^+/Li) ascribed to the high inductive effect of the nitridophosphate group. The obtained value of 3.1 V suggests an even higher inductive effect of more electronegative fluorine atom in $Na_3Li(TiF_6)_2$.

Further characterization is required to fully understand the electrochemical performance of $Na_3Li(TiF_6)_2$. As this phase was obtained by the chemical oxidation of $Na_3Li_3Ti_2F_{12}$ garnet, one would expect that upon electrochemical reduction of $Na_3Li(TiF_6)_2$ the reverse process occurs with transformation into garnet cubic structure. Validation of this hypothesis will require *ex situ* XRD measurement of the fully discharged electrode, followed by the *in situ* XRD tracking the eventual phase transformation upon cycling. If the tetragonal structure is preserved upon discharge, *ex situ* XRD could help to identify the position of the inserted Li and *in situ* XRD could help to understand the mechanism of this reaction.

Likewise, the analysis *vs.* Na metal could reveal the possibility of Na insertion into the structure. All these studies are underway but unfortunately could not be completed at the time of this thesis submission.

DFT calculations of all the systems – $Na_3Li_3M_2F_{12}$ garnets and $Na_3Li(TiF_6)_2$ would be very helpful to support the conclusions from the electrochemical and chemical oxidation/reduction tests. Only the titanium phase was found to undergo phase transitions upon chemical oxidation. Comparative calculations of the stability of all oxidized $Na_3Li_{3-x}M_2F_{12}$ (M = V, Fe, Ti) phases could explain the difficulties with obtaining same results for vanadium and iron.

BVEL calculations predicted facile mobility of Na^+/Li^+ cations, however poor electrochemical performance of garnets, large hysteresis and low capacities indicate possible limitations of the charge transfer processes. These issues can be related to the highly insulating nature of fluorides. Microstructural modification such as carbon coating of the electrode material could be investigated in order to improve the electrochemical performance.

5.8. Conclusion

In this chapter a family of garnet fluorides with general formula of $Na_3Li_3M_2F_{12}$ was explored, where M is a trivalent transition metal. Based on the performed BVEL calculations, these materials appeared as interesting potential cathode materials due to the presence of low-energy migration pathways for alkali cations. These compounds have not been investigated as electrode materials previously.

Three different fluoride garnets ($Na_3Li_3Fe_2F_{12}$, $Na_3Li_3V_2F_{12}$ and $Na_3Li_3Ti_2F_{12}$) were obtained using microwave-assisted solvothermal synthesis (iron and vanadium) and mechanosynthesis using ball milling (all three). Attempts to synthesize manganese and cobalt garnets were unsuccessful.

The SEM study revealed distinct size of the particles depending on the type of the garnet with round hollow shell-type for vanadium and cubes and platelet shape for iron garnet. Particles of titanium garnet obtained from ball-milling synthesis concentrate in agglomerates of nano-sized particles.

Poor electrochemical performance of garnets obtained in the first tests reveals difficulties with charge transfer process within the garnet structure. Only $Na_3Li_3Ti_2F_{12}$ garnet exhibit slight activity of the $Ti^{III/IV}$ redox couple at an average voltage of 2.8 V *vs*. Li^+/Li. Electrode processing such as extended ball-milling with carbon or use of carbon nanotubes may be needed to enhance the electrochemical performance.

Chemical oxidation of vanadium garnet was unsuccessful and resulted with no reaction suggesting that removal of cation from $Na_3Li_3V_2F_{12}$ is limited, which is in contrary to BVEL calculations. Chemical reduction performed on $Na_3Li_3V_2F_{12}$ and $Na_3Li_3Fe_2F_{12}$ also did not result with incorporation of alkali cation. Nevertheless, chemical oxidation of $Na_3Li_3Ti_2F_{12}$ resulted with the formation of the new phase indexed as $Na_3Li(TiF_6)_2$, indicating extraction of two Li^+ cations. This transformation is associated with structural changes from cubic garnet into tetragonal $Na_3Li(TiF_6)_2$. The preliminar electrochemical characterization of this material resulted with stable insertion/extraction of one Li^+ at an average voltage of 3.1 V *vs*. Li^+/Li, being the highest working voltage of the $Ti^{III/IV}$ redox couple among polyanionic compounds reported to date.

Chapter 6 - Vanadium VF$_3$-type fluorides as cathode materials for Na-ion and Li-ion batteries

Outline

Chapter 6 - Vanadium VF$_3$-type fluorides as cathode materials for Na-ion and Li-ion batteries

6.1. Introduction

The most used cathode materials in batteries include oxides and phosphates which are typically intercalation compounds, therefore their capacities are limited to 100 – 200 mAh.g^{-1}.[10,11,295,296] To satisfy the requirement of rapidly expanding applications, cathode materials require further improvements to enhance their key properties such as specific capacity and working voltage. The low molar weight of transition metal binary fluorides, together with their high voltage (compared to oxides and sulfides), has attracted researchers' attention as potential cathode materials.[104,297,298] Additionally, the possibility to use several oxidation states by employing conversion reaction can highly increase the capacity. For example, the theoretical capacity of 243 mAh.g^{-1} originating from the intercalation reaction of Fe^{II}/Fe^{III} redox couple in in FeF$_3$ can be increased up to 731 mAh.g^{-1}, while involving complete reduction of Fe^{III} upon conversion reaction.[299,300] Already in the mid-'60s CoF$_3$ and CuF$_3$ were suggested as conversion electrode materials in primary Li cells for specific space-flight applications as the operation voltage of these materials lies above 3 V *vs.* Li$^+$/Li.[301,302] The theoretical energy density of the metal fluoride conversion reaction (i) (see equation below) exceeds the one expected for the metal oxides due to the higher average voltage, as shown in Table 6.1.

It is expected that these materials react following equation (i), reducing the transition metal to its metallic state and forming lithium fluoride upon discharge.

$$Li^+ + MF_n \rightarrow nLiF + M \qquad \text{(i)}$$
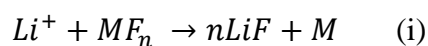
Table 6.1: Theoretical average voltage, specific capacity and specific energy expected during the conversion reaction with Li for a variety of divalent and trivalent oxides and fluorides.[104]

	Voltage *vs.* Li$^+$/Li (V)	Capacity (mAh.g^{-1})	Energy density* (Wh.kg^{-1})
Me^{II}X			
MnF$_2$	1.92	577	1108
MnO	1.03	756	779
FeF$_2$	2.66	571	1519
FeO	1.61	746	1201
CoF$_2$	2.854	553	1578
CoO	1.8	715	1287
NiF$_2$	2.96	554	1640
NiO	1.95	718	1400
CuF$_2$	3.55	528	1874
CuO	2.25	674	1517
Me^{III}X			
VF$_3$	1.86	745	1386
V$_2$O$_3$	0.945	1073	1014
CrF$_3$	2.28	738	1683
Cr$_2$O$_3$	1.09	1058	1153
MnF$_3$	2.65	719	1905
Mn$_2$O$_3$	1.43	1018	1455
FeF$_3$	2.74	712	1951
Fe$_2$O$_3$	1.63	1007	1641

* considering a Li metal anode

Although these primary batteries benefit from the expected extremely high theoretical capacities, their practical application was hampered due to the large volume expansion upon discharge.

The concept of reversible conversion reaction was first introduced by Tarascon et *al.* [303] on the example of lithium with transition metal oxide. It was expected to occur following equation (ii):

$$b \times n\, Li^+ + M_a X_b + b\, e^- \leftrightarrow b\, Li_n X + a\, M \text{ (ii)}$$
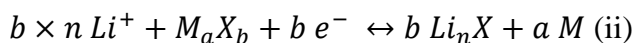
where M is a transition metal and X an anion (*i.e.* F, O, P, S, N, H…).

The reversibility of this reaction was explained by the formation of the fine metallic nanoparticles embedded in the insulating matrix of the lithium binary compound (Li$_n$X). Short diffusion distances allow rapid mass transport during the redox process and the system remains unchanged upon subsequent cycling. [304] This concept has been

exhaustively studied on several binary transition metal oxides. In most of the cases, high temperatures using molten salts as electrolytes are required to enable the reversible processes (*i.e.* for Fe_2O_3 and FeS_2),[73,305] however some reports can be found on compounds operating at room temperatures (CuO, Co_3O_4, MnO).[306–309] Stable capacities, three times higher than from intercalation compounds, obtained upon reversible conversion reactions brought researchers` attention in binary M_aX_b compounds.

Since increasing the M-X bond ionicity results in an increase of the voltage of the conversion reaction (ii), highly ionic metal fluorides are perfect candidates for cathode materials. The first reports show however very limited capacities of ~80mAh.g^{-1}, [310] explained by the insulative nature of the metal fluorides arising from the characteristic large band gap.[104] Exhaustive work on the electrode preparation such as reduction of the crystal size to the nanoscale by advanced ball milling and the use of highly conducting carbon to improve the electronic conductivity significantly improved the electrochemical performance of metal fluorides.[311–314]

The iron-based fluoride compounds are without a doubt the most popular owing to the abundance and low-toxicity of iron and its high reaction voltage, and therefore they are described with more detail in the following part.

i.   Iron fluorides

Different polymorphs of iron fluorides are known, including commercial anhydrous FeF_3 and two hydrated pyrochlore and Hexagonal Tungsten Bronze (HTB) networks (Figure 6.1).

As shown in Figure 6.1a, anhydrous FeF_3 possesses an hexagonal ReO_3-type lattice crystallizing in the R-3*c* space group with open tunnels developed by the layer of ordered Fe cations along the (012) plane. Badway et al.[298] prepared nano-sized particles (<30 nm) of carbon-metal fluoride nanocomposites by high-energy milling commercial FeF_3 with carbon. This concept significantly improved the electrochemical performance reaching almost full theoretical capacity corresponding to the 1e$^-$ reaction (235 mAh.g^{-1} vs 237 mAh.g^{-1}) in the 4.5 – 2.5 V *vs.* Li^+/Li^0 voltage window during first discharge, followed by reversible capacity of 200 mAh.g^{-1} during subsequent cycles. Opening the voltage window down to 1.5 V resulted in a second reaction occurring at ~2 V *vs.* Li^+/Li^0 identified as a reversible conversion reaction.
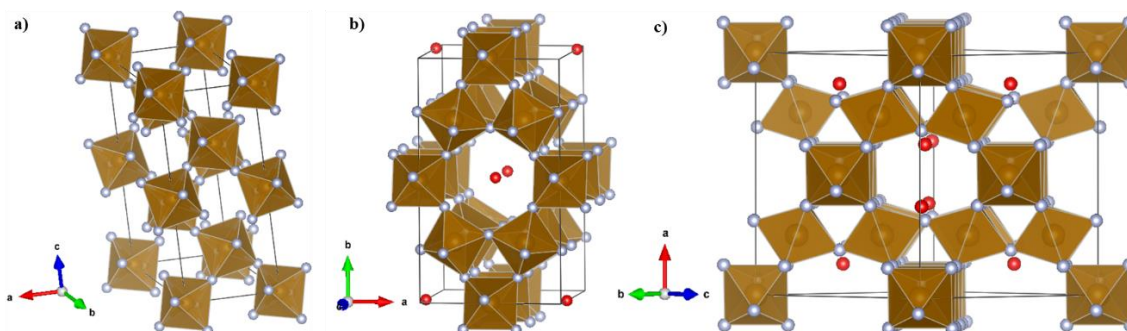
Figure 6.1: (a) Hexagonal unit cell of ReO3-type FeF$_3$ along the (012) plane; (b) HTB-type structure of FeF$_3$•0.33H$_2$O; (c) pyrochlore-type of structure of FeF$_3$•0.5H$_2$O. FeF$_6$ octahedra are denoted in brown; iron and fluorine atoms are denoted as brown and grey spheres, respectively. Red spheres are indicating the oxygen atoms of the water molecules position in HTB and pyrochlore structure (H are omitted).

The electrochemical reaction of FeF$_3$ was described as initial Li$^+$ insertion at the plateau region (3.35 V *vs.* Li$^+$/Li^0) followed by the conversion reaction producing metallic Fe^0 and LiF at around 2.1 V *vs.* Li$^+$/Li^0. The Li$^+$ insertion was topotactic up to the composition of Li$_{0.5}$FeF$_3$ followed by large variation of the unit cell volume in the remaining discharge process up to 1 Li$^+$. Interestingly, the charge does not follow the same reaction path, and the final charge product was identified as rutile-type phase with the cell parameters close to those of FeF$_2$. [298,315]

Anhydrous ReO$_3$-type FeF$_3$ was also evaluated as a potential cathode material for sodium ion batteries by Nishijima et. al. [316] In their work reversible Fe^{II}/Fe^{III} redox reaction was observed at 2.2 V vs. Na$^+$/Na^0 with the reversible capacity of 100 mAh.g^{-1} obtained while cycling the cell at 0.2 mAcm^{-2} rate in the 1.5 – 4.0 V voltage window.

Apart from commercial ReO$_3$-type, there are two other known structures of FeF$_3$ – hexagonal tungsten bronze (HTB) and cubic pyrochlore-type structure (Figure 6.1 b&c, respectively). Both are partially hydrated: FeF$_3$•0.33H$_2$O (HTB) and FeF$_3$•0.5H$_2$O (pyrochlore) due to the highly hydroscopic nature of FeF$_3$ and aqueous synthesis conditions. The crystallographic parameters of all three structures are compared in Table 6.2. Among all these three structures, the pyrochlore one has the largest volume, almost three times larger volume than the ReO$_3$-type.

Table 6.2: Crystallographic data of three different structures of FeF₃.

Structure	Space group	a [Å]	b [Å]	c [Å]	V [Å³]	Z
α -FeF₃ (ReO₃-type)[310]	R-3c	5.120	5.120	13.340	349.70	3
FeF₃•0.5H₂O (pyrochlore)[317]	Fd-3m	10.325	10.325	10.325	1100.70	4
FeF₃•0.33H₂O (HTB)[318]	Cmcm	7.423	12.730	7.526	711.17	12

Both pyrochlore and HTB-type structures were obtained in the beginning of '80s, but their application as cathode materials is quite recent.[311,317–325] Table 6.3 gathers electrochemical properties of these two polymorphs, as well as those of the ReO₃-type FeF₃.

Table 6.3: Electrochemical properties of three different structures of FeF$_3$.

Structure	Synthesis type	Theoretical capacity for 1e$^-$ [mAh.g^{-1}]	Voltage window [V]	Average voltage [V]	Capacity of first discharge [mhA.g^{-1}]	Average capacity [mhA.g^{-1}]	Nr of cycles, C rate	Ref.
α -FeF$_3$	solid-state	237	4.5-2.0	3.0 *vs.* Li$^+$/Li^0	140	80	3 (0.2C)	[310]
α -FeF$_3$/C	Ball milling	237	4.5-2.5	3.0 *vs.* Li$^+$/Li^0	200	150	50 (0.08C)	[298]
			4.5-1.5	3.0 & 2.0 *vs.* Li$^+$/Li^0	600	400	14 (0.08C)	[298]
			4.0-1.5	2.2 *vs.* Na$^+$/Na^0	155	100	10 (0.2C)	[316]
FeF$_3$•0.33H$_2$O (HTB)	Precipitation with Ionic liquid	150	4.5-1.6	2.7 *vs.* Li$^+$/Li^0	154	130	30 (0.01C)	[320]
	solvothermal		4.5-1.5	3.0 *vs.* Li$^+$/Li^0	276.4	193	50 (1C)	[324]
			4.0-1.0	2.2 *vs.* Na$^+$/Na^0	213.2	140	20 (1C)	[324]

FeF₃•0.5H₂O (pyrochlore)	Precipitation with Ionic liquid	110	4.5-1.7	3.0 *vs.* Li⁺/Li⁰	143	135	300 (0.1C)	[317]
			4.5-1.5	2.8 *vs.* Na⁺/Na⁰	158	130	100 (0.05C)	[326]
	solvothermal		4.0-2.0	3.0 *vs.* Li⁺/Li⁰	200	85	50 (0.2C)	[325]

FeF$_3$•0.33H$_2$O (HTB-type) structure was obtained for the first time via hydrothermal synthesis of commercial FeF$_3$•3H$_2$O in aqueous media at 360 °C, 200MPa for 4 days.[318] Light-green crystals were indexed in orthorhombic unit cell with *Cmcm* space group. As visible in Figure 6.1b, the HTB FeF$_3$•0.33H$_2$O structure is built around very large hexagonal cavities of ~550 pm size, forming channels in the [001] direction. The water molecules occupy 1/3 of the free position in the channels and serve as a strong structural stabilizer during the electrochemical lithiation with the possibility to accommodate Li$^+$ up to 2/3 of the remaining vacant positions. The presence of such large cavities is expected to allow fast Li$^+$ diffusion with the theoretical capacity of 150 mAh.g^{-1}.[319,324]

The first electrochemical studies were performed in 2010 by Li *et al.*[320] They also suggested alternative, low-temperature synthesis route by using 1-butyl-3methylimidazolium tetrafluoroborate (BmimBF$_4$) ionic liquid and iron (III) nitrate nanohydrate (Fe(NO$_3$)$_3$•9H$_2$O) as precursors, which leads to obtain nanostructural hydrated iron fluoride. The electrochemical performance of this material used as cathode *vs.* metallic Li is presented in Figure 6.2a. It reveals a reversible discharge capacity of 154 mAh.g^{-1} (corresponding to 0.66 Li$^+$) during first 10 cycles with the working voltage of 2.7 V *vs.* Li$^+$/Li^0. The irreversible plateau in the first cycle was explained by the subtle structural rearrangement and the subsequent cycling proceed through solid-solution mechanism.
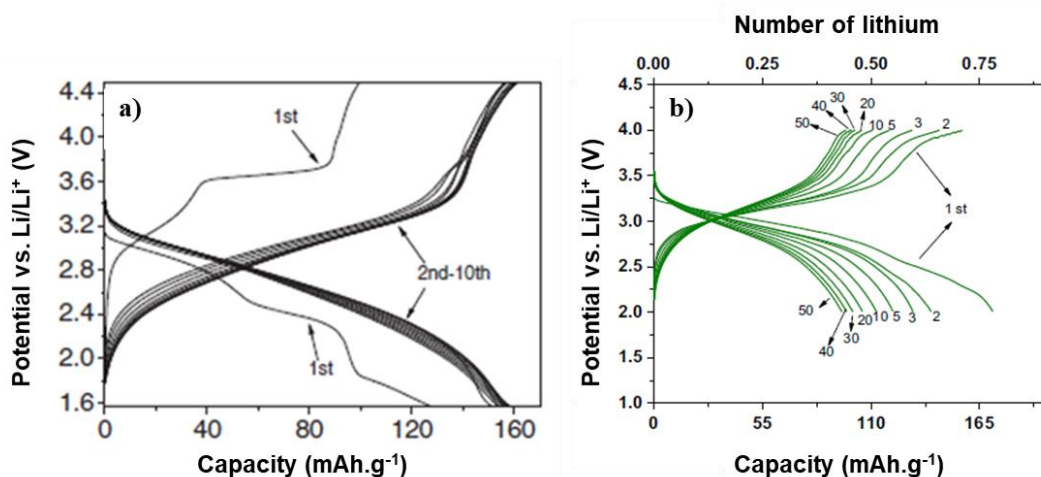
Figure 6.2: (a) Galvanostatic charge-discharge profile of HTB FeF$_3$•0.33H$_2$O electrode cycled with a current density of 14mA/g in a voltage window 1.6-4.5V at 25°C.[320]; (b) Galvanostatic charge/discharge profile of pyrochlore FeF$_3$•0.5H$_2$O in a voltage window 2-0 – 4.0 V at a rate of C/20.[325]

A faster synthesis route was proposed by Di Carlo – microwave-assisted fluorolytic sol-gel synthesis.[327] In this work instead of ionic liquid, methanolic solution of HF and benzyl alcohol as solvent were used and the product was mixed with reduced graphene oxide-based composite. The as-prepared $FeF_3 \cdot 0.33H_2O$/RGO composite (44 mg of RGO per 120 mg of $FeF_3 \cdot 0.33H_2O$) was cycled at full theoretical capacity at C/10 rate for more than 50 cycles and delivered stable 100 mAh.g^{-1} capacity at 1C rate.

The last form of iron fluoride, pyrochlore-type $FeF_3 \cdot 0.5H_2O$ is an open framework structure characterized by much larger cell volume than that of HTB-type. As shown in Figure 6.2c, it possesses large 3D ion channels favoring Na^+/Li^+ ion insertion. The water molecules are located in the zigzag channels, and thus are more confined than the straight channels of HTB-type phase.[321,328]

For the first time, the pyrochlore structure of metal fluoride was obtained in 1986 by De Pape and Ferey by topotactic oxidation of mixed valence fluoride $NH_4Fe_2F_6$ in a boiling solution of Br_2 in acetonitrile at 81°C.[329] Stabilizing pyrochlore-type structure is much more difficult than HTB, therefore the first direct synthesis is quite recent – 2013.[317]

A fast synthesis method was proposed by Rao *et al.* [325] Pyrochlore $FeF_3 \cdot 0.5H_2O$ was obtained with a solvothermal synthesis by dissolving iron nitrate, $Fe(NO_3)_3 \cdot 9H_2O$ and HF in absolute ethanol solution. During the first discharge almost one Li was inserted, and after 50 cycles stable capacity of 80 mAh.g^{-1} was obtained (Figure 6.2b).

ii.   Vanadium fluorides

Compared to the previously described iron fluorides, much less literature records could be found regarding vanadium fluorides.

The only electrochemical studies were performed on commercial ReO_3-type VF_3. The first electrochemical studies resulted with the capacities of 80 mAh.g^{-1} in the voltage range 2.0-4.5 V, corresponding to the reaction of V^{III}/V^{II} redox couple at 2.2 V *vs.* Li^+/Li^0.[310] Opening the voltage window to 0.02-4.3V resulted with registering the conversion reaction with the reversible capacities of ~500 mAh.g^{-1} (Figure 6.3).[330]
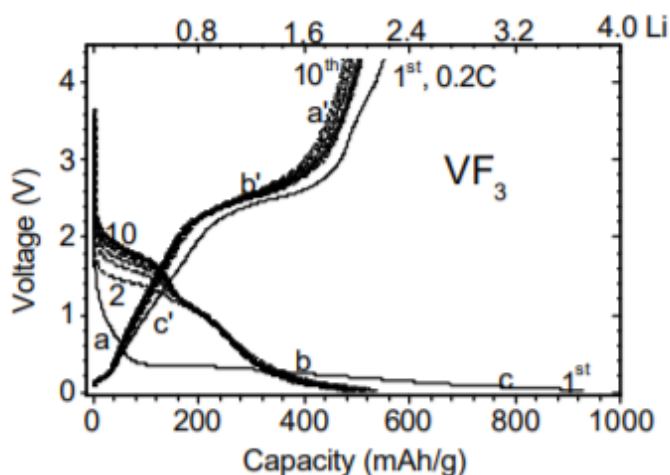
Figure 6.3: Galvanostatic charge-discharge profile of VF₃ cycled in a voltage window 0.02-4.3V with 0.2C cycling rate. [330]

A mixed iron-vanadium HTB fluoride $(Fe_{0.53}V_{0.47})F_{2.67}(OH)_{0.33}$ was cycled in the voltage window 2 – 4 V at a cycling rate of C/20. During the first discharge, a capacity of 180 mAh.g^{-1}, corresponding to insertion of 0.7 Li$^+$ was obtained. During the following cycles a drop of the capacity was observed with eventual stable reversible intercalation of ~0.5 Li$^+$. It was observed that the presence of vanadium in the structure prevents the phase transition from the HTB framework to the more thermodynamically stable of allotropic forms of FeF₃, as was observed for $FeF_{2.67}(OH)_{0.33}$.[282,331]

Up to date, no electrochemical activity has been reported for pyrochlore-type VF₃•0.5H₂O nor HTB phase.

The following part will be devoted to the experimental results for all investigated fluoride-based materials.

6.2. Synthesis of vanadium fluoride VF₃

There are many different synthesis routes to obtain metal fluorides as described in examples above. For the synthesis of vanadium fluoride, a microwave-assisted solvothermal route was selected due to the successful results obtained with garnet fluorides (Chapter 5.2.1).

Prior to this work, an exhaustive study on the microwave-assisted synthesis of iron fluoride was conducted at the Institute of Molecules and Materials of Le Mans.[332] The chemical system of $Fe(NO_3)_3 \cdot 9H_2O$ / HF / methanol was explored and the dependence of different solvothermal synthesis conditions (time, temperature) was investigated. It was proven experimentally that the optimization of the molar ratio of Fe:F and the temperature can result with obtaining different forms of FeF_3 – pyrochlore and HTB. [282] With the Fe:F ratio of 2 and 3 and temperatures of 160 and 190°C, pure pyrochlore phase was obtained, whereas increasing the Fe:F ratio to 4 resulted in the synthesis of the HTB phase. Additionally, the appearance of an amorphous phase was observed for the Fe:F ratio of 1, tentatively assigned to the FeOF-type phase. [333]

A similar approach was adopted to synthesize VF₃. Different molar ratios of VCl₃ and HF were investigated, ranging from 1.0:10.0 to 1.0:0.33, as indicated in Figure 6.4, according to the following reaction:

$$VCl_3 + HF \rightarrow VF_3 + HCl$$
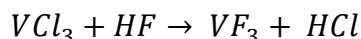
Due to the highly hazardous nature of hexafluoric acid, special safety measurements were applied. Contrary to other acids, HF has a highly corrosive nature, can penetrate the skin extremely easily and decalcify the bones leading to the destruction of the deep tissue layers. While handling the HF acid, personal protective clothing including goggles, laboratory coat and neoprene gloves was always employed. Special laboratory safety training was also carried out to prevent potential risks.

First, VCl₃ powder was dissolved in methanol, next the 40% HF solution was added and mixed for 15 min in a 50 ml Teflon autoclave. The reactor was then tightly closed and placed in the microwave. The same conditions as for the garnet synthesis were selected, – 190 °C and 30 min. After cooling down, the reactor was opened, the powder was washed once with methanol and twice with ethanol, filtered and dried overnight at 60 °C.

Figure 6.4 shows all the XRD patterns obtained for the prepared samples. Three distinct types of XRD patterns could be observed, denoted as green, blue and black. Powders from syntheses using a ratio ranging from 1:10 to 1:2 were indexed as the HTB-type structure (green) using as a reference HTB $FeF_3 \bullet 0.33H_2O$ phase,[318] as vanadium-HTB VF_3 phase had never been reported to date. Each reflection could be indexed as pure HTB phase signifying successful stabilization of this phase for the first time. Powders prepared using a ratio between 1:1.5 and 1:1 were indexed with a pyrochlore-type structure (blue), using the pyrochlore $VF_3 \bullet 0.5H_2O$ phase reported by Barthelet *et al.*[334] as reference. All reflections could be indexed, indicating a pure phase. From these results it can be concluded that the synthesis of pyrochlore phase requires three times less amount of HF than the synthesis of HTB, and the resulting green powder was much darker. It is worth mentioning that comparing to the reported above syntheses of FeF_3 polymorphs, the pyrochlore VF_3 phase was already obtained with the V:F ratio of 1. However, based on the very low amount of obtained powder and intense blue color of the solution, only small part of VCl_3 was involved in the reaction and residues of the vanadium remained in the solution.

The materials obtained for synthesis using a ratio of 1:0.67 and 1:0.33 could not be indexed. These materials exhibit broad reflections that do not correspond to any known MF_3 structure, and the number of peaks was insufficient to allow indexation with the crystallographic program Dicvol.[335] Since this compound is expected to be formed with V, O and F elements, the <<VOF>> name will be used for the future descriptions. The powder obtained using a ratio of 1:0.33 was black and very fine, completely different than others. Synchrotron XRD data of this <<VOF>> sample was also collected (Figure 6.5), however still was insufficient for the identification of this phase.
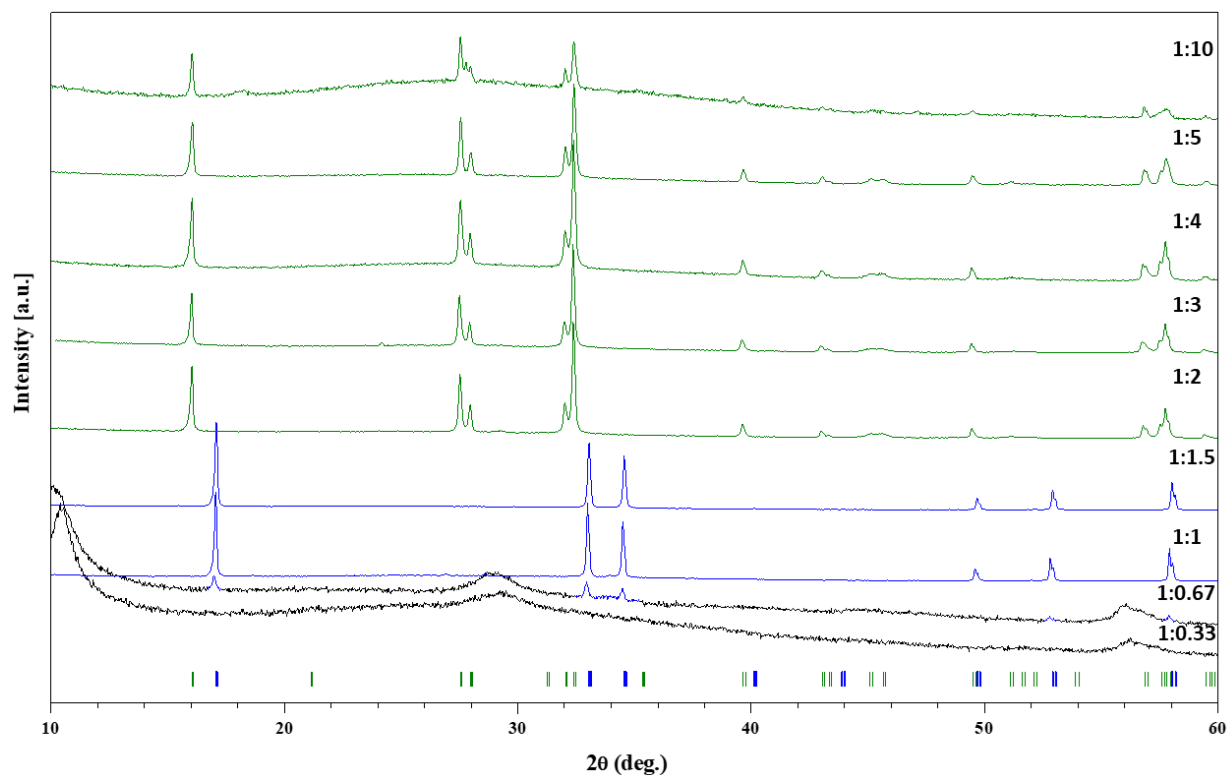
Figure 6.4: XRD patterns of the powders obtained from the synthesis of the targeted VF3 at different molar VCl₃ : HF ratios. The used molar ratio VCl₃ : HF are indicated in the figure. Three different series of resulting patterns was obtained and indicated in black, blue and green, respectively. Vertical blue lines correspond to the position of peaks pyrochlore-type phase, and green ones to the HTB-type phase.
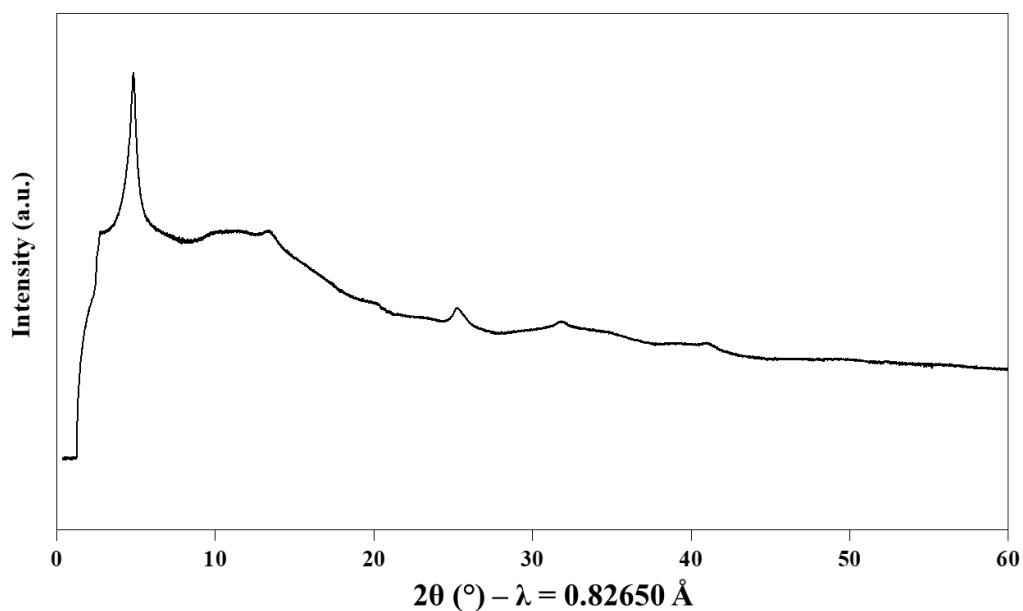
Figure 6.5: Synchrotron XRD data of the unknown <<VOF>> phase.

Most of the samples could be indexed as a single phase, whereas sample with the ratio 1:0.67 corresponds to a mixture of the pyrochlore-type structure and the unknown structure.

277

6.3. Structural and chemical analysis

The sharp peaks of both pyrochlore and HTB phases indicate a high crystallinity of the obtained powders. The size of the crystallites was estimated using the Scherrer formula, resulting with an average value of 0.3 µm and 1.2 µm for HTB and pyrochlore phase, respectively.

6.3.1.   Synchrotron X-ray powder diffraction study

High resolution X-ray patterns were measured for a pure composition of the pyrochlore and HTB phases (ratios 1:5 and 1:1.5) at the MSPD beamline of ALBA Synchrotron Light facility and the obtained patterns were Rietveld-refined using the FullProf program. [336,222]

- **HTB VF$_3$•0.33H$_2$O**

As mentioned before, the HTB VF$_3$•0.33H$_2$O phase has not yet been described in the literature, therefore the refinement was performed by using the model of HTB FeF$_3$•0.33H$_2$O phase (Ref [318]). The XRD patterns were indexed with the hexagonal cell with *Cmcm* space group. The refined atomic positions resulted very similar as the corresponding iron phase, justifying the selection of the model phase for the refinement. The location of the oxygen atom of water molecules in hexagonal cavities was first confirmed by Fourier difference maps, that were calculated with the use of GFourier program[337] within FullProf program[222,336]. Figure 6.6a shows the calculated Fourier difference map suggesting the position of a water molecule around the (0,0, ¼) position, being in agreement with the position of water molecules in the iron HTB phase. The calculated bond distances between V^{III} – F$^-$ ($d_{average}$=1.859 Å) (Table 6.6) are in good agreement with the ones determined by Shannon[187] and confirm the absence of oxygen or water molecules in VF$_6$ octahedra.
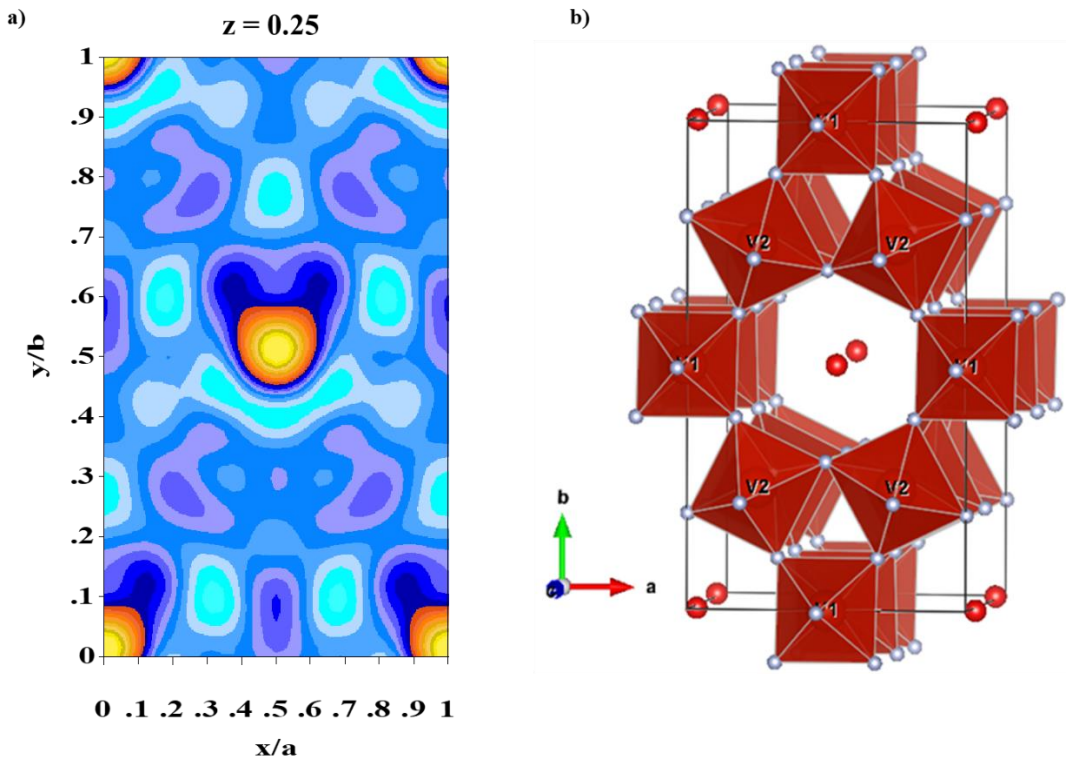
Figure 6.6: (a) Fourier difference map obtained from the refinement of the XRD pattern of HTB $VF_3 \cdot 0.33H_2O$ phase. Yellow spheres denote the expected position of water molecules; (b) crystal structure of HTB $VF_3 \cdot 0.33H_2O$ phase with the position of water molecules determined by Fourier maps represented as red spheres. VF_6 octahedra are shown as red octahedra.

The collected synchrotron XRD pattern revealed the coexistence of two HTB $VF_3 \cdot 0.33H_2O$ phases, which can be observed as a splitting of each peak (see inset in Figure 6.7). Based on the Rietveld refinement both phases differ only slightly with the size of the unit cell and the amount of water – 0.23 and 0.32 as obtained from the data refinement (details in Table 6.4 & Table 6.5). The difference is so small, that could not be detected by laboratory XRD.

Vanadium atoms occupy two crystallographic sites, indicated as V1 and V2 in Figure 6.6b, each coordinated by six fluorine atoms creating VF_6 octahedra, presented in red. Oxygen atoms of water molecules, are located in the hexagonal cavities, depicted as red spheres.

A comparison of the characteristic interatomic distances between $VF_3 \cdot 0.23H_2O$ and $FeF_3 \cdot 0.33H_2O$ HTB phases is presented in Table 6.6. While in $FeF_3 \cdot 0.33H_2O$ HTB, both $Fe(1)F_6$ and $Fe(2)F_6$ octahedra are nearly perfectly symmetrical, in $VF_3 \cdot 0.23H_2O$ HTB two different types of the octahedra can be observed – symmetrical $V(1)F_6$ and slightly distorted $V(2)F_6$ with elongated $V(2)-F(2)$ bond.
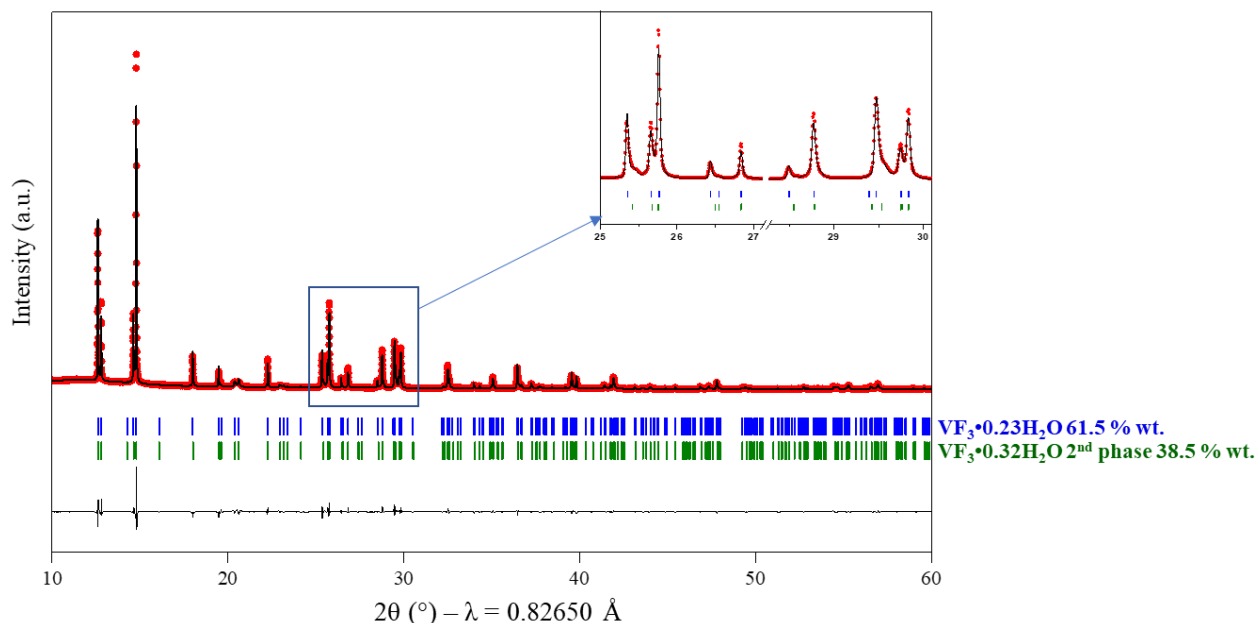
Figure 6.7: Rietveld refinement of the SXRD pattern of HTB VF$_3$•0.23H$_2$O.

Table 6.4 : Crystallographic data and atomic coordinates of HTB VF$_3$•0.23H$_2$O (phase 1) deduced from the Rietveld refinement of the SXRD pattern.

S.G.: *Cmcm*	$a = 7.414(3)$ Å $b = 12.844(1)$ Å $c = 7.514(2)$ Å	$V = 717.3(6)$ Å^3	$R_{Bragg} = 3.89$ %	$\chi^2 = 36.6$ Fraction (%$_{mol}$): 61.5		
Atom	**Wyckoff position**	***x/a***	***y/b***	***z/c***	***B$_{iso}$***	***Occ***
V1	4*b*	0	½	0	1.5(13)	¼
V2	8*d*	¼	¼	0	1.5(13)	½
F1	8*f*	0	0.222(2)	0.517(2)	1.9(3)	½
F2	16*h*	0.31(3)	0.09(3)	0.97(3)	1.9(3)	1
F3	4*c*	0	0.50(4)	¼	1.9(3)	¼
F4	8*g*	0.24(2)	0.24(2)	¼	1.9(3)	½
Ow1	4*c*	0	0.00(12)	¼	3.2(5)	0.23(3)

Table 6.5: Crystallographic data and atomic coordinates of HTB VF$_3$•0.32H$_2$O (phase 2) deduced from the Rietveld refinement of the SXRD pattern.

S.G.: *Cmcm*	$a = 7.418(2)$ Å $b = 12.839(2)$ Å $c = 7.514(1)$ Å	$V = 715.7(2)$ Å^3	R$_{Bragg}$=5.31 %	$\chi^2 = 36.6$ Fraction (%$_{mol}$): 38.5		
Atom	**Wyckoff position**	***x/a***	***y/b***	***z/c***	B_{iso}	***Occ***
V1	4*b*	0	½	0	1.3(12)	¼
V2	8*d*	¼	¼	0	1.3(12)	½
F1	8*f*	0	0.205(7)	0.558(8)	1.0(10)	½
F2	16*h*	0.31(8)	0.10(8)	0.95(8)	1.0(10)	1
F3	4*c*	0	0.545(2)	¼	1.0(10)	¼
F4	8*g*	0.19(8)	0.21(3)	¼	1.0(10)	½
Ow1	4*c*	0	0.00(5)	¼	2.04(8)	0.32(2)

Table 6.6: Comparison of interatomic distances with the structures of iron and vanadium HTB phase.

	FeF$_3$•0.33H$_2$O HTB[318]	VF$_3$•0.33H$_2$O HTB
4xM1-F2	1.948(1) Å	1.833(1) Å
2xM1-F3	1.945(1) Å	1.884(1) Å
2xM2-F1	1.945(1) Å	1.891(3) Å
2xM2-F2	1.945(1) Å	2.086(4) Å
2xM2-F4	1.949(1) Å	1.886(1) Å
2xH$_2$O-F1	3.119(4) Å	3.38(4) Å
2xH$_2$O-F1	3.565(4) Å	3.48(4) Å
4xH$_2$O-F2	3.086(5) Å	3.123(15) Å
4xH$_2$O-F2	3.467(5) Å	3.314(14) Å
2xH$_2$O-F3	3.745(4) Å	5.285(6) Å
2xH$_2$O-F4	3.186(5) Å	5.23(3) Å
2xH$_2$O-F4	4.183(4) Å	5.34(3) Å

- **Pyrochlore VF$_3$•0.5H$_2$O**

The synchrotron XRD pattern of Pyrochlore VF$_3$•0.5H$_2$O phase (Figure 6.8) was indexed with the *Fd*-3*m* space group. Atomic positions were refined using the reported structural model of pyrochlore VF$_3$•0.5H$_2$O phase.[334] This cubic phase possesses an open framework with large 3D channels and is characterized by a much larger cell volume (~1140 Å^3) than the HTB-type (715-717 Å^3). The vanadium atoms are located in the middle of VF$_6$ octahedra, occupying one

crystallographic position. The position of water molecules was also verified by combining Rietveld refinement and analysis of the difference Fourier maps. As in FeF$_3$•0.5H$_2$O, oxygen atoms of water molecules were confirmed to be located in the zigzag channels, as indicated by red spheres in Figure 6.9.
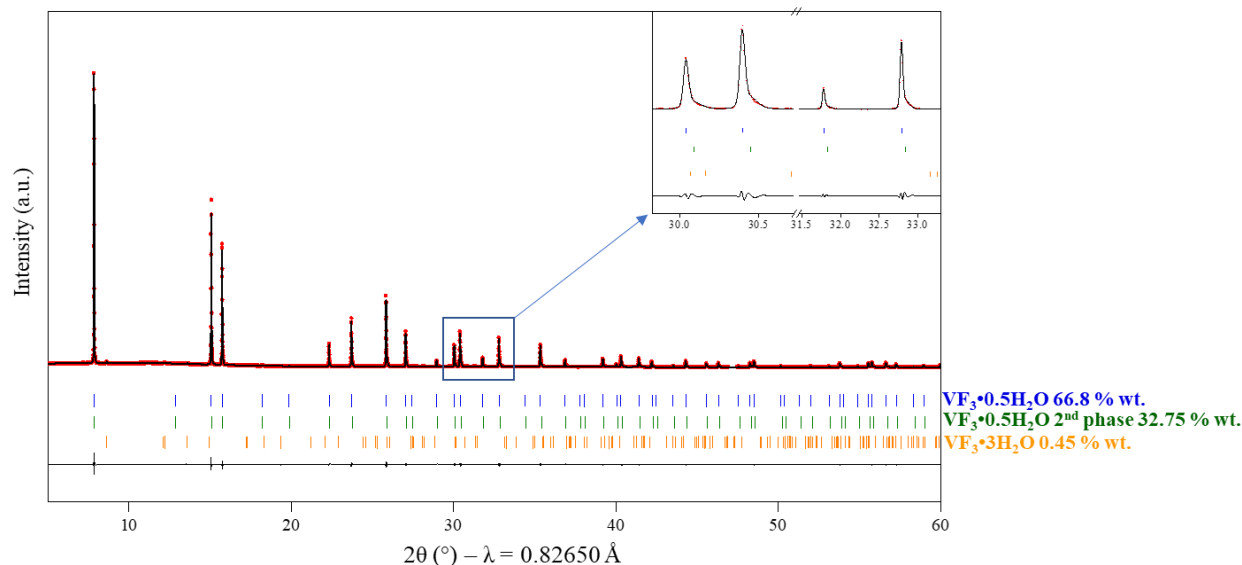
Figure 6.8: Rietveld refinement of the XRD pattern of pyrochlore-type VF$_3$•0.5H$_2$O.

Table 6.7: Crystallographic data and atomic coordinates of pyrochlore-type VF$_3$•0.54H$_2$O (phase 1) deduced from the Rietveld refinement of the SXRD pattern.

S.G.:	a =10.4557(6) Å	V = 1143.0(14) Å^3	R$_{Bragg}$ =4.22%	χ^2 = 40.3		
Fd-3m				Fraction (%$_{mol}$) = 66.8		
Atom	**Wyckoff position**	***x/a***	***y/b***	***z/c***	***B$_{iso}$***	***Occ***
V1	16*c*	0	0	0	0.31(6)	0.0833
F1	48*f*	0.314(5)	⅛	⅛	1.1(13)	¼
Ow1	32*e*	0.59(11)	0.59(11)	0.59(11)	2.56(4)	0.06(2)

Table 6.8: Crystallographic data and atomic coordinates of pyrochlore-type VF$_3$•0.4H$_2$O (phase 2) deduced from the Rietveld refinement of the SXRD pattern.

S.G.:	a =10.439(3) Å	V = 1137.6(4) Å^3	R$_{Bragg}$ =6.01%	χ^2 = 40.3		
Fd-3m				Fraction (%$_{mol}$) = 32.75		
Atom	**Wyckoff position**	***x/a***	***y/b***	***z/c***	***B$_{iso}$***	***Occ***
V1	16*c*	0	0	0	0.2(13)	0.0833
F1	48*f*	0.31(11)	⅛	⅛	1.2(3)	¼
Ow1	32*e*	0.60(4)	0.60(4)	0.60(4)	0.36(4)	0.03(3)
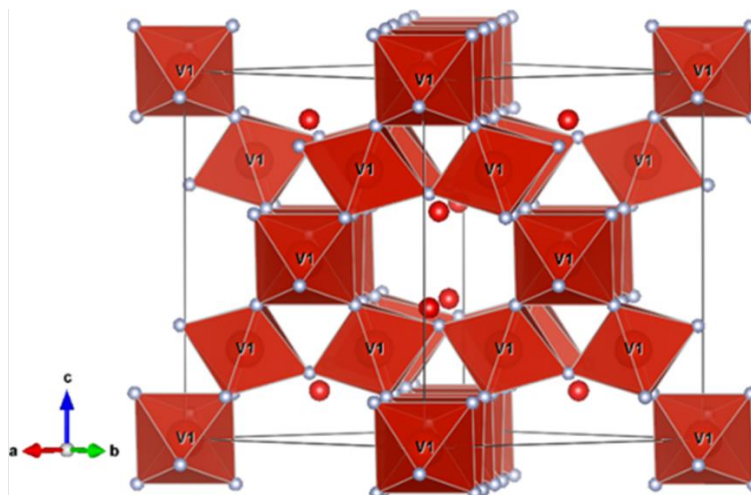
Figure 6.9: Structure of pyrochlore-type VF$_3$•0.5H$_2$O.
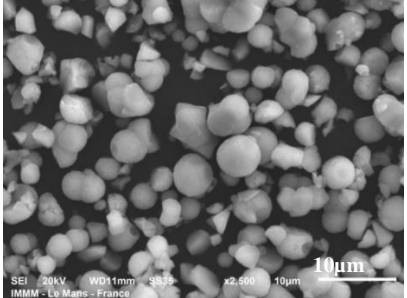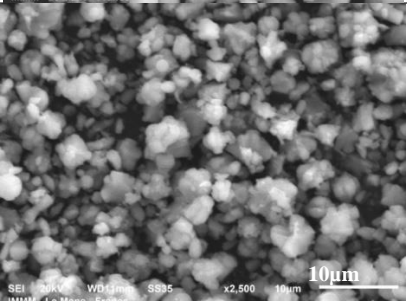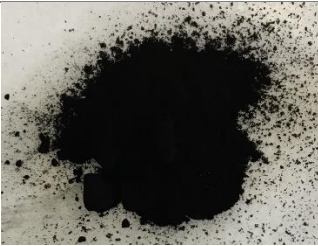
Analogous to HTB phase, the collected synchrotron XRD pattern revealed the coexistence of two pyrochlore VF$_3$•0.5H$_2$O phases, which can be observed as a doubling of each peak. Based on the Rietveld refinement, the second pyrochlore phase is characterized by a smaller unit cell. Additionally, these two phases differ by the amount of structural water (0.54 and 0.4, respectively), however considering the phase fraction of each phase deduced from the refinement, the average amount of water is approximately 0.5, which is in good agreement with the theoretical content (details in Table 6.7 &

Table 6.8). In addition, a very small (<0.5%) amount of VF$_3$•3H$_2$O phase was also observed, which has been also previously reported as an impurity in a synthesis of FeF$_3$•0.5H$_2$O pyrochlore phase.[321]

6.3.2. Electron microscopy and chemical composition

Table 6.9 gathers images of the obtained powders and SEM images of the three obtained phases. The powders of HTB phase are light green. Based on SEM images, the particles are well separated with dominating round-shaped spheres of 2-5 micrometer size. The dark green powders of the pyrochlore phase possess a different morphology – the shape of the particles is more irregular, no more spherical form could be observed. Small 1-2 µm particles are agglomerating into bigger clusters of ~10 µm.

Table 6.9: Powders and SEM images of obtained three phases.

Structure type	powder	SEM image
HTB		
pyrochlore		
Unknown <<VOF>> phase		
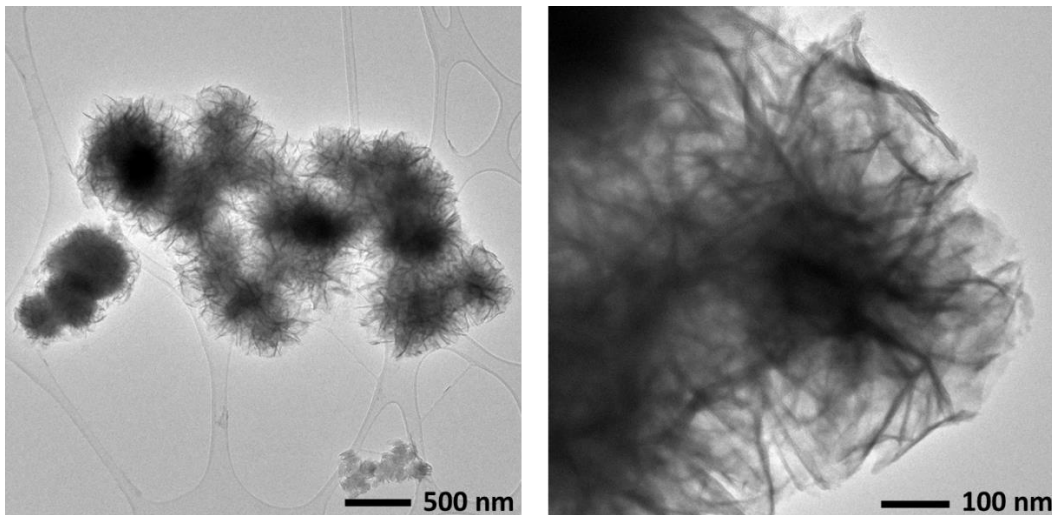
Figure 6.10: TEM images of third, unknown <<VOF>> phase.

Both the powder and SEM images of the third phase differ significantly from the others, as a very fine dust-type black powder is obtained, which consists of spherical nano-sized particles with "needles" on a surface self-assembling into spherical aggregates. The specific shape of those particles has been closely evaluated by TEM, as shown in Figure 6.10. It was observed that the particles possess ~200 nm size dark cores surrounded with very fine interconnected branches.

The chemical composition was evaluated by EDX measurement using the detector of the SEM equipment. The results of all three phases are gathered in Table 6.10. Based on ten measurements the ratio between V and F for HTB and pyrochlore type structures matches well theoretical and expected values. As the samples for the measurement were prepared under air, the obtained amount of O does not correspond only to the structural water and the final water content will be determined by the TGA measurements.

Table 6.10: Composition of three different phases determined by EDX.

Element	Theoretical content	Experimental atomic ratio determined from EDX		
		HTB	Pyrochlore	<<VOF>>
V	1	1	1	1
F	3	3.06	2.76	0.03
O	x	0.57	0.63	1.30

The composition of the unknown phase was evaluated by EDX in TEM, the results in Table 6.10 are an average of 10 measurements. The detected amount of F was very low, suggesting that the obtained material could correspond to vanadium oxide. Additionally, a small amount of Cl was also detected (average 0.03, same as F), whose presence is correlated to the use of vanadium chloride as a precursor. However, in the HTB and pyrochlore samples Cl was not detected, indicating complete reaction of VCl_3, with creation of HCl which was removed while washing the powders after synthesis.

6.3.3.   X-ray absorption spectroscopy

X-ray absorption spectroscopy (XAS) analysis was conducted on the pristine powders of the three obtained phases ($VF_3 \cdot 0.5H_2O$ pyrochlore, $VF_3 \cdot 0.33H_2O$ HTB and <<VOF>>) at the BOREAS beamline of the ALBA Synchrotron facility in Barcelona. The computed spectra were generated with the program CTM4XAS. [166,216]

Figure 6.11 shows the XAS spectra of V $L_{2,3}$-edge and O K-edge of both VF_3 polymorphs–pyrochlore and HTB. The exact same position and shape of both curves indicates the same vanadium oxidation state in both structures. As a reference, spectra for V^{III} computed with O_h coordination symmetry and a crystal field splitting energy of 2.5 eV are also plotted.

The same features can be observed in both $VF_3 \cdot xH_2O$ spectra as was previously described for $Na_3Li_3V_2F_{12}$ garnet, confirming pure V^{III} oxidation state.

The distribution of the two peaks at 530 and 532.5 eV within the O K-edge region, and their intensity ratio is characteristic for the V^{III} oxidation state and is related to the t_{2g}-e_g splitting.[168] The energy difference of 2.5 eV between these two peaks supports well the calculated crystal field splitting energy. The more intense spectra of the O K-edge for the $VF_3 \cdot 0.5H_2O$ pyrochlore phase than for the HTB phase is related to the higher water content of this phase.
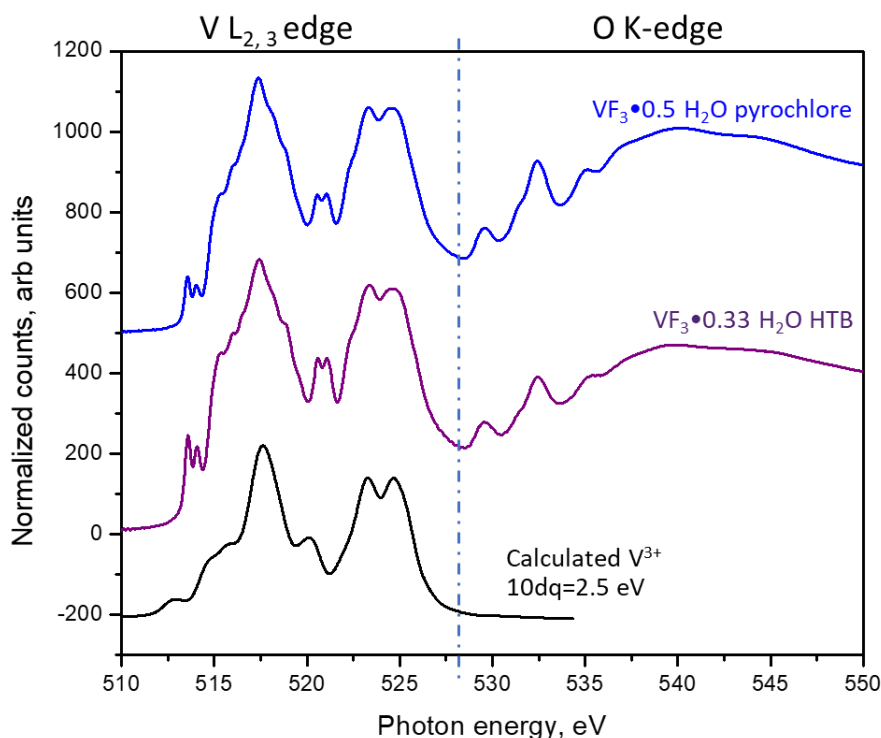
Figure 6.11: XAS V $L_{2,3}$-edge & O K-edge spectra in $VF_3 \cdot xH_2O$ pyrochlore & HTB. Signals from electron detection mode (EY) corresponding to the surface are represented in violet color for pyrochlore and blue for HTB. Black curve corresponds to the calculated XAS V^{III} $L_{2,3}$-edge spectra with Oh coordination symmetry and a crystal field splitting energy of 2.5 eV.

The V $L_{2,3}$-edge spectrum of the third, unknown, <<VOF>> phase differs a lot from the others, and thus was plotted separately (Figure 6.12). Based on the analysis of the peak position and

comparison with the literature, the most matching result is the V^V oxidation state, therefore, the experimental spectrum of V_2O_5 was used as a reference.

The V $L_{2,3}$-edge spectrum of V_2O_5 corresponds to the *d*-projected unoccupied density of states, whereas the O K-edge spectra corresponds to the *p*-projected unoccupied density of states. As in the previous samples, the two broad peaks centered at 518 eV and 525 eV are associated to the electronic transitions from $2p_{3/2}$ and $2p_{1/2}$ levels. The O K-edge spectra corresponds to the transition from the O 1*s* core level to unoccupied O 2*p* level. Within V_2O_5, O 2*p* orbitals are strongly hybridized with the narrow V 3*d* orbitals, therefore the shape of the two peaks at 530 and 532.5 eV significantly differs from the one of VF_3. The distorted octahedral symmetry within the VO_6 polyhedra results in the $t_{2g} - e_g$ splitting with the higher intensity of the t_{2g} band (530 eV).
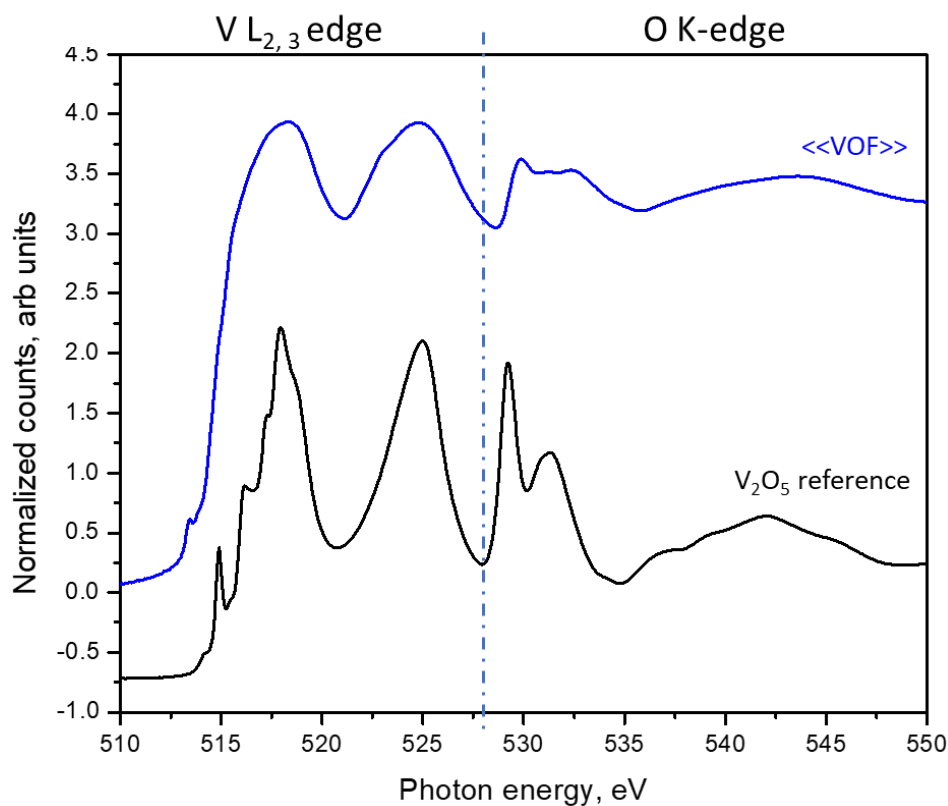
Figure 6.12: XAS V $L_{2,3}$-edge & O K-edge spectra in the unknown <<VOF>> phase. Signals from electron detection mode (EY) corresponding to the surface are represented in blue color. Black curve corresponds to the V $L_{2,3}$-edge & O K-edge spectra in V_2O_5, used as a reference.

Comparison of the spectra of <<VOF>> with the spectra of V_2O_5 allows to draw a first conclusion regarding the structure of the primary phase and suggest octahedral $VO_{6-x}Y_x$ (Y=F,Cl) environment of vanadium. Partial substitution of the oxygen by fluorine is expected to influence the shape of

the two peaks at 530 and 532.5 eV. Based on these observations, the suggested oxidation state for vanadium is +5, and considering the results from EDX, the composition might be a fluorine/chlorine substituted - $VOOF_{0.5}Cl_{0.5}$.

6.3.4. Thermogravimetric analysis

To determine the water content of the obtained materials, thermogravimetric analyses of all samples were carried out by heating the powders from room temperature to 600 °C with a heating ramp of 5 °C/min under constant flow of synthetic air (20% of oxygen +80% of nitrogen). The obtained TGA curves are shown in Figure 6.13.

Analysis of the results was supported by the reported thermal analysis of other metal fluorides: HTB $FeF_3\bullet0.33H_2O$ [13]; pyrochlore $FeF_3\bullet0.5H_2O$ [282,329]; pyrochlore $VF_3\bullet0.5H_2O$ [334]; $(NH_4)_3VOF_5$ [338] and HTB-$(Fe_{0.53}V_{0.47})F_{2.67}(OH)_{0.33}$ [331].

a)

b)
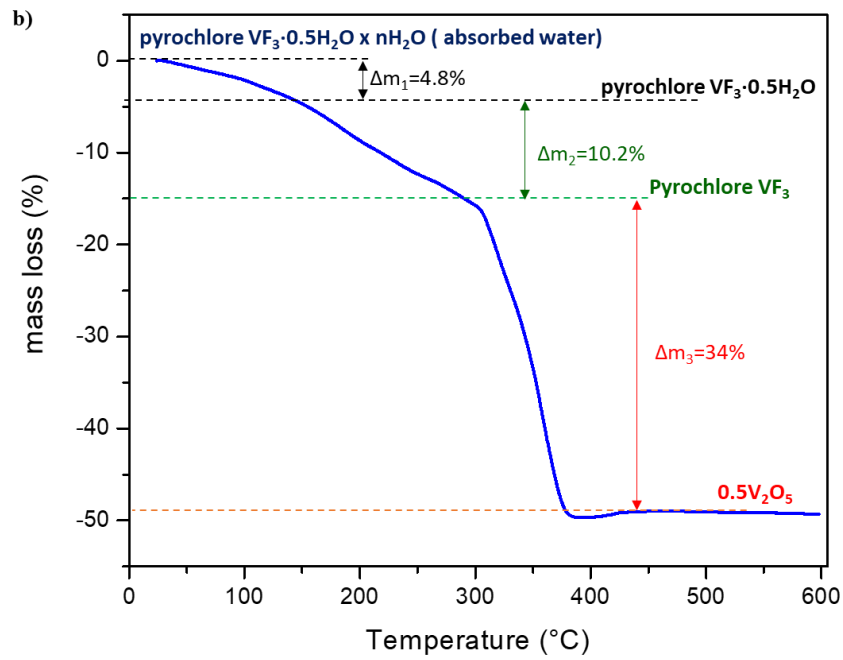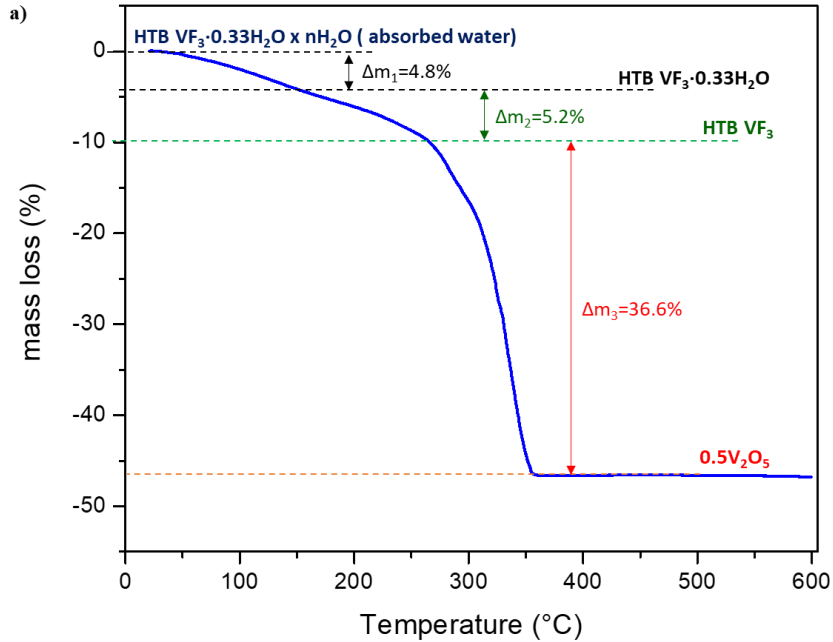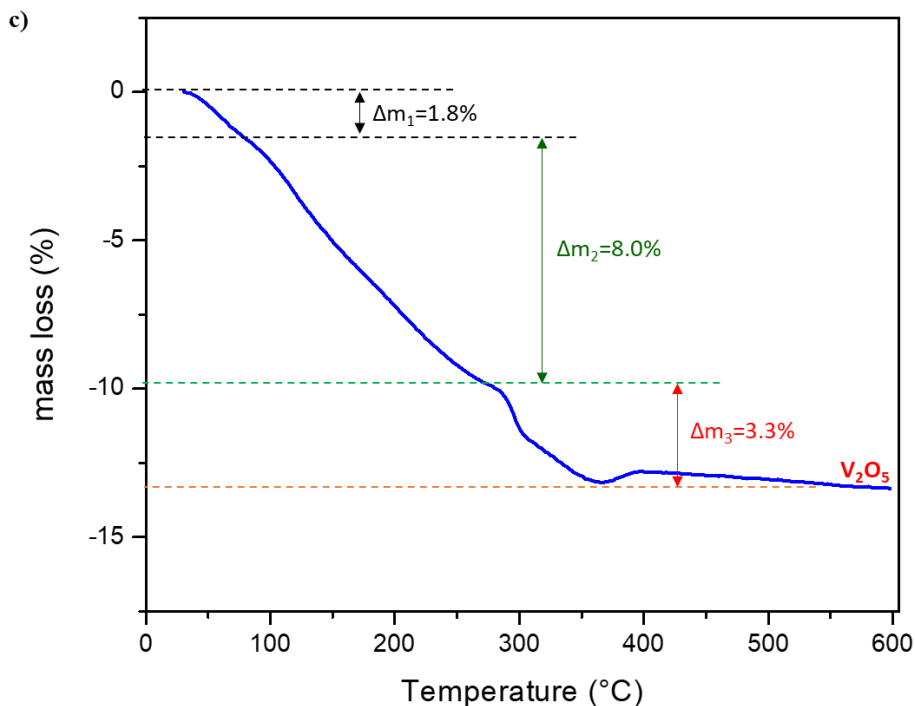
Figure 6.13: Thermogravimetric analysis of (a) HTB VF₃•0.33H₂O; (b) pyrochlore VF₃•0.5H₂O and (c) unknown <<VOF>> phase under air.

Based on Figure 6.13, for all three samples three different processed could be observed, as indicated in the figures:

- First – hydration, related to the water which was absorbed on the surface, for pyrochlore and HTB phases was around 5%, and occurred between RT and ~150 °C, whereas for <<VOF>> 1.8% between RT and 80 °C.

- Second – loss of the structural water from the cavities. As explained in the literature, dehydration process leads to formation of stable HTB-MF₃ or pyrochlore-MF₃ phase.[318,334] For the vanadium fluoride, it can be observed that the dehydration process occurs in the temperature range 160-270 °C for the HTB phase, resulting with the formation of HTB-VF₃ and in the temperature range 170-300 °C for the pyrochlore resulting with pyrochlore-VF₃.

a) $HTB\ VF_3 \cdot 0.33H_2O + O_2 \rightarrow HTB\ VF_3 + 0.33\ H_2O$ $\qquad$ (Δm/m calc. = 5.3%)

b) $pyrochlore\ VF_3 \cdot 0.5H_2O + O_2 \rightarrow pyrochlore\ VF_3 + 0.5\ H_2O$ (Δm/m calc. = 7.7%)
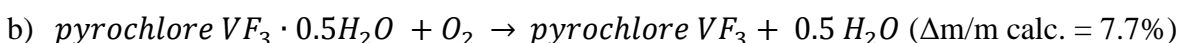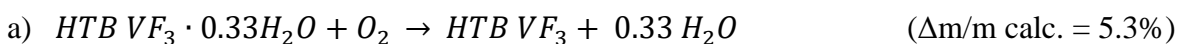
- Third – above 270 °C for the HTB phase, and 300 °C for the pyrochlore phase, decomposition process with the final crystallization into V_2O_5 phase. For both phases same reaction is expected to occur:

$$VF_3 + 1.5H_2O + 0.5O_2 \rightarrow 0.5V_2O_5 + 3HF \qquad\qquad (\Delta m/m \text{ calc.} = 15.74\%)$$
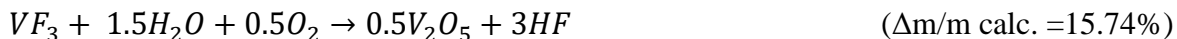
For HTB $VF_3 \bullet 0.33H_2O$ the experimental value corresponding to water loss is very close to the theoretical one (5.2% vs. 5.3%). It can therefore be concluded that the HTB $VF_3 \bullet 0.33H_2O$ phase has 0.33 molecules of water, which is also in good agreement with the results from Rietveld refinement of this sample.

In the case of the pyrochlore $VF_3 \bullet 0.5H_2O$, the experimental value of the lost mass is higher than the calculated one (10.2% vs. 7.7%). However, it supports well the results from the Rietveld refinement, where $VF_3 \bullet 3H_2O$ phase was indexed as an impurity, which decomposition could correspond to the observed higher amount of released water.

For both HTB and pyrochlore phases, during the third step (decomposition into V_2O_5) the experimental loss of water is much higher than the theoretical one. It might be related to the concomitant oxidation of vanadium fluoride into vanadium oxytrifluoride VOF_3 and its sublimation occurring between 300 and 400 °C.[339] This phenomena was observed for $(NH_4)_3VOF_5$ [338] and HTB-$(Fe_{0.53}V_{0.47})F_{2.67}(OH)_{0.33.}$ [331]

To test the hypothesis of creating VOF_3 during the third step and avoid this reaction, thermogravimetric analysis of HTB-type phase was repeated with the use of the ambient air instead of synthetic air. Ambient air provides a small amount of water to the environment (which is absent in synthetic air), therefore it is expected to hinder the oxidation reaction of fluoride into hydroxyfluoride and favor the hydrolysis reaction. As a substitute of gas bottle, a mechanical pump was connected to the system providing a flow of ambient air. The results of the performed experiment with the same temperature range and heating conditions are presented in Figure 6.14.
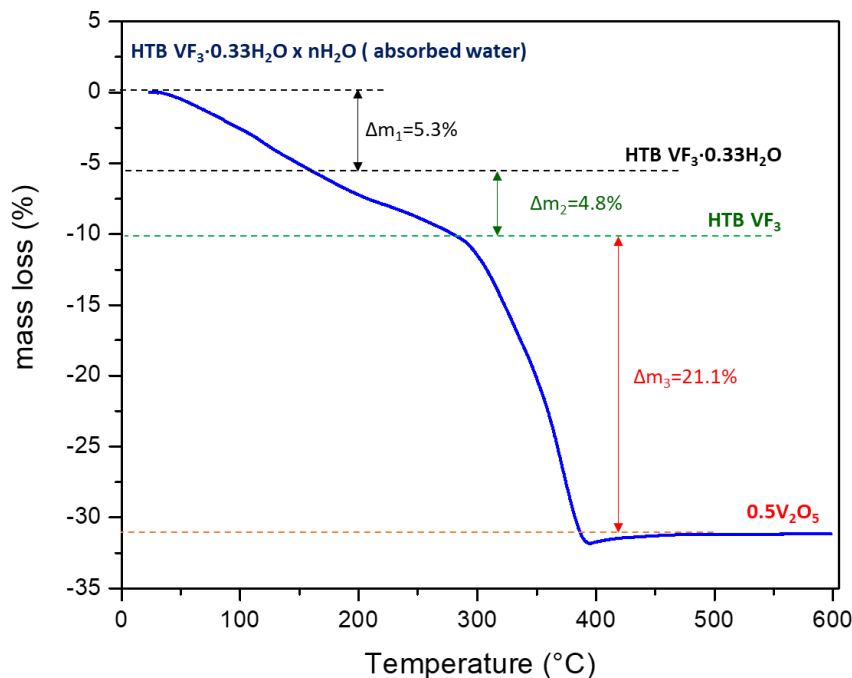
Figure 6.14: Thermogravimetric analysis of HTB VF$_3$ •0.33H$_2$O under ambient air.

The obtained experimental value of mass loss is now in good agreement with the theoretical one, which confirms that the hydrolysis reaction was favored under these conditions. The same results are expected for the pyrochlore phase as the mass loss in first two stages (RT – 270 °C) did not differ from the ones from previous experiment, signifying that the loss of structural water does not depend on the use of ambient or synthetic air.

Based on the performed thermal analyses, the experimental water content in both HTB and pyrochlore phases was found to be corresponding well to the theoretical ones, resulting with the chemical formulas of VF$_3$•0.33H$_2$O for the HTB-type, and VF$_3$•0.5H$_2$O for the pyrochlore-type. Comparing the decomposition temperatures for both VF$_3$•xH$_2$O phases, it can be observed that the pyrochlore-type structure is more stable than HTB-type, which could be related to more stable cubic framework of this fluoride.

The yellow powder obtained after the thermal treatment of each phase could be successfully indexed with the *Pmn*2$_1$ space group of V$_2$O$_5$ as dominating phase, as presented in Figure 6.15 on an example of the powder recovered after TG analysis of HTB VF$_3$•0.33H$_2$O.
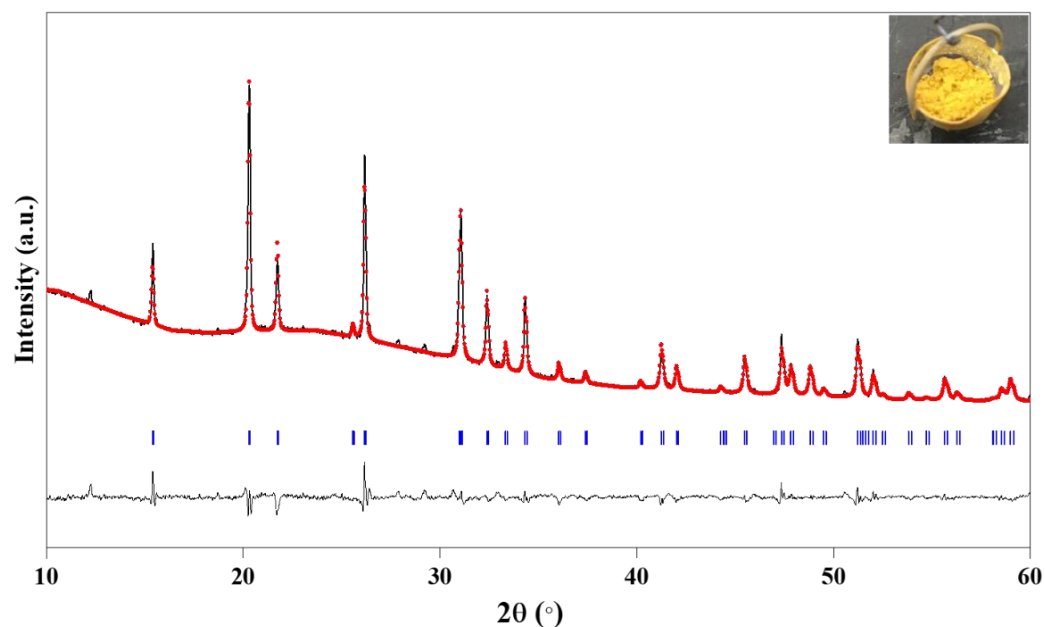
Figure 6.15: Profile matching of the XRD pattern of the yellow powder recovered after thermogravimetric analysis of HTB VF$_3$•0.H$_2$O. In the inset photo of the recovered yellow powder after the reaction.

For the <<VOF>> phase, contrary to the other two materials, the largest mass loss of 8% occurs in the second step, between 80 and 280 °C and is followed by the third mass loss of 3.3% with eventual decomposition at ~400 °C. It could be associated with much lower amount of fluorine in the structure and related to much lower amount of formed HF. This observation is in good agreement with the outcomes from the EDX analysis, where only very small amount of fluorine was detected. Considering the total mass loss and observed final formation of solely V$_2$O$_5$, the conclusions from the XAS analysis with proposed VOOF$_{0.5}$Cl$_{0.5}$ formula of this phase could be supported by the performed TGA analysis. To fully understand the thermal behavior and confirm the formula, TGA measurement should be coupled with the mass spectroscopy analysis to detect and identify the departing gases.

6.3.5.   Operando high temperature XRD measurement

High temperature XRD measurement was performed to investigate the structure evolution upon heating treatment. The samples were heated from 40 °C to 600 °C at a heating rate of 10 °C/min under a constant flow of synthetic air. X-ray diffraction patterns were collected in the 5-70 ° range with a scan time of 10 min at 10 °C intervals from room temperature to 400 °C and 50 °C intervals from 400 °C to 600 °C.

- **HTB VF₃•0.33H₂O**
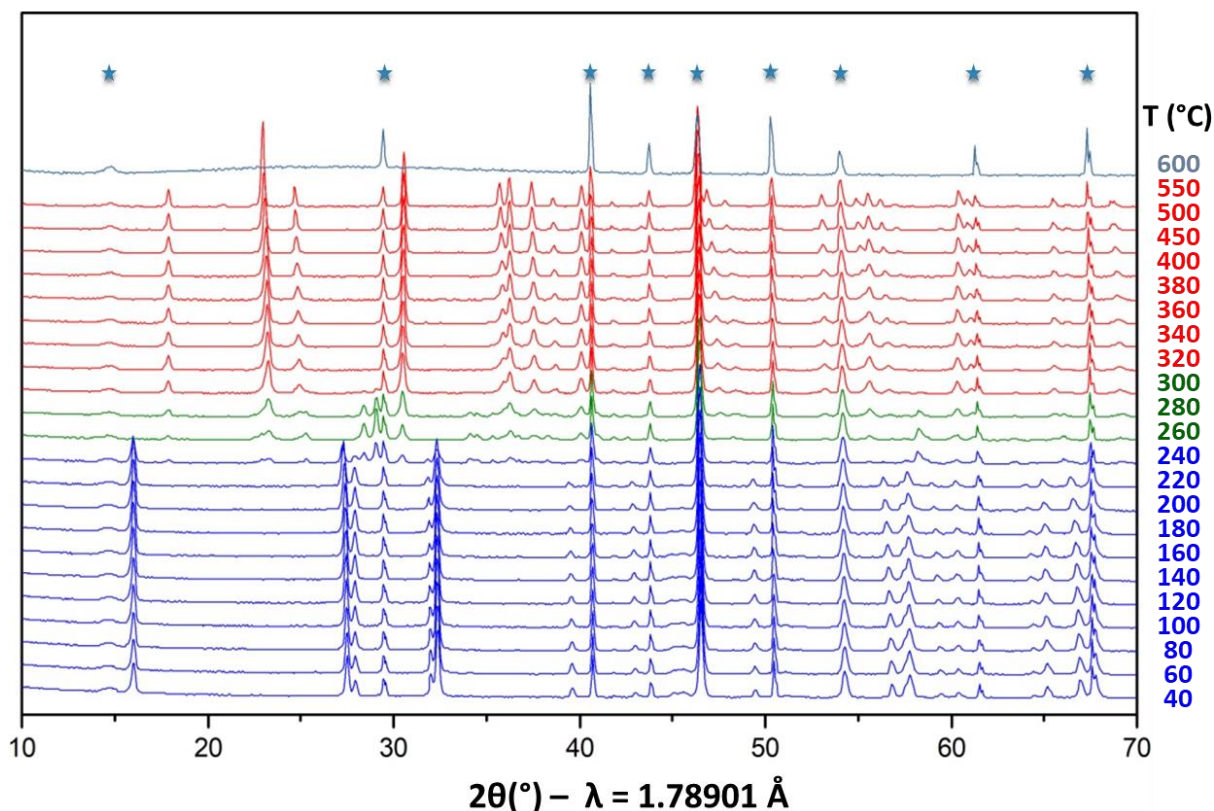
Figure 6.16: Thermal evolution of X-ray diffraction patterns of HTB VF₃•0.33H₂O (Co Kα). By stars are denoted peaks of Pt disk used in the alumina holder.

Figure 6.16 shows the thermodiffractograms of the HTB $VF_3•0.33H_2O$ phase. It can be observed that the HTB structure remains stable up to 240 °C, as indicated with the blue color of the patterns. A small shift of the peaks can be observed with minor changes in the intensities of several peaks above 160 °C, which could be related to the slight framework expansion upon heating. Above 240 °C the appearance of two new phases can be observed, indicated with green color, indexed as a mix of vanadium oxides – V_3O_7 and V_2O_5. Above 300 °C V_3O_7 phase is further decomposing into V_2O_5 (red patterns) which is eventually melting at 600 °C. The only remaining peaks belong to the Pt disk used in the holder due to the small amount of powder.

These results remain in agreement with the TGA measurement. Although in the HT XRD measurement the decomposition of the $VF_3•0.33H_2O$ phase starts earlier than in the TGA measurement (250 °C *vs.* 300 °C), it might be explained by the much longer exposition of the powder to the high temperatures – after each 10 ° XRD pattern was being collected for 10 min, whereas in the TGA powder was constantly heated.

After cooling down to 40 °C the powder recrystallized into the orthorhombic V_2O_5 structure, which was confirmed by performing the profile matching of the obtained XRD pattern (Figure 6.17).
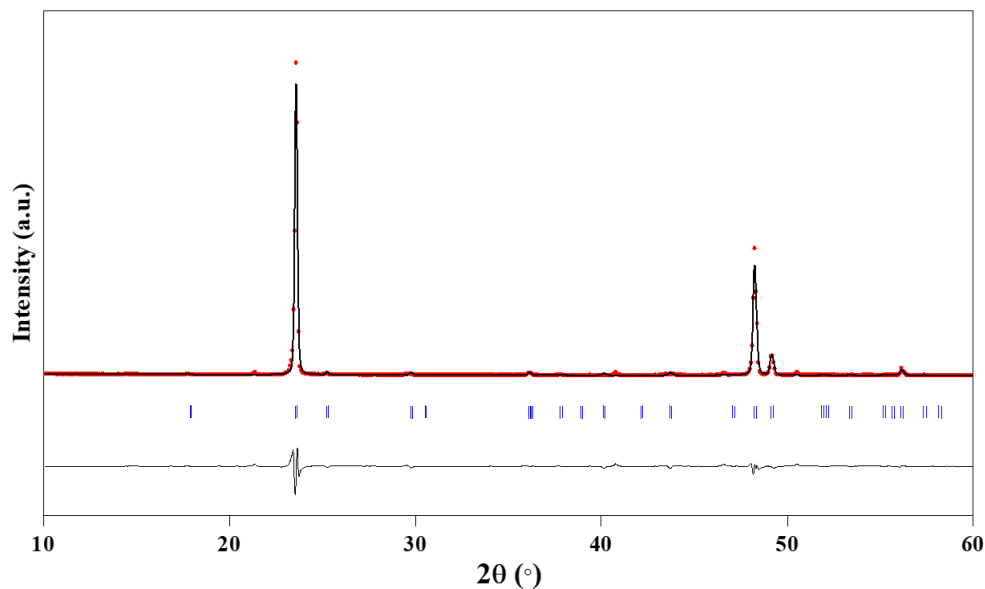
Figure 6.17: Profile matching of the XRD pattern of a recrystallized powder after thermodiffractometry analysis of HTB VF₃•0.33H₂O. (Co Kα).

- **Pyrochlore VF₃•0.5H₂O**

The results of the measurement performed on the pyrochlore $VF_3•0.5H_2O$ phase are presented in Figure 6.18. To avoid the contribution of the foreign signals, no Pt disc was used in this measurement.
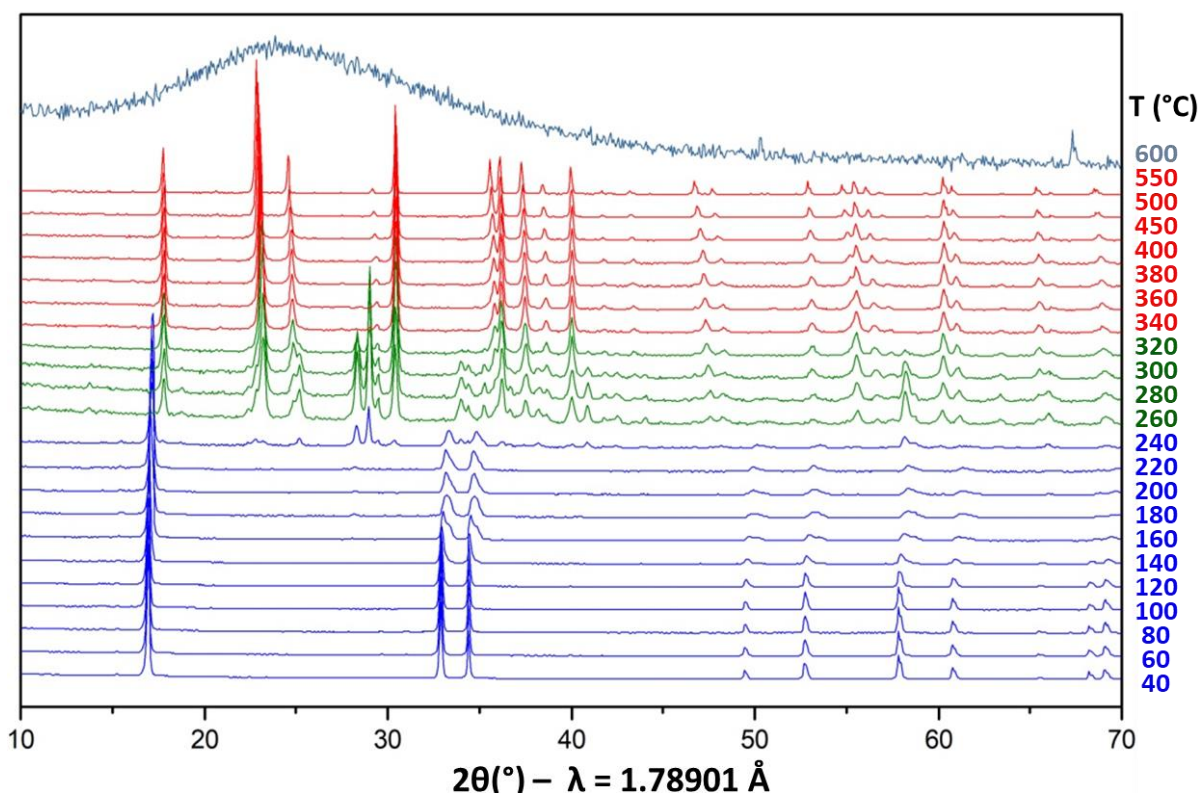
Figure 6.18: Thermal evolution of X-ray diffraction patterns of pyrochlore VF₃•0.5H₂O (Co Kα).

The pyrochlore type framework remains stable up to 240 °C, however significant structural changes can be observed: above 140 °C an important broadening of the peaks can be observed which could be related to the changes in the crystallinity of the pyrochlore phase. At 240 °C the appearance of the new phase indexed as V_3O_7 can be observed, which is next decomposing in to V_2O_5, similarly to HTB-type VF₃•0.33H₂O. As for the HTB phase, again good correlation can be observed between TGA and HT XRD measurements. The observed evolution of the peaks belonging to the pyrochlore phase in the 160 – 240 °C temperature range can be supported by the observed in TGA large mass loss – departure of the structural water causing large deformation in the pyrochlore phase. Analogous behavior observed Ali et. *al.*[326] in pyrochlore FeF₃•0.5H₂O, where the removal of the structural water resulted with the deformation of the framework upon water departure, following by the decomposition of the structure after complete removal of the water,

At 600 °C the powder melts resulting with an amorphous profile in the XRD pattern. After cooling down to room temperature the powder recrystallizes into V_2O_5 phase, as confirmed by performing profile matching on the corresponding XRD pattern (Figure 6.19). Figure 6.20 shows an image of

the powder of pyrochlore $VF_3 \cdot 0.5H_2O$ before the thermodiffraction (a) and recrystallized powder indexed as V_2O_5 (b).
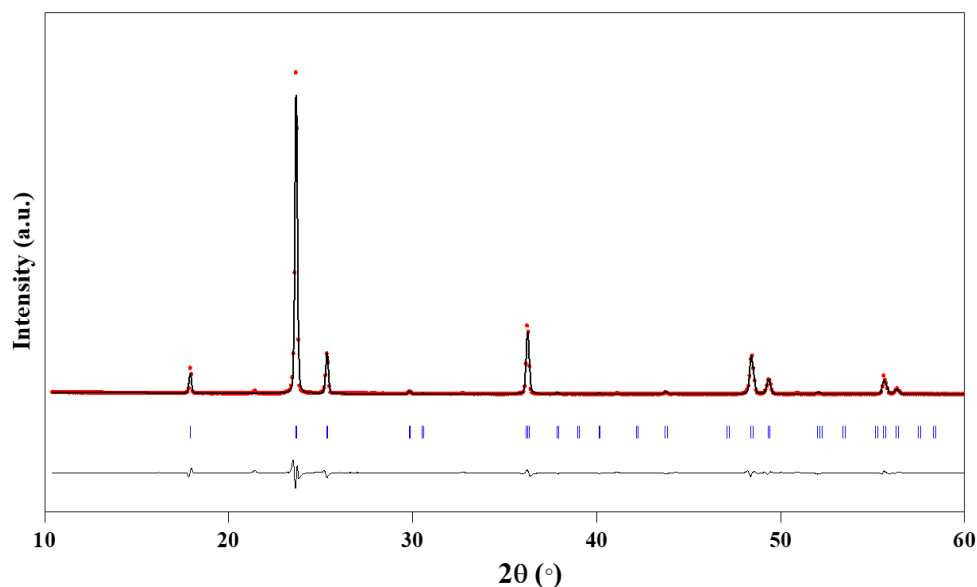
Figure 6.19: Profile matching of the XRD pattern of a recrystallized powder after thermodiffractometry analysis of pyrochlore $VF_3 \cdot 0.5H_2O$. (Co Kα).
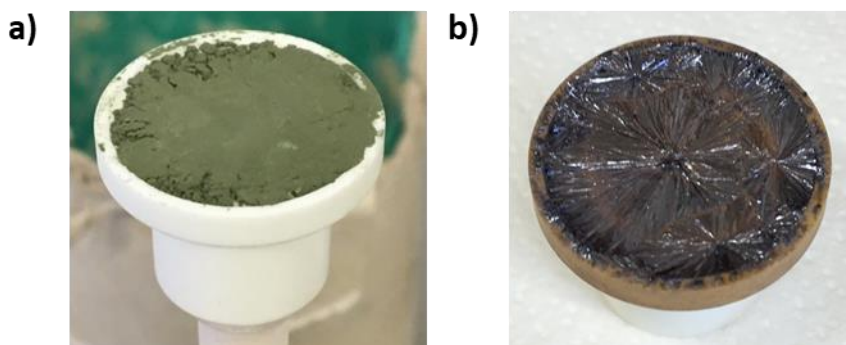
Figure 6.20: (a) Powder of pyrochlore $VF_3 \cdot 0.5H_2O$ before the thermodiffraction; (b) recrystallized powder of V_2O_5. Combined TGA and HT XRD measured confirm the essential role of the water as the structure stabilizing agent in both pyrochlore and HTB polymorphs of $VF_3 \cdot xH_2O$.

- **Unknown <<VOF>> phase**

Hight temperature XRD measurement was also performed on the unknown <<VOF>> phase in order to investigate possible crystallization at higher temperature which would be helpful with the identification of the phase. Measurement conditions were analogous to previous experiments. Results of the measurement are shown in Figure 6.21.
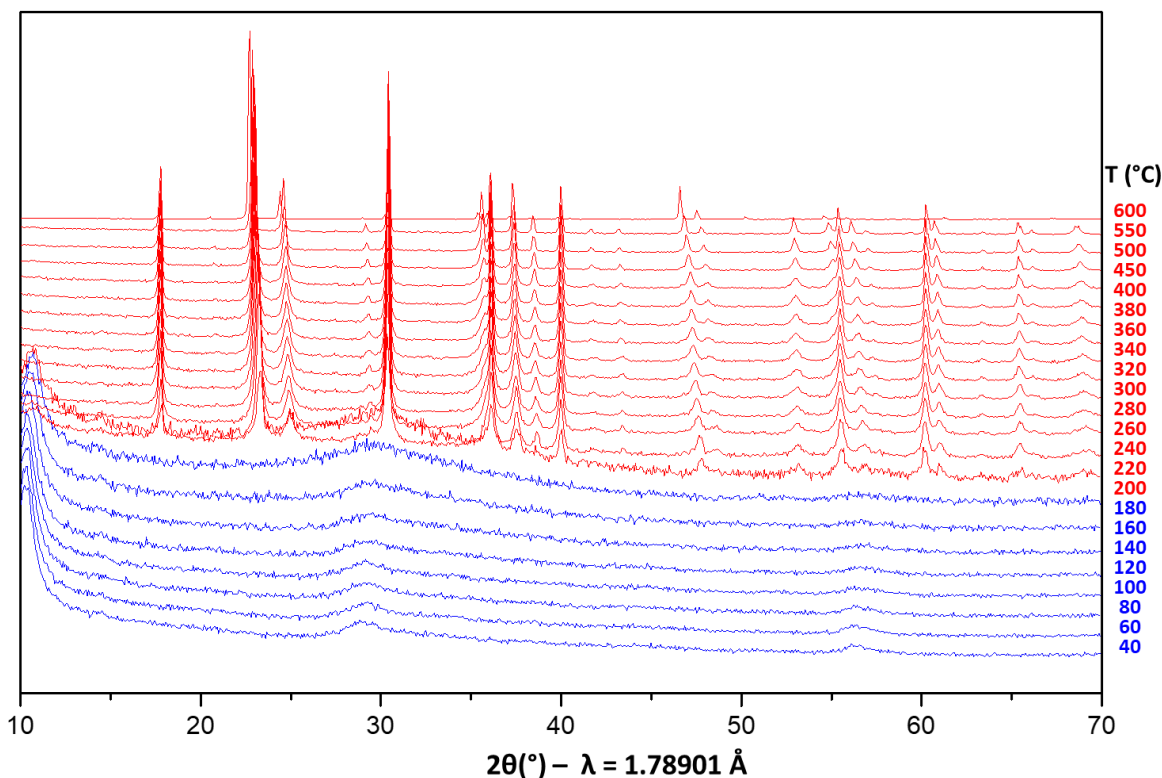
Figure 6.21: Thermal evolution of X-ray diffraction patterns of unknown <<VOF>> phase (Co Kα).

Unfortunately, no crystallization of the unknown phase could be observed. At 200 °C a new phase crystallized, which was indexed as V_2O_5 phase. With temperature, the diffraction peaks of this phase are becoming more intense which indicates the increasing crystallization of this phase. No other phase was observed during the measurement. These results confirms that the observed weight in TGA loss is related to the formation of V_2O_5. Lack of the formation of the new phase upon heating could suggest absence of the oxidation of vanadium, which was observed in $VF_3 \bullet xH_2O$ and corroborate the conclusions from the XAS analysis regarding +5 oxidation state of vanadium.

6.4. Electrochemical characterization

Up to date, vanadium fluorides have not been investigated as potential cathode materials. As described in the introduction, iron fluorides revealed interesting electrochemical performance as a host material for Li^+ or Na^+ cations. The open framework of the pyrochlore structure as well as the large hexagonal channels in the HTB structure favoring cation insertion and mobility make metal fluorides interesting candidates. The theoretical capacity corresponding to the insertion of the

Li$^+$/Na$^+$ into the free vacancies within the VF$_3 \cdot$xH$_2$O phases related to the reduction of V^{III} into V^{II} is equal to 156.8 mAh.g^{-1} for the HTB phase and 114.5 mAh.g^{-1} for pyrochlore.

All three synthesized vanadium fluoride phases were evaluated as potential hosts for Li$^+$/ Na$^+$ insertion. Electrochemical performance of these materials was evaluated in Swagelok-type cell with metallic Li or Na as an anode. The same preparation technique was performed to formulate the electrode material with either HTB VF$_3 \cdot$0.33H$_2$O; pyrochlore VF$_3 \cdot$0.5H$_2$O and <<VOF>> phases. Prior to preparing the electrode materials, powders of active material were dried for 12h in an oven at 120 °C to remove absorbed water. After drying, the powders were manually grinded with 20% carbon (Ketjen Black) in a glovebox. Swagelok cells were assembled using as prepared powder as active material, a disk of metallic Li or Na and commercial LP30 or NaClO$_4$ in EC:PC electrolyte. The choice of the perchlorate over persulfate while cycling *vs.* Na anode was made by the reported superior performance observed while cycling FeF$_3$ polymorphs.[311,317,324,326]

Initial electrochemical tests were performed at the Institute of Molecules and Materials of Le Mans on a single channel potentiostat, therefore only first cycles were registered. Further electrochemical tests were performed at CIC energiGUNE using self-standing electrodes with mass loading ~3 mg.cm^{-2}. Electrode materials were prepared by manually mixing powder of active material with carbon and an aqueous solution of PTFE in a mass ratio 70:20:10. Few drops of ethanol were used to facilitate mixing and preparation of the film, from which disks of diameter 12 mm were punched. Prepared disks were next dried in a vacuum oven for 12h at 120 °C. Swagelok cells were assembled using as prepared electrodes as, a disk of metallic Li or Na and commercial LP30 or NaClO$_4$ in EC:PC electrolyte. The tests performed using self-standing electrodes were realized in a broader voltage window – down to 1 V, to follow the processes occurring around this voltage. As expected, it was demonstrated that opening the voltage window is associated with the occurrence of conversion reactions resulting with high capacities.[289,340–345]

- **HTB VF$_3 \cdot$0.33H$_2$O**

Figure 6.22 presents the electrochemical performance of HTB VF$_3 \cdot$0.33H$_2$O (powder electrode) against Li and Na metal. Cells were cycled in a voltage window 1.5 – 4.0 V at C/20 rate. The low cut-off voltage was chosen to avoid the conversion reaction to metallic vanadium, which may

occur below 1.5 V in vanadium fluoride-type materials and follow solely Li^+/Na^+ intercalation reaction related to the redox reaction of V^{III}/V^{II} couple.
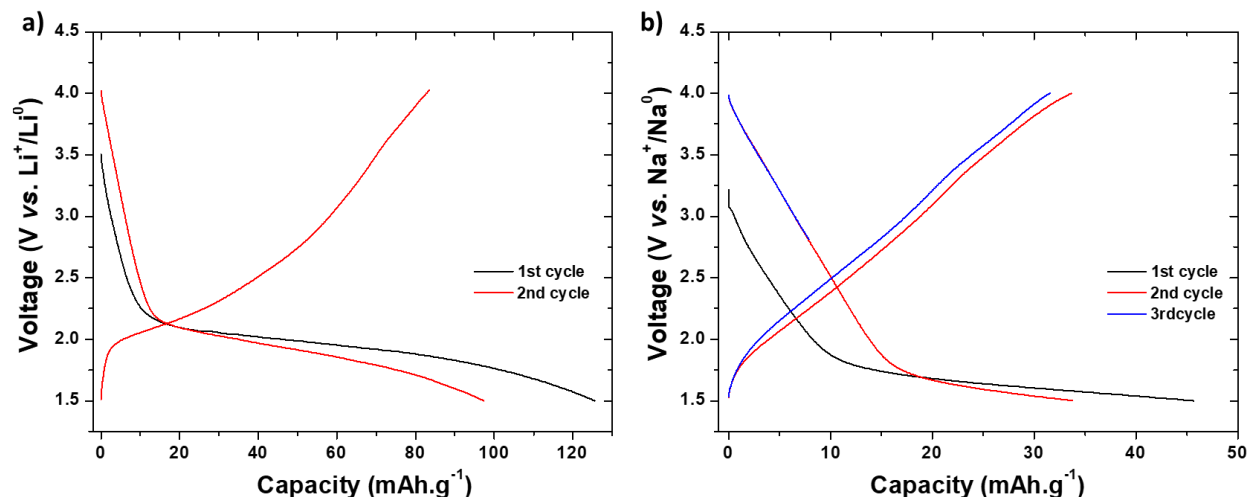
Figure 6.22: Electrochemical performance of HTB VF$_3$•0.33H$_2$O against (a) Li metal; (b) Na metal anode at C/20 rate.

Based on the Figure 6.22a, the capacity obtained during the first discharge of the cell cycled *vs.* Li anode corresponds to the insertion of ~0.8Li$^+$ at a voltage of ~2V *vs.* Li$^+$/Li^0 related with the reduction reaction of V^{III}/V^{II} redox couple. Around 0.65 Li$^+$ can be next reversibly removed and reinserted.

After stopping at 1.5 V at the second discharge, the cell was opened and the *ex situ* XRD was performed in order to validate the structure after reversible insertion of Li$^+$ cation.
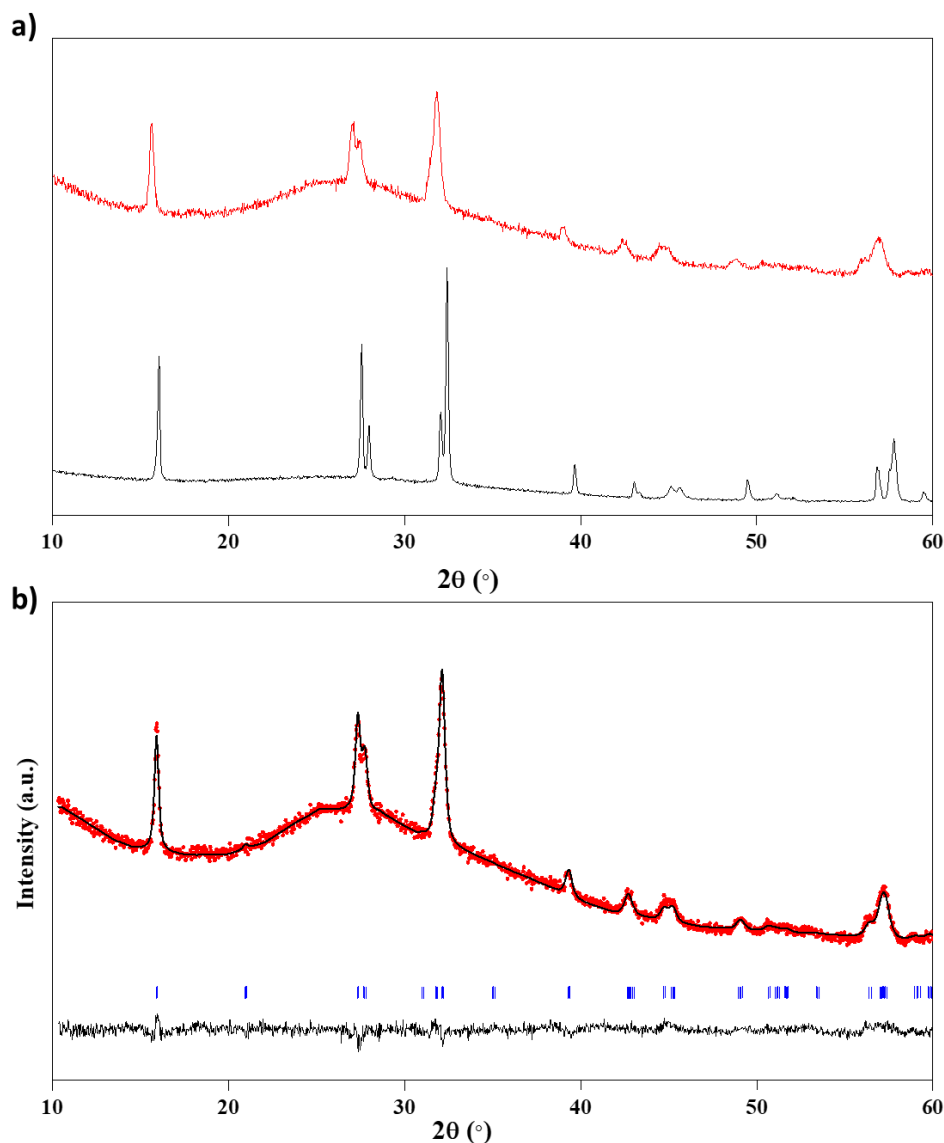
Figure 6.23: a) XRD pattern of HTB-type VF₃•0.33H₂O phase (black) and *ex situ* XRD pattern of the powder recovered from the Swagelok at 1.5V (red); b) Le Bail refinement of the XRD pattern of the cycled powder.

Figure 6.23a show the comparison of the XRD patterns of HTB-type VF$_3$•0.33H$_2$O and powder after reversible insertion of Li$^+$. Based on the Le Bail refinement of the XRD pattern of the cycled powder (Figure 6.23b), the HTB structure was preserved with a ~10% increase of the cell volume. Comparison of the cell parameters of two phases is presented in Table 6.11. It can be observed that indeed the structural water support the reversible mobility of the Li$^+$ cation within the formed large cavities and the volume expansion is correlated with the accommodation of the Li$^+$.

Table 6.11: Comparison of the cell parameters of the HTB phase before and after Li⁺ insertion.

VF$_3$•0.33H$_2$O HTB	VF$_3$•0.65Li HTB
S.G.: *Cmcm*	S.G.: *Cmcm*
a = 7.403(4) Å	a = 7.480(2) Å
b = 12.860(3) Å	b = 12.924(3) Å
c = 7.558(2)	c = 7.576(2) Å
V =719.57(2) Å^3	V = 732.395(2) Å^3

While cycling the cell *vs.* Na (Figure 6.24b), during first charge much lower capacity was registered, only ~0.3 Na⁺ was inserted. Additionally, the working voltage related with the reduction reaction of V^{III}/V^{II} redox couple was found to be ~1.8V *vs.* Na⁺/Na⁰, around 0.2 V lower than in the Li cell. Much lower obtained capacity might be related with larger Na⁺ while comparing with Li⁺ and difficulties with intercalation into the free vacancies within the cavities. Indeed, similar conclusion drawn Wei et. *al.* while cycling HTB FeF$_3$•0.33H$_2$O *vs.* Na.[324]

While following the shape of the curve it can be observed that the curve exhibits two regions – sloppy in the range 4.0 – 1.8 V, followed by a plateau at 1.7 V, which has not finished and could be related to the beginning of the conversion reaction. To verify this hypothesis next measurement requires opening the low cut-off voltage to follow this second reaction. The opening of the voltage window down to 1.0 V indeed resulted in a great increase of the capacity, both for Li and Na cells (Figure 6.25a and b respectively) which is expected to result from the contribution of reversible conversion reaction.
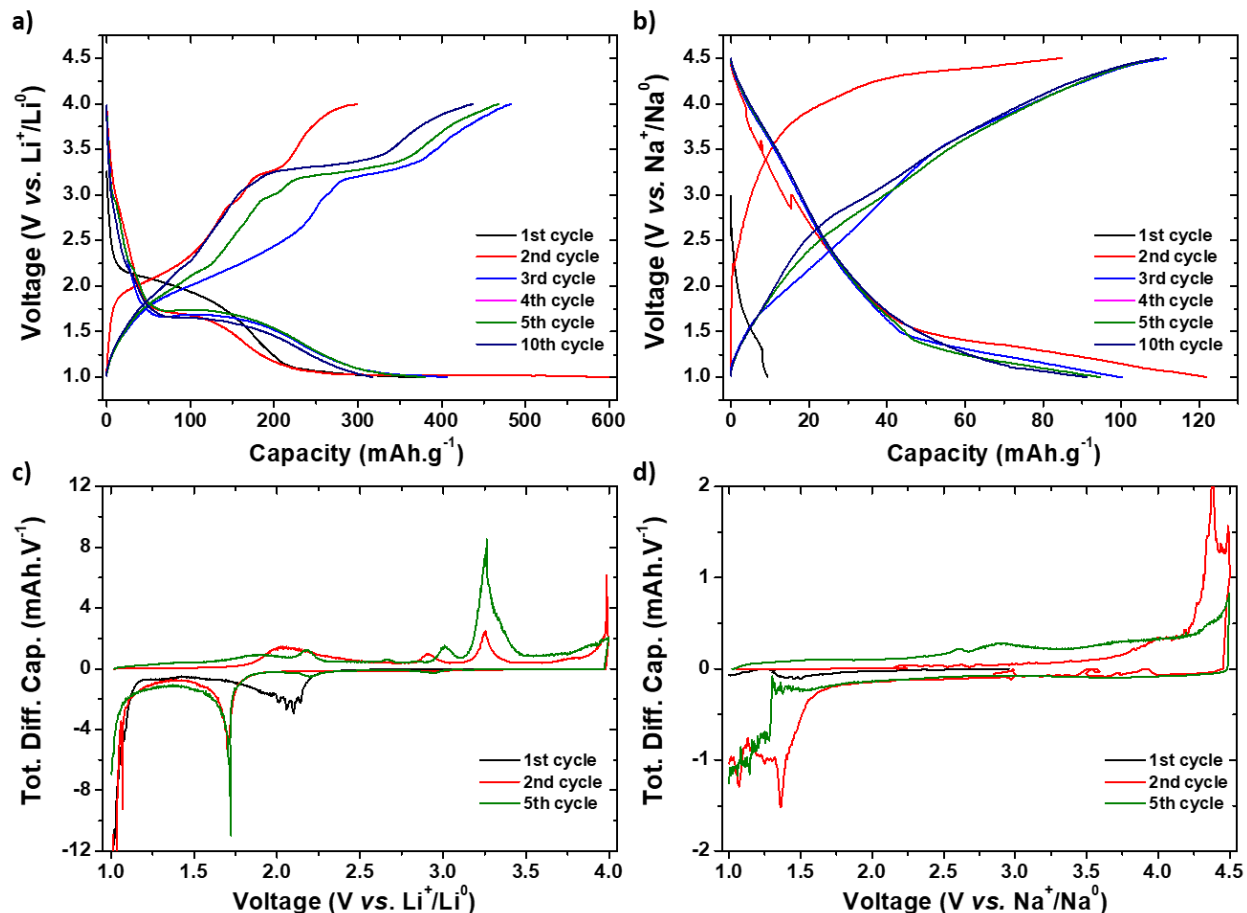
Figure 6.24: (a&b) electrochemical performance of self-standing electrode material consisting of HTB-type VF₃•0.33H₂O as an active material, against (a) Li metal; (b) Na metal at C/20 rate. For better legibility, the x axes (Capacity) are in different ranges for Li and Na cell; (c&d) corresponding derivative dQ/dV curves *vs.* (c) Li and (d) Na metal.

Following the derivative dQ/dV curves registered for the cell cycled *vs.* Li metal (Figure 6.24c), during the first discharge the plateau at ~2 V *vs.* Li^+/Li^0 is expected to result from the reduction of V^{III} to V^{II} and insertion of Li^+ while the large plateau at 1 V *vs.* Li^+/Li^0 can be ascribed to the reversible conversion reaction. During subsequent charge, two different processes centered at ~1.7 V *vs.* Li^+/Li^0 in discharge and 3.25 V *vs.* Li^+/Li^0 in charge were observed resulting with the capacities of ~400 mAh.g⁻¹. The observed reaction mechanism is expected to follow these reactions:

$$V^{III}F_3 + Li^+ + e^- \rightarrow LiV^{II}F_3 \qquad (i)$$

$$LiV^{II}F_3 + 2Li^+ + 2e^- \rightarrow V^0 + 3LiF \qquad (ii)$$
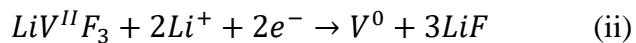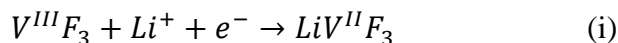
Where reaction (i) describes intercalation mechanism while (ii) a conversion reaction. Subsequent cycles reveal stable position of the discharge peaks at ~1.7 V confirming the reversibility of the reaction between V^{II} and metallic V^0 based on the conversion reaction. Small variation of the charge peaks located ~3.2 V originates from the increasing polarization caused by highly insulating nature of formed LiF.[346]

Although electrochemical tests performed *vs.* Na metal in a voltage window 4.5 – 1.0 V also resulted with higher capacities than previous measurements yet are much lower than one obtained while cycling *vs.* Li metal. During the first discharge the corrugated shape of the curve and low capacity could indicate problems with the contact, which also repeated in next cycle, however subsequent cycling revealed no further problems. After two cycles stable capacity of ~100 mAh.g^{-1} was achieved. Two regions could be observed in discharge curve – steady sloping profile between 4.5 – 1.5 V, and a pseudo-plateau between 1-5 – 1.0 V with gradual decrease of the voltage which as in the cell cycled *vs.* Li could be assigned to the intercalation and conversion reactions, respectively. While following the derivative curves (Figure 6.24d), no clear anodic or cathodic peaks could be distinguished as for the cell cycled *vs.* Li, however, as described above, that might be related to the larger radius of Na^+ than Li^+.

These findings remain in good agreement with the electrochemical mechanism reported for HTB $FeF_3 \cdot 0.33H_2O$ cycled in the voltage window 1.0 – 4.5 V where both intercalation and conversion reactions were observed.[296,324,346]

- **Pyrochlore VF$_3$•0.5H$_2$O**

Figure 6.25 presents electrochemical performance of pyrochlore $VF_3 \cdot 0.5H_2O$ against Li and Na metal anode. Cells were cycled in a voltage window 1.4 – 4.5 V (cell *vs.* Li) and 1.3 – 4.5 V (*vs.* Na) at C/20 rate. By mistake in the settings, after 1st cycle in a cell cycled *vs.* Li the voltage window was changed to 1.4 – 4.2 V.
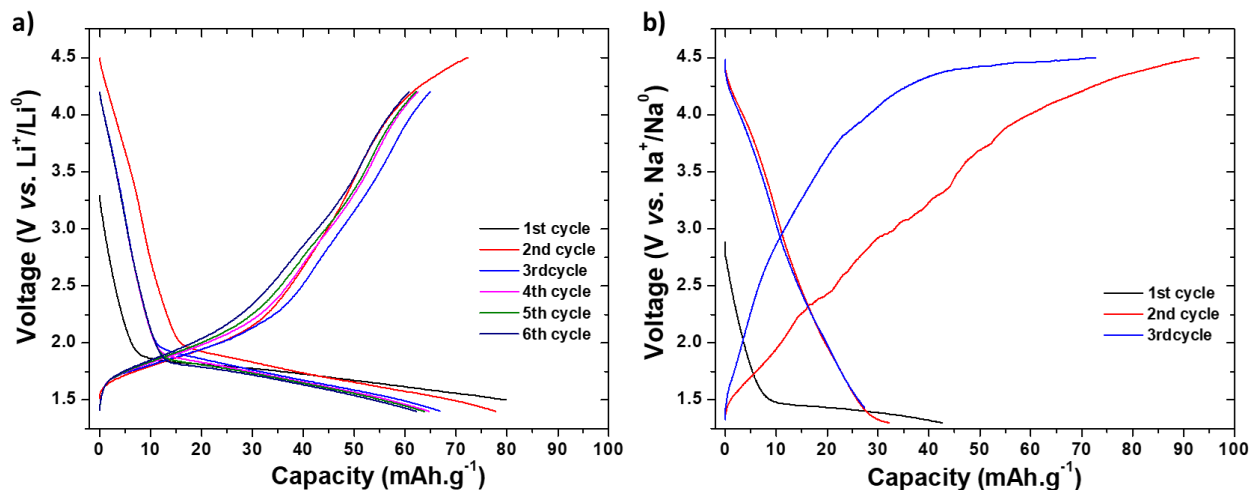
Figure 6.25: Electrochemical performance of pyrochlore VF$_3$•0.5H$_2$O against (a) Li metal; (b) Na metal at C/20 rate.

While cycling the cell *vs.* Li anode (Figure 6.25a), the obtained capacity at the first discharge corresponds to the insertion of 0.7 Li$^+$ at a voltage of 1.8 V *vs.* Li$^+$/Li^0, being slightly less than the amount inserted into the HTB structure. The capacity of the following cycle was almost fully retained but decreased after changing the voltage window. Subsequent cycling corresponds to the slightly fading capacity, stabilizing after fifth cycle and corresponding to the reversible mobility of ~0.55 Li$^+$. This phenomenon was also observed in pyrochlore FeF$_3$•0.5H$_2$O by Li et. *al.*[317] and explained by the irreversible trapping of Li in the cavities.

While cycling the cell *vs.* Na anode, at the first discharge approximately half of the capacity was obtained while comparing the cell cycled *vs.* Li anode, suggesting difficulties with the accommodation of the larger Na$^+$ cation. This observation can be supported by the very large polarization observed in the following cycle. While following the shape of the second discharge curve, the beginning of some process can be observed ~1.3 V, however it requires opening the voltage window for the identification.

Next electrochemical tests were performed with opening the voltage window down to 1.0 V to follow the processes observed in the plateau range below 2 V.
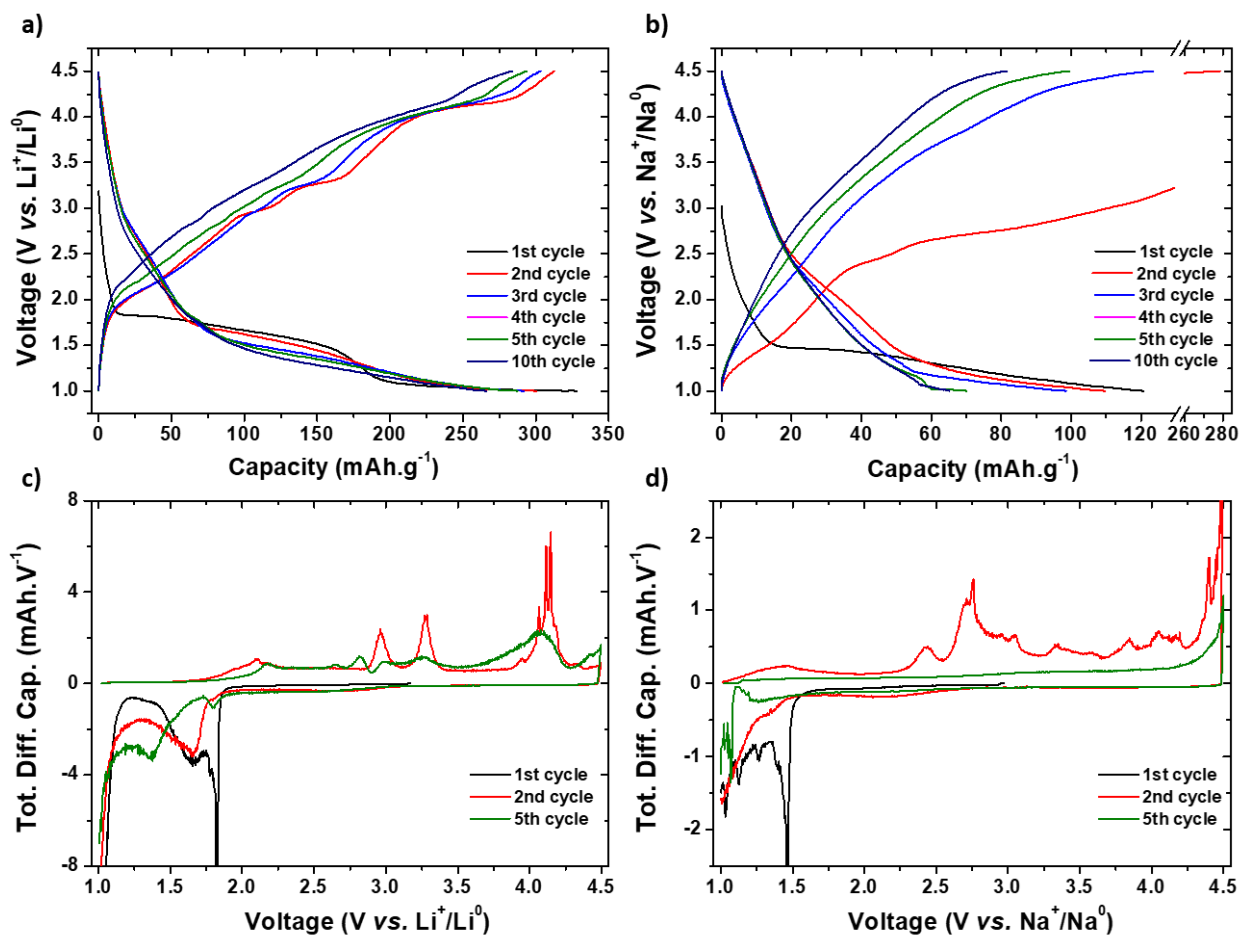
Figure 6.26: (a&b) electrochemical performance of self-standing electrode material consist of pyrochlore-type VF₃•0.5H₂O as an active material, against (a) Li metal; (b) Na metal at C/20 rate; (c&d) corresponding derivative dQ/dV curves *vs.* (c) Li and (d) Na metal.

As for the HTB phase, opening the voltage window down to 1 V resulted with significant increase of the capacity related to the contribution of the conversion reaction observed around 1 V. During the first discharge a long plateau between $1.8 - 1.5$ V *vs.* Li^+/Li^0 could be observed with the resulting capacity of 330 mAh.g^{-1}. While following the derivative curves of subsequent charge-discharge processes (Figure 6.26c), it can be observed that the shape of the curve is gradually changing. Various peaks observed in the first charge and absent in the discharge may suggest slight framework reorganizations upon migration of the Li^+ ions, however, are gradually fading. The observed reversible conversion reaction is expected to follow analogous mechanism as one explained above for the HTB phase.

During first discharge *vs.* Na anode (Figure 6.26b) two different regions can be distinguished – sloping profile between $3.0 - 1.5$ V *vs.* Na^+/Na^0 and a plateau ~1.5 V *vs.* Na^+/Na^0 resulting with

306

the capacity of 120 mAh.g^{-1}. The shape of the curve of subsequent charge process reveals a pseudo-plateau around 2.5 V *vs.* Na$^+$/Na^0, followed by the sloping profile up to 4.5 V *vs.* Na$^+$/Na^0. The high irreversible capacity (around 280 mAh.g^{-1}) in the first cycle indicates side reactions occurring while charging. The profile of the following discharge-charge curves changed into sloping shape without distinguishable plateau range, as observed in HTB VF$_3$•0.33H$_2$O. Additionally, as in the cell cycle *vs.* Li, gradual decrease of the capacity while cycling was observed.

The operating voltage of the pyrochlore-type phase was found to be around 0.2 V lower than the HTB-type phase. It might correspond to the differences in the structures of those two polymorphs – within HTB structure there is only one possible migration pathway for the cations (along c axis), whereas in open pyrochlore structure there are large three-dimensional interconnected channels. Additionally, firmly confined water molecules in zigzag channels are also expected to improve the accommodation of the Li$^+$ ions.
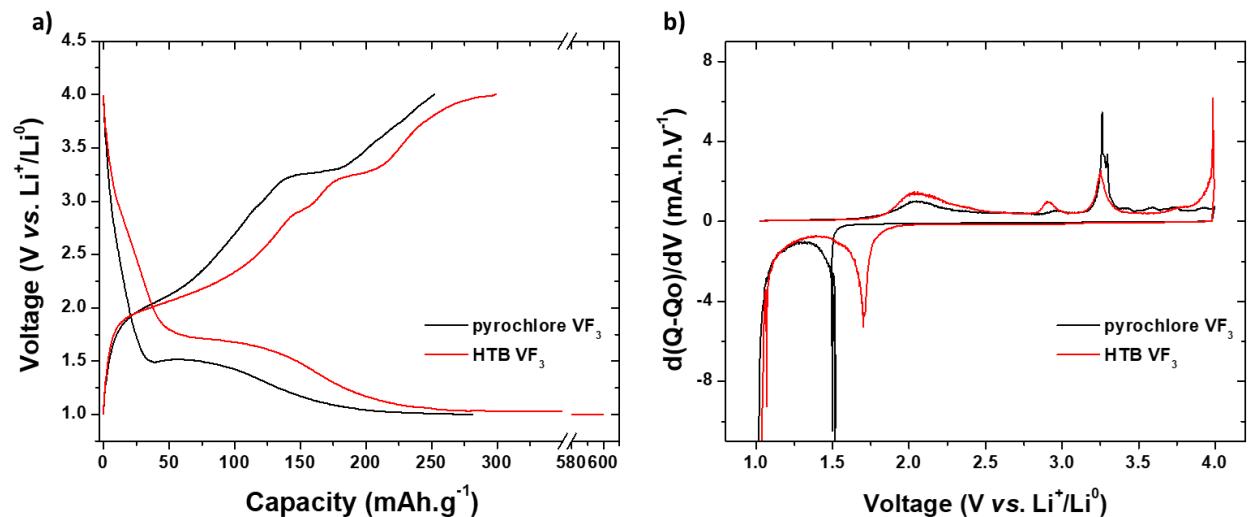
Figure 6.27: (a) Galvanostatic charge-discharge curve of the second cycle of pyrochlore VF$_3$•0.5H$_2$O (black curve) and HTB VF$_3$•0.33H$_2$O (red curve) together with the corresponding derivative dQ/dV curve (b).

Compared to iron fluoride, FeF$_3$•xH$_2$O, both HTB and pyrochlore phases of VF$_3$•xH$_2$O exhibit much higher stability upon cycling. Suggested in the literature preparation of the graphene composite revealed significant improvement of the electrochemical performance of both polymorphs of FeF$_3$•xH$_2$O [317,325] and likewise is expected to improve the performance of investigated VF$_3$•xH$_2$O. The operating voltage of the V^{III}/V^{II} couple of ~2 V *vs.* Li$^+$/Li^0, although higher than the one of the oxides is too low for the application as positive electrode, however

performed tests demonstrated successful Li insertion followed by the reversible conversion reaction. Additionally, it was shown that the electrochemical performance of both HTB and pyrochlore $VF_3 \cdot xH_2O$ is superior while cycling the cell *vs.* Li than *vs.* Na which might be related to the more facile mobility of the smaller Li^+ than Na^+.

Other reported vanadium fluorides, such as Li_3VF_6 reveal successful lithium insertion however with relatively poor electrochemical performance (capacities limited to 30 mAh.g^{-1}) and the operating voltage of V^{III}/V^{II} couple was found to be 2 V *vs.* Li^+/Li^0, very similar to the one presented for VF_3. Yet again it was shown that ball milling with carbon improves the electrochemical performance by significantly increasing the capacity. [250]

The uncovered electrochemical activities of both pyrochlore and HTB $VF_3 \cdot xH_2O$ already shows relatively good electrochemical performance of these compounds and is expected to be significantly improved while ball milling with carbon or preparing the graphene composite.

- **Unknown <<VOF>> phase**

The last obtained phase, <<VOF>>, was also investigated as potential electrode material. For the calculations of the charge/discharge current which will correspond to the C/20 rate, the composition of the phase was assumed to be $VOOF_{0.5}Cl_{0.5}$, according to the assumptions from XAS analysis suggesting V^V oxidation state. The cell was cycled in the 1.5 – 4.7 V voltage window. Theoretical capacity of this phase corresponding to the insertion of one Li^+ is equal to 243 mAh.g^{-1}.

Figure 6.28 shows the electrochemical performance of the <<VOF>> phase as an active material against metallic Li. The expected redox reaction was the reduction of vanadium, therefore the cell was launched in discharge. During the first cycle the cell developed the capacity of 225 mAh.g^{-1} which corresponds to the insertion of ~0.9 Li^+. The shape of the subsequent charge curve – sloping in the range 1.5 – 4.0 V and plateau above 4.0 V suggests occurring side reactions which also are responsible for the additional capacity. Lack of clear peaks in the discharge in the derivative dQ/dV curves (Figure 6.28b) corroborates this statement.
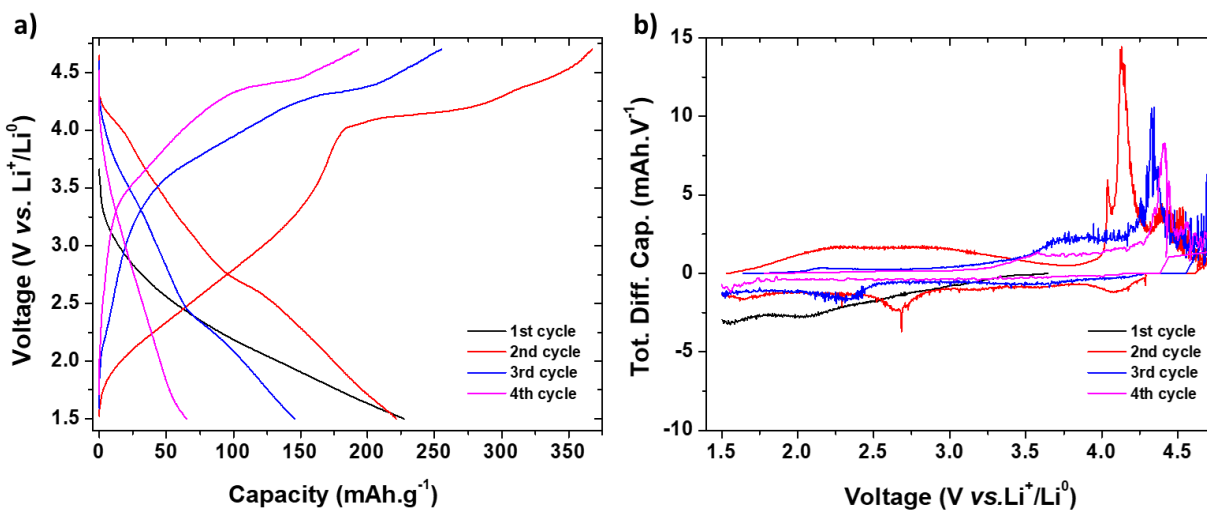
Figure 6.28: (a) electrochemical performance of <<VOF>> phase against Li metal together with (b) corresponding dQ/dV curve.

During the following discharge-charge reactions a gradual decrease of the capacity is observed with large changes in the shape of the curves. Such changes could be related to the structural changes occurring upon lithium insertion and removal. To follow these eventual structural changes and possible crystallization upon lithiation/delithiation, which could help with the identification of the phase, a couple of *ex situ* XRD curves were acquired – at different charge state.
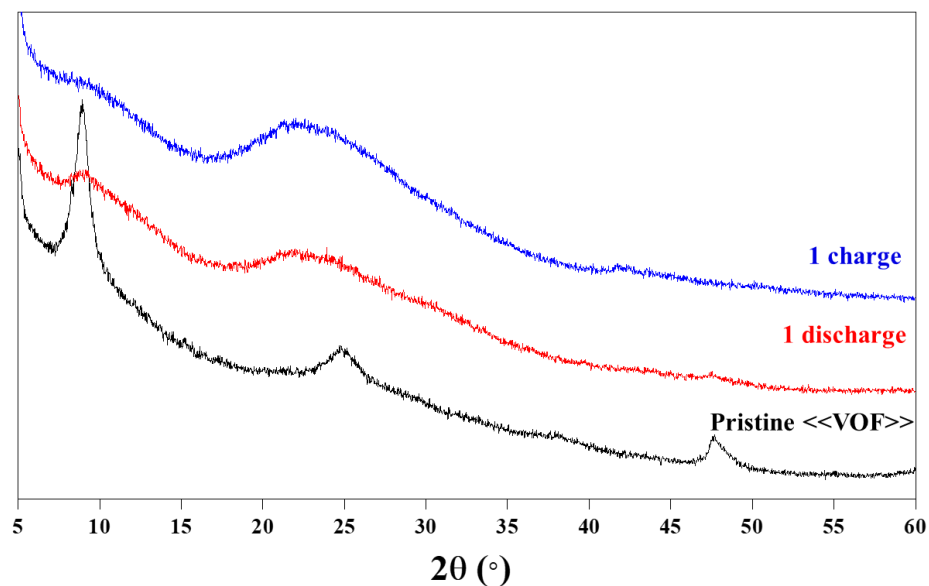
Figure 6.29: *Ex situ* XRD patterns of <<VOF>> phase at three different charge states: pristine (black); after one discharge (red); and after one charge (blue).

Figure 6.29 shows three XRD patterns – before cycling, after one discharge and after one discharge. Unfortunately, it can be observed that with charging the structure undergoes further amorphization, which makes impossible to identify created lithiated/delithiated phases with this technique.

6.5. Conclusion

In this chapter an interesting family of metal fluorides was investigated with the focus on vanadium transition metal. For the first time, the vanadium-based HTB $VF_3 \cdot 0.33H_2O$ compound was obtained via solvothermal microwave-assisted synthesis. It crystallizes in *Cmcm* space group and its framework presents hexagonal channels, confirming the HTB structure.

With the same synthesis approach, a second polymorph of vanadium fluoride with pyrochlore $VF_3 \cdot 0.5H_2O$ structure was obtained. Additionally, a third vanadium fluoride phase was also obtained from same synthesis route by changing the amount of HF precursor, however its XRD pattern could not be indexed due to insufficient and broad reflections. Based on the coupled XAS and EDX analyses, the proposed formula was deduced to $VOOF_{0.5}Cl_{0.5}$.

The morphology of all three compounds was characterized by SEM revealing entirely different shapes of the particles of each phase.

High temperature study was performed on HTB and pyrochlore phases showing its thermal stability to ~240 °C with final thermal decomposition into V_2O_5. No crystallization at high temperature of the third synthesized phase was observed, but above 200°C decomposed into V_2O_5.

The electrochemical study of these phases as potential electrode materials resulted with an insertion of ~0.8 Li^+ at 2 V *vs.* Li^+/Li^0 into HTB structure and ~0.7 Li^+ at 1.8 V *vs.* Li^+/Li^0 into pyrochlore structure. Only one migration pathway along *c* axis in HTB structure in comparison to 3D migration in pyrochlore structure is expected to be answerable for the difference of 0.2 V between the operating voltage of these two polymorphs.

The performed *ex situ* XRD measurements after electrochemical insertion of Li^+ ion into HTB structure revealed the preservation of the HTB framework with the ~10% expansion and observation of the Jahn Teller distortion of the (4)T(2)(g) state suggesting the redox reduction of V^{III} to V^{II}. Opening the voltage window to 1 V in both polymorphs resulted with observation of

reversible conversion reaction which contributed into significant increase of the capacities. The electrochemical performance of both HTB and pyrochlore VF_3 is superior while cycling the cell *vs.* Li than *vs.* Na which might be related to the more facile mobility of the smaller Li^+ than Na^+. Ball milling with carbon or preparation of the graphene composite as suggested in the literature is expected to translate into improvement of the electrochemical performance.

General conclusions for Part B

This part of the thesis was dedicated to fluorine-based compounds as potential cathode materials.

In Chapter 5, the family of garnet fluorides with general formula of $Na_3Li_3M_2F_{12}$ was revisited. The presence of both alkali cation and transition metal which could participate in the redox reactions attracted our attention and triggered the detailed investigation of these materials. The BVEL calculations revealed low-energy migration pathways for alkali cations, which was expected to translate into appealing electrochemical performance. Two synthesis routes were employed in the synthesis of selected garnets - microwave assisted solvothermal synthesis route and mechanochemical using ball milling. Three different fluoride garnets (iron $Na_3Li_3Fe_2F_{12}$, vanadium $Na_3Li_3V_2F_{12}$ and titanium $Na_3Li_3Ti_2F_{12}$) were successfully prepared. Detailed structural analysis confirmed proper stoichiometry and +3 oxidation state of the transition metal. Morphological analysis revealed distinct size of the particles depending on the type of the garnet with round hollow shell-type for vanadium and cubes and platelet shape for iron garnet. Particles of titanium garnet obtained from ball-milling synthesis concentrate in agglomerates of nano-sized particles.

Early electrochemical study of these materials resulted in rather poor activity – very low capacity and large polarization. Only $Na_3Li_3Ti_2F_{12}$ cycled versus Li exhibit activity of the $Ti^{III/IV}$ redox couple at an average voltage of 2.8 V $vs.$ Li^+/Li^0. In the next stage of the work, electrode processing such as extended ball-milling with carbon or use of carbon nanotubes would be recommended to enhance the electrochemical performance.

In parallel to the attempts of the electrochemical oxidation / reduction of the garnet materials, chemical oxidation and reduction was performed to compare the results. Both attempts of the chemical oxidation and reduction resulted unsuccessful for the vanadium garnet, no changes in the composition in the mild conditions with eventual decomposition in the more concentrated oxidizing/reducing agent were observed. No change either was observed after trying to reduction the iron garnet, even with the use of highly concentrated reducing agent, revealing exceptional stability of $Na_3Li_3Fe_2F_{12}$ structure. On the contrary, effective oxidation of Ti^{III} to Ti^{IV} was observed by performing chemical oxidation of $Na_3Li_3Ti_2F_{12}$. This reaction is associated with the extraction of two Li^+ cations and with structural changes from cubic garnet into tetragonal $Na_3Li(TiF_6)_2$.

Initial electrochemical study of this material showed stable mobility of one Li^+ at an average voltage of 3.1 V *vs.* Li^+/Li^0, being the highest working voltage of the $Ti^{III/IV}$ redox couple. Further research in this material is highly recommendable with detailed *ex situ* and *operando* analysis of the structure to verify if tetragonal structure is maintained, or reversible transformation into cubic structure is occurring.

In Chapter 6, we investigated the family of binary metal fluorides with the focus on vanadium transition metal. We reported for the first time the successful solvothermal microwave-assisted synthesis of vanadium based HTB $VF_3 \cdot 0.33H_2O$ structure, crystallizing in *Cmcm* space group. With the same synthesis approach, a second polymorph of vanadium fluoride with pyrochlore structure $VF_3 \cdot 0.5H_2O$ was obtained. Additionally, a third vanadium fluoride phase was also obtained from same synthesis route by changing the amount of HF precursor, however its XRD pattern could not be indexed due to insufficient and very broad reflections.

The electrochemical study of these phases as potential electrode materials resulted in an insertion of ~0.8 Li^+ at 2 V *vs.* Li^+/Li^0 into HTB the structure and ~0.7 Li^+ at 1.8 V *vs.* Li^+/Li^0 into the pyrochlore structure. Only one migration pathway along the *c* axis in HTB structure in comparison to 3D migration in pyrochlore structure is expected to be answerable for the difference of 0.2 V between the operating voltage of these two polymorphs. Although the operating voltage was found to be higher than the one reported for oxides yet is too low to be considered for a practical application as battery material. However, it is another example of a structure hosting lithium/sodium cation upon combined reversible intercalation and conversion reaction. The ex-situ XRD measurements performed after electrochemical insertion of Li^+ ion into the HTB structure revealed the preservation of the HTB framework with the ~10% expansion and observation of the Jahn Teller distortion of the (4)T(2)(g) state suggesting the redox reduction of V^{III} to V^{II}. Ball milling with carbon or preparation of the graphene composite as suggested in the literature is expected to translate into improvement of the electrochemical performance.

Third, the unknown phase was also tested electrochemically, assuming the composition of $VOOF_{0.5}Cl_{0.5}$, according to the results from XAS analysis suggesting V^V oxidation state and the analysis of the TGA curve. The discharge capacity of 225 mAh.g^{-1} obtained in the first cycle is expected to correspond to the insertion of ~0.9 Li^+. The shape of the subsequent charge curve –

sloping in the range 1.5 – 4.0 V and plateau above 4.0 V suggests occurring side reactions which also are responsible for the additional capacity. The following discharge-charge reactions resulted in a gradual decrease of the capacity and large changes in the shape of the curves suggesting morphological changes occurring in the structure.

In perspective, the confirmation of the assumed composition is essential for the further insight into this phase. So far, the synchrotron XRD, TEM and NMR analyses were unfruitful. Although high temperature XRD did not show the appearance of new signals in the XRD pattern, recrystallization of the powder would be suggested to get more crystalline phase. Next, *operando* measurement should help to follow the structural changes upon reversible Li^+ migration.

Chapter 7 GENERAL CONCLUSION

This thesis aimed at searching for new electrode materials which could be applied in lithium-ion and sodium-ion batteries. More precisely, we focused on the materials with high-voltage and high-capacity, that could compete with the current state-of-art/commercial cathode material. Material databases such as Inorganic Crystal Structure Database[125] (ICSD) and Crystallographic Open Database[126] (COD) are a great source of thousands of compounds among which true gems can be found if only proper identification techniques can be applied. The screening of the compounds can be accelerated with the help of computational methods. In our work, we applied high-throughput Bond Valence Energy Landscape (BVEL) calculations [128] looking for structures presenting a 3D migration pathway with migration energies below 1.5 eV, that could include a 3d transition metal and with a relatively low molar mass in order not to penalize the expected capacity. Using this method we identified two families of compounds – the CUBICON nitrodophosphates of general formula $Na_{3-n}M_{1+n}(PO_3)_3N$ and the garnet fluorides of general formula $Na_3Li_3M_2F_{12}$ for which 3D migration pathways for Na^+ were predicted with E_m = 1.08 eV (M = Al, n=0), E_m = 0.81 eV (M = Mg, n=1) and E_m = 0.58 eV (M = V), respectively. As a first choice, vanadium was selected as a transition metal since it is expected to offer high working voltage and deliver high capacity due to the use of both $V^{III/IV}$ and $V^{IV/V}$ redox couples, as in NASICON $Na_3V_2(PO_4)_3$.[98] Focusing on low cost and earth abundant 3d metals, iron and manganese were selected as a divalent transition metals. Although being less popular dopant owing to its higher cost and mining ethics, cobalt substitution usually has a beneficial effect by elevating the working voltage and improving the cyclability, therefore also this metal was included in the investigation.

PART A was dedicated to CUBICON nitridophosphates, the first identified family by BVEL. In Chapter two, we introduced the first member of the CUBICON family, $A_3V(PO_3)_3N$ (A=Na/Li). We presented the direct synthesis of $Na_3V(PO_3)_3N$ and an ion-exchange method to obtain the Li analog, $Li_3V(PO_3)_3N$. BVEL calculations suggest a presence of low-energy 3D mobility pathway allowing the mobility of two alkali cation within the $A_3V(PO_3)_3N$ structure. The performed electrochemical studies on $Na_3V(PO_3)_3N$ revealed a very high working potential of the V^{IV}/V^{III} redox couple, 4.0 V *vs.* Na^+/Na^0 and 4.1 V *vs.* Li^+/Li^0 with stable capacity and very low voltage hysteresis. Although, contrary to BVEL predictions, only one Na was found to be active. DFT

calculations revealed that the extraction of more than one sodium cation seems to be prevented because the potential of the redox couple V^V/V^{VI} is predicted to be beyond the voltage stability window of the electrolytes available up to now. Yet, on the example of $Na_3V(PO_3)_3N$ we demonstrated the beneficial effect of the nitrogen inductive effect on the working voltage of V^{IV}/V^{III} redox couple.

Chapter three was dedicated to different solid solutions of CUBICON nitridophosphates, investigating Fe, Mn and Co transition metals. A highlight from this chapter is the first synthesis of $Na_2Co_2(PO_3)_3N$ and improved electrochemistry of $Na_2Fe_2(PO_3)_3N$ while comparing with the ones reported up date. $Na_2Fe_2(PO_3)_3N$ was found to deliver stable capacity of 60 mAh.g^{-1} *vs.* Li corresponding to the reversible mobility of one alkali cation in hybrid-ion configuration with average voltage of 3 V *vs.* Li^+/Li^0. The removal of the second alkali cation upon electrochemical and chemical oxidation was not achieved, suggesting very high stability of the oxidized $NaFe_2(PO_3)_3N$ phase requiring very high additional energy to transform into less favorable desodiated $Fe_2(PO_3)_3N$ state. Stabilization of Mn-based CUBICON was found to be only possible in the presence of foreign cation such as Al^{III} or Fe^{II}. Changes of the synthesis conditions resulted in obtaining a novel family of sodium manganese nitrodophosphate $A_{1.1}Mn_3P_3O_8N_2$ (A = Na/Li), to which Chapter 4 was dedicated. Additionally, the evaluated preparation of the lithium counterpart, to the best of our knowledge, is the first direct synthesis of lithium nitrogen-based polyanionic compound. DTF calculations predicted activity of the $Mn^{II/III}$ redox couple at a potential compatible with common organic electrolytes (3.25 V *vs.* Na^+/Na^0 and 3.30 V *vs.* Li^+/Li^0), however based on the performed experimental tests, sodium and lithium extraction from these structures was not achieved. The BVEL calculations revealed very high values of percolation energies (>4 eV), indicating a difficile diffusion of the alkali cations within the structure, most probably resulting from the presence of narrow bottlenecks on the course of the alkali cations diffusion pathways. Unfortunately for this new compound, but these results confirmed the successful application of the BVEL calculations in search for new materials.

In PART B, we focused on the second family identified by BVEL calculations, the garnet fluorides of general formula $Na_3Li_3M_2F_{12}$ (M=Fe, Ti, V). The garnet fluorides were expected to offer high capacities upon removal of two alkali cation at elevated voltage resulting from the inductive effect of fluorine. Apart from garnet fluorides, other fluoride-based compounds were decided to be

316

explored in this thesis – the family of binary vanadium fluorides. These compounds were expected to offer high capacity through using all oxidation states involving reversible conversion reaction. Although the first electrochemical study on garnet showed rather poor activity – very low capacity and large polarization, chemical oxidation of one of the garnet, $Na_3Li_3Ti_2F_{12}$ brought interesting results. This reaction indicates the extraction of two Li^+ cations and is associated with structural changes from cubic garnet into tetragonal $Na_3Li(TiF_6)_2$. Initial electrochemical study of this material resulted in reversible insertion/extraction of one Li^+ at an average voltage of 3.1 V *vs.* Li^+/Li^0, being the highest working voltage of the $Ti^{III/IV}$ redox couple. Investigating binary vanadium fluorides in Chapter 6, we reported for the first time the successful microwave-assisted solvothermal synthesis of vanadium based HTB $VF_3•0.33H_2O$ compound. Changing the V:F ratio in the synthesis, we also obtained second polymorph of vanadium fluoride with pyrochlore structure $VF_3•0.5H_2O$. The electrochemical measurements revealed the operating voltage of the V^{III}/V^{II} couple at ~2 V *vs.* Li^+/Li^0, which although higher than the one usually observed for vanadium oxides, is too low for the application as positive electrode and too high for a negative electrode. However, we demonstrated successful Li insertion followed by the reversible conversion reaction.

Summarizing all the experimental results, we can confirm that high-throughput BVEL calculations can be successfully applied as a tool in search for novel cathode materials. This method allows fast identification of interesting structures with appealing electrochemical performances.
Additionally, on the examples of $A_{1.1}Mn_3P_3O_8N_2$ and $Na_3Li(TiF_6)_2$, two compounds identified upon modification of conditions/ chemical modifications, we hopefully demonstrated that nitrogen and fluorine-containing polyanionic compounds are chemical spaces that worth to be investigated to discover new attractive materials.

Annex - Experimental section

Outline

A.1. Synthesis of the active material

To prepare described samples, three different synthesis routes were used – solid state synthesis under ammonia flow (ammonolysis) or argon flow, solvothermal synthesis method with the use of the microwave and mechanochemical using ball milling. All three routes will be described below with details. First synthesis method, ammonolysis, was carried out at CIC energiGUNE, whereas both microwave-assisted solvothermal route and mechanochemical using ball milling were carried out at Institut des Molécules et des Matériaux du Mans (IMMM) with the support of Jérôme Lhoste.

A.1.1.   Ammonolysis

This synthesis method involves the direct reaction of solid components at high temperature in the reducing atmosphere of ammonia. Apart from the role of the reducing agent, ammonia also acts as a nitriding agent. Nitridation of oxides is not possible to be achieved by thermal treatment under air or nitrogen due to much higher stability of triple bond in molecular nitrogen than double bond in molecular oxygen. Therefore, a heating process under flow of ammonia allows the formation of nitrides following the reaction:

$MO_x + NH_3 \rightarrow MN_y + H_2O + 0.5\ H_2$

Additionally, the presence of H_2 may lead to the reduction of the cations.
Due to the toxic and corrosive nature of ammonia gas, special safety precautions are required to be taken into account while carrying out the reaction. Personal protective equipment including goggles, laboratory coat and gloves must be always employed. In the beginning of each reaction the potential leak of ammonia is verified in each end of the tubular furnace with soaked lackmus paper. The reaction is carried out under closed fume hood with powerful ventilation. Additionally, special laboratory safety training was also carried out to prevent potential risks and to explain the emergency actions.

In the syntheses of the $Na_3MP_3O_9N$ nitridophosphates, sodium phosphate, $NaPO_3$ and transition metal oxide have been used as precursors, while in the syntheses of $Na_2M_2P_3O_9N$ additionally

ammonium dihydrogen phosphate, $NH_4H_2PO_4$ was also used as a precursor to balance the stoichiometry. The reagents were taken in a molar ratio and milled in a FRITSH Pulverisette 7 ball-miller under air for 20 min in 45 ml zirconium oxide jar in a 1:20 powder-to-ball mass ratio (15 mm zirconium oxide balls were used). The as-prepared mixture of precursors was placed into an alumina or graphite crucible and deposited in a tubular furnace for the heat treatment. Depending on the chosen formulation, different synthesis conditions (temperature, time, gas flow) were adapted. Details on these conditions can be found in the synthesis section in chapters 2 to 4.

A.1.2.   Microwave-assisted solvothermal synthesis

A CEM MARS5 microwave oven (Figure A.1a) was used to perform the solvothermal syntheses of the fluoride materials from part B. The reactants were placed into the 50ml Teflon autoclave and closed in the support module showed in Figure A.1b. The as-prepared reactor was fixed inside the microwave oven and subjected the thermal treatment. For most of the reactions the selected conditions were heating at 160 °C for 30 min and cooling till room temperature.
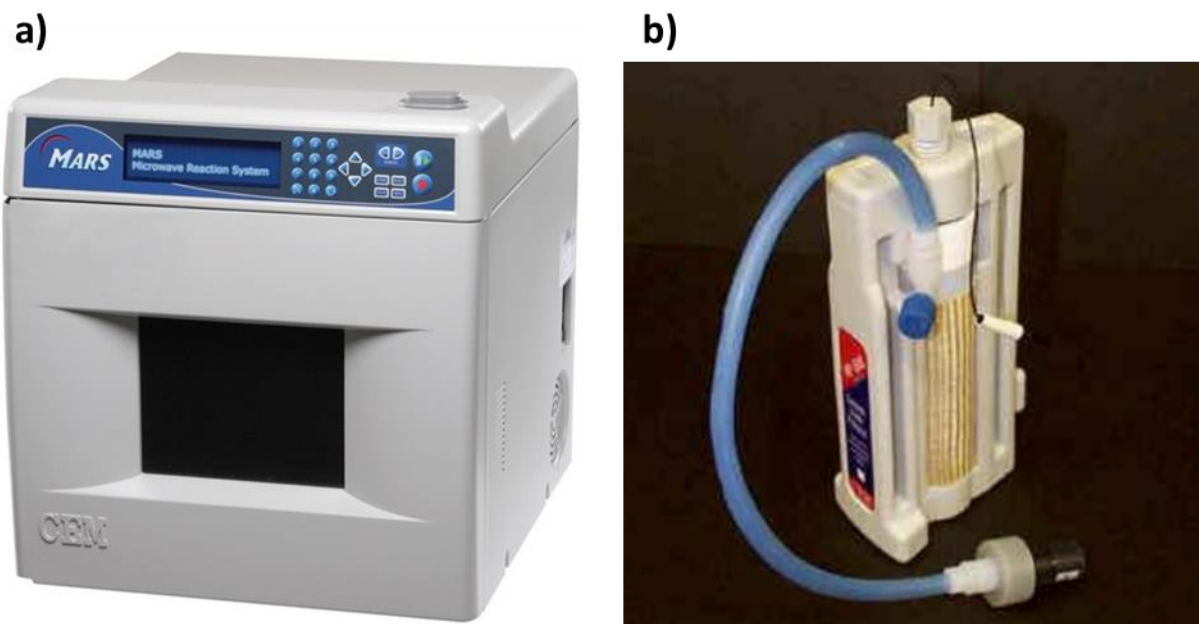
Figure A.1: (a) CEM MARS5 microwave used for the syntheses; (b) control vessel assembled and housed in the support module.

A.1.3. Ball milling

Fluoride garnets from chapter 5 were prepared by the mechanochemical synthesis using ball milling. FRITSH Pulverisette 7 ball-miller equipped with the 45 ml zirconium oxide jar was used. This ball miller allows thoroughly mix the powders through the high energy milling process. For the synthesis of $Na_3Li3M_2F_{12}$ garnet, the mix of M_2O_3, LiF and NaF powder precursors was introduced into the jar together with the zirconium oxide balls in the 1:5 powder-to-ball ratio. Next, the jar was closed in the planetary mill to undergo the grinding cycles. During them, the jars rotate at a very high rotation speed in the opposite direction to the main disc generating centrifugal forces. The friction between the grinding balls and the jar walls results in the formation of the high energy grinding the material into ultra-fine nanopowders. To avoid overheating of the jars, the milling process was divided into 36 cycles of 30 min separated by the 2 min pause. Additionally, the jars were tightly closed under argon to avoid oxidation process.

Figure A.2: FRITSH Pulverisette 7 ball-miller together with the 45 ml zirconium oxide jar.

A.2. Structural characterization

A.2.1. X-ray diffraction (XRD)

X-ray powder diffraction (XRD) is a non-destructive and rapid analytical technique used for the phase identification of a crystalline sample. This technique has been used as a routine characterization for a verification of the purity of obtained samples and detailed crystallographic structure determination by performing Rietveld refinement of the obtained XRD patterns.

Laboratory XRD patterns were acquired using a Bruker D8 Discover diffractometer (Figure A.3a) equipped with a monochromatic Cu radiation: ($\lambda_{Cu,K\alpha1}$ =1.54053 Å) and a LynxEye detector operating at 40 kV in reflection mode with a θ/θ Bragg-Brentano geometry (Figure A.3b). *Operando* XRD measurements were performed in Bruker D8 Advance diffractometer using a Cu K $_{\alpha2}$ ($\lambda_{Cu,K\alpha1}$ =1.54053 Å and $\lambda_{Cu,K\alpha2}$ =1.5444 Å) Cu tube and Co K $_{\alpha2}$ ($\lambda_{Co,K\alpha1}$ =1.78896 Å and $\lambda_{Co,K\alpha2}$ =1.7928 Å) Co tube. The tube was substituted from Cu to Co during the course of this thesis. All the regular and *operando* measurements were realized at CIC energiGUNE with the support of María Jáuregui and Damien Saurel.
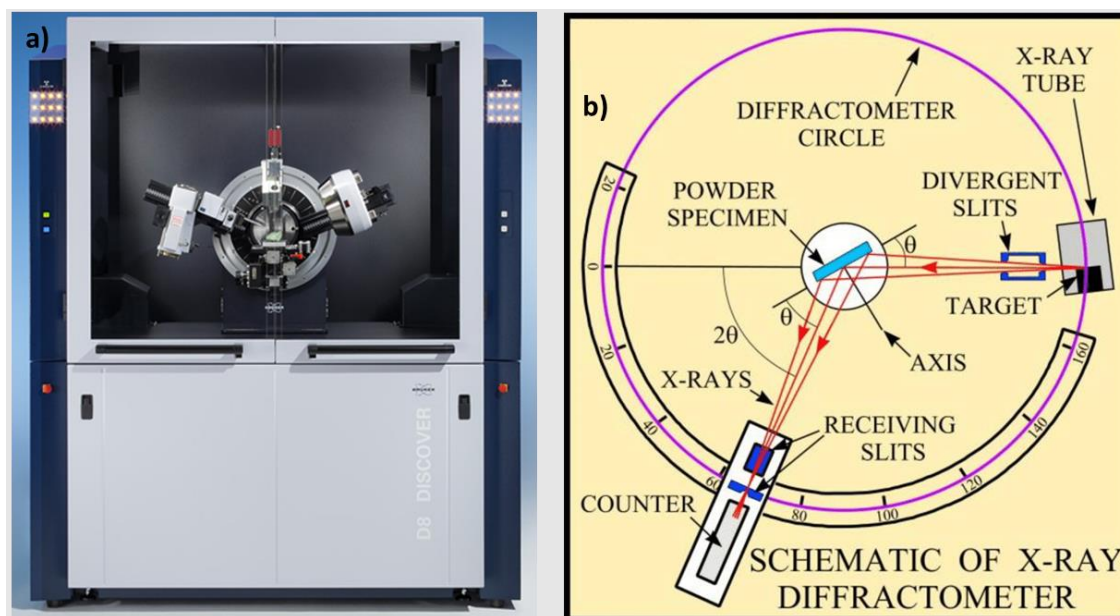
Figure A.3:(a) Bruker D8 Discover diffractometer; (b) scheme of the Bragg-Brentano geometry. Adapted from B.D. Cullity[348]

A.2.1.1. Operando XRD experiment

Operando XRD measurements were performed in a specially designed cell[349] (Figure A.4b). The shape of the cell was adapted for the Bruker D8 advance diffractometer. The cell is equipped with a beryllium window being almost completely transparent to the X-ray and serving as a current collector. The Be window was covered with a thin layer (3 µm) of aluminum foil to prevent its oxidation at high voltage. The cell was assembled in an argon filled glovebox in the usual configuration – cathode material ‖ separator ‖ anode material and closed tightly. Next, the cell was placed in the diffractometer and connected to a portable VMP Biologic potentiostat to control the electrochemical measurement. The XRD patterns were recorded in the selected 2θ range while

performing a galvanostatic cycling at C/20 – C/50 rate (details on the selected 2θ range and the C-rate can be found in the experiment description in Chapter 2).

A.2.1.2. Synchrotron XRD (SXRD)

High resolution XRD measurements were performed at the BL04-MPSD beamline of ALBA Synchrotron in Barcelona., with the support of Dr. François Fauth. The reason for using this facility was the high flux of the X-ray allowing to perform the measurement in highly reduced time and at significantly higher resolution. Samples for the measurements were packed inside 0.25 mm capillaries and air-tightly closed with the epoxy raisin (Figure A.4a). For the *operando* XRD measurements the same home-made cell (Figure A.4b) was used. As can be seen in the image, the plunger possesses a beryllium-covered hole allowing the transmission of the X-rays through it.
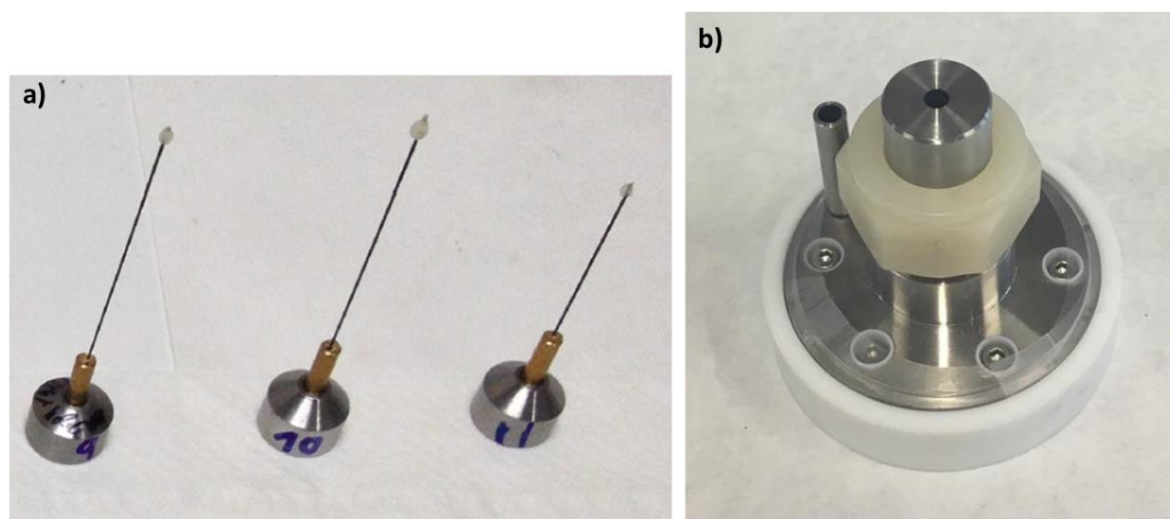
Figure A.4: (a) Borosillicate capillaries filled with the samples and mounted into specific holders for the synchrotron measurements; (b) CIC home-made *in situ* cell used for the *operando* measurements.

The experimental set-up for the *operando* measurement is shown in Figure A.5. As can be observed, the holder was adapted to mount three cells which allowed to measure three cells at the same time. The beamline can be observed at the back of the cells (left photo with the cables connected to the plungers) and detector on the front of the cells (right photo where the Be windows in the cells can be visible). Each *in situ* cell was connected to the potentiostat and well centered which allowed collecting SXRD patterns without manual changes of the position. After verifying that the positions of the peaks from the *in situ* cell perfectly superimpose the positions of the peaks of the material in the capillary, the *operando* measurements were performed.
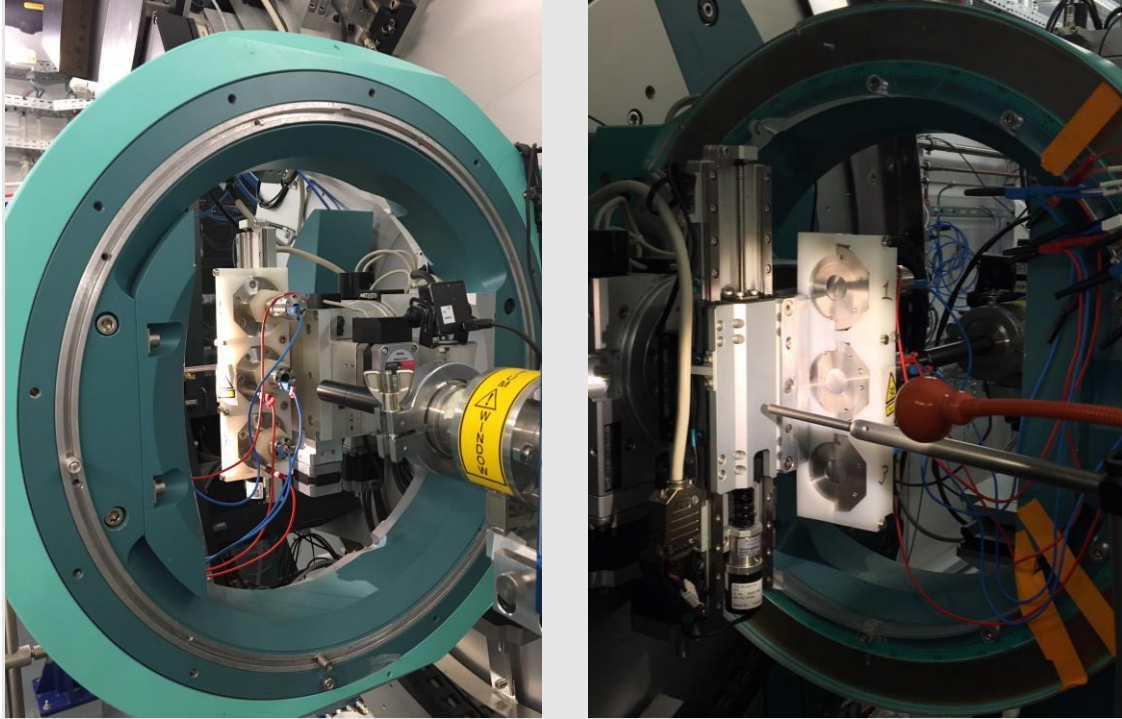
Figure A.5: Set up for the *operando s*ynchrotron measurement presenting three *in situ* cells placed in the holder in the BL04-MSPD beamline.

A.2.2.　　Neutron powder diffraction (NPD)

Neutron powder diffraction (NPD) data were collected at the ECHIDNA high-resolution diffractometer at ANSTO facilities (Australia) in collaboration with Dr. Max Avdeev. The schematic of this diffractometer is shown in Figure A.6. The instrument uses a single wavelength and a highly collimated neutron beam to improve resolution. The NPD patterns were acquired using a wavelength of $\lambda = 1.622$ Å in the 2θ range $4 \leq 2\theta \leq 164°$ with a step size of $0.05°$.
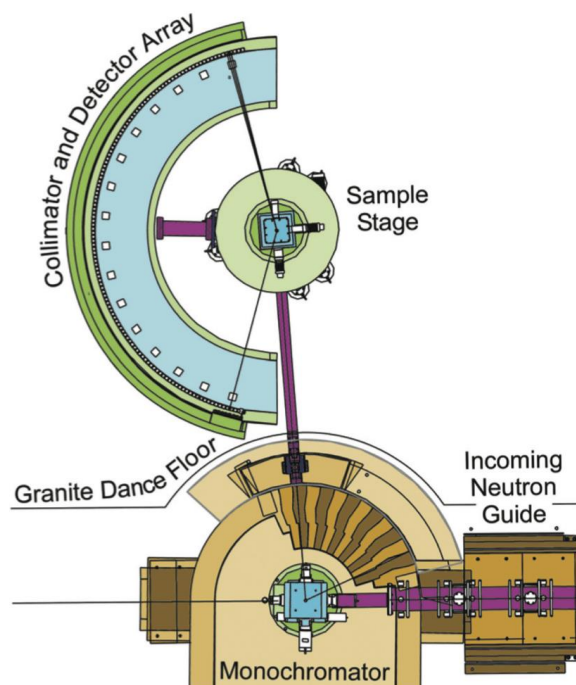
Figure A.6: Schematic of the high-resolution powder diffractometer Echidna at ANSTO. From Hudspeth.[350]

A.2.3.   X-ray Absorption Spectroscopy (XAS)

X-ray Absorption Spectroscopy measurements were performed at the BL29-BOREAS beamline of ALBA Synchrotron in Barcelona with the support of Manuel Valvidares. The BL29-BOREAS beamline is a soft X-ray beamline dedicated to polarization-dependent spectroscopic investigations of advanced materials and allows to analyze the magnetic materials composed of 3d metals. The beamline is equipped with two state-of the-art end-stations: a High-field vector magnet (HECTOR) for Soft X-ray absorption Spectroscopy and Dichroism techniques such as NEXAFS, XMCD or XMLD; and a UHV reflectometer (MARES) for scattering and reflection approaches including resonant soft X-ray reflectivity, resonant magnetic scattering and GISAXS. An X-ray absorption spectra can be acquired routinely in 2-3 min with high accuracy and repeatability (typically 100-200 eV wide with <0.05 eV step). BOREAS beamline instrumentation is shown in Figure A.7.

All data were analyzed with the use of CTM4XAS program. Data treatment was realized with the support of Gene Nolis (CIC energiGUNE).
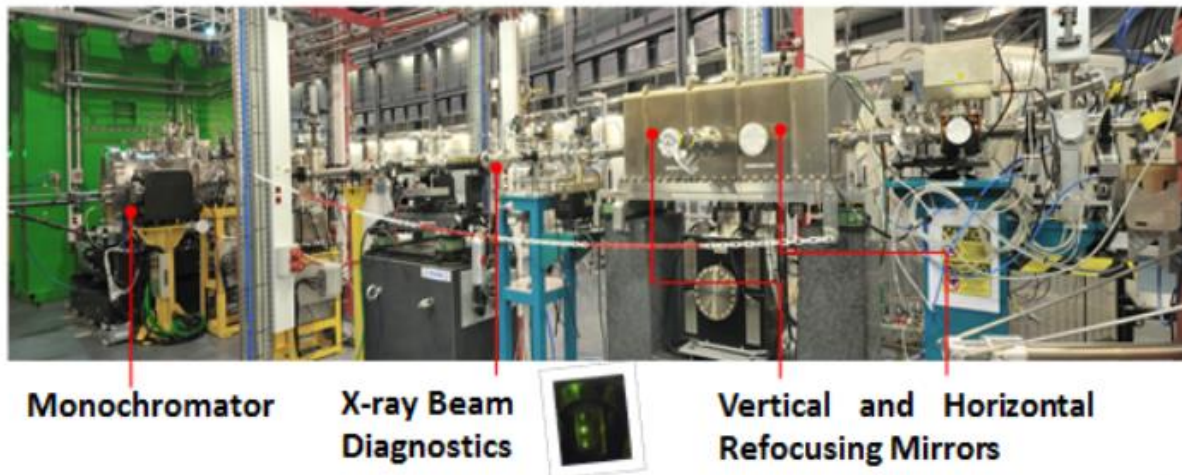
Figure A.7: Instrumentation at BL29-BOREAS beamline at ALBA.[351]

A.2.4. Nuclear Magnetic Resonance (NMR)

All the measurements were performed using a Bruker Advance III 300 MHz wide-bore magnet at CIC energiGUNE (Figure A.8a), with the support of Dr. Juan Miguel López del Amo (CIC energiGUNE). The spectrometer was charged to a field of 4.69 T (corresponding to 200MHz) and equipped with a standard 1.3 mm MAS probe (Figure A.8b). A rotor synchronized spin–echo pulse sequence (90˚-τ–180˚-τ acquisition) was used with typical 90° and 180° pulses of 1.2 and 2.4 us, respectively, and a recycle delay of 0.8 s. For each measurement the spinning frequencies were set to 50kHz. The spectra were referenced to 0.1 M solutions of NaCl and LiCl. EXSY (2D EXchange SpectroscopY) experiments were performed using standard three-pulse sequences with the mixing times indicated in each case. The obtained spectra were fitted using the Dmfit software.[352]
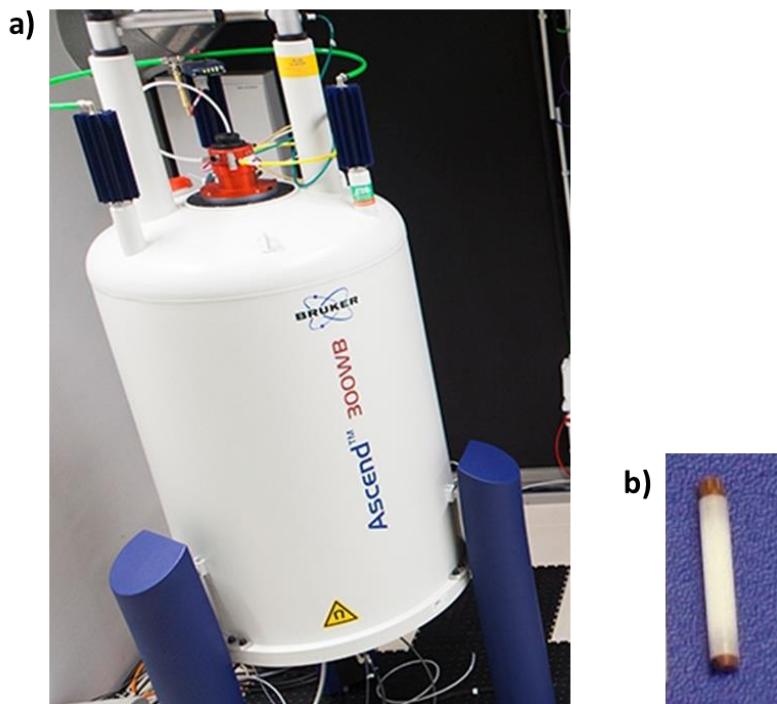
Figure A.8: (a) Bruker Advance III 300 MHz wide-bore magnet at CIC energiGUNE; (b) 1.3 mm rotor.

A.2.5. Gas Chromatography – Mass Spectroscopy analysis (GCMS)

Gas Chromatography – Mass Spectroscopy (GCMS) analysis was performed to analyze the gases released upon chemical and electrochemical oxidation of $Na_3V(PO_3)_3N$ (Chapter 2). All the measurements were performed at Laboratoire de Réactivité et Chimie des Solides (LRCS) with the support of Sylvie Grugeon, Matthieu Courty and Grégory Gachot. For the mass spectroscopy analysis, special home-made set-up was designed (visible in Figure A.9 and Figure A.10) to tightly connect the Thermo Scientific high resolution Mass Spectrometer with the vial or cell.

Figure A.9: Set-up for the mass spectrometry analysis of the gases released upon chemical oxidation of Na$_3$V(PO$_3$)$_3$N – the vial from the left photo was tightly connected to the Mass Spectrometer by the set of cables and valves, which were gradually opened upon the measurement.

For the analysis of the gases released upon chemical oxidation, first the reaction was performed in the glovebox, following the protocol described in Chapter 2, section 2.2.5). Next, the cap of the vial was pierced by the needle with the valve on top. The valve was closed and the vial was taken out from the glovebox. The Mass Spectrometer with the connected set-up was purged with Ar prior the collection of the gases. Next, the vial was connected to the set-up by the cable and the valves were opened to collect the gases from the vial.

Next set of experiments was performed on the electrochemically oxidized Na$_3$V(PO$_3$)$_3$N. Tests were performed in two types of cells: Swagelok, with the capillary fixed inside of the plunger through which gases can be collected (Figure A.10, left), and the EL-cell with the valve to manipulate the release of the formed gases (Figure A.10, right). Advantage of the EL-cell is the bigger surface area of the electrode which could correspond to the higher amount of the gases, however Swagelok provides much tighter closure and better contact between electrodes.
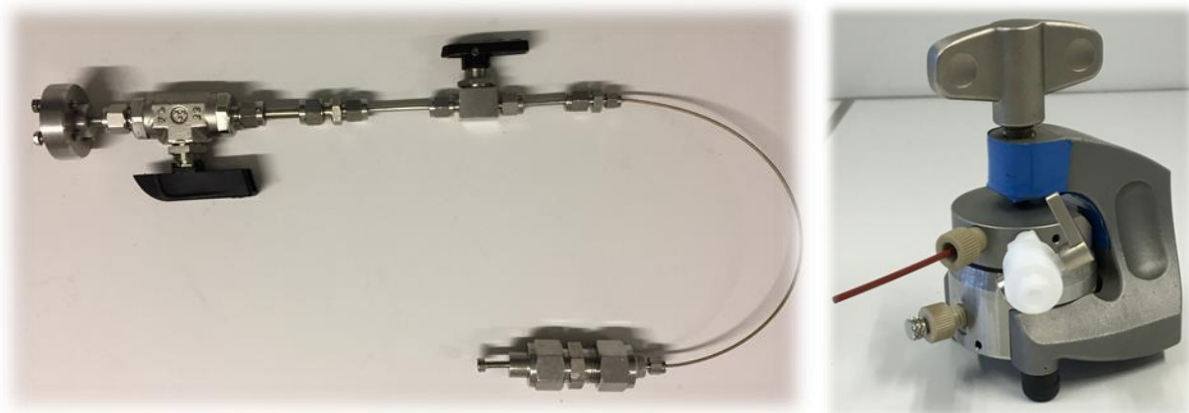
Figure A.10: Two different cell types for the gas analysis upon electrochemical oxidation: Swagelok and modified EL-cell.

A.2.6. Scanning electron microscopy (SEM) and Transition Electron Microscopy (TEM)

Scanning electron microscopy (SEM) was performed on FEI Quanta 200FEG. The measured powders were dispersed on the top of the conducing carbon tape. X-ray Dispersive Energy (EDX) spectrometer was used to detect the elements and perform a semi-quantitative composition analysis.

Transition Electron Microscopy (TEM) was performed using a FEI Tecnai F20 electron microscope operated at 200 keV and equipped with a High Angle Annular Dark Field (HAADF) detector and an X-ray Dispersive Energy (EDX) spectrometer, in collaboration with Dr. Francisco Bonilla (CIC energiGUNE). The samples for TEM were prepared on 3 mm cupper grids and mounted on a double tilt specimen holder with maximum tilt angle + 40°. Simulations of the ED patterns used for the indexation of the experimental SAED patterns were performed with the programs Single Crystal® and CaRIne Crystallography.[353]

A.2.7. Inductively coupled plasma optical emission spectrometry (ICP-OES)

Inductively coupled plasma optical emission spectrometry (ICP-OES) measurements were performed using a Horiba Ultima 2 Sequential ICP-OES equipment with support of Ismael García

and Nuria Gomez (CIC energiGUNE). Prior to the measurements samples were diluted in a 20% HNO_3 solution. The digestion was performed in the microwave by heating the samples at 180°C for 15 min. Next, the solution was dissolved with ICP grade H_2O.

A.3. Electrochemical characterization

Electrode materials were prepared by ball milling the active material with carbon (C_{65} or Ketjen Black) and PVDF (polyvinylidene fluoride) solubilized in NMP (N-Methylpyrrolidone) for 20 min in SPEX 8000M Grinding Ball Miller (a) under air. Typically, for the 500 mg mix of precursor, stainless steel jar with fifteen 1.5mm size stainless steel balls was used.

Figure A.11: (a) SPEX 8000M Grinding Ball miller; (b) SPEX ball mill mechanism with the back-and-forth shaking motion together with the lateral movements of the end of the jar. From SPEX SamplePrep[354]

The obtained viscous slurry was coated on a 100μm thick aluminum foil using dr. Blade. As-obtained laminate was then dried overnight under vacuum at 120°C. Next, 12mm or 11mm diameter electrodes were punched from the laminate and pressed at 2 T/cm2. The electrodes were then again dried at 120°C before introducing them into an Ar filled glove box for the cell assembly.

These as-prepared electrodes were used to assemble cells against lithium and sodium metal anodes using 1M $LiPF_6$ or $NaPF_6$ in EC:DMC as electrolyte. Two types of cells were used: coin cells

(Figure A.12a) for the galvanostatic and cyclic voltammetry tests and Swagelok cells (Figure A.12b) for the initial galvanostatic tests.
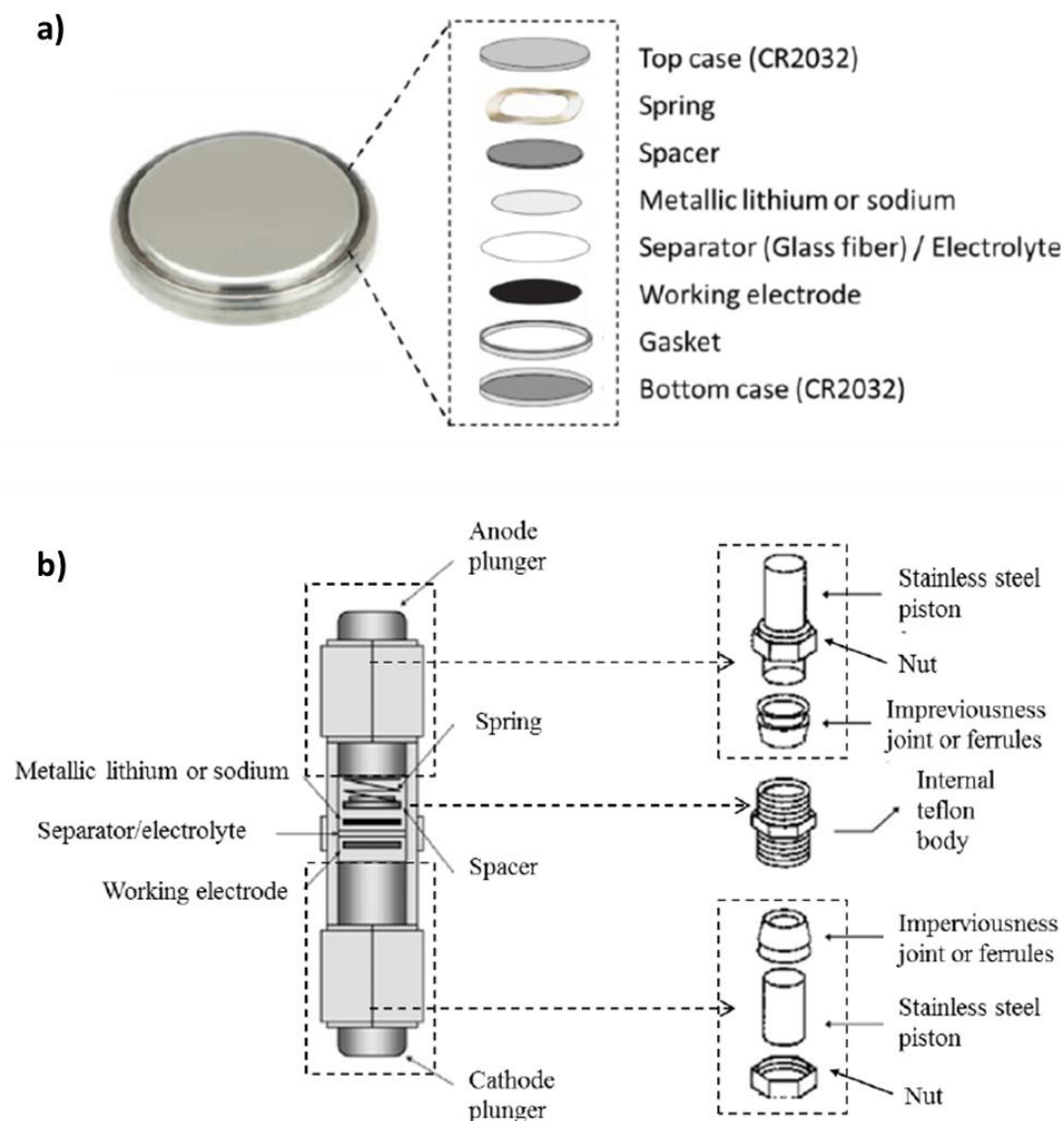
Figure A.12: (a) coin cell components; Swagelok cell components. [355]

The electrochemical characterization was performed using two different devices: a Maccor battery tester series 4000 for the coin cells (Figure A.12a) and a Biologic VMP3 Multi-Channel Potentiostat for the coin cells and Swagelok cells (Figure A.12b). Maccor battery tester was typically used for the long-term galvanostatic cycling, while VMP3 potentiostat for the cyclic voltammograms and initial galvanostatic tests.

List of Figures

333

List of Tables

BIBLIOGRAPHY

1. Wrigley, E. A. Energy and the English Industrial Revolution. *Phil. Trans. R. Soc. A.* **371**, 20110568 (2013).
2. Smil, V. *Energy transitions: global and national perspectives*. (Praeger, an imprint of ABC-CLIO, LLC, 2017).
3. Hannah Ritchie, M. R. CO_2 and Greenhouse Gas Emissions. (2020).
4. Lacis, A. A., Schmidt, G. A., Rind, D. & Ruedy, R. A. Atmospheric CO_2 : Principal Control Knob Governing Earth's Temperature. *Science* **330**, 356–359 (2010).
5. Jackson, R. B. *et al.* Persistent fossil fuel growth threatens the Paris Agreement and planetary health. *Environ. Res. Lett.* **14**, 121001 (2019).
6. Tomabechi, K. Energy Resources in the Future. *Energies* **3**, 686–695 (2010).
7. Daim, T. U., Li, X., Kim, J. & Simms, S. Evaluation of energy storage technologies for integration with renewable electricity: Quantifying expert opinions. *Environmental Innovation and Societal Transitions* **3**, 29–49 (2012).
8. Goodenough, J. B. Energy storage materials: A perspective. *Energy Storage Materials* **1**, 158–161 (2015).
9. Ibrahim, H., Ilinca, A. & Perron, J. Energy storage systems—Characteristics and comparisons. *Renewable and Sustainable Energy Reviews* **12**, 1221–1250 (2008).
10. Armand, M. & Tarascon, J.-M. Building better batteries. *Nature* **451**, 652–657 (2008).
11. Massé, R. C., Liu, C., Li, Y., Mai, L. & Cao, G. Energy storage through intercalation reactions: electrodes for rechargeable batteries. *National Science Review* **4**, 26–53 (2017).
12. Sudduth, W. M. The Voltaic Pile and Electro-Chemical Theory in 1800. *Ambix* **27**, 26–35 (1980).
13. Kurzweil, P. Gaston Planté and his invention of the lead–acid battery—The genesis of the first practical rechargeable battery. *Journal of Power Sources* **195**, 4424–4434 (2010).
14. https://www.upsbatterycenter.com/blog/history-batteries-timeline/.
15. Hirsh, H. S. *et al.* Sodium-Ion Batteries Paving the Way for Grid Energy Storage. *Adv. Energy Mater.* **10**, 2001274 (2020).
16. Wieboldt, D., Matthias Hahn, & Ines Ruff. Techniques for Raman Analysis of Lithium-Ion Batteries. *Spectroscopy Supplements* **30**, (2015).
17. Tarascon, J.-M. & Armand, M. Issues and challenges facing rechargeable lithium batteries. *Nature* **414**, 359–367 (2001).
18. Goodenough, J. B. Design considerations. *Solid State Ionics* **69**, 184–198 (1994).
19. Goodenough, J. B. & Kim, Y. Challenges for Rechargeable Li Batteries. *Chem. Mater.* **22**, 587–603 (2010).
20. https://www.batterypowertips.com/difference-between-lithium-ion-lithium-polymer-batteries-faq/.
21. Goodenough, J. B. & Park, K.-S. The Li-Ion Rechargeable Battery: A Perspective. *J. Am. Chem. Soc.* **135**, 1167–1176 (2013).

22. https://www.statista.com/statistics/268790/countries-with-the-largest-lithium-reserves-worldwide/.

23. https://www.spglobal.com/marketintelligence/en/news-insights/blog/top-electric-vehicle-markets-dominate-lithium-ion-battery-capacity-growth.

24. Ellis, B. L. & Nazar, L. F. Sodium and sodium-ion energy storage batteries. *Current Opinion in Solid State and Materials Science* **16**, 168–177 (2012).

25. Palomares, V. *et al.* Na-ion batteries, recent advances and present challenges to become low cost energy storage systems. *Energy Environ. Sci.* **5**, 5884–5901 (2012).

26. Whittingham, M. S. Electrical Energy Storage and Intercalation Chemistry. *Science* **192**, 1126–1127 (1976).

27. Tofield, B. C., Dell, R. M. & Jensen, J. Advanced batteries. *Nature* **276**, 217–220 (1978).

28. https://en.wikipedia.org/wiki/Abundance_of_elements_in_Earth%27s_crust.

29. Goikolea, E. *et al.* Na-Ion Batteries—Approaching Old and New Challenges. *Adv. Energy Mater.* **10**, 2002055 (2020).

30. Fang, C., Wang, X. & Meng, Y. S. Key Issues Hindering a Practical Lithium-Metal Anode. *Trends in Chemistry* **1**, 152–158 (2019).

31. Besenhard, J. O. The electrochemical preparation and properties of ionic alkali metal-and NR4-graphite intercalation compounds in organic electrolytes. *Carbon* **14**, 111–115 (1976).

32. Asenbauer, J. *et al.* The success story of graphite as a lithium-ion anode material – fundamentals, remaining challenges, and recent developments including silicon (oxide) composites. *Sustainable Energy Fuels* **4**, 5387–5416 (2020).

33. Fong, R., von Sacken, U. & Dahn, J. R. Studies of Lithium Intercalation into Carbons Using Nonaqueous Electrochemical Cells. *J. Electrochem. Soc.* **137**, 2009–2013 (1990).

34. Nishi, Y. The development of lithium ion secondary batteries. *Chem. Record* **1**, 406–413 (2001).

35. Peled, E., Menachem, C., Bar-Tow, D. & Melman, A. Improved Graphite Anode for Lithium-Ion Batteries Chemically: Bonded Solid Electrolyte Interface and Nanochannel Formation. *J. Electrochem. Soc.* **143**, L4–L7 (1996).

36. Xu, K. Nonaqueous Liquid Electrolytes for Lithium-Based Rechargeable Batteries. *Chem. Rev.* **104**, 4303–4418 (2004).

37. Yamada, Y., Iriyama, Y., Abe, T. & Ogumi, Z. Kinetics of Lithium Ion Transfer at the Interface between Graphite and Liquid Electrolytes: Effects of Solvent and Surface Film. *Langmuir* **25**, 12766–12770 (2009).

38. Jung, Y. S. *et al.* Ultrathin Direct Atomic Layer Deposition on Composite Electrodes for Highly Durable and Safe Li-Ion Batteries. *Adv. Mater.* **22**, 2172–2176 (2010).

39. Sawicki, M. & Shaw, L. L. Advances and challenges of sodium ion batteries as post lithium ion batteries. *RSC Adv.* **5**, 53129–53154 (2015).

40. Hou, H., Qiu, X., Wei, W., Zhang, Y. & Ji, X. Carbon Anode Materials for Advanced Sodium-Ion Batteries. *Adv. Energy Mater.* **7**, 1602898 (2017).

41. Stevens, D. A. & Dahn, J. R. High Capacity Anode Materials for Rechargeable Sodium-Ion Batteries. *J. Electrochem. Soc.* **147**, 1271 (2000).

42. Stevens, D. A. & Dahn, J. R. The Mechanisms of Lithium and Sodium Insertion in Carbon Materials. *J. Electrochem. Soc.* **148**, A803 (2001).

43. Chevrier, V. L. & Ceder, G. Challenges for Na-ion Negative Electrodes. *J. Electrochem. Soc.* **158**, A1011 (2011).

44. Kubota, K. *et al.* Structural Analysis of Sucrose-Derived Hard Carbon and Correlation with the Electrochemical Properties for Lithium, Sodium, and Potassium Insertion. *Chem. Mater.* **32**, 2961–2977 (2020).

45. Bauer, A. *et al.* The Scale-up and Commercialization of Nonaqueous Na-Ion Battery Technologies. *Adv. Energy Mater.* **8**, 1702869 (2018).

46. https://faradion.co.uk/.

47. Whittingham, M. S. Chemistry of intercalation compounds: Metal guests in chalcogenide hosts. *Progress in Solid State Chemistry* **12**, 41–99 (1978).

48. Fischer, J. E. & Kim, H. J. Elastic effects in intercalation compounds: Comparison of lithium in graphite and TiS 2. *Phys. Rev. B* **35**, 3295–3298 (1987).

49. Suslov, E. A., Bushkova, O. V., Sherstobitova, E. A., Reznitskikh, O. G. & Titov, A. N. Lithium intercalation into TiS2 cathode material: phase equilibria in a Li–TiS2 system. *Ionics* **22**, 503–514 (2016).

50. Godshall, N. A., Raistrick, I. D. & Huggins, R. A. Thermodynamic investigations of ternary lithium-transition metal-oxygen cathode materials. *Materials Research Bulletin* **15**, 561–570 (1980).

51. Godshall, N. Lithium transport in ternary lithium-copper-oxygen cathode materials. *Solid State Ionics* **18–19**, 788–793 (1986).

52. Mizushima, K., Jones, P. C., Wiseman, P. J. & Goodenough, J. B. LixCoO2 (0<x<-1): A new cathode material for batteries of high energy density. *Materials Research Bulletin* **15**, 783–789 (1980).

53. Yano, A., Shikano, M., Ueda, A., Sakaebe, H. & Ogumi, Z. LiCoO2 Degradation Behavior in the High-Voltage Phase Transition Region and Improved Reversibility with Surface Coating. *J. Electrochem. Soc.* **164**, A6116–A6122 (2017).

54. Akira Yoshino, Nakajima, T. & Kenichi Sanechika. Secondary battery.

55. Dahn, J. Structure and electrochemistry of Li1±yNiO2 and a new Li2NiO2 phase with the Ni (OH)2 structure. *Solid State Ionics* **44**, 87–97 (1990).

56. Moshtev, R., Zlatilova, P., Manev, V. & Tagawa, K. Synthesis of LiNiO2 in air atmosphere: X-ray diffraction characterization and electrochemical investigation. *Journal of Power Sources* **62**, 59–66 (1996).

57. Markevich, E. *et al.* High-Performance LiNiO 2 Cathodes with Practical Loading Cycled with Li metal Anodes in Fluoroethylene Carbonate-Based Electrolyte Solution. *ACS Appl. Energy Mater.* **1**, 2600–2607 (2018).

58. Bianchini, M., Roca-Ayats, M., Hartmann, P., Brezesinski, T. & Janek, J. There and Back Again—The Journey of LiNiO2 as a Cathode Active Material. *Angew. Chem. Int. Ed.* **58**, 10434–10458 (2019).

59. Capitaine, F. A new variety of LiMnO2 with a layered structure. *Solid State Ionics* **89**, 197–202 (1996).

60. Huang, Z.-F., Meng, X., Wang, C.-Z., Sun, Y. & Chen, G. First-principles calculations on the Jahn–Teller distortion in layered LiMnO2. *Journal of Power Sources* **158**, 1394–1400 (2006).

61. Marianetti, C. A., Morgan, D. & Ceder, G. First-principles investigation of the cooperative Jahn-Teller effect for octahedrally coordinated transition-metal ions. *Phys. Rev. B* **63**, 224304 (2001).

62. Ohzuku, T. & Makimura, Y. Layered Lithium Insertion Material of LiCo1/3Ni1/3Mn1/3O2 for Lithium-Ion Batteries. *Chem. Lett.* **30**, 642–643 (2001).

63. Rozier, P. & Tarascon, J. M. Review—Li-Rich Layered Oxide Cathodes for Next-Generation Li-Ion Batteries: Chances and Challenges. *J. Electrochem. Soc.* **162**, A2490–A2499 (2015).

64. Thackeray, M. M., Johnson, C. S., Vaughey, J. T., LiCurrent address: eVionyx Inc., Ha, N. & Hackney, S. A. Advances in manganese-oxide 'composite' electrodes for lithium-ion batteries. *J. Mater. Chem.* **15**, 2257 (2005).

65. Dugas, R., Zhang, B., Rozier, P. & Tarascon, J. M. Optimization of Na-Ion Battery Systems Based on Polyanionic or Layered Positive Electrodes and Carbon Anodes. *Journal of The Electrochemical Society* **163**, A867–A874 (2016).

66. Wang, P.-F., You, Y., Yin, Y.-X. & Guo, Y.-G. Layered Oxide Cathodes for Sodium-Ion Batteries: Phase Transition, Air Stability, and Performance. *Adv. Energy Mater.* **8**, 1701912 (2018).

67. Delmas, C., Braconnier, J., Fouassier, C. & Hagenmuller, P. Electrochemical intercalation of sodium in NaxCoO2 bronzes. *Solid State Ionics* **3–4**, 165–169 (1981).

68. Clément, R. J., Bruce, P. G. & Grey, C. P. Review—Manganese-Based P2-Type Transition Metal Oxides as Sodium-Ion Battery Cathode Materials. *Journal of The Electrochemical Society* **162**, A2589–A2604 (2015).

69. Ma, X., Chen, H. & Ceder, G. Electrochemical properties of monoclinic NaMnO2. *Journal of The Electrochemical Society* **158**, A1307–A1312 (2011).

70. Han, M. H., Gonzalo, E., Singh, G. & Rojo, T. A comprehensive review of sodium layered oxides: powerful cathodes for Na-ion batteries. *Energy Environ. Sci.* **8**, 81–102 (2014).

71. Sun, R. *et al.* Secondary-Phase Formation in Spinel-Type LiMn2O4-Cathode Materials for Lithium-Ion Batteries: Quantifying Trace Amounts of Li2MnO3 by Electron Paramagnetic Resonance Spectroscopy. *Appl Magn Reson* **49**, 415–427 (2018).

72. Tan, X. *et al.* Different roles of oxygen deficiency in performance of spinel lithium manganese oxides as the cathodes for aqueous and non-aqueous systems. *Ionics* **27**, 4249–4257 (2021).

73. Thackeray, M. M., David, W. I. F., Bruce, P. G. & Goodenough, J. B. Lithium insertion into manganese spinels. *Materials Research Bulletin* **18**, 461–472 (1983).

74. Liu, X., Li, K. & Li, X. The Electrochemical Performance and Applications of Several Popular Lithium-ion Batteries for Electric Vehicles - A Review. in *Advances in Green Energy Systems and Smart Grid* (eds. Li, K., Zhang, J., Chen, M., Yang, Z. & Niu, Q.) vol. 925 201–213 (Springer Singapore, 2018).

75. Shen, L., Wang, Z. & Chen, L. Prussian Blues as a Cathode Material for Lithium Ion Batteries. *Chem. Eur. J.* **20**, 12559–12562 (2014).

76. Qian, J. *et al.* Prussian Blue Cathode Materials for Sodium-Ion Batteries and Other Ion Batteries. *Adv. Energy Mater.* **8**, 1702619 (2018).

77. Huang, T. *et al.* A Prussian blue analogue as a long-life cathode for liquid-state and solid-state sodium-ion batteries. *Inorg. Chem. Front.* **7**, 3938–3944 (2020).

78. Wang, L. *et al.* A Superior Low-Cost Cathode for a Na-Ion Battery. *Angew. Chem. Int. Ed.* **52**, 1964–1967 (2013).

79. Wu, X. B. *et al.* Polyanion Compounds as Cathode Materials for Li-Ion Batteries. in *Rechargeable Batteries* (eds. Zhang, Z. & Zhang, S. S.) 93–134 (Springer International Publishing, 2015).

80. Gutierrez, A., Benedek, N. A. & Manthiram, A. Crystal-Chemical Guide for Understanding Redox Energy Variations of $M^{2+/3+}$ Couples in Polyanion Cathodes for Lithium-Ion Batteries. *Chem. Mater.* **25**, 4010–4016 (2013).

81. Sapra, S. K. *et al.* A comprehensive review on recent advances of polyanionic cathode materials in Na-ion batteries for cost effective energy storage applications. *WIREs Energy Environ.* **10**, (2021).

82. Padhi, A. K., Nanjundaswamy, K. S. & Goodenough, J. B. Phospho-olivines as Positive-Electrode Materials for Rechargeable Lithium Batteries. *J. Electrochem. Soc.* **144**, 1188–1194 (1997).

83. Laffont, L. *et al.* Study of the $LiFePO_4$/$FePO_4$ Two-Phase System by High-Resolution Electron Energy Loss Spectroscopy. *Chem. Mater.* **18**, 5520–5529 (2006).

84. Yamada, A., Chung, S. C. & Hinokuma, K. Optimized $LiFePO_4$ for Lithium Battery Cathodes. *J. Electrochem. Soc.* **148**, A224–A229 (2001).

85. Yuan, L.-X. *et al.* Development and challenges of $LiFePO_4$ cathode material for lithium-ion batteries. *Energy Environ. Sci.* **4**, 269–284 (2011).

86. Prosini, P. P., Carewska, M., Scaccia, S., Wisniewski, P. & Pasquali, M. Long-term cyclability of nanostructured $LiFePO_4$. *Electrochimica Acta* **48**, 4205–4211 (2003).

87. Doeff, M. M., Wilcox, J. D., Kostecki, R. & Lau, G. Optimization of carbon coatings on $LiFePO_4$. *Journal of Power Sources* **163**, 180–184 (2006).

88. Damen, L., Hassoun, J., Mastragostino, M. & Scrosati, B. Solid-state, rechargeable Li/$LiFePO_4$ polymer battery for electric vehicle application. *Journal of Power Sources* **195**, 6902–6904 (2010).

89. Zaghib, K. *et al.* Characterization of Na-based phosphate as electrode materials for electrochemical cells. *Journal of Power Sources* **196**, 9612–9617 (2011).

90. Moreau, P., Guyomard, D., Gaubicher, J. & Boucher, F. Structure and Stability of Sodium Intercalated Phases in Olivine FePO $_4$. *Chemistry of Materials* **22**, 4126–4128 (2010).

91. Goodenough, J. B., Hong, H. Y.-P. & Kafalas, J. A. Fast Na+-ion transport in skeleton structures. *Materials Research Bulletin* **11**, 203–220 (1976).

92. Hong, H. Y.-P. Crystal structures and crystal chemistry in the system Na1+xZr2SixP3−xO12. *Materials Research Bulletin* **11**, 173–182 (1976).

93. Fang, Y. *et al.* Phosphate Framework Electrode Materials for Sodium Ion Batteries. *Advanced Science* **4**, 1600392 (2017).

94. Lim, S. Y., Kim, H., Shakoor, R. A., Jung, Y. & Choi, J. W. Electrochemical and Thermal Properties of NASICON Structured Na3V2(PO4)3 as a Sodium Rechargeable Battery Cathode: A Combined Experimental and Theoretical Study. *Journal of the Electrochemical Society* **159**, A1393–A1397 (2012).

95. Song, W. *et al.* First exploration of Na-ion migration pathways in the NASICON structure Na3V2(PO4)3. *Journal of Materials Chemistry A* **2**, 5358 (2014).

96. Song, W. *et al.* First exploration of Na-ion migration pathways in the NASICON structure Na3V2(PO4)3. *Journal of Materials Chemistry A* **2**, 5358 (2014).

97. Zhu, Q. *et al.* Na3V2(PO4)3/C nanofiber bifunction as anode and cathode materials for sodium-ion batteries. *J Solid State Electrochem* **21**, 2985–2995 (2017).

98. Lim, S. Y., Kim, H., Shakoor, R. A., Jung, Y. & Choi, J. W. Electrochemical and Thermal Properties of NASICON Structured Na3V2(PO4)3 as a Sodium Rechargeable Battery Cathode: A Combined Experimental and Theoretical Study. *Journal of the Electrochemical Society* **159**, A1393–A1397 (2012).

99. Liu, J. *et al.* Electrospun Na3V2(PO4)3/C nanofibers as stable cathode materials for sodium-ion batteries. *Nanoscale* **6**, 5081 (2014).

100. Julien, C. M., Mauger, A. & Groult, H. Fluorosulfates and Fluorophosphates As New Cathode Materials for Lithium Ion Battery. in *Advanced Fluoride-Based Materials for Energy Conversion* 77–101 (Elsevier, 2015). doi:10.1016/B978-0-12-800679-5.00004-X.

101. Masquelier, C. & Croguennec, L. Polyanionic (Phosphates, Silicates, Sulfates) Frameworks as Electrode Materials for Rechargeable Li (or Na) Batteries. *Chemical Reviews* **113**, 6552–6591 (2013).

102. Tsuyoshi Nakajima, H. G. *Advanced Fluoride-Based Materials for Energy Conversion*. (Elsevier, 2015).

103. Sharma, L., Adiga, S. P., Alshareef, H. N. & Barpanda, P. Fluorophosphates: Next Generation Cathode Materials for Rechargeable Batteries. *Adv. Energy Mater.* **10**, 2001449 (2020).

104. Amatucci, G. G. & Pereira, N. Fluoride based electrode materials for advanced energy storage devices. *Journal of Fluorine Chemistry* 20 (2007).

105. Tripathi, R., Ramesh, T. N., Ellis, B. L. & Nazar, L. F. Scalable Synthesis of Tavorite LiFeSO4F and NaFeSO4F Cathode Materials. *Angewandte Chemie International Edition* **49**, 8738–8742 (2010).

106. Ati, M. *et al.* Synthesis and electrochemical properties of pure LiFeSO4F in the triplite structure. *Electrochemistry Communications* **13**, 1280–1283 (2011).

107. Dong, J. *et al.* Triplite LiFeSO4F as cathode material for Li-ion batteries. *Journal of Power Sources* **244**, 716–720 (2013).

108. Sobkowiak, A. LiFeSO4F as a Cathode Material for Lithium-Ion Batteries: Synthesis, Structure, and Function. (Acta Universitatis Upsaliensis, 2015).

109. Barker, J., Saidi, M. Y. & Swoyer, J. L. A Sodium-Ion Cell Based on the Fluorophosphate Compound NaVPO$_4$F. *Electrochemical and Solid-State Letters* **6**, A1 (2003).

110. Barker, J., Saidi, M. Y. & Swoyer, J. L. Electrochemical Insertion Properties of the Novel Lithium Vanadium Fluorophosphate, LiVPO$_4$F. *J. Electrochem. Soc.* **150**, A1394–A1398 (2003).

111. Barker, J. *et al.* Structural and electrochemical properties of lithium vanadium fluorophosphate, LiVPO4F. *Journal of Power Sources* **146**, 516–520 (2005).

112. Park, Y.-U. *et al.* Tailoring a fluorophosphate as a novel 4 V cathode for lithium-ion batteries. *Sci Rep* **2**, 704 (2012).

113. Zhang, Y. *et al.* Nearly monodispersed LiFePO4F nanospheres as cathode material for lithium ion batteries. *J Solid State Electrochem* **22**, 1995–2002 (2018).

114. Fedotov, S. S. *et al.* Tuning the Crystal Structure of A $_2$ CoPO $_4$ F (A = Li, Na) Fluoride-Phosphates: A New Layered Polymorph of LiNaCoPO $_4$ F: Tuning the Crystal Structure of A $_2$ CoPO $_4$ F (A = Li, Na) Fluoride-Phosphates: A New Layered Polymorph of LiNaCoPO $_4$ F. *Eur. J. Inorg. Chem.* **2019**, 4365–4372 (2019).

115. Khasanova, N. R., Drozhzhin, O. A., Storozhilova, D. A., Delmas, C. & Antipov, E. V. New Form of Li $_2$ FePO $_4$ F as Cathode Material for Li-Ion Batteries. *Chem. Mater.* **24**, 4271–4273 (2012).

116. Jin, D., Qiu, H., Du, F., Wei, Y. & Meng, X. Co-doped Na2FePO4F fluorophosphates as a promising cathode material for rechargeable sodium-ion batteries. *Solid State Sciences* **93**, 62–69 (2019).

117. Sukkabot, W. Structural and electronic properties of non-metal doping in Li $_2$ FePO $_4$ F compound: spin density functional theory. *Philosophical Magazine* **100**, 3155–3164 (2020).

118. Tripathi, R., Wood, S. M., Islam, M. S. & Nazar, L. F. Na-ion mobility in layered Na2FePO4F and olivine Na[Fe,Mn]PO4. *Energy Environ. Sci.* **6**, 2257 (2013).

119. Recham, N. *et al.* Ionothermal Synthesis of Sodium-Based Fluorophosphate Cathode Materials. *J. Electrochem. Soc.* **156**, A993 (2009).

120. Ellis, B. L., Makahnouk, W. R. M., Makimura, Y., Toghill, K. & Nazar, L. F. A multifunctional 3.5 V iron-based phosphate cathode for rechargeable batteries. *Nature Mater* **6**, 749–753 (2007).

121. Gover, R., Bryan, A., Burns, P. & Barker, J. The electrochemical insertion properties of sodium vanadium fluorophosphate, Na3V2(PO4)2F3. *Solid State Ionics* **177**, 1495–1500 (2006).

122. Deng, Z., Mo, Y. & Ong, S. P. Computational studies of solid-state alkali conduction in rechargeable alkali-ion batteries. *NPG Asia Mater* **8**, e254–e254 (2016).

123. Ceder, G., Hautier, G., Jain, A. & Ong, S. P. Recharging lithium battery research with first-principles methods. *MRS Bull.* **36**, 185–191 (2011).

124. Meng, Y. S. & Arroyo-de Dompablo, M. E. First principles computational materials design for energy storage materials in lithium ion batteries. *Energy Environ. Sci.* **2**, 589 (2009).

125. Inorganic Crystal Structure Database – ICSD. Available at https://www.fiz-karlsruhe.de/en/produkte-und-dienstleistungen/inorganic-crystal-structure-database-icsd.

126. Crystallography Open Database. Available at http://www.crystallography.net/cod/.

127. Brown, I. D. Recent Developments in the Methods and Applications of the Bond Valence Model. *Chem. Rev.* **109**, 6858–6919 (2009).

128. Katcho, N. A. *et al.* An investigation of the structural properties of Li and Na fast ion conductors using high-throughput bond-valence calculations and machine learning. *J Appl Crystallogr* **52**, 148–157 (2019).

129. Brown, I. D. & Altermatt, D. Bond-valence parameters obtained from a systematic analysis of the Inorganic Crystal Structure Database. *Acta Crystallogr. B* **41**, 244–247 (1985).

130. Adams, S. From bond valence maps to energy landscapes for mobile ions in ion-conducting solids. *Solid State Ionics* **177**, 1625–1630 (2006).

131. Adams, S. & Rao, R. P. High power lithium ion battery materials by computational design: High power Li ion battery materials by computational design. *Phys. Status Solidi A* **208**, 1746–1753 (2011).

132. Adams, S. & Rao, R. P. Modelling of Ion Transport in Solids with a General Bond Valence Based Force-Field. *Atom Indo.* **36**, 95 (2011).

133. Adams, S. & Rao, R. P. Understanding Ionic Conduction and Energy Storage Materials with Bond-Valence-Based Methods. in *Bond Valences* (eds. Brown, I. D. & Poeppelmeier, K. R.) vol. 158 129–159 (Springer Berlin Heidelberg, 2014).

134. Sale, M. & Avdeev, M. *3DBVSMAPPER*: a program for automatically generating bond-valence sum landscapes. *Journal of Applied Crystallography* **45**, 1054–1056 (2012).

135. Rodríguez-Carvajal, J. FullProf Suite.

136. Momma, K. & Izumi, F. *VESTA*: a three-dimensional visualization system for electronic and structural analysis. *Journal of Applied Crystallography* **41**, 653–658 (2008).

137. Ouyang, C. & Chen, L. Physics towards next generation Li secondary batteries materials: A short review from computational materials design perspective. *Sci. China Phys. Mech. Astron.* **56**, 2278–2292 (2013).

138. Bölle, F. T., Bhowmik, A., Vegge, T., Maria García Lastra, J. & Castelli, I. E. Automatic Migration Path Exploration for Multivalent Battery Cathodes using Geometrical Descriptors. *Batteries & Supercaps* **4**, 1516–1524 (2021).

139. Morgan, D., Van der Ven, A. & Ceder, G. Li Conductivity in Li[sub x]MPO[sub 4] (M = Mn, Fe, Co, Ni) Olivine Materials. *Electrochem. Solid-State Lett.* **7**, A30 (2004).

140.   Yang, J. & Tse, J. S. Li Ion Diffusion Mechanisms in LiFePO $_4$: An ab Initio Molecular Dynamics Study. *J. Phys. Chem. A* **115**, 13045–13049 (2011).

141.   Xu, Y.-N., Chung, S.-Y., Bloking, J. T., Chiang, Y.-M. & Ching, W. Y. Electronic Structure and Electrical Conductivity of Undoped LiFePO[sub 4]. *Electrochem. Solid-State Lett.* **7**, A131 (2004).

142.   Delacourt, C. *et al.* Toward Understanding of Electrical Limitations (Electronic, Ionic) in LiMPO[sub 4] (M=Fe, Mn) Electrode Materials. *J. Electrochem. Soc.* **152**, A913 (2005).

143.   Moriwake, H. *et al.* First-Principles Calculations of Lithium-Ion Migration at a Coherent Grain Boundary in a Cathode Material, LiCoO $_2$. *Adv. Mater.* **25**, 618–622 (2013).

144.   Xu, B. & Meng, S. Factors affecting Li mobility in spinel LiMn2O4—A first-principles study by GGA and GGA+U methods. *Journal of Power Sources* **195**, 4971–4976 (2010).

145.   Kim, M. & Kim, S.-J. Synchrotron powder study of Na₃V(PO₃)₃N. *Acta Crystallographica Section E Structure Reports Online* **69**, i34–i34 (2013).

146.   Liu, J. *et al.* Ionic Conduction in Cubic Na3TiP3O9N, a Secondary Na-Ion Battery Cathode with Extremely Low Volume Change. *Chem. Mater.* **26**, 3295–3305 (2014).

147.   Armand, M., Tarascon, J.-M. & Arroyo-de Dompablo, M. E. Comparative computational investigation of N and F substituted polyoxoanionic compounds: The case of Li2FeSiO4 electrode material. *Electrochemistry Communications* **13**, 1047–1050 (2011).

148.   Armand, M. & Arroyo y de Dompablo, M. E. Benefits of N for O substitution in polyoxoanionic electrode materials: a first principles investigation of the electrochemical properties of Li2FeSiO4−yNy (y = 0, 0.5, 1). *Journal of Materials Chemistry* **21**, 10026 (2011).

149.   Kageyama, H. *et al.* Expanding frontiers in materials chemistry and physics with multiple anions. *Nat Commun* **9**, 772 (2018).

150.   Rousseau, B., Timoshevskii, V., Mousseau, N., Côté, M. & Zaghib, K. Na3Fe2(SO4)2(SO3N) as a potential high capacity cathode material. *Materials Science and Engineering: B* **211**, 185–190 (2016).

151.   Marchand, R., Laurent, Y., Guyader, J., L'Haridon, P. & Verdier, P. Nitrides and oxynitrides: Preparation, crystal chemistry and properties. *Journal of the European Ceramic Society* **8**, 197–213 (1991).

152.   Marchand, R. Caractes specifiques de I'azote dans les nitrures et oxynitrures. *C.R.Acad.Sc.Paris* 669–673 (1999).

153.   Marchand, R., Conanec, R., Gueguen, E. & Laurent, Y. A New Class of Phosphate Compounds: Introduction of Nitrogen in the Tetrahedral Phosphorus Environment. *Phosphorus, Sulfur, and Silicon and the Related Elements* **76**, 277–280 (1993).

154.   Feldmann, W. Über Natriumnitridophosphate [NanPnO3n-3N2]x (n = 4; 6). *Z. Chem.* **23**, 139–140 (1983).

155.   Feldmann, W. Über Natrium-aluminium-nitridophosphat Na₃AlP₃O₉N und Natrium-magnesium-nitridophosphat Na₂Mg₂P₃O₉N. *Z. Chem.* **27**, 100–101 (1987).

156. Feldmann, W. Über Nitridophosphate $M^I_3M^{III}P_3O_9N$ (M^I = Na; K, M^{III} = Al; Ga; Cr; Fe; Mn). *Z. Chem.* **27**, 182–183 (1987).

157. Feldmann, W. Crystalline Nitridophosphates Obtained by Thermal Reactions. *Phosphorus, Sulfur, and Silicon and the Related Elements* **51**, 141–144 (1990).

158. Conanec, R., L'haridon, P., Feldmann, W., Marchand, R. & Laurent, Y. Crystal structure determination of the nitridophosphate $Na_3AlP_3O_9N$. *European journal of solid state and inorganic chemistry* **31**, 13–24 (1994).

159. Lee, M. S., Kang, J. K. & Kim, S. J. Crystal Structure and Ionic Conductivity of $Na_2Mg_2(PO_3)_3N$. *Bull. Korean Chem. Soc.* **33**, 2083 (2012).

160. Liu, J. *et al.* Divalent Iron Nitridophosphates: A New Class of Cathode Materials for Li-Ion Batteries. *Chem. Mater.* **25**, 3929–3931 (2013).

161. Khalifah, P. G. & Jue Liu. Cubic ionic conductor ceramics for alkali ion batteries. (2013).

162. Conanec, R., Feldmann, W., Marchand, R. & Laurent, Y. Les Phosphates Azotés Cristallisés de Type $Na_3AlP_3O_9N$ et $Na_2Mg_2P_3O_9N$. *Journal of Solid State Chemistry* **121**, 418–422 (1996).

163. Agnieszka Wizner. Nitridophosphates as positive electrode materials for Na-ion batteries. (2016).

164. Zhang, H., Buchholz, D. & Passerini, S. Synthesis, Structure, and Sodium Mobility of Sodium Vanadium Nitridophosphate: A Zero-Strain and Safe High Voltage Cathode Material for Sodium-Ion Batteries. *Energies* **10**, 889 (2017).

165. Sears, V. F. Neutron scattering lengths and cross sections. *Neutron News* **3**, 26–37 (1992).

166. Stavitski, E. & de Groot, F. M. F. The CTM4XAS program for EELS and XAS spectral shape analysis of transition metal L edges. *Micron* **41**, 687–694 (2010).

167. Groot, F. de & Kotani, A. *Core level spectroscopy of solids*. (CRC Press, 2008).

168. Abbate, M. *et al.* Soft X-ray absorption spectroscopy of vanadium oxides. *Journal of Electron Spectroscopy and Related Phenomena* **62**, 185–195 (1993).

169. Chen, M. *et al.* Development and Investigation of a NASICON-Type High-Voltage Cathode Material for High-Power Sodium-Ion Batteries. *Angew. Chem. Int. Ed.* **59**, 2449–2456 (2020).

170. Tessier, F., Le Gendre, L., Cheviré, F., Marchand, R. & Navrotsky, A. Thermochemistry of a New Class of Materials Containing Dinitrogen Pairs in an Oxide Matrix. *Chemistry of Materials* **17**, 3570–3574 (2005).

171. Jian, Z. *et al.* Atomic Structure and Kinetics of NASICON $Na_xV_2(PO_4)_3$ Cathode for Sodium-Ion Batteries. *Advanced Functional Materials* **24**, 4265–4272 (2014).

172. Cahill, L. S., Chapman, R. P., Britten, J. F. & Goward, G. R. 7Li NMR and Two-Dimensional Exchange Study of Lithium Dynamics in Monoclinic. 7.

173. Davis, L. J. M., Heinmaa, I. & Goward, G. R. Study of Lithium Dynamics in Monoclinic $Li_3Fe_2(PO_4)_3$ using ^{6}Li VT and 2D Exchange MAS NMR Spectroscopy †. *Chem. Mater.* **22**, 769–775 (2010).

174. Davis, L. J. M. *et al.* [6]Li 1D EXSY NMR Spectroscopy: A New Tool for Studying Lithium Dynamics in Paramagnetic Materials Applied to Monoclinic Li $_2$ VPO $_4$ F. *J. Phys. Chem. C* **115**, 22603–22608 (2011).

175. Smiley, D. L. & Goward, G. R. Ex Situ 23Na Solid-State NMR Reveals the Local Na-Ion Distribution in Carbon-Coated Na2FePO4F during Electrochemical Cycling. *Chem. Mater.* **28**, 7645–7656 (2016).

176. Dudarev, S. L., Botton, G. A., Savrasov, S. Y., Humphreys, C. J. & Sutton, A. P. Electron-energy-loss spectra and the structural stability of nickel oxide: An LSDA+ U study. *Physical Review B* **57**, 1505 (1998).

177. Fradkin, E. *Field theories of condensed matter systems*. (Addison-Wesley, 1991).

178. Aryasetiawan, F., Karlsson, K., Jepsen, O. & Schönberger, U. Calculations of Hubbard U from first-principles. *Physical Review B* **74**, (2006).

179. Debbichi, M. & Lebègue, S. Crystal and electronic structures of nitridophosphate compounds as cathode materials for Na-ion batteries. *Physical Review B* **92**, (2015).

180. Armand, M., Endres, F., MacFarlane, D. R., Ohno, H. & Scrosati, B. Ionic-liquid materials for the electrochemical challenges of the future. *Nature Mater* **8**, 621–629 (2009).

181. MacFarlane, D. R. *et al.* Energy applications of ionic liquids. *Energy Environ. Sci.* **7**, 232–250 (2014).

182. Neale, A. R., Murphy, S., Goodrich, P., Hardacre, C. & Jacquemin, J. Thermophysical and Electrochemical Properties of Ethereal Functionalised Cyclic Alkylammonium-based Ionic Liquids as Potential Electrolytes for Electrochemical Applications. *ChemPhysChem* **18**, 2040–2057 (2017).

183. Brutti, S. *et al.* Ionic liquid electrolytes for high-voltage, lithium-ion batteries. *Journal of Power Sources* **479**, 228791 (2020).

184. Bach, R. D., Holubka, J. W. & Taaffee, T. A. Reaction of alkyl halides and alkyl methyl ethers with nitronium tetrafluoroborate in acetonitrile. *J. Org. Chem.* **44**, 1739–1740 (1979).

185. Reynaud, M. *et al.* Sodium vanadium nitridophosphate Na 3 V(PO 3) 3 N as a high-voltage positive electrode material for Na-ion and Li-ion batteries. *Electrochemistry Communications* **84**, 14–18 (2017).

186. Liu, J. *et al. In Situ* Neutron Diffraction Studies of the Ion Exchange Synthesis Mechanism of Li$_2$Mg$_2$P$_3$O$_9$N: Evidence for a Hidden Phase Transition. *Journal of the American Chemical Society* **139**, 9192–9202 (2017).

187. Shannon, R. D. & Prewitt, C. T. Effective ionic radii in oxides and fluorides. *Acta Crystallogr B Struct Sci* **25**, 925–946 (1969).

188. Mueller, D. N., Machala, M. L., Bluhm, H. & Chueh, W. C. Redox activity of surface oxygen anions in oxygen-deficient perovskite oxides during electrochemical reactions. *Nat Commun* **6**, 6097 (2015).

189. Grimaud, A., Hong, W. T., Shao-Horn, Y. & Tarascon, J.-M. Anionic redox processes for electrochemical devices. *Nature Mater* **15**, 121–126 (2016).

190. Rozier, P. *et al.* Anionic redox chemistry in Na-rich Na 2 Ru 1−y Sn y O 3 positive electrode material for Na-ion batteries. *Electrochemistry Communications* **53**, 29–32 (2015).

191. Park, J. *et al.* Anionic Redox Reactions in Cathodes for Sodium-Ion Batteries. *ChemElectroChem* **8**, 625–643 (2021).

192. Xu, H., Guo, S. & Zhou, H. Review on anionic redox in sodium-ion batteries. *J. Mater. Chem. A* **7**, 23662–23678 (2019).

193. Armand, M. & Dompablo, M. E. A. y de. Benefits of N for O substitution in polyoxoanionic electrode materials: a first principles investigation of the electrochemical properties of Li2FeSiO4−yNy (y = 0, 0.5, 1). *J. Mater. Chem.* **21**, 10026–10034 (2011).

194. Junaid Bushiri, M., Antony, C. J. & Aatiq, A. Raman and FTIR studies of the structural aspects of Nasicon-type crystals; AFeTi(PO4)3 [A=Ca, Cd]. *Journal of Physics and Chemistry of Solids* **69**, 1985–1989 (2008).

195. Boukbir, L. *et al.* A structural investigation of phosphorus oxynitride glasses. *Journal of Solid State Chemistry* **87**, 423–429 (1990).

196. Bunker, B. C. *et al.* Structure of Phosphorus Oxynitride Glasses. *Journal of the American Ceramic Society* **70**, 675–681 (1987).

197. Reidmeyer, M. R. & Day, D. E. Phosphorus oxynitride glasses. *Journal of Non-Crystalline Solids* **181**, 201–214 (1995).

198. Paraschiv, G. L. *et al.* Mixed alkali silicophosphate oxynitride glasses: Structure-property relations. *Journal of Non-Crystalline Solids* **462**, 51–64 (2017).

199. Mascaraque, N., Fierro, J. L. G., Durán, A. & Muñoz, F. An interpretation for the increase of ionic conductivity by nitrogen incorporation in LiPON oxynitride glasses. *Solid State Ionics* **233**, 73–79 (2013).

200. Shannon, R. D. Revised effective ionic radii and systematic studies of interatomic distances in halides and chalcogenides. *Acta Crystallogr. A* **32**, 751–767 (1976).

201. Deng, C., Zhang, S. & Zhao, B. First exploration of ultrafine Na7V3(P2O7)4 as a high-potential cathode material for sodium-ion battery. *Energy Storage Materials* **4**, 71–78 (2016).

202. Masquelier, C. & Croguennec, L. Polyanionic (Phosphates, Silicates, Sulfates) Frameworks as Electrode Materials for Rechargeable Li (or Na) Batteries. *Chem. Rev.* **113**, 6552–6591 (2013).

203. Aparicio, P. A. & de Leeuw, N. H. Electronic structure, ion diffusion and cation doping in the Na 4 VO(PO 4) 2 compound as a cathode material for Na-ion batteries. *Phys. Chem. Chem. Phys.* **22**, 6653–6659 (2020).

204. Kim, J. *et al.* Tailoring a New 4V-Class Cathode Material for Na-Ion Batteries. *Adv. Energy Mater.* **6**, 1502147 (2016).

205. Oh, S.-M., Myung, S.-T., Hassoun, J., Scrosati, B. & Sun, Y.-K. Reversible NaFePO4 electrode for sodium secondary batteries. *Electrochemistry Communications* **22**, 149–152 (2012).

206. Ling, R. *et al.* Double-shelled hollow Na2FePO4F/C spheres cathode for high-performance sodium-ion batteries. *J Mater Sci* **53**, 2735–2747 (2018).

207. Ong, S. P. *et al.* Voltage, stability and diffusion barrier differences between sodium-ion and lithium-ion intercalation materials. *Energy & Environmental Science* **4**, 3680 (2011).

208. Pagot, G. *et al.* High-Performance Olivine for Lithium Batteries: Effects of Ni/Co Doping on the Properties of LiFeαNiβCoγPO4 Cathodes. *Adv. Funct. Mater.* **25**, 4032–4037 (2015).

209. Shakoor, R. A., Park, C. S., Raja, A. A., Shin, J. & Kahraman, R. A mixed iron–manganese based pyrophosphate cathode, $Na_2 Fe_{0.5} Mn_{0.5} P_2 O_7$, for rechargeable sodium ion batteries. *Phys. Chem. Chem. Phys.* **18**, 3929–3935 (2016).

210. Kresse, G. & Furthmüller, J. Efficiency of ab-initio total energy calculations for metals and semiconductors using a plane-wave basis set. *Computational Materials Science* **6**, 15–50 (1996).

211. Kresse, G. & Hafner, J. Ab initio molecular dynamics for liquid metals. *Phys. Rev. B* **47**, 558–561 (1993).

212. Perdew, J. P., Burke, K. & Ernzerhof, M. Generalized Gradient Approximation Made Simple. *Phys. Rev. Lett.* **77**, 3865–3868 (1996).

213. Jain, A. *et al.* Commentary: The Materials Project: A materials genome approach to accelerating materials innovation. *APL Materials* **1**, 011002 (2013).

214. Van der Ven, A., Deng, Z., Banerjee, S. & Ong, S. P. Rechargeable Alkali-Ion Battery Materials: Theory and Computation. *Chem. Rev.* **120**, 6977–7019 (2020).

215. Aydinol, M. K., Kohan, A. F., Ceder, G., Cho, K. & Joannopoulos, J. Ab initio study of lithium intercalation in metal oxides and metal dichalcogenides. *Phys. Rev. B* **56**, 1354–1365 (1997).

216. de Groot, F. M. F., Fuggle, J. C., Thole, B. T. & Sawatzky, G. A. L 2 , *3* x-ray-absorption edges of d 0 compounds: K + , Ca 2 + , Sc 3 + , and Ti 4 + in O h (octahedral) symmetry. *Phys. Rev. B* **41**, 928–937 (1990).

217. DIFFRAC.EVA; https://www.bruker.com/content/bruker/int/en/products-and-solutions/diffractometers-and-scattering-systems/x-ray-diffractometers/diffrac-suite-software/diffrac-eva.html.

218. The HighScore suite, T. Degen, M. Sadki, E. Bron, U. König, G. Nénert; Powder Diffraction / Volume 29 / Supplement S2 / December 2014, pp S13-S18.

219. Boultif, A. & Louër, D. Indexing of powder diffraction patterns for low-symmetry lattices by the successive dichotomy method. *J. Appl. Crystallogr.* **24**, 987–993 (1991).

220. Aydinol, M. K., Kohan, A. F., Ceder, G., Cho, K. & Joannopoulos, J. *Ab initio* study of lithium intercalation in metal oxides and metal dichalcogenides. *Phys. Rev. B* **56**, 1354–1365 (1997).

221. Rodríguez-Carvajal, J. Recent advances in magnetic structure determination by neutron powder diffraction. *Physica B: Condensed Matter* **192**, 55–69 (1993).

222. J. Rodríguez-Carvajal. FullProf Suite. Available at http://www.ill.eu/sites/fullprof/index.html.

223. Altomare, A. *et al.* EXPO : a program for full powder pattern decomposition and crystal structure solution. *Journal of Applied Crystallography* **32**, 339–340 (1999).

224. Altomare, A. *et al. EXPO2009*: structure solution by powder data in direct and reciprocal space. *Journal of Applied Crystallography* **42**, 1197–1202 (2009).

225. Altomare, A. *et al. EXPO2013*: a kit of tools for phasing crystal structures from powder data. *J Appl Crystallogr* **46**, 1231–1235 (2013).

226. Sun, J., Ruzsinszky, A. & Perdew, J. P. Strongly Constrained and Appropriately Normed Semilocal Density Functional. *Phys. Rev. Lett.* **115**, 036402 (2015).

227. Sun, J. *et al.* Accurate first-principles structures and energies of diversely bonded systems from an efficient density functional. *Nature Chemistry* **8**, 831–836 (2016).

228. Kitchaev, D. A. *et al.* Energetics of ${\mathrm{MnO}}_{2}$ polymorphs in density functional theory. *Phys. Rev. B* **93**, 045132 (2016).

229. Kitchaev, D. A., Dacek, S. T., Sun, W. & Ceder, G. Thermodynamics of Phase Selection in MnO2 Framework Structures through Alkali Intercalation and Hydration. *J. Am. Chem. Soc.* **139**, 2672–2681 (2017).

230. Kim, J. *et al.* New 4V-class and zero-strain cathode material for Na ion batteries. *Chemistry of Materials* (2017) doi:10.1021/acs.chemmater.7b02477.

231. Kuznetsov, V. G. & Imanakunov, B. X-ray diffraction investigation of solid phases in ternary aqueous systems consisting of nickel, sodium, and aluminum sulfates at 25?65�C. *J Struct Chem* **3**, 44–55 (1962).

232. Treushnikov, E. N., Ilyukhin, V. V. & Belov, N. V. Crystal structure of sodium-calcium triorthosilicate Na 2 Ca 3 [Si 3 O 10]. *Kristallografiya* **16**, 76–79 (1971).

233. Tessier, F., Le Gendre, L., Cheviré, F., Marchand, R. & Navrotsky, A. Thermochemistry of a New Class of Materials Containing Dinitrogen Pairs in an Oxide Matrix. *Chem. Mater.* **17**, 3570–3574 (2005).

234. *Advances in Inorganic Phosphate Materials: Ceramic Transactions*. vol. 233 (Wiley, 2012).

235. El Khalfaouy, R., Elabed, A., Addaou, A., Laajeb, A. & Lahsini, A. Synthesis and Characterization of LiMnPO4 Cathode Material via Dittmarite-Type NH4MnPO4 · H2O as an Intermediate Compound. *Arab J Sci Eng* **44**, 123–129 (2019).

236. Katcho, N. A. *et al.* An investigation of the structural properties of Li and Na fast ion conductors using high-throughput bond-valence calculations and machine learning. *J Appl Cryst* **52**, 148–157 (2019).

237. Adams, S. From bond valence maps to energy landscapes for mobile ions in ion-conducting solids. *Solid State Ionics* **177**, 1625–1630 (2006).

238. Liu, J., Yin, L., Yang, X.-Q. & Khalifah, P. G. Li3VP3O9N as a Multielectron Redox Cathode for Li-Ion Battery. *Chem. Mater.* **30**, 4609–4616 (2018).

239. Zhao, P., Feng, K., Wang, Y. & Gao, J. Syntheses, structure and properties of a new Fillowite-type compound Na0.48Mn1.22PO4. *Journal of Alloys and Compounds* **734**, 229–234 (2018).

240. Ong, S. P. *et al.* Voltage, stability and diffusion barrier differences between sodium-ion and lithium-ion intercalation materials. *Energy Environ. Sci.* **4**, 3680–3688 (2011).

241. Tsuyoshi Nakajima, H. G. *Fluorinated Materials for Energy Conversion*. (Elsevier, 1995).

242. de Dompablo, M. E. A. y, Amador, U. & Tarascon, J.-M. A computational investigation on fluorinated-polyanionic compounds as positive electrode for lithium batteries. *Journal of Power Sources* **174**, 1251–1257 (2007).

243. Barpanda, P., Lander, L., Nishimura, S. & Yamada, A. Polyanionic Insertion Materials for Sodium-Ion Batteries. *Advanced Energy Materials* **8**, 1703055 (2018).

244. Nanjundaswamy, K. S. *et al.* Synthesis, redox potential evaluation and electrochemical characteristics of NASICON-related-3D framework compounds. *Solid State Ionics* **92**, 1–10 (1996).

245. Arroyo-de Dompablo, M. E., Rozier, P., Morcrette, M. & Tarascon, J.-M. Electrochemical Data Transferability within Li $_y$ VOXO $_4$ (X = Si, Ge $_{0.5}$ Si $_{0.5}$, Ge, Si $_{0.5}$ As $_{0.5}$, Si $_{0.5}$ P $_{0.5}$, As, P) Polyoxyanionic Compounds. *Chem. Mater.* **19**, 2411–2422 (2007).

246. Kitajou, A. *et al.* Novel synthesis and electrochemical properties of perovskite-type NaFeF3 for a sodium-ion battery. *Journal of Power Sources* **198**, 389–392 (2012).

247. Kitajou, A. *et al.* Cathode Properties of Perovskite-type NaMF3 (M= Fe, Mn, and Co) Prepared by Mechanical Ball Milling for Sodium-ion Battery. *Electrochimica Acta* **245**, 424–429 (2017).

248. Steward, E. G. & Rooksby, H. P. Transitions in crystal structure of cryolite and related fluorides. *Acta Cryst* **6**, 49–52 (1953).

249. Basa, A., Gonzalo, E., Kuhn, A. & García-Alvarado, F. Reaching the full capacity of the electrode material Li3FeF6 by decreasing the particle size to nanoscale. *Journal of Power Sources* **197**, 260–266 (2012).

250. Basa, A., Gonzalo, E., Kuhn, A. & García-Alvarado, F. Facile synthesis of β-Li3VF6: A new electrochemically active lithium insertion material. *Journal of Power Sources* **207**, 160–165 (2012).

251. Gonzalo, E., Kuhn, A. & García-Alvarado, F. On the room temperature synthesis of monoclinic Li3FeF6: A new cathode material for rechargeable lithium batteries. *Journal of Power Sources* **195**, 4990–4996 (2010).

252. Euchner, H., Clemens, O. & Reddy, M. A. Unlocking the potential of weberite-type metal fluorides in electrochemical energy storage. *npj Comput Mater* **5**, 31 (2019).

253. *Li, Wai-Kee, et al. Advanced structural inorganic chemistry. Vol. 10. Oxford University Press, 2008.*

254. Geller, S., Williams, H. J., Sherwood, R. C. & Espinosa, G. P. Substitutions of divalent manganese, iron and nickel in yttrium iron garnet. *Journal of Physics and Chemistry of Solids* **23**, 1525–1540 (1962).

255. Geller, S. Crystal chemistry of the garnets. (1967).

256. Pawlak, D. A., Woźniak, K. & Frukacz, Z. Correlation between structural parameters of garnet and garnet-like structures. *Acta Crystallogr B Struct Sci* **55**, 736–744 (1999).

257. Xu, Y.-N., Ching, W. Y. & Brickeen, B. K. Electronic structure and bonding in garnet crystals Gd3Sc2Ga3O12, Gd3Sc2Al3O12, and Gd3Ga3O12 compared to Y3Al3O12. *Phys. Rev. B* **61**, 1817–1824 (2000).

258. Awaka, J. *et al.* Crystal Structure of Fast Lithium-ion-conducting Cubic Li ₇ La ₃ Zr ₂ O ₁₂. *Chem. Lett.* **40**, 60–62 (2011).

259. Xie, H., Park, K.-S., Song, J. & Goodenough, J. B. Reversible lithium insertion in the garnet framework of Li3Nd3W2O12. *Electrochemistry Communications* **19**, 135–137 (2012).

260. Geiger, C. A. *et al.* Crystal Chemistry and Stability of "Li 7 La 3Zr2O12" Garnet: A Fast Lithium-Ion Conductor. *Inorg. Chem.* **50**, 1089–1097 (2011).

261. Murugan, R., Weppner, W., Schmid-Beurmann, P. & Thangadurai, V. Structure and lithium ion conductivity of garnet-like Li5La3Sb2O12 and Li6SrLa2Sb2O12. *Materials Research Bulletin* **43**, 2579–2591 (2008).

262. Buschmann, H. *et al.* Structure and dynamics of the fast lithium ion conductor "Li7La3Zr2O12". *Phys. Chem. Chem. Phys.* **13**, 19378 (2011).

263. Ramakumar, S., Deviannapoorani, C., Dhivya, L., Shankar, L. S. & Murugan, R. Lithium garnets: Synthesis, structure, Li + conductivity, Li + dynamics and applications. *Progress in Materials Science* **88**, 325–411 (2017).

264. de Pape, J. P. Les grenats floures des elements de transition Na3Li3M2F12 (M=Ti,V,Cr,Fe ou Co). *C.R.Acad.Sc.Paris* 1244–1246 (1967).

265. de Pape, J. P. R. de. Sur quelques noveaux grenats fluores. **269**, 1120–1121 (1969).

266. Menzer, G. 17. Die Kristallstrnktur von Kryolithionit. *Zeitschrift für Kristallographie - Crystalline Materials* **75**, 265–287 (1930).

267. Geller, S. Refinement of the crystal struture of Cryolithionite, Na3[AI2](Li3)F12. **50**, 6 (1971).

268. Grzechnik, A., Krüger, H., Kahlenberg, V. & Friese, K. Thermal expansion of Li ₃ Na ₃ In ₂ F ₁₂ garnet. *J. Phys.: Condens. Matter* **18**, 8925–8934 (2006).

269. Massa, W. & Babel, D. Crystal structure and bonding in transition-metal fluoro compounds. *Chem. Rev.* **88**, 275–296 (1988).

270. S. Naka, Y. T. Synthesis of Fluoride Garnets Na3M2Li3F12 (M=Al,Cr, and Fe) from aqueous solution and their properties. *Journal of Solid State Chemistry* **20**, 261–265 (1977).

271. Katcho, N. A. *et al.* An investigation of the structural properties of Li and Na fast ion conductors using high-throughput bond-valence calculations and machine learning. *J Appl Crystallogr* **52**, 148–157 (2019).

272. Yoshiko Suwa, S. N. Synthesis of the fluoride garnets Na3M2Li3F12 (M=Al,Cr,Fe). *Chemistry Letters* 653–654 (1975).

273. Langley, R. H. & Sturgeon, G. D. Synthesis of transition-metal fluoride garnets. *Journal of Fluorine Chemistry* **14**, 1–6 (1979).

274. Cablewski, T., Faux, A. F. & Strauss, C. R. Development and Application of a Continuous Microwave Reactor for Organic Synthesis. *J. Org. Chem.* **59**, 3408–3412 (1994).

275. Rao, K. J., Vaidhyanathan, B., Ganguli, M. & Ramakrishnan, P. A. Synthesis of Inorganic Solids Using Microwaves. *Chem. Mater.* **11**, 882–895 (1999).

276. Cresswell, S. L. & Haswell, S. J. Microwave Ovens—Out of the Kitchen. *J. Chem. Educ.* **78**, 900 (2001).

277. Lemoine, K. Nouveaux matériaux fluorés d'électrodes positives à cations 3d mixtes pour batteries à ions lithium. (2019).

278. Goldstein, J. I. *et al. Scanning Electron Microscopy and X-ray Microanalysis*. (Springer US, 2003). doi:10.1007/978-1-4615-0215-9.

279. Vandi, L.-J. *et al.* Fluorine Mobility During SEM-EDX Analysis: A Challenge for Characterizing Epoxy/Fluoropolymer Interfaces. *J. Phys. Chem. C* **117**, 16933–16941 (2013).

280. Azua Jamari, N. L., Behrens, A., Raab, A., Krupp, E. M. & Feldmann, J. Plasma processes to detect fluorine with ICPMS/MS as $[M–F]^+$: an argument for building a negative mode ICPMS/MS. *J. Anal. At. Spectrom.* **33**, 1304–1309 (2018).

281. Burbano, M. *et al.* Anionic Ordering and Thermal Properties of $FeF_3 \cdot 3H_2O$. *Inorg. Chem.* **54**, 9619–9625 (2015).

282. Lemoine, K. *et al.* Synthesis by Thermal Decomposition of Two Iron Hydroxyfluorides: Structural Effects of Li Insertion. *Chem. Mater.* **31**, 4246–4257 (2019).

283. Krasnikov, S. A. *et al.* Electronic structure of FeF_2 and FeF_3 studied by x-ray absorption and fluorescence spectroscopy. *Phys. Scr.* **T115**, 1074–1076 (2005).

284. Vinogradov, A. S. *et al.* High resolution F1s absorption spectra of solid fluorides of 3d elements. *Opt. Spectrosc.* **93**, 862–869 (2002).

285. Nakai, S. *et al.* F–K XANES Studies of Alkali Fluorides. *J. Phys. Soc. Jpn.* **55**, 2436–2442 (1986).

286. Qiao, R., Chin, T., Harris, S. J., Yan, S. & Yang, W. Spectroscopic fingerprints of valence and spin states in manganese oxides and fluorides. *Current Applied Physics* **13**, 544–548 (2013).

287. Solomon, E. I., Hedman, B., Hodgson, K. O., Dey, A. & Szilagyi, R. K. Ligand K-edge X-ray absorption spectroscopy: covalency of ligand–metal bonds. *Coordination Chemistry Reviews* **249**, 97–129 (2005).

288. Neuville, D. R., Cormier, L., Flank, A.-M., Prado, R. J. & Lagarde, P. Na K-edge XANES spectra of minerals and glasses. *ejm* **16**, 809–816 (2004).

289. Krahl, T., Marroquin Winkelmann, F., Martin, A., Pinna, N. & Kemnitz, E. Novel Synthesis of Anhydrous and Hydroxylated CuF_2 Nanoparticles and Their Potential for Lithium Ion Batteries. *Chem. Eur. J.* **24**, 7177–7187 (2018).

290. Luo, J.-Y., Li, X.-L. & Xia, Y.-Y. Synthesis of highly crystalline spinel LiMn2O4 by a soft chemical route and its electrochemical performance. *Electrochimica Acta* **52**, 4525–4531 (2007).

291. Jiang, Y. *et al.* Chemical lithiation route to size-controllable LiFePO4/C nanocomposite. *J Appl Electrochem* **43**, 611–617 (2013).

292.   Zhong, W. *et al.* New Prelithiated V2O5 Superstructure for Lithium-Ion Batteries with Long Cycle Life and High Power. *ACS Energy Lett.* **5**, 31–38 (2020).

293.   Popov, D. Yu., Antokhina, T. F., Gerasimenko, A. V., Kaidalova, T. A. & Sergienko, V. I. Crystal Structure of Na $_3$ Li(TiF $_6$) $_2$. *Russian Journal of Coordination Chemistry* **30**, 27–29 (2004).

294.   De Groot, F. M. F. *et al.* Oxygen 1s X-ray-absorption edges of transition-metal oxides. *Physical Review B* **40**, 5715–5723 (1989).

295.   Lee, W. *et al.* Advances in the Cathode Materials for Lithium Rechargeable Batteries. *Angew. Chem. Int. Ed.* **59**, 2578–2605 (2020).

296.   Liu, C., Neale, Z. G. & Cao, G. Understanding electrochemical potentials of cathode materials in rechargeable batteries. *Materials Today* **19**, 109–123 (2016).

297.   Amatucci, G. G., Badway, F., DuPasquier, A., Cosandey, F. & Plitz, I. Next Generation Positive Electrode Materials Enabled by Nanocomposites: Metal Fluorides. 10.

298.   Badway, F., Pereira, N., Cosandey, F. & Amatucci, G. G. Carbon-Metal Fluoride Nanocomposites. *Journal of The Electrochemical Society* 10.

299.   Conte, D. E. & Pinna, N. A review on the application of iron(III) fluorides as positive electrodes for secondary cells. *Mater Renew Sustain Energy* **3**, 37 (2014).

300.   Wang, F. *et al.* Conversion Reaction Mechanisms in Lithium Ion Batteries: Study of the Binary Metal Fluoride Electrodes. *J. Am. Chem. Soc.* **133**, 18828–18836 (2011).

301.   Bauman, H. F. Lithium-anode limited cycle battery investigation. 95 (1965).

302.   Bauman H. Limited-cycle secondary battery using lithium anode. 43 (1964).

303.   Tarascon, J.-M. *et al.* New concepts for the search of better electrode materials for rechargeable lithium batteries. *Comptes Rendus Chimie* **8**, 9–15 (2005).

304.   Grugeon, S., Laruelle, S., Dupont, L. & Tarascon, J.-M. An update on the reactivity of nanoparticles Co-based compounds towards Li. *Solid State Sciences* **5**, 895–904 (2003).

305.   Thackeray, M. M. & Coetzer, J. A preliminary investigation of the electrochemical performance of α-Fe2O3 and Fe3O4 cathodes in high-temperature cells. *Materials Research Bulletin* **16**, 591–597 (1981).

306.   Ikeda, H. & Narukawa, S. Behaviour of various cathode materials for non-aqueous lithium cells. *Journal of Power Sources* **9**, 329–334 (1983).

307.   Novák, P. CuO cathode in lithium cells—II. Reduction mechanism of CuO. *Electrochimica Acta* **30**, 1687–1692 (1985).

308.   Butala, M. M. *et al.* MnO Conversion in Li-Ion Batteries: In Situ Studies and the Role of Mesostructuring. *ACS Appl. Mater. Interfaces* **8**, 6496–6503 (2016).

309.   Thackeray, M., Baker, S., Adendorff, K. & Goodenough, J. Lithium insertion into Co3O4: A preliminary investigation. *Solid State Ionics* **17**, 175–181 (1985).

310.   Arai, H., Okada, S., Sakurai, Y. & Yamaki, J. Cathode performance and voltage estimation of metal trihalides. *Journal of Power Sources* **68**, 716–719 (1997).

311.   Bao, T., Zhong, H., Zheng, H., Zhan, H. & Zhou, Y. One-pot synthesis of FeF3/graphene composite for sodium secondary batteries. *Materials Letters* **158**, 21–24 (2015).

312. Kim, T. *et al.* A cathode material for lithium-ion batteries based on graphitized carbon-wrapped FeF$_3$ nanoparticles prepared by facile polymerization. *J. Mater. Chem. A* **4**, 14857–14864 (2016).

313. Liu, M. *et al.* Unveiling the Role and Mechanism of Nb Doping and In Situ Carbon Coating on Improving Lithium-Ion Storage Characteristics of Rod-Like Morphology FeF$_3$·0.33H$_2$O. *Small* **18**, 2105193 (2022).

314. Zhang, L. *et al.* FeF$_3$·0.33H$_2$O@carbon nanosheets with honeycomb architectures for high-capacity lithium-ion cathode storage by enhanced pseudocapacitance. *J. Mater. Chem. A* **9**, 16370–16383 (2021).

315. Doe, R. E., Persson, K. A., Meng, Y. S. & Ceder, G. First-Principles Investigation of the Li−Fe−F Phase Diagram and Equilibrium and Nonequilibrium Conversion Reactions of Iron Fluorides with Lithium. *Chem. Mater.* **20**, 5274–5283 (2008).

316. Nishijima, M. *et al.* Cathode properties of metal trifluorides in Li and Na secondary batteries. *Journal of Power Sources* **190**, 558–562 (2009).

317. Li, C. *et al.* An FeF3·0.5H2O Polytype: A Microporous Framework Compound with Intersecting Tunnels for Li and Na Batteries. *J. Am. Chem. Soc.* **135**, 11425–11428 (2013).

318. Leblanc, M., Ferey, G., Chevallier, P., Pape, R. D. & Calage, Y. Hexagonal Tungsten Bronze-Type Ferll Fluoride: (H20)0.33FeF3; Crystal Structure, Magnetic Properties, Dehydration to a New Form of Iron Trifluoride. 6.

319. Murata, Y. *et al.* A fundamental study on carbon composites of FeF3·0.33H2O as open-framework cathode materials for calcium-ion batteries. in 020005 (2017). doi:10.1063/1.4974787.

320. Li, C., Gu, L., Tsukimoto, S., van Aken, P. A. & Maier, J. Low-Temperature Ionic-Liquid-Based Synthesis of Nanostructured Iron-Based Fluoride Cathodes for Lithium Batteries. *Adv. Mater.* **22**, 3650–3654 (2010).

321. Liu, L. *et al.* A comparison among FeF3·3H2O, FeF3·0.33H2O and FeF3 cathode materials for lithium ion batteries: Structural, electrochemical, and mechanism studies. *Journal of Power Sources* **238**, 501–515 (2013).

322. Bai, Y. *et al.* 3D Hierarchical nano-flake/micro-flower iron fluoride with hydration water induced tunnels for secondary lithium battery cathodes. *Nano Energy* **32**, 10–18 (2017).

323. Chu, Q. *et al.* Reduced graphene oxide decorated with FeF3 nanoparticles: Facile synthesis and application as a high capacity cathode material for rechargeable lithium batteries. *Electrochimica Acta* **111**, 80–85 (2013).

324. Wei, S. *et al.* The FeF3·0.33H2O/C nanocomposite with open mesoporous structure as high-capacity cathode material for lithium/sodium ion batteries. *Journal of Alloys and Compounds* **689**, 945–951 (2016).

325. Rao, R. S., Pralong, V. & Varadaraju, U. V. Facile synthesis and lithium reversible insertion on iron hydrated trifluorides FeF3·0.5H2O. *Materials Letters* **170**, 130–134 (2016).

326.   Ali, G. *et al.* An open-framework iron fluoride and reduced graphene oxide nanocomposite as a high-capacity cathode material for Na-ion batteries. *J. Mater. Chem. A* **3**, 10258–10266 (2015).

327.   Carlo, L. D., Conte, D. E., Kemnitz, E. & Pinna, N. Microwave-assisted fluorolytic sol–gel route to iron fluoride nanoparticles for Li-Ion batteries. *Chem. Commun.* **50**, 460–462 (2014).

328.   Aleshin, E. & Roy, R. Crystal Chemistry of Pyrochlore. *J American Ceramic Society* **45**, 18–25 (1962).

329.   De Pape, R. & Ferey, G. A new form of FeF3 with the pyrochlore structure : Soft chemistry synthesis, crystal structure, thermal transitions and structural correlations with the other forms of FeF3. *Materials Research Bulletin* **21**, 971–978 (1986).

330.   Li, H., Richter, G. & Maier, J. Reversible Formation and Decomposition of LiF Clusters Using Transition Metal Fluorides as Precursors and Their Application in Rechargeable Li Batteries. *Adv. Mater.* **15**, 736–739 (2003).

331.   Lemoine, K. *et al.* Stabilization of a mixed iron vanadium based Hexagonal Tungsten Bronze hydroxyfluoride HTB-(Fe0.53V0.47)F2.67(OH)0.33 as positive electrode for lithium-ion batteries. *Dalton Trans.* 10.1039.D0DT01310B (2020) doi:10.1039/D0DT01310B.

332.   IMMM - Institut des Molécules et des Matériaux du Mans. Available at http://www.univ-lemans.fr/en/research/laboratories/immm.html.

333.   Typhaine Despres. Synthese de fluorures de fer et mise au point dúne methode pour le dosage des ions fluorures. Rapport de stage. (2019).

334.   Barthelet, K., Marrot, J., Riou, D. & Férey, G. (H2O)"VIII2F6" and Pyr-VF3:Hydrothermal Synthesis, Structure Determination, and Magnetic Characterization of New Fluorides with the Pyrochlore Type. *Journal of Solid State Chemistry* **162**, 266–269 (2001).

335.   Boultif, A. & Louër, D. Powder pattern indexing with the dichotomy method. *Journal of Applied Crystallography* **37**, 724–731 (2004).

336.   Rodríguez-Carvajal, J. Recent advances in magnetic structure determination by neutron powder diffraction. *Physica B: Condensed Matter* **192**, 55–69 (1993).

337.   https://www.ill.eu/sites/fullprof/php/programse811.html?pagina=Fourier.

338.   Bukovec, P., Bukovec, N. & Demšar, A. Thermal analysis of complex fluorides. *Journal of Thermal Analysis* **36**, 1751–1760 (1990).

339.   Trevorrow, L. E. The Vapor Pressure of Vanadium Oxytrifluoride. *J. Phys. Chem.* **62**, 362–362 (1958).

340.   Groult, H. *et al.* Nano-CoF 3 prepared by direct fluorination with F 2 gas: Application as electrode material in Li-ion battery. *Journal of Fluorine Chemistry* **196**, 117–127 (2017).

341.   Li, W., Groult, H., Borkiewicz, O. J. & Dambournet, D. Decomposition of CoF3 during battery electrode processing. *Journal of Fluorine Chemistry* **205**, 43–48 (2018).

342.   Kitajou, A. *et al.* Electrochemical properties of titanium fluoride with high rate capability for lithium-ion batteries. *Journal of Power Sources* **419**, 1–5 (2019).

343.   Senoh, H. *et al.* Degradation Mechanism of Conversion-Type Iron Trifluoride: Toward Improvement of Cycle Performance. *ACS Appl. Mater. Interfaces* **11**, 30959–30967 (2019).

344.   Demourgues, A. *et al.* About MX3 and MX2 (Mn+=Mg2+, Al3+, Ti4+, Fe3+; Xp−=F−, O2−, OH−) nanofluorides. *Journal of Fluorine Chemistry* **134**, 35–43 (2012).

345.   Zhou, M., Zhao, L., Okada, S. & Yamaki, J. Thermal characteristics of a FeF3 cathode via conversion reaction in comparison with LiFePO4. *Journal of Power Sources* **196**, 8110–8115 (2011).

346.   Myung, S.-T., Sakurada, S., Yashiro, H. & Sun, Y.-K. Iron trifluoride synthesized via evaporation method and its application to rechargeable lithium batteries. *Journal of Power Sources* **223**, 1–8 (2013).

347.   Yin, S. F., Xu, B. Q., Zhou, X. P. & Au, C. T. A mini-review on ammonia decomposition catalysts for on-site generation of hydrogen for fuel cell applications. *Applied Catalysis A: General* **277**, 1–9 (2004).

348.   Cullity, B. D. *Elements of x-ray diffraction*. (Addison-Wesley Pub. Co, 1978).

349.   https://chemistry-europe.onlinelibrary.wiley.com/doi/full/10.1002/cmtd.202100009.

350.   J. M. Hudspeth. Short-Range Order in Ferroelectric Triglycine Sulphate. (2012).

351.   Simonelli, L. *et al.* CLAESS: The hard X-ray absorption beamline of the ALBA CELLS synchrotron. *Cogent Physics* **3**, (2016).

352.   Massiot, D. *et al.* Modelling one- and two-dimensional solid-state NMR spectra: Modelling 1D and 2D solid-state NMR spectra. *Magn. Reson. Chem.* **40**, 70–76 (2002).

353.   CaRIne Crystallography Software. http://carine.crystallography.pagesperso-orange.fr/index.html.

354.   https://www.spexsampleprep.com/8000M-mixermill.

355.   https://www.mtixtl.com/index.aspx.